ISSN 0911-5730
UVSOR-28
April 2001

UVSOR

ACTIVITY REPORT

2000

Ultraviolet Synchrotron Orbital Radiation Facility
Institute for Molecular Science

CONTENTS

3. Gas-phase Spectroscopy

4. Solid State Spectroscopy 1 (IR, VUV, etc.)

5. Solid State Spectroscopy 2 (XAFS, PES)

UVSOR
ACTIVITY REPORT
2000

edited by
M. Katoh, T. Gejo, K. Takahashi, and H. Hagiwara

Preface

This Activity Report covers the research activities done at the UVSOR facility in the Institute for Molecular Science (IMS) in FY2000. This is the seventh volume in the red-covered Activity Report series for the second 10 years in UVSOR. For these years the total beam time and the total number of beamlines are almost constant, ~40 weeks/year (~2,500 hours/year) and ~20 beamlines, and the users to be accepted are restricted to almost the constant number, ~800 persons/year (with ~180 projects/year). We have to focus our scientific policy on quality rather than quantity. The reader will find a lot of reports describing new scientific insights by using good and stable equipments, progress in beamlines under development, and reconstructive designs for very old equipments. I would like to acknowledge various kinds of efforts and supports by the UVSOR users and staff, respectively.

In Japan we have three public and national facilities, Photon Factory, SPring-8, and our UVSOR. Since January 6, 2001, all of them have belonged to the same ministry, Ministry of Education, Culture, Sports, Science and Technology (MEXT). Photon Factory and UVSOR are of nearly the same age, and UVSOR is in charge of the lower energy region than soft X-rays as well as the advanced use for molecular science and chemistry. We are trying to get an additional budget for the upgrade of the light source of UVSOR to maintain and enhance our activities even for the third 10 years. We hope that we can start the upgrade project and successfully increase the number of undulator sections and reduce the emittance as soon as possible.

March, 2001

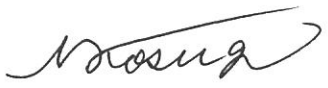

Nobuhiro Kosugi
Director of UVSOR

Current Status of Light Source and Beam Lines

Light Source in 2000

Masahiro KATOH

UVSOR Facility, Institute for Molecular Science,
Okazaki 444-8585 Japan

1. Machine Operation

In 2000, the UVSOR accelerator complex was operated for about 43 weeks (including machine tunings) as scheduled. Fortunately, there was no serious trouble during this year. Monthly statistics of the operation time is shown in Figure 1. Three weeks in this year were assigned for single bunch users operation and other two weeks were dedicated for machine studies. We had four shut down period, around the new years day (two weeks), in spring (three weeks), in summer (three weeks) and in autumn (one week).

Typical operation pattern in a week is as follows. Monday and Saturday morning (from 9 to 13 o'clock), are assigned for machine tunings and machine studies. From Tuesday to Friday, the machine is operated for users. The beam is injected twice a day, at 9 and 13 o'clock. The beam is stopped at 18 o'clock. It can be extended until 21 o'clock as requested by users. On Thursday, the beam is injected additionally at 17 o'clock and is stopped at 21 o'clock. The filling beam current is 250 mA in multi-bunch mode and 70 mA in single bunch mode. Typical beam current histories in both modes are shown in Figure 2.

During the operation periods, there were a few minor troubles, on the magnet power supplies of the booster-synchrotron and on the power source of the harmonic cavity. Both of them are repaired quickly and did not affect the users experiments.

Before the summer shut down, it was observed that the injection efficiency tended to decrease, in spite of the careful tunings. Later, this was found to be due to the troubles on the linac and the extraction kicker, as described later. After the shut down, the injection efficiency was recovered to normal level. In addition, by adjusting the RF voltage of the synchrotron, the electron capture efficiency was increased by a factor of 2. As the result, the injection rate reached 3mA/sec.

In users operations, the closed orbit distortion is corrected after every injection. The deviation from the golden orbit just after the correction is smaller than 100μm (r.m.s.) in horizontal and 50μm (r.m.s.) in vertical. However, it was observed in the beam position measurement that the orbit was drifting slowly by a few hundreds of microns over one injection interval (4 hours). After installing the new beam position monitor system, which will be described in the following section, this phenomenon can be investigated more precisely.

During the shut down in spring, about one fourth of the storage ring was vented for the reconstruction works on the SR beam-lines and the optical cavity for FEL. After the baking of the beam pipes, vacuum conditioning with stored beam

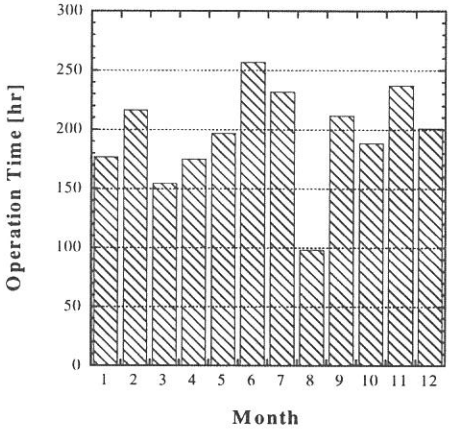

Fig. 1 Monthly statistics of the operation time in 2000.

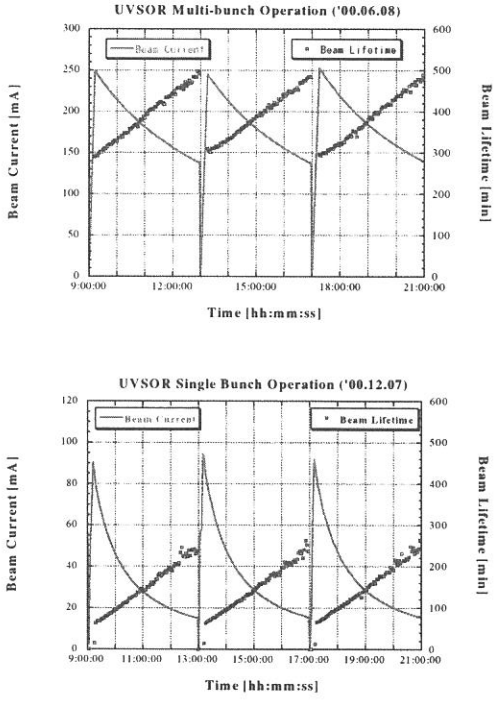

Fig. 2. Typical beam current histories in multi-bunch mode (upper) and single-bunch mode (lower).

started and continued for one week. When the users operation started, the beam lifetime reached to about 80% of that before the shut down. After a few weeks of users operation, the lifetime recovered almost completely.

The summer and autumn shut down were assigned for annual maintenance works. A few problems were found on the RF power source of the linac and on the power supply of the extraction kicker of the booster-synchrotron. Although the latter was successfully repaired during the shut down, the former was not solved completely. By temporally adjusting the operating conditions, it does not affect daily operation so seriously. It will be repaired as soon as possible after the necessary parts arrive. During the summer shut down, the circulator of the main RF cavity was replaced, that had been malfunctioned for long time.

It was decided that the super-conducting wiggler at BL7A, which has serious trouble on the refrigerator, would be removed from the ring. An in-vacuum undulator will be installed as described later.

2. Improvements

2-1. New beam position monitor system

The beam position monitor (BPM) system, which has been used for 16 years, is being replaced. Since the old system uses mechanical switches to accumulate the signals from the pick-up electrodes (totally 64), it takes about one minutes to measure an orbit. In addition, since the attenuator control of the BPM signals is not automated, the operator must adjust the attenuation level before the measurement depending on the beam current

The new system comprises 16 signal-processing modules, which are commercial products by Bergoz Co. [1]. These modules give the beam positions in horizontal and vertical as DC voltages. They are AD-converted and accumulated in a PC. A schematic drawing of the system is shown in Figure 3. It is expected to measure an orbit within 1 second, with an accuracy of a few microns. The new system will shorten the time for injection procedure. It will also shorten the time to get orbit correction data for undulators. An orbit feedback system can be constructed based on this system. Construction of the entire system will be completed until March 2001. Performance test will be started in April.

2-2. High Current Operation

The filling beam current in multi-bunch mode has been set at 250 mA for these years. In December, multi-bunch mode operation with 300 mA was tested. The beam stability, the temperature rises of the vacuum chambers and the radiation level of the experimental floor were observed and no problem was found. The beam current history and the temperature rise of the vacuum ducts are shown in Figure 4. The users operation with 300 mA will be realized in near future.

3. Research and Developments

3-1. New Lattice

A new lattice for UVSOR storage ring was designed [2, 3], which has four new short straight sections and much smaller emittance (27nm-rad). The optical functions are shown in Figure 5. All the quadrupoles and sextupoles will be replaced with combined function magnets, which have capabilities of producing both quadrupole and sextupole fields by utilizing

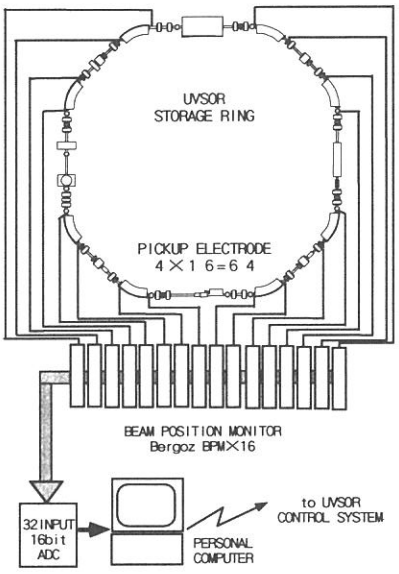

Fig. 3 Schematic drawing of new BPM system.

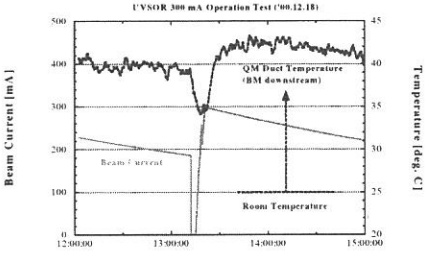

Fig. 4 Beam Current History and temperature rise of the vacuum duct at 300 mA test operation

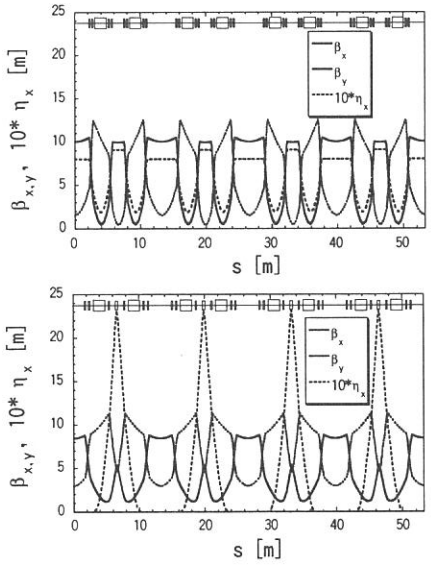

Fig.5 Present (lower) and new (upper) lattice

auxiliary windings. A prototype is under construction and will be completed in March 2001. Field measurements will be started soon after.

3-2. Development of In-vacuum undulator

In the new lattice described in the previous section, each straight section has small vertical betatron function, which enables us to install in-vacuum and small gap devices. A prototype of such a device is now under construction [4]. In this fiscal year, the magnetic arrays are being constructed (Fig. 6). The remaining parts will be constructed in next fiscal year. This undulator will be installed at the straight section between B06 and B07, after removing the super-conducting wiggler. The effects of this device on the circulating beam will be investigated as well as the property of the radiation. Main parameters of the undulator are listed in Table 1.

3-3. Free Electron Laser

Efforts to realize stable oscillation are being continued, such as improving the mechanical stability of the optical cavity and introducing a new feedback system [5]. A two-color experiment using FEL and synchrotron radiation was proposed and is being prepared. Transportation of the FEL beam to a SR beam line (BL7A) was successfully demonstrated and the synchronization between FEL and SR was confirmed [5].

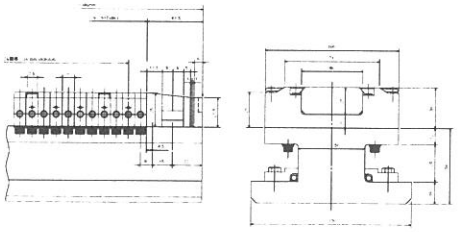

Fig. 6. Magnetic poles of in-vacuum undulator (under construction by Sumitomo Special Metals Co. Ltd.)

Table 1. Parameters of In-vacuum Undulator

Magnet type	Pure Permanent (Nd-Fe-B)
Remanent Field	1.17 Tesla
Period Length	36 mm
Number of Period	26
Magnetic Length	936 mm
Overall Length	1.4 m
Minimum Gap	10 mm for low-β optics 20 mm for present optics
Max. K-parameter	2.77 for low-β optics 1.15 for present optics
Polarization	linear (horizontal)

References

[1] http://www.bergoz.com/

[2] M. Katoh et al. in this report

[3] M. Katoh et al., Nuclear Instruments and Methods in Physics Section A (accepted)

[4] M. Katoh et al., in this report

[5] S. Koda et al., in this report

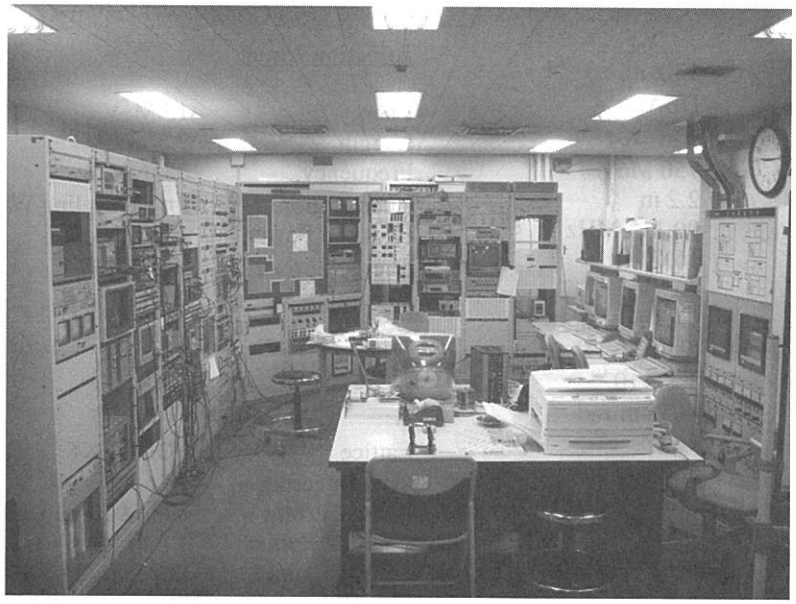

Control Room of UVSOR

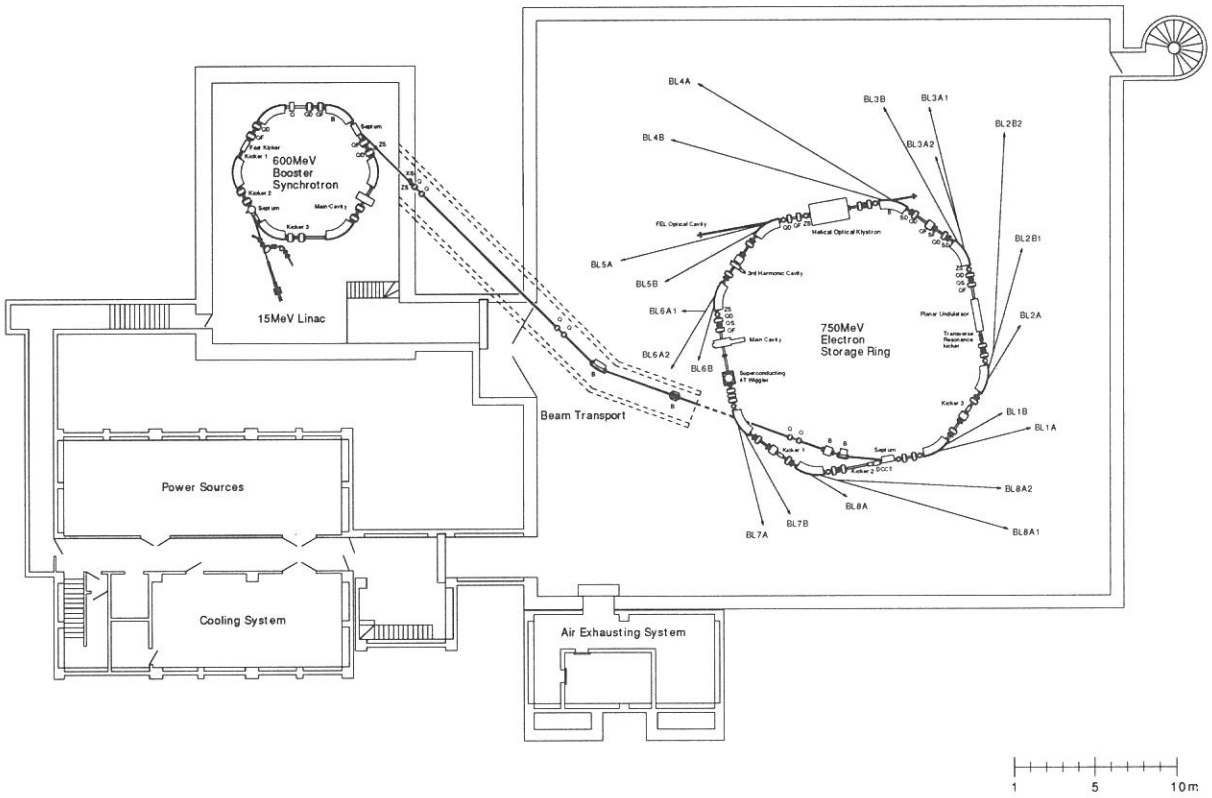

UVSOR Accelerator Complex

Parameters of UVSOR Storage Ring

Circumference	53.2 m
Lattice	DBA ×4
Straight Sections	3 m ×4
Beam Energy	750 MeV
Bending Radius	2.2 m
RF Frequency	90.115 MHz
Harmonic Number	16
RF Voltage	46 kV
Mom. Comp. Factor	0.026
Betatron Tunes	(3.16, 1.44)
Natural Energy Spread	4.2×10^{-4}
Natural Emittance	165 nm-rad
Natural Bunch Length	160 psec[#1]
Max. Beam Current	300mA (multi-bunch)[#2]
	70 mA (single bunch)

#1) About three times longer with harmonic cavity on

Parameters of UVSOR Injector

Injection Linac

Energy	15 MeV
Length	2.5 m
Frequency	2856 MHz
Acceleration	2π/3Traveling Wave
Klystron Power	1.8 MW
Energy Spread	~1.6MeV
Repetition Rate	2.6 Hz

Booster Synchrotron

Lattice	FODO ×8
Circumference	26.6 m
Beam Current	32 mA (8-bunch filled)
Bending Radius	1.8 m
Betatron Tune	(2.25, 1.25)
Mom. Comp. Fac.	0.138
Harmonic Number	8
RF Frequency	90.115 MHz
Repetition Rate	2.6 Hz

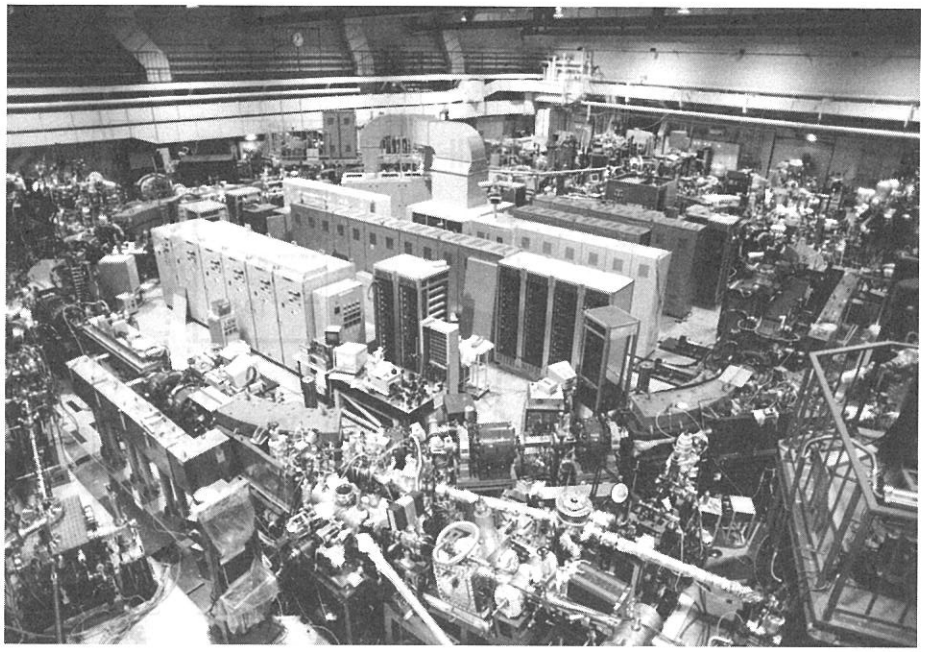

UVSOR Storage Ring

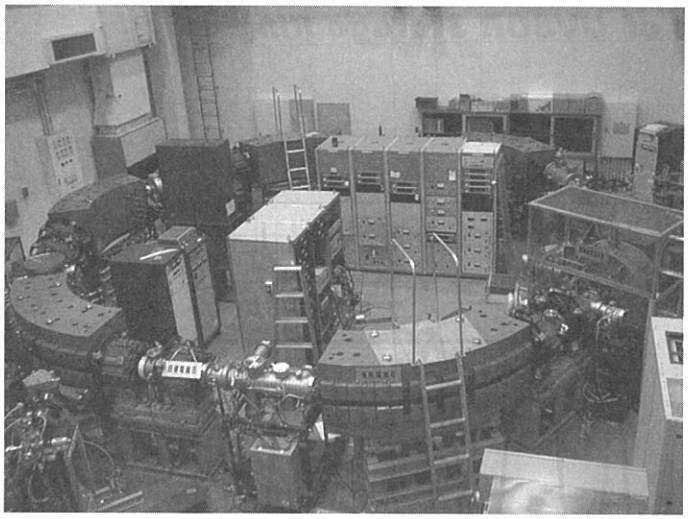

Booster Synchrotron

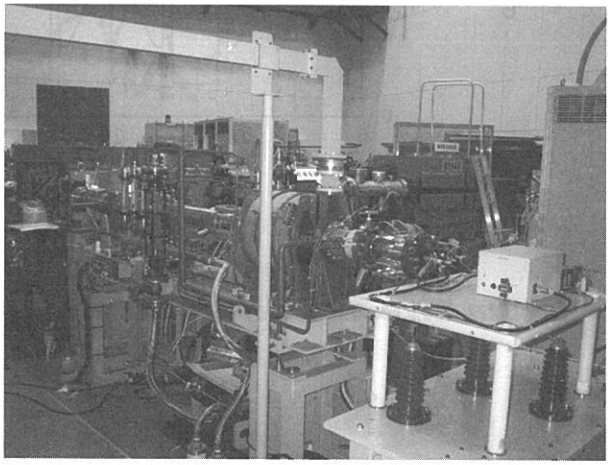

Injection Linac

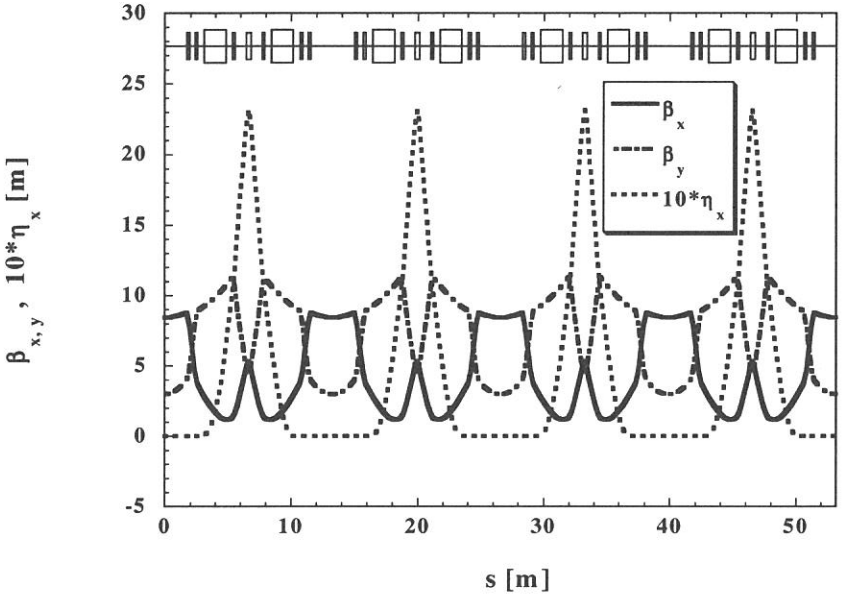

Optical Functions of UVSOR Storage Ring

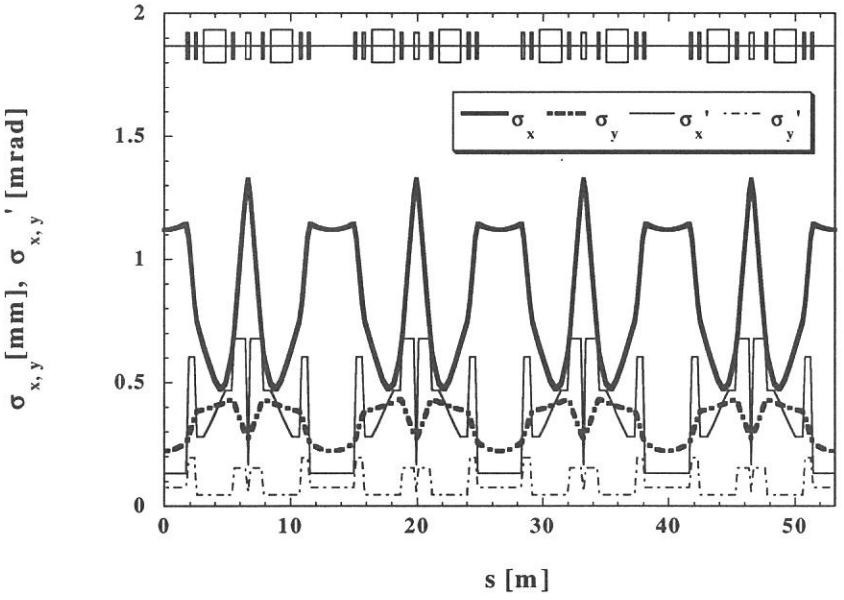

Beam Size and Divergence of UVSOR Storage Ring

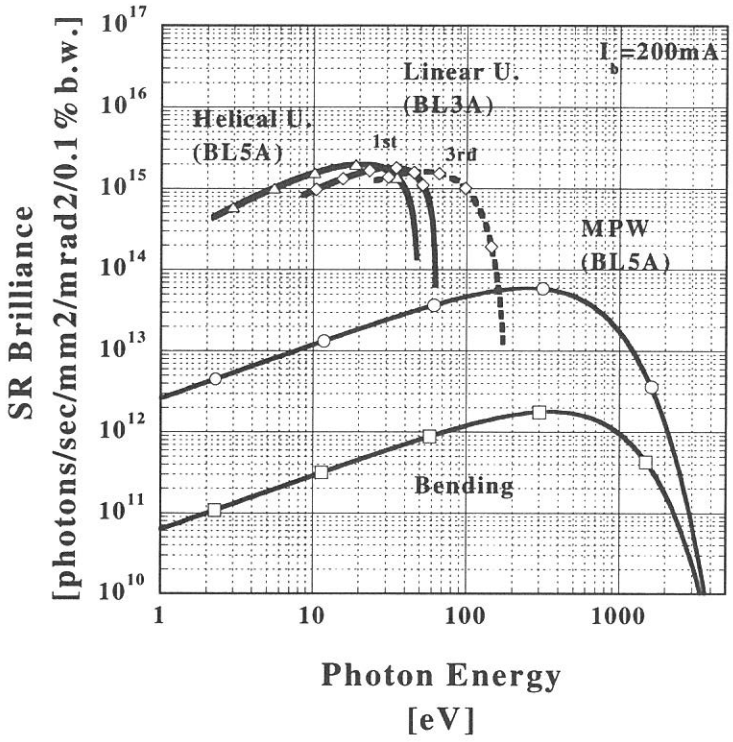

Synchrotron Radiation Spectra at UVSOR

Light Source Parameters

Bending Magnets

Bending Radius	2.2 m
Critical Photon Energy	425 eV

Linear Undulator (BL3A)

Number of periods	24
Period Length	84 mm
Total Length	2016 mm
Remanent Field	0.9 T
Magnetic gap	30 – 90 mm
Deflection parameter (K)	0.6 – 3.6

Helical Undulator/Optical Klystron (BL5A)

Number of periods	18
Period length	110 mm
Length of dispersive part	302.5 mm
Total Length	2351.2 mm
Remanent field	1.3 T
Magnetic gap	30 – 150 mm
Deflection parameter (K)	0.07 – 4.6 (helical mode)
	0.15 – 8.5 (linear mode)

Basic Parameters of UVSOR-FEL

Free Electron Laser	
Wave Length	240～570 nm
Spectral Band Width	$\sim 10^{-4}$
Polarization	Circular
Pulse Rate	11.26 MHz
Typical Average Power	～100 mW (at 520nm)
Storage Ring	
Beam Energy	600 MeV
Natural Emittance	106 nm-rad
Natural Energy Spread	3.4×10^{-4}
Natural Bunch Length	3.4 cm
Number of Bunches	2
Max. Beam Current	50 mA/bunch
RF Frequency	90.1 MHz
Optical Cavity	
Type	Fabry Perot
Cavity Length	13.3 m
Mirror	HfO_2, Ta_2O_5 multi-layer
Optical Klystron	
Polarization	Circular
Length	2.35 m
Period Length	11 cm
Number of Periods	9 + 9

BL5A Helical Undulator (Optical Klystron for FEL)

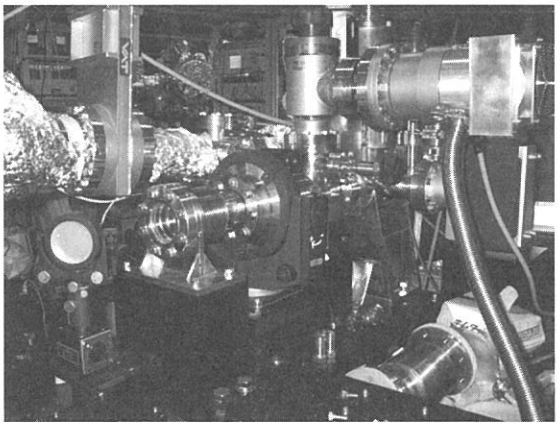

Optical Cavity for FEL at BL5A

Beam Lines in 2000

Masao KAMADA
UVSOR Facility, Institute for Molecular Science

There are 20 beam lines operational in UVSOR facility, 11 beam lines of which are opened beam lines for many users coming from outside of IMS, while the rest 9 beam lines are in-house beam lines dedicated to the research groups in IMS. The followings are the status of the beam lines in 2000.

<Open beam lines>

○BL1B

This beam line is one of the busiest beam line in UVSOR. The beam line has been used for general purposes in VUV region and has welcome many users all the time since the beam line has the following advantages. 1) It has large acceptance angles to provide high flux VUV light. 2) Standard measurements such as absorption, reflection, and luminescence can be conducted at low temperatures down to 10 K. 3) This beam line covers the wavelength ranges from 650 to 30 nm, which overlaps with those of the usual light sources in users' institute or university. 4) Since windows are available in the wavelength more than 110 nm, beginners can start their experiments by themselves without feeling any restriction. 5) The window makes it possible for us to try many materials such as liquid, high-pressure, gaseous phase, high-vapor-pressure, bio-specimens, and so on. 6) Only usual vacuum techniques are required to conduct their experiments. 7) There is no similar beam line in other facilities in Japan.

In 2000, a second-monochromator system has been upgraded but there was a bug in the software of its CCD system, resulting in the delay of the use. The computer control system of a 1-m Seya-Namioka monochromator as well as the moter drivers, which were renewed last year, work well without any serious problems. The instruments including the multi-channnel analyzer and MCP-PM have been improved for time-resolved experiments. Several interesting experiments such as two-photon excitation, photo-reflectance, photo-ionization of liquids, and so on are in progress.

○BL2B1

This beam line consists of a grasshopper monochromator, a double-pass CMA, and a coincidence analyzer. This beam line has been used mainly for surface science because useful equipments for surface science such as LEED, Auger, Ar-ion gun, and gas doser are installed at BL2B1. This beam line covers soft x-ray regions up to 800 eV and therefore it is useful for core-level spectroscopy for C, N, and O elements. Photoelectron spectroscopy and electron-ion-coincidence spectroscopy can be carried out on adsorbed surface and bulk materials. Besides these spectroscopies, NEXAFS/XAFS are also powerful techniques for molecular science.

In 2000, the electron-ion-coincidence instrument had small trouble in electronics during the installation, resulting in the loss of the beam times. The active scientists in the coincidence group worked well to fix it. There were no serious problems on the Grasshopper monochromator and photoelectron spectrometer. However, the resolving power of the monochromator is not good in comparison with similar beam lines in other facilities. This will push us to consider the future of this beam line. We expect users' collaboration and proposal for future.

We would like to express our thanks to Prof. S. Nagaoka and EICO group for their collaboration to maintain the activity of this beam line.

○BL3A1/BL3A2

These beam lines can share intense synchrotron radiation from a planar-type undulator. At BL3A1 the intense undulator radiation has been used without monochromator for SR-CVD, light-amplification, desorption, and luminescence experiments. At BL3A2, a constant-length SGM has been used with the undulator radiation for SR-laser combined experiments in gaseous phase.

On the last user's day in 20th century, the accident happened on the gaseous line, causing the leakage of BF3. Fortunately, the amout of the gas was so small that nobody had any effect from this accident. However, the facility decided to confirm the safety system to avoid future

undesirable accidents.

○BL5A

This beam line consists of a high-resolution photoelectron spectrometer and a spin and angle resolved photoelectron spectrometer. Besides SR from a dipole magnet, circularly polarized radiation from a helical undulator can be used at BL5A.

In 2000, the lens system of the spin analyzer was repaired and the vacuum system of the main sample chamber was improved. The first signal after the reinstallation was obtained in January 2001. Both of right and left circulary polarized light from the helical undulator became available in user times. The instruments for time-resolved photoelectron spectroscopy were installed. The combined experiments with SR and the powerful laser system consisting of a TiS laser, RegA, and OPA are in progress too.

○BL5B

This beam line was constructed for calibration of many optical elements and detectors in VUV and soft x-ray regions. Since there are no similar beam lines in other facilities, BL5B has been contributing to the various fields such as astro-science, nano-science, besides synchrotron science and technology.

In 2000, there were small problems on the mechanics of the goniometer, and we decided to improve it in a coming year.

○BL6A1

The BL6A1 has been used as a unique IR and FIR beam line. It consists of FT-IR and FT-FIR interferometers and covers wide wavelength range from sub-milli to near IR. Lots of research studies such as high-pressure with DAC, magnetic circular Dichroism, and time-dependence have been carried out.

In 2000, the optical arrangement of this beam line was upgraded to conduct the experiments more precisely. Also the super-conducting magnet was installed for MCD experiments by Prof. S. Kimura of Kobe University. This arrangement may avoid the loss of the beam time and the inefficient labor works for installation.

○BL7A

This beam line was constructed at the first construction stage of the UVSOR facility in mid of 1980 for soft x-ray spectroscopy. This beam line has been providing soft x-rays in the energy range from 0.6 to 3 keV without the 4T-wiggler and up to 6 keV with the wiggler. However, the mechanical problem happened on the cryogenics for the wiggler in 1998. In 1999, the 4T-wiggler was shutdown completely. We have decided to provide better SR from a dipole magnet with good crystals such as beryl, YB66, InSb, and KTP, to cover the soft x-ray region less than 3 keV.

○BL7B

The 3-m NIM at BL7B was constructed to provide good SR with a high resolving power in a wide wavelength range from near IR to VUV. Although the installation took long times, users have started taking good data at He temperature and showed the good performance of BL7B in 2000. The CCD system was also installed to have fluorescence spectra in 2000. The wall for the radiation protection was constructed in October.

We would like to express our thanks to many members in the 7B-working group, especially Profs. K. Fukui, for their efforts to construct this beam line.

○BL8A

This beam line has no monochromator and any special equipment. This means that users can install their own instruments which are brought from their institute or university. The UVSOR facility will support the users of course. For examples, a differential pump system can be provided for SR-CVD experiments. In 2000, the vacuum condition of the pre-mirror chamber and the differential pump system were improved.

○BL8B1

This beam line can provide soft x-rays with a high resolving power and cover the energy

range of K-shell excitation in light elements. The TOF-mass instrument makes it possible to take ionization spectra of various molecules. Yield experiments on solid-state phase are also available. In 2000, the alignment of the CL-SGM monochromator was improved to provide good linear polarization, which was monitored by a multi-layer polarizer with a help from Prof. M. Watanabe of Tohoku University.

<In-house beam lines>

○BL1A

This beam line was constructed for solid-state experiments in soft x-ray region. High performance photoelectron analyzer produces good data in recent years.

○BL2A

This beam line was constructed for experiments in gaseous phase and have produced a lots of scientific results. This beam line was rearranged for bio-science with bio-scientists in Okazaki institutes. We are expecting many active bio-scientists come to use UVSOR soon.

○BL2B2

The construction of a dragon-type new monochromator has commissioned in 1999. The scientific instruments for gaseous experiments have been installed or tested to conduct future experiments in 2000.

○BL3B

This beam line consists of a 3-m NIM and a two-dimensional photoelectron analyzer. This has been used for experiments in gaseous phase, providing interest results. However, the optical elements become worse in recent years, and the gratings will be replaced in coming Spring to achieve higher performance.

○BL4A/4B and BL6B

The re-arrangement of the beam lines at BL4A , 4B, and 6B has started in 2000. The SR-CVD instruments installed at 4B were moved to BL4A, and the SR-STM system at BL4B was installed to BL6B. The old IR station at BL6B was completely removed. A new soft x-ray beam line with a VLS monochromator was constructed at BL4B. The first high-resolution spectra were obtained in January 2001. A party will be arranged in February.

○BL6A2

The post-mirror system was completely changed to get a small spot for the micro-ESCA system. The achievement of the performance was successfully tested. The femto-second laser system was also installed to conduct the combination experiments of SR and lasers.

○BL8B2

The high-performance multi-channel photoelectron spectrometer was installed to measure the precise angle distributions of photoelectrons from well-organized molecules. The performance are under investigation.

Therefore, the UVSOR facility has twenty stations operational; two soft-x-ray stations equipped with a double-crystal monochromator, ten extreme-ultraviolet stations with a glancing incidence or a plane-grating monochromator, four vacuum-ultraviolet stations with a Seya-Namioka-type or a normal incidence-type monochromator, one (far) infrared station equipped with a FT interferometer, a multi-layer monochromator, and two white-light stations without any monochromator. In 2000, many interesting results were obtained at these UVSOR beam lines and they are presented in this activity report.

The UVSOR facility strongly asks all users to conduct their experimental procedures according to the beam line manuals and the guidebook. The persons who want to use the open and the in-house beam lines are recommended to contact with the following station master or supervisor and the representative, respectively. The persons who want to know updated information of the UVSOR facility are recommended to open http://www.uvsor.ims.ac.jp/.

Table I. Station masters and supervisors of open beam lines in 2000

Beam Line	Station Master	Sub Master	Supervisor
1B	M. Hasumoto	M. Kamada	M. Kamada
2B1	S. Nagaoka	E. Nakamura, K. Takahashi	M. Kamada
3A1	M. Kamada	E. Nakamura	M. Kamada
3A2	N. Kondo	T. Gejo	E. Shigemasa
5A	K. Takahashi	M. Hasumoto	M. Kamada
5B	M. Hasumoto	E. Nakamura	E. Shigemasa
6A1	E. Nakamura	O. Matsudo	M. Kamada
7A	E. Shigemasa	N. Kondo, O. Matsudo	E. Shigemasa
7B	K. Fukui	M. Hasumoto	M. Kamada
8A	T. Gejo	E. Nakamura	E. Shigemasa
8B1	T. Gejo	N. Kondo	E. Shigemasa

Table II. Representatives of in-house beam lines in 2000.

Beam Line	Representative	Department/Facility
1A	N. Kosugi	VUV Photo Science
2A	N. Kosugi	VUV Photo Science
2B2	K. Mitsuke	VUV Photo Science
3B	K. Mitsuke	VUV Photo Science
4A	T. Urisu	VUV Photo Science
4B	E. Shigemasa	UVSOR
6A2	M. Kamada	UVSOR
6B	T. Urisu	VUV Photo Science
8B2	T. Urisu	VUV Photo Science

Beamlines of UVSOR

Beam line	Monochromator, Spectrometer	Wavelength Region	Acceptance Angle (mrad) Horiz.	Vert.	Experiment
BL1A	Double Crystal	2.1 - 0.3 nm	4	1	Solid (photoemission)
BL1B	1m Seya-Namioka	650 - 30 nm	60	6	Solid (absorption)
BL2A	1m Seya-Namioka	400 - 30 nm	40	6	Bio-science (irradiation)
BL2B1	2m Grasshopper	60 - 1.5 nm	10	1.7	Solid & Surface (photoemission, absorption)
BL2B2	18m Spherical Grating	60 - 6 nm	15	6	Gas (photoionization, photodissociation)
BL3A1	None (Filter, Mirror)	(U)	0.3	0.3	Solid & Irradiation (photodissociation)
BL3A2	2.2m Constant Deviation Grazing Incidence	100 - 10 nm (U)	10 0.3	4 0.3	Gas & Solid (photoionization & photodissociation)
BL3B	3m Normal Incidence	400 - 30 nm	20	6	Gas (photoemission)
BL4A1	Multi-Layered-Mirror Monochromator	23 - 13 nm Mo/Si MLMs	16.6	12.8	Irradiation
BL4A2	None				SR-CVD
BL4B	3m Varied-line Plane Grating Monochromator	2 - 10 nm	8.3	6	Gas (absorption)
BL5A	None SGM-TRAIN	(OK) 250 - 5 nm	 10	 3	Free Electron Laser Solid (photoemission)
BL5B	Plane Grating	200 - 2nm	10	2.2	Calibration, Gas & Solid (photodissiociation & absorption)
BL6A1	Martin-Puplett FT-IR Michelson FT-IR	3000 - 30 mm 100 - 1 mm	80 80	60 60	Solid (absorption)
BL6A2	Plane Grating	650 - 8 nm	10	6	Solid (photoemission)
BL6B	None		8.3	6	Irradiation
BL7A	Doble-crystal	1.5 - 0.8 nm	2	0.3	Solid (absorption)
BL7B	3m Normal Incidence	1000 - 50 nm	65	10	Solid (absorption)
BL8A	None (Filter)		25	8	Irradiation & User's Instruments
BL8B1	15m Constant Deviation Grazing Incidence	40 - 2 nm	10	1.5	Gas & Solid (absorpton)
BL8B2	Plane Grating	650 - 8 nm	10	6	Solid (photoemission)

SGM-TRAIN : Spherical Grating Monochromator with Translating and Rotating Assembly Including Normal-incidence-mount

U : with an undulator, OK : with an optical klystron

BL1A

Soft X-Ray Beamline for Photoelectron-Photoabsorption Spectroscopy

BL1A is a soft x-ray beamline for photoelectron-photoabsorption spectroscopy. The beamline is equipped with a focusing premirror and a double crystal monochromator [1]. The monochromator serves soft x-rays in the energy range from 585 to 4000 eV by using several kind of crystals such as β-Al_2O_3, beryl, KTP ($KTiOPO_4$), quartz, InSb and Si crystals. The throughput spectra are shown in Fig. 1. Typical energy resolution (E/ΔE) of the monochromator is about 1500 for beryl and IbSb.

For photoelectron-photoabsorption spectroscopy, an ultra-high-vacuum (UHV) apparatus is connected. The top view of the apparatus is shown in Fig. 2. It is equipped with a high-performance electron energy analyzer (SES-200, SCIENTA Co.). The pass energy can be varied between 1 and 500 eV. Using the apparatus, resonant photoelectron spectra for solid samples can be obtained with the total energy resolution of 0.7eV around hν=1000 eV.

Reference

[1] A. Hiraya et al., Rev. Sci. Instrum., **63** (1992) 1264.

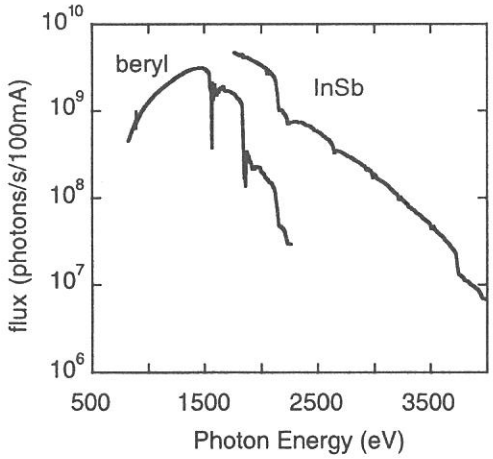

Figure 1. Throughput spectra of the double crystal monochromoator at BL1A.

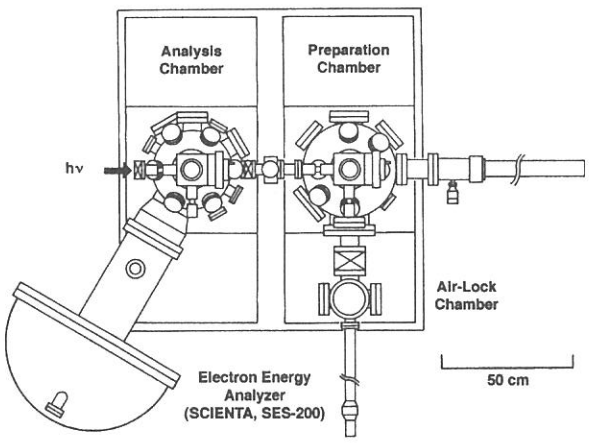

Figure 2. Top view of the UHV apparatus for photoelectron-photoabsorption spectroscopy.

Specification

Monochromator	: double crystal monochromator
Monochromator crystals (2d value, energy range)	: β-Al_2O_3 (22.53Å, 585-1609eV), beryl (15.965Å, 826-2271eV), KTP (10.95Å, 1205-3310eV), quartz (8.512Å, 1550-4000eV), InSb (7.481Å, 1764-4000eV), Si (6.271Å, 2104-4000eV)
Resolution	: E/ΔE=1500 for beryl and InSb
Experiment	: photoelectron-photoabsorption spectroscopy for solid

BL1B

Seya-Namioka Monochromator for General Purpose in VUV Region

The beam line 1B has been used for many experiments such as absorption, reflectivity, photo-ionization, and luminescence in condensed phase. The system consists of a pre-mirror, a 1-m Seya-Namioka type monochromator, and a post-mirror. Three gratings with 600, 1200, and 2400 gr/mm can cover the wavelength range from 40 nm to 650 nm, and two post mirror make it possible to change the focus point. A long-focus mirror is usually used with a LiF window to separate a main chamber for spectroscopy in liquids and biospecimens, while a short-focus mirror is suited to solid-state spectroscopy. The output flux from this monochromator is about 10^{10} phs/s around 200 nm with 0.1 mm slits. The spectral distributions obtained with three gratings are shown in the figure, although they are not the best data because of the contamination of the mirrors and gratings due to the recent careless accident.

A second monochromator (Spex 270M) and a LN-cooled CCD detector (Princeton Inc.) are available for luminescence experiments, together with a liquid helium-flow type cryostat. A time-resolved system to observe luminescence and excitation spectra with three time-gates is also possible. The decay measurement is one of the highlights of this station. A couple of weeks are supplied for the decay measurements under single bunch operation. A TAC system is therefore one of the standard instruments at this beam line.

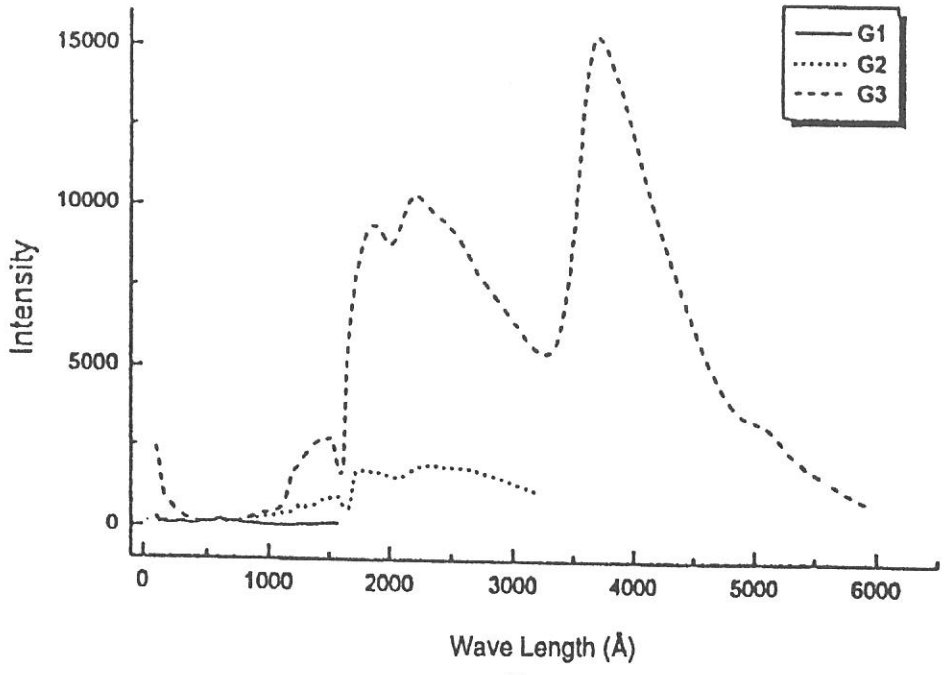

BL2A

Gas Phase Photoabsorption and Fluorescence Spectroscopy

Photoabsorption cross section and fluorescence excitation spectra of gaseous sample are simultaneously measured in a vacuum cell or effusive jet condition. The primary photons in the 30-400 nm region are dispersed by a 1-m Seya monochromator. Higher order light in the 80-120 nm range is suppressed by using a long channel with a cross section 2.5 × 5.0 × 170 mm long filled with argon gas at a pressure ≅0.3 Torr as shown in fig. 1. No filter is used between 30 and 80 nm since the photon flux at $\lambda<40$ nm is very weak (see fig. 1). The gas filter and cell are placed in a main chamber which is evacuated by a 5000 *l*/s diffusion pump (Varian, Model VHS10). A LiF window is used for the measurement at the $105<\lambda<210$ nm range as usual. Thus, the total photo-absorption cross section and fluorescence excitation spectra are available in the wide wavelength region 30-210 nm without or with little contamination by the higher order light.

Dispersed fluorescence and polarity of emission from the excited fragment are also measurable in addition to the total photoabsorption and emission cross sections. In the single bunch operation of synchrotron radiation with the period of 178 ns, a radiative life time can be measured.

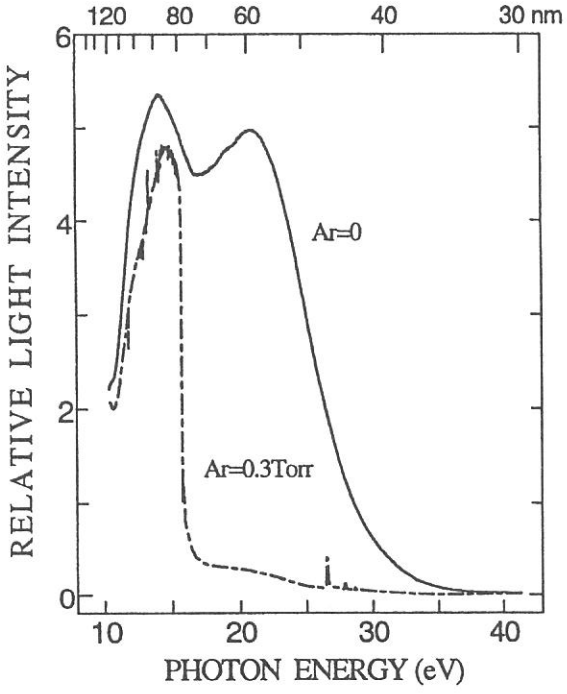

Fig. 1. Transmitted I_0 intensity with and without an Ar gas filter.

Specification

Monochromator :	1-m Seya
Wavelength range :	30-400 nm
Resolution :	$\Delta E/E \cong 10^{-3}$ at 100 nm
Grating :	1200 *l*/mm blazed at 96 nm
Experiments :	
	•Vacuum cell or effusive jet
	•Total photoabsorption cross section
	•Fluorescence cross section
	•Dispersed fluorescence
	•Radiative lifetime
	•Emission polarity

BL2B1

Soft X-ray Beamline for Solids and Surfaces

BL2B1 has been used for soft X-ray absorption and photoelectron spectroscopies of solids and surfaces. A 2-meter grazing incidence monochromator ('Grasshopper' type, Mark XV; Baker Manufacturing Co.) is installed. The monochromator serves soft X-rays in the energy range from 95 to 1000 eV using a 1800 l/mm grating. The resolving power is better than 600 at C K-edge (about 290 eV). Figure 1 shows the total photoelectron yield from a Au mesh of 90%-transmission located between the refocusing mirror and the sample. The dips around 290 and 550 eV originate from the carbon and oxygen contamination of optical elements, respectively.

The analyzing chamber is located at the focusing point of the monochromized light. A double-pass cylindrical mirror analyzer (CMA), a LEED optics of reverse type, a quadrupole mass spectrometer, and an ion-gun for sputtering are installed in the analyzing chamber. A pulsed leak-valve and a variable leak-valve are also installed in order to introduce various kinds of gases. The samples can be cooled with a liquid helium cryostat. The base pressure of the analyzing chamber is better than 1×10^{-10} Torr. The photoelectron spectroscopy including constant initial-state spectroscopy (CIS) and constant final-state spectroscopy (CFS) can be conducted using the double-pass CMA. Besides these standard photoemission measurements, electron-ion-coincidence (EICO) spectroscopy can be carried out on adsorbed surfaces and bulk materials. In 1999, a new version of an EICO instrument has been installed, resulting in better efficiency on collecting data. The users who plan to perform the EICO measurement should make contact with the EICO users group. The sample preparation chamber equipped with a load-lock chamber is connected to the analyzing chamber. Sample treatments such as cleaving, filing, and deposition can be made under the ultra-high vacuum condition.

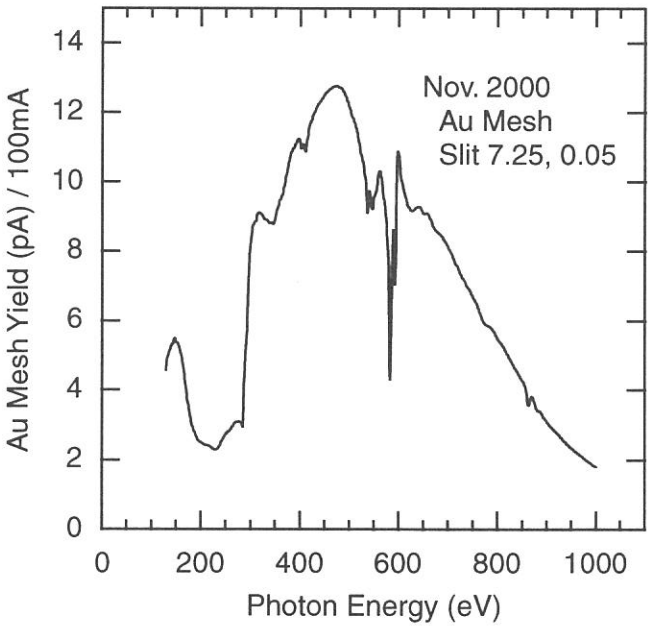

Fig. 1.

Specification

Monochromator	: 2 m grasshopper type
Energy range	: 95-1000 eV (1800 l/mm)
Resolution of photon	: < 0.4 eV at 300 eV
Resolution of photoelectron	: < 0.3 eV for hν = 150 eV
Experiment	: Photoelectron spectroscopy, X-ray absorption spectroscopy, Electron-ion-coincidence spectroscopy

BL2B2

Beamline for Gas Phase Photoionization and Photodissociation Dymanics

This beamline has been developed for the purpose of studying ionization and decay dynamics involving excitation of inner-valence electrons or 2*p* electrons of the third-row atoms. The monochromator is a spherical grating Dragon-type with 18 m focal length. High throuput (1×10^{10} photons s^{-1}) and high resolution ($E/\Delta E$ = 2000 – 8000) are achieved simultaneously (Fig. 1).

The optical system consists of two prefocusing mirrors, an entrance slit, spherical gratings (G1, G2 and G3), two folding mirrors, a movable exit slit and a refocusing mirror. The monochromator is designed to cover the energy range of 20 – 200 eV with the three gratings: G1 (2400 lines mm^{-1}, R = 18 m) at 80 – 200 eV; G2 (1200 lines mm^{-1}, R = 18 m) at 40 – 100 eV, G3 (2400 lines mm^{-1}, R = 9.25 m) at 20 – 50 eV. The including angles are 160° for G1 and G2 and 140° for G3. The detailed parameters of the optical elements [1] and performance [2] are described elsewhere.

References

[1] H. Yoshida and K. Mitsuke, *J. Synchrotron Radiat.* 5, 774 (1998).

[2] M. Ono *et al. Nucl. Instrum. Meth. Phys. Res. A*, in press.

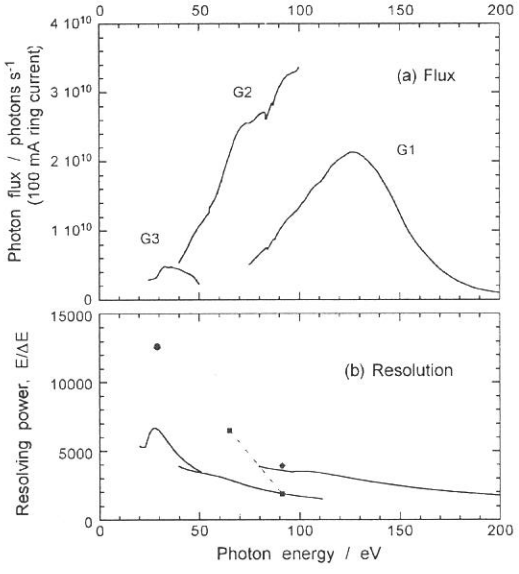

Fig. 1. The photon flux at a 100 mA ring current (a) and resolving power (b) when the entrance and exit slit widths are set to 100 μm. The solid lines in (b) show the expected values[1].

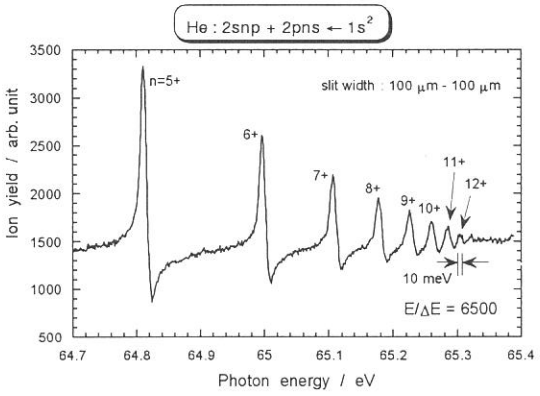

Fig. 2. Ion yield spectrum of He in the doubly excitation region obtained with the slit widths of 100 μm. The resolving power is estimated to be 6500 from the peak width (FWHM) of He(2*s*12*p*+2*p*12*s*).

Specification

Monochromator	:	Dragon-type (18 m spherical grating)
Energy Range	:	20 - 200 eV
Resolution	:	$E/\Delta E$ = 6500 (@65 eV, 100 μm slit width)

BL3A1

Irradiation Port with Undulator Radiation

The beam line 3A1 has been used for various kinds of experiments need intense undulator radiation. In recent years, photo-desorption photo-chemical reaction, SR-CVD, photo-etching, irradiation damage effects in condensed phase, light amplification induced by core-revel excitation, and so on have been carried out at this beam line. The luminescence yield of which is not high enough at beam lines for bending radiation, has been observed, A time-response measurement of SR-induced desorption. A planar-type undulator installed in a long straight section of the UVSOR storage ring provides an intense quasi-monochromatic radiation to beam lines 3A1or 3A2. The undulator consists of 24 sets of magnets, a period length of which is 80mm,the photon energy range from 8 to 52eV can be covered by the fundamentals with a K-values form 0.62 to3.6, although higher harmonics are mixed into the spectral distribution in case of high K-value. The beam line 3A1 has no monochromator between the undulator and a sample chamber. The radiation is introduced by a toroidal focusing mirror into sample chamber through a pinhole of 1mm in diameter and metallic filter (Al, Sn, and In), A gold mesh is always installed in the sample chamber to monitor the incident photons. Atypical spectrum distribution measured by the monochromator at BL3A2 is shown in the figure, where the undulator gap is 60mm and the photon flux is estimated to be abut 10^{14}-10^{15}phs/s on the samples. A differential pumping system can be provided for the users who want to use gaseous materials. A second monochromator (Jobin-YvonHR-302),another vuv monochromator (home-made one of normal-incident type),and a helium storage-type cryostat are available for luminescence experiments. A TAC system is also one of the standard instruments of this beam line. For liquid or gaseous-phase experiments, MgF_2 windows can be installed to separate the sample chamber from the beam line.

Specifications

Type	planar-type undulator
Source emittance	164nmrad
Period	80mm
Number of periods	24
Magnetic field	Kmax 3.6
Photon Fulux	10^{14}phs/s at 34eV
Energy range	8-52eV

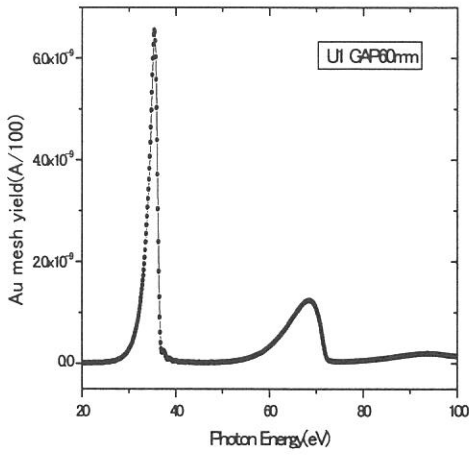

BL3A2

Gas-Phase Dissociative Photoionization Apparatus

This machine has been constructed to study the formation of multiply charged ions and their dissociation processes. The monochromator is constant-deviation grazing incidence type with 2.2-m focal length and covers wide wavelength region (10-100 nm) where many kinds of molecules and multiply charged ions are effectively measured. High intensity photon beam is available by introducing the radiation emitted from the undulator to the monochromator. The apparatus contains an angle-resolved time-of-flight mass spectrometer (TOFM) equipped with automatic data acquisition system for photoion-photoion coincidence measurements. For full understanding of dissociative multiple photoionization, the coincidence signals of two fragment ions produced from a parent ion are detected, the kinetic energy release in "Coulomb explosion" is evaluated, and the angular distributions for the fragment ions are measured. The sensitivity with respect to energetic fragment ions (several tens of electron volts) is much improved in comparison with commercial TOFMs.

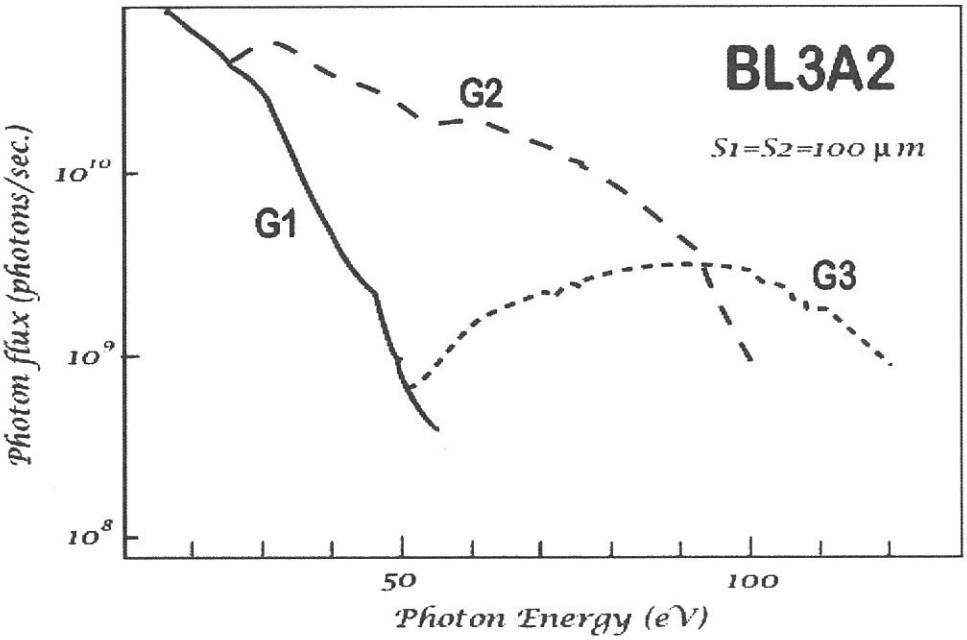

Figure 1. Throughput from the 2.2-m CDM monochromator on BL3A2.
(SR from the bending magnet)

Specification

Monochromator: 2.2-m Constant-Deviation Grazing-incidence
Energy range: 10 to 100 nm (15-120 eV)
Resolution: E/ΔE~550-800 (ΔE~0.03-0.18 eV)
Experiments: TOF photoion spectroscopy for gaseous targets
(variable drift-tube-length: 0.2-1.0 m)
Rotatable angle: 0-90° relative to the electric vector of SR

BL3B

Beam Line for Gas Phase Two-Dimensional Photoelectron Spectroscopy

This beam line is devoted to studies of elementary atomic and molecular processes induced by excitation of valence electrons. A monochromator is a vertically dispersed normal incidence type with 3m focal length and 10° angle between the incident and diffracted photon beams. The maximum wavelength resolution of 0.007nm is narrow enough to separate vibrational levels of excited states for various molecules. A main component in an experimental chamber is a spherical sector electrostatic energy analyzer which has been designed and setup for photoelectron spectroscopy. One can perform two-dimensional photoelectron spectroscopy with good resolution (≤ 30meV) in which the photoelectron yield is measured as a function of both photon energy and electron kinetic energy (binding energy). A two-dimensional spectrum, usually represented as a contour plot (*e.g.* Fig. 1), contains rich information on photoionization dynamics and properties of superexcited states. A great variety of interesting high-lying states involved in autoionization have been studied as follows: (1) a bound valence state of nitric oxide whose autoionization gives rise to a number of irregularly spaced peaks in its photoionization efficiency curve,[1] (2) the $(3\sigma_g)^{-1}(3\sigma_u)^1$ valence state of acetylene which dominates photoionization cross section and leads to strong vibrational excitation,[2] (3) Rydberg states of NO or SO_2 which undergo dissociation into N** + $O(^1D^e, {}^3P^e)$ [3], or S** + $2O(^3P^e)$, [5] respectively, followed by autoionizing transitions of the superexcited N or S atoms, respectively, and (4) multiple-electron-excited Rydberg states of carbonyl sulfide which are primarily produced by conversion from the Rydberg states converging to $OCS^+(B^2\Sigma^+)$ and subsequently dissociate into S** + $CO(X^1\Sigma^+)$ giving rise to autoionizing transitions of the superexcited sulfur atoms.[4]

1) K. Mitsuke *et al.*, *J. Electron Spectrosc. Rel. Phenom.* **79**, 395 (1996).
2) H. Hattori and K. Mitsuke, *ibid.* **80**, 1 (1996); H. Hattori *et al.*, *J. Chem. Phys.* **106**, 4902 (1997).
3) Y. Hikosaka *et al.*, *ibid.* **105**, 6367 (1996).
4) Y. Hikosaka *et al.*, *ibid.* **107**, 2950 (1997); **110**, 335 (1999).
5) K. Mitsuke *et al.*, *J. Electron Spectrosc. Rel. Phenom.* **112**, 137 (2000).

Specification

Monochromator	: 3 m normal incidence
Wavelength range	: 30 - 200 nm
Resolution	: 0.007 nm at 100 nm

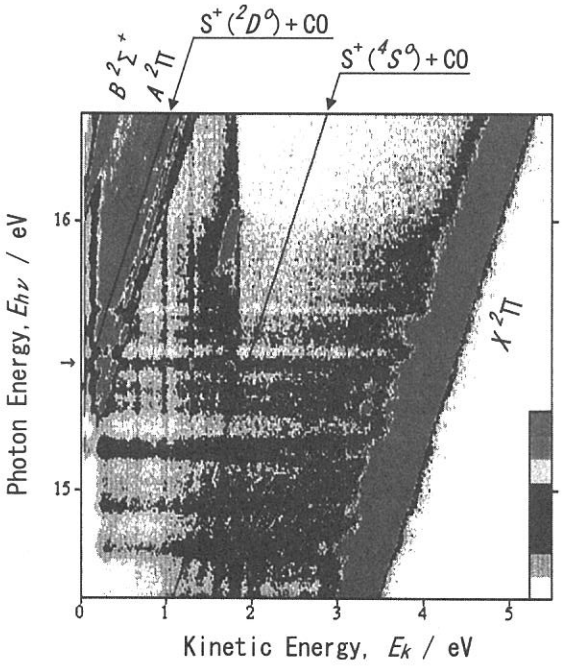

Figure 1. Two-dimensional photoelectron spectrum of OCS taken at the photon energy range from 14.2 to 16.8eV. The electron yield is presented by the plots with eight tones from light to dark on a linear scale.[4]

BL4A1

Multilayered-mirror monochromator beam line for the study of synchrotron radiation stimulated process

A multilayered-mirror (MLM) monochromator beam line designed specially for synchrotron radiation (SR) stimulated process experiments has been constructed for the first time. The most important point in constructing a MLM monochromator beam line for the study of SR-stimulated processes is the optimization of the beam line optics to obtain a large photon flux. The second most important point is to remove the background existing in the low energy region caused by the total reflection. Optimization conceming the reduction of the low-energy background due to the total reflection has been made for the combination of the Mo/Si MLMs and the C filter. Mo/Si MLMs have a (normal incident) reflectivity of over 60% can be made for the energy region around 100 eV, which contains the core electron binding energies of Al and Si (important materials in semiconductor processes). The beam line was designed by the criteria ; a beam spot size on the sample surface $\geqq 3\times3$ mm^2, a density of total irradiated photons $\geqq 10^{18}$ photons/cm^2 (for an irradiation time of a few tens of minutes to a few hours) and low-energy background $\leqq$ 1% of the output.[1]

[1] H. Mekaru, *et. al.*, Rev. Sci. Instrum., 70, 2601-2605 (1999).

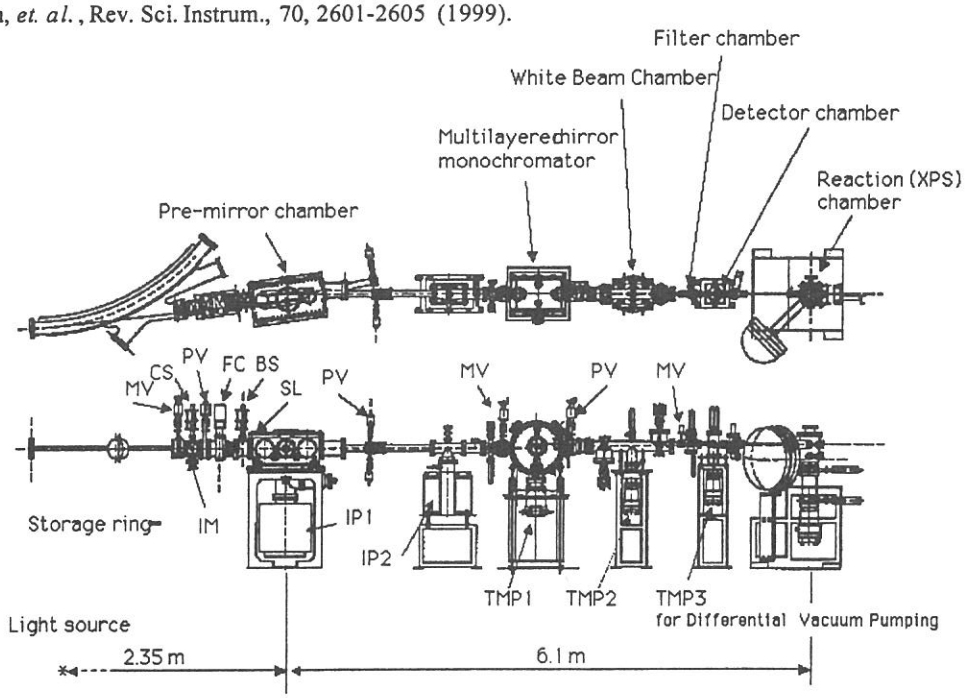

Figure 1. Top and side views of the MLM monochromator beam line (BL4A1) constructed at the UVSOR facility of the IMS.

Specifications

Monochromator	:Multilayered-mirror monochromator
Wavelength range	:13.3 - 22.5 nm
Resolution	:5 – 9 eV (FWHM)
Experiments	:Excitation energy dependence of the SR processing

BL4A2

SR-CVD beam line

SR-CVD experimental station, which had been installed at the end of the beam line 4B until 1999, was moved to the end of the new beam line 4A2 at April 2000. The reaction chamber system has been modified as shown in Fig.1. Adjustments of the reaction chamber, in situ observation system of IRRAS and gas supply and extinction systems have already been finished. The pre-mirror chamber is already at high vacuum but the downstream beam line is still under construction. The legally controlled high pressure gases such as SiH4, Si2H6 and GeH4 gas can be used at this beam line and SR stimulated reactions such as SR etching and SR stimulated gas source MBE. The ultra high vacuum STM chamber is also under construction as a blanch experimental station of BL4A2.

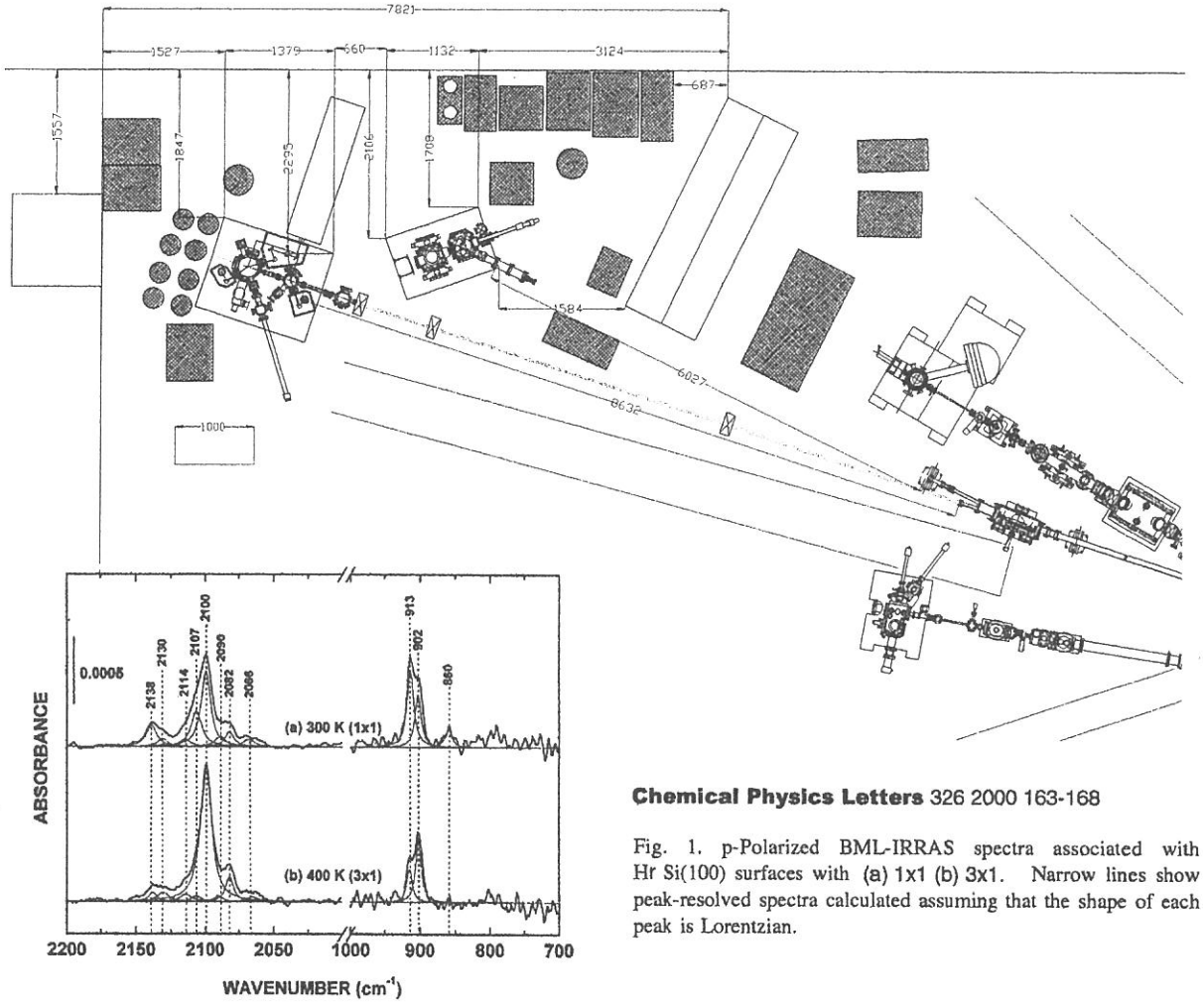

Chemical Physics Letters 326 2000 163-168

Fig. 1. p-Polarized BML-IRRAS spectra associated with Hr Si(100) surfaces with (a) 1x1 (b) 3x1. Narrow lines show peak-resolved spectra calculated assuming that the shape of each peak is Lorentzian.

BL4B

Varied-line-spacing Plane Grating Monochromator for Molecular Soft X-ray Spectroscopy

The beamline BL4B equipped with a varied-line-spacing plane grating monochromator was constructed for various spectroscopic investigations in a gas phase and/or on solids in the soft X-ray range. Two holographically ruled laminar profile plane gratings with SiO_2 substrates are designed to cover the photon energy range from 80 eV to 1000 eV. The gratings with the groove densities of 267 and 800 l/mm cover the spectral ranges of 75-300 and 220-1000 eV, respectively, and are interchangeable without breaking the vacuum. Figure 1 shows the absolute photon flux for each grating, with the entrance- and exit-slit openings set at 25 and 10 μm, respectively. Under this condition, the corresponding resolving power is expected to be more than 3000.

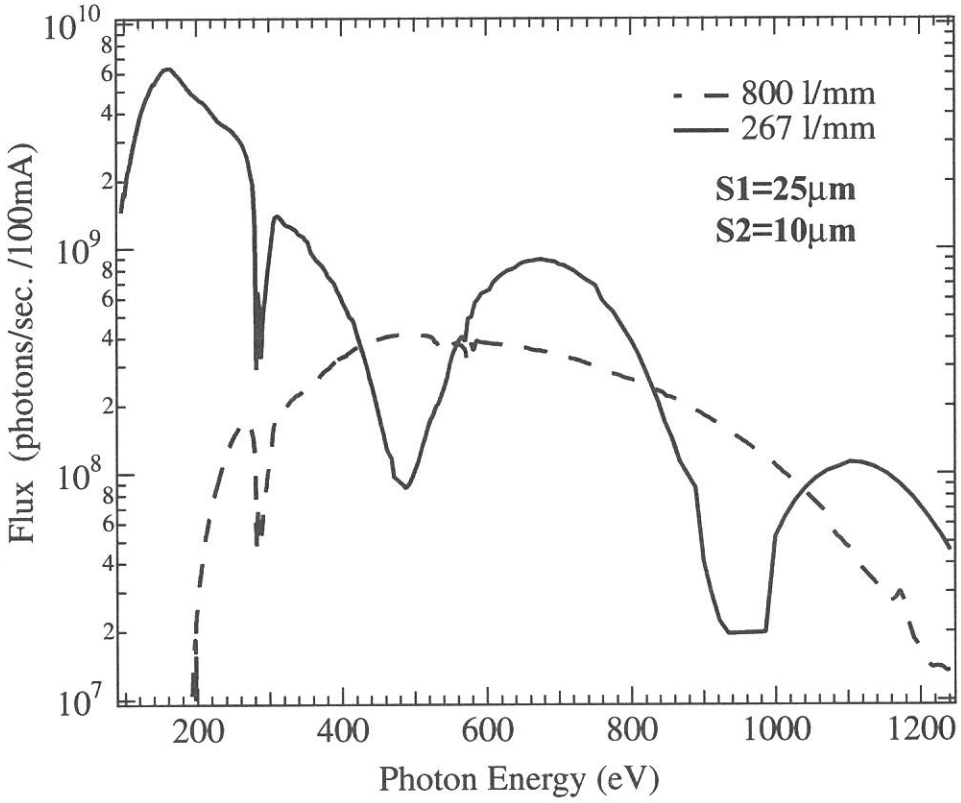

Figure 1. Throughput from the VPGM monochromator on BL4B.

Specification

Monochromator: Varied-line-spacing plane grating monochromator

Energy range: 75 to 1000 eV

Resolution: E/ΔE>5000 (at maximum)

Experiments: Soft X-ray spectroscopy (mainly, angle resolved photoion spectroscopy for gaseous targets and photoelectron spectroscopy for gaseous and solid targets)

BL5A

Photoelectron Spectrometer for Solids and Surfaces

This beamline is designed for spin- and angle-resolved photoemission study for solids and surfaces with the circularly polarized synchrotron radiation from a helical undulator and for high-resolution photoemission spectroscopy with bending magnet radiation. The beamline consists of a Spherical Grating Monochromator with Translational and Rotational Assembly Including a Normal incidence mount (SGM-TRAIN), a spin- and angle-resolved photoelectron spectrometer, and a high-resolution photoelectron spectrometer.

The SGM-TRAIN is an improved version of a constant-length SGM to aim the following points; (1) wide energy range of 5-250 eV, (2) high resolving power, (3) use of linearly and circularly polarized light, (4) reduction of second-order light, and (5) two driving modes by a computer control. The second-order light is well suppressed by using laminar-profile gratings and combinations of mirrors and gratings.

Specifications

1. Monochromator

Type : SGM-TRAIN
(two glancing-incidence and one normal-incidence)
Energy range : 5-250 eV
Resolution : 0.5-80 meV (with slits of 0.01 mm)
Flux : 3×10^{10} phs/sec for bending magnet radiation
1×10^{12} phs/sec for undulaor radiation in MPW mode
(at 120 eV with slits of 0.1 mm)

2. Main Instruments

Two-levels UHV chamber (1×10^{-10} Torr)
Hemispherical electron energy analyzer
(OMICRON, EA125-HR)
Spin- and Angle-resolved spectrometer
(low-energy diffused scattering type)
LEED of reverse type (OMICRON)
Ion-gun (ULVAC-Phi)
Low-temperature cryostat (above 30 K)

3. Helical Undulator (Optical Klystron)

Number of periods	18
Period length	110 mm
Length of dispersive part	302.5 mm
Total length	2351.2 mm
Deflection parameter, $K_{x,y}$	0.07-4.6 (helical mode)
Deflection parameter, K	0.15-8.5 (planar mode)
Fundamentals	2-45 eV (Circularly polarized)

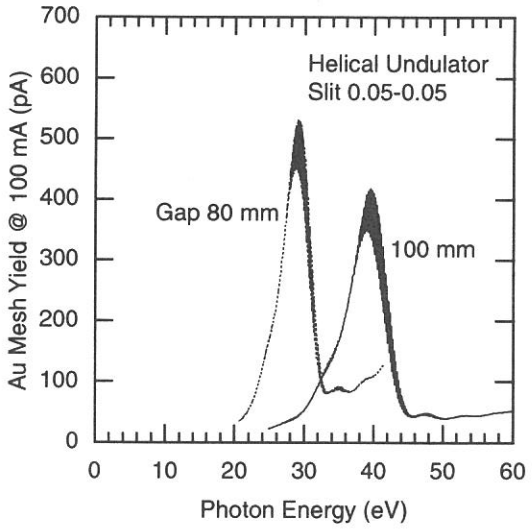

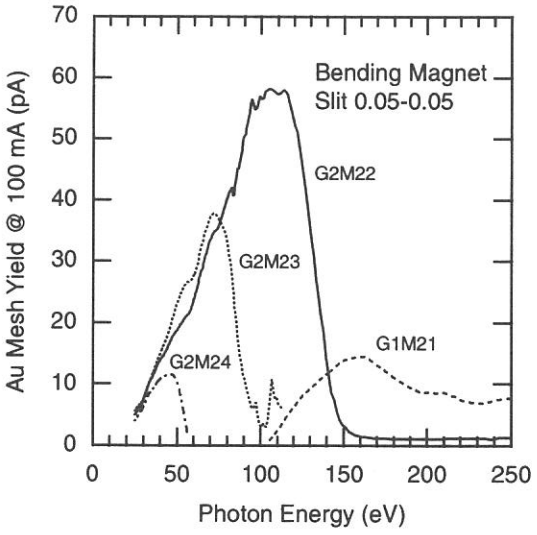

BL5B

Calibration Apparatus of Optical Elements

BL5B has been constructed to calibrate optical elements. The beam line consists of a plane grating monochromator (PGM) and three chambers (Fig. 1). The chamber A is used for calibration of optical elements, the camber B for optical measurements of solids and the chamber C for photo-stimulated desorption (PSD) experiments. The chamber C is sometimes changed to a chamber for photoemission microscopy.

The calibration chamber is equipped with a goniometer. The goniometer, which was installed for the characterization of optical components, has six degrees for freedom; X-Y translation of a sample, and interchange of samples and filters. They are driven by vacuum pulse motors. Since the polarization of SR is essential for such measurement, axis of the rotation can be made in either horizontal or vertical direction (s- or p-polarization).

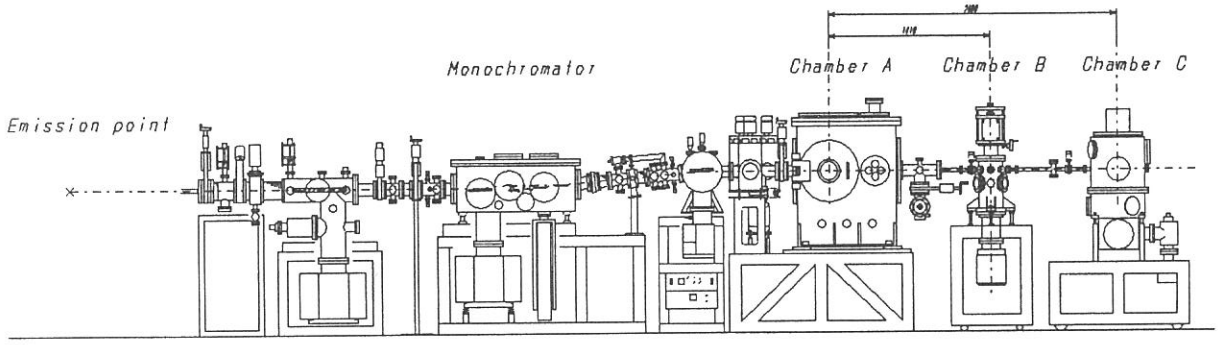

Figure 1. Schematic figure of BL5B spectrometer system.

Specification

Monochromator: Plane grating

Wavelength range: 2 - 200 nm (Fig. 2)

Resolution: $\lambda / \Delta\lambda = 300 \sim 500$

Experiments: Calibration of optical elements, absorption of solids, photo-stimulated desorption from rare gase solids, photoelectron microscopy.

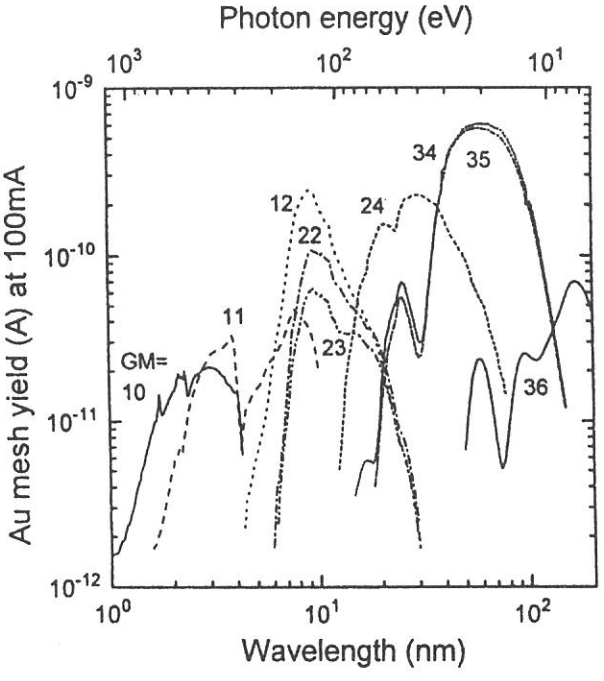

Figure 2. Throughput spectra of BL5B detected by a gold mesh (84% transmission).

BL6A1

Fourier-Transform Middle and far Infrared spectrometers for solids

UVSOR covers a very wide energy region from a soft-X ray to a millimeter wave. BL6A1 was constructed in order to cover a long wavelength part in the spectral distribution of UVSOR from a near infrared to a milli-meter wave. Beamline are composed of two kinds of interferometers, a Martin Puplett type and a Bruker-IFS66v. The spectrum from 1 μ m to 3 μ m regions is measureable by changing of three kinds of detectors, MCT, Si-bolometer and InSb hot electron detector, according to each available region. Owing to the high brightness of the SR in the long wavelength region, the present spectroscopic system is specially favorable to the transmission and reflection measurements on so tiny specimens..

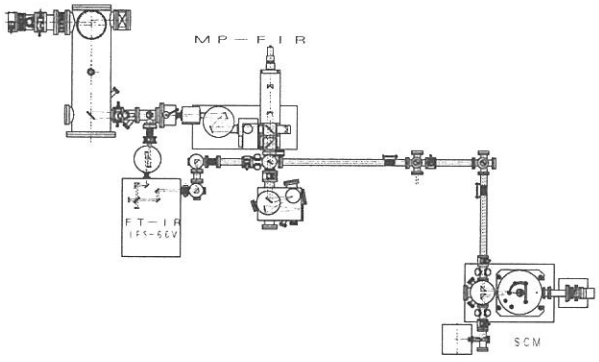

Top view of BL6A1

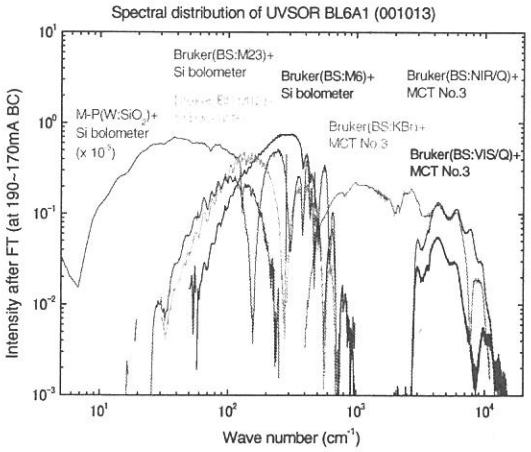

Throughput spectra of BL6A1

Spccification

Energy resolution :	500-20000
Energy range :	0.0005-1.5eV
Interferometers :	5-300cm^{-1} by Martin-puplett interferometer
	50-30000cm^{-1} by Michelson type interferometer
Detectors :	Si bolometer(20-1000cm^{-1})
	Ge bolometer(with polyethylene window,30-300cm^{-1})
	Ge bolometer(with quartz window,10-200cm^{-1})
	InSb bolometer(5-50cm^{-1})
	MCT(400-10000cm^{-1}) Photovoltaic type
	MCT(400-10000cm^{-1},time response10nsec)

BL6A2

Photoelectron Spectrometer for Solids and Surfaces

The beamline BL6A2 has been used for photoelectron spectroscopy on solids and surfaces with bending magnet radiation. The beamline consists of a Plane Grating Monochormator (PGM) and a photoelectron micro-spectrometer.

The PGM has several combinations of mirrors and gratings to cover the wide energy range of 2-150 eV with less higher-order light. Since the monochromator has no entrance slit, the resolving power depends on the beam size and the divergence. The beamline was re-arranged to have a small spot for the photoelectron micro-spectrometer. Also the femto-second laser system was installed to conduct the combination experiments with synchrotron radiation and laser.

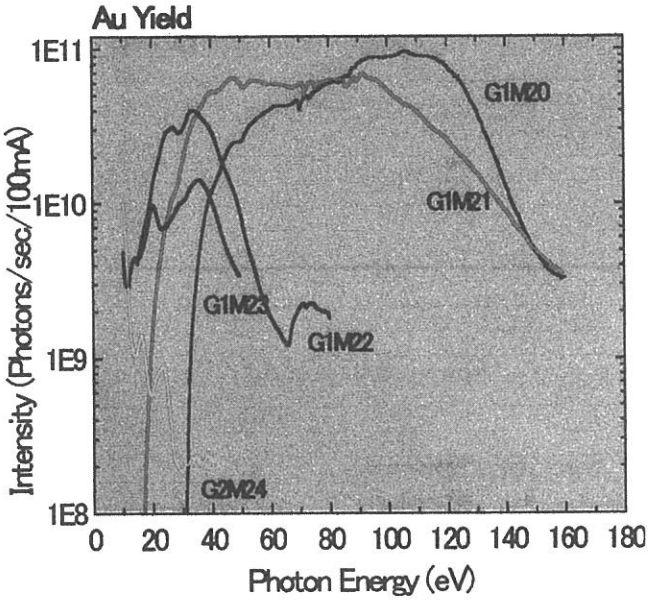

Specifications

Monochromator;

Type:Plane-Grating Monochromator

Energy range;2-150 eV

Resolution:0.1 eV at 70 eV

Flux:1x10^{11} phs/s at 100 eV

Photoelectron micro-spectrometer;

Type:FISONS, ESCALAB 220i-XL

Spatial Resolution:20 μm for spectroscopy

2 μm for imaging

others:XPS, LEED, Ion-gun

Laser;

Type:Spectra Physics, Hurricane

Fundamentals:750-850 nm

SR=>

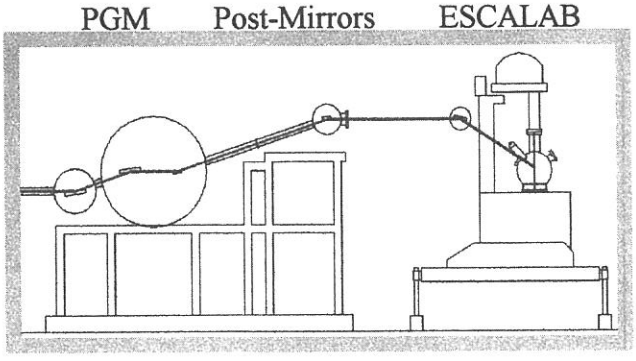

BL6B

UHV-STM beam line

This beam line is constructed for the atom level characterization of the SR illuminated surfaces by the in situ observation of STM. The STM experimental systems, ultra-high-vacuum chamber and STM, have been installed at the upstream of the BL4B SR-CVD chamber until the end of March 2000 and moved here at the last summer shut down.

When it was working at BL4B, the atomic image of clean Si(111) surface was clearly observed even under the SR storage ring operation and STM in situ observation of SR stimulated decomposition of thin SiO_2 film was successfully demonstrated. The BL6B beam line construction has almost finished. The STM experimental systems are now under remodeling. The design of the STM system is changed so that the SR beam can illuminate the sample surface just under the STM chip. By this change, the STM observation can be made just after the SR illumination without the sample transfer. The short undulator which is going to be inserted to the strait part of the storage ring and emit the beam for BL7A, is under construction. The beam line and the UHV STM station are going to be moved to the end of the new BL7A after the completion of the undulator.

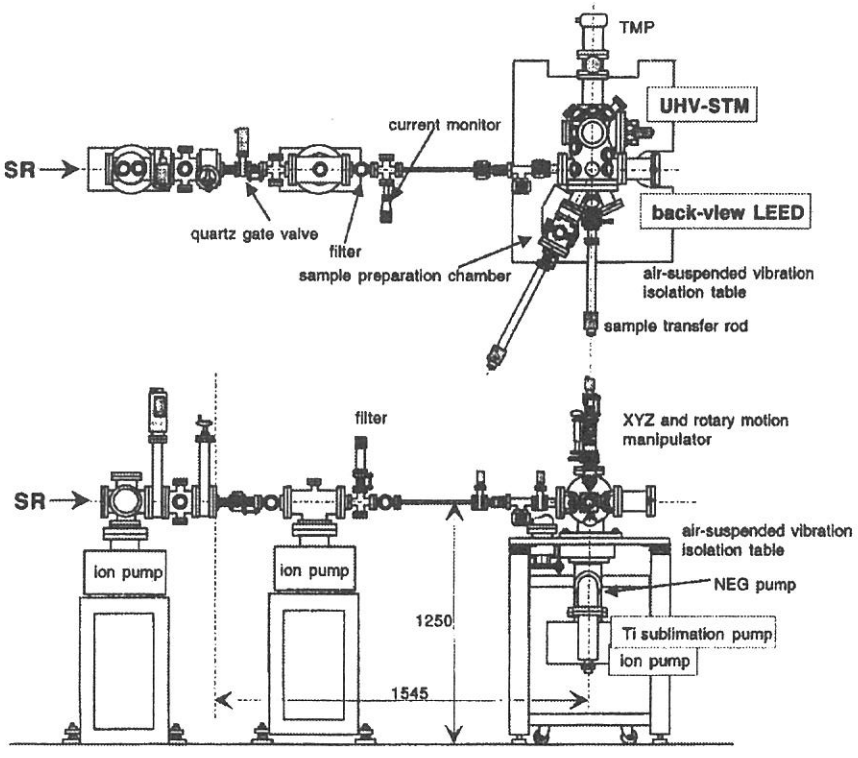

BL7A

Soft X-ray Spectrometer for Solids

The beamline BL7A equipped with a double crystal monochromator was constructed for spectroscopic investigation on solids in the soft X-ray range (0.6 to 5 keV). In order to make the EXAFS experiments at the Mg (~1300 eV) and Al (~1550 eV) *K*-edges possible, a pair of $KTiOPO_4$ [KTP] (011) crystals was introduced and its performance test was done in 1999. In the past, it has been necessary to use beryl and quartz crystals to approach these two edges. The combination of an artificial crystal, YB_{66}(400), with the wiggler has been another possibility to access the Al and Mg *K*-edges. However, YB_{66} is unsuitable for the radiation from the bending magnet, due to its low reflectivity, and there is a disadvantageous characteristic caused by a anomalous (600) reflection at the Y *L*-edge for carrying out the EXAFS experiments with the YB_{66} crystals.

Figure 1 shows the photon flux of the KTP monochromator crystals over the photon energy range 1200–3000 eV. It is found that the photon intensity from the KTP crystals without the wiggler is almost the same as that from the YB_{66} crystals combined with the wiggler. The ability to cover the Mg, Al, and Si *K*-edges with a single pair of the KTP crystals seems to be attractive for many users.

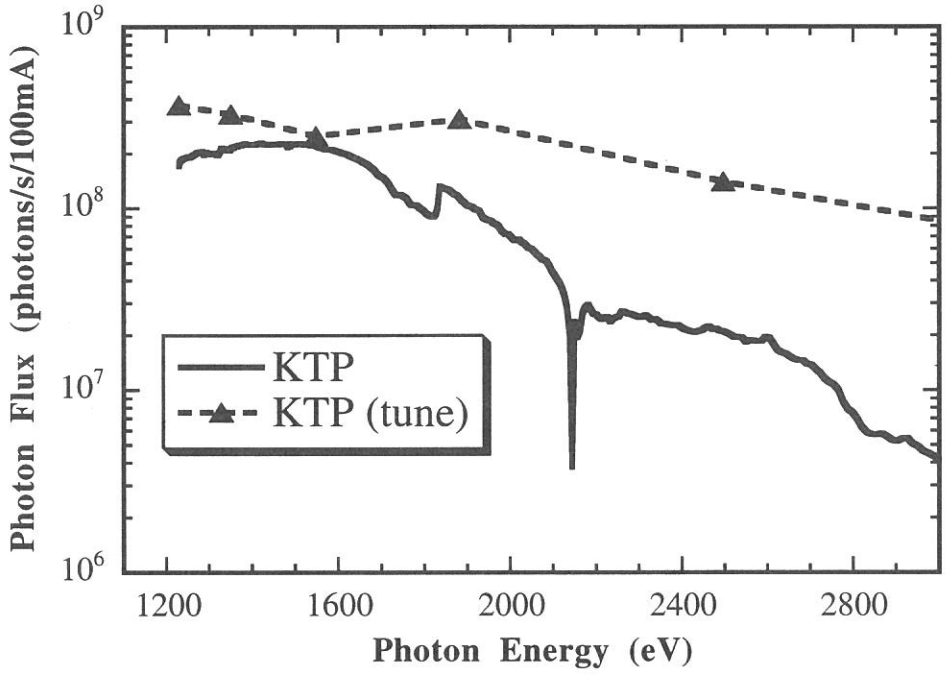

Figure 1. Throughput from KTP monochromator crystals on BL7A.

Specification

Monochromator: Double-Crystal

Energy range: 0.6～4.0 keV

Experiments: X-ray absorption (by total electron- or fluorescence-yield methods)

BL7B

3m Normal Incidence Monochromator for UV, VIS and IR Spectroscopy of Solids

The beamline BL7B is a dedicated beamline for solid-state spectroscopy, and has been reconstructed to provide sufficiently high resolution for solid-state spectroscopy, enough intensity for luminescence measurements, a wide wavelength coverage for Kramers-Kronig analysis, and the minimum deformation to the polarization characteristic of the incident synchrotron radiation for polarization measurements. It is also expected in the future that combined experimental systems are realized at this beamline, for example, with synchronization to the synchrotron radiation pulse or with the external magnetic field. The reconstructed BL7B mainly consists of a 3m normal incidence monochromator which covers the vacuum ultraviolet, ultraviolet, visible and infrared, *i.e.* the wavelength range 40 – 1000 nm, with three gratings and has been opening for users from April 1999.

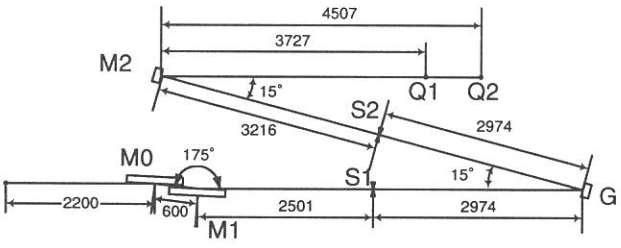

Fig. 1

Figure 1 shows the optical configuration of the beamline which consists of four parts; pre-mirror system (M0, M1), 3 m normal incidence monochromator (modified version of McPherson model 2253)(S1, G, S2), post-mirror system (M2) and experimental area (Q1, Q2). All of the optical elements are on a vertical plane. The beam spot size of the zeroth light at Q1 is about 3 mm (H) × 2 mm (V). Figure 2 shows the output spectra. A silicon photodiode (AXUV-100, IRD Inc.) was used for measurement, and the photon number was calculated from the quantum efficiency table for AXUV-100 photodiodes. The slit widths of both entrance and exit slits are 0.5 mm. The labels a to f represent output spectrum of G1 (a), G2 (b), G2 with a LiF filter (c), G3 with a quartz filter (d), G3 with a pyrex glass filter (e) and G3 with a colored glass cut filter (Toshiba Ltd. O-53) (f). All of these filters are located just before Q1 in Fig. 1. Under normal operation of UVSOR, the average beam current is more than 100 mA, so that the typical output photon number per second is in the range of $10^8 \sim 10^9$ and $10^{11} \sim 10^{12}$ for 0.05-0.05 mm and 1-1 mm slit widths, respectively. In general, the reduction of the higher order light becomes important if a monochromator covers a wide wavelength region. As shown in Fig. 2, the required good spectral purity of the monochromated light is almost fulfilled over the whole spectral range by mean of the lower wavelength cut-off filters and the reflection thresholds of the gratings themselves. It is difficult to estimate the intensity of scattered light, but the transmission spectra at the absorption region of the filters indicate that the intensity of the visible scattered light can be expected to be less than 0.5% of the average output.

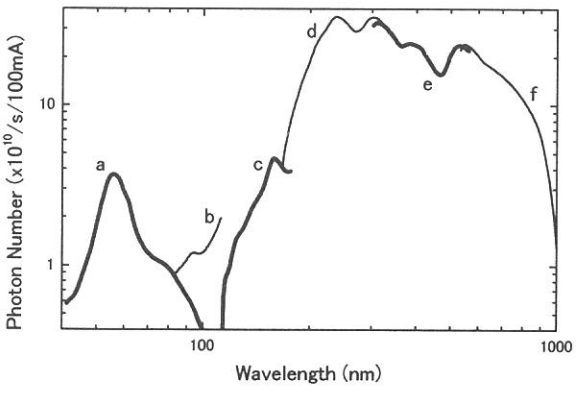

Fig. 2

Specification

Monochromator	: 3m Normal Incidence Monochromator
Wavelength range	: 50 nm – 1000 nm
Typical resolution	: E/ΔE = 4000 – 8000 for 0.01 mm slits
Experiments	: absorption, reflection, fluorescence spectroscopy, mainly for solids

BL8A

Free Port

This beamline was constructed as a free port to which user can connect their own instruments. The beamline consists of a front end, a focusing premirror chamber and a separation chamber. Both focused and unfocussed beam can be used. A general purpose reaction chamber and a two (or three) stage differential pumping system are available for the experiments that use gas samples without window. With using three stage differential pumping system, gas pressure at the reaction chamber upto 0.5 torr can be used while keeping ultra high vacuum at the premirror chamber.

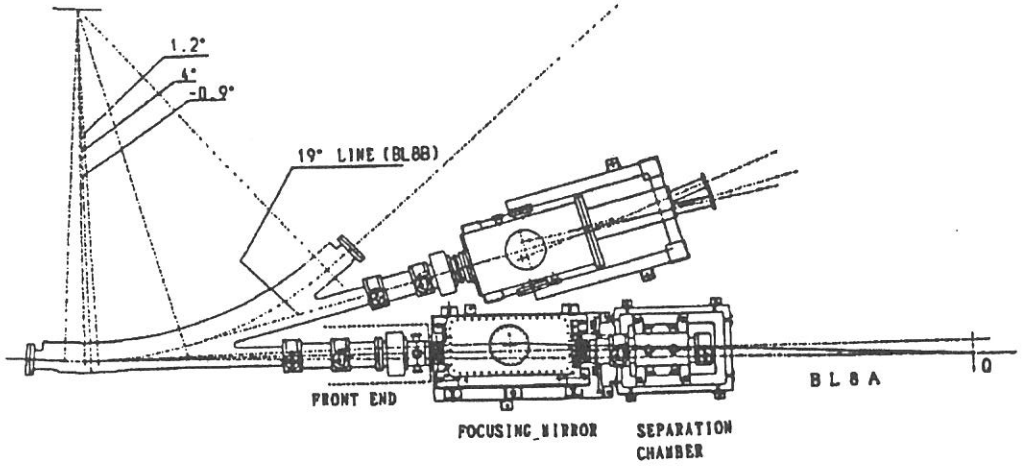

UP VEW OF BL8A

Specification

Spectral range : whole range of synchrotron radiation from UVSOR

Acceptance angle

Unfocused beam : 25 mrad (horizontal) × 8 mrad (vertical)
0.6 mrad (horizontal) × 0.6 mrad (vertical)
(with ϕ 3 mm aperture before sample)

Focused beam : 7.7 mrad (horizontal) × 8 mrad (vertical)
Beam spot size at focu : 3 mm (horizontal) × 2 mm (vertical)
Source - mirror distance : 2500 mm
Mirror - focus distance : 2807 mm

BL8B1

Photoabsorption and Photoionization Spectrometer

Last year a new beam line BL8B1 was constructed for observation of high resolution photoabsorption and photoionization experiments in the photon energy range from 30 to 800 eV, which includes the 1s core excitation energy of C, N and O atoms. For high resolution measurement among these energy, a constant-deviation constant-length spherical grating monochromator (CDCL-SGM) with three gratings (G1: R = 15 m; 1080 l/mm, G2: R = 15 m 540 l/mm, G3: R = 7.5 m; 360 l/mm) has been employed, in which entrance and exit slit positions and directions of incident and exit photon beams do not change during its scan. Consequently, it provides us with resolutions (E/ΔE) of 4000 at 400 eV and of 3000 at 245 eV. A drain current of gold foil reveals the absolute photon flux normalized by an ring current when two slit widths are 10μm. (Fig. 1)

Being Equipped at the downstream of the monochrometer, an chamber with a time-of-flight ion detector and a photoelectron detector allows us to measure photoelectron - photoion coincidence (PEPICO) and photoion - photoion coincidence (PIPICO) spectra. Measurements of absorption, electron yield and emission spectra of solid samples are also available.

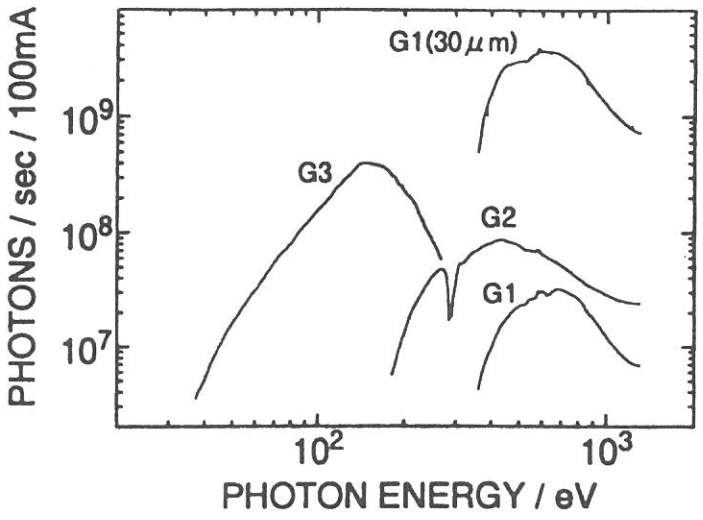

Figure 1. Absolute photon fluxes measured by a drain current of gold foil

Specification

Monochrometer	: 2.2 m constant-deviation grazing incidence
Wavelength range	: 30 to 800 eV
Resolution	: E/ΔE = 4000 at 400 eV and 3000 at 245 eV
Available Experiments	: Measurement of photoabsorption and photoionization spectra for gas and solid sample

BL8B2

Angle-Resolved Ultraviolet Photoelectron Spectrometer for Solids

BL8B2 is a beamline for angle-resolved ultraviolet photoemission spectroscopy (ARUPS) system which is designed for measuring various organic solids such as molecular crystals, organic semiconductors, and conducting polymers. The beamline consists of a plane-grating monochromator (PGM), a sample preparation chamber with a fast entry Load-Lock chamber, a measurement chamber with an accurate for temperature dependence (base pressure 1×10^{-10}Torr), a cleaning chamber (base pressure 1×10^{-10}Torr), and a sample evaporation chamber (base pressure 3×10^{-10}Torr). The cleaning chamber is equipped with a back-view LEED/AUGER, an ion gun for Ar^+ sputtering, and an infrared heating unit. The PGM consists of premirrors, a plane grating, focusing mirror, and a post-mirror, with an exit slit. It covers the wide range from 2 to 150eV with exchanging two gratings (G1: 1200l/mm, G2: 450l/mm) and five cylindrical mirrors. The toroidal mirror focuses the divergent radiation onto the sample in the measurement chamber. The spot size of the zeroth-order visible light at the sample surface is about $1\times1mm^2$. The energy resolution at a slit width of 100μm was found to be 0.004-0.3eV in the wavelength range from 2 to 130eV. A hemi-spherical electron energy analyzer of 75mm mean radius with an angular resolution less than 2° can be rotated around vertical and horizontal axes. The sample mounted on a manipulator can be also rotated around two axes.

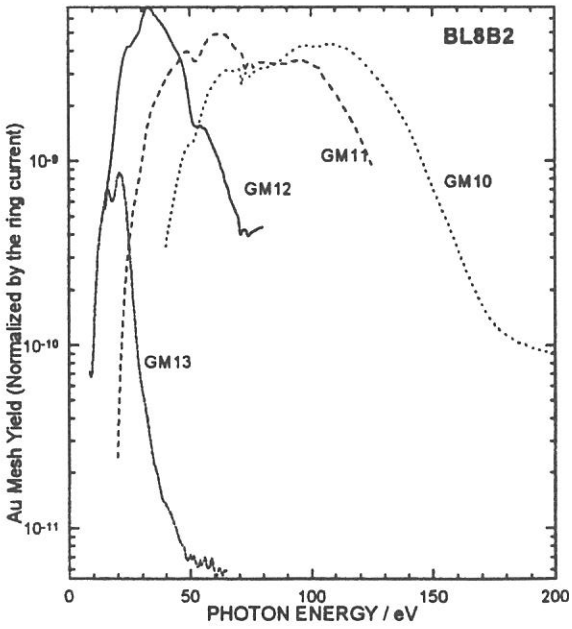

Figure Throughput spectra of plane-grating monochromator at BL8B2 with 100 μm exit slit.

Specification

Monochromator : plane grating monochromator
Spectral range : 2-150eV
Resolution : 100meV at 40eV as determined by the Fermi edge of gold
Experiment : angle-resolved ultraviolet photoelectron spectroscopy (ARUPS) for various organic solids
Polarization : 85~91% at 500nm

Open Beam Lines (Apr. 2000 - Mar. 2001)

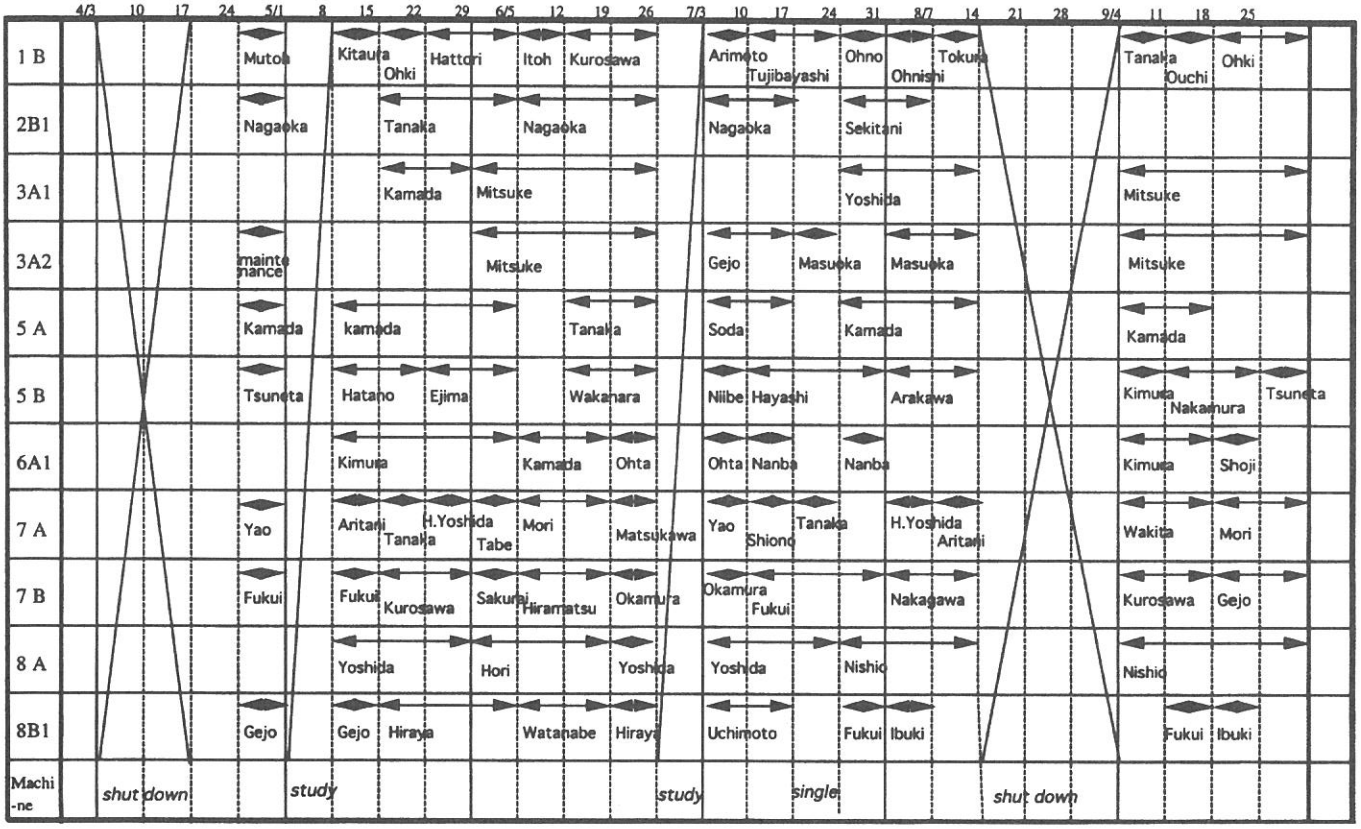

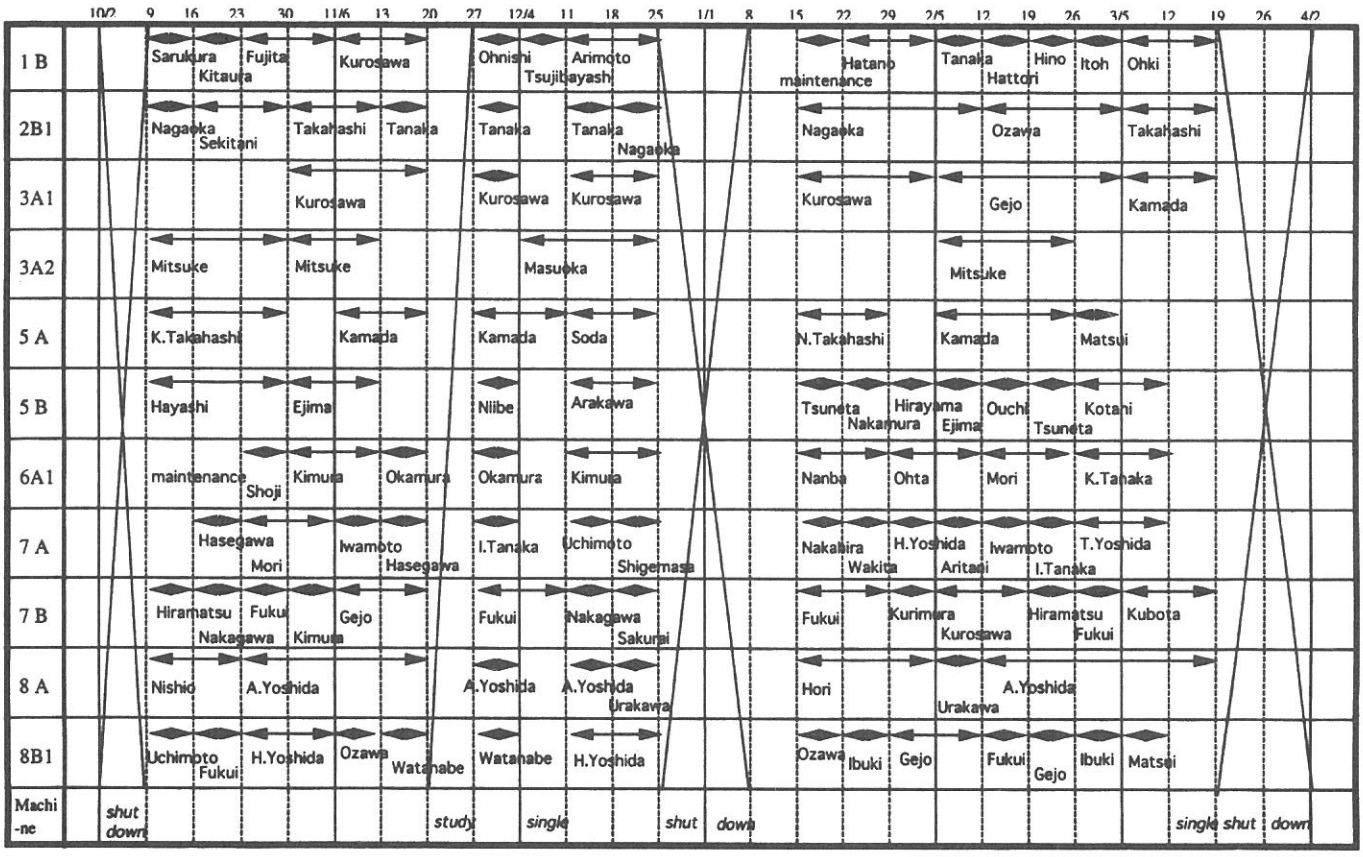

In-house Beam Lines (Apr. 2000 - Mar. 2001)

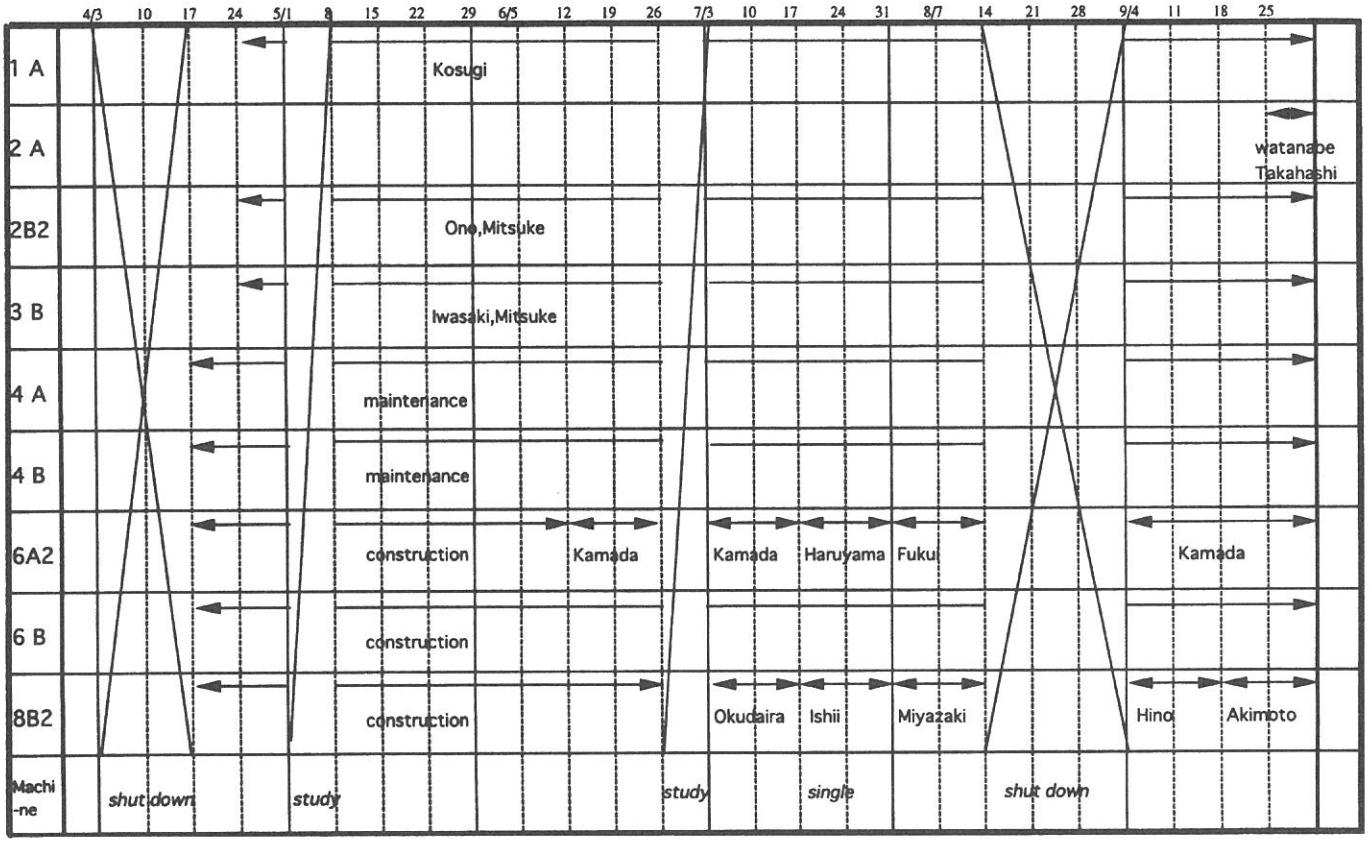

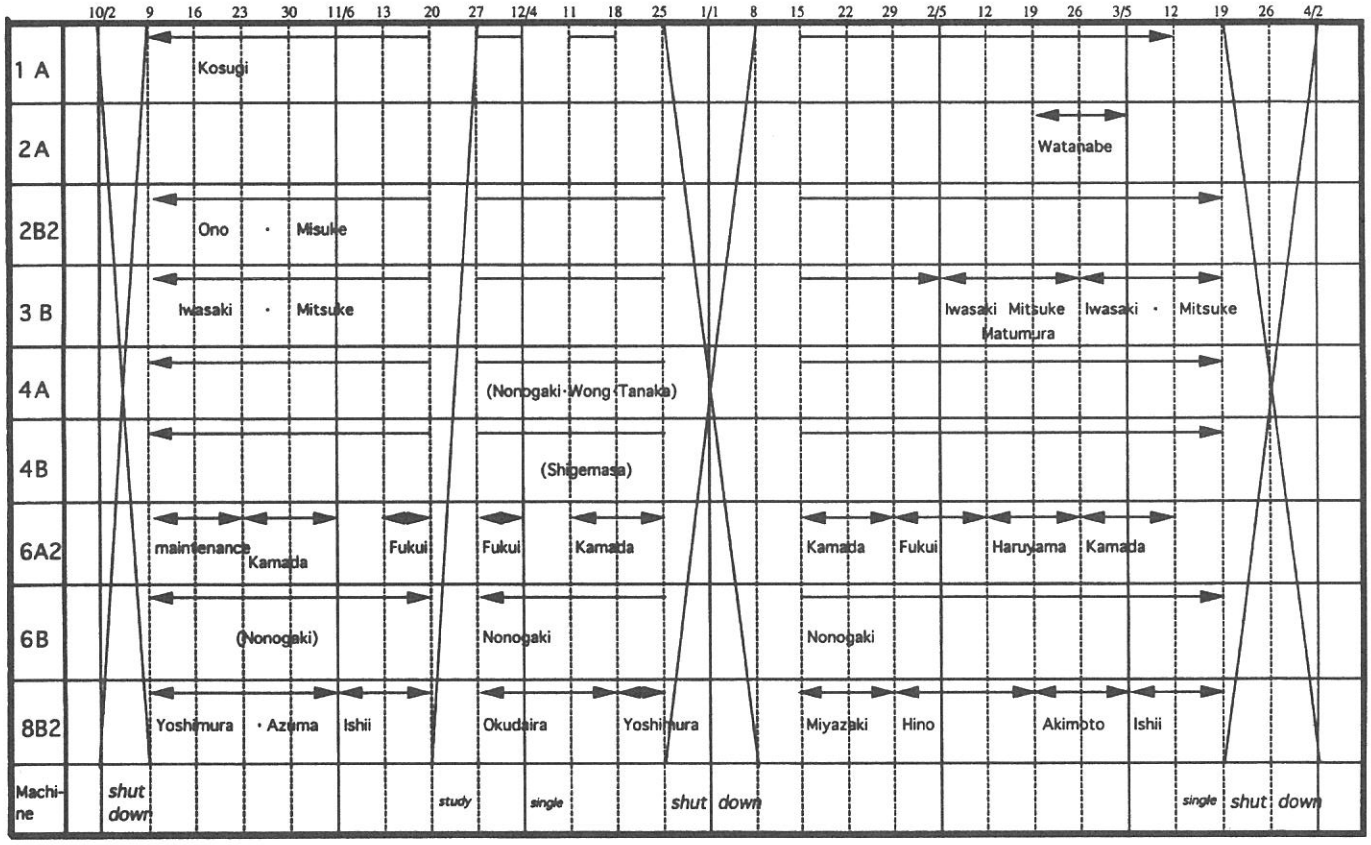

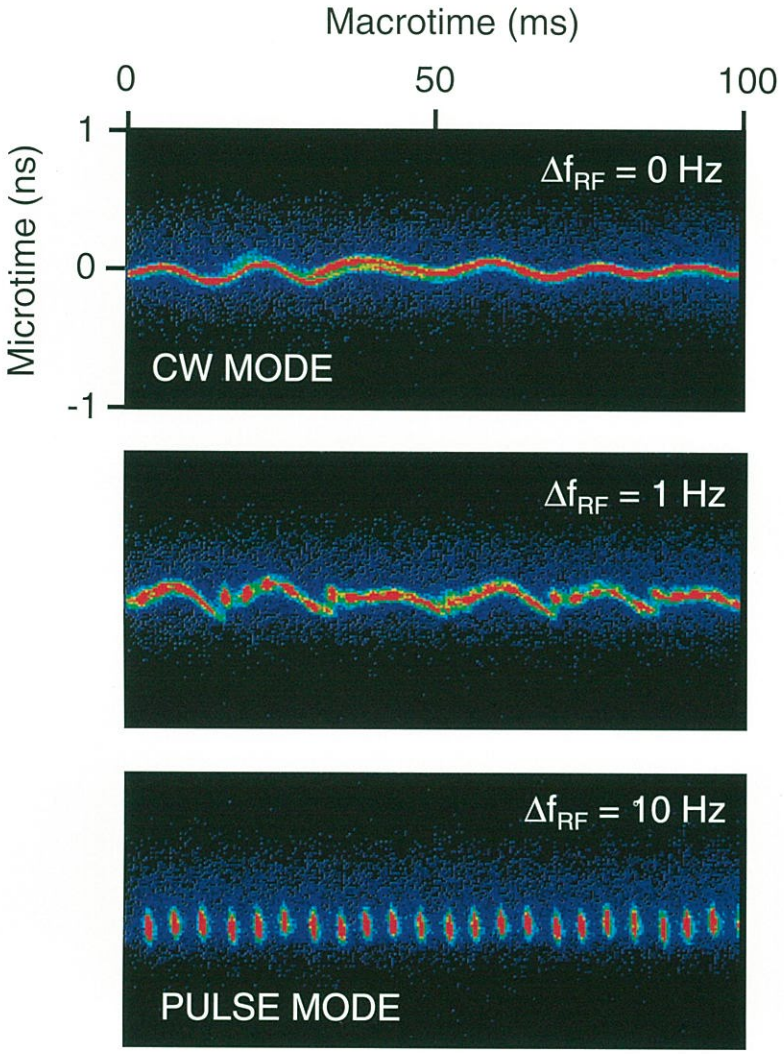

Beam Physics

Development of In-vacuum Undulator for UVSOR

Masahiro KATOH, Masahito HOSAKA, Shigeru KODA,
Jun-Ichiro YAMAZAKI, Toshio KINOSHITA, Kenji HAYASHI, Yoshifumi TAKASHIMA[A],
Hideo KITAMURA[B], Toru HARA[B], Takashi TANAKA[B]

UVSOR Facility, Institute for Molecular Science, Okazaki 444-8585 Japan
[A)]Department of VUV Photo-science, Institute for Molecular Science, Okazaki 444-8585 Japan
[B)]SPring-8, Institute of Physical and Chemical Research (RIKEN), Mikazuki-cho 679-5148 Japan

An upgrade plan is proposed for UVSOR [1]. In this plan, new four straight sections of 1.5 m long will be created. These sections have small vertical betatron function of less than 1m. They are suitable for installing in-vacuum short period undulators [2]. The gap between the magnetic poles can be reduced down to 10 mm without reducing the beam lifetime. To investigate the effects of this type of devices on electron beams and to evaluate the undulator radiation, we have started developing an in-vacuum undulator.

The main parameters of the undulator are shown in Table 1. The minimum gap of the magnetic poles is 10 mm for upgraded lattice. The period length is decided to be 36 mm, which will result in very wide tunability in VUV and soft X-ray region, as shown in Figure 1.

Before the upgrade of the ring, this undulator will be installed in the ring for performance test, at a free space that will be created by removing the super-conducting wiggler. In this case, the minimum gap is limited to be 20 mm because of relatively large betatron function of the present beam optics. As a result, the tunability is limited as shown in Figure 1. However, the fundamental and the third harmonic of the undulator radiation will come to the photon energy range around 100 eV and 300 eV, which are close to L-edge of Si and K-edge of C respectively. After the performance test, some users are planning to use the undulator as a high flux and moderately monochromatic light source.

This fiscal year, only the magnetic pole is being constructed. The remaining parts will be constructed in next fiscal year. The construction of the undulator will be completed in next fiscal year. In March 2002, it will be installed in the ring.

Table 1. Parameters of In-vacuum Undulator

Magnet type	Pure Permanent (Nd-Fe-B)
Remanent Field	1.17 Tesla
Period Length	36 mm
Number of Period	26
Magnetic Length	936 mm
Overall Length	1.4 m
Minimum Gap	10 mm for low-β optics
	20 mm for present optics
Max. K-parameter	2.77 for low-β optics
	1.15 for present optics
Polarization	linear (horizontal)

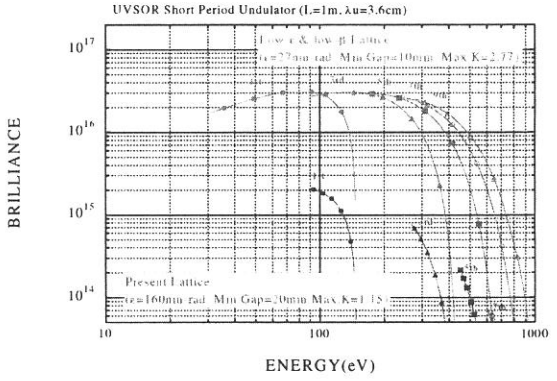

Fig. 1 Brilliance of the in-vacuum undulator for present and upgraded optics, calculated by SPECTRA [3]

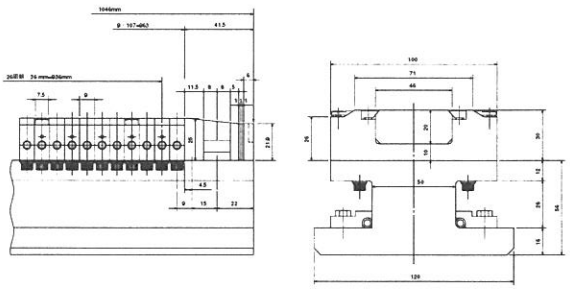

Fig. 2. Magnetic poles of in-vacuum undulator (under construction by Sumitomo Special Metals Co. Ltd.)

References

[1] M. Katoh et al., in this report
[2] H. Kitamura, J. Synchrotron Rad. (1998), 5, 184
[3] H. Kitamura and T. Tanaka, Synchrotron Radiation Calculation Program for Win32 Ver. 1.1 (1996)

An Upgrade Plan for UVSOR

Masahiro KATOH, Masahito HOSAKA, Shigeru KODA,
Jun-Ichiro YAMAZAKI, Toshio KINOSHITA, Kenji HAYASHI, Yoshifumi TAKASHIMA[A],
Yoichiro HORI[B], Toru HONDA[B]

UVSOR Facility, Institute for Molecular Science, Okazaki 444-8585 Japan
[A)]Department of VUV Photo-science, Institute for Molecular Science, Okazaki 444-8585 Japan
[B)]Photon Factory, Institute of Materials Structure Science,
High Energy Accelerator Research Organization (KEK), Tsukuba, 305-0801 Japan

1. Introduction

In these years, some of the second-generation synchrotron light sources has been or will be upgraded to compete with the third generation light sources [1, 2]. As stimulated by these works, we have started a design study on upgrading UVSOR. The goal is to realize (1) smaller emittance, (2) more straight sections for insertion devices with much smaller budget than that to construct a new ring.

2. Magnetic Lattice

The basic structure of the UVSOR magnetic lattice is double-bend achromat, which has totally eight straight sections between the bending magnets. However, four short straight sections are occupied by quadrupoles and sextupoles, as shown in Fig. 1. We have designed a new lattice, in which, the original DBA cells are modified as shown in Fig. 1. New four free space of 1.5 m are created at the short straight sections. There is no change on the bending magnets. All the quadrupole and sextupole magnets are replaced with combined function type magnets which are capable of producing both quadrupole and sextupole fields. The parameters of the new magnets are shown in Table 2.

Optical functions of the present and new lattice are shown in Fig. 2. The beam parameters are summarized in Table 1. A small emittance of 27 nm-rad can be achieved by making horizontal focussing stronger and by distributing the momentum dispersion in all the straight sections. The vertical betatron function is 1.5 m and 0.5 m at the center of the long and short straight sections respectively, which is optimized for installing narrow gap undulators.

Four families of sextupoles are used to compensate the linear chromaticity and to optimize the dynamic aperture. A tracking simulation has proved that the dynamic aperture is sufficiently large for injection and storage, as shown in Fig. 3.

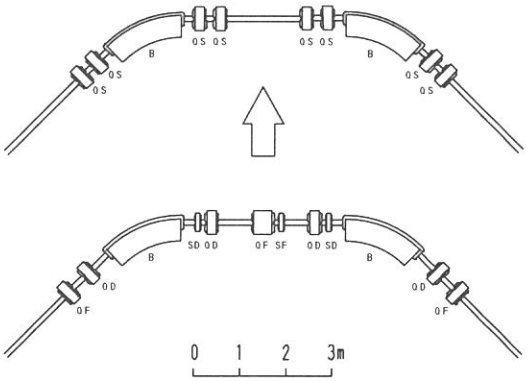

Fig. 1. Lattice modification. The lower is the present configuration and the upper is the upgraded one. One quadrant of the ring is shown. The sextupoles are integrated in the quadrupole magnets in the new lattice.

Table 1. Main Parameters of UVSOR

	Present	Upgraded
Circumference	53.2 m	
Lattice Type	DBA	extended DB(A)
Number of Cells	4	4
Straight Sections	3m x 4	4m x 4, 1.5m x 4
Beam Energy	750 MeV	
Emittance	165 nm-rad	27.4 nm-rad
Energy Spread	4.2×10^{-4}	
Betatron Tunes	(3.16, 1.44)	(3.75, 3.20)
Nat. Chromaticity	(-3.4, -2.5)	(-8.1, -7.3)
XY Coupling	~10%	
Mom. Comp. Factor	0.026	0.028
RF Frequency	90.115 MHz	
Harmonic Number	16	
RF Voltage	46 kV	>80 kV
RF Bucket Height	0.74 %	>1.1 %
Max. Beam Current	250 mA	> 250 mA
Beam Lifetime (200mA)	~6 hr	> 6hr

Table 2. Parameters of focusing magnets

Core Length	0.2 m
Bore Diameter	94 mm
Maximum Quadrupole Field	15 T/m
Maximum Sextupole Field	35 T/m^2

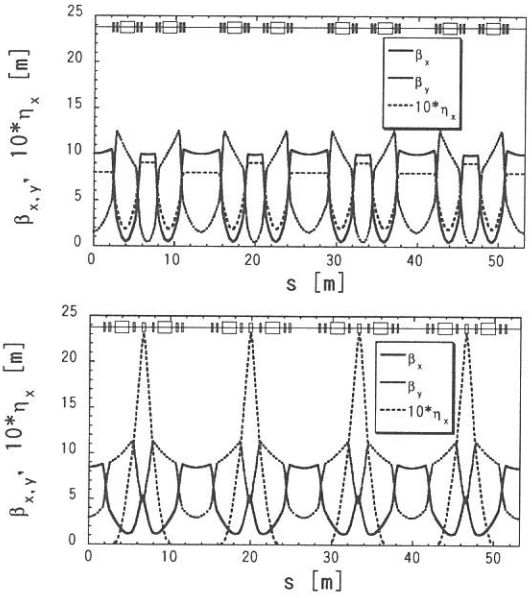

Fig.2. Optical functions of present (lower) and upgraded (upper) lattice.

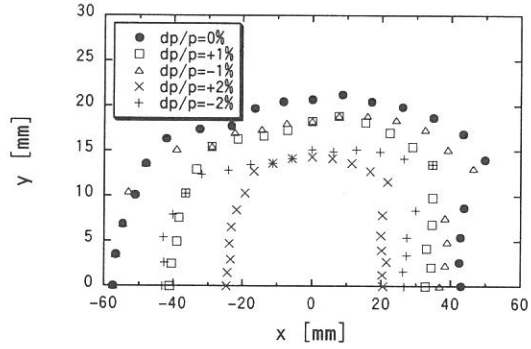

Fig. 3. Dynamic aperture calculated at the center of the long straight section of the new lattice. The results for momentum deviation within 2% are shown. A computer code SAD [3] is used for the simulation.

The reduced emittance will cause strong Touschek effect, which will dominantly limit the beam lifetime. This problem can be solved by increasing the RF accelerating voltage and by utilize the existing third harmonic RF cavity [4] in bunch lengthening mode.

3. Synchrotron Radiation Spectra

On the new lattice, totally six straight sections will be available for insertion devices. The existing undulators will cover the energy range from 10 to 100 eV with higher brilliance by one order of magnitude, as shown in Fig. 4. The small betatron function enables installation of in-vacuum and short period undulators. Their magnetic gap can be as small as 10 mm without reducing the lifetime. They can cover the energy range up to 500 eV and more, as shown in Fig. 4.

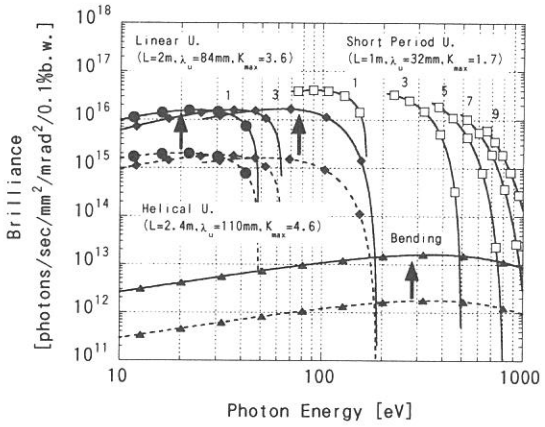

Fig.4. Synchrotron Radiation Spectra from the existing linear (black diamonds), helical (black circles) undulators, the bending magnet (black triangles) and an example of future short period undulator (white squares). The dashed lines are for the present lattice. The increase of the brilliance, as the result of lower emittance, is indicated with arrows. A computer code, SPECTRA [5] is used for the calculation. The beam current is 200 mA and the XY coupling is 10%. The undulator parameters are shown in the figure.

4. Summary

We have designed a new lattice for UVSOR, which has smaller emittance and more straight sections. The emittance will be 27 nm-rad, which is close to those of the third generation light sources. Totally six insertion devices can be installed. The small vertical betatron function at the straight sections enables us to install small gap and short period devices, which will cover much shorter wavelength than the existing undulators.

By introducing the new lattice as well as by replacing old accelerator components, the UVSOR will be converted to a high brilliance synchrotron light source in VUV and soft X rays, which can compete with the third generation light sources in next decade.

References

[1] M. Katoh et al., J. Synchrotron Rad. (1998). 5, 366

[2] S. Brennan and R. Hettel, Synchrotron Radiation News (1998). Vol. 11, No. 1, 25

[3] K. Hirata, 2nd Advanced ICFA Beam Dynamics Workshop, CERN 88-04 (1988)

[4] K. Tamura et al., Jpn. J. Appl. Phys. Vol. 33 (1994) p. L59

[5] H. Kitamura and T. Tanaka, Synchrotron Radiation Calculation Program for Win32 Ver. 1.1 (1996)

A New Method for Monitoring Bunch Length

M. Hosaka, S. Koda, M. Katoh, J. Yamazaki and H. Hama[a]

UVSOR Facility, Institute for Molecular Science, Myodaiji, Okazaki 444-8585
[a]Laboratory of Nuclear Science, Tohoku University, Mikamine, Taihaku-ku, Sendai 980-0826

We have developed a new method to measure bunch length by the detection of the synchronous phase shift on the UVSOR storage ring. Conventionally bunch length is measured by using optical methods in which a longitudinal profile of bunch is evaluated from synchrotron radiation. For example, a dual-sweep streak camera can provide a lot of information about electron distribution in a bunch over a wide dynamic range, but it takes at least several minutes to evaluate one numerical result and an instantaneous resolution is limited. In our new method, a longitudinal profile of the bunch is picked up using an electrode and bunch length is obtained through synchronous phase information. Although information available is limited, a continuous observation is possible using the method.

The principle of the methods is based on the bunch length dependence of the loss factor of beam bunch. The loss factor is a parameter used to characterize an energy loss of the electron beam due to the interaction with the vacuum chamber impedance and is defined by

$$k = \frac{\Delta E}{e^2 N_b^2}, \tag{1}$$

where ΔE, e and N_b are the energy loss per tune for an electron bunch, the electron charge and the total number of electron in the bunch, respectively. Assuming that the bunch distribution is Gaussian with RMS bunch length σ_τ, the loss factor can be expressed as

$$k = \frac{\pi I_0^2}{e^2 N_b^2} \int_{-\infty}^{\infty} Z_{res}(\omega) e^{-\omega^2 \sigma_\tau^2} d\omega, \tag{2}$$

where I_0 and $Z_{res}(\omega)$ is the total bunch current and the resistive part of the longitudinal coupling impedance at the frequency of ω. With Eq. (2), one can get for example

$$k \propto \begin{cases} \sigma_\tau^{-1} & \text{for } Z_{res} \text{ is constant} \\ \sigma_\tau^{-2} & \text{for } Z_{res} \propto \omega \end{cases}. \tag{3}$$

Thus the loss factor depends strongly on the bunch length.

In order to obtain a scaling law between the loss factor and the bunch length in the UVSOR storage ring, simultaneous measurements between the loss factor and the bunch length have been performed. In the UVSOR storage ring, the most efficient way to lengthen the electron bunch is by using FEL-induced bunch heating [1]. A visible wavelength of 520 nm for the FEL oscillation was chosen because the FEL gain at the wavelength is rather high, and then the phase shift would be measured over a wide range of the bunch length. Since the energy loss of the electron bunch is compensated by the rf cavity field, the loss factor can be deduced from the synchronous phase shift $\Delta\phi$ as

$$k = \frac{V_{rf} \left| \sin(\phi_{s0} + \Delta\phi) - \sin\phi_{s0} \right|}{eN_b} \tag{4}$$

where ϕ_{s0} corresponds to the synchronous phase for a zero beam current and V_{rf} the peak accelerating voltage in the rf cavity. The setup for the synchronous phase detection is shown in Fig. 1. In order to obtain the beam

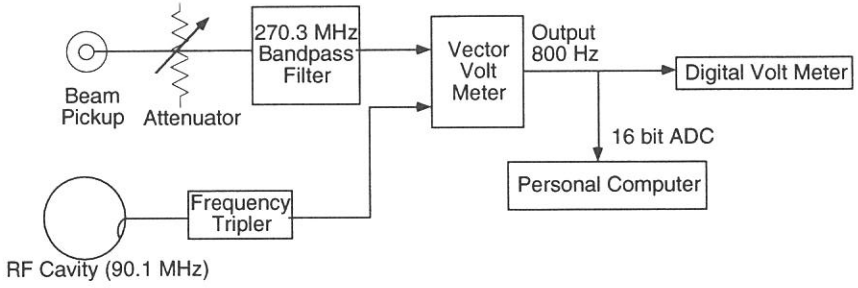

Fig. 1 Setup for the synchronous phase detection.

phase with high resolution, a frequency of 270 MHz which correspond to the 3rd harmonics of the rf frequency has been chosen for the measurement. In the system, the phase information of the bunch can be recorded at a rate of 800 Hz. At the same time, longitudinal bunch profiles have been taken by using a dual-sweep streak camera. The bunch length has been varied up to 400 ps (RMS) with a higher beam current from the natural bunch length of 115 ps.

The loss factors are deduced from the measured phase shift using Eq. (4) and are plotted as a function of the bunch length in Fig. 2. As seen in the figure, the relation between the loss factor and the bunch length does not completely obey the simple scaling law as in the SPEAR storage ring [2]. It is probably due to the resistive-wall impedance, which plays an important role at the low frequency region. Accordingly we introduce offsets for both the bunch length and the loss factor and perform a fitting with these parameters. The result of fitting is shown as a solid line in Fig. 2 and the fit is apparently good. The relation between the loss factor and the bunch length is written using the fitting parameters as

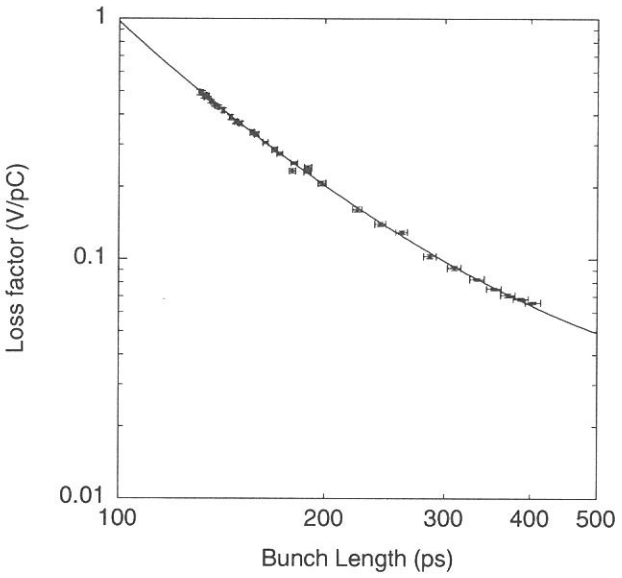

Fig. 2 Dependence of the loss factor on the bunch length. The solid line is the result of the fitting given in Eq. (5).

$$(k - 0.0234) = 3180(\sigma_\tau - 28.9)^{-1.90} \qquad (5)$$

where the loss factor k and the bunch length σ_τ are measured in units of [V/pC] and [ps], respectively. In the UVSOR storage ring the resistive part of the longitudinal coupling impedance is seemed to depends linearly on the frequency (see Eq. (3)). With the scaling low given in Eq. (5), we can deduce the bunch length from the information of the synchronous phase shift. In our present system shown in Fig. 2, we can detect the phase shift at the rate of 800 Hz that is the sampling rate of the vector volt meter used in the system. This allows measuring the variation of bunch length continuously within the rate. The new method for monitoring bunch length has already been used for experiments on the bunch lengthening associated with the FEL power variation [3].

References

[1] M. E. Couprie, D. Garzella, A. Delboulbe, M. Velghe and M. Billardon, Nucl. Instr. and Meth. A 331 (1993) 84.

[2] P. B. Wilson, R.V. Servanckx, A. P. Sabersky, J. Gareyte, G. E. Fischer and A.W. Chao, IEEE Trans. NS-24 (1977) 1211.

[3] M. Hosaka, S. Koda, M. Katoh, J. Yamazaki and H. Hama Nucl. Instr. and Meth. A (in press)

Study for pump and prove experiment using the UVSOR-FEL

Shigeru KODA, Masahito HOSAKA, Jun-ichiro YAMAZAKI, Masahiro KATOH, Kenji HAYASHI, Hiroyuki HAMA[1], Tatsuo GEJO and Eiji SHIGEMASA

UVSOR Facility, Institute for Molecular Science, Myodaiji, Okazaki 444-8585, Japan

[1]Laboratory of Nuclear Science, Tohoku University, Sendai 982-0826, Japan

Storage ring free electron lasers (SRFELs) have potentially advantages for pump and prove (two-color) experiments because of spectral tunability and natural synchronism between synchrotron radiation (SR). However, in a practical operation of the SRFEL extreme stable lasing and higher out-coupled power are crucial for the pump prove experiment. Performance of the UVSOR-FEL has been steadily improved by installation of sturdy cavity-mirror chambers employing simple structure and heavy bases against mechanical vibrations [1], and development of a longitudinal feedback system for stable FEL oscillation [2]. At present, we are planning a pump and prove experiment to investigate dynamics of highly excited state of atomic Xe. A shown in Fig. 1, the target Xe is excited to the $5p^5(^2P1/2)4f[5/2]_2$ autoionization resonance via the $5p^5(^2P3/2)5d[5/2]_1$ intermediate state by using a sequential two-color photoreaction with SR (119 nm) and the FEL (570 nm). Photoelectron energy spectra emitted from the resonance state will be measured. According to an estimation of the photoelectron rate, an FEL average-power of 50 mW would be at least required.

The first test experiment to provide the FEL and SR into a Xe target chamber was carried out at an SR beam line of BL7B in November 2000. In order to increase the out-coupled power, a multilayer of Ta_5O_2/SiO_2 with large transmission 1100 ppm were used as the optical cavity mirrors. In addition, an FEL transport system to the BL7B was newly developed. A schematic figure is shown in Fig. 2. The transport path-length of the FEL is longer than the SR path-length by just a half circumference of the storage ring to synchronize the FEL with SR.

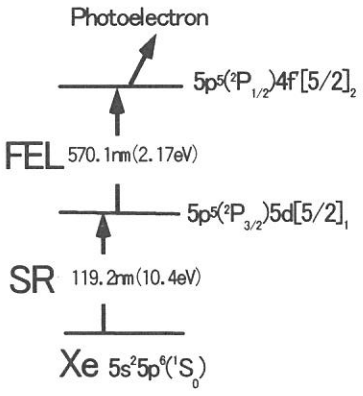

Fig. 1 Energy diagram of the Pump & prove experiment.

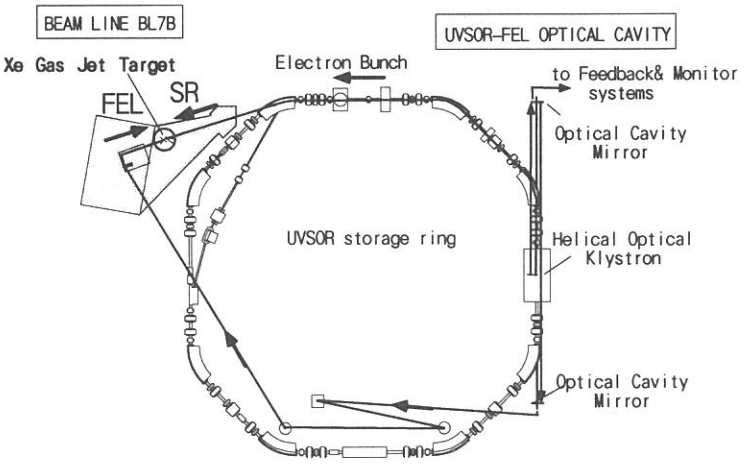

Fig.2 The FEL and SR transport system

Synchronism between the FEL and SR at the Xe target position was roughly measured by a photo diode. A result after a preliminary adjustment of the FEL path-length is shown in Fig. 3. Arrival time of the FEL pulse at the target position was successfully adjusted within an accuracy of 1 ns (in the actual experiment, the path length will be precisely adjusted by detecting of the photoelectron event rate).

The longitudinal feedback system of the UVSOR-FEL detects temporal deviation between an electron bunch and an FEL micropulse by measuring higher harmonics of those signals in the frequency domain, and regulates the accelerating rf frequency of the storage ring to reduce the temporal deviation [2]. The synchronism between the electron bunch and the FEL micropulse is able to be held with high accuracy, and as a result CW lasing is maintained with small power fluctuation for long time. However we have experienced that the FEL power sometimes drops because of a transverse mode change due to probably thermal deformation of the optical cavity. Consequently we has to change manually the transverse axes of the cavity mirrors several times in an hour. In addition, the FEL wavelength drifts slowly (a rate of approximately 0.1 nm/hour), we changes the optical-klystron gap by about 10 μm.

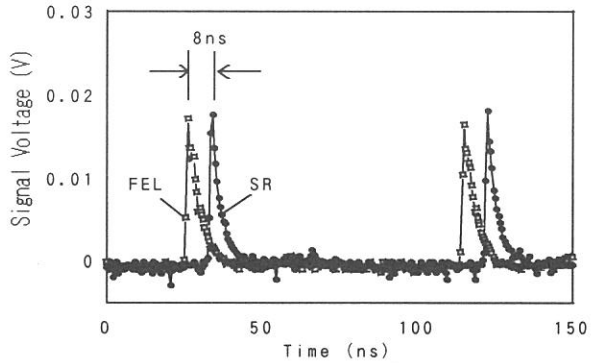

Fig. 3 Measurement of synchronism between SR and the FEL signals by a photodiode whose response time of about 1 ns. The photodiode detected SR and the FEL at a downstream position located 1.2 m from the Xe target position along the SR beam axis. Therefore arrival time of SR and the FEL at the photodiode has to be shifted by 8 ns.

The performance of the UVSOR-FEL is briefed in Table 1. The FEL property attained roughly the required power and the stability. At the moment, the photoelectron from the resonance state was not clearly observed in the experiment because of high background event rate due to SR scattering in the target chamber. The chamber and the detector system are being improved to suppress the background efficiently. On the other hand further developments of the UVSOR-FEL is discussed to reduce the power degradation and the drift of the wavelength.

Table 1 Attained performance of the UVSOR-FEL

Wavelength	570.1 nm
Line width (σ)	0.1 nm
Optical pulse width(σ)	~10 ps
Tunable range	10～20 nm
FEL out-coupled power (100mA/2bunch)	150 mW(=13nJ/pulse)
at BL7B (including transport loss)	100 mW
FEL power fluctuation	～5 %
Time jitter between SR and FEL (σ)	～30 ps (with the feedback)
Repetition rate	11.26 MHz (2 bunch operation)
Electron beam lifetime	100～150 min

Reference

[1] S. Koda, J. Yamazaki, M. Hosaka, H. Hama, Proceedings of the 4th Asian Symposium on Free Electron Lasers and Korea-Russia Joint Seminar on High-Power FELs, Korea (1999), 36-41, KAERI.

[2] S. Koda, M. Hosaka, J. Yamazaki, M. Katoh and H. Hama, Proceedings of the 22nd International Free Electron Laser Conference and 7th FEL Users Workshop, Durham, North Carolina USA, August 2000

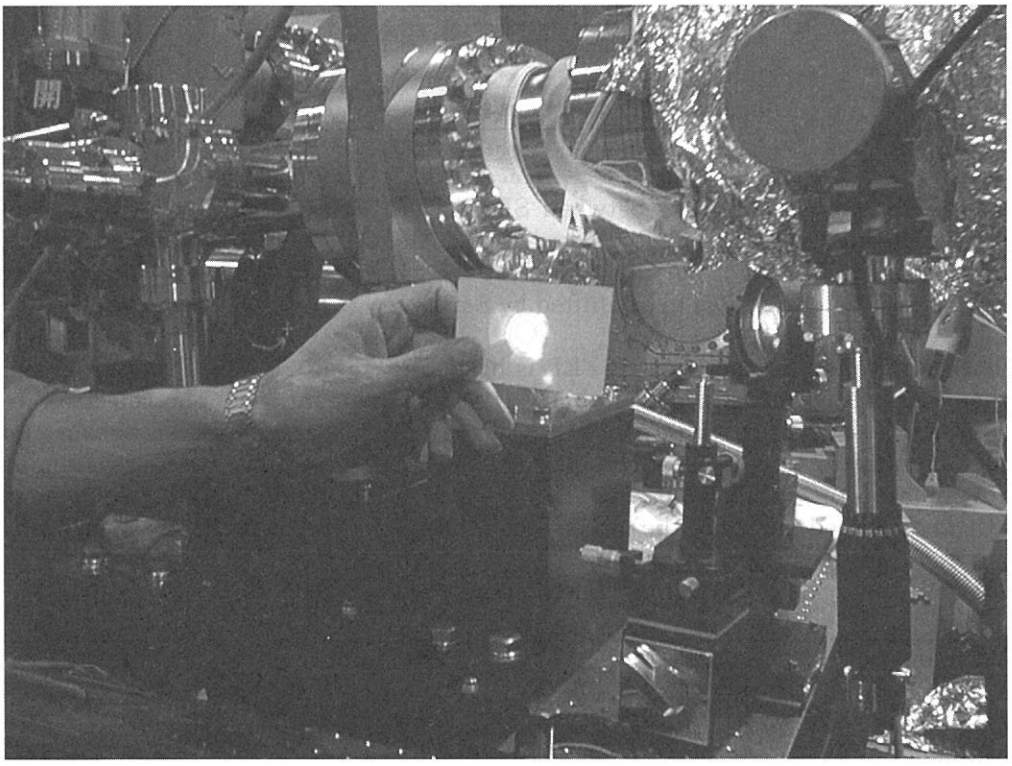

UVSOR

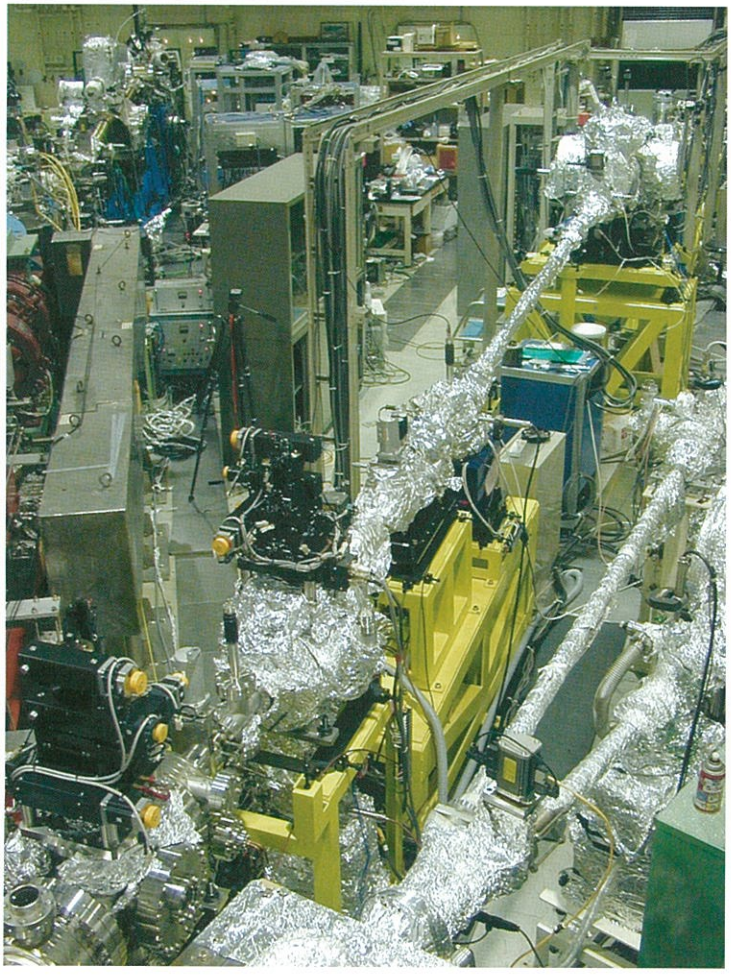

Instrumental Developments

(BL2B1)

Fourth electron-ion coincidence spectroscope adapting a Siegbahn-type coaxially symmetric electron energy analyzer

Koji Isari, Kenichiro Tanaka, Kazuhiko Mase,[A] Shin-ichi Nagaoka,[B]

Department of Physics Science, Faculty of Science, Hiroshima University, 1-3-1Kagamiyama, Higashi-Hiroshima 739-8527
[A]Photon Factory, Institute of Materials Structure Science, High Energy Accelerator Research Organization, 1-1 Oho, Tsukuba 305-0801
[B]Institute for Molecular Science, Myodaiji Okazaki 444-8585

Energy-selected electron ion coincidence (EICO) spectroscopy is an ideal tool for investigations of the ion desorption mechanism induced by electronic transitions, because it provides mass spectra for the ion desorption channels related to the selected electron transitions [1]. One of the authors has developed three EICO analyzers at BL-2B1 for the study of surface dynamics so far [2]. To achieve a fair signal-to-background ratio, the solid angles of the electron energy analyzer and the time-of-flight mass spectrometer (TOF-MS) have been improved. In the present article, we report the design of the fourth EICO analyzer. The EICO analyzer is constructed on a 203-mm-diameter conflat flange as a bolt-on instrument, which consists of a Siegbahn-type coaxially symmetric mirror electron energy analyzer [3] for detection of energy-resolved electrons, a TOF-MS for ion detection and an xyz stage for position adjustment. Figure 1 shows a photograph of the fourth EICO apparatus. The solid angle of the electron energy analyzer (1.2 sr) is designed to achieve a fair signal-to-background ratio within a reasonable data collection time. The TOF-MS is located coaxially to the electron energy analyzer. The surface normal of sample is set coaxially to the electron energy analyzer and the TOF-MS. The performance of the electron energy analyzer was examined at BL-2B1. The sample was a gold film without surface cleaning. The electron states of the surface were excited by *p*-polarized radiation with an incident angle of 60° with respect to the surface normal. The base pressure was 1.8×10^{-10} Torr. Figure 2 shows the photoelectron spectrum at hυ = 350 eV in Au 4f region. Based on Gaussian curve fitting the energy resolution was estimated to be $E/\Delta E = 130$ at the $4f_{7/2}$ peak, full width at half maximum (FWHM) of which was 2.0 eV.

References

[1] K. Mase *et al.*, *J. Electron Spectros. Relat. Phenom.* **101-103**, 13 (1999).
[2] K. Mase *et al.*, *UVSOR ACTIVITY REPORT 1999*, 35 (2000).
[3] K. Siegbahn *et al.*, *Nucl. Instr. and Meth. in Phys. Res.* **A384**, 563-574 (1997).

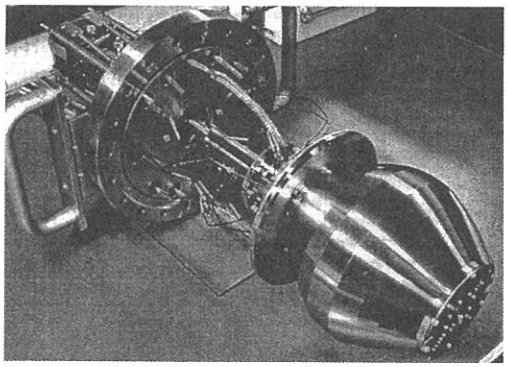

Figure1. Photograph of the fourth EICO analyzer.

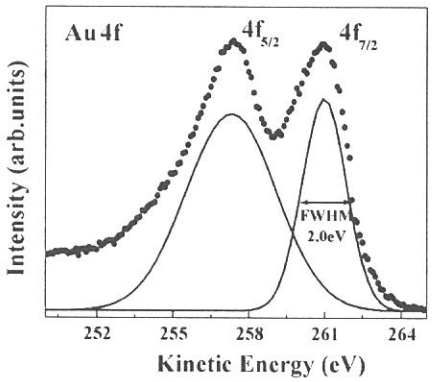

Figure 2. Au 4f photoelectron spectrum taken at a photon energy of 350 eV with the Siegbahn-type coaxially symmetric mirror electron energy analyzer.

(BL2A)

Development and evaluation of a video-microscope-computer system for observiation and analyses of behavioral responses of microorganisms to ultraviolet light from the synchrotron radiation light source

Shigeru Matsunaga[1] , Terumitsu Hori[1], Sho-ichi Higashi[2], Shinji Ito[2,3], Tetsuo Takahashi[4], Yasutaka Takata[5], Takaki Hatsui[5], Nobuhiro Kosugi[5] and Masakatsu Watanabe[2,3]

[1]Institute of Biological Sciences, University of Tsukuba, Tsukuba 305-8532 ; [2]National Institute for Basic Biology, Okazaki 444-8585; [3]Department of Photoscience, School of Advanced Sciences, Graduate University for Advanced Studies, Hayama 240-0193; [4]Japan Advanced Institute for Science and Technology, Tatsunokuchi 923-1292; [5]Institute for Molecular Science, Okazaki 444-8585

Single-celled microorganisms such as cyanobacteria, halophilic archaea (formerly called archaebacteria) and unicellular flagellate algae show behavioral responses to visible and UV light so that they can accumulate in suitable or avoid harmful light conditions (e. g.[1-4]). Because they originated in Precambrian era, much before the establishment of the stratospheric ozone layer, they must have had, thus may well even now have, sensitive behavioral responses to avoid shorter-wavelength UV (e. g. 220-300 nm), than the present-day terrestrial UV (of wavelengths longer than ca. 300 nm because of the ozone layer). Indeed, we have demonstrated that the unicellular flagellate alga *Euglena* ("Midorimushi" in Japanese) cells do show clear photoavaidance as well as photoaccumulation responses even at 280 nm [3]. It is therefore interesting and meaningful to extend such wavelength-dependency studies into shorter wavelength regions of UV, artificially obtainable from the synchrotron radiation, in order to understand bio-molecular mechanisms as well as ecological and evolutionary significance of the short-wavelength-UV-sensing in such microorganisms.

Preliminary measurement with calibrated Si photodiodes indicated that the maximun monochromatic UV light fluence rate at BL2A of UVSOR at 200 nm at the ring current of 180 mA is ca. $2x10^{10}$ photons/mm^2/s (ca. 0.03 μmole/m^2/s) , which is 1 order of magnitude lower than that needed to induce the behavioral responses of *Euglena* cells [5]. Therefore a quartz lens was mounted on the otpical axis to condense the monochromatic UV light on to the sample suspension in a qurarts chamber on the stage of a microscope connected to a CCD camera (Fig.1a, b). Slantly projocted observation light beam from a microscopic projector was usually filtered through an infrared- or a red-transmitting filter before reaching the sample. The images of the *Euglena* cells were recorded at the viedo-rate of 30 frames/s using a video-recorder and were thereafter analysed on a Macintosh computer using the public domain NIH Image program (developed at the U.S. National Institutes of Health and available on the Internet at http://rsb.info.nih.gov/nih-image/) .

By using the above-described system, we have succeeded in detecting the behavioral responses of the *Euglena* cells to avoid the monochromatic UV light of 220 nm in wavelength: Fig. 2 shows that the cells avoid the central round area which is irradiated with the 220 nm UV light condensed by the quarts lens. After some more refinement of the system especially in terms of microscopic-scale positional reproducibility and numerical quantification of the behavioral responses, extensive experiments on wavelength- and fluence-rate-depencency of the behavioral responses in various microorganisms will become possible.

Acknowledgements

We thank Profs. Toshio Ibuki (Kyoto University of Education), Kazumichi Nakagawa (Kobe University), Kotaro Hieda (Rikkyo University) and Mr. Mamoru Kubota (National Institute for Basic Biology) for their advice and help in measurement of fluence rates of the monochromatic UV light at BL2A. Shigeru Matsunaga acknowledges support from Technology Department of IMS under the Technical Staff Training Progaram.

References

[1] Choi, J.-S., Chung, Y.-H., Moon, Y.-J., Kim, C., Watanabe, M., Song, P.-S., Joe, C.-O., Bogorad, L. and Park, Y. M.: *Photochem. Photobiol.* 70, 95-102 (1999). [2] Takahashi, T., Yan, B., Mazur, P., Derguini, F., Nakanishi, K. and Spudich, J. L.: *Biochem.* 29, 8467-8474 (1990). [3] Matsunaga, S., Hori, T., Takahashi, T., Kubota, M., Watanabe, M., Okamoto, K., Masuda, K. and Sugai, M. : *Protoplasma* 201, 45-52 (1998). [4] Watanabe, M.: In *CRC Handbook of Organic Photochemistry and Photobiology.* pp. 1276-1288 (1995). [5] Matsunaga, S.: Doctoral Thesis, Univ. Tsukuba (1999).

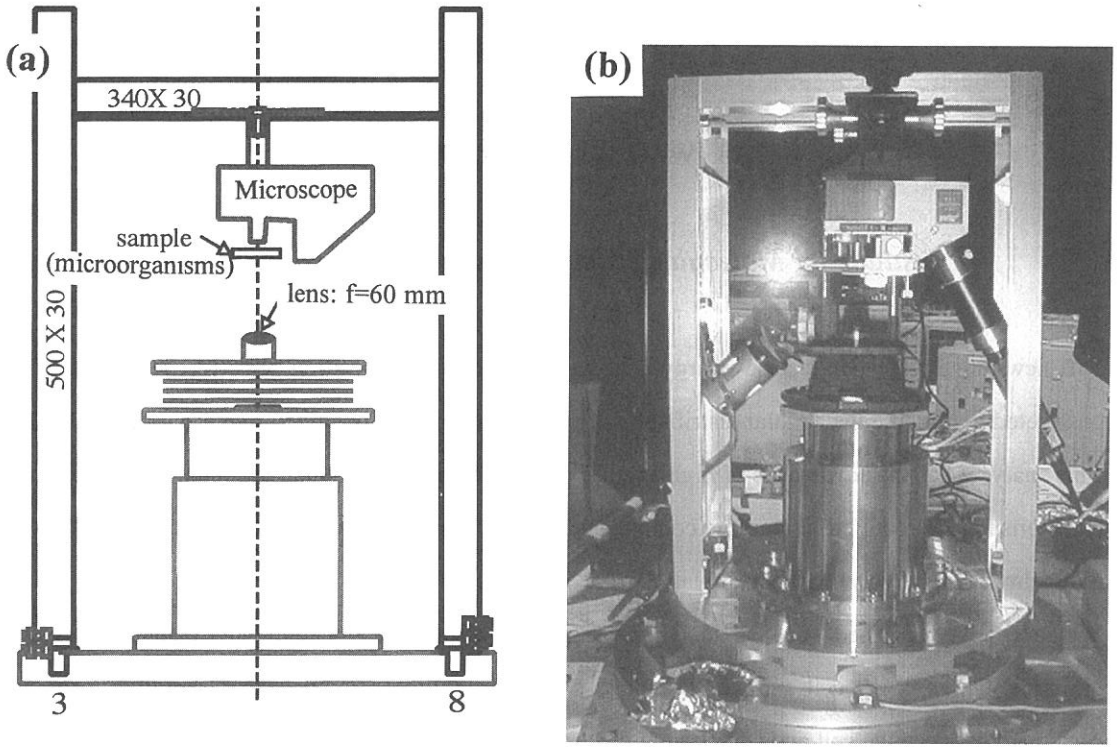

Fig. 1 a, b. Schematic layout (**a**) and photograph (**b**) of the video-microscopic system for observation of behavioral responses of microorganisms to monochromatic UV light from BL2A of UVSOR. The UV light beam is projected vertical-upwardly.

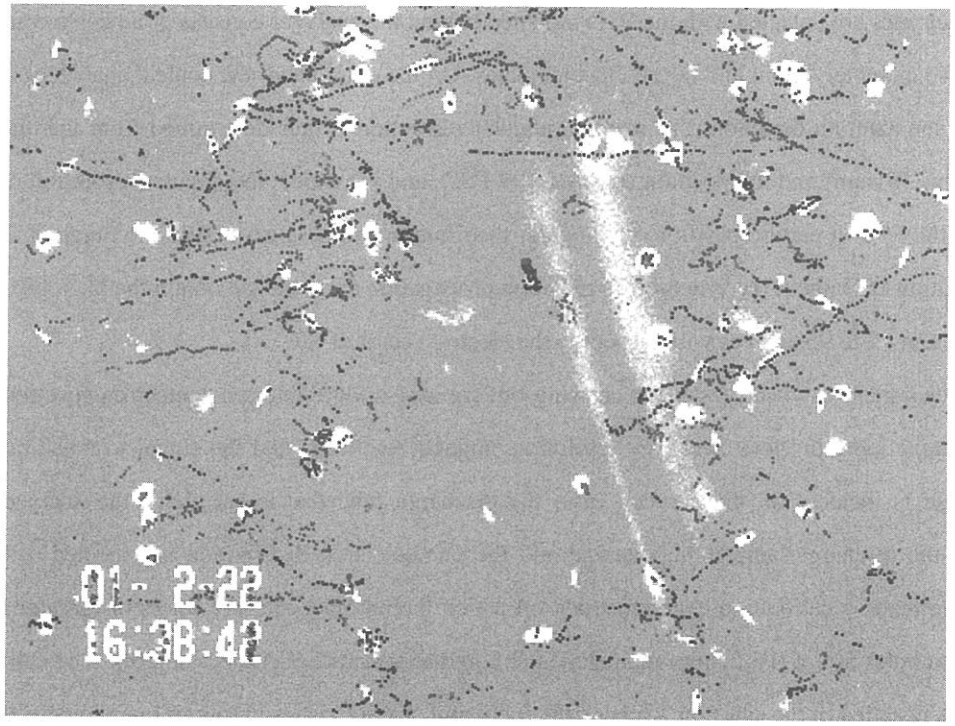

Fig. 2. Swimming tracks, in 8 s, of *Euglena* ("Midorimushi" in Japanese) cells. The cells are avoiding the central round area irradiated with monochromatic UV light of 220 nm in wavelength.

(BL-3B)

Construction of a conical energy analyzer for angle-resolved photoelectron spectroscopy

Kota IWASAKI and Koichiro MITSUKE

Institute for Molecular Science, Myodaiji, Okazaki 444-8585, Japan

A new angle-resolved electron energy analyzer incorporating a position sensitive detector (PSD) has been constructed to measure the angular distribution of photoelectron from polarized rare gas atoms in BL3B.

This analyzer has the advantages of high angular resolution and wide angular acceptance simultaneously. These characteristics are required to measure complicated angular distributions of photoelectrons caused by the atomic alignment with relatively short accumulation time of signals.

We have newly designed a conical analyzer consisting of a set of an inner and outer conical deflector electrode, cylindrical lenses, a gas cell and a PSD unit as shown in Figure 1. Photoelectrons emitted in the gas cell are accelerated between the cell and an extractor electrode, then focused on an entrance slit by the cylindrical lenses. The electron trajectories between the inner and the outer conical electrodes are similar to those expected for a conventional parallel-plate analyzer. However, the conical analyzer has considerably larger energy dispersion and larger angular aberration than the parallel-plate analyzer. Energy selected electrons exiting out of the conical deflector electrodes are detected with the PSD mounted behind the analyzer consists of a resistive anode encoder of an effective diameter 40mm and micro-channel plates. On the other hand, the conical analyzer is incapable of focussing in the azimuth direction. The azimuth angular resolution is thus determined from the diameter of the sample volume (ϕ1mm) and the position sensitivity of PSD, and we expect the angular resolution of 1.5 degree. With fixing the PSD at certain position, the angular distribution can be measured in the range of 25 degrees at once. By rotating PSD about the synchrotron radiation propagation axis, we can obtain the photoelectron angular distribution from –5 to 95 degrees with respect to the electric vector of SR.

Our analyzer system has been tested by carrying out gas phase ultraviolet photoelectron spectroscopy with a helium discharge lamp in view of energy resolution, angular resolution and the signal to noise ratio. The HeI (58.4nm) light is incident on the gas cell from the discharge tube that is set above the analyzer. The light produced in the discharge lamp is unpolarized and the photoelectron distribution is expected to be isotropic. Therefore, we made a calibration cone electrode on which the entrance slit is a series of circular holes as test objects. These holes are of 0.5-2.0mm diameters and bored at intervals of 4.5-8.5 degrees. The calibration cone electrode was installed in the analyzer to check the focussing characteristics by observing photoelectrons passing through the circular holes.

In the first stage of the performance test, extremely high background due to low energy electrons was a serious problem. We have measured the dependence of the rate of the background on the transmission energy, deceleration energy of cylindrical lens and the Ar gas pressure to examine the origin of background electrons. The result showed that the background signals are caused by the photoelectrons emitted from the metal surfaces near the gas cell.

We have therefore tried to prevent the photoelectrons from entering the detector by setting a photoelectron shield applied at a potential of 20V. Consequently, the background signals have been suppressed to about 1/100 comparing to those before the improvement. The following performance test is being carried out.

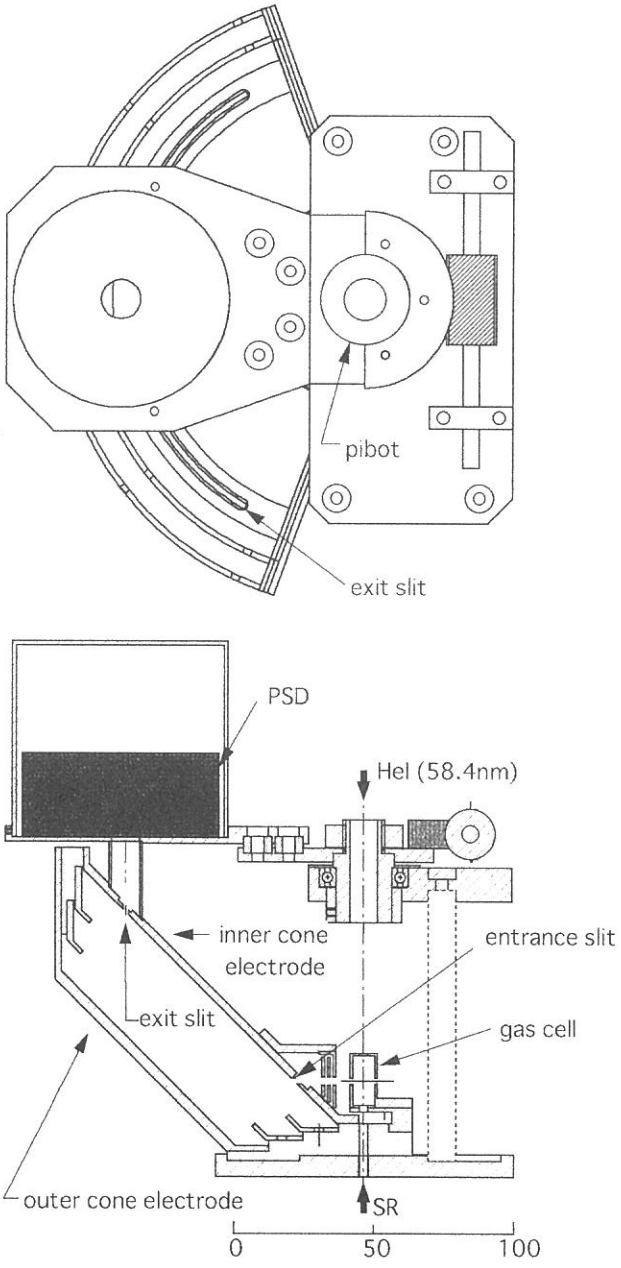

Figure 1. Schematic diagram of the conical analyzer. Synchrotron radiation is introduced in the gas cell through a plate holding all the electrodes and HeI light is so as to counterpropagate the SR.

BL4A-2

Reconstruction of BL4A Beam Line and Infrared Reflection Absorption Spectroscopy System

Zhihong Wang[1], Hideyuki Noda[1], Youichi Nonogaki[2] and Tsuneo Urisu[1,2]

([1]The Graduate University for Advanced Studies, [2]Institute for Molecular Science)

Re-arrangement of the beam line at BL4A has already started this year. Now it is still under construction. The IRRAS(Infrared Reflection Absorption Spectroscopy) system has been moved from BL4B to BL4A2. The reaction gas lines have been reconstructed connecting with new interlock system. The reaction chamber for IRRAS measurement was also reconstructed. The new system only use one chamber instead of formal two for the sample transfer to the measurement chamber to make the transfer more easy and efficient. The interlock system connecting these chambers and turbo molecular pumps also has been changed to the more simple and practical one.

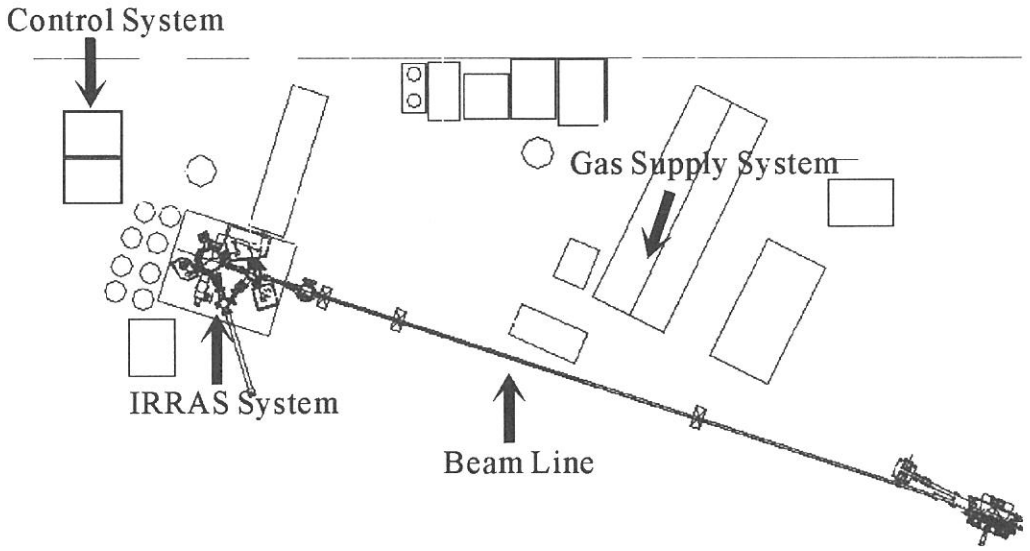

Figure 1 BL4A2 and IRRAS system after reconstruction

(BL6B)

Construction of BL6B for UHV-STM Observation of Si Surfaces Irradiated by Synchrotron Radiation

Y. Nonogaki, Y. Gao[a], H. Noda, Z. Wang, T. Urisu

Institute for Molecular Science, Myodaiji, Okazaki, 444-8585, Japan

[a]*The Graduate University for Advanced Studies, Myodaiji, Okazaki, 444-8585, Japan*

Synchrotron radiation (SR) processing including selective cleaving of chemical bonds through the tunability of the photon energy by exciting certain dissociative energy levels, has advantages of lower damage in comparison to plasma processes, high spatial resolution and aspect ratio because of the shorter wavelengths, and the applicability to thick insulating materials were nanofablication techniques based on charged particles such as electron beam lithography cannot be used.

STM observations are important for investigation of the SR illumination effect on Si surface for surface photochemistry and semiconductor technology for nanostructure fabrication. Our group has reported the SR stimulated cleaning of Si (111) by using BL4B in UVSOR[1-3]. In a pure thermal cleaning, the Si wafer had to be heated to > 850°C and, additional long hours of annealing at 700 °C was required to obtain the thermal equilibrium surface. In a SR stimulated cleaning, on the other hand, the desorption of SiO_2 occurred at much lower temperatures (650-700°C) and atomically flat surfaces free of voids, which inevitably appeared in a pure thermal desorption at these low temperatures, were observed.

We also found an interesting nanostructure formed on Si (111) surface by SR stimulated cleaning. At upper right corner in Fig. 1 a strip terrace of which width quantized to the unites of 7x7 unit cell were observed. It shows that the steps align along the boundaries of the 7x7 unit cell. We think combination of the SR stimulated cleaning and a vicinal surface realize an ordered structure on the surface with the straight steps separated by the width quantized terraces. Now we are preparing to investigate surface misorientation effects on step alignment.

In last year, we moved all the BL4B beam line components into BL6B and reconstructed them. The base pressures achieved now at the pre-mirror and beam line are ~1x10^{-9} Torr and ~3 x 10^{-9} Torr, respectively. However, the vacuums, introducing SR light into beam line, become worse due to the degas from mirror and beam line itself. We are now drying beam line components.

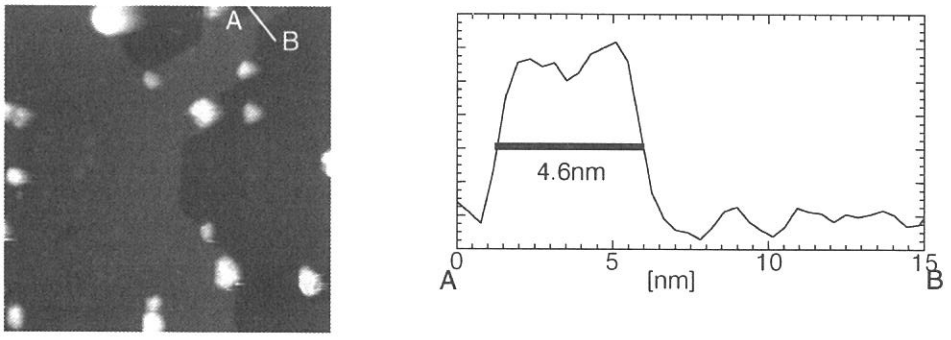

Figure 1: 100 nm x 100 nm STM topograph and line profile across the stripe at the upper-right-hand side coner. The sample is a Si (111) substrate after 5 h of SR irradiation at 650°C.

[1] T. Miyamae, H. Uchida, I.H. Munro and T. Urisu, J. Vac. Sci. Technol. A18, 1 (1999).

[2] Y. Gao, H. Mekaru, T. Miyamae and T. Urisu, Appl. Phys. Lett. 76, 1392 (2000).

[3] Y. Gao, H. Mekaru, T. Miyamae and T. Urisu, J. Vac. Sci. Technol. A 18, 1053 (2000).

(BL4B)

The first performance tests for a new monochromator on BL4B

Eiji Shigemasa, Tatsuo Gejo, Naonori Kondo, Hiroshi Oji, Mitsuru Nagasono, Takaki Hatsui, and Nobuhiro Kosugi

Institute for Molecular Science, Okazaki 444-8585, JAPAN

In order to realize various studies on vibrational spectroscopy in the soft x-ray range (100 ~ 1000 eV), which contains the *K*-shell thresholds of chemically important elements like C, N, and O, the construction of a new grazing incidence monochromator on BL4B at the UVSOR has begun. The Varied-line-spacing Plane Grating Monochromator (VPGM) has been chosen for this work [1] and its installation has been successfully finished in October 2000. The vacuum condition was ready for obtaining the first SR light until the end of December 2000, and the first performance tests for the monochromator have just been started.

The absolute photon flux for two gratings available so far (267 and 800 l/mm) has been measured using a Si photodiode supplied by IRD Inc. With the entrance and exit slit openings set at 25 and 10 μm, corresponding to the resolving power of 10000 at 400 eV with the 800 l/mm grating, the photocurrent from the photodiode was measured after the sample position, and converted into the absolute photon flux, taking account of the quantum efficiency of the photodiode. In this case, the resolving power in the regular spectral region for each grating is more than 3000. The throughput photon flux measured ranges from 10^8 to 10^9 photons/sec for the ring current of 100 mA, which is a little smaller than that estimated.

The inner-shell photoabsorption spectra of Ar and N_2 were measured, to demonstrate the instrumental resolution. The *K*-shell photoabsorption spectrum of N_2 at the N 1s $\rightarrow \pi^*$ resonance is presented in Fig. 1. The entrance and exit slits were set for achieving the resolving power of 10000. From the comparison with all available spectra of the N 1s $\rightarrow \pi^*$ resonance of N_2, it seems to be reasonable that the resolving power obtained here is more than 5000. The photoabsorption spectrum in the vicinity of the 2p ionization thresholds of Ar (~250 eV) was also recorded using the 800 l/mm grating, with slit openings of 50 and 10 μm, for the entrance and exit slits, respectively. The Ar 2p $\rightarrow$ nd Rydberg series up to n=7 are observed. This implies that the resolving power is more than 8000 at this photon energy region, and is in good accord with the theoretically predicted value.

To improve the total throughput of the monochromator, further fine tunings for all optical elements through the performance tests is obviously necessary. Experiments for angle-resolved photoion spectroscopy and photoelectron spectroscopy in a gas phase are expected to be started in the near future.

Reference

[1] Y. Takata, T. Gejo, and E. Shigemasa, UVSOR Activity Report 1999, p. 42.

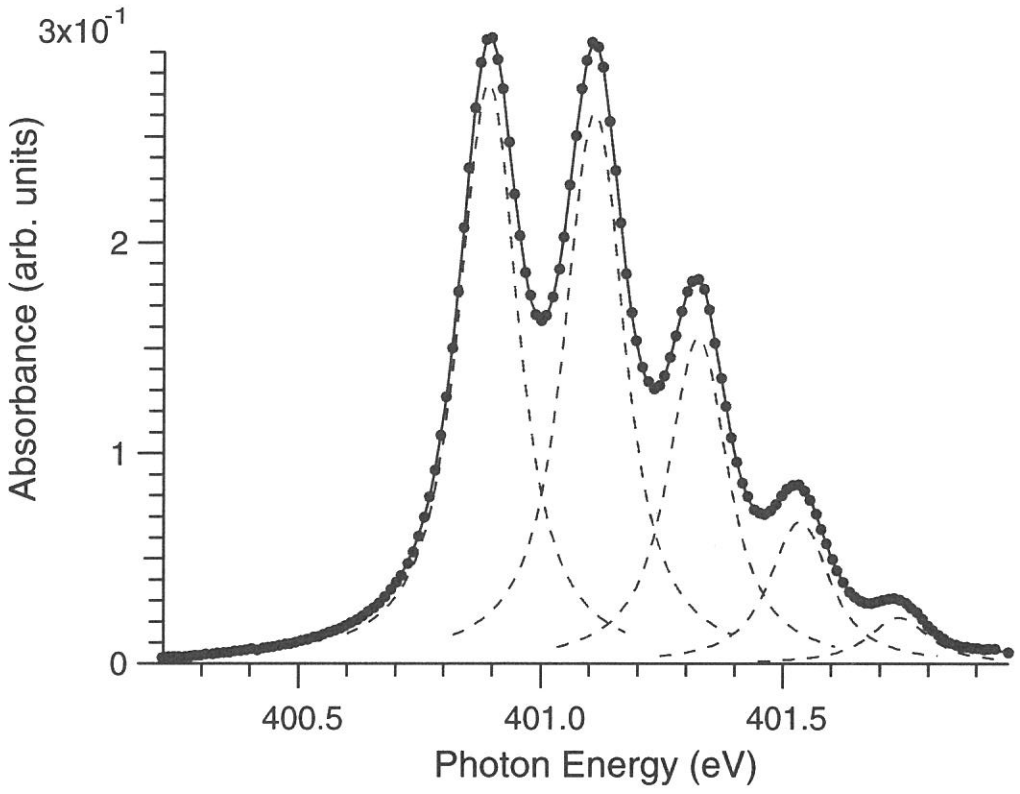

Figure 1. *K*-shell photoabsorption spectrum of N_2 at the N 1s $\rightarrow \pi^*$ resonance.

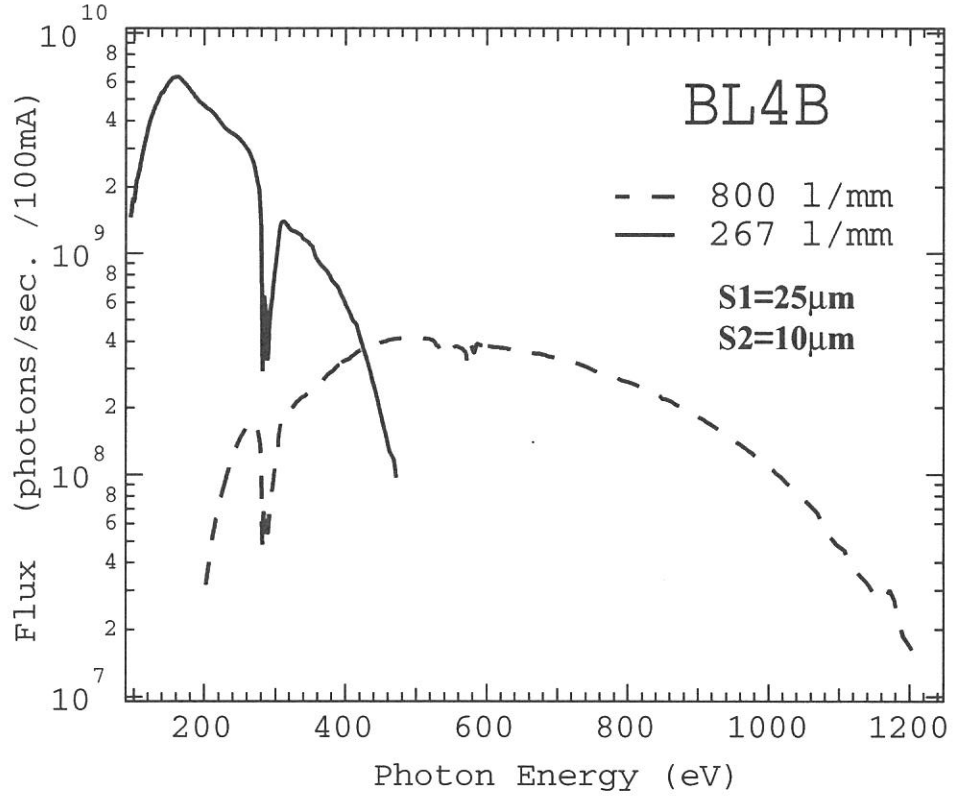

Figure 2. Absolute photon flux measured by a Si photodiode.

(BL4B)

The Resolving Power of the New Monochromator at BL4B

Mitsuru Nagasono, Eiji Shigemasa, Tatsuo Gejo, Hiroshi Oji, Takaki Hatsui, and Nobuhiro Kosugi

Institute for Molecular Science, Okazaki 444-8585, JAPAN

Resolution is an important index for the performance of monochromators. In order to demonstrate the instrumental resolution, the inner-shell photoabsorption spectra of N_2 and O_2 were measured with the grating having the groove density of 800 l/mm.

The resolving power dependences of the *K*-shell photoabsorption spectra of N_2 at the N 1s $\rightarrow \pi^*$ resonance are presented in Fig. 1. The combinations of the entrance and exit slit openings utilized were 50-20, 25-10, and 12.5-5 μm. The corresponding resolving powers are expected to be 5000, 10000, and 20000, respectively. It is difficult to determine the transmission function of the monochromator with the N 1s $\rightarrow \pi^*$ excitation of N_2, because the natural linewidth is not well-established. This is due to the existence of several nearly overlapping vibrational bands as clearly seen in Fig. 1. However, in comparison with the recent data for the N 1s$\rightarrow\pi^*$ resonance of N_2 measured at Spring-8, the best energy resolution obtained might be less than 40 meV at 400 eV, which corresponds to a resolving power of more than 10000.

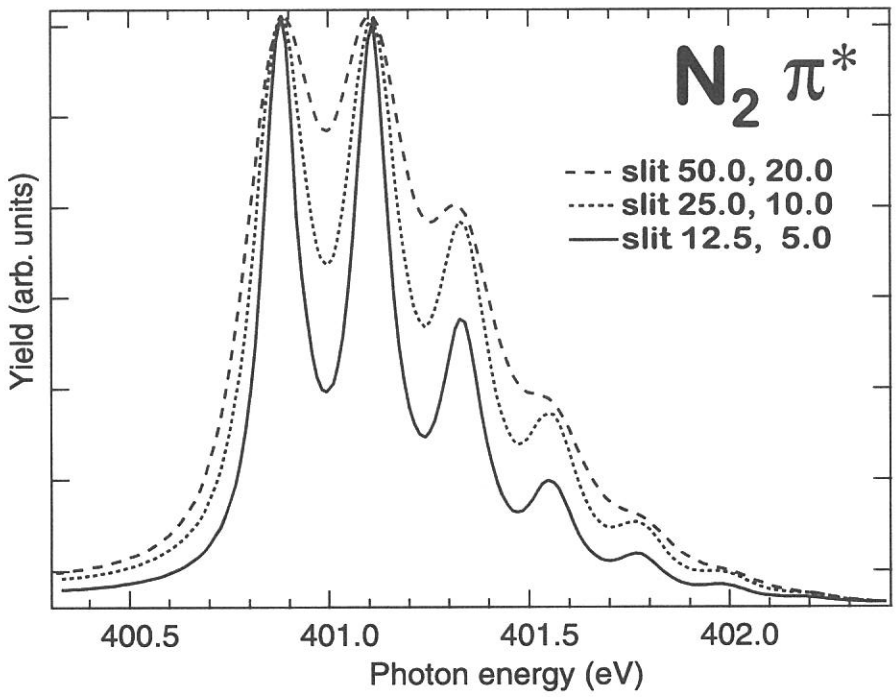

Fig. 1. High-resolution *K*-shell photoabsorption spectra in the π* resonance region of N_2.

The entrance and exit slit openings were set at 15 and 7.5 μm, which corresponds to the resolving power of 10000 at the oxygen *K*-edge region. Many fine structures due to the Rydberg excitations and their vibrational side bands are detected on the broad enhancements owing to the σ* resonances. Due to these complicated absorption features, the estimation of the monochromator resolution from the measured spectrum is difficult in the case of O_2. From the comparison with all available spectra of the Rydberg resonances around 530 eV, it seems possible to safely say that the resolving power obtained here is more than 5000. The estimated resolving powers for all the spectra obtained are a little worse than those expected from the numerical calculations, which may be attributable to the imperfection of the alignments of the optical elements.

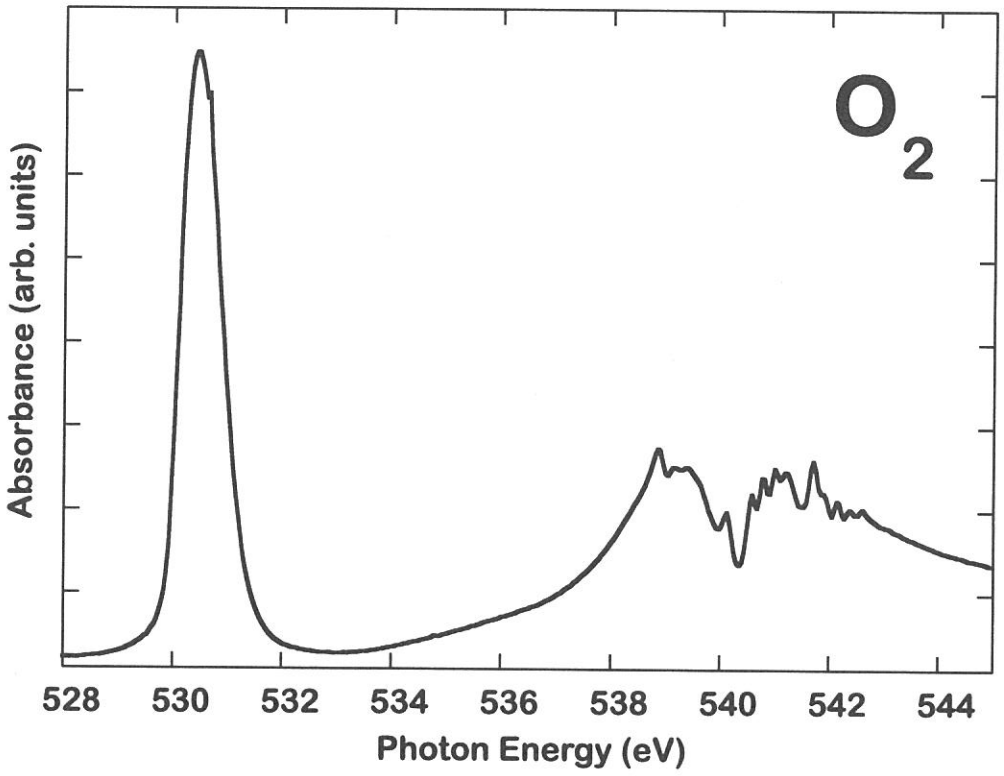

Fig. 2. *K*-shell photoabsorption spectrum of O_2.

(BL 5A)

Experimental system for time-dependent photoelectron spectroscopy

Senku Tanaka[A], Kazutoshi Takahashi[B], Sam D Moré[B], and Masao Kamada[A, B]

[A] *The Graduate University for Advanced Studies, Myodaiji, Okazaki, 444-8585*
[B] *UVSOR Facility, Institute for Molecular Science, Myodaiji, Okazaki, 444-8585*

Photoelectron spectroscopy is one of the most powerful experimental methods to investigate the electronic structures in the wide energy range. However, many experiments have been carried out by means of static way, where synchrotron radiation (SR) itself is assumed as a continuum light source like a helium lamp and an x-ray in the laboratory. These experiments use the high brilliance, continuum wavelength, polarization, cleanness of SR, and so on. On the other hand, SR has also the advantage in the temporal structure and few groups in the worldwide synchrotron radiation facilities have been trying to apply the pulse nature of the synchrotron radiation for time-dependent experiments of photoelectron spectroscopy. Moreover, the combinational use of SR and laser lights has been developing the time-dependent photoelectron spectroscopy. In this report, we present a part of our recent experimental system for temporal resolution of SR photoelectron spectroscopy.

Roughly speaking, there are two ways for the time-dependent photoelectron spectroscopy. One is the pump-probe method, where the first pulse such as laser light, electric field, pressure, and gaseous jet stimulates the material to cause remarkable changes in the electronic structures, and then the second pulse (namely, SR pulse) probes the response from the material using photoelectron spectroscopy. This pump-probe method requires the pulse nature of the SR and also the stimulation (for example, laser light), and the temporal coincidence between them. Since the UVSOR has a duration time of about 1.5 ns and a repetition of 90 MHz, this system is restricted in the temporal range of 1.5 to 11 ns under usual multi-bunch operation and can be extended to the range of 0.5 to 178 ns for a single-bunch operation. The present shortest duration of SR in the world is about few tens of pico-seconds and also the duration of few pico-seconds will be achieved in the next generation sources. Therefore time-dependent photoelectron spectroscopy using SR may attract much interest from basic researches and applications.

Another way is based on the direct measurement of the photoelectron signals decaying after the stimulation, where the fast stimulation pulse causes the change in the electronic structures of the materials and then the decaying signals following the stimulation are detected using a fast storage oscilloscope or a time-to-amplitude converter. The SR is assumed as a continuum light source and the performance of the system is restricted by the response time of the experimental system and the repetition of the stimulation. This second way is described in more details in the followings.

Experimental systems have been constructed at BL5A, UVSOR facility. Figure.1 shows the schematic block diagram of the time-dependent photoelectron spectroscopy system. We used the laser (COHERENT Mira 900-F (90 MHz, 800 nm) & RegA (10 KHz, 800 nm)) as the excited light source to cause the stimulation. The laser light was transported to the view-port of the main sample chamber using an optical fiber and focused on the sample surface using a quartz lens. SR is monochromatized by an SGM-TRAIN type monochromator and then SR photons of about 100 eV are introduced on the sample surface to observe the photoelectron spectra. The spatial overlap between laser and SR spots were carefully adjusted by the optical system of the laser. The photoelectrons are observed by an OMICRON hemi-spherical

electron-energy analyzer (EA-125HR). The electron analyzer was used in a single energy-analyzer mode. Photoelectron signals from the electron analyzer were changed to LED signals in the pre-amplifier circuit and sent to the optical receiver using an optical fiber in order to decrease the noises. Photoelectron signals acquired in the receiver were fed to the gate circuit. The gate circuit and the shutter were controlled by the timing circuit. Photoelectron signals were transferred into time-to-amplitude converters (TACs) as the start signals. Laser pulses, which were detected by a PIN photodiode, were used as the stop signals. A couple of TACs has been used to take both of laser-on/off signals, simultaneously. By changing the fixed kinetic energy, it is also possible to observe the time dependence of photoelectron spectra as well as the time-dependence of the photoelectron signals. The time-range of the present system is restricted by the response time of the system (0.1μs) and the laser repetition time (100 μs). Further improvement is under progress.

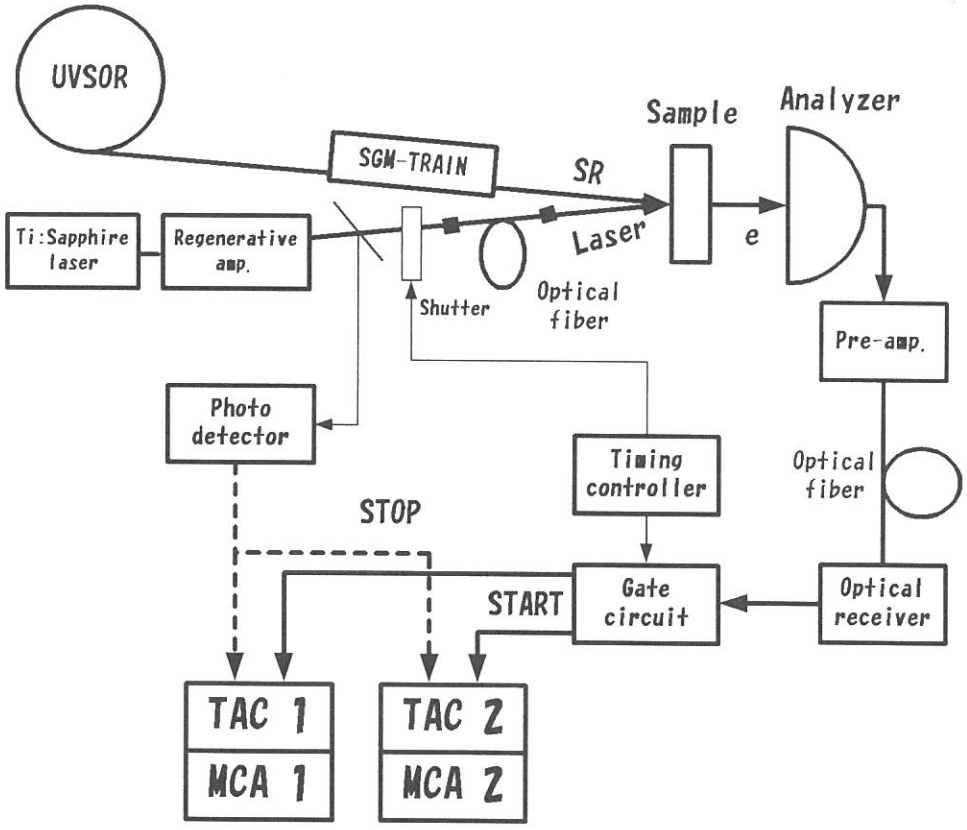

Figure 1. Schematic block diagram of the experimental system.

In summary, we have been studying the dynamical behaviors of electronic structures. We constructed the experimental system to investigate the time-dependence of the photoelectron spectra, which is based on the combinational use of the SR and laser light. The system has been applied to investigate the photo-induced phenomena on the semiconductors.

References

[1] M. Kamada et al., *UVSOR Activity Report*, 1999, p 180.

[2] M. Kamada et al., *Surf. Sci.*, **454-456** (2000) 525.

(BL5B)

Characterization of Optical Units and a $[SnO_2/SiO_2]_{20}$ Multilayer Spacemen for the Use of Plasma X-ray Laser Experiment

Kazumichi NAMIKAWA, RenZhong TAI, Etsuo ARAKAWA, Hisatak TAKENAKA*, Masao KAMADA**, Masami HASUMOTO**, Eiji SHIGEMASA**

Tokyo Gakugei University, Koganei, Tokyo184-8501

** NTT Advance Technology, Musashino, Tokyo 180-0012*

*** Institute for Molecular Science, Okazaki, Aichi 444-8584*

1. Introduction

Among existing soft x-ray sources the plasma x-ray laser is known as the most bright souse; Bose degeneracy is an order of 10^9. This means the plasma x-ray is the most suitable source to be utilized in the non-liner x-ray optical experiments. However, the plasma x-ray is a single shot souse whose repetition rate, for example, at the Laser Institute of Osaka University is 1 shot per two hours. Prior to the plasma x-ray laser experiment, we oblige to characterize the spacemen and the optical units, and to prepare an off beam aliment of these materials. We report here the results of the experiments characterized a two axis goniomator and a $[SnO_2/SiO_2]_{20}$ multilayer spacemen which we fabricated for Ni-like Ag plasma x-ray laser experiment; stimulated x-ray parametric scattering (SXPS).

2. Experimental

A new-designed goniomator, which consists of an entrance slit, a sample and an exit slit closely attached by a silicon photodiode, as shown in Figure 1, was installed in the scattering chamber at BL-5B. The design parameters of this sample are a multilayer period at 10 nm with a thickness of top layer SnO_2 at 2 nm, a number of periods at 20, and a substrate of SiO_2. The widths of the two slits were set to 1 mm. The change of the photon energy is given by the monochromator of the beam line.

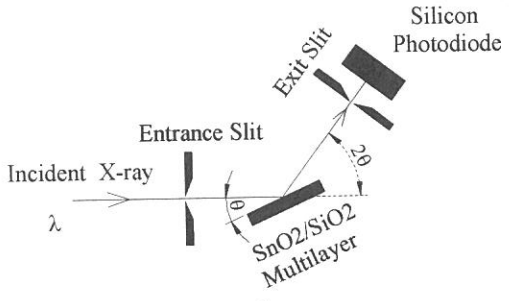

Fig. 1 Experimental set-up

3. Results and Discussion

Bragg reflections were measured for various wave lengths. Figure 2 shows a typical Bragg reflection of the

sample, with a peak reflectance estimated at 10% and a FWHM at around 5° due to the finite number of layers.

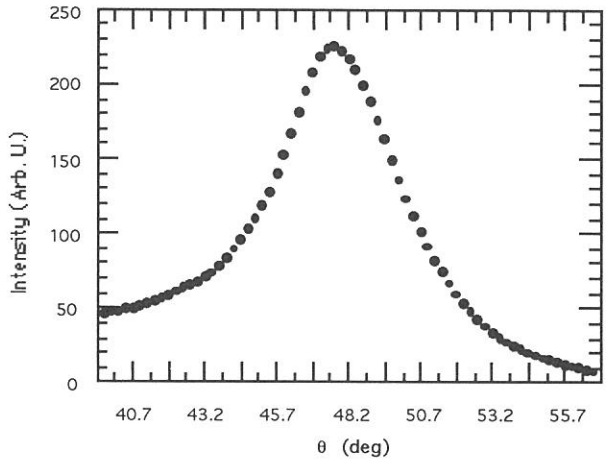

Fig. 2 Bragg reflection for the $[SnO_2/SiO_2]_{20}$ multilayer. The incident x-ray wave length is 14.437 nm, the peak appears at 47.63 degree.

The broad tail of Fig. 2 will inevitably contribute a background noise to the SXPS with this sample. This influence was measured as shown in Fig. 3 by 2-theta scanning, with the theta set at 55.36° , which is the designed value of SXPS. At the signal direction, a background was measured to be with magnitude of 0.38% of the peak Bragg reflection.

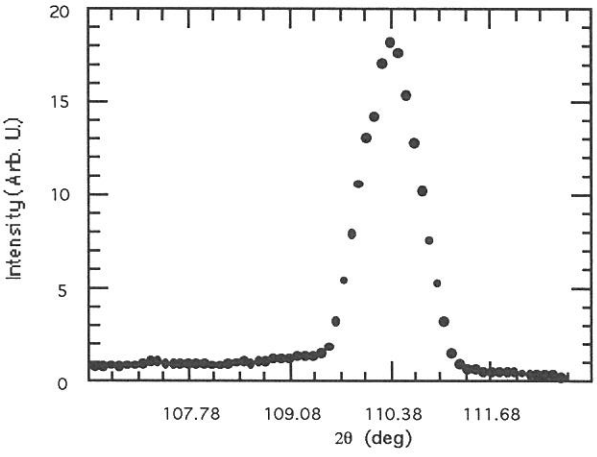

Fig. 3 Background from the tail of specular reflection. The peak arises from the broad tail of Bragg reflection as shown in Fig. 2. The SXPS signal is expected to appear -3.74° off this peak.

A clear N_3, N_4 absorption edge of Sn^{4+} was also observed by measuring the reflected intensities for different incident photon energies. This is a good verification of the transition between 4p and the lower edge of 5d-conduction band of Sn4+, which has been presumed to exist in the process of SXPS.

(BL5B)

Measurement of SELENE/UPI-TEX FM mirror reflectivity

Masato Nakamura[A], Tetsunori Murachi[A], Ichiro Yoshikawa[B],
Atsushi Yamazaki[A], Kei Shiomi[A] and Yoshiyuki Takizawa[C]

[A]*Department of Earth and Planetary Science, University of Tokyo, Bunkyo-ku, Tokyo 113-0033, Japan*

[B]*Institute of Space and Astronautical Science, Sagamihara, Kanagawa 229-8510, Japan*

[C]*The Institute of Physical and Chemical Research, Wako, Saitama 351-0198, Japan*

As one of the calibrations for the reflectivity characteristics of the multi-layer coated mirror (UPI (Upper-atmosphere and Plasma Imager)-TEX (Telescope of EXtreme ultra-violet) FM (Flight Model) mirror) for the Lunar orbiter SELENE (SELenological and ENgineering Explorer), the purpose of this experiment is to measure the reflectivity of multi-layered mirror at different areas and different incident angles.

The UPI-TEX on board SELENE will measure the abundance and distribution of Helium gas and ions in the Terrestrial Plasmasphere. Neutral Helium gas scatter the 58.4nm (He I emission) and those ions scatter 30.4nm (He II emission) Extreme Ultra-Violet (EUV) light from the sun which are the target of this telescope. Mo/Si multi-layered mirror reflects preferentially 30.4nm EUV light.[1] Maximum reflectivity that peaks at 30.4nm is about 24% and the full width at half of maximum is about 4nm. The reflectivity above 50nm again increases. This type of mirror was used in the Helium Emission Monitor (HEM) boarded on the sounding rocket S-520-19[2], eXtreme Ultra-Violet (XUV) Scanner boarded on the Mars orbiter NOZOMI[3,4] (Fig.1) and will be SELENE.

Below is why we measure the reflectivity of multi-layered mirror at different areas and different incident angles. As shown in Fig.1, the black line and the gray line, which come from different directions, are reflected by different incident angles at same mirror area, and are detected at different areas of MicroChannel Plates (MCPs). As it is well known that the reflectivity depends on incident angles, the light reflected at same area by different incident angles, which originally have same intensity, are measured at different intensity by MCPs. And by the curvature of mirror the light, which from same direction and reflected at different mirror areas are reflected to same MCPs area, result in different intensity. In brief, the 2D-intensity-distributions detected by MCPs may differ from TRUE 2D-intensity-distributions of light from the objects.

To measure the reflectivity of multi-layered mirror at different areas and different incident angles we did below. We got the pure EUV light free from the contamination of multi-order light.[5] We fixed the mirror that the frame plane of mirror was perpendicular to beam line and the center of mirror corresponded to beam line. We decided measurement points: (r, i) = (30, 6.5), (40, 5.0), (40, 6.5), (50, 3.2), (50, 5.0), (50, 6.5), where r is the distances [mm] at the measurement point from the mirror center, i is the incident angles [degree] (6.5 degrees are corresponding to a 6.5-degree half

field of view). We injected XUV light to measurement points of mirror, and measured the reflectivity of the multi-layered mirror.

The result is shown in Fig.2. The large (small) markers have less error than 10% (20%) of reflectivity. It is ascertained that this multi-layered mirror reflects preferentially 30.4nm XUV light. The reflectivity above 50nm again increases. The reflectivity varies with incident angles: at 30.4nm in Fig.2 (a), (b) the reflectivity of 5.0 degrees differs from that of 6.5 degrees significantly. This result implies that the reflectivity of 0.0 degrees might have remarkable difference from that of 5.0 degrees. Because this mirror designed at 0.0-degree incident angle, this thought must be ascertained. We will measure the reflectivity characteristics of 0.0~6.5 degrees and different areas in detail.

References

1) T. Yamazaki et al., *J. Electron Spectrosc. Relat. Phenom., 80,* 229, 1996.

2) I. Yoshikawa et al., *J. Geophys. Res., 102,* 19897, 1997.

3) M. Nakamura et al., *Earth, Planets and Space, 51,* 61, 1999.

4) M. Nakamura et al., *Geophys. Res. Lett., 27,* 141, 2000.

5) M. Nakamura et al., *UVSOR Activity Report,* 152, 1998.

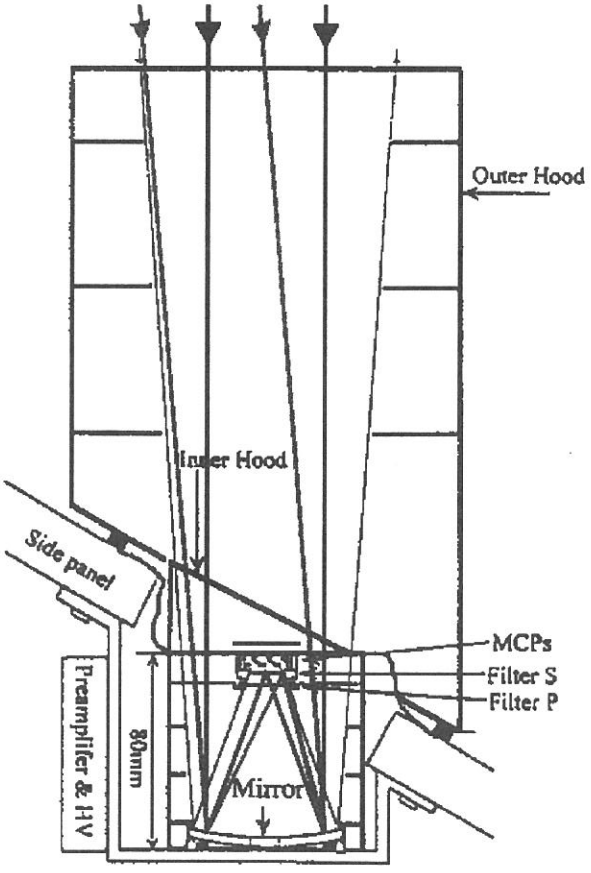

Fig.1 A cross section of the XUV scanner on board the Mars orbiter NOZOMI.

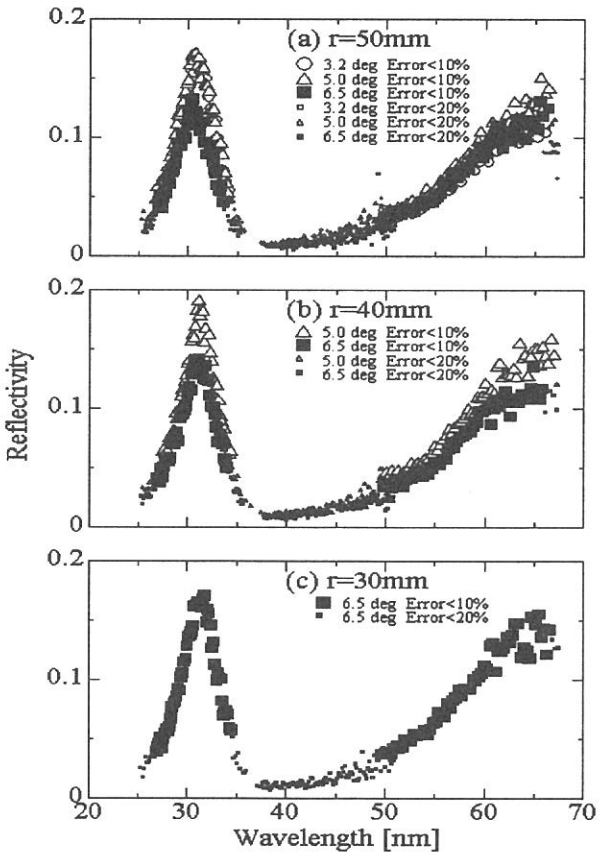

Fig.2 Reflectivity characteristics of UPI-TEX FM mirror for the Lunar orbiter SELENE at (a) r=50mm (b) r=40mm (c) r=30mm from mirror center.

(BL–5B)

Charge Spreading in Back Illuminated CCD

Ryouhei KANO[1], Kazuyoshi KUMAGAI[1], Tomonori TAMURA[1], Saku TSUNETA[1], Taro SAKAO[2], Yukio KATSUKAWA[3]

[1] *National Astronomical Observatory, 2-21-1 Osawa, Mitaka, Tokyo 181-8588, Japan*
[2] *The Institute of Space and Astronautical Science, 3-1-1 Yunodai, Sagamihara, Kanagawa 229-8510, Japan*
[3] *Department of Astronomy, School of Science, The University of Tokyo, Bunkyo, Tokyo 113-0033, Japan*

A cloud of electrons generated by an incident X-ray in a CCD are dispersed, while they travel to electrodes on the CCD surface. If these electrons spread out of a CCD pixel, the image taken with the CCD is blurred.

We investigated the charge spreading in a commercial-based back-illuminated CCD device developed by Marconi Applied Technologies (MAT): CCD42–40, by utilizing beam lines located at UVSOR Facility in Okazaki National Research Institute and Photon Factory in High Energy Accelerator Research Organization. The same type of the CCD will be used for the X-ray Telescope (XRT) abroad the Solar-B satellite, which will be launched in summer of 2005.

In order to obtain the CCD spatial response with sub-pixel resolution, we used the mesh technique which was developed by Tsunemi et al. (1997). We prepared a copper mesh whose pinhole is 4μm in diameter, and whose pitch length is twice larger than the CCD pixel size (13.5μm). Just in front of a test CCD, we put the mesh, and rotated it by a few degree around the normal of the CCD surface. The moire pattern clearly appears in raw images (Fig.1). Because of its geometrical regularity, it is easy to derive the relative position of each pixels from pinholes of the mesh. Figure 2 shows the intensity distribution based on the mesh coordinates. The electrons generated by X-ray photons passing through a pinhole located at (1.5, 1.5) spread out of a pixel (bashed box). The modulation pattern is blurred not only by the charge spreading in a CCD but also by the diffraction of a pinhole. We, therefore, subtracted the effect of the diffraction. We approximated the distribution of the charge spreading in CCD 42–40 by a Gaussian function, and then plotted its standard deviation as a function of the absorption depth in silicon at the measured wavelengths (Fig. 3). Because X-ray photons with the shorter wavelength penetrate closer to the electrodes at the front surface, we expected that the shorter wavelength made the smaller spreading size. However, we also expected that the dependence of the spreading size on the absorption depth might be small, because most of X-ray photons are absorbed near the back surface even in the case of the shorter wavelength. In fact, Figure 3 shows the size is almost constant around 0.5 pixel (6.25μm), except for the data at 100Å. The constant spreading size may be a general character of back-illuminated CCDs.

As a practical point of view, this experiment shows that the charge spreading in MAT CCD42–40 is one of the primary factors for the image blurring. In fact, we have to pay attention to the charge spreading as well as the optical aberrations and the spacecraft jitter, to evaluate the spatial resolution of XRT.

We would like to thank Prof. Tsunemi and his colleagues of Osaka University for supporting this experiment based on their mesh technique.

References:

Tsunemi, Yoshita & Kitamoto 1997, Jpn. J. Appl. Phys., Vol.36, pp2906-2911

Fig. 1.. *A part of a raw image, which shows the clear moire pattern produced by pinholes of the mesh and CCD pixels.*

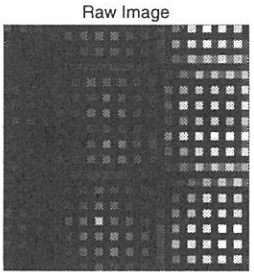

Fig. 2.. *The normalized intensity distribution shown on the mesh coordinated. Pinholes are located at (1.5, 1.5), (1.5, 3.5), (3.5, 1.5) and (3.5, 3.5).*

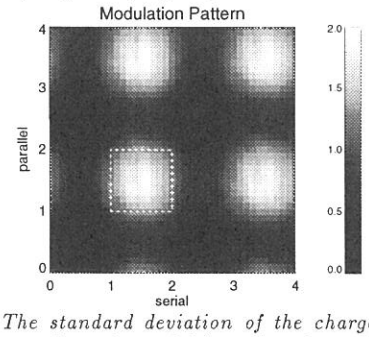

Fig. 3.. *The standard deviation of the charge spreading in CCD42-40 along the serial (stars) and parallel (diamonds) resistors, as a function of the absorption depth in silicon. The data points correspond to the measured wavelengths; 100, 80, 60, 40, 20 and 10 Åfrom the left.*

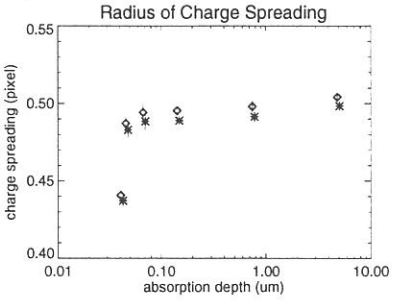

(BL8A)

Study of the carbon contamination of the SR irradiated optical devices

Takashi Naito, Mikio Tadano, Junji Urakawa,[1]
Eiken Nakamura, Masami Hasumoto,[2]
[1]*High energy Accelerator research organization(KEK), Accelerator Division,1-1 Oho Tsukuba 305-0801, Japan*
[2]*Insitute of Molecular Science, Okazaki 444-8585, Japan*

A carbon contamination of the optical devices is a serious problem for the operation of synchrotron radiation beam lines(SR-BL) and for the measurements by the optical monitors of the accelerator. From the experience of the SR-BL, we had to replace the gratings or the mirrors after several operation periods. From the experience of the SR interferometer of Accelerator Test Facility in KEK(ATF-KEK), the carbon contamination for the visible light of the first mirror has limited the resolution of the beam size measurement. The purpose of this study is to find out the dependence of the growth rate of the carbon contamination and to investigate the key parameter for keeping the clean mirror surface.
In order to investigate the growth rate of the carbon contamination, the experiments were carried out at BL8A. The growth rate of the carbon contamination was measured with a reflected light power of 670nm laser light at different conditions. The measurement set up is shown in fig. 1. The optical mirror(BK7, Aluminum+MgF2 coated) was used as a test sample. The reflected laser power was measured by PIN Photo Diodes(Hamamatsu S3590). Two photo diodes were used to compare the reflection of the SR irradiated part and the normal part. Fig. 2 shows the reflectivity as a function of dose(time x current) in two cases of mirror temperature of 25 degrees and 100 degrees, respectively. The clearly temperature dependence of the carbon contamination was measured. For the more, the series of the study is scheduled at various conditions.

References

[1] K. Boller et. al., "INVESTIGATION OF CARBON CONTAMINATION OF MIRROR SURFACES EXPOSED OT SYNCHROTRON RADIATION" DESY SR-82-18 Oct. 1982

[2] A. Kumao et. al., " Study on Specimen Contamination by Transmission Electron Microscopy", J. Electron Microsc., Vol 30, No.3, 161-170

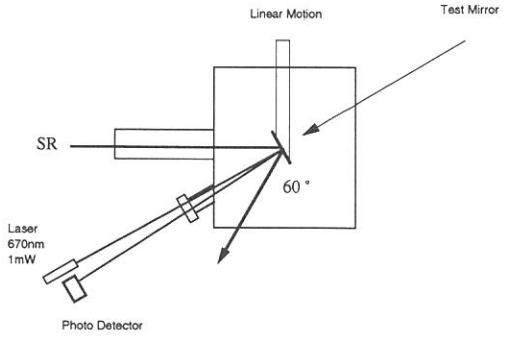

Fig.1 Measurement setup:
The incident SR is reflected with high angle (60degrees). The reflectivity of the mirror of the irradiated position is measured by 670nm laser.

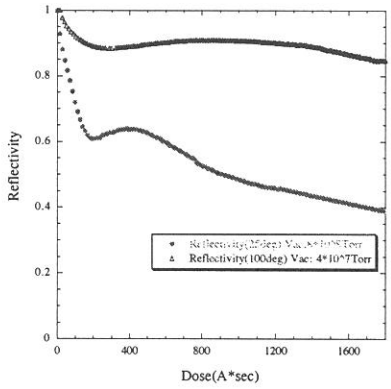

Fig.2 Reflectivity as a function of dose for different temperature.

(BL6A2)

Beamline Upgrade for Photoelectron Microscopy with the Combination of Synchrotron Radiation and Laser

Kazutoshi Takahashi[A], Yoichiro Doi[B], Kazutoshi Fukui[C], Yuichi Haruyama[D], Toyohiko Kinoshita[E], and Masao Kamada[A]

[A]*UVSOR Facility, Institute for Molecular Science, Okazaki 444-8585*
[B]*Faculty of Engineering, Fukui University, Fukui 910-8507*
[C]*VUV Photo-Science, Institute for Molecular Science, Okazaki 444-8585*
[D]*LASTI, Himeji Institute for Technology, Ako 678-1201*
[E]*ISSP, University of Tokyo, Kashiwa 277-8581*

Photoelectron spectroscopy is one of the most powerful techniques to investigate the electronic structures of various materials. BL6A2 has been used for the photoemission study for solids and surfaces using the home-made angle-integrated and angle-resolved photoelectron spectrometers for more than 10 years. However, it has been suggested that these spectrometers should be replaced by newer one due to their poor resolution and low efficiency on collecting data. Recently, various photo-induced phenomena such as the electronic non-equilibrium on the photo-excited semiconductor surface, photo-induced phase transition on transition metal complexes has been attracting much interest. The combinational use of the synchrotron radiation and laser is attractive and promising, since it is powerful to investigate the various photo-induced phenomena. Moreover, newly developed photoelectron micro-specroscopic method has many applied usages compared with ordinary one, because it can measure the specific small area of the sample. In this report, we present the new experimental system for photoelectron micro-spectroscopy with the combination of synchrotron radiation and laser.

Figure 1 shows the schematic view of the upgraded BL6A2. In order to connect the photoelectron micro-spectroscope (FISIONS Instruments, ESCALAB 220i-XL) to the plane grating monochromator, a post-mirror M3 was replace by plane mirror and a new post-mirror M4 was installed. M4 is a toroidal mirror with the radius of R_h = 4266.3 mm and R_v = 446.9 mm. These parameters have been determined to minimize the beam size at the sample by raytrace simulation. Figure 2(a) shows the beam spot at the sample obtained from the raytrace simulation. The photoelectron micro-spectroscope has been installed at the focusing point of the monochromized light. The laser light from the cw Ar^+ ion laser, Nd:YAG laser with the pulse width of 300 ps, and Ti:Sapphire laser with the pulse width of 100 fs can be introduced through the quartz view-port of the main sample chamber. The base pressure of the analyzing chamber is about 2×10^{-8} Pa. The samples can be cooled with a flow-type He cryostat. The sample preparation chamber equipped with a load-lock chamber is connected to the main sample chamber.

The photon flux at the sample determined by the total electron yield of Au sample is about 6×10^{10} photons/sec/100mA at $h\nu$ = 60-100 eV and the slit width of 100 μm. Figure 2(b) shows the

beam spot measured by the photoelectron imaging for valence band of Cu sample at hν = 100 eV. As shown in Fig 2(a), the beam size at the sample is about 0.5 mm in diameter, which is almost same as that of raytrace simulation. Total instrumental energy resolution is 0.1-0.2 eV, dependent on the photon energy. The spatial resolution was determined by the photoelectron imaging for the C 1s core-level from knife-edge sample excited by Mg Kα line. The spatial resolution were about 8 and 6 μm for the measuring area of 1.0×1.0 and 0.5×0.5 mm^2, respectively.

In summary, the new experimental system for photoelectron micro-spectroscopy with the combination of synchrotron radiation and laser has been constructed at beamline BL6A2. Using this system, photoelectron spectro-microscopic studies of various photo-induced phenomena can be conducted.

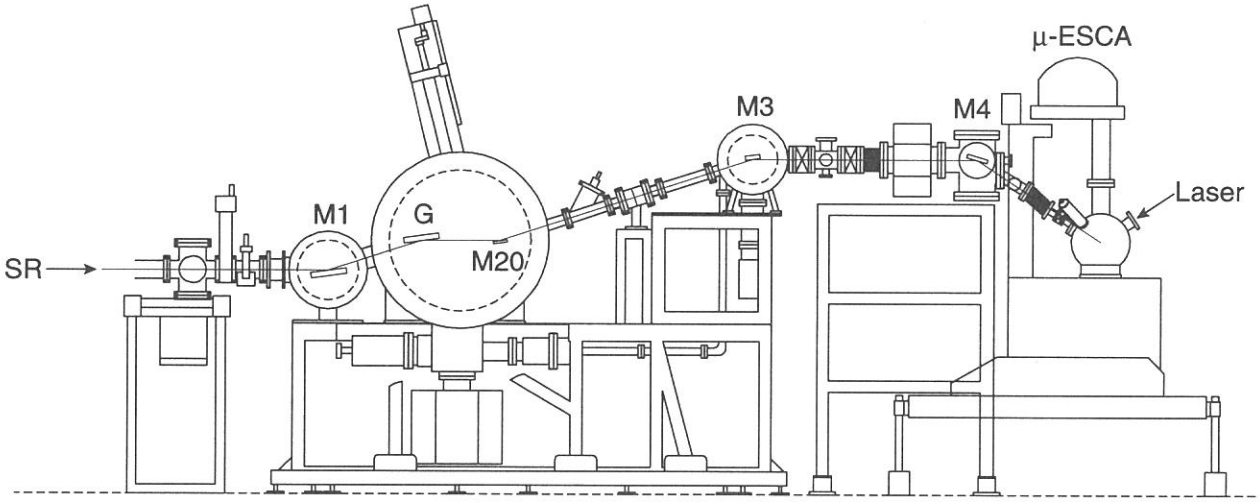

Fig. 1 Schematic view of the upgraded BL6A2.

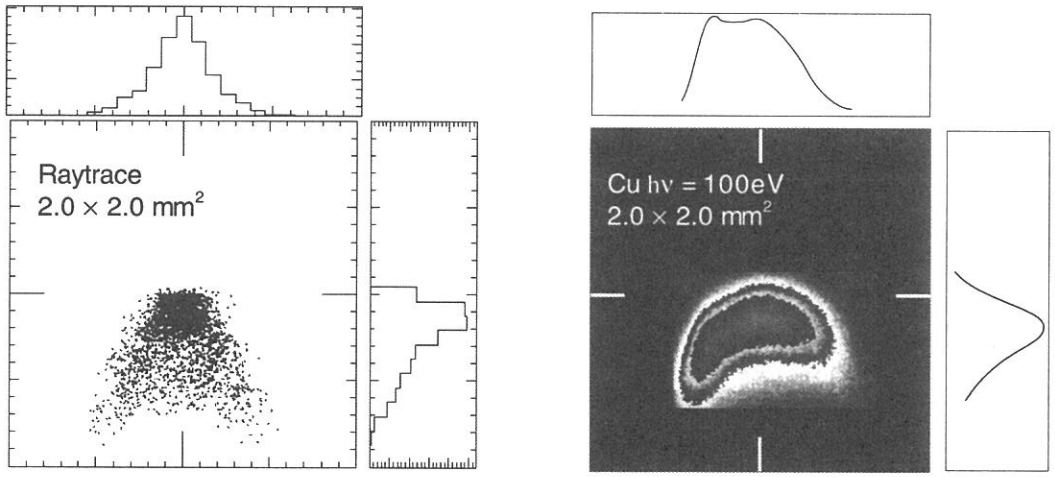

(a) (b)

Fig. 2 The beam spot at the sample determined by (a) raytrace simulation and (b) photoelectron imaging for gold sample at hν = 100 eV.

(BL8B1)

Development of Siegbahn-type coaxially symmetric mirror electron energy analyzer for photoemission and electron-ion coincidence spectroscopy in gas phase

Koji Isari, Kenichiro Tanaka, Masaki Morita, Yasumitsu Suto, Hiroaki Yoshida, Kazuhiko Mase,[A] Tatsuo Gejo,[B] Shin-ichi Nagaoka[B]

Department of Physics Science, Faculty of Science, Hiroshima University, 1-3-1 Kagamiyama, Higashi-Hiroshima 739-8527
[A]Photon Factory, Institute of Materials Structure Science, High Energy Accelerator Research Organization, 1-1 Oho, Tsukuba 305-0801,
[B]Institute for Molecular Science, Myodaiji Okazaki 444-8585

Coincidence method is one of the most powerful tools for investigating ionization process, dissociation dynamics and auger decay process. We have developed a coaxially symmetric mirror electron energy analyzer proposed by Kai Siegbahn et al.[1] for photoemission spectroscopy and electron-ion coincidence spectroscopy in gas phase. Figure 1 shows a schematic diagram of the analyzer. It consists of inner and outer electrodes, five sets of electrodes for maintaining a coaxial electric field, a 0.8-mm-diameter exit slit and tandem micro channel plates (MCP), a magnetic shield, a 203-mm-diameter conflat flange with feedthroughs, and an xyz stage for position adjustment. The solid angle of the analyzer is designed to be 1.2sr. The performance of the analyzer was examined by measuring resonant Auger spectrum of N_2 at BL-8B1. Synchrotron radiation was cut by a pin hole with a diameter of 1 mm to reduce the ionization area of sample. The N_2 pressure at the experimental chamber was kept at 5 x 10^{-6} Torr. Figure 2 shows a resonant Auger electron spectrum of N_2 at π^* ← $1s$. The energy resolution was estimated as E/ΔE = 110 at the $3\sigma_g^{-1}$ peak, which is twice better than that of a cylindrical mirror analyzer (CMA) which was used before at BL-8B1. The brilliance of the analyzer, however, was one order of magnitude poorer than that of CMA, because the ionization area of the N_2 is much larger than the exit slit area of the analyzer. Energy resolution and brilliance will be improved with a suitable slit in future.

References

[1] K. Siegbahn *et al.*, *Nucl. Instr. and Meth. in Phys. Res.* **A384**, 563-574 (1997).

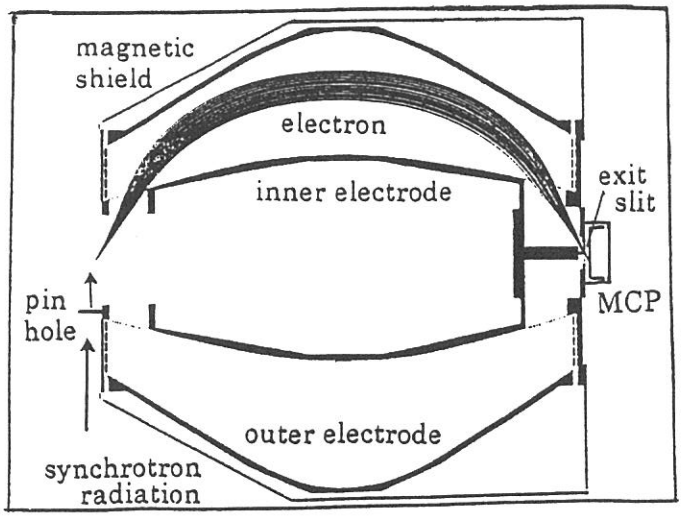

Figure 1. Schematic drawing of the Siegbahn-type coaxially symmetric mirror electron energy analyzer.

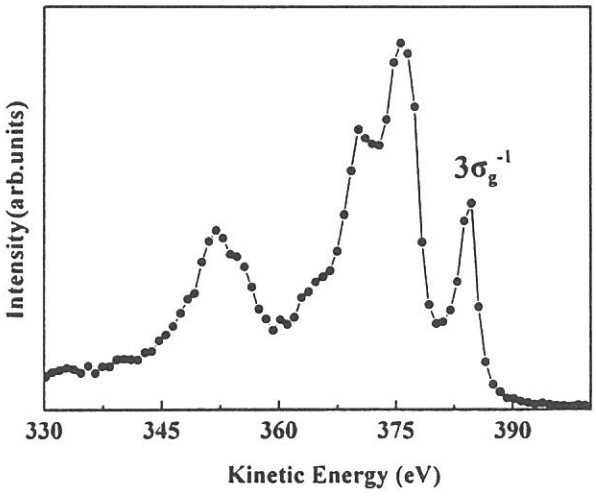

Figure 2. Resonant Auger electron spectrum of N_2 at π^* ←$1s$.

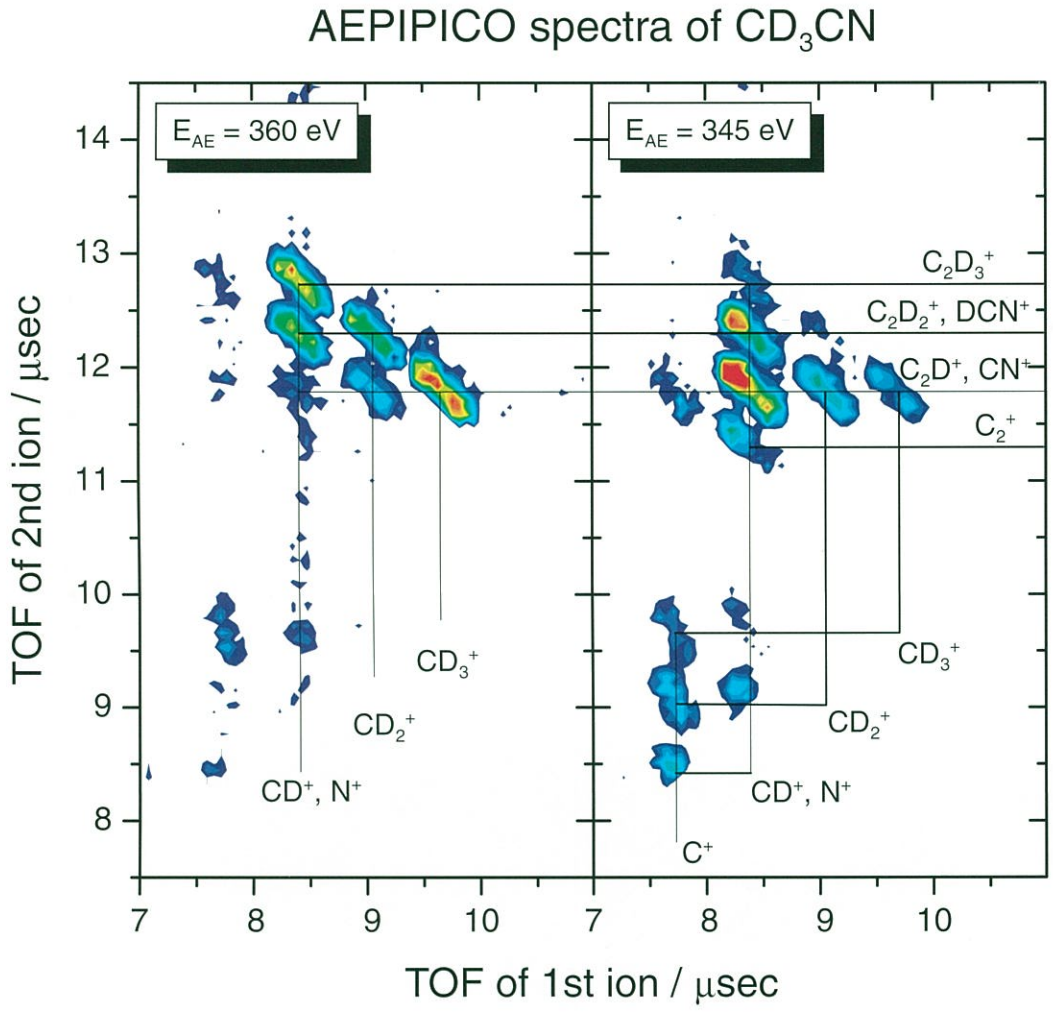

Gas-Phase Spectroscopy

BL2B2, 3A2, 3B, 8A1

(BL7B)

Two-dimensional imaging of photoelectron from Xe

Tatsuo GEJO, Eiken Nakamura, Kazutishi Fukui and Eiji Shigemasa
Institute for Molecular Science, Myodaiji, Okazaki 444-8585, Japan

The dynamics of atoms in highly excited states can be investigated by preparing to a given state at a well-defined energy and analyzing energy spectra and anisotropy of photoelectrons emitted. When a count rate is extreme low, two dimensional imaging technique is one of the most powerful tools for obtaining reasonable signals, because it allow us to detect all low energy electrons emitted around. At BL7B we have launched this two-dimensional imaging technique with using a position sensitive detector (PSD). We have successfully measured the image of Xe^+ signal at the valence region (12.1-14 eV).

Experimental setup is as follows: After the acceleration by ion lens, electrons hit the PSD (Roendek). The determination of position on the detector is based on the time delay between two signals from each end of a wire behind the MCP. The position is obtained by the subtracting of time when each two signals arrive. Since the direction of polarization of SR is parallel to the axis of the tube, and the position of the electrons on the detector provide its velocity and direction. Figure 1 shows the 2D imaging of photoelectons from Xe excited at 13.5 eV. The inner circle shows the electrons generated via $^2P_{3/2}$ state and the outer one shows via $^2P_{1/2}$ state.

This two-dimensional technique is particularly suitable for pump and probe technique with laser and SR, since its count rate is expected to be less than 10 cps. Although we have tried to measure the ion signal via $5p^55d$ state of Xe* combined with the free electron laser (FEL) at UVSOR as the first stage, we have not obtain signals due to low flux photon density of BL7B and relatively high background signals. We are going to apply this technique with the FEL and a undulator in order to investigate of the dynamics of Xe excited state.

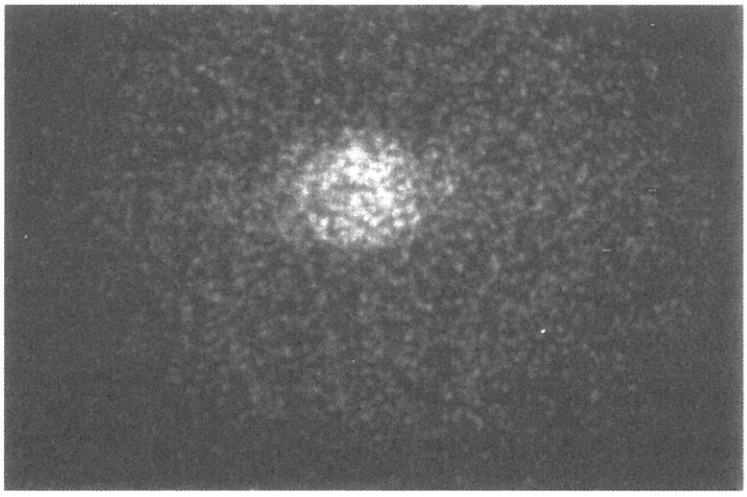

Fig. 1: 2D imaging of photoelecton from Xe excited at 13.5 eV.

(BL2B2)

Anisotropy of Fragment Ions from SF_6 with Valence- and Sulfur L-Electron Excitation

Masaki ONO, Masakazu MIZUTANI and Koichiro MITSUKE

Department of VUV Photoscience, Institute for Molecular Science, Okazaki, 444-8585, Japan

Sulfurhexafluoride (SF_6) is one of the most well-known molecules that dissociate to multiple species of fragment ions after photoionization. Therefore, formation of SF_n^+ ($0 \leq n \leq 5$) has been studied by many authers [*e.g.* 1,2]. Recently it was reported that the angular distribution of SF_5^+ is anisotropic with respect to the electric vector of the light in the region of the valence electron excitation (18 – 23 eV) [3]. In the present report the asymmetry parameter β of the fragment ion has been measured in the energy region from the outer-valence to sulfur 2*p* electron excitation (23 – 200 eV).

The apparatus for the measurements of the anisotropy of fragment ions has been constructed at the endstation of BL2B2. At this beam line a Dragon-type monochromator is placed, which provides 23 – 200 eV photons with high-resolution and high-photon flux [4, 5]. The apparatus consists with two sets of an ion detector and three grids, as shown in Fig. 1. The two ion detectors were mounted in the parallel and perpendiclar direction against the electric vector of synchrotron radiation. Retarding voltages were applied to the two grids near the detector to reject the parent ion. The last grid nearest the photoionization region was put on the electrical ground level. All fragment ion species have been observed. The base and sample pressure were 5×10^{-8} and 2×10^{-5} Torr, respectively. The photon flux was estimated by measuring the photocurrent of the gold mesh at the downstream of the photoionization region.

Figure 2 shows the fragment ion yield from SF_6 and β. The β parameter is calculated by

$$\beta = \frac{2(I_{//} - I_{\perp})}{I_{//} + 2I_{\perp}} ,$$

where $I_{//}$ and $I_{\perp}$ are the ion yields in the parallel and perpendiclar direction against the SR electric vector, respectively. The spectral range includes various regions from the outer-valence electron to sulfur 2*p* electron excitation. The three peaks at > 170 eV are assigned to the resonance excitations from $2t_{1u}$ (sulfur 2*p*) to unoccupied valence orbitals ($6a_{1g}$, $2t_{2g}$ and $4e_g$).

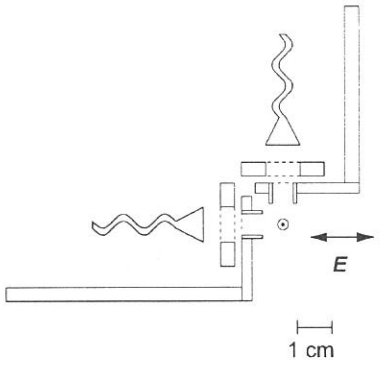

Fig. 1. The schematical layout of the apparatus for measurement of the anisotropy of fragment ions.

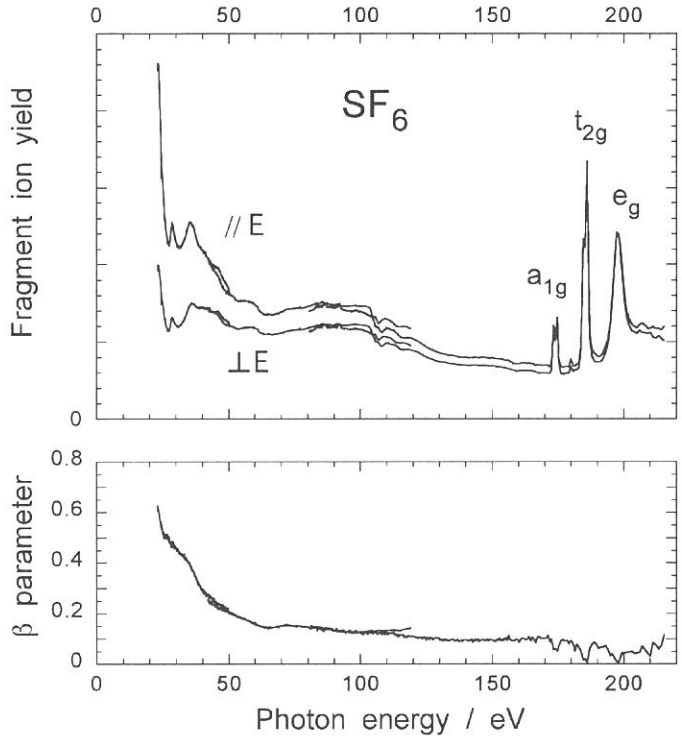

Fig. 2. Ion yield spectra and asymmetry parameter of the fragment ions from SF_6. A retarding voltage is set to 0.4 V.

The β value involving the contribution only of the 2*p* electron excitation is constant at these resonance positions. Then the β parameter has been set deliberately to 0, because it is likely that the fragmentation occurs isotopically, and because no correction has been made on the difference in the detection efficiency between the two detctors.

Several features around 20 – 60 eV are found to resemble those in the absorption spectrum. The structures around 110 eV are artifact and arise from an imperfect photon flux normalization process. The β parameter increases with decreasing photon energy. This trend can be explained qualitatively by the assumption that SF_5^+ ions has much more anisotropic distribution than other fragments from SF_6.

References

[1] M. Evans, C. Y. Ng, C. -W. Hsu and P. Heimann, *J. Chem. Phys.* **106**, (1997) 978.

[2] A. P. Hitchcock and M. J. Van der Wiel, *J. Phys. B* **12**, (1979) 2153.

[3] D. S. Peterka, M. Ahmed, C. Y. Ng and A. G. Suits, *Chem. Phys. Letter* **312**, (1999) 108.

[4] H. Yoshida and K. Mitsuke, *J. Synchrotron Rad.* 5, (1998) 774.

[5] M. Ono, H. Yoshida, H. Hattori and K. Mitsuke, *Nucl. Instrum. Meth. Phys. Res. A in press.*

(BL3A2)

Dissociative single and double photoionization of CF_4 and ionic fragmentation of CF_4^+ and CF_4^{2+} in the range from 23 to 120 eV

Toshio MASUOKA, Atsuo OKAJI, and Ataru KOBAYASHI

Department of Applied Physics, Faculty of Engineering,, Osaka City University, Sugimoto 3, Sumiyoshi-ku, Osaka 558-8585

Single and particularly double photoionization and subsequent dissociation processes of CF_4 have not quite been examined so far. Therefore, we have studied these processes with time-of-flight mass spectrometry and the photoion-photoion-coincidence (PIPICO) method by use of synchrotron radiation in the photon energy range of 23-120 eV. The TOF mass spectra and the PIPICO spectra were measured at an angle of ~55° with respect to the polarization vector where the second-order Legendre polynomial is close to zero. Under these conditions, the effects of anisotropic angular distributions of fragment ions are minimized [1]. Appropriate optical filters (Sn and Al) were used to eliminate higher order radiation. To obtain accurate ion branching ratios, the radio frequency (rf) signal of the storage ring was used as the start signal of a time-to-amplitude converter (TAC) under the single bunch mode operation of the storage ring [2].

The present study focuses on the determination of the ratio of double to single photoionization (σ^{2+}/σ^{+}) and the partial cross sections for single (σ^{+}) and double (σ^{2+}) photoionization as a function of photon energy. Second, the ion branching ratios and the partial cross sections for the individual ions produced from the parent CF_4^+ and CF_4^{2+} ions are separately determined. Third, the dissociation ratio of the parent CF_4^{2+} ions into two ionic fragments is determined. Some of the results are presented in this report.

Shown in Fig. 1 is a typical time-of-flight mass spectrum measured at a photon energy of 100 eV. The spectrum is complicated because two or three bunches pass the front end of the beam line in the time range of the mass spectrum. Metastable CF_4^{2+} ions are not observed. The ion branching ratios and the absolute partial cross sections for the production of singly charged CF_3^+, CF_2^+, CF^+, F^+, and C^+ ions, as well as doubly charged CF_3^{2+} and CF_2^{2+} ions have previously reported [3]. The ratio of double to single photoionization is shown in Fig. 2, increasing monotonically with photon energy. The threshold of double ionization 37.5±0.5 eV is in good agreement with the value 37.6±0.6 eV reported by Codling et al. [4]. Above 100 eV, the ratio exceeds 0.3. Since the total photoabsorption cross section of CF_4 in this photon energy range has been reported by Au, Burton, and Brion [5], the σ^{2+}/σ^{+} ratio can be converted to the absolute cross sections for single and double photoionization.

Ion branching ratios for the individual ions respectively produced from the parent CF_4^+ and CF_4^{2+} ions are determined separately, thus enabling more detailed study of the dissociation processes of the CF_4^+ and CF_4^{2+} ions. These results are shown in Figs. 3 and 4. Looking at the ion branching ratios of CF_4^+ (Fig. 3), we notice that the major ions produced are CF_3^+ and their ratio still increases at higher photon energies. The ratio for C^+ also increases with photon energy up to about 85 eV. In Fig. 4, we see interesting behavior of the fragmentation of CF_4^{2+} as a function of photon energy. Two body dissociation F^++CF_3^+ takes place first. Depending on the number of neutral fluorine atoms in the dissociation, the different channels (F^++CF_2^++F, F^++CF^++2F, and F^++C^++3F) appear one after another. This matter will be discussed in a separate report.

REFERENCES

[1] T. Masuoka, I. Koyano, and N. Saito, J. Chem. Phys. **97**, 2392 (1992).
[2] T. Masuoka and E. Nakamura, Phys. Rev. A **48**, 4379 (1993).
[3] T. Masuoka and A. Kobayashi, J. Chem. Phys. **113**, 1559 (2000).
[4] K. Codling, L. J. Frasinski, P. A. Hatherly, M. Stankiewicz, and F. P. Larkins, J. Phys. B **24**, 951 (1991).
[5] J. W. Au, G. R. Burton, and C. E. Brion, Chem. Phys. **221**, 151 (1997).

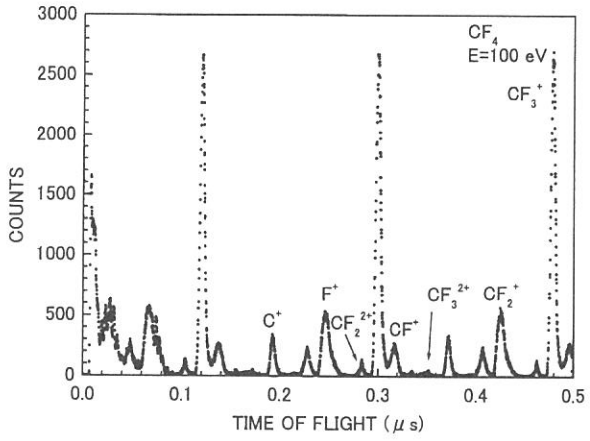

FIG. 1. A typical time-of-flight mass spectrum measured at a photon energy of 100 eV.

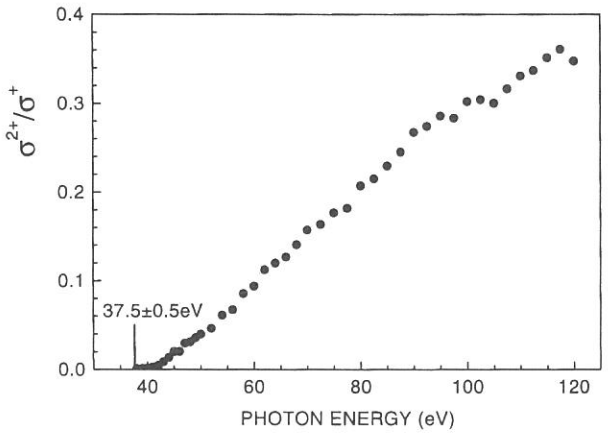

FIG. 2. Ratios of double to single photoionization cross section of CF_4.

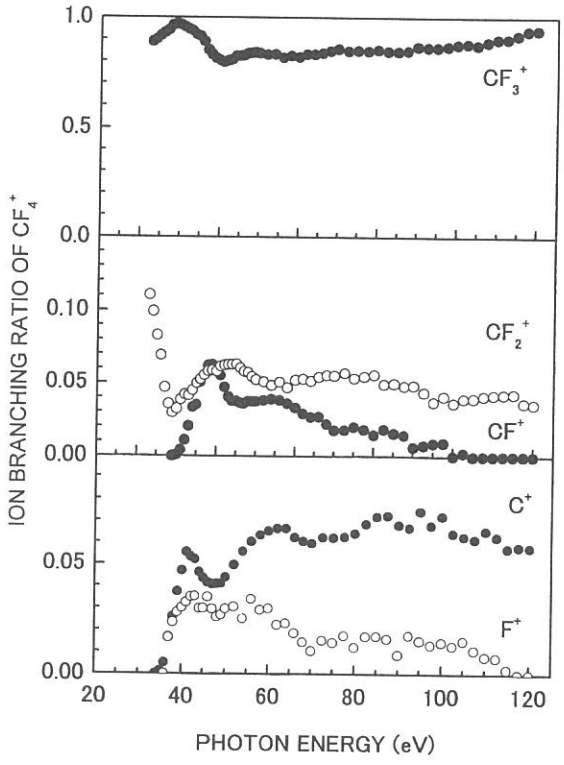

FIG. 3. Ion branching ratios of single photoionization of CF_4.

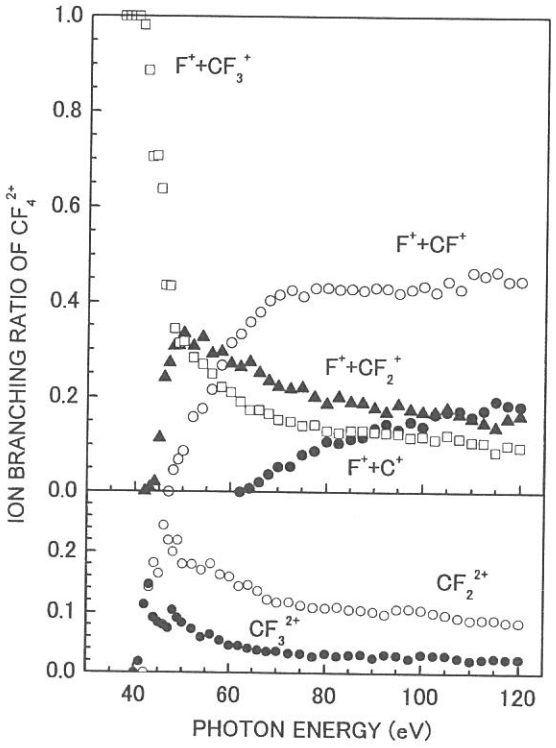

FIG. 4. Ion branching ratios of double photoionization of CF_4.

(BL3A2)

Fragmentation of doubly charged CF_4^{2+} ion

Toshio MASUOKA, Atsuo OKAJI, and Ataru KOBAYASHI

Department of Applied Physics, Faculty of Engineering,, Osaka City University, Sugimoto 3, Sumiyoshi-ku, Osaka 558-8585

The doubly charged CF_4^{2+} ion has received much attention recently by the advent of synchrotron radiation. Recently Hall et al. [1] reported the threshold for double ionization to be 37.5±0.5 eV using threshold photoelectron(s) coincidence (TPEsCO) spectroscopy and presented direct information on the two-hole states of CF_4. Experimental information on the CF_4^{2+} dication has also been obtained via Auger spectroscopy, double-charge-transfer (DCT) spectroscopy, PIPICO, and PEPIPICO experiments. Among these experiments, Codling et al. [2] determined the thresholds for the ion-pair formation of CF_4^{2+} into F^++CF_3^+ (37.6 eV), F^++CF_2^+ (42.4 eV), F^++CF^+ (47.5 eV), and C^++F^+ (62.0 eV) and tentatively correlated these thresholds with specific two-hole states of CF_4 calculated by Lurkins and Tulea [3].

In the present study, we have studied dissociative double photoionization processes with the photoion-photoion-coincidence (PIPICO) method by use of synchrotron radiation. The PIPICO spectra were measured at an angle of ~55° with respect to the polarization vector to minimize any effects of anisotropic angular distributions of fragment ions [4]. Al optical filter was used to eliminate higher order radiation.

Shown in Fig. 1 are the PIPICO branching ratios of CF_4^{2+}. The thresholds for the respective fragmentation channels reported by Codling et al. are indicated with vertical lines. The two-body fragmentation F^++CF_3^+ may occur in the narrow energy range of 37.6-42.4 eV. The three-body fragmentation F^++CF_2^++F starts at 42.4 eV. The four-body (F^++CF^++2F) and the five-body (F^++C^++3F) fragmentation channels appear according to priority with increasing photon energy. The PIPICO branching ratios for these many-body fragmentation channels increase at different photon energies, indicating the existence of fragmentation pathways at these different photon energies. In order to correlate these fragmentation pathways more clearly to the electronic states of CF_4^{2+}, the PIPICO branching ratios for these fragmentation channels were differentiated with respect to the photon energy.

The results are shown in Fig. 2 with electronic states of the dication calculated by Larkins and Tulea [3] by vertical lines. They have calculated the energy of the 107 two-hole states associated the seven outermost orbitals. The electron configuration of the ground electronic state of CF_4 is $(1a_1^2 1t_2^2)(2a_1^2)(3a_1^2 2t_2^6)(4a_1^2 3t_2^6 1e^4 4t_2^6 1t_1^6)$: $^1A_1$. The important bonding orbitals are $4t_2$, $4a_1$, $2t_2$, and $3a_1$ [2]. In the attempt to correlate initial states of the CF_4^{2+} ion with the above thresholds for fragmentation, Codling et al. [2] used various simplifying assumptions: the first one is that no fragmentation occurs where both orbitals are non-bonding or antibonding ($1t_1$, $1e$, $3t_2$), and they shifted the calculation of Larkins and Tulea by 4.8 eV. The 80 electronic states shown in Fig. 2 are those concerned with fragmentation following the above description with the shift by 4.8 eV. First, we notice that the three-body fragmentation occurs in a relatively narrow energy range from the threshold to about 49 eV, where 14 two-hole states, $1t_1$, $4t_2(2)$, $3t_2$, $4t_2(7)$, $1e$, $4t_2$ (2), $4a_1$, $1t_1$ (2), and $4a_1$, $4t_2$ (1) lies. The value in the parentheses represents the number of the states in this range. That is, only the outer-valence electrons are involved. The four-body fragmentation takes place in a rather wide energy range from the threshold to about 80 eV, where both inner-valence and outer-valence electrons are involved.

REFERENCES

[1] R. I. Hall, L. Avaldi, A. G. McConkey, M. A. MacDonald, and G. C. King, Chem. Phys. **187**, 125 (1994).
[2] K. Codling, L. J. Frasinski, P. A. Hatherly, M. Stankiewicz, and F. P. Larkins, J. Phys. B **24**, 951 (1991).
[3] F. P. Larkins and L. C. Tulea, J. Phys. (Paris), Colloq. C9(12) **48**, 725 (1987).
[4] T. Masuoka, I. Koyano, and N. Saito, J. Chem. Phys. **97**, 2392 (1992).
[5] F. P. Larkins, private communication.

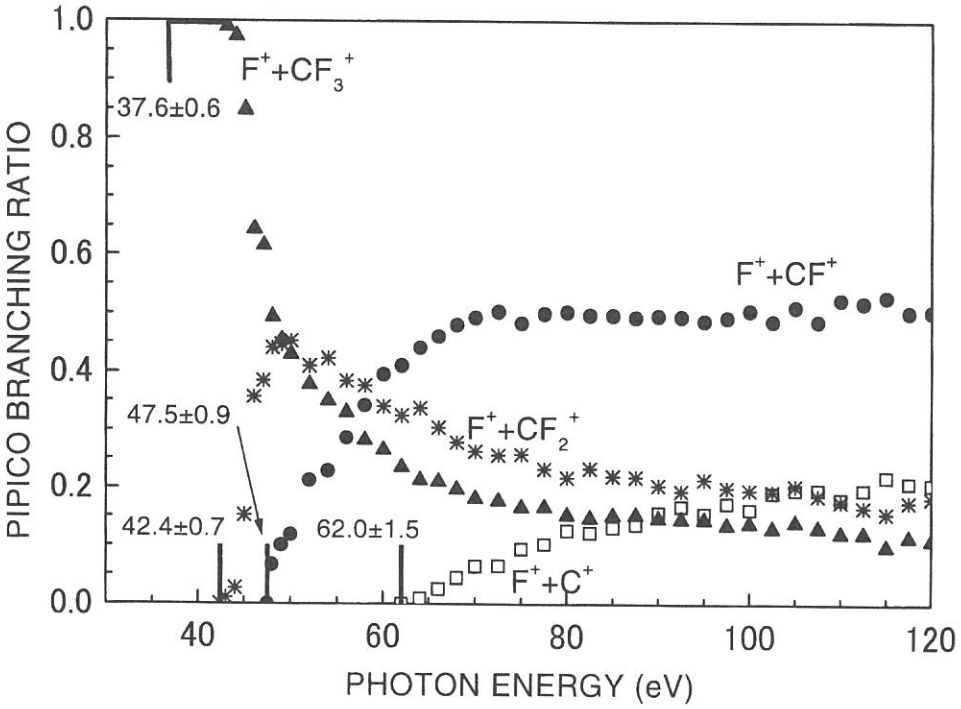

FIG. 1. PIPICO branching ratio of CF_4^{2+}.

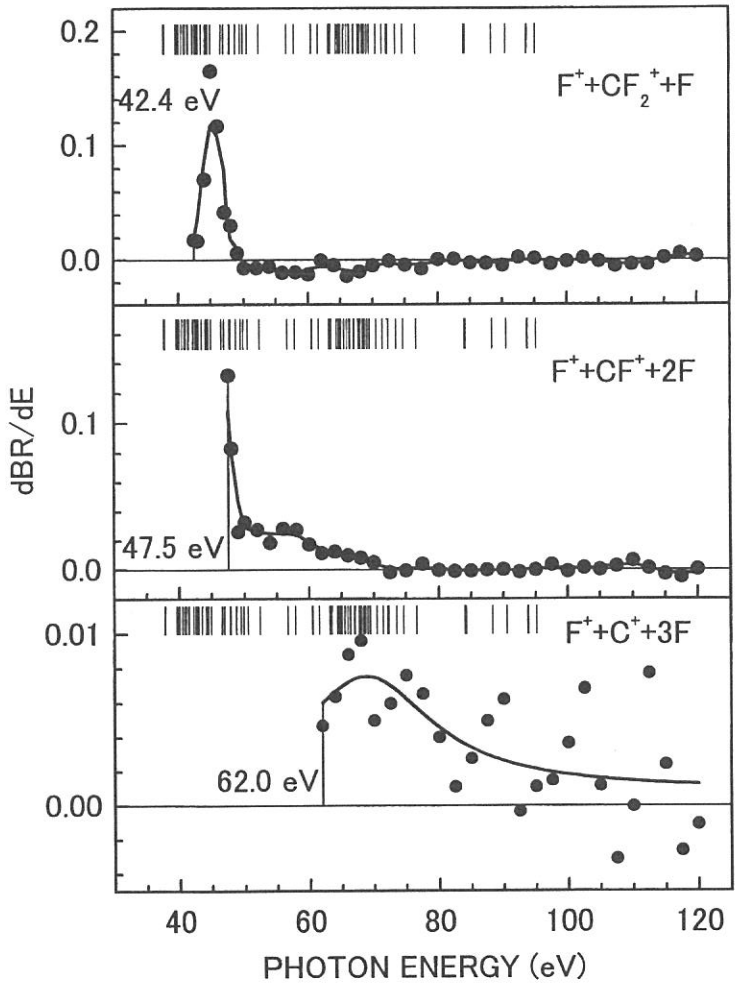

FIG. 2. Differential spectrum of PIPICO branching ratios for the three fragmentation channels.

(BL3A2)

Molecular and dissociative single and double photoionization of CS_2

Toshio MASUOKA, Atsuo OKAJI, and Ataru KOBAYASHI

Department of Applied Physics, Faculty of Engineering,, Osaka City University, Sugimoto 3, Sumiyoshi-ku, Osaka 558-8585

Molecular and dissociative single and double photoionization processes of carbon disulfide have been studied with time-of-flight (TOF) mass spectrometry in the 20-120 eV range by the use of synchrotron radiation. Sn and Al optical filters were used to eliminate higher order radiation. The TOF mass spectra were measured at an angle of about 55° with respect to the polarization vector of synchrotron radiation to minimize any effects of anisotropic angular distributions of fragment ions. To obtain accurate ion branching ratios, the radio frequency (rf) signal (90.115 MHz) of the storage ring was used as the start input of a time-to-amplitude converter (TAC) under the single bunch mode operation of the storage ring.

The observed ions are CS_2^+, S_2^+, CS^+, S^+, C^+, and CS_2^{2+}. The ion branching ratios for these fragment ions increase at various photon energies, indicating the presence of dissociation pathways at these photon energies. In order to correlate these dissociation pathways more clearly to the electronic states of CS_2^+ and CS_2^{2+}, the ion branching ratios for these ions were differentiated with respect to the photon energy. These differential spectra are similar by nature to those measured by threshold photoelectron-photoion coincidence spectroscopy (TPEPICO) except for a low spectral resolution of the present spectra.

Typical examples of the resultant photoion spectra (dBR/dE) are shown in Figs. 1 and 2 for CS^+ and CS_2^{2+}, respectively. The first peak in the photoion spectrum for CS^+ (Fig. 1) indicates that the C state of CS_2^+ dissociates into CS^+ (and also into S^+) in agreement with the observation of Brehm et al. [1] and dipole breakdown scheme of Carnovale et al. [2]. The satellite bands due to configuration interaction have been observed in the 19.1-35 eV range by Carnovale et al. [3]. The first peak in Fig. 1 covers the lower part of the satellite bands, meaning that the lower part of the satellite bands dissociates into CS^+. The threshold for formation of the metastable CS_2^{2+} ions lies at 27.05±0.02 eV (the best previously reported value) measured by TPEsCO spectroscopy [4]. Roy et al. suggested that the bands with binding energies above 27 or 28 eV originate from direct double ionization continua [5]. Theoretical calculation of the energies of the low-lying electronic states of the dication is available [6]. These states are shown in the figure by vertical lines. The second peak in Fig. 1 locates in the double ionization region, probably indicating that the CS^+ ions are formed by the charge separation $CS^+ + S^+$ of the dication. It is interesting to note that the CS^+ ions are formed only in a restricted energy range from about 31 to about 42 eV.

Fig. 2 shows an interesting behavior for the formation of the CS_2^{2+}ions, i.e., the dication is formed only in a narrow energy range from 27.05 to about 35 eV with a peak at about 29 eV. Hochlaf et al. have reported the potential energy curves along the SC-S coordinate for 14 electronic states of CS_2^{2+} using complete active space self-consistent field (CASSCF) approach and have shown that all low-lying electronic states of CS_2^{2+} are separated by large barriers from their dissociation asymptotes [6]. They have further mentioned that all electronic states up to about 32-33 eV have bound parts on their potential curves and are stable with respect to the dissociation. The present observation is essentially in agreement with their calculation.

REFERENCES

[1] B. Brehm, J. H. D. Eland, R.Frey, and A. Küstler, Int. J. Mass Spectrom. Ion Phys. **12**, 213 (1973).
[2] F. Carnovale, A. P. Hitchcock, J. P. D. Cook, and C. E. Brion, Chem. Phys. **66**, 249 (1982).
[3] F. Carnovale, M. G. White, and C. E. Brion, J. Electron Spectrosc. Relat. Phenom. **24**, 63 (1981).
[4] M. Hochlaf, R. I. Hall, F. Penent, J. H. D. Eland, and P. Lablanquie, Chem. Phys. **234**, 249 (1998).
[5] P. Roy, I. Nenner, P. Millié, P. Morin, and D. Roy., J. Chem. Phys. **87**, 2536 (1987).
[6] M. Hochlaf, G. Chambaud, and P. Rosmus, J. Chem. Phys. **108**, 4047 (1998).

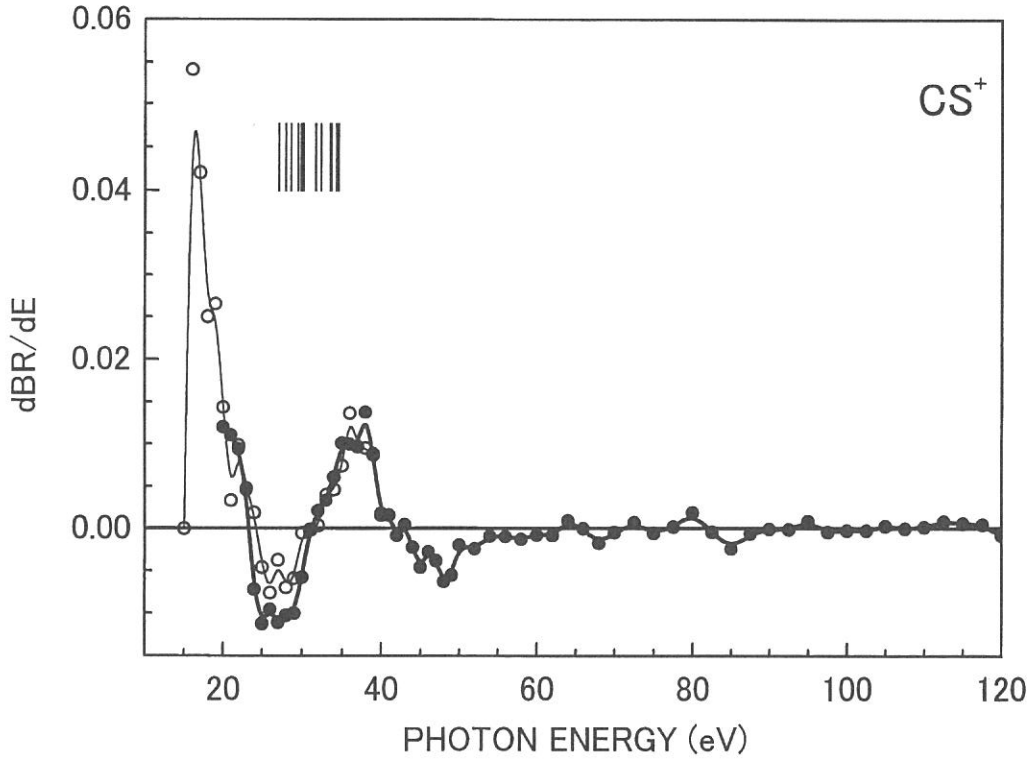

FIG. 1. Differential spectrum of ion branching ratios for CS^+. ● and fat solid line, present result; ○ from ref. 3, thin solid curve is a fitting result to their data. Vertical lines indicate the electronic states of CS_2^{2+} from ref. 6.

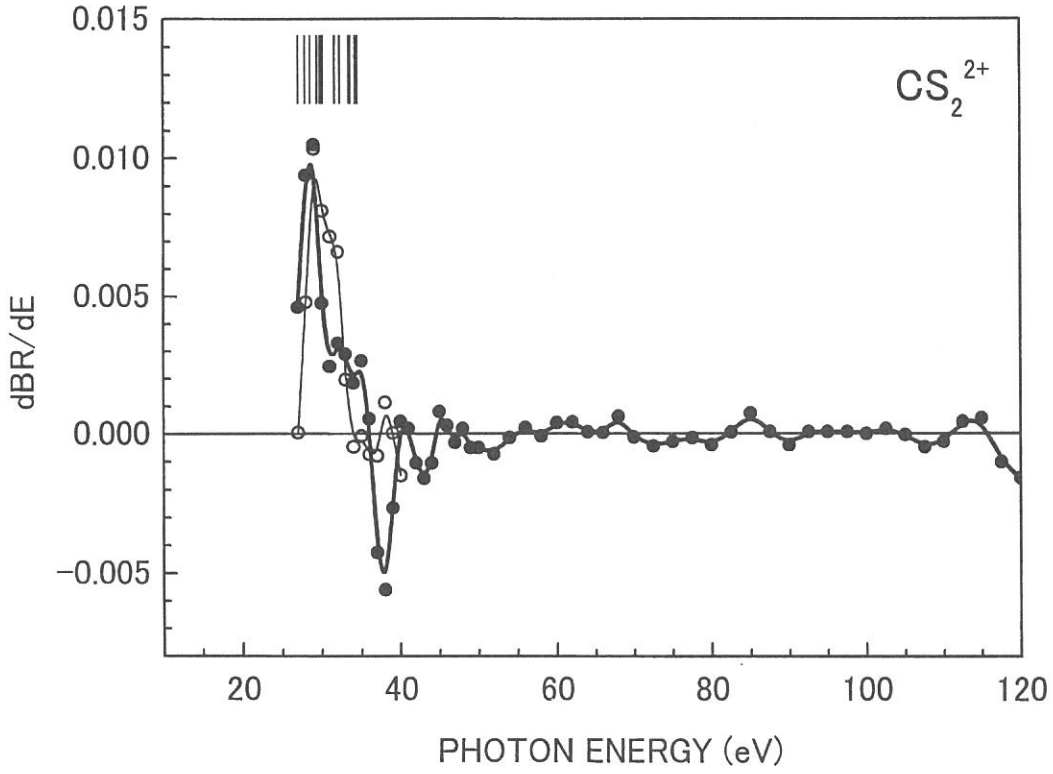

FIG. 2. Differential spectrum of ion branching ratios for CS_2^{2+}. ● and fat solid line, present result; ○ from ref. 3, thin solid curve is a fitting result to their data. Vertical lines indicate the electronic states of CS_2^{2+} from ref. 6.

(BL3A2)

Laser Induced Fluorescence Spectroscopy of CN($X\,^2\Sigma^+$) Radicals Produced by Vacuum UV Photoexcitation of CH_3CN with Synchrotron Radiation

Koichiro Mitsuke and Masakazu Mizutani

Institute for Molecular Science, Myodaiji, Okazaki 444-8585, Japan

Department of Structural Molecular Science, The Graduate University for Advanced Studies

Synchrotron radiation-pump and laser-probe spectroscopy is employed to observe CN radicals in the vibronically ground state produced from CH_3CN. The photon energy of synchrotron radiation is changed from 13.6 to 18.6 eV. The laser induced fluorescence signal is measured as a function of the photon energy with the laser wavelength fixed at the CN($B\,^2\Sigma^+$, $v_B = 0 \leftarrow X\,^2\Sigma^+$, $v_X = 0$) transition. The onset of 15.4 eV of the fluorescence signal indicates that the detected CN($X\,^2\Sigma^+$) radicals result from dissociative ionization of CH_3CN. The partial cross section for the formation of CN($X\,^2\Sigma^+$) is estimated to be 0.1 – 0.5 Mb and is compared with that for the CH_3^+ formation.

A wide wavelength range of synchrotron radiation was searched for the LIF signal of CN($X\,^2\Sigma^+$) with the laser and monitored wavelength fixed at 388 and 420.8 nm, respectively. Fig. 1 shows a plot of the LIF intensity, the difference between the fluorescence signal counts with and without the laser, as a function of the photon energy E_{SR} of synchrotron radiation in the range of 13.6 – 18.6 eV. This plot represents the yield curve for the formation of CN($X\,^2\Sigma^+$, $v_X = 0$). Though the data points show some scatter around the background level, the LIF intensity has an onset at E_{SR} = 15.4 eV and makes a peak around 15.6 eV. Similar E_{SR} dependences of the LIF intensity have been obtained at other laser wavelengths between 387 and 388.5 nm. The onset energy of 15.4 eV is in a reasonable agreement with the appearance potential of the CH_3^+ ion reported in the photoionization mass spectrometric study of CH_3CN [2]. This indicates that the CN radical detected by LIF spectroscopy originates from CH_3CN^+ which subsequently dissociates:

$$CH_3CN^+ \rightarrow CN(X\,^2\Sigma^+) + CH_3^+(X\,^1A_1'). \qquad (1)$$

The photoionization efficiency of CH_3^+ has an onset of 15.34 eV, increases gradually with the photon energy up to 17.5 eV and almost levels off thereafter [2]. On the contrary, the LIF signal intensity in Fig. 1 rapidly decreases beyond the peak at 15.6 eV and settle down to the background level at > 16 eV. The absence of the LIF signal above 16 eV is ascribed to a large kinetic energy release on the way of the

dissociation of CH_3CN^+. The quicker the $CN(X\,^2\Sigma^+)$ fragment escapes from the probe region, the lower its time-averaged number density becomes.

References

[1] K. Mitsuke and M. Mizutani, *J. Electron Spectrosc. Relat. Phenom.* submitted.

[2] D.M. Rider, G.W. Ray, E.J. Darland and G.E. Leroi, *J. Chem. Phys.* **74** 1652 (1981).

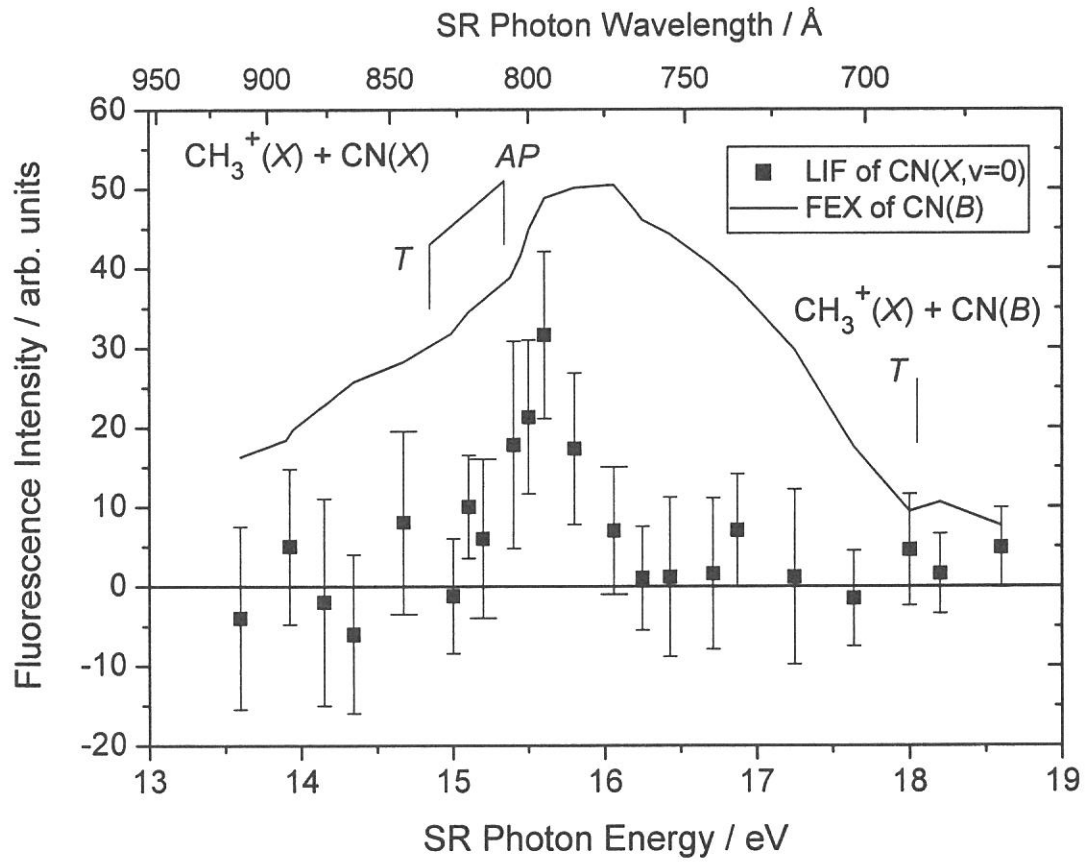

Fig. 1. LIF signal intensity (■) of the $CN(X\,^2\Sigma^+, v_X = 0)$ fragment produced from CH_3CN plotted against the photon energy of synchrotron radiation. The solid curve represents the fluorescence excitation spectrum of CH_3CN for the CN(*B*-*X*) emission. In both cases, the $(X\,^2\Sigma^+, v_X = 1) \leftarrow (B\,^2\Sigma^+, v_B = 0)$ transition was monitored. The thermochemical thresholds (T) for the dissociative ionization of CH_3CN and the appearance potential (AP) of CH_3^+ are indicated.

(BL3A2)

UV and Visible Emission Spectra from Photodissociation of Carbonyl Sulfide Using Synchrotron Radiation at 15 – 30 eV

Koichiro Mitsuke and Masakazu Mizutani

Institute for Molecular Science, Myodaiji, Okazaki 444-8585, Japan

Department of Structural Molecular Science, The Graduate University for Advanced Studies

Photofragmentation of OCS in the excitation photon energy range of 15 – 30 eV has been studied by dispersed fluorescence spectroscopy using monochromatized undulator radiation supplied from the UVSOR facility. The following emission band systems have been identified: $OCS^+[A^2\Pi_\Omega(0,0,0) \rightarrow X^2\Pi_\Omega(0,0,v_3'')]$, $CO^+(A^2\Pi_\Omega \rightarrow X^2\Sigma^+)$, $CS^+(B^2\Sigma^+ \rightarrow A^2\Pi_\Omega)$, and $CO(d^3\Delta \rightarrow a^3\Pi)$. All the transitions except $OCS^+[A^2\Pi_\Omega \rightarrow X^2\Pi_\Omega]$ are newly obtained from photodissociation of OCS in the vacuum UV region. The fluorescence excitation spectra for the $OCS^+[A^2\Pi_\Omega\ (0,0,0) \rightarrow X^2\Pi_\Omega(0,0,v_3'')]$ and $CS^+(B^2\Sigma^+ \rightarrow A^2\Pi_\Omega)$ transitions were measured in the photon energy range of 15.1 – 15.75 and 21.8 – 26 eV, respectively. The emission spectra obtained at 20.85 and 22.9 eV exhibit atomic transitions of $S[nd^3D^o \rightarrow 4p^3P^e\ (n=6\text{-}9)]$ which result from neutral dissociation of superexcited Rydberg states of OCS into $S(nd^3D^o)$ + CO. Possible excited states of the counterpart CO were discussed on the basis of the difference in the n distribution between the two spectra.

Reference

[1] K. Mitsuke and M. Mizutani, *Bull. Chem. Soc. Jpn.* submitted.

Fig. 1. Dispersed fluorescence spectra of OCS encompassing the wavelength region of 360 – 530 nm at five photon energies between 19.85 and 29.8 eV. All spectra were measured by using the imaging spectrograph equipped with a 600 grooves/mm grating which has a nominal blaze wavelength of 500 nm. A 1200 grooves/mm grating with a nominal blaze wavelength of 300 nm was employed to obtain the dashed curve in the panel of E_{hv} = 22.9 eV. The entrance slit width of the imaging spectrograph was set to 500 μm at E_{hv} = 19.85 eV and 250 μm at the other four photon energies. The thin vertical lines indicate a vibrational progression in the antisymmetric stretch v_3 mode of the $OCS^+[A^2\Pi_\Omega(0,0,0) \rightarrow X^2\Pi_\Omega(0,0,v_3'')]$ transition with $v_3'' = 2 - 5$. The number of the excited quanta are given in the panel of E_{hv} = 19.85 eV. Each vibrational band is split into two spin-orbit components specified with Ω = 3/2 and 1/2. The thick vertical lines indicate the band origins of the $CO^+(A^2\Pi_\Omega, v' \rightarrow X^2\Sigma^+, v'')$ emission band system. The (v',v'') mark denotes the vibrational band due to the upper vibrational state v' and the lower state v''.

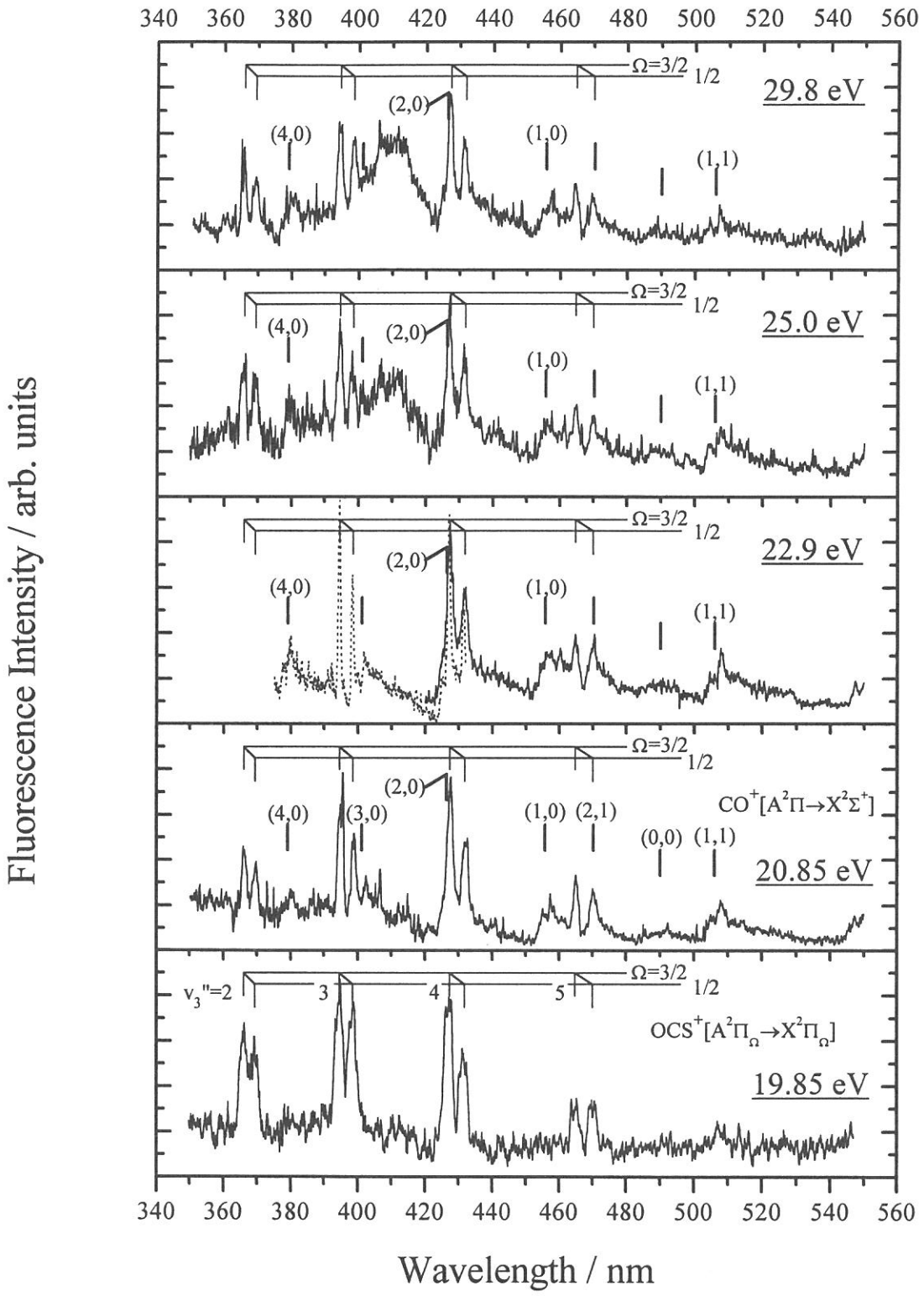
340 360 380 400 420 440 460 480 500 520 540 560
Ω=3/2
1/2
29.8 eV
(2,0)
(4,0)
(1,0)
(1,1)
25.0 eV
22.9 eV
(3,0)
(2,1)
(0,0)
CO+[A2Π→X2Σ+]
20.85 eV
v3"=2
3
4
5
OCS+[A2Π3/2→X2Π3/2]
19.85 eV
Fluorescence Intensity / arb. units
Wavelength / nm

(BL3B)

Superexcitation and Subsequent Decay of Triatomic Molecules Studied by Two-Dimensional Photoelectron Spectroscopy

Koichiro Mitsuke, [a] Hideo Hattori [b] and Yasumasa Hikosaka [c]

[a] *Institute for Molecular Science, Myodaiji, Okazkai 444-8585, Japan*
Department of Structural Molecular Science, The Graduate University for Advanced Studies
[b] *Nitto Technical Information Center Co., Ltd., Toyohashi, Aichi 441-3194, Japan*
[c] *Photon Factory, Institute of Materials Structure Science, 1-1 Oho, Tsukuba, 305-0801, Japan*

Photoionization and photodissociation processes of SO_2 and CS_2 in the vacuum UV are studied by using two-dimensional photoelectron spectroscopy with a monochromatized synchrotron radiation source. The principal focus is on the mechanisms of autoionization and neutral dissociation of superexcited states. Photoelectron spectra of SO_2 exhibit characteristic peaks at the electron kinetic energy below 1.8 eV which are assigned as resulting from autoionizing transitions of excited atomic sulfur, S*, into the ground $S^+(^4S^o)$ state. These S* atoms are in the singlet Rydberg states converging to $S^+(^2D^o)$. The precursor molecular states, SO_2*, are considered to be multiple-electron excited Rydberg states lying at the photon energy above ~22 eV. The onset of the photoelectron yield due to the atomic autoionization accords with that expected from the thermochemical threshold for the formation of S* through three-body dissociation $SO_2^* \rightarrow S^* + O + O$. The two-dimensional photoelectron spectrum of CS_2 provides tangible evidence for the formation of a dipole-forbidden Rydberg state $(6\sigma_g)^{-1}(3d\sigma_g)^1\ ^1\Sigma_g^+$ at the photon energy of 14.88 eV which autoionizes into the $v_3 = 1$ vibrational state of the antisymmetric stretch v_3 mode of CS_2^+ ($X\ ^2\Pi_{g,\Omega}$, Ω=1/2 and 3/2). This Rydberg state is expected to borrow substantial oscillator strength from the $(6\sigma_g)^{-1}(5p\sigma_u)^1\ ^1\Sigma_u^+$ state through vibronic coupling involving the v_3 vibration.

Reference

[1] K. Mitsuke, H. Hattori and Y. Hikosaka, *J. Electron Spectrosc. Relat. Phenom.* **112**, 137-150 (2000).

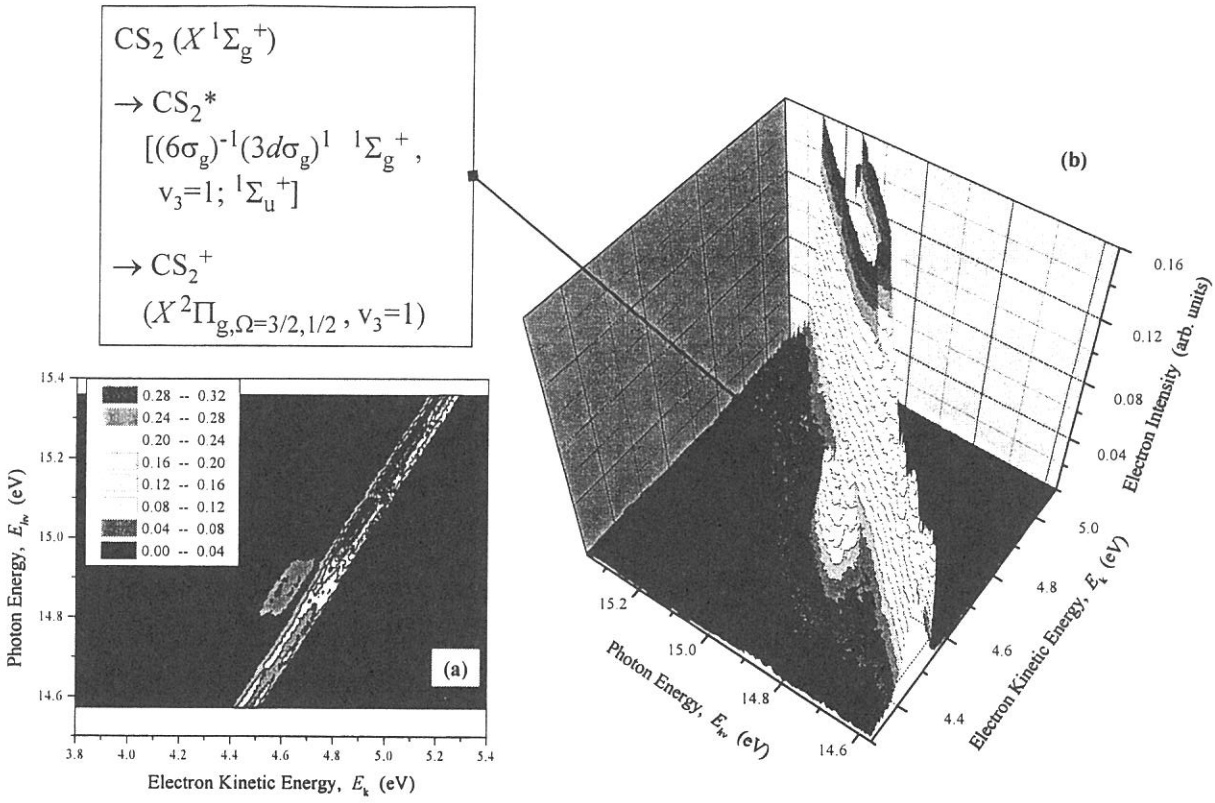

Fig. 1. (a): Two-dimensional photoelectron spectra of CS_2 in the photon energy range of 14.57 – 15.36 eV. The photoelectron yield, measured as a function of both photon energy $E_{h\nu}$ and electron kinetic energy E_k, is presented by the contour plots filled with 8 different colors according the photoelectron intensity on the plot. The photon wavelength resolution is 0.8 Å, which corresponds to 15 meV at $E_{h\nu}$ =15.0 eV. The energy resolution of the analyzer is set to 40 meV. The spectrum is taken at wavelength intervals of 0.3 Å. The diagonal stripes at I_E = $E_{h\nu}$ - E_k = 10.08 and 10.13 eV are identified as direct ionization and/or autoionization into the spin-orbit components (Ω=3/2 and 1/2, respectively) of the vibrational ground state of CS_2^+ ($X\,^2\Pi_{g,\Omega}$).

(b): Surface plot mapped with 16 differently-colored bands according the electron intensity on the surface. This plot is gained by converting the contour plot in panel (a).

(BL4B)

Symmetry resolved photoabsorption spectra of N_2 in the *K*-shell excitation region

Eiji Shigemasa, Tatsuo Gejo, Hiroshi Oji, Mitsuru Nagasono, Takaki Hatsui, and Nobuhiro Kosugi
Institute for Molecular Science, Okazaki 444-8585, JAPAN

In order to identify the symmetries of molecular inner-shell excited states, polarization dependent studies have been widely applied to both chemisorbed and free molecules. The photodissociating molecules produced by a subsequent Auger decay of the *K*-shell vacancy are not isotropically distributed in relation to the exciting radiation, because the absorption probability is greatest when the transition dipole moment is aligned with the electric vector of the incident radiation. Since the lifetime of the molecular inner-shell excited state is much shorter than the molecular rotation period, the angular distribution of the fragments should show a corresponding anisotropy. For diatomic molecules, the measurements of the energetic fragment ions emitted parallel and perpendicular to the electric vector of the incident light achieve complete symmetry resolution between the $\Delta\Lambda=0$ (parallel) and $\Delta\Lambda=1$ (perpendicular) transitions [1].

The angle-resolved photoion measurements were performed on the newly constructed beamline BL4B, equipped with a varied-line-spacing plane grating monochromator. Two identical ion detectors with retarding grids were used to detect energetic photoions (>5 eV) emitted at 0° and 90° relative to the electric vector of the incident light. The $\Delta\Lambda=0$ component spectrum (I_0) and $\Delta\Lambda=1$ component spectrum (I_{90}) were obtained by counting the signals from the 0° and 90° positioned detectors, as a function of the photon energy, respectively.

The symmetry-resolved nitrogen *K*-edge photoabsorption spectra of N_2 measured with a monochromator bandpass of 0.4 eV are shown in Fig. 1. It is clear that the obtained I_0 and I_{90} spectra nicely demonstrate the symmetry decomposition of the conventional photoabsorption spectrum. Fig. 2 shows the high-resolution symmetry-resolved photoabsorption spectra, with a monochromator bandpass of 0.08 eV, in the so-called double excitation region. The I_{90} spectrum exhibits three broad bands centered around 411, 415, and 419 eV, which have not been of interest so far. The strongest band displays fine structures, which have been attributed to the double excitations tentatively. The structure just above the threshold has recently been found [2] and assigned to the double excitations. No special attention has been paid to the band detected at the shape resonance position in the I_{90} spectrum. In the I_0 spectrum, a very weak shoulder on the left-hand side of the shape resonance enhancement can be seen, which may be due to the double excitations having Σ symmetries. The detailed theoretical analyses on such double excitations are now in progress.

References

[1] E. Shigemasa et al., Phys. Rev. A **45**, 2915 (1992).

[2] M. Neeb et al., Chem. Phys. Lett. **320**, 217 (2000).

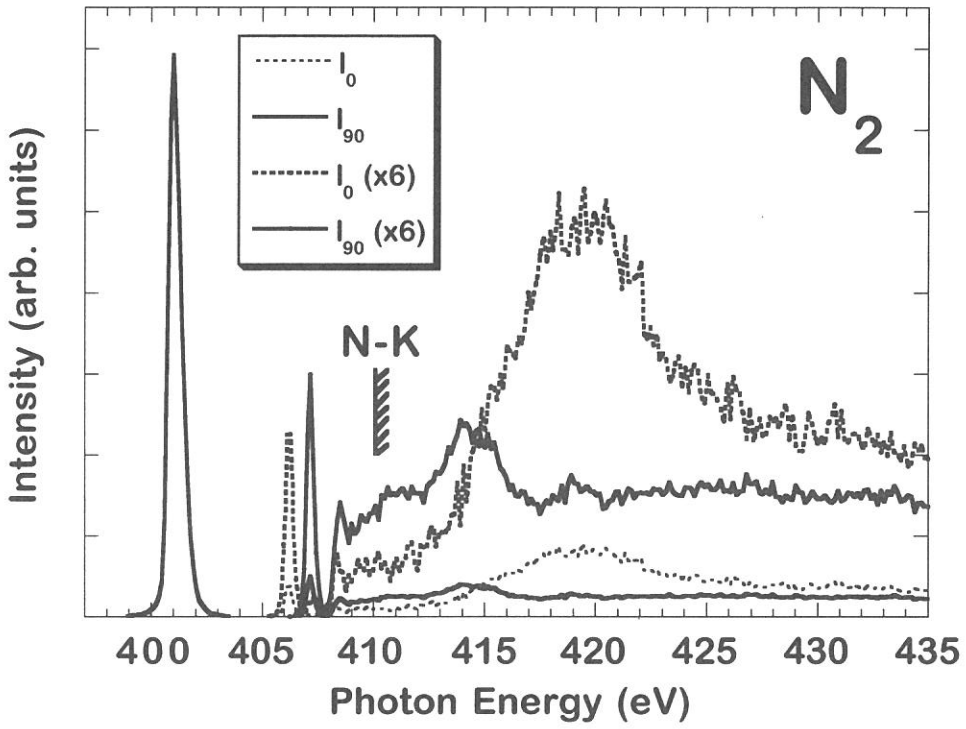

Fig. 1. Symmetry-resolved *K*-shell photoabsorption spectra of N_2.

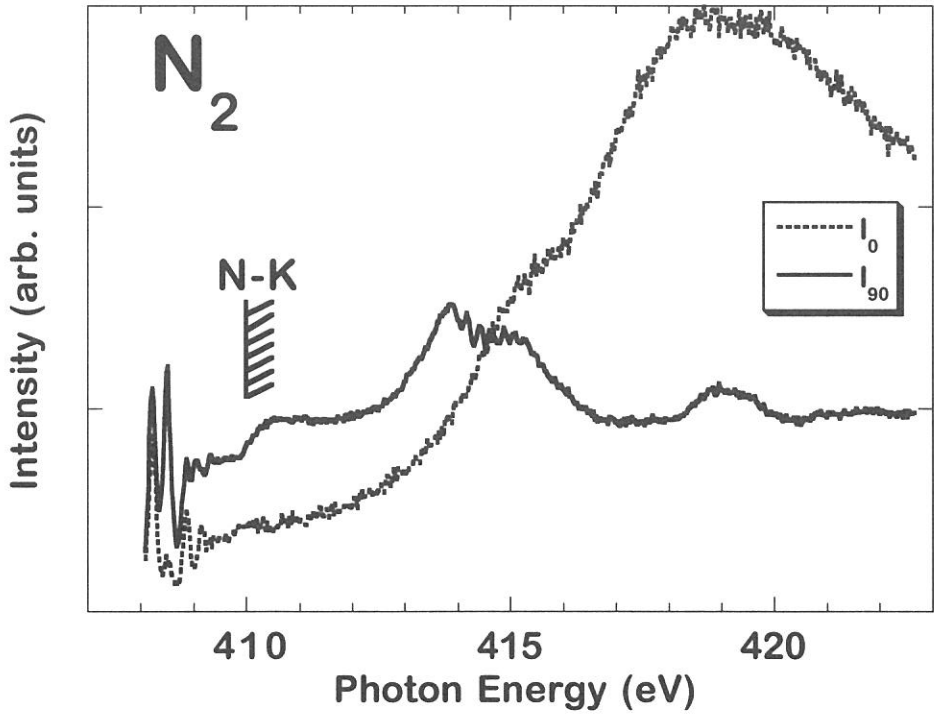

Fig. 2. High-resolution symmetry-resolved *K*-shell photoabsorption spectra of N_2.

(BL8B1)

Study on dissociation dynamics of core-excited acetonitrile using Auger electron-photoion-photoion coincidence measurements

Y. Senba [a], H. Yoshida [a], K. Kato [a], Y. Mishima [a], M. Morita [a], T. Muneyoshi [a], T. Gejo [b], K. Mase [c], and A. Hiraya [a]

[a] *Department of Physical Science, Hiroshima University, Higashi-Hiroshima 739-8526, Japan.*

[b] *UVSOR, Institute for Molecular Science, Okazaki 444-8585, Japan.*

[c] *Photon Factory, Institute of Materials Structure Science, Tsukuba 305-0801 Japan.*

Auger electron-photoion(-photoion) coincidence (AEPI(PI)CO) measurement is a powerful tool to investigate dissociation dynamics of core-excited molecules. However, few AEPI(PI)CO results for complex organic molecules have been reported. We have measured AEPI(PI)CO spectra of acetonitrile-d_3 (CD_3CN) for the N1s $\rightarrow \pi^*$ excitation ($h\nu \sim 400$ eV) at the soft X-ray beamline BL8B1 of UVSOR by using a cylindrical mirror analyzer (CMA) and a high-resolution time-of-flight mass spectrometer. Electrons and ions are extracted by a weak electrostatic field (40 V/cm). Energy resolution (E/ΔE) of the CMA is about 40.

The resonant Auger spectrum of CD_3CN obtained under the present experimental conditions has two broad maximum at around 378 and 360 eV and a shoulder at around 345 eV. A remarkable dependence on Auger-electron energy is observed for the formation of CD_2CN^{2+}, which is only one doubly charged ion among observed ion species. The AEPICO yield spectrum of CD_2CN^{2+} as a function of the Auger-electron energy has a maximum well coincide with the second maximum (~360 eV) of the resonant Auger spectrum. This unique doubly-charged CD_2CN^{2+} ion may be produced efficiently by autoionization and subsequent D atom elimination from the singly-charged parent ions in Auger-final states with ~40 eV binding energy, because this energy is slightly higher than the threshold of doubly-charge parent ion (CD_3CN^{2+}) which is estimated to be ~ 33 eV from the normal AEPICO spectrum.

A part of the AEPIPICO 2D-coincidence maps of CD_3CN at N1s$\rightarrow\pi^*$ excitation for different Auger-electron energies (E_{AE}= 360 eV and 345 eV) are shown in Fig.1. As shown in Fig. 1(a), the resonant-Auger-final states with low binding energy (~40 eV) mainly lead to dissociation into (①$C_2D_3^+$+N^+) and (②CD_3^++CN^+) by single bond-cleavage. Two-body dissociation to (③CD_2^++DCN^+) with rearrangement is also observed. On the other hand, for the higher binding energy (~55 eV, Fig. 1(b)) multiple bond-cleavage is enhanced, and ion-pairs like (④CD_3^++C^+) and

(C_2^++N^+) are formed. The slope of the contour of coincidence peaks for the two-body dissociations (①~③) is −1, while that of (④CD_3^++C^+) peak is about −2. This value is in good agreement with the calculated value of −2.17 for the assumed sequential dissociation process as following.

$CD_3CN^{2+} \rightarrow CD_3^+ + CN^+ \rightarrow CD_3^+ + C^+ + N$

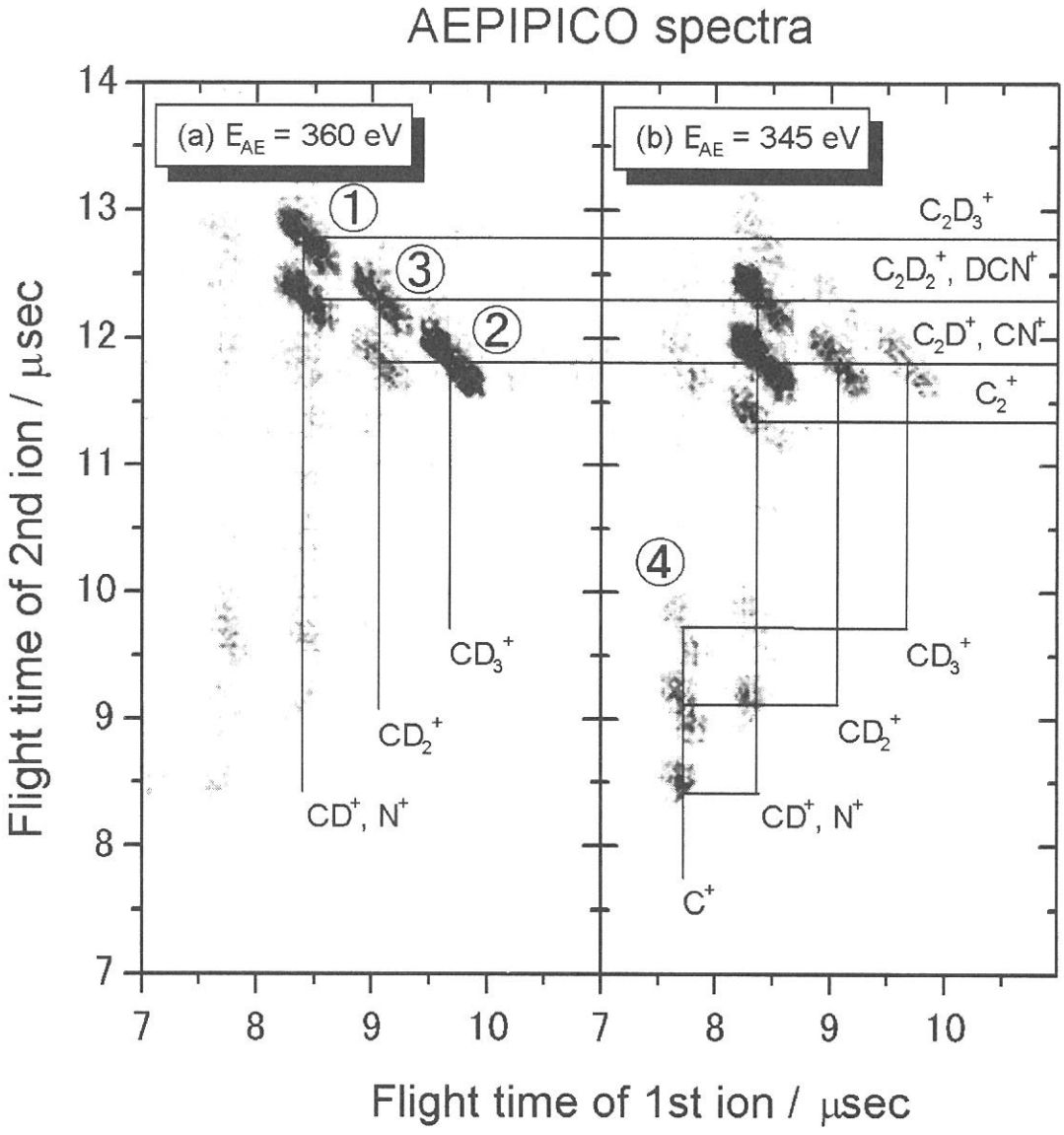

Fig.1 AEPIPICO 2D-coincidence maps of CD_3CN at N1s π* excitation for different Auger-electron energies ((a)E_{AE} = 360 eV and (b)345 eV).

(BL8B1)

Angle-, energy- and mass-resolved photofragmentation of the N and C *K*-shell excited CF_3CN molecule

Shuichiro TANIMOTO, Kazumasa OKADA, Toshio IBUKI[a], Ko SAITO, and Tatsuo GEJO[b]

Department of Chemistry, Hiroshima University, Higashi-Hiroshima 739-8526

[a] *Kyoto University of Education, Kyoto 612-8522*

[b] *Institute for Molecular Science, Okazaki 444-8585*

When an inner-shell electron of a molecule is photoexcited, a multiply ionized molecule is formed through Auger decays. The Coulomb explosion in this multiply charged molecular ion follows the loss of bonding electrons. One of the goals in the studies of inner-shell photoexcitation dynamics is to develop a more detailed understanding of the electronic relaxation and fragmentation processes and, applicably, to take advantage of the localized nature of the core hole to induce a specific bond rupture in a molecule. Inner-shell electrons of an atom in a specific chemical environment can be selectively excited with a monochromatized soft x-ray synchrotron radiation, because the energy levels of the inner-shell electrons differ from one atom to another. The dynamics can be probed by the measurement of mass, angular, and kinetic energy distributions of the fragment ions [1].

Trifluoroacetonitrile (CF_3CN) is one of the intriguing molecules in two respects. Firstly, we can selectively excite a specific atom (F, N or either C). Fluorine is the most electronegative atom and induces the largest chemical shift around it in a molecule. Secondly, we can investigate the fragmentation dynamics of the inner-shell excited molecule noticing the linearity of the C–C≡N skeleton. Whether anisotropic fragmentation can be observed in the polyatomic molecule is our concern here. Thus, in the present study we investigate the angle-resolved time-of-flight (TOF) mass spectra of the N and C *K*-shell excited CF_3CN molecule.

The experiments were performed on the beamline BL8B1 at UVSOR facility. Photoabsorption spectra were observed at room temperature in the N and C *K*-shell regions with the typical energy resolution $E/\Delta E$ of 2000–4000. An ion chamber with two 10-cm long electrodes was used. The photon beam entered through an Al thin filter. The ion current was fed to a picoammeter and stored in a personal computer, together with the pressure of the sample CF_3CN gas monitored with a capacitance manometer. The photon energy was calibrated using the published soft x-ray peaks, i.e., the π^* resonance transitions of N_2 and CO at 401.0 and 287.3 eV, respectively [2].

The TOF mass spectra were also measured at the several prominent resonance peaks observed. An energy resolution of about 1 eV was employed for the measurement. The sample gas was introduced into the main experimental chamber as an effusive molecular beam through a gas nozzle which is mounted orthogonal to both the photon beam axis and the TOF mass spectrometer tube. An Al thin filter was inserted upstream in order to suppress the scattered stray light. The pressures in the chamber during the measurements were kept 1×10^{-5} Torr. The spectrometer was operated under a Wiley–McLaren space-focusing condition [3] with an extraction field of –250 V/cm. This extraction field results from a proper compromise between the sensitivity to the angular distributions and the moderate coincidence count rate of the photofragment ions. Detection of an electron defines the time zero of the TAC for the TOF mass

spectrum. The TOF mass spectra were acquired at 0° and 90° angles with respect to the linearly polarized electric vector of the incident photon. The sample gas for the present study was purchased from SynQuest Laboratories, Inc. and was used without further purification.

The earlier studies of inner-shell photoexcitation dynamics of diatomic molecules have clearly shown that an anisotropic photofragmentation is characteristically observed at the photon energy corresponding to the excitation of a 1s electron into the π^* unoccupied molecular orbital. Figure 1 shows the enlarged TOF mass spectra recorded at the $\pi^* \leftarrow C_N(1s)$ resonance excitation of CF_3CN. In these spectra the contribution of background originating from the ionization of valence electrons was subtracted by the measurement of the spectra at around 283 eV. It is noteworthy that the peaks of CN^+ and CF_3^+ observed at the 90° angle distinctly split into triplets: The central peak is formed by the ions with almost zero or small kinetic energies, while the wings in the lower- and the higher-mass regions arise from the fragment ions with kinetic energies initially toward and away from the TOF tube, respectively. Similar spectra were obtained at the $\pi^* \leftarrow N(1s)$ excitation.

The profiles of CN^+, CF^+, and CF_3^+ peaks were reproduced by the fitting method developed by Saito and Suzuki [4]. The results are also shown in Fig. 1. The CN^+ and CF_3^+ ions are produced by typical Π–Σ transition, which means that the symmetry basically holds also for the relatively large CF_3CN molecule. The anisotropy parameters for CN^+ were found to be +0.10, –0.57, and –0.85 for kinetic energies 0.01–0.41, 0.67–3.61, and 4.33–6.86 eV, respectively. More distinct results were obtained for the N(1s) excitation.

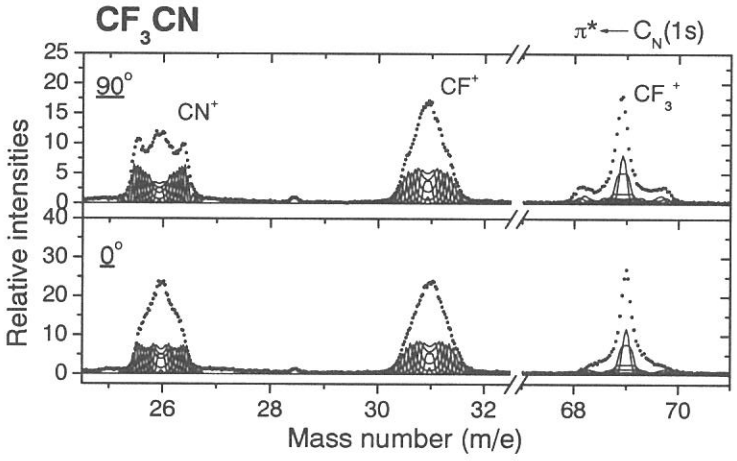

Fig. 1: Experimental and simulated angle-resolved TOF mass spectra recorded at the $\pi^* \leftarrow C_N(1s)$ resonance excitation of CF_3CN. The dots indicate the experimental data. The solid curves are the simulated profiles for the kinetic energy components of 0.01–6.86, 0.01–6.86, and 0.01–3.17 eV for CN^+, CF^+, and CF_3^+ ions, respectively.

References

[1] A. P. Hitchcock and J. J. Neville, in: T. K. Sham (Ed.), "Chemical Applications of Synchrotron Radiation," World Scientific, Singapore, in press.

[2] A. P. Hitchcock and C. E. Brion, *J. Electron Spectrosc. Relat. Phenom.* **18**, 1 (1980).

[3] W. C. Wiley and I. H. McLaren, *Rev. Sci. Instrum.* **26**, 1150 (1955).

[4] N. Saito and I. H. Suzuki, *Int. J. Mass Spectrom. Ion Processes* **82**, 61 (1988).

(BL8B1)

Study on dissociation dynamics of core-excited acetone using Auger electron-photoion-photoion coincidence measurements

H. Yoshida [a], Y. Senba [a], K. Kato [a], Y. Mishima [a], M. Morita [a], T. Gejo [b], K. Mase [c], and A. Hiraya [a]

[a] *Department of Physical Science, Hiroshima University, Higashi-Hiroshima 739-8526, Japan.*

[b] *UVSOR, Institute for Molecular Science, Okazaki 444-8585, Japan.*

[c] *Photon Factory, Institute of Materials Structure Science, Tsukuba 305-0801, Japan.*

To elucidate the detail of the core-excited dissociation processes of organic molecules, especially those from the dicationic states produced after Auger decay, Auger electron–photoion–photoion coincidence (AEPIPICO) method has been applied to acetone. Correlations between different ions produced by an Auger process are recorded in a fast multiscaler, by using the signal of an energy-selected resonant Auger electron as a start signal and the ion signals as multi-stop signals. AEPIPICO signals at the O 1s to π^* resonance, from where only singly charged ionic states is formed by Auger decays, were observed at the lower Auger electron energy side. When the energy of resonant Auger final state is higher than the threshold of dication formation, autoionization channels to form dication states and therefore dissociation to form ion-pairs become possible. By selecting the energy of Auger electron, it is found that only a unique ion-pair CH_3^+ and CH_3CO^+ is produced from the ground state of acetone dication whereas various ion-pairs such as "$H_3C_3^+$ – O^+" and "CH_3^+ – CH_3C^+" are produced from the excited states (see Fig.1).

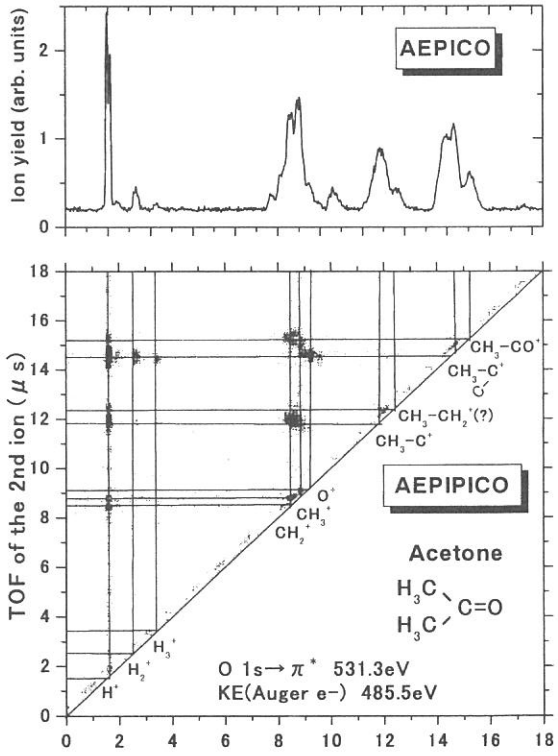

Fig.1 AEPI(PI)CO spectra of $(CH_3)_2CO$ at O1s π^* excitation for the Auger-electron energy of 485.5 eV.

(BL8B1)

Details of H_3^+ Formation from Core-Excited Methanol Revealed by Electron-Ion-Ion Coincidence (PEPIPICO) Measurements.

T. Tokushima, T. Yanagihara, Y.Senba, H. Yoshida, and A. Hiraya

Department of Physical Science, Hiroshima University, Higashi-hiroshima 739-8526, Japan

A number of researches on the dissociation processes of core-excited molecules have been carried out extensively. In those studies, PEPIPICO (Photoelectron-Photoion-Photoion Coincidence) technique was used as the powerful tool to investigate the ionic dissociation from doubly or highly charged molecular ions. However, there are only a few reports applying this technique to complex organic molecules [2]. To investigate ionic dissociation processes of core-excited organic molecules, especially the molecular elimination process to form H_3^+, high mass-resolution PEPIPICO measurements were performed for methanol CH_3OH and CD_3OH.

Measurements were carried out at BL8B1 of UVSOR using the reflectron time-of-flight (RTOF) mass spectrometer [1], which is featured by a high-mass resolution for fragment ions with kinetic energies of several eV while preserving kinetic energy information of the fragment ions.

Figure 1 shows the PEPICO and PEPIPICO spectra of methanol-d_3 (CD_3OH) measured at 544 eV, 4.9 eV above the O 1s ionization threshold (539.1 eV) [5], with using a moderate extraction field (200 V/cm) and the linear TOF mode. In the PEPICO spectrum, D_3^+ is clearly observed with partial yield of 0.6 %, while D_2H^+ is not discernible. From the present result for CD_3OH, it can be concluded that the dominant reaction pathway to form H_3^+ from core excited $CH(D)_3OH$ is the $H(D)_3$ elimination from the methyl group.

PEPIPICO spectra of methanol plotted as the correlation of second-ions to each first-ions are shown in Fig. 2. The spectra reveal that H_3^+ ion is formed exclusively with COH^+, and CH_3^+ with OH^+. Another strong correlation is observed for CH_x^+/OH_y^+ ion pairs (x=0-3, y=0,1), in which x and y has negative correlation. This results suggests that the two type of ion-pairs, CH_3^+ and OH^+ ion-pair formed by single C-O bond scission without further C-H bond scissions and completely cracked (C^+ and O^+) ion-pair formed with further C-H bond scission(s), originate from different dissociation channels, possibly different Auger final states.

References

[1]. A. Hiraya *et al.*, J. Electron Spectrosc. Rel. Phenom. **101-103** (1999) 1025.
[2]. A. Hempelmann *et al.*, J. Phys. B: At. Mol. Opt. Phys. **32** (1999) 2677

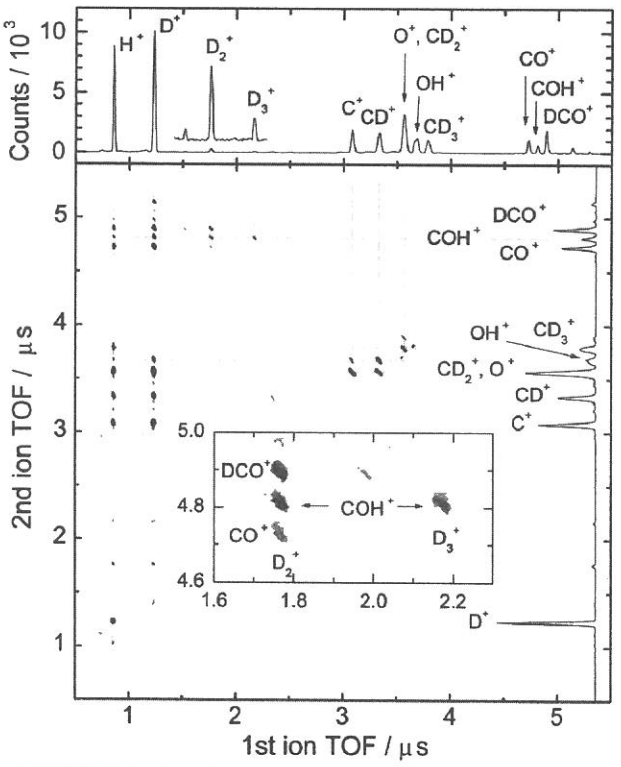

Fig. 1. PEPICO (top) and PEPIPICO spectra of CD_3OH measured at the O1s ionization. Inset shows the mass region of the first ions D_2^+ - D_3^+ and the second ions CO^+ - DCO^+.

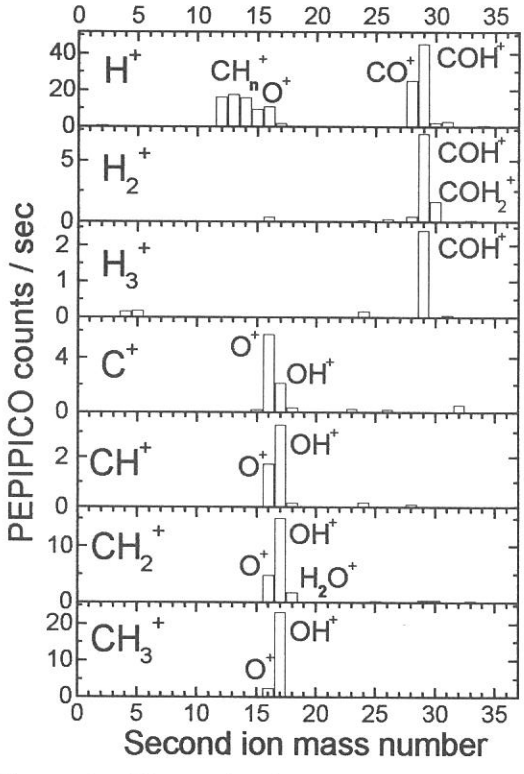

Figure 2. Electron-ion-ion correlation spectra plotted for each first-ion, obtained by the O1s excitation to the ionization continuum of CH_3OH.

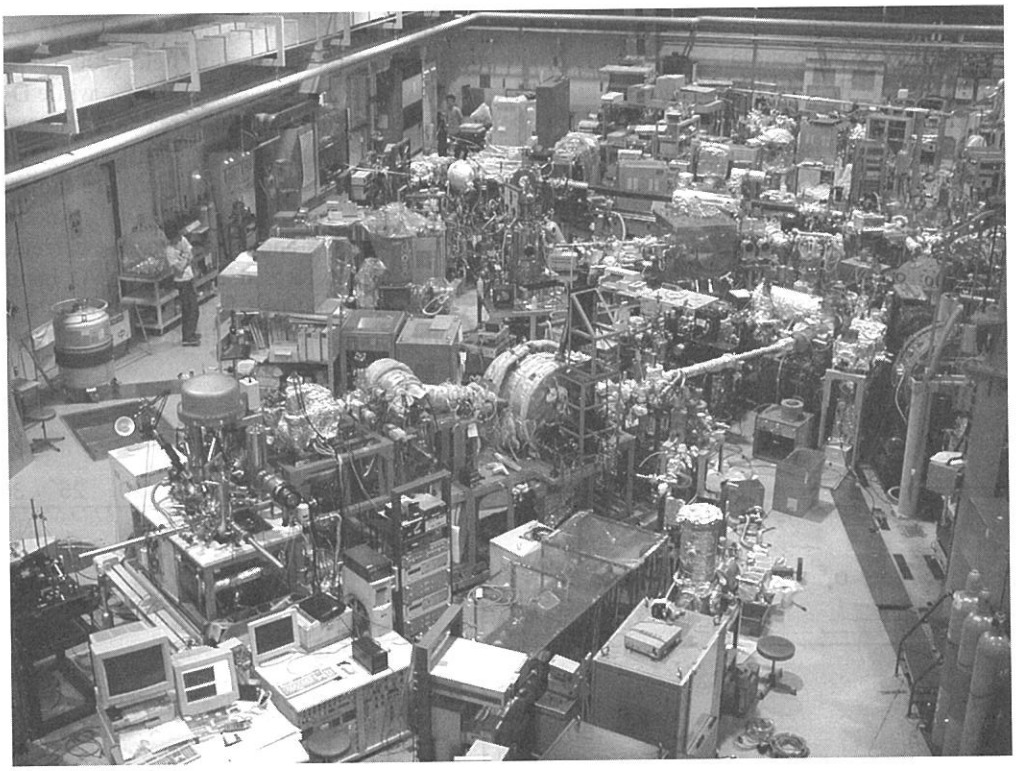

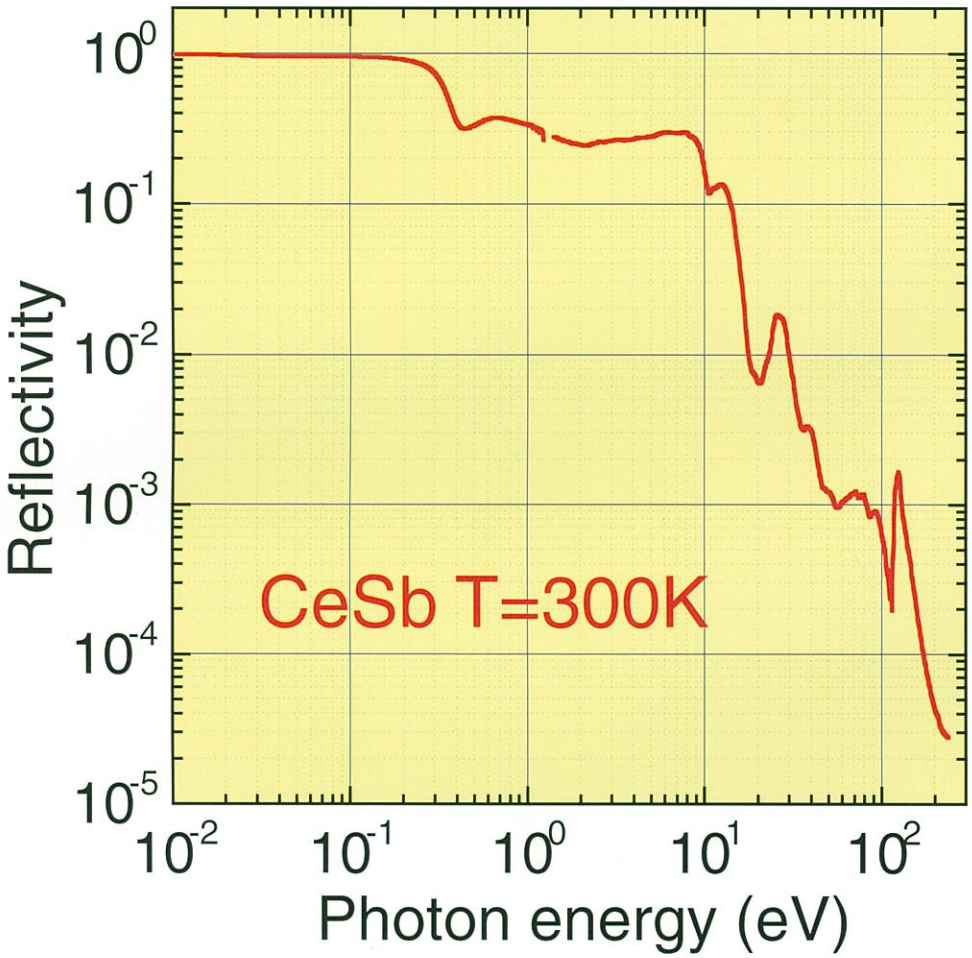

Solid State Spectroscopy I

(IR, VUV etc.)
BL1B, 3A1, 6A1, 7A, 7B

(BL1B)

Observation of new excitation channel of Cerium ion through LiCAF host crystal

Toshimasa KOZEKI, Masahiro SAKAI, Hideyuki OHTAKE, and Nobuhiko SARUKURA
Institute for Molecular Science (IMS), Myodaiji, Okazaki 444-8585, Japan
Tel: +81 564 55 7477, Fax: +81 564 55 7218, e-mail: sakai@ims.ac.jp

Zhenlin LIU, Kiyoshi SHIMAMURA, Kenji NAKANO, Na MUJILATU, and Tsuguo FUKUDA
Institute for Materials Research, Tohoku University, Katahira 2-1-1, Aoba-ku, Sendai 980-8577, Japan

Ce^{3+}:$LiCaAlF_4$ (Ce:LiCAF) [1] is already known as practical tunable ultraviolet laser crystal pumped with the fourth harmonic of an Nd:YAG laser. 60 mJ output from this laser medium was already demonstrated with large-sized CZ-grown crystal [2]. If other pumping schemes were available, it would expand the applicability of this laser medium. In this paper, we report on the observation of new excitation channel of Ce^{3+} through LiCAF host crystal.

The transmission, luminescence and excitation characteristics of Ce:LiCAF crystal were measured using Ultraviolet Synchrotron Orbital Radiation Facility (UVSOR) using 1-m focal length Seya-Namioka monochrometer with a photomultiplier. It was already known that the luminescence spectrum of Ce:LiCAF is around 290 nm. Therefore we measured the excitation characteristics of Ce:LiCAF with observation wavelength 290 nm through band-pass filters as shown in Fig.1. The two peaks in the excitation spectrum corresponded to the absorption of Ce ions. Moreover new excitation channel at around 112 nm was found. The transmission edge of the crystal is known to be about 112 nm. That is completely coincided with the peak of excitation spectrum. Therefore, this excitation can be considered as electron transfer from host crystal to the active Ce ions.

In conclusion, new excitation channel of Ce^{3+} through LiCAF host crystal was discovered. It is interesting that this excitation channel indicate the bandgap of the crystal. This excitation channel will be used as potential pumping channel.

The authors are grateful to Mr. M. Hasumoto, Dr. T. Gejo, and Prof. K. Kamada for their experimental support and stimulated discussion.

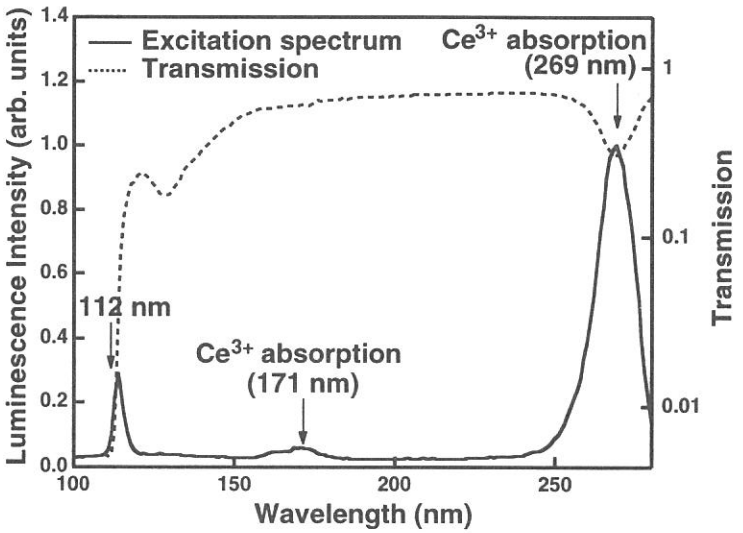

Fig.1 The excitation spectrum and transmission curve for the Ce:LiCAF crystal. The transmission edge 112 nm corresponded to the peak of excitation spectrum.

[1] N. Sarukura, Z. Liu, H. Ohtake, Y. Segawa, M. A. Dubinskii, R. Y. Abdulsabirov, S. L. Korableva, A. K. Naumov, and V. V. Semashko, "Ultraviolet short pulses from an all-solid-state Ce:LiCAF master oscillator and power amplifier system," Opt. Lett. **22**, 994-996 (1997).

[2] Z. Liu, S. Izumida, H. Ohtake, N. Sarukura, K. Shimamura, N. Mujilatu, S. L. Baldochi, and T. Fukuda, "High-pulse-energy, all-solid-state, ultraviolet laser oscillator using large Czochralski-grown Ce:LiCAF crystal," Jpn. J. Appl. Phys. **37**, L1318-L1319 (1998).

(BL1B)

Reflectance Modulation Spectroscopy of Semiconductors by Using Synchrotron Radiation and Laser

Osamu ARIMOTO, Shigeo UMEMOTO, Junpei AZUMA[A], Syuji ASAKA[B,*], Mieko SAKAMOTO, Keita NAKANISHI, Michihiro HORIMOTO[C], Toru TSUJIBAYASHI[D], Masayuki WATANABE[E], Koichiro TANAKA[A], Syunsuke NAKANISHI[F], Hiroshi ITOH[F], Minoru ITOH[C] and Masao KAMADA[G]

Department of Physics, Okayama University, Okayama 700-8530
[A]*Department of Physics, Kyoto University, Kyoto 606-8502*
[B]*Equipment Development Center, Institute for Molecular Science, Okazaki 444-8585*
[C]*Department of Electrical & Electronic Engineering, Shinshu University, Nagano 380-8553*
[D]*Department of Physics, Osaka Dental University, Hirakata 573-1121*
[E]*Department of Fundamental Sciences, Kyoto University, Kyoto 606-8501*
[F]*Department of Advanced Materials Science, Kagawa University, Takamatsu 761-0396*
[G]*UVSOR Facility, Institute for Molecular Science, Okazaki 444-8585*

Combination of synchrotron radiation (SR) and laser is an attractive and promising technique for solid-state research such as two-photon spectroscopy or pump-probe experiments focused on inner-shell electronic states. We have so far investigated exciton structures in wide-gap materials BaF_2 and CaF_2, in which the luminescence induced by two-photon excitation with SR and laser is detected [1-6]. In order to ascend a new step in the combined experiments, we have developed in the present work an experimental system of reflection-type, that is, reflectivity changes induced by laser irradiation are detected in the VUV region with probe light from SR. This system will be useful and powerful especially in the cases where measurements of luminescence or absorption are difficult. Measurements for ZnSe and n-GaAs crystals have been made in order to check the suitability of our system.

In Fig. 1 is shown a schematic diagram of the experimental setup for ZnSe. A second harmonics of CW mode-locked Ti:sapphire laser (Coherent, Mira 900-F/P) was generated with a harmonic generator (Coherent, 5-140 UltraFast Harmonic Generator), and was used as an excitation light source. The synchronization of SR and laser pulses was achieved by a phase-locked loop circuit (Coherent, Mira Synchro-lock 9300), which locked the laser timing to the 90 MHz signal from the RF master oscillator. In order to enlarge the temporal overlap between the SR pulse (1.5 ns) and the laser pulse (160 fs), the laser beam was injected into a multi-mode optical fiber with length of 50 m, which stretches the pulse width to about 300 ps [6]. A ZnSe crystal with thickness of 6000 A grown onto GaAs substrate by molecular beam epitaxy was studied. The band gap energy of ZnSe is 2.82 eV, so that interband excitation was made with the laser light (3.12 eV,13 mW). A glass envelope of the photomultiplier tube (PMT) with CsI photocathode (Hamamatsu Photonics, R2032) was cut down, and it was installed into a sample chamber. Reflected light from the sample was detected with the PMT, and reflectivity change synchronized with the chopped laser light was measured with a lock-in amplifier. In luminescence-detected SR-laser combined experiments, one has to eliminate strong laser scattering light for observing weak luminescence signal. In the present system, on the other hand, the PMT of solar-blind type has no sensitivity for the laser light, so that the problem of laser scattering is cleared away. At present, the system has sensitivity of reflectivity change $\Delta R/R = 10^{-5}$.

Figure 2 shows reflectance modulation spectrum of ZnSe at 15 K. The spectrum was not measured below 6.2 eV, where the PMT does not have enough sensitivity. Significant reflectivity changes are seen in the region from 6.2 to 7.5 eV. As an origin of the reflectivity change, we first checked an effect of temperature increase of the sample due to the laser irradiation, i.e., temperature modulation of the reflectance. The temperature change induces an energy shift of the reflection spectrum. In a rough approximation, therefore, thermoreflectance is to be the same as the wavelength modulation reflectance [7]. However, the derivative of the observed reflection spectrum with respect to energy was found not to agree with the modulation spectrum observed, indicating

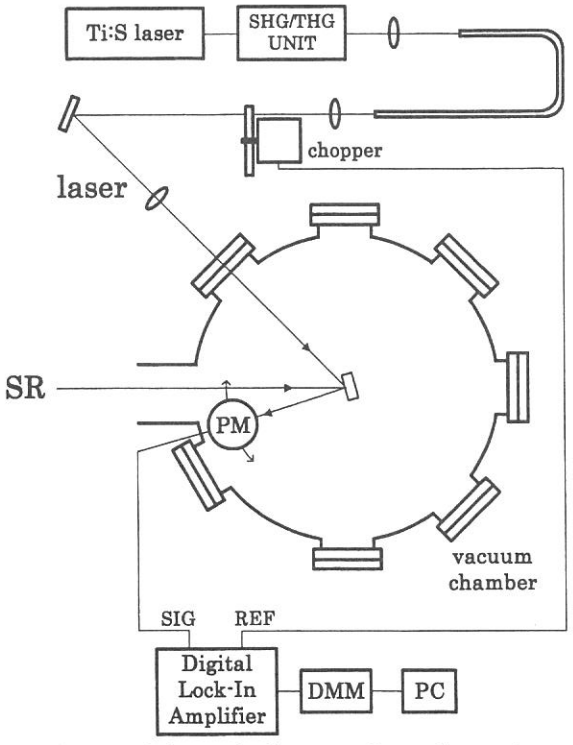

Fig. 1. Schematic diagram of experimental system for reflectance modulation.

negligible contribution of the temperature modulation in the present system.

We consider that the reflectivity change arises from an electric field modulation. The ZnSe crystal has usually an n-type conductivity, and the band bending is inherently induced in a depletion region near the surface. The electrons and holes photoexcited by laser light find themselves in that electric field, and separate spatially in a manner so as to reduce the built-in field. Consequently the reflectance is modulated by the periodic cancellation of the built-in surface field due to the free carriers created by chopped laser light, that is, the present modulation reflectance is originated from the electroreflectance. In general, electroreflectance shows the well-known Franz-Keldysh oscillation under a medium or strong electric field, which allows us identification of critical points. Under a weak electric field, on the other hand, it is shown that the $\Delta R(\omega)$ spectrum is identical with the third derivative of original spectrum $R(\omega)$ [7]. In fact, it was found that d^3R/dE^3 spectrum agrees with the observed $\Delta R(\omega)$ spectrum except an energy range from 6.8 to 7.3 eV; the d^3R/dE^3 spectrum shows no structure there. It has been reported that ZnSe shows reflectivity structures at 6.50 eV and 6.63 eV at room temperature and they are assigned to transitions at Δ_5^v- Δ_5^c and plateau near (0.8, 0.2, 0.2) in the Brillouin zone, respectively, from the band calculation [8]. The structures peaking at 6.45 and 6.62 eV in Fig. 2 are related with these transitions. It is plausible that the observed structures around 7.0 eV appear due to other transitions, which are hidden in the reflection spectrum.

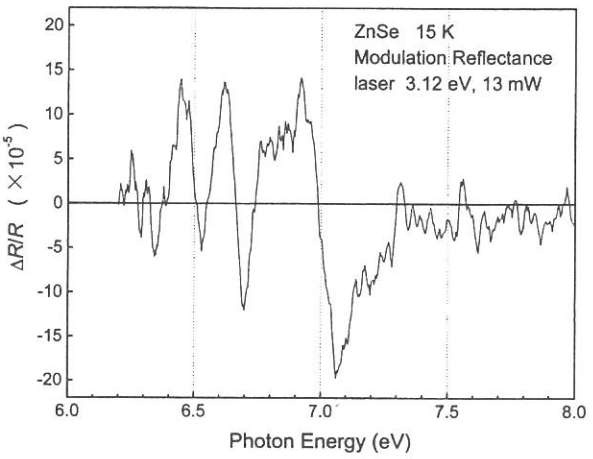

Fig. 2. Reflectance modulation spectrum of ZnSe at 15 K.

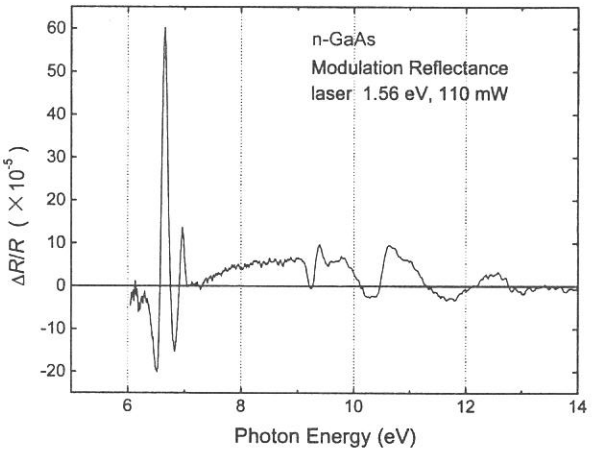

Fig. 3. Reflectance modulation spectrum of n-GaAs at 15 K.

In Fig. 3 is shown modulation reflectance spectrum of n-GaAs (band gap energy 1.520 eV, donor concentration ~10^{18} /cm^3) at 15 K. In this case, fundamental light of Ti:sapphire laser (1.56 eV, 110 mW) was used to create free carriers. An intense reflectivity change is seen at 6.6 eV. Spectral position and shape agree well with those of the electroreflectance [9], if the sign of ΔR is reversed. This fact definitely shows that the observed reflectivity change is caused by the electric field modulation mentioned above. The reverse sign indicates the quenching of the built-in surface electric field due to photocarriers.

In conclusion, we have developed the SR-laser combined experimental system of reflection-type. The system provides non-contact electric field modulation spectroscopy in VUV region without any electrodes, and will be effective for the study on dynamics of photoexcited carriers in semiconductors.

The present work was partly supported by a Grant-in-Aid for Scientific Research from the Ministry of Education, Culture, Sports, Science and Technology.

References

[1] M. Kamada *et al.*: J. Synchrotron Radiation **5** (1998) 1035.
[2] O. Arimoto: J. Electron Spectrosc. Relat. Phenom. **92** (1998) 219.
[3] S. Asaka *et al.*: Rev. Sci. Instrum. **69** (1998) 1931.
[4] T. Tsujibayashi *et al.*: Phys. Rev. B **60** (1999) R8442.
[5] T. Tsujibayashi *et al.*: J. Lumin. **87** (2000) 254.
[6] J. Azuma *et al.*: Nucl. Instrum. Methods (2001) (in press).
[7] P. Y. Yu and M. Cardona: *Fundamentals of Semiconductors* (Springer-Verlag, Berlin, 1996).
[8] J. R. Chelikowsky and M. L. Cohen: Phys. Rev. B **14** (1976) 556.
[9] D. E. Aspnes, C.G. Olson and D. W. Lynch: Phys. Rev. B **12** (1975) 2527.

* Present address: Elementary and Secondary Education Bureau, Ministry of Education, Culture, Sports, Science and Technology, Tokyo 100-0013

(BL1B)

Polarized Reflectivity Spectra of Exciton Band in $PbWO_4$

Masami FUJITA, Minoru ITOH[A], Michihiro HORIMOTO[A],
Hisanobu KUNISAKI[A] and Yoshiyuki USUKI[B]

Japan Coast Guard Academy, Wakaba, Kure 737-8512
[A] *Department of Electrical and Electronic Engineering, Faculty of Engineering, Shinshu University, Nagano 380-8553*
[B] *Materials Research Laboratory, Furukawa Co., Kannondai, Tsukuba 305-0856*

Lead tungstate ($PbWO_4$; PWO) is a well-known scintillating substance. Although the luminescence properties have been extensively studied in the application field, basic investigations on the optical constants such as reflectivity spectra have been still scarce [1-4]. The PWO has two structural modifications, scheelite (tetragonal) and raspite (monoclinic) structures. Recently we measured optical spectra of both phases [3,4]. Belsky *et al.* [1] have reported that the intensity of the exciton band of scheelite crystals is strongly affected by the stoichiometry of samples. However, if one wants to discuss the change in spectra, the polarization dependence of optical constants should be examined in detail, because the scheelite crystal has an anisotropic structure. In the present study we have measured polarized reflectivity spectra of pure and impurity-doped PWO crystals in order to reveal the optical anisotropy and the effect of impurity doping in the exciton band region.

Single crystals of undoped and impurity-doped PWO were grown by the Czochralski method. The dopants investigated here were Cd^{2+}, La^{3+}, Gd^{3+}, Y^{3+}, Th^{4+}, Nb^{5+} and Mo^{6+} ions. Reflectivity spectra were measured at 6 K on the cleaved surfaces of (011) plane [5], with the electric vector parallel ($\boldsymbol{E} \parallel \boldsymbol{a}$) and perpendicular ($\boldsymbol{E} \perp \boldsymbol{a}$) to the $\boldsymbol{a}$-axis.

Figure 1 shows reflectivity spectra of undoped PWO single crystal in the 3–7 eV region. A strong exciton band is observed for the polarization $\boldsymbol{E} \parallel \boldsymbol{a}$. The band consists of two components at 4.25 eV and 4.38 eV as reported in Refs. [3,4]. On the other hand, weak structures are observed at 4.22 eV and 4.45 eV for $\boldsymbol{E} \perp \boldsymbol{a}$. A broad peak is found at 5.27 eV for $\boldsymbol{E} \perp \boldsymbol{a}$, while it is not observed for $\boldsymbol{E} \parallel \boldsymbol{a}$. The peaks at 3.3 eV and 4.0 eV are spurious structures due to the reflection from the rear surface of the sample, because no structures are observed in the absorption spectrum shown in Fig. 1. The absorption band at 3.5 eV is likely ascribed to some lattice imperfection.

In Fig. 2 are shown reflectivity spectra of samples doped with Mo^{6+} (1350 ppm) for $\boldsymbol{E} \parallel \boldsymbol{a}$ and with La^{3+} (1350 ppm) for $\boldsymbol{E} \perp \boldsymbol{a}$. The spectral features above 4.1 eV are essentially the same as those for the corresponding polarization in Fig. 1. Similar polarized reflectivity spectra were obtained for PWO crystals doped with the other impurity ions. When the polarization of light was arbitrary chosen with respect to the crystal orientation, the spectrum exhibits a mixed character of the $\boldsymbol{E} \parallel \boldsymbol{a}$ and $\boldsymbol{E} \perp \boldsymbol{a}$ spectra, as exemplified by the spectrum of the sample doped with Cd^{2+} (1%) in Fig. 2. The humps and peaks below 4.0 eV in Fig. 2 are again due to the reflection from the rear surface of samples.

No appreciable change of the reflectivity spectrum, as well as its polarization dependence, is seen between Fig. 1 and Fig. 2, except for a small broadening of the exciton band of doped samples. This fact indicates that the electronic structures of PWO are hardly affected by the doping of various types of impurity ions.

The present result strongly suggests that the intensity variation of the exciton band pointed out by Belsky *et al.* is ascribed to the anisotropy of the transition intensity, rather than the difference in the stoichiometry of samples [1]. According to the energy band calculation of PWO [6], the valence band is formed by the 2*p* state of O^{2-} ions, and the conduction band is built up of the 5*d* state of W^{6+} ions. Furthermore, the Pb^{2+} 6*s* state hybridizes throughout the valence band, and the Pb^{2+} 6*p* state contributes to the conduction band. The dichroism of the exciton band observed in the present experiment would be ascribed to the crystal-field splitting of the Pb^{2+} 6*p* states in the axial crystal field along the *c*-axis.

The authors would like to thank Prof. M. Kobayashi (KEK) for useful comments on PWO crystals.

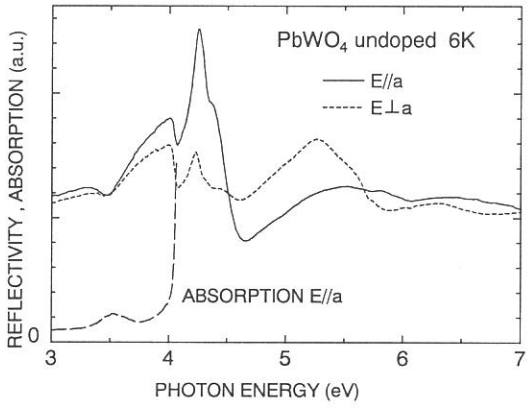

Fig. 1 Reflectivity and absorption spectra of undoped $PbWO_4$ crystal.

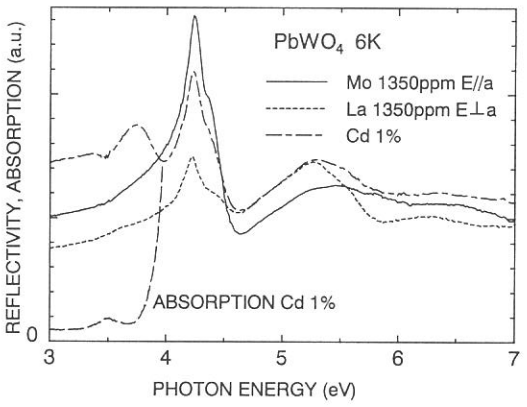

Fig. 2 Reflectivity and absorption spectra of $PbWO_4$ crystals doped with impurities.

References

[1] A. N. Belsky, S. M. Klimov, V. V. Mikhailin, A. N. Vasil'ev, E. Auffray, P. Lecoq, C. Pedrini, M. V. Korzhik, A. N. Annenkov, P. Chevallier, P. Martin and J. C. Krupa: Chem. Phys. Lett. **277** (1997) 65.

[2] I. N. Shpinkov, I. A. Kamenskikh, M. Kirm, V. N. Kolobanov, V. V. Mikhailin, A. N. Vasil'ev and G. Zimmerer: Phys. Status. Solidi (A) **170** (1998) 167.

[3] M. Itoh, D. L. Alov and M. Fujita: J. Lumin. **87-89** (2000) 1243.

[4] M. Itoh and M. Fujita: Phys. Rev. B **62** (2000) 12825.

[5] M. Ishii, K. Harada, M. Kobayashi, Y. Usuki and T. Yazawa: Nucl. Instrum. Methods Phys. Res. A **376** (1996) 203.

[6] Y. Zhang, N. A. W. Holzwarth and R. T. Williams: Phys. Rev. B **57** (1998) 12738.

(BL1B)

Optical Spectra of MoO_3 Single Crystals Investigated by Polarized Light

K. Hayakawa, M. Itoh, S. Oishi[1] and M. Fujita[2]

Department of Electrical and Electronics Engineering, Shinshu University, Nagano 380-8553

[1]Department of Environmental Science and Technology, Shinshu University, Nagano 380-8553

[2]Japan Coast Guard Academy, Wakaba, Kure 737-8512

Molybdenum trioxide (MoO_3) has been widely used as a catalyst in the chemical industry. Recently, this material is attracting attention as an optical substance from the viewpoint of technical engineering, because it has a special character such as photochromism or electrochromism. An early study of this material was performed by Deb and Chopoorian in 1966 [1]. Although there are many investigations on amorphous and thin MoO_3 films, few studies have been done for the single crystals.

Single crystals investigated in this work were grown by the sublimation method. The crucible filled with reagent-grade MoO_3 powder was heated to 780－900℃ for 5－10 hours. The temperature gradient along the crucible allowed us to grow single crystals at the relatively cooler upper edge and crucible lid. The MoO_3 crystals obtained were transparent in the visible region.

Figure 1 shows reflectivity spectra of MoO_3 measured at 6 K in the energy range between 3 and 25 eV for the polarization parallel to the *a* axis (E // a) and to the *c* axis (E // c). The absolute values of the reflectivity were not measured in the present experiment. Fortunately, the refractive indices of MoO_3 at 2.1 eV have been measured to be 2.29 for E // a and 2.54 for E // c [2]. Using these values, we obtained the reflectivity spectra of Fig. 1.

The reflectivity spectra exhibit remarkable polarization dependence. The spectrum for E // c rises at lower energy than that for E // a, as shown clearly in Fig. 2. Both spectra are structure-rich in the energy region below 12.5 eV, and have a broad structure at around 20－25 eV.

The imaginary part of the dielectric function and the absorption coefficient have been derived through the Kramers-Kronig analysis of the reflectivity spectra in Fig. 1. The obtained results are shown in Fig. 3. For E // c, three sharp bands are observed at 4.7, 6.1 and 8.6 eV. A weak peak is also seen at 10.5 eV. For E // a, one can see three sharp bands at 4.9, 8.4 and 10.0 eV. Furthermore, doublet structure peaking at 5.5 and 5.9 eV is observable.

No information on the electronic structures of MoO_3 has been available in the literature. Therefore, we calculated the electronic states of a model cluster of MoO_3 by using the DV-Xα method. The crystal structure of MoO_3 belongs to the orthorhombic type, in which molybdenum ions are connected with oxygen ions to form the chain parallel to the *c* axis. The oxygen ion in the direction of *a* axis is connected with this chain, and that in the *b* axis combines weakly with one molybdenum ion. Accordingly, the MoO_3 forms a layered structure. Because of the low symmetry of MoO_3, we used an embedded cluster model for a more accurate calculation. The oxygen ions surrounding a molybdenum ion are divided into two groups. One is the O^{2-}[I] ion aligned

along the *c* axis, and the other is the O^{2-}[II] ion along the *a* axis.

The present calculation indicates that the valence band is dominated by the 2*p* state of oxygen ions, and the lowest conduction band is mainly built up of the 4*d* state of molybdenum ions. The calculated band-gap is 3.9 eV, which is in satisfactorily agreement with the experimental result. The top of the valence band originating from O^{2-}[II] is located at 1.8 eV below that from O^{2-}[I]. This result may explain the difference between the solid and dotted curves in Fig. 2. The absorption spectra of Fig. 3 show a clear dip at around 7 eV higher than the absorption edges. Since the valence-band width is calculated to be about 7.0 eV, the structures observed below the dip are attributed to the transitions from the valence band to the bottom of the conduction band.

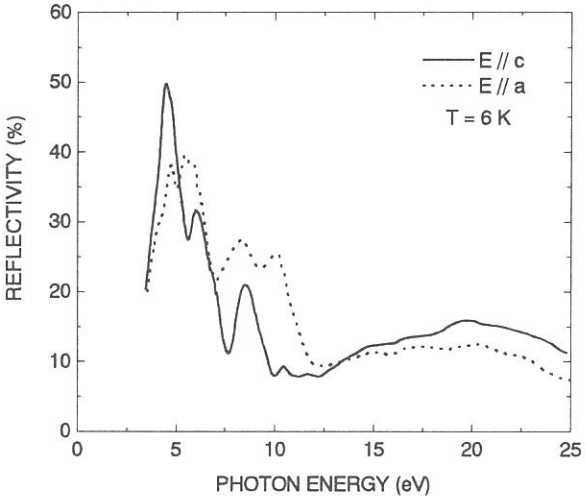

Fig. 1. Reflectivity spectra of single crystal MoO_3 (solid curve ; *E* // *c* and dotted curve; *E* // *a*) at 6 K.

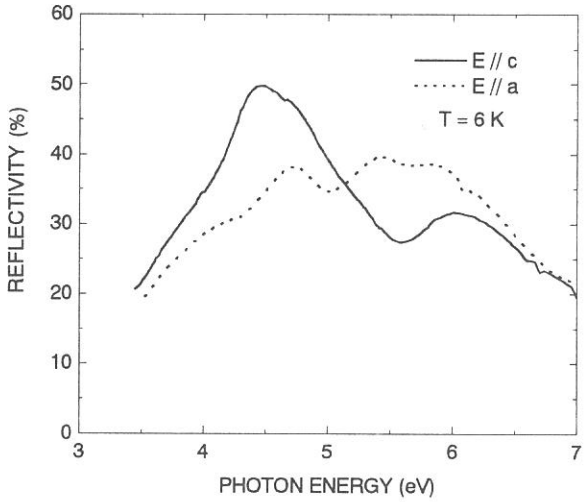

Fig. 2. Reflectivity spectra of MoO_3 in the energy region between 3 and 7 eV at 6 K.

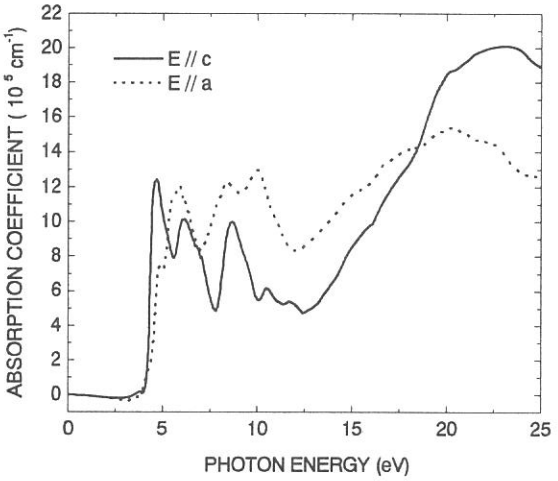

Fig. 3. Absorption spectra of MoO_3 derived through the Kramers-Kronig analysis of the reflectivity spectra in Fig. 1.

References

[1] S. K. Deb and J. A. Chopoorian: J. Appl. Phys. **37** (1966) 4818.

[2] S. K. Deb: Proc. Roy. Soc. A. **304** (1968) 211.

(BL1B)

in-situ VUV absorption spectra and emission spectra of mesoporous silica powder using quartz *in-situ* cell

Yoshitaka Inaki,[1] Hisao Yoshida,[1] Tomoko Yoshida [2] and Tadashi Hattori [1]

[1] *Department of Applied Chemistry, Graduate School of Engineering, Nagoya University, Nagoya 464-8603, Japan.*

[2] *Center for Integrated Research in Science and Engineering, Nagoya University, Nagoya 464-8603, Japan.*

Introduction

We have been studied for a several years about amorphous silica powder catalyst having high surface area (above 500 m^2 g^{-1}) and large amount of surface SiOH groups (~5 OH/nm^2). In our previous study, we discovered that pure silica materials evacuated at high temperature exhibit the photometathesis activity [1]. Metathesis reaction is known to occur only on transition metal catalyst including Mo, Re and W, and therefore, metathesis activity over silica is very unique. We expected that the active sites for photometathesis would be the strained siloxane bridges (≡Si−O⋯⋯Si≡) generated by dehydroxylation of surface isolated SiOH at high temperature such as above 673 K [1, 2]. However the strained siloxane bridges were observed only by infrared spectra and those detailed structure has not been revealed.

Vacuum UV (VUV) and UV spectroscopy is a useful tool for the observation of the defect center on the silica surface and in the bulk silica. The aim of this study is to observe the specific sites on silica materials evacuated at high temperature. In order to measure the spectra of such treated samples without exposure to air, the quartz *in-situ* cell shown in Fig. 1 was used.

Experimental

The silica powder samples we used were amorphous silica and mesoporous silica materials (FSM-16 and MCM-41). Amorphous silica was prepared by sol-gel method. FSM-16 and MCM-41 were prepared by referring the reports [2].

Fig. 1 shows the pretreatment cell. The sample in the pretreatment part (A) was performed at 1073 K in O_2 for 1h, followed by the evacuation at 1073 K for 1h by a diffusion pump (the pressure reached to 10^{-4} ~ 10^{-5} Torr). After pretreatment, the sample was transferred to the measurement part (B) made of quartz and the glass tube was sealed and cut without exposure to air. Then, measurement part was attached to the sample folder (C) by using the carbon adhesive sheet.

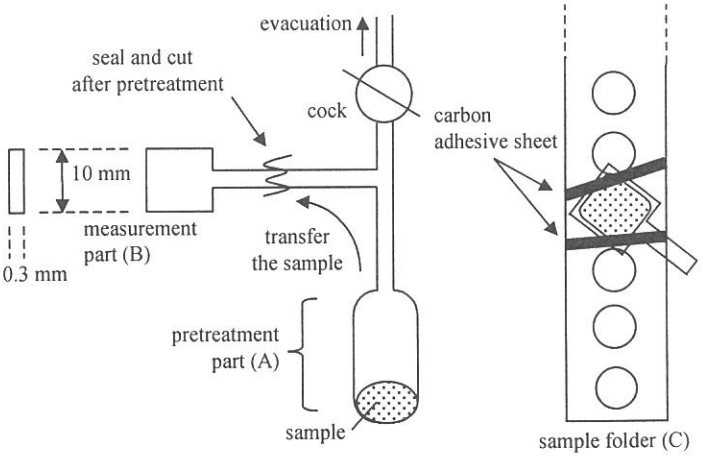

Figure 1 The pretreatment cell (left) and the attachment of sample (right).

VUV spectra and photoluminescence spectra were measured at room temperature using synchrotron radiation at the beam line 1B station (BL-1B) attached with an 1 m Seya-Namioka monochrometer at UVSOR, Institute for Molecular Science, Okazaki, Japan, operated at electron energy of 750 MeV. Photoluminescence spectra were measured by using monochrometer (Spex 270M) and photomultiplier (Hamamatsu R4220).

Results and Discussion

Fig. 2 shows the VUV spectra of FSM-16, MCM-41 and amorphous silica, evacuated at various temperatures. FSM-16 and MCM-41 showed the complex spectra (Fig. 2Aa, 2Ab), which were probably consisted of four absorption bands and the threshold at band gap of silica (8.1 eV, 153 nm) (Fig. 2B). The four bands could be assigned to the defect centers in the bulk silica and on the silica surface [3], respectively: ≡Si-Si

≡ at 7.6 eV (163 nm), ≡Si...Si≡ at 6.9 eV (180 nm), ≡Si·(E' center) at 6.1 eV (203 nm) and =Si : center ($B_2\beta$) and/or ≡Si-O· center (non-bridging oxygen hole center, NBOHC) at 4.75 eV (261 nm). On the other hand, only small absorption band was observed on amorphous silica (Fig. 2Ac), although absorption intensities could not be discussed because these were varied easily by the sample density in the *in-situ* cell. Since effective wavelength for photometathesis over silica is in UV region below ca. 370 nm (> 3.4 eV) [2], either of two defect centers at 261 nm are candidate for the photocatalytic active sites.

Fig. 3 shows the photoluminescence spectra of silica materials evacuated at 1073 K. Only on FSM-16, emission peak was observed at 390 nm (Fig. 3B), which emission was excited by the light at 250 nm (Fig. 3A). This emission band would be assigned to =Si : ($B_2\beta$ center) [3]. On the other hand, $B_2\beta$ center was not observed on MCM-41 and amorphous silica, although these were also active for photometathesis. These suggest that the $B_2\beta$ center should not be the photometathesis active sites. Probably, the another defect sites also showing the absorption band at 261 nm, i. e., ≡Si-O· (NBOHC), should be photometathesis active site rather than $B_2\beta$ center, and ≡Si-O· may relate to the strained siloxane bridges.

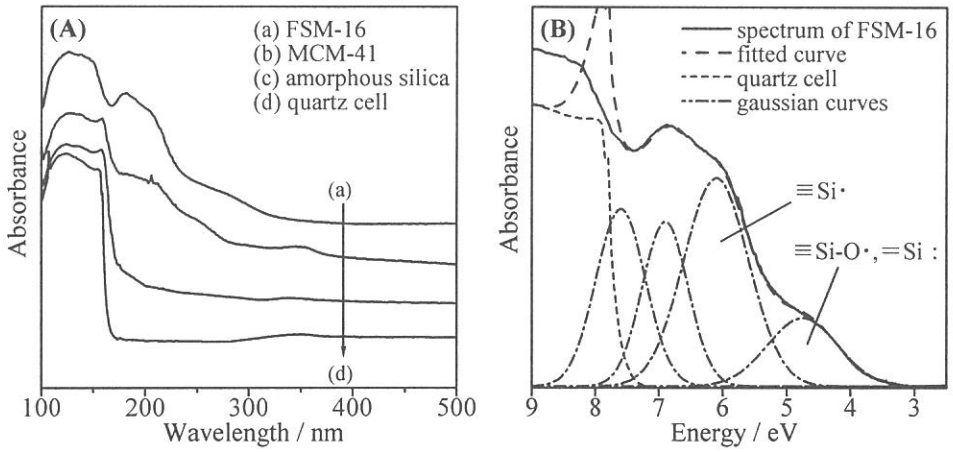

Figure 2 VUV-UV-visible spectra of silica materials evacuated at 1073 K, and of the quartz cell (A), and the spectrum of FSM-16 fitted by a curve of the quartz cell and four Gaussian curves at 7.6 eV, 6.9 eV, 6.1 eV and 4.75 eV (B). Fitting curve did not fit above 7.6 eV, because very large band of the band gap of silica existed and transmittance was extremely low.

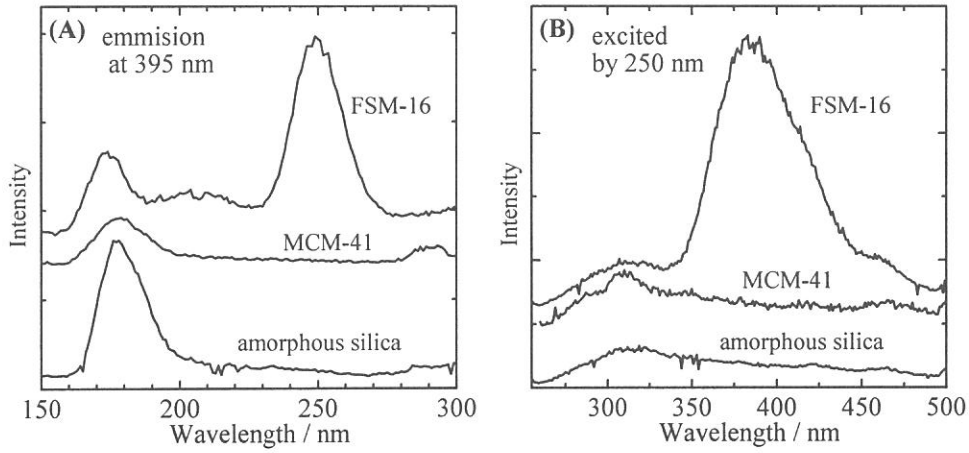

Figure 3 Photoexcitation spectra (A) and photoemission spectra (B) of silica materials evacuated at 1073 K. Peaks around at 175 nm in (A) would be emission from the lens attached to the monochrometer.

[1] Y. Inaki, H. Yoshida, K. Kimura, S. Inagaki, Y. Fukushima and T. Hattori, *Phys. Chem. Chem. Phys.* **2**, 5293 (2000).

[2] Y. Inaki, H. Yoshida and T. Hattori, *J. Phys. Chem. B* **104**, 10304 (2000).

[3] L. Skuja, *J. Non-Cryst. Solids* **239**, 16 (1998).

(BL1B)

Photoionization of Soluble Dye Molecules at the Water Surface

T. Ishioka, K. Seno, T. Sugiyama, A. Harata, and Y. Hatano

Department of Molecular and Material Sciences, Kyushu University, Kasuga-shi, Fukuoka, 816-8580, Japan

Understanding of the spectroscopy and dynamics of photoexcitation and photoionization of molecules at the liquid surface is of essential importance in fundamental and applied sciences. Since little is known such interesting behavior of molecules,[1] RhodamineB (RhB) is chosen in this study as an example of soluble molecules at the liquid water surface for photoionization experiments because of our previous studies of this molecule in laser two-photon ionization experiments.[2]

The experimental setup for photoionization is shown in Fig. 1. Synchrotron radiation obtained at BL-1B of the UVSOR was used as an excitation source. Its intensity was calibrated using a photodiode (Hamamatsu Photonics, S2281-01) for each measurement. The solution of RhB with liquid water was kept on a stainless-steel vessel and high voltage (2000 V/cm) was applied between water surface and an electron-trapping electrode settled in the vessel purged with He gas. The photoionization current was measured using a current meter (Keithley, 617).

Figure 2 shows the photon energy dependence of the photoionization current on RhB solution surface with its threshold at 5.4 eV, which is identified with the lowest photoionization threshold of RhB at the water surface. This result is consistent with the previous one.[2] In the photon energy range above 5.4 eV, the increase in the magnitude of the observed photocurrent I is observed and explained by the following empirical power law represented by

$$I = C\,(h\nu - E_{th})^{\alpha} \qquad (1)$$

with α=2.5, where C is a constant and E_{th} is the ionization threshold.[3] The change in the slope value with increasing the photon energy starting from the threshold, which is observed also in pure liquid hydrocarbons,[4] is explained by the multiple photoionization thresholds corresponding to different molecular orbitals. It is interesting to apply this explanation to the present experiment of the photoionization behavior of RhB molecules on the water surface since RhB is composed of different moieties such as xanthene structure, carboxyphenyl group, and substituted amines. At the water surface, it is also possible to account for the above result by the condition of RhB with different hydration state, depth profile from the surface, and aggregation at the surface. Further experiments are greatly needed to understand the spectroscopy and dynamics of photoexcitation and photoionization of molecules at the liquid surface as opposed to those of isolated molecules in the gas phase.[5]

References

[1] T. Inoue, S. Sasaki, M. Tokeshi, and T. Ogawa, *Chem. Lett.*,**1998**, 609.

[2] T. Ishioka, K. Seno, S. Sasaki, and A. Harata, *UVSOR Activity Report*, **1999**, 70.

[3] J. Casanovas, R. Grob, D. Delacroix, J. P. Guelfucci, and D. Blanc, *J. Phys. Chem.*, **75**, 4661 (1981).

[4] H. Koizumi, K. Lacmann, and W. F. Schmidt, *J. Elec. Spectrosc. Relat. Phenom.*, **67**, 417 (1994).

[5] Y. Hatano, *Phys. Reports*, **313**, 110 (1999).

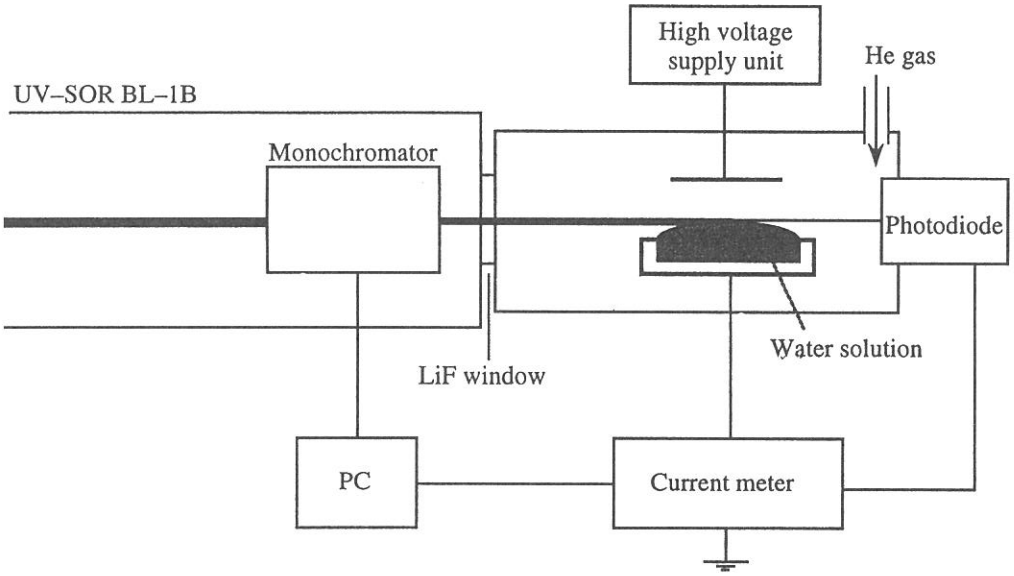

Fig. 1 Schematic diagram of the photoionization spectrometer using SR light.

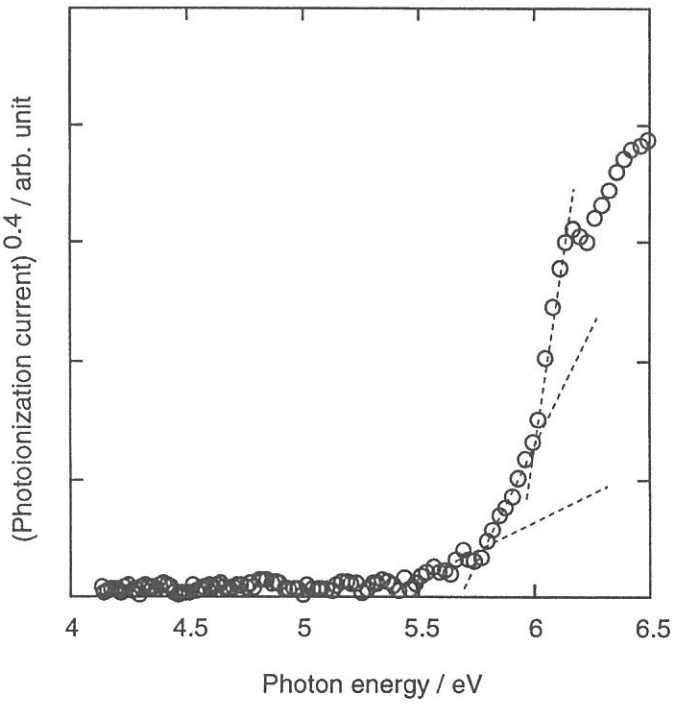

Fig. 2 Photon energy dependence of photoionization current from the surface of aqueous RhodamineB solution. The concentration of RhodamineB was 3.9 μM.

(BL1B)

Luminescence Properties of Tb^{3+} Ions in Mg_2SiO_4 Crystals

M. Kitaura[A], H. Nakagawa[B], K. Ebisu[B] and R. Mizuno[B]

[A]*Fukui National College of Technology, Sabae, 916-8507*

[B]*Department of Electrical and Electronics Engineering, Fukui University, Fukui 910-8507*

Magnesium silicate (Mg_2SiO_4) activated with Tb^{3+} ion has been studied for application in a thermoluminescence dosimeter under irradiation with VUV- light, X- ray and electrons. The thermo-luminescence is certainly induced by electron- hole recombination at the Tb^{3+} ion sites; however, the process has not yet been understood. In the present study, we have investigated luminescence properties of Tb^{3+} ions in Mg_2SiO_4 under excitation with UV- and VUV-light.

The crystals of Mg_2SiO_4:Tb were grown in air from the sintered rods by the floating zone method using an infrared imaging furnace. The concentration of Tb^{3+} ions in the crystals was weighed to 0.1 mol%. The sample was cut off from a crystal ingot, and was mounted on the copper holder of a temperature variable cryostat. The present experiments were carried out at BL1B of UVSOR, where monochromatic light from a 1-m Seya-Namioka type monochromator is available for excitation. Luminescence from the sample was detected by a combination of quartz lenses, a monochromator (Jobin-Yvon HR 320) and a photomultiplier tube (Hamamatsu R955). Excitation spectra reported here were corrected for the spectral distribution of excitation light by using sodium-salycilate phosphor.

Figure 1 shows the absorption spectrum of Mg_2SiO_4:Tb measured at 9 K. Three bands are observed at 4.57, 5.11 and 5.58 eV. These bands were not observed in pure Mg_2SiO_4. This result indicates that the incorporation of Tb^{3+} ions is responsible for the three bands. In addition, their peak energies are in agreement with those of $4f \rightarrow 5d$ bands of Tb^{3+} ions in Y_2SiO_5 [1]. Therefore, the three bands in Fig. 1 are assigned to the $4f \rightarrow 5d$ bands of Tb^{3+} ions in Mg_2SiO_4. In the high-energy side, the absorption spectrum rises drastically. Such a rise corresponds to the fundamental absorption edge of host Mg_2SiO_4. Figures 2 (a) and (b) show emission spectra of Mg_2SiO_4:Tb at 10 K. The excitation photon energy in (a) corresponds to the fundamental absorption region, and that in (b) to a $4f \rightarrow 5d$ absorption peak. In Figs. 2 (a) and (b), sharp emission bands are seen in the range of 1.7-3.5 eV. From comparison with emission spectra of Tb^{3+} ions in Y_2SiO_5 [1] and $YAlO_3$

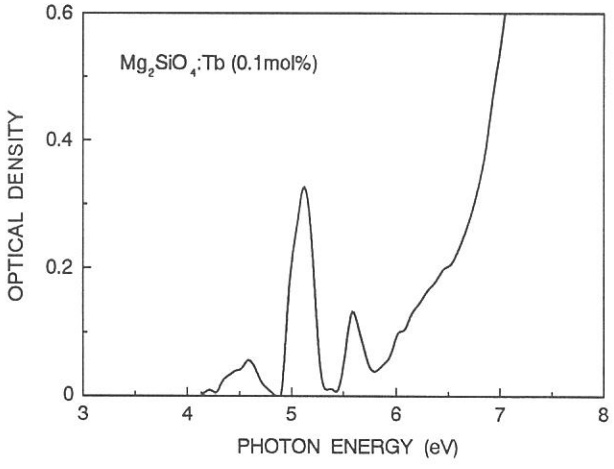

Fig. 1: Absorption spectrun of Mg_2SiO_4:Tb (0.1mol%) at 10 K.

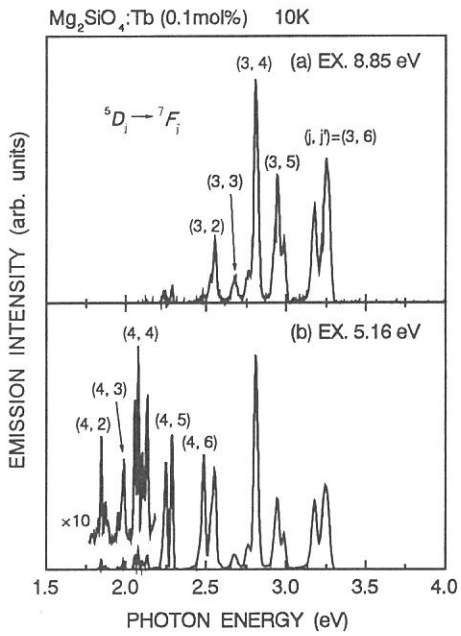

Fig. 2: Emission spectra of Mg_2SiO_4:Tb (0.01 mol%) at 10 K under excitation in (a) the fundamental region and in (b) the $4f \rightarrow 5d$ absorption region.

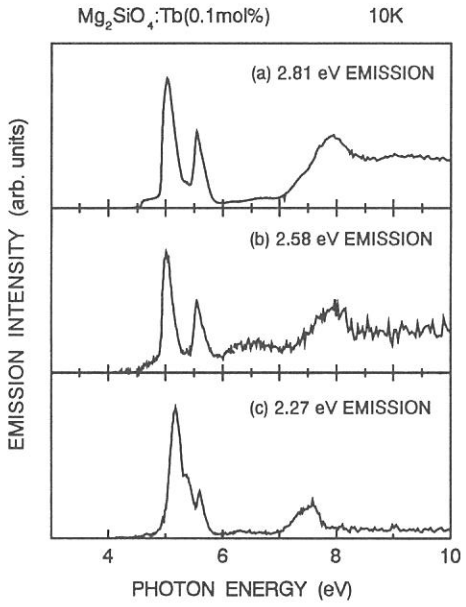

Fig. 3: Excitation spectra for the emission bands at (a) 2.81, (b) 2.58 and (c) 2.27 eV at 10 K.

[2], it is most likely that the emission bands in Figs. 2 (a) and (b) result from the $^5D_j \rightarrow {}^7F_j$ transitions in the Tb^{3+} ion.

Excitation spectra for the emission bands at (a) 2.81, (b) 2.58 and (c) 2.27 eV emission bands are shown in Fig. 3. The 2.81 and 2.58 eV bands originating from the $^5D_3$ level are excited not only in the $4f \rightarrow 5d$ absorption bands, but also in the fundamental absorption region. In Fig. 2 (a), we cannot see any other emission band under excitation in the fundamental absorption region. These results suggest that energy transfer from excited states of host Mg_2SiO_4 to the $^5D_3$ level of the Tb^{3+} ions takes place efficiently. On the other hand, the 2.27 eV band originating from the $^5D_4$ level is also excited in the $4f \rightarrow 5d$ absorption region, though in this region, the excitation spectrum for the 2.27 eV band is different from those for the 2.81 and 2.58 eV bands. Furthermore, it is scarcely excited in the fundamental absorption region. That is, the 2.27 eV band is not produced by energy transfer from host Mg_2SiO_4. The reasons for the differences in the excitation features of the 2.27 eV band from the 2.81 and 2.58 eV bands are not clear.

References

[1] D.Meiss, W.Wischert and S.Kemmler-Sack: Phys. Stat. Sol. (a) **141** (1994) 495.

[2] P.A.Arsenev, K.E.Bienert and A.V.Potemkin: Phys. Stat. Sol. (a), **26** (1974) K71.

(BL-1B)

Multi Lanthanide Doped Fluoride Phosphors for VUV Excitation

T. Kunimoto, R. Yoshimatsu, K. Ohmi and S. Tanaka

Dept. of Electrical and Electronic Eng., Tottori University
Koyama, 4-101, Tottori, Japan, 680-8552

There has been a growing interest recently in the luminescent spectroscopy of lanthanide ions in the vacuum ultraviolet (VUV) region. This has become important because of the need for new phosphors with high quantum efficiencies under VUV excitation and high stability in the plasma environment for VUV applications such as mercury free lamps and plasma display panels (PDPs). Three aspects are important in the development of VUV phosphors : a higher efficiency, a higher stability, and an optimum VUV absorption. For VUV applications, Xe discharge such as 147 nm resonance line and 173 nm excimer band are used as excitation radiation sources. However the power efficiency is quite low because of large stokes shift resulting from the conversion of one VUV photon (> 8 eV) to only one visible photon (1.6~3.2 eV), and the energy transfer probability is relatively small due to the enormously large absorption coefficient in the fundamental absorption of oxide host. To overcome this problem, a concept based on a combination of two or more lanthanide ions which is termed as quantum cutting through down conversion in large band gap material has been reported.[1-3] Other possibility for obtaining higher efficiency VUV phosphors is employing a sensitizer together with the emitting ions or activators in the fluoride host which is transparent in VUV region. The sentitizer efficiently absorbs the VUV radiation and transfers this energy efficiently to the activators. As a possible sentitizer for VUV region we investigated Pr^{3+} ion in fluoride host such as YF_3. The lowest $4f5d$ band of Pr^{3+} ion in YF_3 is predicted to lie above 45000 cm^{-1}[4]. If another lanthanide ion whose $4f$ energy levels happen to coincide with this $4f5d$ band of Pr^{3+} is incorporated in fluoride host, it might be possible for Pr^{3+} ion after absorbing VUV excitation photon to transfer this energy to the $4f$ levels of the incorporated ion instead of relaxing to its $^1S_0$ energy level which lies just below the $4f5d$ band. In this paper, we report our preliminary studies of YF_3:Pr, Gd phosphors under VUV excitation. The enhancement of Gd^{3+} 311 nm emission line with addition of Pr^{3+} ions and the quantum cutting phenomena in Gd^{3+} were observed.

Gd and Pr co-doped YF_3 phosphors were prepared by conventional solid state reaction. Powder samples were first fired at 200 °C for 1 hour and subsequently fired at 1000 °C for 3 hours in Ar atmosphere. Photoluminescence (PL) and PL excitation spectra of the phosphors were measured by BL-1B line of UVSOR. The PL spectra for $Y_{0.7-y}Gd_{0.3}Pr_yF_3$ under 170 nm excitation are represented in Fig. 1. In the range from 300 to 600 nm (16670 ~ 33330 cm^{-1}), the strong emission line of Gd^{3+} at 311 nm (32100 cm^{-1}) and a very weak emission at 407 nm (24570 cm^{-1}) of Pr^{3+} are observed. Above 300 nm (> 33330 cm^{-1}), the weak emission lines due to the ^6D_J - $^8S_{7/2}$ and ^6I_J - $^8S_{7/2}$ were observed. In addition the weak emission line was observed at about 611 nm (16370 cm^{-1}), which shhould correspond to ^6G_J - ^6P_J transitions. We consider that the observation of these emission lines is one of the confirmation of quantum cutting phenonena in Gd^{3+} ion. The peak intensity of Gd^{3+} 311 nm emission increases with increasing Pr content reaching a maximum at y=0.1. It can be seen that the Gd^{3+} 311 nm emission increased by about 5 times in comparison to y=0 sample. To clarify this enhancement, PL excitation spectra of the Gd^{3+} 311 nm emission for both $Y_{0.7}Gd_{0.3}F_3$ and $Y_{0.6}Gd_{0.3}Pr_{0.1}F_3$ were measured. As shown in Fig. 2, with the addition of Pr, a large increase in the excitation band which is mainly for corresponding state above ^6G_J levels of Gd^{3+} is found. The increased excitation band is based on the $4f5d$ absorption band of Pr^{3+}. A possible enhancement mechanism can be represented as follows. The VUV excitation energy is absorbed by $4f5d$ band of Pr^{3+} and the excited electron relaxes to the bottom of $4f5d$ band which is estimated to lie at about 48000 cm^{-1}. In $Y_{0.99}Ce_{0.01}F_3$, we have observed $4f$-$5d$ emission band

with the Stoke's shift of about 5000 cm^{-1}. In $Y_{1-z}Pr_zF_3$, we have observed only $4f^2$-$4f^2$ emissions, and this phenomenon can be explained by configuration coordinate model using the speculation that the Stoke's shift of the lowest $4f5d$ -$4f^2$ emission of Pr^{3+} is about 6000 cm^{-1}. The lattice constant of $Y_{0.6}Gd_{0.3}Pr_{0.1}F_3$ is larger than YF_3. In $Y_{0.6}Gd_{0.3}Pr_{0.1}F_3$, we therefore speculate the energy of $4f5d$-$4f^2$ emission of Pr^{3+} to be about 49000 cm^{-1} (Stoke's shift ; ~3000 cm^{-1}). In $Y_{0.6}Gd_{0.3}Pr_{0.1}F_3$, instead of $4f5d$-$4f^2$ emission of Pr^{3+}, this energy is immediately transferred to the ^6G_J and above levels of Gd^{3+} by resonant energy transfer. This excited state relaxes to the lower ^6D_J, ^6I_J and ^6P_J through the nonradiative processes ($^6G \rightarrow {}^6D \rightarrow {}^6I \rightarrow {}^6P$) and the radiative process ($^6G \rightarrow {}^6P$), resulting in the enhanced Gd^{3+} 311 nm emission corresponding to ^6P_J-$^8S_{7/2}$ transition.

In conclusion the enhancement of Gd^{3+} 311 nm emission (^6P_J-$^8S_{7/2}$) in YF_3 host with the addition of Pr was observed. The energy transfer from this level to other $4f$ levels in suitable activators such as Eu and Tb may produce efficient VUV phosphors.

This work is supported by "Research for the Future Program" through grant JSPS-RFTF 96 R12501 from Japan Society for the Promotion of Science (JSPS)".

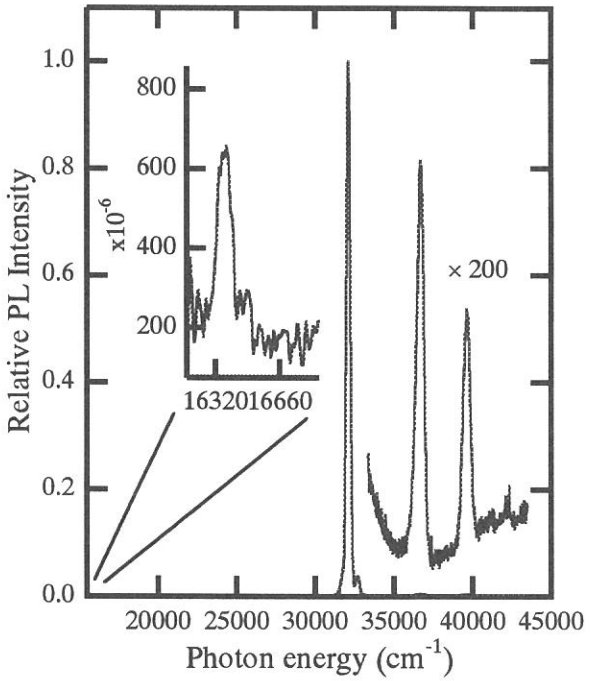

Fig. 1 PL spectra of $Y_{0.6}Gd_{0.3}Pr_{0.1}F_3$ for 170 nm excitation. The inset shows the magnification of emission spectrum around 16500 cm^{-1}. The intensity is normlized by the peak height of Gd^{3+} 311 nm (32100 cm^{-1}) emission.

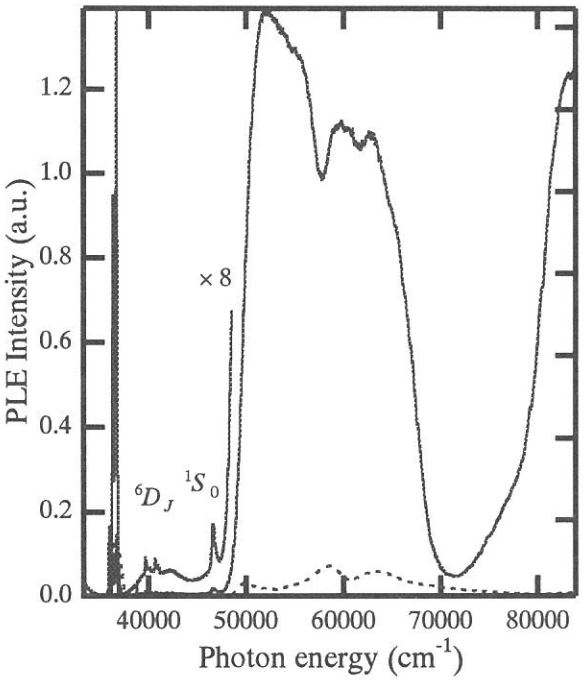

Fig. 2 PL excitation spectra of $Y_{0.6}Gd_{0.3}Pr_{0.1}F_3$ (solid line) and $Y_{0.7}Gd_{0.3}F_3$ (broken line) monitored at 311 nm emission line of Gd^{3+} ion. ^6D_J and ^6I_J levels of Gd^{3+} and $^1S_0$ level of Pr^{3+} can be observed.

REFERENCE

[1] R. T. Wegh, H. Donker, A. Meijerink, R. J. Lamminmäki and J. Hölsä: Phys. Rev. **B56**(1997)13841.

[2] R. T. Wegh, H. Donker, K. D. Oskam and A. Meijerink: Science **283**(1999)663.

[3] R. T. Wegh, E. V. D. van Loef and A. Meijerlink: J. Lumin. **90**(2000)111

[4] W. W. Piper, J. A. DeLuca and F. S. Ham: J. Lumin. **8**(1974)344.

(BL-1B)

Reflection Spectra of Ethyl-Ammonium Cadmium Halides and Ethyl-Ammonium Halides

Akimasa OHNISHI[A], Takafumi OTOMO[A] and Mamoru Kitaura[B]

[A]*Department of Physics, Yamagata University, Yamagata 990-8560*

[B]*Fukui National College of Technology, Sabae 916-8507*

So far, we have investigated optical reflection spectra of $(C_2H_5NH_3)_2CdCl_4$ layered crystals to clarify the energy band structure.[1,2] In this materal, two types of exciton absorption bands are observed at 6.2 and 8.2 eV at 7 K. We proviously assigned that the 6.2 eV band comes from the electronic transition from the Cl^- 3*p* VB to the Cd^{2+} 5*s* CB, and the 8.2 eV band that from the Cl^- 3*p* VB to the NH_3^+ *s*-like CB. As for the assignment of the 8.2 eV band, however, there still remains ambiguity. In the present study, the reflection spectrum of $C_2H_5NH_3Cl$ layered crystal has been investigated to obtain the information about the origin of the 8.2 eV exciton band in $(C_2H_5NH_3)_2CdCl_4$. The reflection spectra for $(C_2H_5NH_3)_2CdBr_4$ and $C_2H_5NH_3Br$ layered crystals have been also investigated.

$(C_2H_5NH_3)_2CdBr_4$ crystals were grown by slow evaporation method from the aqueous solution of stoichiometric amount $C_2H_5NH_3Br$ and $CdBr_2$ at room temperature in dark. $C_2H_5NH_3Cl$ and $C_2H_5NH_3Br$ crystals were also obtained by the similar method. Experiments were perforemed at the BL-1B of UVSOR equipped with a 1m Seya-Namioka VUV monochromator. Reflection spectra from samples for the polarization perpendicular to the *c*-axis (E⊥c) were measured with a combination of a photomultiplier (Hamamatsu R105) and sodium salycilate phosphor.

Figures 1(a) and (b) show the reflection spectra of the cleaved surface of $(C_2H_5NH_3)_2CdCl_4$ and $C_2H_5NH_3Cl$ at 7 K in the range of 3-30 eV for E⊥c. The reflection spectrum of $(C_2H_5NH_3)_2CdCl_4$ is the same as that reported in previous paper.[2] In $C_2H_5NH_3Cl$, the lowest exciton absorption band is observed at 7.8 eV, which is located at the energy position similar to the 8.2 eV band in $(C_2H_5NH_3)_2CdCl_4$. The band-peak energy is in good agreement with that of the lowest exciton band in NH_4Cl.[3] This agreement indicates that the VB and the CB of $C_2H_5NH_3Cl$ are constructed from the Cl^- 3*p* and the NH_3^+ *s*-like states, respectively. Thus, it is most likely that the 8.2 eV band of $(C_2H_5NH_3)_2CdCl_4$ comes from the electronic transition from the Cl^- 3*p* VB to the NH_3^+ *s*-like CB, being in line with our previous assignment.

Figure 2(a) shows the reflection spectrum of $(C_2H_5NH_3)_2CdBr_4$ at 10 K for E⊥c in 3-20 eV. Two exciton bands with splitting energy of 0.5 eV are observed at 4.9 and 5.4 eV. Since the splitting energy is comparable with the spin-orbit splitting energy of a Br atom, they are related to the transition from the VB constructed from Br^- 4*p* states (so-called halogen doublet). In addition, the band-peak energies agree well with those of the lowest exciton bands in $CdBr_2$.[4] Therefore, the 4.9 and 5.4 eV bands in $(C_2H_5NH_3)_2CdBr_4$ are attributed to the transitions from the Br^- 4*p* VB to the Cd^{2+} 5*s* CB. Two exciton bands with the splitting of 0.5 eV are also observed at 6.9 and 7.4 eV. By the analogy with the case of

$(C_2H_5NH_3)_2CdCl_4$, they are suggested to be due to the transition from the Br^- $4p$ VB to the NH_3^+ s-like CB.

In Fig. 2(b) is shown the reflection spectrum of $C_2H_5NH_3Br$ at 10 Kfor E⊥c in 3-20 eV. At 6.5 and 7.0 eV the peaks due to halogen doublet are observed. The peak energies of the 6.5 and 7.0 eV bands are in good agreement with those of the lowest exciton bands in NH_4Br, [3] and thus the exciton bands are attributed to the electronic transitions from the Br^- $4p$ VB to the NH_3^+ s-like CB. From this, the 6.9 and 7.4 eV bands of $(C_2H_5NH_3)_2CdBr_4$, which are peaked at the almost same energy positions as the 6.5 and 7.0 eV bands in $C_2H_5NH_3Br$, must come from the transition from the Br^- $4p$ VB to the NH_3^+ s-like CB.

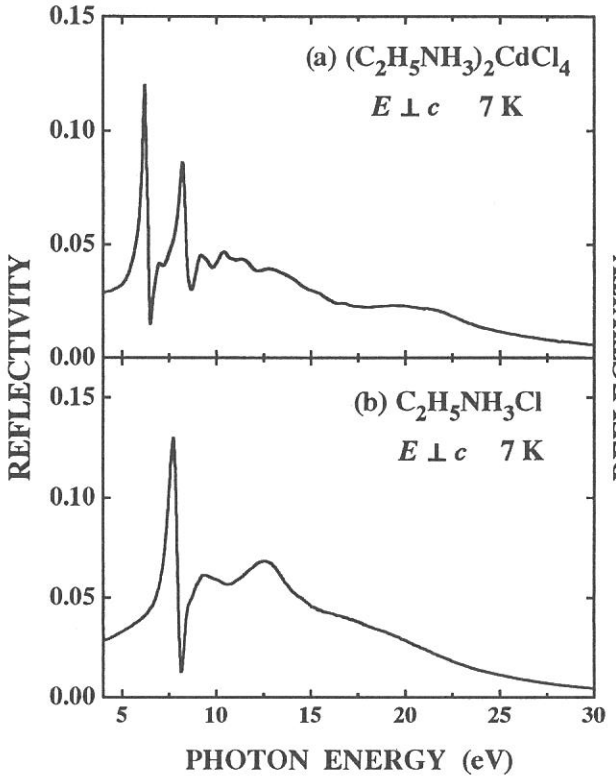

Fig.1 Reflection spectra of (a) $(C_2H_5NH_3)_2CdCl_4$ and (b) $C_2H_5NH_3Cl$ layered crystals

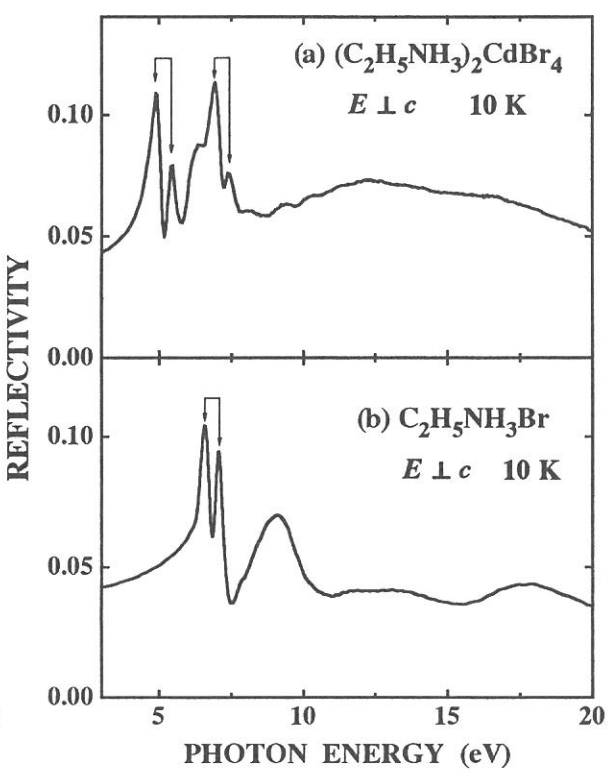

Fig.2 Reflection spectra of (a) $(C_2H_5NH_3)_2CdBr_4$ and (b) $C_2H_5NH_3Br$ layered crystals

References

1) A. Ohnishi, K. Tanaka and T. Yoshinari: J. Phys. Soc. Jpn. **68** (1999) 288.

2) A. Ohnishi, K. Tanaka, T. Otomo, T. Yoshinari and M. Kitaura: UVSOR-27, *p.*80.

3) H. Yamashita: J. Phys. Soc. Jpn. **29** (1990) 338.

4) M. Fujita, H. Nakagawa, H. Matsumoto, T. Miyanaga, M. Watanabe, K. Fukui, E. Ishiguro, Y. Fujii and Y. Sakisaka: J. Phys. Soc. Jpn. **59** (1990) 338.

(BL1B)

Fluorescence Spectra of Uniaxially Oriented Polyethylene 2,6-Naphthalate Films

Isuke OUCHI, Ikuo NAKAI[A] and Masao KAMADA[B]

Faculty of Engineering, Tokushima Bunri University, Shido, Kagawa 769-2193
[A]Faculty of Engineering, Tottori University, Koyama, Tottori 680-8552
[B]UVSOR, Institute for Molecular Science, Myodaiji, Okazaki 444-8585

Polyethylene 2,6-naphthalate (PEN) is a polyester having naphthalene rings in the main chain, one each in a repeat unit. The fluorescent nature of PEN has been known since long ago. The first description about it appeared in 1969;[1] high-energy electron excited luminescence of PEN films was compared with that from dimethyl 2,6-naphthtalate solutions and crystals, indicating that the former was broader and shifted its peaks toward longer wavelengths. The red shift therein was interpreted to be due to emission from excimer states. Since then, several researchers including one of the present authors treated the luminescence of PEN for various purposes.[2-4] According to them, the excitation peaks nearly corresponded to those of absorption; and the fluorescence spectrum looked roughly like a mirror image of the absorption. Its fluorescence occurred from the lowest energy level of the singlet excited states, which was conformed to the Kasha law.

In the present study, it was intended to look into the emission behaviour of PEN in the vacuum ultraviolet region and also to reveal more details of the spectrum in the ultraviolet and visible regions in respect to the molecular orientaion.

Relatively thick samples of undrawn, uniaxially or biaxially drawn films of 60-100 μ m thickness, were supplied from the Film Research Laboratory of Teijin Limited. Cut samples of 10 - 15 mm square were held by screws between a copper frame and a holder, keeping the original machine direction. Eight circular holes of 10 mm diameter were opened in the copper holder plate; eight samples were measured during a series of experiments.

The Seya-Namioka type monochromator installed at the BL-1B was utilized for reflection and emission measurements in the range between 500A and 6500A. In most cases, the G3 grating of 600 lines/mm was utilized. Incidence angle was set as 12.5° for reflection measurements. The exit slit width was set as 100 μ m for reflection and overall excitation measurements; here, the overall excitation spectra mean the spectra taken without filter nor monochromator for emitted light. Namely, only excitation light is monochromatized by a grating; and the observed light intensity is the sum of all the light of various wavelenghts emitted from the sample and passed through the detector window. Therefore, one concerns only which wavelength of incident light is effective to excite the luminescence. Contribution of stray light to the luminescence was corrected by substracting the fluorescence taken with a pyrex glass before the sample; this correction was less than 1 %. In the measurements of fluorescence or ordinary excitation spectra, the slit width was set as 500 μ m; fluorescence was lead to the MIC monochromator placed outside of the vacuum chamber. Although the incident light is fairly polarized as a nature of synchrotron radiation, the emitted light was detected without polarizers.

Separate measurements were further made by use of Shimazu Fluorescence Spectrometer Model RF 5300PC with a xenon lamp as light source. A pair of polarizers were placed before and after the sample, when necessary. A Jusco spectrometer, consisting of a monochromator for excitation and a double monochromator for luminescence, having a halogen lamp as a source was also used in parallel.

An example of the overall excitation spectra is shown in Fig. 1, for a biaxialy drawn PEN film, where

absorption spectra of a uniaxially drawn PEN film[5] are superposed on the overall excitation spectra. If looked at closer, the excitation peaks therein correspond to the tails of the absorption rather than the peaks. This may be related to the fact that the intensity of fluorescence increases with the depth reached by the incident light, depending on the absorption coefficient at the wavelength of emitted light.

Although effects of stray light were corrected, there may be some effects of reflected light by scattering. Nevertheless, it seems that there must be a considerable amount of emission in vacuum ultraviolet region on top of the detected fluorescene in ultraviolet region.; because, the excitation at 1200A gave rise to only about tenth of the fluorescence if observed at 4300A, comparing with those excited at 2500A and observed at 4300A. This problem is yet to be examined.

Fig. 2 shows the fluorescence spectra of undrawn PEN films taken with a pair of polarizers before and after the specimen; this measurement was made separately by use of Shimazu Fluorescence Spectromer RF5300PC. Since undrawn films are isotropic in the film plane, these curves indicate that the monochromator for emission is horizontally polarized in this wavelength region. (Monochromator for incidence light has the same character.) Furthermore, Fig. 2 indicates that the fluorescence of PEN is composed of two peaks about 200A apart; also, the longer wavelength peak at about 4550A is parallel-polarized, as clearly manifested by measurements by use of uniaxially drawn films, which are not shown here.

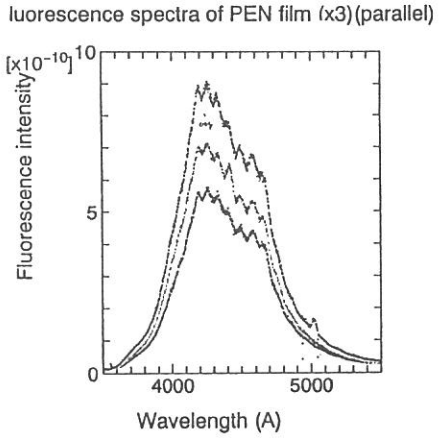

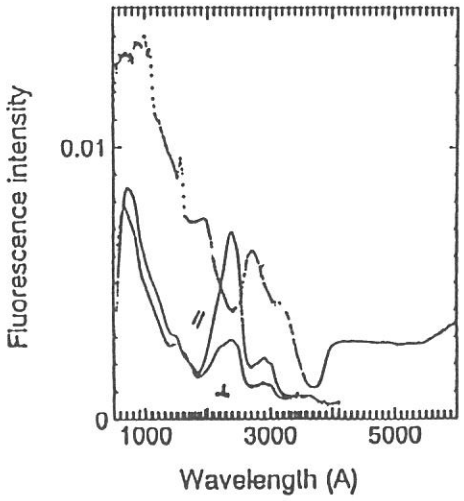

Fig. 1. Overall excitation spectra of a biaxially drawn PEN film (Upper curve). Lower curves are the absorption spectra, either parallel or perpendicular, of a uniaxially drawn PEN film in an arbitrary unit.

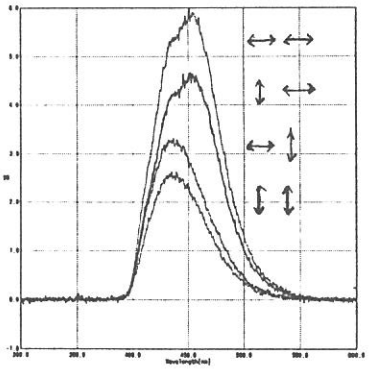

Fig. 2. Fluorescence of undrawn PEN films excited at 3500 A. First arrow indicates the polarization of incident light, and the second that of fluorescence.

Fig. 3 shows an example of fluorescence spectra of a uniaxially drawn PEN film excited at 2550A, 2000A, 3500A (from the top to the bottom), where the electric vector of the synchrotron radiation was parallel to the draw direction. In addition to the two components shown in Fig. 2, fine structures are clearly manifested. Further analyses are yet to be made.

1. D.H. Phillips and J.C. Schug, J. Chem. Phys., 50 (1969) 3297.
2. I. Ouchi, M. Hosoi and F. Matsumoto, J. Appl. Polym. Sci., 20 (1976) 1983.
3. P.-S. Cheung, C.W. Roberts and K. Wagener, ibid 24 (1979) 1809.
4. I. Ouchi, R. Miyamura, M. Sakaguchi, S. Hosaka and M. Kitagawa, Polym. Adv. Technol., 10(1999)195.
5. I. Ouchi, I. Nakai and M. Kamada, UVSOR Act. Rept. 1999,(2000) 82.

(BL1B)

Photoluminescence in Polypropylene Induced by Ultraviolet Laser Irradiation

Takehiko TOYODA, Hiromitsu KATO, Toshihide ITO, Naoshi HIRAI and Yoshimichi OHKI
Department of Electrical, Electronics, and Computer Engineering, Waseda University
Shinjuku-ku, Tokyo 169-8555

Category 4. Solid- and liquid- phase spectroscopy 1 (IR, VUV, etc)

I. EXPERIMENTAL PROCEDURES

The samples tested are PP sheets of 50 μm thick. The sample is just general PP sheets, in which some kinds of additives and antioxidants are added. This material only contains saturated C-C and C-H bonds which are not chromophores. Therefore, in PP, luminescence contribution of chromophores is rather low leading to an easier observation of luminescence due to degradation. We have measured photoluminescence (PL) spectra and photoluminescence excitation (PLE) spectra induced in PP by irradiation of photons from an ArF excimer laser (photon energy: 6.4 eV, power intensity: ca 50 mJ/pulse, repetition frequency: 1 Hz) and synchrotron radiation (SR) at BL1B line in UVSOR at 300 K.

II. RESULTS AND DISCUSSION

The PL spectrum excited by synchrotron radiation photons with an energy of 6.4 eV at 300 K is shown in Fig. 1. The change of the PL spectrum as a function of the irradiation time is shown in Fig. 2 for the case that the excitation by the ArF excimer laser was continued in air at room temperature. Because the repetition frequency of the laser was 1 Hz, it is thought that the temperature increase and its effect on the chemical change are negligible. The luminescence around 4 eV decreases rapidly with continuous laser irradiation, and a new luminescence band with a peak around 3 eV is induced. The luminescence due to the oxidation that relates essentially to the degradation of PP is examined by comparing luminescence spectrum induced by the irradiation in a vacuum and the one induced in an O_2 atmosphere. So, the PL spectra are compared in Fig. 3 between two cases where the sample was put in vacuum (1×10^{-1} Pa) and in oxygen at 1 atm at room temperature. The PL intensity is found to be enhanced significantly around 3 eV by the irradiation in vacuum, although it diminishes almost completely if irradiated in oxygen.

As an alternative possibility, it is considered that the excitation band has been moved to an energy different from the one of the ArF excimer laser (= 6.4 eV). Therefore, the PLE spectrum was measured using synchrotron radiation at 300 K in a vacuum at 1.3×10^{-7} Pa for the samples that had been irradiated by the ArF excimer laser for 1000 s either in air, in oxygen, or in vacuum at room temperature. The PLE spectra obtained at different detecting energies (4.1, 3.5, and 2.9 eV) are shown in Fig. 4. The PL intensity becomes smaller with an increase in the oxygen content of the atmosphere. In Fig. 4(a), it is also found that the PLE spectrum measured after the irradiation in vacuum has its peak at a lower energy than the peak position before irradiation.

As for the PLE spectra detected at 3.5 eV, the intensity becomes larger and a new PLE band appears around 5.7 eV if the sample was irradiated in vacuum, while the PL intensity becomes smaller for the samples irradiated in air or in oxygen. When the PLE was detected at 2.9 eV, the PL was observable only in the sample that had been irradiated in vacuum as shown in Fig. 4(c). These results suggest that different chemical groups were formed through different processes depending on the point that oxygen was present or not when the sample was irradiated for 1000 s by the ArF excimer laser. Namely, the luminescence center disappears by the continuous photon irradiation in the presence of oxygen, while a new luminescence center is induced by similar irradiation if oxygen is not present.

When the photons from an ArF excimer laser are irradiated to PP, the luminescence component around 4 eV decreases with an increase in irradiation time irrespective of the irradiation atmosphere. This is probably due to the decomposition of unsaturated ketone which is present in PP as an impurity. The luminescence component

around 3 eV increases with an increase in irradiation time only in the case that the laser irradiation was done in vacuum. This is probably caused by the double bonds induced by the irradiation. These results suggest that different chemical groups are induced depending on the irradiation atmosphere.

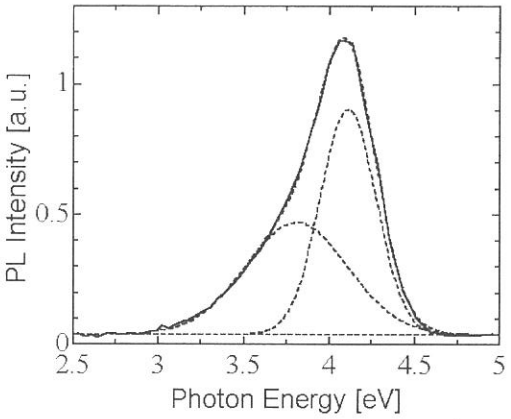

Fig.1. PL spectrum excited at 6.4 eV induced in PP by irradiation of photons from synchrotron radiation, and its Gaussian-fit spectra.

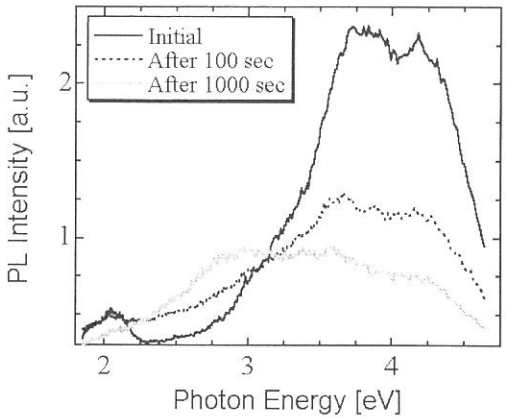

Fig.2. Change of PL spectrum excited by the excimer laser photons with irradiation time in air at room temperature.

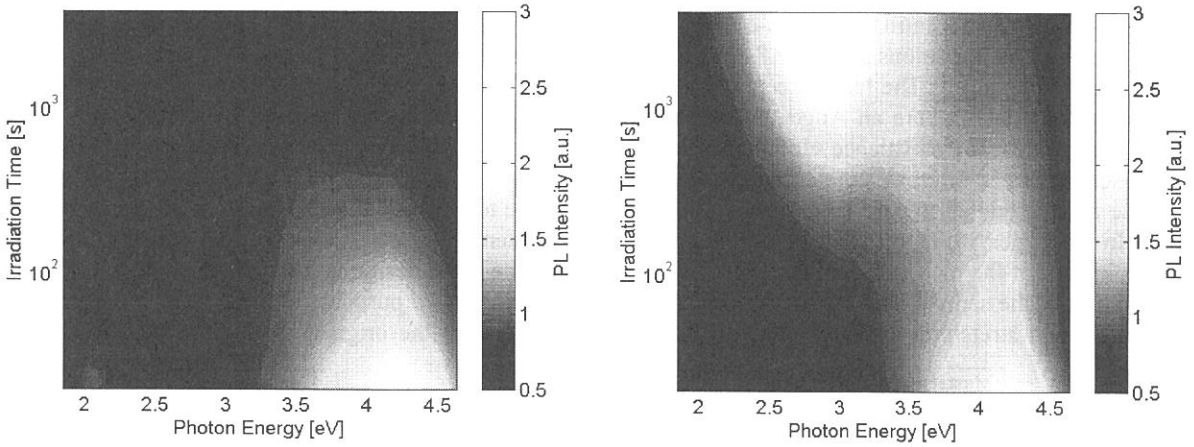

Fig.3. Change of PL spectrum with irradiation time excited by the excimer laser photons in oxygen (a) or in vacuum (b) at room temperature.

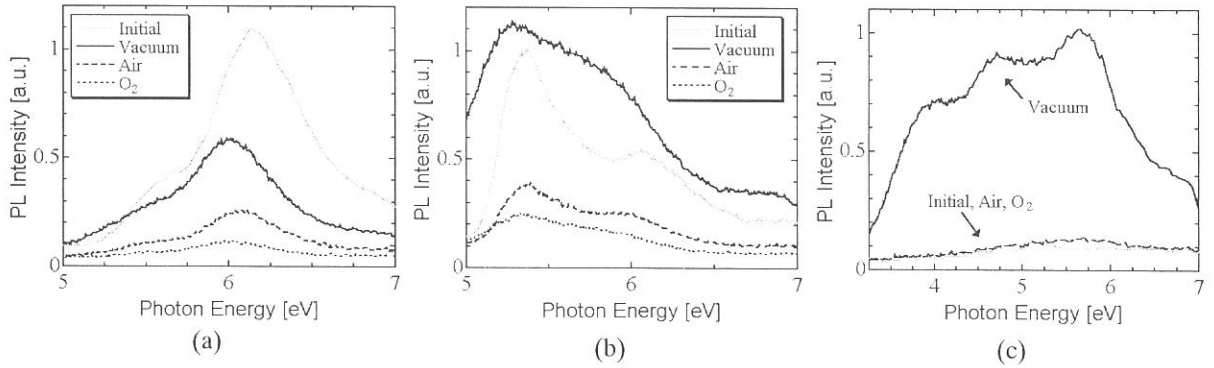

Fig.4. PLE spectra measured using synchrotron radiation.
Detected at 4.1 eV (a), at 3.5 eV (b), and at 2.9 eV (c).

(BL1B)

Laser-Induced Increase of Auger-free Luminescence under Excitation of Core-Electrons in BaF_2

T. Tsujibayashi[a], J. Azuma[b], K. Hayakawa[c], M. Horimoto[c], M. Itoh[c], M. Watanabe[d], O. Arimoto[e], S. Nakanishi[f], H. Itoh[f], S. Asaka[g*], and M. Kamada[h]

[a]*Department of Physics, Osaka Dental University, Hirakata 573-1121*
[b]*Department of Physics, Kyoto University, Kyoto 606-8502*
[c]*Department of Electrical & Electronic Engineering, Shinshu University, Nagano 380-8553*
[d]*Department of Fundamental Sciences, Kyoto University, Kyoto 606-8501*
[e]*Department of Physics, Okayama University, Okayama 700-8530*
[f]*Department of Advanced Materials Science, Kagawa University, Takamatsu 760-8526*
[g]*Equipment Development Center, Institute for Molecular Science, Okazaki 444-8585*
[h]*UVSOR Facility, Institute for Molecular Science, Okazaki 444-8585*

We have been developing a spectroscopic system in which both synchrotron radiation (SR) and laser are used [1, 2]. The system is designed for investigation of dynamical behaviors of excitations in inner-shell electronic states of solids through non-linear spectroscopy such as two-photon and pump-probe spectroscopy. The wide spectral range of SR, from X-ray to infrared, and the high power of lasers are combined in the system.

BaF_2 is known as a scintillator with 6-eV luminescence in high-energy physics. The luminescence is observed under excitation with photons above 17.8 eV. This energy corresponds to that between the outermost core state to the conduction band [3]. The luminescence is attributed to the transition of a valence electron to the hole in the outermost core state, where an Auger process is suppressed since the energy released by the transition is not enough to excite another valence electron to the conduction band. The luminescence is known as Auger-free luminescence (AFL) or cross luminescence.

Since AFL is related to core holes, it should be a good probe to examine the relaxation of core electrons and holes. In this paper, we report laser-induced increase of AFL intensity of BaF_2 under excitation through SR. The block diagram of the measuring system is depicted in Fig. 1. The basic design is the same as that in Ref. 2. The temperature of the sample was 295 K. An optical fiber was used for two purposes: introducing the laser light to the sample and stretching the laser pulse to 0.5 ns. The duration of the original laser pulse was 160 fs. The

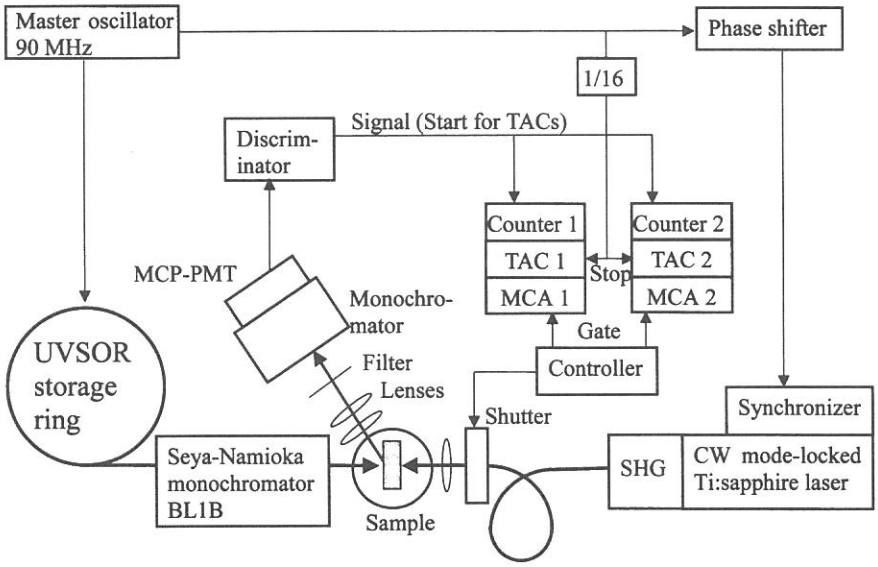

Fig. 1 The block diagram of the experimental setup.

---

*Present address: *Elementary and Secondary Education Bureau, Ministry of Education, Culture, Sports, Science and Technology, Tokyo 100-0013.*

shapes of excitation pulses of the laser and SR are shown in panels (a) and (b), respectively, of Fig. 2.

Panels (c) and (d) of Fig. 2 show the time responses of the AFL under the simultaneous excitation by SR and laser and the excitation by SR alone, respectively. The photon energy of SR was 18.4 eV. The signal was accumulated for about an hour for each curve. The humps at –12.5 ns are not caused by AFL or other luminescence [4]. The absence of signal at 11 ns indicates that the filter and monochromator prevent the false light-signal due to the scattered laser-light completely.

The intensity of AFL under SR-laser excitation is larger by several percent than that under excitation by SR alone as shown in Fig. 2. However, the ratio of the increase was varied significantly in separate measurements at the same beam line.

Searching for the cause of this uncertain value of the ratio, we noticed the existence of defects in the sample at low temperatures. Defects-related enhancement of luminescence under SR-laser excitation was reported previously [5]. In this report, a crystal of BaF_2 was kept 15 K and luminescence of self-trapped excitons was detected. We observed that the AFL intensity decreased after irradiation of SR light for a few tens hours at 295 K. It is implied that defects are created and remain to decrease the AFL intensity even at a room temperature.

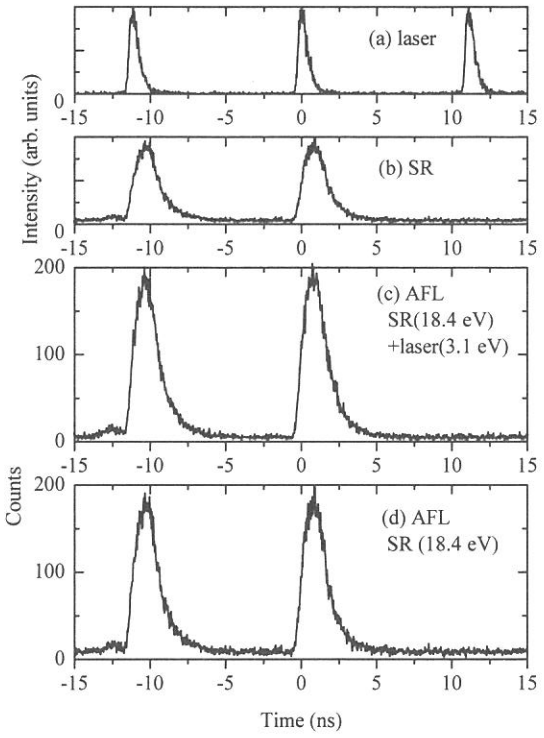

Fig. 2 Temporal behaviors of (a) laser pulses, (b) SR pulses, (c) AFL under SR-laser excitation, and (d) AFL under SR alone excitation.

If breaking defects by the laser light causes the increase of the AFL intensity, the ratio depends on the number of defects. Assuming that this number varies with the time-length of irradiation of SR prior to the measurement, there is a possibility that the increase rate varies sample to sample in separate measurements.

The present work was partially supported by a Grant-in Aid for Scientific Research from the Ministry of Education, Culture, Sports, Science and Technology.

References

[1] S. Asaka *et al.*: Rev. Sci. Instrum. **69** (1998) 1931.
[2] S. Asaka *et al.*: UVSOR Activity Report **26** (1999) 34.
[3] M. Itoh *et al.*: Solid State Commun. **65** (1988) 523.
[4] J. Azuma *et al.*: Nucl. Instrum. & Methods (in press).
[5] M. Watanabe *et al.*: UVSOR Activity Report **26** (1999) 66.

(BL1B)

Luminescence due to Self-Trapped Excitons in Orthorhombic $SnBr_2$

Y. YAMASAKI and N. OHNO

Division of Electronics and Applied Physics, Graduate School of Engineering,

Osaka Electro-Communication University, Neyagawa 572-8530, Japan

Optical properties of lead halides have been studied extensively so far by several groups. Especially, luminescence studies of these materials have been carried out since they give complimentary information on the photolysis phenomena. Orthorhombic tin halides, $SnBr_2$ and $SnCl_2$, have the same crystal structure (space group *Pmnb*) and the similar electronic configurations as orthorhombic lead halides. It is interesting to know the electronic structures and exciton states in Sn halides. The investigation of the optical properties of $SnBr_2$ and $SnCl_2$ would deepen our understanding the energy relaxation processes in this system. However, only a few studies on optical properties of Sn halides have been reported so far. [1-3]

Reflection measurement of $SnBr_2$ has revealed a pronounced polarization dependence of the first exciton band at 3.4 eV.[4,5] The polarization dependence has been well interpreted as a cationic interband transition in Sn^{2+} ($5s \rightarrow 5p$) under the crystal field with C_S symmetry.[5] Moreover, the observed first exciton structures in $SnBr_2$ are considerably sharp as compared with those in orthorhombic Pb halides.[6,7] The exciton binding energy has also been estimated as 32 meV. The logarithmic plot of the absorption spectra at the absorption edge has been found to give a straight line, [5] that is, the absorption tail of $SnBr_2$ is described as the Urbach rule. The obtained small value of the steepness parameter $\sigma_0 = 0.7$ suggests that the electron-phonon interaction is in a strong case, and the free carriers are expected to be self-trapped in $SnBr_2$.

Luminescence measurements of $SnBr_2$ single crystals were carried out at BL1B in the UVSOR facility. The samples were mounted on a copper block attached to a temperature-variable cryostat of liquid helium-flow type. The light beam passed through a 1-m Seya-Namioka type monochromator was incident on the sample surface. Luminescence emitted from the illuminated surface was collected by lenses, and analyzed through a Jovin-Yvon HR320 monochromator equipped with an R955 photomultiplier.

Figure 1 shows the luminescence spectra of $SnBr_2$ measured at 12 K. The polarization of excitation light was along the *b*-axis of the crystal. The spectrum shown by solid curve was obtained under the excitation with 3.39-eV light whose energy falls in the first exciton region. Two luminescence bands are observed at 2.17 eV and 1.85 eV. The 2.17-eV band has a Gaussian lineshape and a large Stokes shift of 1.24 eV from the lowest exciton energy for *E//b* polarization. When the excitation was made with higher-energy light than the bandgap energy, on the other hand, the luminescence spectrum changed drastically as shown by hatched curve in the figure, where the excitation energy was 6.20 eV. The spectrum consists of a broad band peaking at 2.52 eV, and the weak structures around 2.3 and 2.9 eV. The intensities of these luminescence bands become weak when the sample is warmed above 50 K, and almost disappear at 100 K.

Figure 2 show the excitation spectra for the 2.17-eV band (solid) and 2.52-eV band (hatched) measured at 12 K. Arrows indicate the first exciton energies for *E//b* polarization. As clearly seen, the 2.17-eV band is efficiently produced under the photo-excitation in the first exciton region. On the other hand, the 2.52-eV luminescence is hardly excited under the exciton region, but stimulated by photons with energies higher than the bandgap. It is thus confirmed that under excitation in the lowest exciton band the

2.52-eV luminescence is not observed while the 2.17 eV luminescence appears strongly. Although not shown in the figure, the excitation spectrum for the 1.85-eV band exhibits a strong peak at 3.11 eV, suggesting this band is ascribed to some impurity.

There have been found two types of luminescence in $PbBr_2$ at low temperatures.[8,9] One is the B luminescence (2.75 eV) produced under the excitation in the first exciton region, attributed to the radiative decay of self-trapped excitons at Pb^{2+} ion sites in $PbBr_2$. The other is the BG luminescence (2.62 eV) stimulated by photons with energies above the band gap, which originates from tunneling recombination of holes released from some trapping centers with electrons trapped at the Pb_2^{3+} STEL centers.[10] The 2.17-eV band in $SnBr_2$ is probably ascribed to self-trapped excitons similar to the B band in $PbBr_2$ since the 2.17-eV band appears under the excitation of the first exciton region, that is, this band is originated from the radiative decay of self-trapped excitons at Sn^{2+} ion sites. On the other hand, it is probable that the origin of the 2.52-eV band is due to the similar relaxed excited states to the BG luminescence in $PbBr_2$, namely the tunneling recombination of holes with electrons trapped at the Sn_2^{3+} STEL centers.

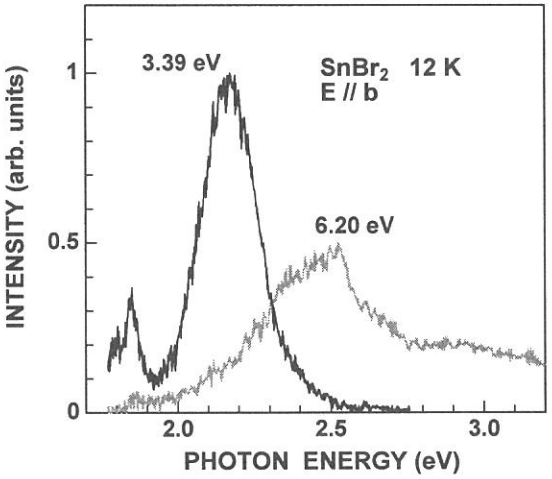

Fig. 1. Luminescence spectra of $SnBr_2$ excited with 3.39-eV light (solid) and 6.20-eV light (hatched) with *E//b* polarization at 12 K.

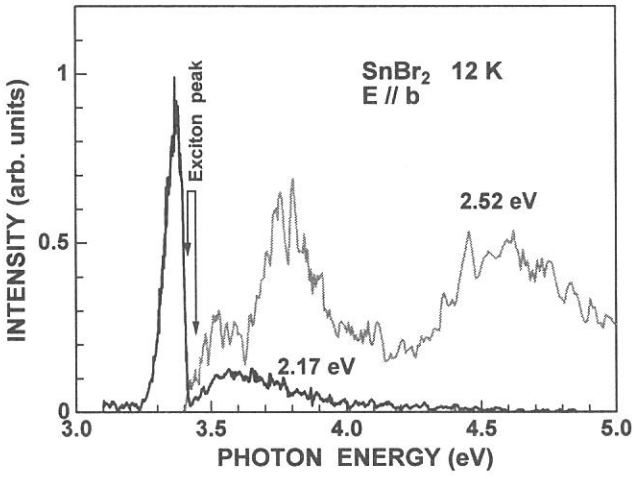

Fig. 2. Excitation spectra for 2.17-eV (solid) and 2.52-eV band (hatched) of $SnBr_2$ measured at 12 K.

References

[1] N.S. Pidsyrailo, A.S. Voloshinovskii, N.G. Stan'ko and Z.A. Khapko: Sov. Phys. Solid State **24** (1982) 708.
[2] A.S. Voloshinovskii, S.V. Myagkota, N.S. Pidsyrailo and Z.A. Khapko: Opt. Spectrosc. **52** (1982) 457.
[3] A.S. Voloshinovskii: Phys. Solid State **35** (1993) 1588.
[4] Y. Yamasaki and N. Ohno, UVSOR Activity Report **1999** (2000) 84.
[5] N. Ohno, Y. Yamasaki, H. Yoshida and M. Fujita, Phys. Status Solidi (b), in press.
[6] J. Kanbe, H. Takezoe and R. Onaka, J. Phys. Soc. Jpn. **41** (1976) 942.
[7] M. Fujita, H. Nakagawa, K. Fukui, H. Matsumoto,T. Miyanaga and M. Watanabe, J. Phys. Soc. Jpn. **60** (1991) 4393.
[8] M. Kitaura and H. Nakagawa: J. Electron Spectrosc. and Relat. Phenom. **9** (1996) 171.
[9] M. Kitaura and H. Nakagawa: J. Lumin. **72-74** (1997) 883.
[10] S.V. Nistor, E. Groovaert and D. Schoemaker: Phys. Rev. **B48** (1993)9575.

(BL1B)

Energy Transfer from Pr^{3+} to Eu^{3+} Ions through Gd^{3+} Sublattices in $NaGdF_4$:Pr,Eu

T. HIRAI[A] and N. OHNO[B]

[A]*Graduate School of Engineering Science, Osaka University, Toyonaka 560-8531, Japan*
[B]*Division of Electronics and Applied Physics, Graduate School of Engineering, Osaka Electro-Communication University, Neyagawa 572-8530, Japan*

Recently, the phosphors to convert vacuum ultraviolet (VUV) photons into visible photons, which are used in mercury-free fluorescent lamps and plasma display panels, have been researched extensively. The materials with a higher quantum efficiency and higher stability for VUV light emitted from Xe dimers (172 nm) and/or monomers (147 nm) are naturally quite needed.

In some of rare-earth activated fluorides, the conversion of one VUV photon into two visible photons is reported to be possible. Such a phenomenon is called "quantum cutting" or "quantum splitting". This indicates that these VUV phosphors have quantum efficiency more than 100%. Especially, $LiGdF_4$:Eu phosphor has been reported to convert one VUV photon into two visible (red) photons with a quantum efficiency close to 200% [1]. This conversion is caused by the energy transfer from the Gd^{3+} site, which absorbs one VUV photon, to two Eu^{3+} ions which emit two red-light photons. However, the *f-f* transition in the Gd^{3+} site is dipole-forbidden in origin, so that the absorption of the VUV photons is quite weak. On the other hand, it has been reported in $NaGdF_4$:Ce,Eu that the absorbed UV-photon energy in Ce^{3+} ions due to the allowed *f-d* transition transfers to Eu^{3+} ions through Gd^{3+} sublattices [2]. In the same manner, Pr^{3+} ions are expected to act as a suitable sensitizer to the VUV photons emitted from a high-pressure Xe discharge at around 172 nm, since the allowed *f-d* absorption in Pr^{3+} ions in fluoride phosphors are observed at around 180 nm. In the present study, we have examined whether the energy transfer occurs or not from Pr^{3+} ions to Eu^{3+} ions in $NaGdF_4$:Pr,Eu phosphor.

On the right-hand side of Figure 1 are shown the luminescence spectra of $NaGdF_4$:Pr,Eu, $NaGdF_4$:Eu, $NaGdF_4$:Pr and $NaYF_4$:Pr at room temperature. The excitation was made by an ArF excimer laser (193 nm). Measurements of the excitation spectra for these luminescence lines are carried out with use of SOR at BL1B in the UVSOR facility. The results are shown on the left-hand side of the figure.

In $NaGdF_4$:Pr, only a luminescence line is observed at 310 nm. This luminescence line is attributed to the *f-f* transition from ^6P_J state to $^8S_{7/2}$ ground state in Gd^{3+} sublattice. It is found that the luminescence is efficiently excited at around 180 nm, which is due to the *f-d* transition in Pr^{3+} ions, since no structure is observable in the excitation spectra for phosphors without Pr^{3+} ions. This fact indicates that the energy transfer occurs from Pr^{3+} ions to Gd^{3+} sublattices in $NaGdF_4$:Pr. In $NaYF_4$:Pr, on the other hand, the *f-d* excited states in Pr^{3+} ions at around 180 nm relax immediately to $^1S_0$ state, and then emit 407-nm photons ascribed to the *f-f* transition in Pr^{3+} ions [3].

The similar energy transfer is found also to occur in $NaGdF_4$:Pr,Eu. In both $NaGdF_4$:Eu and $NaGdF_4$:Pr,Eu, all prominent luminescence lines arise from the *f-f* transition of Eu^{3+} ions. The luminescence line at 615 nm is attributed to the transition from $^5D_0$ to $^7F_0$ state in Eu^{3+} ion. In the excitation spectrum of $NaGdF_4$:Pr,Eu, one can see the excitation peak at around 180 nm, assigned to the *f-d* transition in Pr^{3+} ions.

These results show clearly that the VUV light absorption in Pr^{3+} ions gives the red luminescence of Eu^{3+} ions. It is concluded that the energy transfer from Pr^{3+} ions to Eu^{3+} ions through Gd^{3+} sublattice efficiently occurs in $NaGdF_4$:Pr,Eu. Further study is needed to confirm whether the "quantum cutting" occurs or not in this system.

References

[1] R.T. Wegh, H. Donker, K.D. Oskam and A. Meijerink, Science **283** (1999) 663.
[2] H.S. Kiliaan, J.F.A.K. Kotte and G. Blasse, Chem. Phys. Lett. **133** (1987) 425.
[3] J.L. Sommerdijk, A. Bril and A.W. de Jager, J. Lumin. **8** (1974) 341.

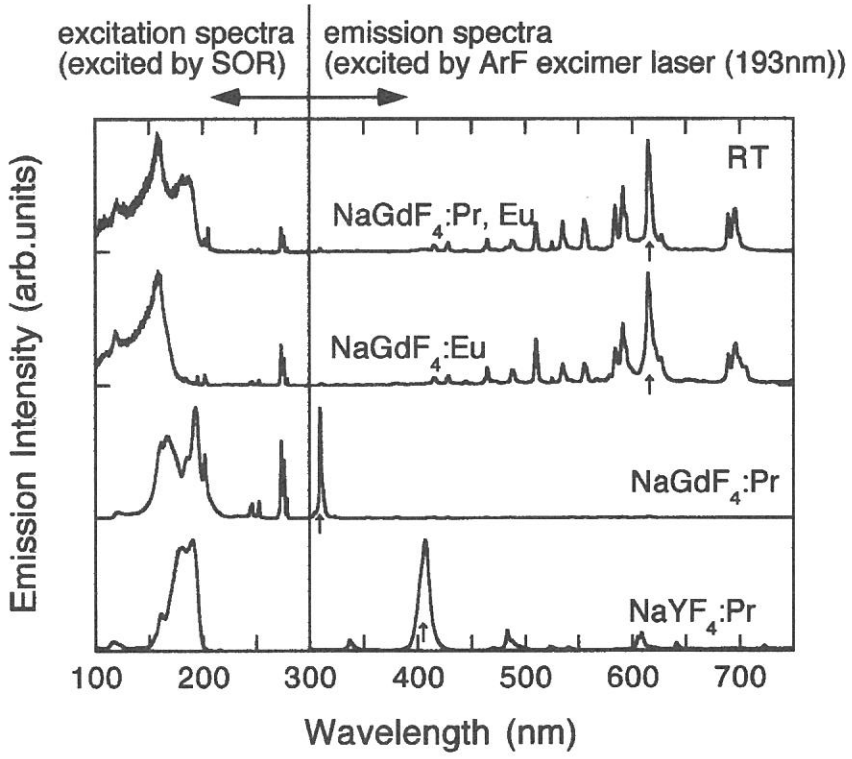

Figure 1. Luminescence spectra excited by 193-nm ArF excimer laser (right) and the excitation spectra for the luminescence lines indicated by arrows (left) at room temperature.

(BL1B)

Study on the defects in silica irradiated by a nuclear reactor

Tomoko Yoshida[1], Tetsuo Tanabe[1], Tatsuya Ii[2], Shunsuke Muto[1] and Yoshitaka Inaki[3]

[1]*Center for Integrated Research in Science and Engineering, Nagoya University, Nagoya 464-8603, Japan*

[2]*Department of Nuclear Engineering, Graduate School of Engineering, Nagoya University, Nagoya 464-8603, Japan*

[3]*Department of Applied Chemistry, Graduate School of Engineering, Nagoya University, Nagoya 464-8603, Japan*

Introduction

Neutron irradiation and radiation effects on silica glasses are one of the main concerns for their application as optical windows, insulators and optical fibers in fusion reactors as well as fission reactors.[1,2] Recently, dynamic effects of the irradiation in silica glasses have been observed as degradations of their good transparency, high electrical resistivity, low optical absorption and luminescence during in-reactor irradiation.[1-5] In order to investigate dynamic effects of in-reactor irradiation on silica, we have tried to make in situ luminescence measurement of silica glasses induced by in-reactor irradiation. In-reactor luminescence (IRL) was expected to originate mainly from the defects in silica. To confirm this, in the present study, IRL was compared with the photoluminescence which would be closely correlated to the defects in silica.

Experimental

The samples used in this work were fused silica glasses (T-1030 and T-2030) and synthesized silica glasses (T-4040) of 13 mm diameter and 2 mm thickness produced by Toshiba Ceramics, Japan with different OH content.

In-reactor irradiation have been carried out using the nuclear reactor YAYOI at the University of Tokyo. YAYOI was operated with a power of 0.5 or 1.5 kW (the neutron flux were about 2×10^{15} n/m^2 s and 6×10^{15} n/m^2 s, respectively) with an average neutron energy of 1.3 MeV and γ ray level was about 3.0 kGy/h.[6]

The photoluminescence (PL) spectra were measured at room temperature using synchrotron radiation at the beam line 1B station (BL-1B) attached with an 1m Seya-Namioka monochromator at UVSOR, Institute for Molecular Science, Okazaki, Japan, operated at electron energy of 750 MeV. The spectra were measured using monochromator (SPEX 270M) equipped with a photomultiplier (Hamamatsu R4220).

Results and Discussion

Fig. 1 shows observed luminescence spectra from various types of silica glasses irradiated in the reactor core. One can see that the IRL spectra of the low-OH fused silica glass (T-2030) consist of two broad bands peaked at 4.2 and 3.1 eV. The intensity of the 4.2 eV IRL band stayed constant during irradiation, while that of the 3.1 eV IRL band decreased linearly with the irradiation time. The high-OH fused silica glass (T-1030) showed similar double peaked spectra but the emission intensity was much less than that for the low-OH fused silica glass (T-2030). The 4.2 eV IRL band also showed no change with the irradiation time, whereas the other IRL band was centered at 2.8 eV not at 3.1 eV, and grew with the irradiation. For the high-OH synthesized silica glass (T-4040), the IRL band at the lower energy side can not be seen in Fig. 1. However, a new IRL band appeared at 2.8 eV and its intensity increased by the prolonged irradiation

Fig. 2 shows the photoluminescence (PL) spectra obtained under excitation at various energy (5.1 eV - 7.7 eV) for both the low-OH fused silica glass (T-2030) and the high-OH synthesized silica glass (T-4040) before and after the irradiation. In the spectrum of the unirradiated low-OH fused silica (Fig. 2a), two PL bands at 3.1 eV and 4.2 eV were observed, and these two PL bands were reduced remarkably by the in-reactor irradiation (Fig. 2b), which is parallel to the 3.1 eV IRL band. On the other hand, the PL spectra of the unirradiated high-OH synthesized silica glass (T-4040) were different from those of the low-OH one (T-2030); no significant PL

band was observed (Fig. 2c). After the in-reactor irradiation, two new PL bands at 2.8 eV and 4.3 eV appeared. This is again parallel to the 2.8 eV IRL band. These results suggest that the origins of the present IRL and PL would be the same.

Thomon *et al.*[7] reported the existence of two B_2 bands excited at 5.1 eV, and it is commonly accepted that the PL emission bands at 2.7 eV and 4.4 eV are attributed to the $B_{2\alpha}$ while the $B_{2\beta}$ center generates the 3.1 eV and 4.2 eV PL bands. Therefore, the PL and IRL bands for the low-OH fused silica glass (T-2030) and the high-OH synthesized silica glass (T-4040) are very likely originate from the different two types of oxygen deficiencies, $B_{2\beta}$ and $B_{2\alpha}$ centers, respectively.

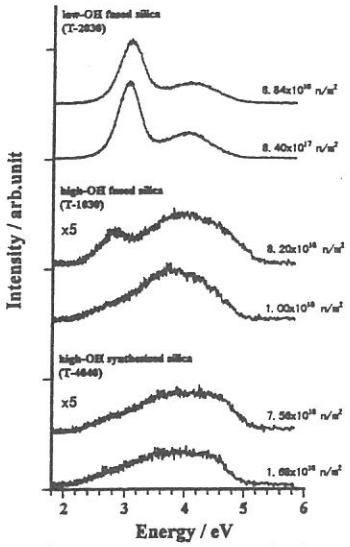

Fig.1 Luminescence spectra of silica glasses during the irradiation in the reactor core.

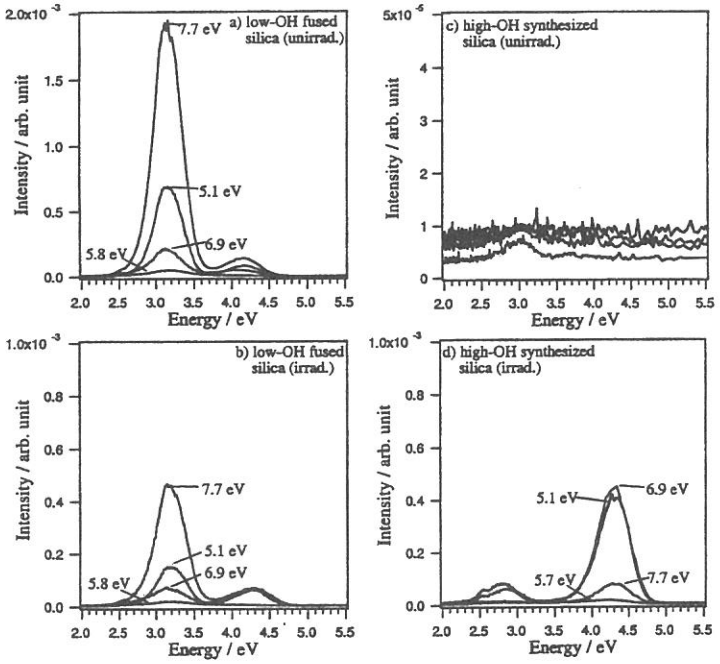

Fig. 2 The photoluminescence emission spectra excited at various energies in (a) an unirradiated low-OH fused silica glass (T-2030), (b) the reactor irradiated low-OH fused silica glass (neutron fluence is 2.8 x 10^{19} n/m^2), (c) an unirradiated high-OH synthesized silica glass (T-4040), and (d) the reactor irradiated high-OH synthesized silica glass (neutron fluence is 2.7 x 10^{20} n/m^2). The excitation energies are shown in the figure. The excitation energies in (c) are the same as those in (d).

References

[1] F. W. Clinard, Jr and L.W. Hobbs, Physics of Radiation Effects in Crystal (Elsevier, Amsterdam, 1986) p. 442.

[2] Proc. US/Japan Workshop on Dynamic Effects of Irradiation in Ceramics, Santa Fe, November 11-14,1992, Los Alamos National Laboratory Report LA-UR-92-4400 (1992)

[3] E. H. Farnum et al., J. Nucl. Mater. 191/194 (1992) 548.

[4] E. R. Hodgson, J. Nucl. Mater. 191/194 (1992) 552.

[5] T. Shikama et al., J. Nucl. Mater. 191/194 (1992) 544 and 575.

[6] M. Nakazawa and A. Sekiguchi, Radiation Dosimetry Data for Reactor YAYOI, Interior, Report of University of Tokyo, R0037 in Japanese.

[7] R. Tohmon, H. Mizuno, Y. Ohki, K. Sasagane, K. Nagasawa and Y. Hama, Phys. Rev. B 44 (1989) 1337.

(BL1B)

Vacuum-ultraviolet reflectance spectroscopy of transition-metal oxides

Katsuhiro TOBE [1], Yasujiro TAGUCHI [1], Kyoko ISHIZAKA [1], Shigeki MIYASAKA [2], Takafumi SAITO [3], Taka-hisa ARIMA [3], and Yoshinori TOKURA [1,2]

[1] *Department of Applied Physics, University of Tokyo, Tokyo 113-8656*

[2] *Joint Research Center for Atom Technology (JRCAT), Tsukuba 305-0046*

[3] *Institute of Materials Science, University of Tukuba, Tsukuba 305-8573*

One of the most important characteristics for the correlated electron systems is the drastic re-construction of electronic structure over an energy scale of eV with changes of temperature, doping concentration, and/or external field. Optical reflectivity measurements over a wide energy range and the optical conductivity spectra derived from the reflectivity spectra provide us with useful information about the strongly correlated electron systems.

In this beam time, we measured the reflectivity spectra of several transition-metal oxides, including Mn-, Ni-, Co-, Mo- and V-oxides, for an energy range of 4 eV < E < 35 eV at room temperature using the beam line BL1B. The measured reflectivity data, together with the lower-energy data below 6 eV, were used to derive the optical conductivity spectra or dielectric function via the Kramers-Kronig analysis. As an example, the imaginary part of the dielectric function of perovskite-type Mn-oxide, a detwinned single crystal of $LaMnO_3$ is shown below. This compound shows the orbital ordering below $T_{OO} \sim 780$ K.

At the orbital-ordered state, the spectra show the strong anisotropy between the polarizations parallel and perpendicular to the *c*-axis in the *Pbnm* orthorhombic structure. These polarization-dependent optical spectra are interpreted in terms of anisotropic electronic structure reflecting orbital ordering. Since the anisotropy is especially pronounced for a peak at 8 eV, this peak is assigned to the transition between O 2*p* and Mn e_g levels.

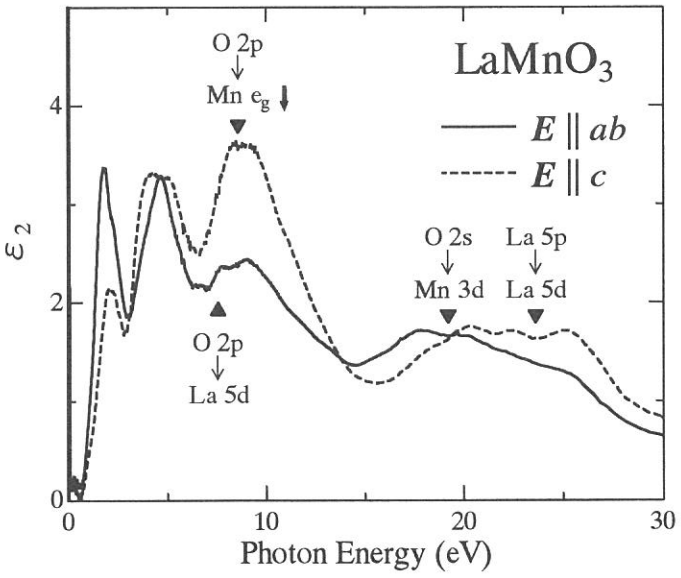

(BL6A1)

Study of Secondary Battery Substances $Li_{1-x}NiO_2$ by Millimeter Wave Reflection Measurements

Hitoshi Ohta, Yuichi Miura, Kenji Hazuki, Takao Nanba[A], Atushi Hirano[B] and Ryoji Kanno[B]

Department of Physics, Faculty of Science, Kobe University, 1-1 Rokkodai, Nada, Kobe 657-8501
[A]The Graduate School of Science and Technology, Kobe University, 1-1 Rokkodai, Nada, Kobe 657-8501
[B]Department of Chemistry, Faculty of Science, Kobe University, 1-1 Rokkodai, Nada, Kobe 657-8501

As $LiNiO_2$ is a promising material for the positive electrode of the Li ion secondary batteries, it attracted much interest. We found the drastic increase of the reflection of $LiNiO_2$ above 300 K in the millimeter wave region previously [1, 2], and we suggested that this increase of reflection is related to the motion of Li ion in the system. Moreover, we extended our study to the low energy region down to 5 cm^{-1} and also extended our study to the study of $Li_{1-x}Ni_{1+x}O_2$ in order to discuss the effect of the non-stoichiometry, which degrades the charge and discharge characteristics [3-5]. However, the study of $Li_{1-x}NiO_2$ is important because it is the intermediate state in the charging and discharging proccesses. Thereofre, we performed the reflection measurement of $Li_{1-x}NiO_2$ in the millimeter wave region.

The reflection measurements of $Li_{1-x}NiO_2$ sample have been performed in the spectra region from 10 to 60 cm^{-1} using the beam line BL6A1 of UVSOR. The temperature was changed from 79 to 380 K. The gold plate was used as a reference and InSb detector was used as a detector. Figure 1 shows our results for $Li_{1-x}NiO_2$ sample. The reflection spectra above 25 cm^{-1} are similar with those for stoichiometric $LiNiO_2$ for all temperatures. However, the reflection spectra of $Li_{1-x}NiO_2$ below 25 cm^{-1} decrease as the temperature is increased above 300 K. This suggests the change of the motion of Li ions at high temperature in $Li_{1-x}NiO_2$. These behaviors are completely different with those of non-stoichiometry samples. For more detailed discussion, the measurements of $Li_{1-x}NiO_2$ in the lower wavenumber region below 10 cm^{-1} are required.

[1] H. Ohta *et al.*: UVSOR Activity Report 1996 (1997) 182.
[2] H. Ohta *et al.*: to appear in Jpn. J. Appl. Phys. (2001).
[3] H. Ohta *et al.*: UVSOR Activity Report 1997 (1998) 128.
[4] H. Ohta *et al.*: UVSOR Activity Report 1998 (1999) 158.
[5] H. Ohta et al.: UVSOR Activity Report 1999 (2000) 93.

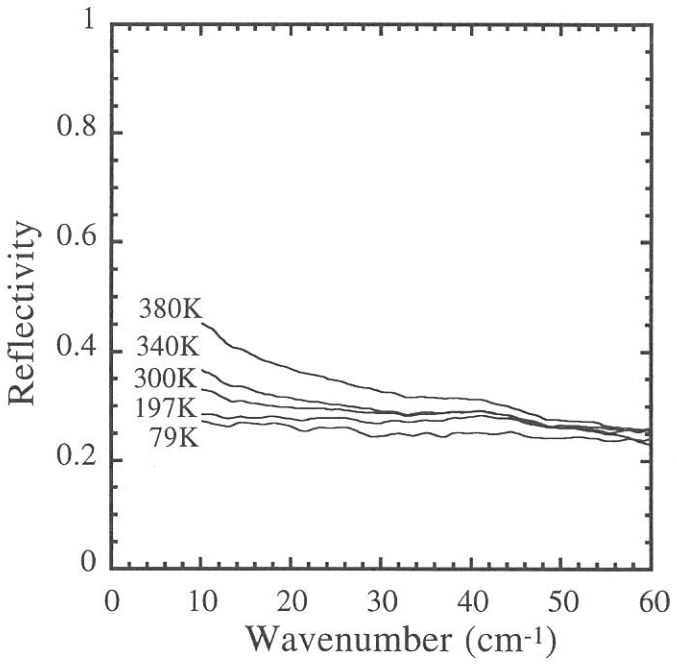

Fig. 1 Reflection spectra of $Li_{1-x}NiO_2$.

(BL5B)

Total Photoyield Spectra of Amorphous Chalcogenide Films in the VUV region

Koji HAYASHI, Yukihiro NAITO and Satoshi NAKAMURA

Department of Electrical and Electronic Engineering, Gifu University, Gifu 501-1193, JAPAN

Today, the natural environment is protected , and to ensure the safe and clean energy resource is the very important problem which must urgently reach solution. The solar cell can solve this problem, and it will be necessary energy supply source in the next generation. At present, there are crystal, polycrystal and amorphous semiconductor as a material of the solar cell. The amorphous semiconductor is the most advantageous material compared to other materials in respect of conversion efficiency and manufacture cost and area expansion, etc. Though the amorphous solar cell had been used as batteries such as electronic calculator and clock practically, the degradation by the light is large problem, when the high power was produced. However, the mechanism of the photodegradation phenomenon[1] is unresolved still. It is known that the amorphous semiconductor shows the photoinduced phenomena which is also very various except for the photodegradation phenomenon[2,3]. The application of the amorphous material to optical function devices is greatly expected by this fact. Although a large number of studies have been made on the photoinduced phenomena, there is seldom a photoinduced phenomenon in which the mechanism is clarified as well as the photodegradation phenomenon. Then, we advance the research on the photoinduced phenomena of the amorphous semiconductor using the synchrotron orbital radiation as a trial of the new research recently. Until now, these phenomena have been studied by exciting and producing the most outer shell electron using the light with the energy which corresponds to optical band gap as a light source. Using the synchrotron orbital radiation, we advance the research from the viewpoint of two. One is a viewpoint of the research of the photoinduced phenomena by the core electronic excitation, and it is a viewpoint of studying the energy structure change over the wide energy region in another. From such viewpoint, the experiment was advanced in the UVSOR facility of the Institute for Molecular Science in Okazaki, and the reversible change of optical band gap was found as a core electronic excitation effect, and it was found that the efficiency of the phenomenon depended on the energy of the exciting light[4,5]. In our recent study, we observed interesting photoinduced change in the photoconductivity and the total photoyield of amorphous chalcogenide films by the irradiation of the VUV light[6-8]. In the previous work, we measured the total photoyield spectra and the VUV reflection spectra in amorphous arsenic sulfide (a-As_2S_3) films in order to study the photoinduced effects of those optical spectra by the irradiation of the bandgap light and the VUV light[9]. In the present work, we measured the total photoyield spectra and the VUV reflection spectra in amorphous arsenic selenide (a-As_2Se_3) films.

Samples used for those measurements were amorphous chalcogenide (a-As_2Se_3 & a-As_2S_3) films. Thin films of amorphous chalcogenide were prepared onto quartz substrates by conventional evaporation technique. For the measurement of the total photoyield spectra, the amorphous chalcogenide film was deposited, after an Al electrode was fabricated on the substrate. A typical thickness of an amorphous film was around 0.5 μm. The samples were annealed at near the glass transition temperature for two hours in a vacuum. The experiments were performed at room temperature at the BL5B beam line of the UVSOR facility of the Institute for Molecular Science. For the measurement of the total photoyield spectra, we obtained the spectrum by measuring the sample drain current. We also monitored the spectrum of light source by measuring the photoyield of the gold mesh. For the measurement of the reflection spectra, the incident angle was near normal to the sample surface and the reflectivity was measured by a silicon photodiode. The reflection spectrum was obtained by normalizing the spectrum by the spectrometer system response. In the measurement of these spectra, the spectra in the equal position of the sample would be able to be measured at the same time.

Figure 1 shows the total photoyield spectra of a-As_2S_3 and a-As_2Se_3 at room temperature in the wavelength region between 15nm and 35nm. In the figure, the photoyield spectrum of the gold mesh is also shown. Two main peaks were observed at this wavelength region. One peak around 22nm corresponds to the 3d core level of Se atom. Another peak around 28nm corresponds to the 3d core level of As atom. Though these peak were also observed at the reflection spectra,

there is slight difference in the peak position. As you see in the figure, the components of the photoyield of the aluminum electrode were included for the photoyield spectra of the amorphous chalcogenide films. It is a problem to remove the components of the electrode from the photoyield spectra. In addition, there was the case in which the peak which corresponds to the core level appeared as a dip at some spectra of a-As_2S_3 films. In the measurement of the present photoyield spectra, it seems to have to consider the influence by the absorption in the thick film with not good conductivity. This point is carrying out the examination at present. Further analysis of these spectra is now in progress. We pay attention to the photoinduced effects near this wavelength region. We now are investigating photoinduced change on these spectra. The detailed experiments and analysis will be done in the next step.

This work was partly supported by grants-in-aid for Scientific Research from the Ministry of Education, Science and Culture of Japan.

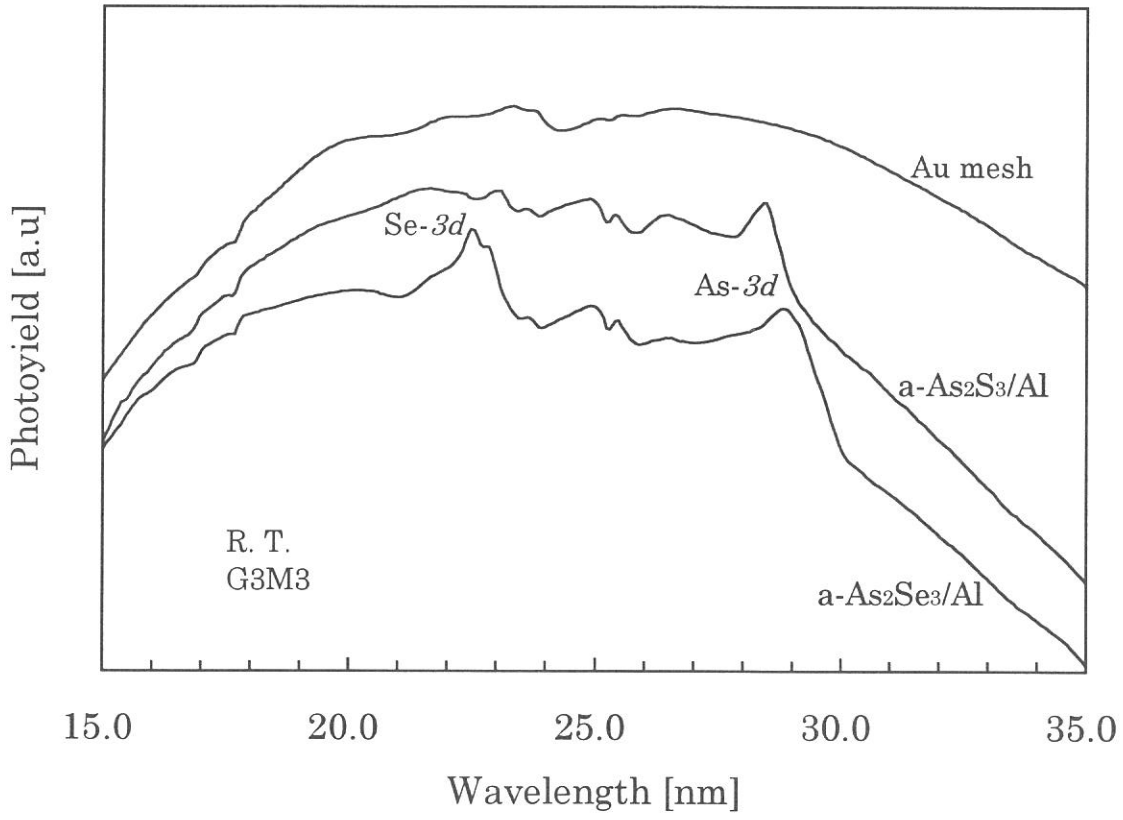

Fig. 1 Total photoyield spectra of a-As_2Se_3/Al, a-As_2S_3/Al and Au mesh at room temperature.

REFERENCES

[1] D. L. Staebler and C. R. Wronski, Appl. Phys. Lett. 31(1977)292.
[2] Ke. Tanaka, Rev. Solid State Sci., 4(1990)641.
[3] K. Shimakawa, A. Kolobov, and S. R. Elliott, Adv. Phys., 44(1995)475.
[4] K. Hayashi, D. Kato, and K. Shimakawa, UVSOR Activity Report 1995(1996)128.
[5] K. Hayashi, D. Kato, and K. Shimakawa, J. Non-Cryst. Solids., 198-200(1996)696.
[6] K. Hayashi, A. Hirai, and K. Shimakawa, UVSOR Activity Report 1996(1997)116.
[7] K. Hayashi, UVSOR Activity Report 1997(1998)118.
[8] K. Hayashi, UVSOR Activity Report 1998(1999)105.
[9] K. Hayashi, UVSOR Activity Report 1999(2000)90.

(BL5B), (BL8B1)

Development of Magnetic Kerr Rotation Apparatus in the 50-70 eV Region

K. Saito, M. Igeta, T. Ejima, T. Hatano and M. Watanabe

Research Institute for Scientific Measurements, Tohoku University
Katahira 2-1-1, Aoba-ku, Sendai 980-8577

A magnetic Kerr rotation apparatus in the 50-70 eV region has been developed. The schematic illustration is shown in Figure 1. It consists of an Al/YB_6 transmission multilyer polarizer, a magnetic circuit, a sample holder and a rotating analyzer unit. It was accommodated in a vacuum chamber equipped with a goniometer, at BL5B of the UVSOR Facility. The magnetic circuit was composed of four Sm-Co permanent magnets which generate a magnetic field of 0.82 T at a sample position. Angles of incidence of 60°-85° and 10°-30° can be chosen for longitudinal and polar Kerr configurations, respectively. A rotating analyzer unit consists of an Al/YB_6 reflection multilayer analyzer, a micro-channel plate and a pulse motor. It can be rotated around an optical axis with a fixed angle of incidence called quasi-Brewster angle. The Al/YB_6 multilayer polarizer and analyzer are similar to those employed in previous Faraday rotation measurements.[1)]

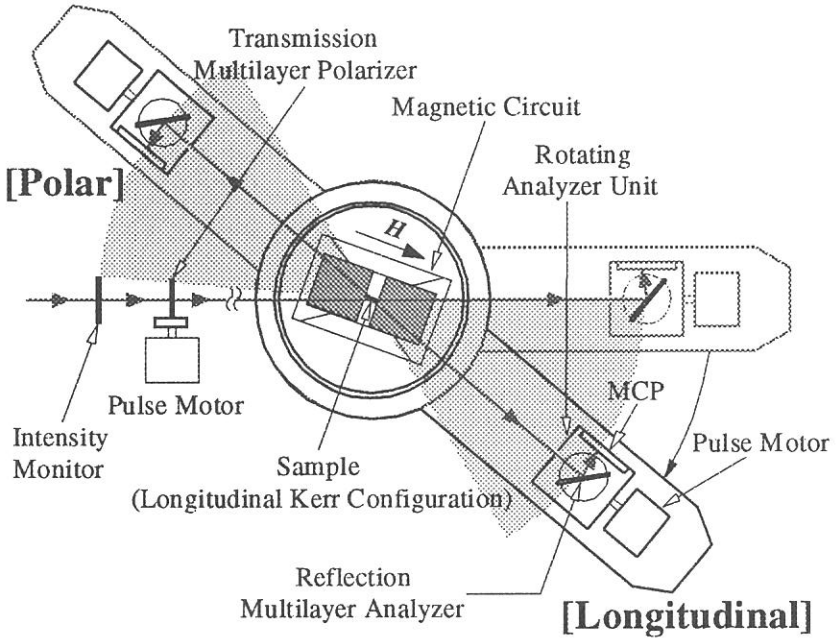

Fig. 1. Magnetic Kerr rotation apparatus.

Employing the apparatus, preliminary measurements of magnetic Kerr rotation were performed on a Co 100 nm thick single layer sputtered on a Si wafer, around Co $M_{2,3}$ absorption edges. The measurements were carried out at room temperature in longitudinal Kerr configuration in which magnetization was parallel to both the sample plane and the plane of incidence, using s-polarized incident light. Angles of incidence were fixed at $\theta = 65°$ and 80°. The experimental results for $\theta = 65°$ and 80° were plotted by closed circles in Figures 2(a) and 2(b), respectively. The maximum rotation angles about 2.5° for $\theta = 65°$ and 1.6° for $\theta = 80°$ were observed at neighborhood of Co $M_{2,3}$ absorption edges as seen in Figures 2(a) and 2(b). For the purpose to confirm the validity of the obtained Kerr rotation spectra, we have compared with those calculated from a Faraday rotation spectrum using equations derived by Zak *et al.* for determining magneto-optic coefficients.[2)] The Faraday rotation spectrum had been measured on a 39.8 nm thick Co film magnetized perpendicular to the sample plane,

in a magnetic field of 0.82 T generated by the same magnetic circuit, at BL8B1 of the UVSOR. In this calculation, we have adopted isotropic optical constants of the nonmagnetized Co film and the nonmagnetic Si wafer, given in a literature.[3] In Figures 2(a) and 2(b), calculated Kerr rotation spectra are shown by solid lines. Calculated results show that the maximum rotation angle is larger for θ = 65° than for θ = 80°, which is consistent with experimental results. However, absolute values of experimental Kerr rotation angles are smaller than those of calculated ones. The main reason for the difference may be due to the difference of magnetization between Kerr and Faraday measurements. In applied magnetic field of 0.82 T, the magnetization of the Co film is saturated in longitudinal Kerr configuration but unsaturated in the Faraday configuration. To confirm the above-mentioned reason we are carrying out the similar measurement on Ni film, of which perpendicular saturation magnetic field is 0.61 T and smaller than the applied magnetic field of 0.82 T.

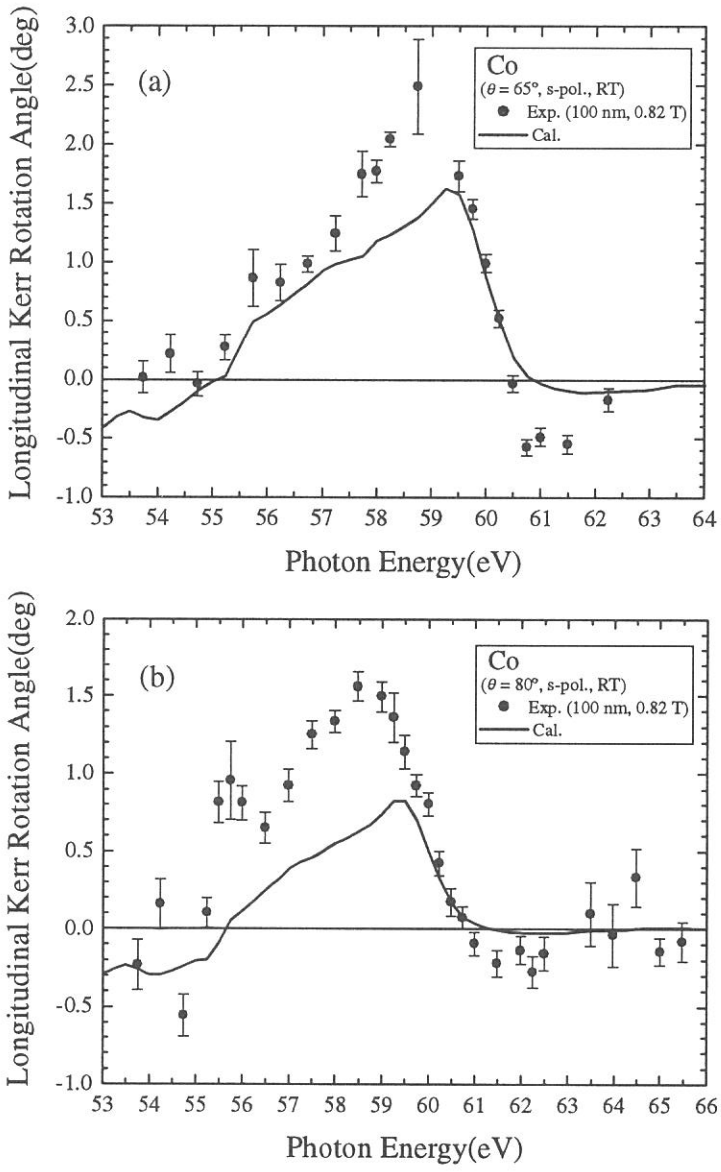

Fig. 2. Experimental (closed circles) and calculated (solid lines) longitudinal Kerr rotation spectra of Co for s-polarized light at angles of incidence of (a) θ = 65° and (b) θ = 80°.

References

1) W. Hu, T. Hatano, M. Yamamoto and M. Watanabe, J. Synch. Rad. **5** (1998) 732.
2) J. Zak, E. R. Moog, C. Liu and S. D. Bader, Phys. Rev. **B 43** (1991) 6423.
3) E. D. Palik: *Handbook of Optical Constants of Solids* (Academic Press, 1985).

(BL5B)

Reflection spectra of $Ga_{1-x}In_xN$ ternary alloy semiconductors

A. Wakahara, T.Misaki, T.Nakajima, and Q. Guo *

Toyohashi University of Technology, Tempaku-cho, Toyohashi, 441-8580, Japan
**Saga University, Saga, Japan*

Group-III nitride semiconductors, such as AlN, GaN, InN, and its alloy, have been paid much attention for application to optoelectronics, those are able to cover from 6.2 to 1.9eV. Recent progress on crystal growth achieved high quality GaN layer on sapphire substrate, and very bright blue/green light-emitting diodes (LEDs) have been commercialized, and also, continuous wave operation of current-injection violet laser has been achieved by means of GaInN/GaN multi-quantum well (MQW) laser structure [1-3]. In order to design the device structure, it is important to know fundamental properties of the materials. However, the fundamental properties of GaInN, such as effective masses, optical constants, and elastic constants, are not well investigated. Moreover, it is difficult to grow GaInN with uniform In composition, because the covalent bond length of In-N is much linger than that of Ga-N and it leads to the phase separation phenomenon, and thus it is interested in the effect of compositional in homogeneity on te band structure of GaInN. In this study, reflection spectra are measured in infra-red to vacuum ultraviolet region and optical constants are calculated via Kramers-Kronig analysis.

GaInN ternary alloy were grown on sapphire (0001) substrate by remote-plasma enhanced organometallic vapor phase epitaxy, in which RF (13.56Mhe) discharging of N_2 generated reactive nitrogen source. The group-III precursors were trimethylgallium (TMGa) and trymethylindium (TMIn). The detailed growth conditions were described in the previous publications [4]. The substrate used in the experiments was (0001)-oriented sapphire wafer. GaInN layers were grown at 680°C. In composition 'X' of GaInN layers was determined from lattice constant measured by X-ray diffraction assuming Vegard's low, and was in the range of 0.07-1.0. The layer thickness of the GaInN layer was about 0.2μm. Reflection spectra were measured by double-beam spectrometer for the photon energy less than 6eV and by BL5A for higher than 6eV. Incident angle defined as the angle between incident light and the normal direction of the sample surface was 10 degree.

Figure 1 shows reflectance spectra of GaInN with different In composition. It can be seen in the figure, that sharp peaks are observed in the range of 2-11eV. For the reflectance of InN, peaks can be seen at 2.1, 4.8, 5.3, 7.9, ~9. 10.7, and 11.2eV, and these are well agree with previously reported value [5]. The peak position of these peaks systematically shifts as decreasing the In contents. Higher energy transition was investigated via dielectric function. The dielectric function was calculated via Kramers-Kronig analysis using reflectance spectra shown in Fig.1. Figure 2 shows the imaginary part of the dielectric function 'ε_2'. In the case of GaN, critical point structures are reported at 3.4 (E_0, $\Gamma 6 \rightarrow \Gamma 1$), 6.9 ($E_1$, critical points in close to *M*), 7.75 (*A-L* and *L-M*), and 9.2eV(*Γ-M* and *A-H*) [6]. For InN, critical point structures can be seen at 2.3, 4.7, 5.3, ~8, ~9, and ~10eV. Critical points at 2.3, 4.7, 5.3, and ~10eV would be corresponding to the transitions of E_0, $U_4 \rightarrow U_1$(critical point in *L-M*), $M_2 \rightarrow M_1$, and critical point in *Γ-M*, respectively [5,7]. In order to see the shift of critical points as a function of

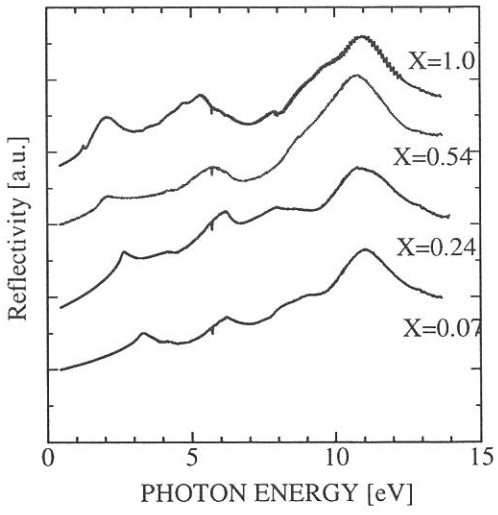

Fig.1. Reflectance spectra of GaInN with different In composition.

In composition, we focused on the peaks corresponding to the similar transitions observed in both GaN and InN. Figure 3 shows relationship between the transition energy of critical point and In composition. As can be seen in the figure, both E_0 and E_1 decrease with increasing In composition. The transition energies of E0 and E1 are well fitted to a relation of $E(x)=E_{GaN}(1-X)+E_{InN}(X)-bX(1-X)$, where X is In composition and b is called bowing parameter. Obtained bowing parameters for E_0 and E_1 transitions estimated from the figure are 1.8eV and 0.6eV, respectively. The obtained bowing parameter for E_0 transition is larger than the reported value of 1eV [8,9]. E_1 and other higher band transitions indicate small bowing.

References

1] S.Nakamura, T.Mukai, and M.Senoh, Appl.Phys.Lett. **64** (1994) 1687.

2] S.Nakamura, M.Senoh, N.Iwasa, S.Nagahama, T.Yamada, and T.Mukai, Jpn.J.Appl.Phys. **34** (1995) L1332.

3] S.Nakamura, M.Senoh, S.Nagahama, N.Iwasa, T.Yamada, T.Matsushita, Y.Sugimoto, and H.Kiyoku, Appl.Phys.Lett. **69** (1996) 4056.

4] T.Tokuda, A.Wakahara, S. Noda, and A. Sasaki, J. Crystal Growth **187** (1998) 178.

5] Q.Guo, O.Kato, M.Fujisawa, and A.Yoahida, Solid State Commun. **83** (1992) 721.

6] J.P.L.Hughec, Y.Wang, and J.E.Sipe, Phys. Rev. **B 55** (997) 13630.

7] A.Wakahara, T.Tsuchiya, and A. Yoshida, Vacuum **41** (1990) 1071.

8] K.Osamura, S.Naka, and Y.Murakami, J. Appl. Phys. **46** (1975) 3432.

9] S. Nakamura, T.Mukai, M.Senoh, S.Nagahama, N.Iwasa, J. Appl. Phys. 74 (1993) 3911.

10] S.Adachi, Optical constants of crystalline and amorphous semiconductors, Chap. B9, (Kluwer Academic Publishers, Boston,1999)

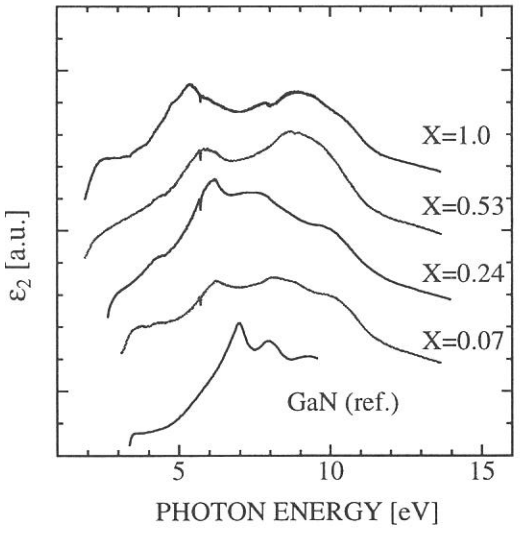

Fig.2. Change of imaginary part of dielectric function ε_2 for different In composition 'X' of GaInN. Dielectric function of GaN is taken from the literature [10].

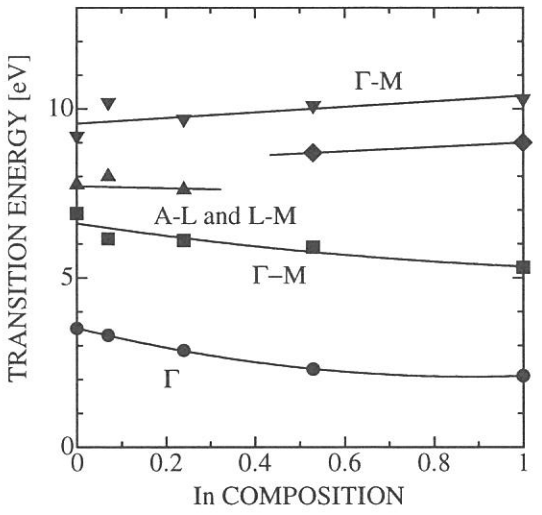

Fig.3. In composition dependence of critical points.

(BL5B, 6A1, 7B)

Spectral Range Effect to the Optical Constants via Kramers-Kronig Analysis: Reflectivity Spectrum of CeSb in the FIR-SX Region

Shin-ichi Kimura[1, 2], Mitsuru Okuno[1], Hideki Iwata[1], Hideaki Kitazawa[3] and Giyu Kido[3]

[1]*Graduate School of Science and Technology, Kobe University, Nada-ku, Kobe 657-8501*
[2]*PRESTO, Japan Science and Technology Corporation*
[3]*Physical Properties Division, National Research Institute for Metals, 1-2-1 Sengen, Tsukuba, 305-0047*

To obtain optical constants of solids, some methods are adopted. In the case of insulators, the ellipsometry that can directly measure the phase shift is a powerful tool for the investigation of the optical constants as well as the electronic structure. However, the method cannot be adapted to metallic materials because these cannot be transparent. In such case, the Kramers-Kronig analysis (KKA) is useful. The KKA needs an accurate reflectivity spectrum in the energy range from 0 to infinity. However, since we cannot measure a spectrum in such energy range, we have to extrapolate below and above the obtained spectrum. Here we report the effect of the limited energy range to the optical constants.

The reflectivity spectrum of CeSb at 300 K is measured in the energy range from far-infrared to soft x-ray (0.01 - 250 eV) by using BL6A1 (0.01 – 1.5 eV), BL7B (1.4 – 30 eV) and BL5B (15 – 250 eV) shown in Fig. 1. CeSb is one of typical strongly correlated electron systems with 4f electrons and low carrier density [1]. It is easy to cleave along a (100)-plane because of the NaCl-type crystal structure. In the BL7B and BL5B region, the clean surface of the sample was obtained by cleavage *in situ*. Because the cleavage surface is flat microscopically, no diffused scattering on the surface occurs. Then absorption peaks in the high-energy range, for instance the Ce 4d-4f absorption at 120 eV, were clearly observed.

The optical conductivity spectra of CeSb obtained by the KKA of the reflectivity spectrum are shown in Fig. 2. Three lines indicate the optical conductivity spectra using the different limited

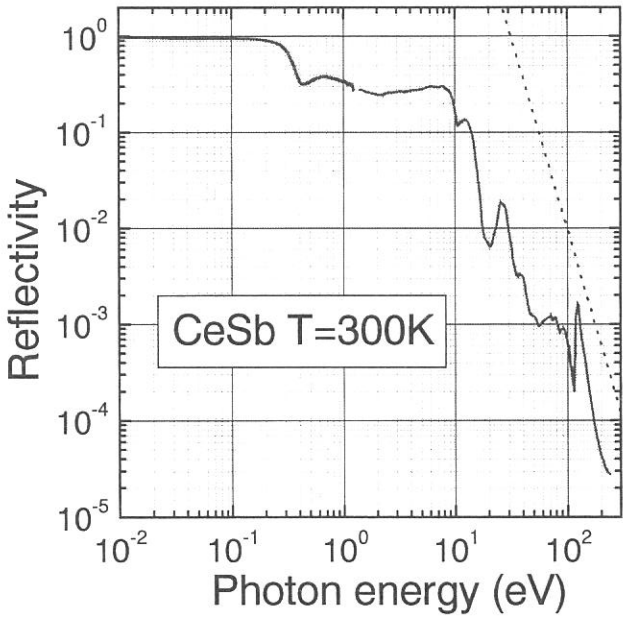

Fig. 1. Reflectivity spectrum of CeSb in the energy range of 0.01 – 250 eV at 300 K (solid line). The dotted line indicates the slope of $R(\omega) \propto \omega^{-4}$.

energy range of the reflectivity spectrum. The solid line is the energy range of 0.01 – 250 eV, the dashed line 0.01 – 30 eV (up to the BL7B and BL1B region) and the dotted line 0.01 – 6 eV (up to the conventional UV spectrometer region). The extrapolations below and above the energy range were commonly adapted to be the Hagen-Rubens function ($R(\omega) = 1 - A\cdot\omega^{1/2}$) and $R(\omega) = B\cdot\omega^{-4}$, respectively [2]. Here, A and B were determined to be smoothly connected to the reflectivity spectrum.

The solid line in Fig. 2 indicates six main structures, the absorption due to carriers below 0.3 eV, Sb 5p → Ce 5d (from the valence band to the conduction band) at 0.5 – 15 eV, Ce 5p → 5d at 25 eV, Sb 4d → 6p at 39 eV, Sb 4p → 5d at 80 eV and Ce 4d → 4f at 120 eV. The solid line is a reasonable spectrum of the electronic structure of CeSb. The dashed line is very similar to the solid line below 30 eV. However the dotted line is much different from the solid line. Particularly, the shape of the Sb 5p → Ce 5d absorption is much different because of the limitation of the energy range. In addition, the shape of the carrier absorption is different from the solid line. This causes a mistake to evaluate the character of carriers.

Since the extrapolation function of $R(\omega) = B\cdot\omega^{-4}$ seems to obey in the energy range above 20 eV roughly as shown in Fig. 1. The 20 eV is the upper limit of the transition from the valence band to the conduction band. The energy is almost equal among all materials. Therefore, if we use the extrapolation function of $R(\omega) = B\cdot\omega^{-4}$, the reflectivity spectrum should be measured in the energy range above 20 eV.

---

[1] T. Suzuki, JJAP Series 8 (1993) 267.
[2] F. Wooten, *Optical Properties of Solids*, Academic Press, (1972).

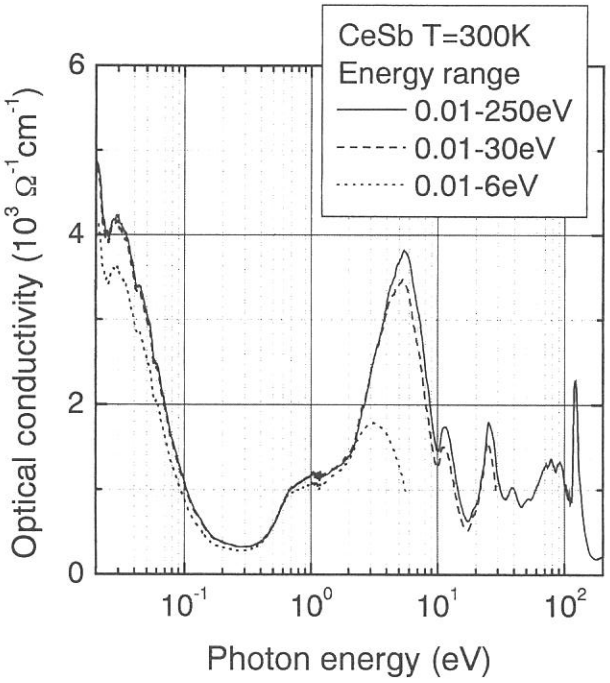

Fig. 2. The difference of the optical conductivity spectra of CeSb due to the spectral range effect. The solid line is used the reflectivity spectrum of 0.01 – 250 eV, the dashed line of 0.01 – 30 eV and the dotted line of 0.01 – 6 eV. The extrapolation functions below and above the spectral range for the Kramers-Kronig analysis were commonly adopted to be the Hagen-Rubens function and $R(\omega) = B\cdot\omega^{-4}$, respectively.

(BL6A1)

Optical conductivity spectra of Pr Ru_4P_{12} due to metal-insulator transition

Lin Chen[2], Masaya Nakayama[a], Takao Nanba[a], Itimin Shirotani[b], and Chihiro Sekine[b]

a Graduate school of Science and Technology, Kobe University, Nada-ku, Kobe 657-8501, Kobe,Japan

b Muroran Institute of Technology, 27-1, Mizumoto,Muroran 050-0071, Japan

$PrRu_4P_{12}$ are ternary metal phosphides with the skutterudite structure ($CoAs_3$-type), which is represented as RT_4P_{12} (R=rare earth element and T=transition metal). $PrRu_4P_{12}$ was found to show a metal-insulator (M-I) transition at Tc=60K [1]. After the success of the synthesis of these compounds, many kinds of experiments has started because its very attractive physical properties. In general, infrared spectroscopy is a useful tool to know the information about the precise change in the electronic structure very close to the Fermi level. The optical measurements ,however, has not yet been done for these materials. We measured the temperature dependence of the optical reflection spectra of RRu_4P_{12} (R=La,Ce,Pr and Sm) in the energy region of 0.005 -4 eV. The optical conductivity spectrum ($\sigma(\omega)$) was obtained from a Kramers-Kronig transformation of the reflectivity spectrum by using each extrapolation function at the both side of the measured spectrum[2].

Figs.1 show the temperature dependence of the low energy part of the obtained optical conductivity spectra of $PrRu_4P_{12}$. We can see that the formation of the shoulder-like structure takes place around 0.04 e V at the low temperature regions instead of the disappearance of the Drude part due to the collective motion of the free carriers in the conduction bands at the higher temperatures. This means that the energy gap was formed with the magnitude of 0.04 eV at 10 K. The position of the shoulder shifts slightly towards the lower energy-side as well as the suppression of the gap by the Drude component according to the increase in the temperatures.

Fig. 2 shows the obtained $\sigma(\omega)$ -spectra of $PrRu_4P_{12}$ at 78 and 300 K in which $PrRu_4P_{12}$ are a metallic state, and the decomposition of the low energy part to the two simple Drude components (broken curves *a* and *b*). The existences of the two Drude components in the $\sigma(\omega)$ -spectra means that there are at least two branches which come across the Fermi level. The component, *a*, corresponds to the band which has a larger Fermi surface between the two bands because the carrier concentration is higher than the component *b*. The possibility of the existence of the two bands which come across the Fermi level in the energy band scheme of $PrRu_4P_{12}$ are pointed out by the recent energy band [3].

References

[1] C.Sekine, T.Uchiumi, I.Shirotani, and T.Yagi, Phys.Rev.Lett.79, (1997)3218.

[2] T.Nanba et.al. Physica B259-261 (1999)853-854.

[3] H.Harima for a private communication.

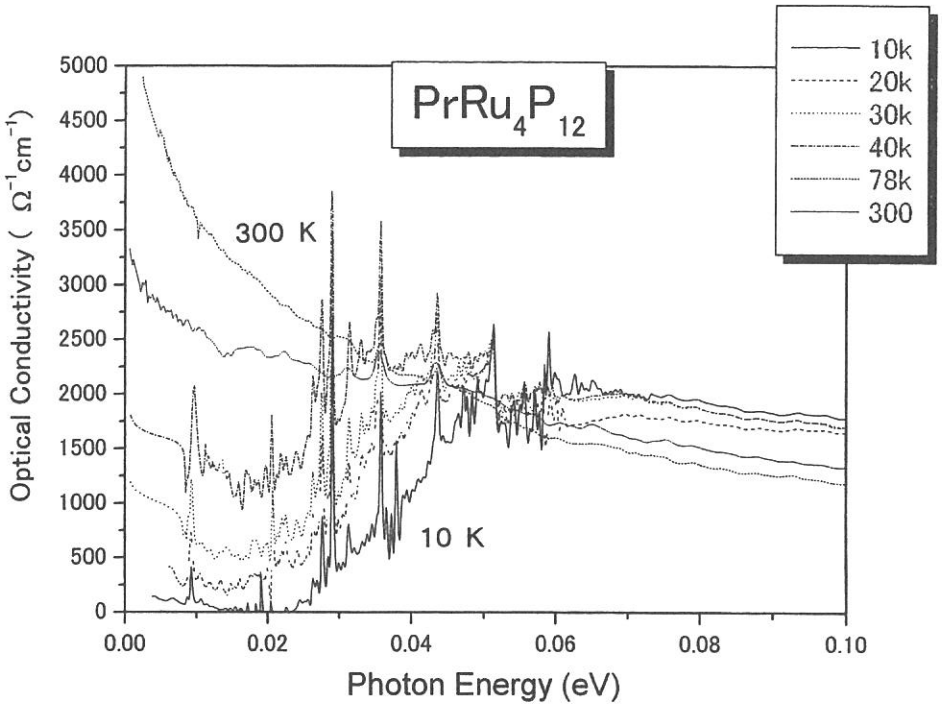

Fig.1

The temperature dependence of the low energy part of the obtained σ-spectra of $PrRu_4P_{12}$.

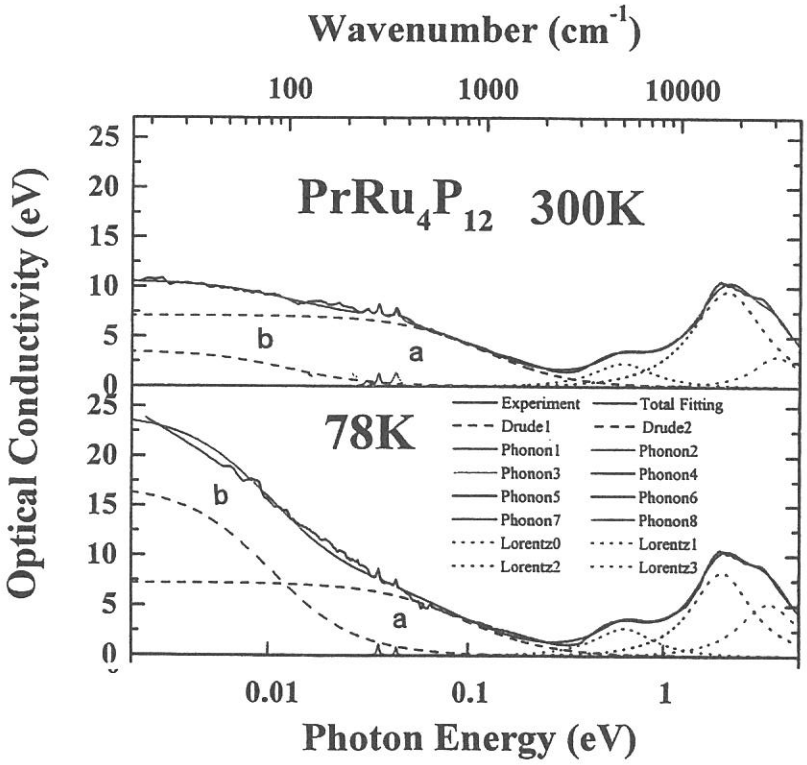

Fig.2 The σ-spectra of $PrRu_4P_{12}$ at 300 and 78 K and its decomposition of the low energy part to two Drude-terms.

(BL6A1)

Infrared absorption spectrum of GaAs

Ichiro Shoji, Sunao Kurimura and Takunori Taira

Laser Research Center for Molecular Science, Institute for Molecular Science, 38 Nishigonaka, Myodaiji, Okazaki 444-8585, Japan

Wide-tunable near-infrared (IR) to mid-IR light sources are needed for a variety of applications, including spectroscopy, chemical monitoring, biomedical applications, and atmospheric and environmental sensing. Frequency down conversion of 1 μm pump sources such as Nd:YAG lasers using optical parametric oscillation or difference-frequency generation is a promising approach to obtain coherent light in the IR region. Since it is necessary to satisfy the phase-matching condition between the pump, signal, and idler light in order to realize high conversion efficiency, the conventional phase-matching method using birefringence in nonlinear-optical crystals limited the wavelength range and materials applicable. On the other hand, quasi-phase matching (QPM) technique which periodically modulates the magnitude of the nonlinear-optical coefficient has many advantages and has been intensively studied. Especially, recent developments in fabrication of periodically poled $LiNbO_3$ (PPLN) [1] have realized high-power pulse and cw optical parametric oscillators which emit up to 4 μm. However, PPLN cannot be used for generating light of wavelength longer than 6 μm, because IR absorption in $LiNbO_3$ becomes significant. Although generation of mid-IR light around 10 μm region, which is often called "fingerprints region for molecules," have been made with birefringent phase matching in some compounds such as $AgGaS_2$, $AgGaSe_2$, and $ZnGeP_2$, these materials are difficult to grow, thermo-mechanically weak, and have low optical damage thresholds.

We are developing QPM devices using GaAs, which can generate mid-IR light up to ~16 μm. GaAs has a large optical nonlinearity: the nonlinear optical coefficient of GaAs is 170 pm/V at wavelength of 1.06 μm, which is more than 6 times larger than that of $LiNbO_3$ [2]. Its transparent range is as wide as 1–16 μm. Moreover, since GaAs is a popular semiconductor, the crystal-growth and processing technologies are matured enough. We are fabricating the GaAs QPM structure by the diffusion-bonding

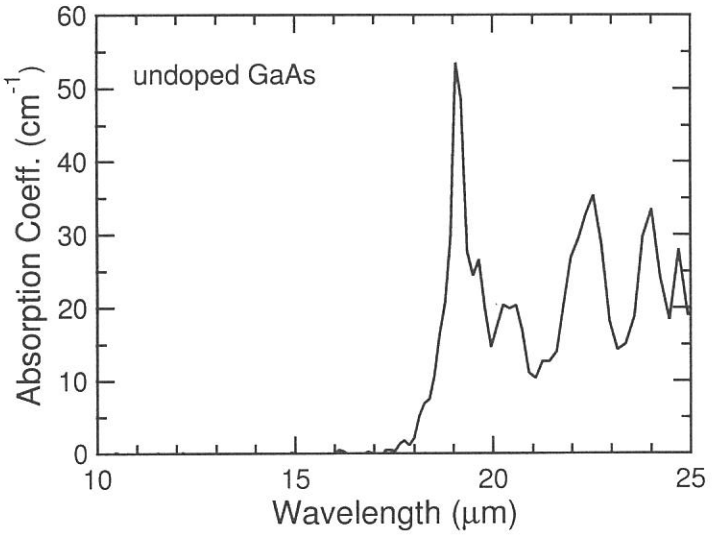

Fig 1. Infrared absorption spectrum of the undoped GaAs.

technique, in which several-tens-to-hundreds of micron-thickness GaAs plates are stacked with the directions alternatively reversed, and bonded at the atomic level by heating. Although this technique was applied first at Stanford University [3], the scattering losses at the interfaces of the plates were significant and only low conversion efficiencies were reported [4]. However, we believe that the optical loss can be greatly reduced by optimizing the fabrication processes. We report here the IR absorption spectra of a raw GaAs sample, which can be used as reference.

Absorption spectra of semiconductors strongly depend on the dopant concentration. Semi-insulating or high-resistivity samples are suitable for frequency-conversion devices because optical absorption is much lower. We have prepared an undoped GaAs sample grown by Hitachi Cable, Ltd. The resistivity was $\geq 10^7\ \Omega\,\mathrm{cm}$, the thickness 465 μm, and the both facets were optically polished. The absorption spectrum was measured with the rapid-scan Michelson FT-IR (Bruker) at the beam line BL6A1. Using the KBr beam splitter and a MCT detector, we made a measurement in the wavelength range of 1–25 μm (10000–400 cm^{-1}).

Figure 1 shows the obtained absorption spectrum. The wavelength range 1–10 μm, where no absorption was observed, is not shown. The obtained result is in agreement with previously reported spectrum of a n-type but high resistivity sample [5]. However, the absorption coefficients in low-absorption region of 12–18 μm, which are important for evaluating the performance of the QPM device, could not be accurately obtained in our measurement because of low signal-to-noise ratios. A much thicker sample should be used in order to measure such small absorption coefficients.

We have a plan to compare the absorption coefficients between the diffusion-bonded stacked sample and the raw bulk sample to evaluate the scattering losses at the interfaces of the stacked sample, and feedback the fabrication processes.

References

[1] L. E. Myers, R. C. Eckardt, M. M. Fejer, R. L. Byer, W. R. Bosenberg, and J. W. Pierce, J. Opt. Soc. Am. B **12,** 2102 (1995).

[2] I. Shoji, T. Kondo, A. Kitamoto, M. Shirane, and R. Ito, J. Opt. Soc. Am. B **14,** 2268 – 2294 (1997).

[3] L. Gordon, G. L. Woods, R. C. Eckardt, R. R. Route, R. S. Feigelson, M. M. Fejer, and R. L. Byer, Electron. Lett. **29,** 1942 (1993).

[4] D. Zheng, L. A. Gordon, Y. S. Wu, R. S. Feigelson, M. M. Fejer, and R. L. Byer, Opt. Lett. **23,** 1010 (1998).

[5] W. Cochran, S. J. Fray, F. A. Johnson, J. E. Quarrington, N. Williams, J. Appl. Phys. **32,** 2102 (1961).

(BL6A1, BL7B)

Optical reflectivity study of colossal magneto-resistance pyrochlore $Tl_2Mn_2O_7$

H. Okamura, T. Koretsune, M. Matsunami, S. Kimura, T. Nanba,
H. Imai[A], Y. Shimakawa[A], Y. Kubo[A]

Department of Physics and Graduate School of Science and Technology, Kobe University, Kobe 657-8501.
[A]Fundamental Research Laboratories, NEC Corporation, Tsukuba 305-8501, JAPAN

Physics of the colossal magneto-resistance (CMR) phenomena has been one of the central issues of condensed matter physics in the last several years. In particular, the ferromagnetic perovskite manganites, e.g., $La_{1-x}Sr_xMnO_3$, have attracted much attention [1]. More recently, the $Tl_2Mn_2O_7$ pyrochlore has been attaining increasing interest, since it exhibits a CMR that is comparable to those observed for the perovskites [2]. $Tl_2Mn_2O_7$ is also a ferromagnet, and its resistivity (ρ) drops rapidly upon cooling through $T_c \sim 120$ K. Near and above T_c, an external magnetic field of 7 T reduces ρ by a factor of ~ 10. Although these features appear very similar to those for the perovskites, various studies have suggested that the underlying mechanism should be very different from that in the perovskites [2]. In order to probe the electronic structures of $Tl_2Mn_2O_7$ and its relation to the CMR, we have studied the infrared optical reflectivity of $Tl_2Mn_2O_7$ under magnetic fields at BL6A1, and the optical reflectivity in the visible, UV, and VUV ranges at BL7B. Figure 1 shows the reflectivity spectra (R) measured at various temperatures (T) and magnetic fields (B). Figure 2 shows the optical conductivity spectra (σ) obtained from R using the Kramers Kronig relations. The sample used had a Curie temperature (T_c) of 120 K, and the T-induced spectral change is very large around T_c. In addition, the B-induced spectral changes are also largest near and above T_c (120 K - 140 K). These spectral changes show that the electronic structures of $Tl_2Mn_2O_7$ become metallic and the carrier density increases below T_c, and the same change occurs also above and near T_c in strong magnetic fields. The range 120-140 K is also where the CMR is observed, and the CMR mechanism in $Tl_2Mn_2O_7$ should be closely related to this carrier density increase.

References

[1] See, for example, Y. Tokura et al. J. Phys. Soc. Jpn. **63**, 3931 (1994).

[2] Y. Shimakawa et al., Nature **379**, 53 (1996); Phys. Rev. B **55**, 6399 (1997).

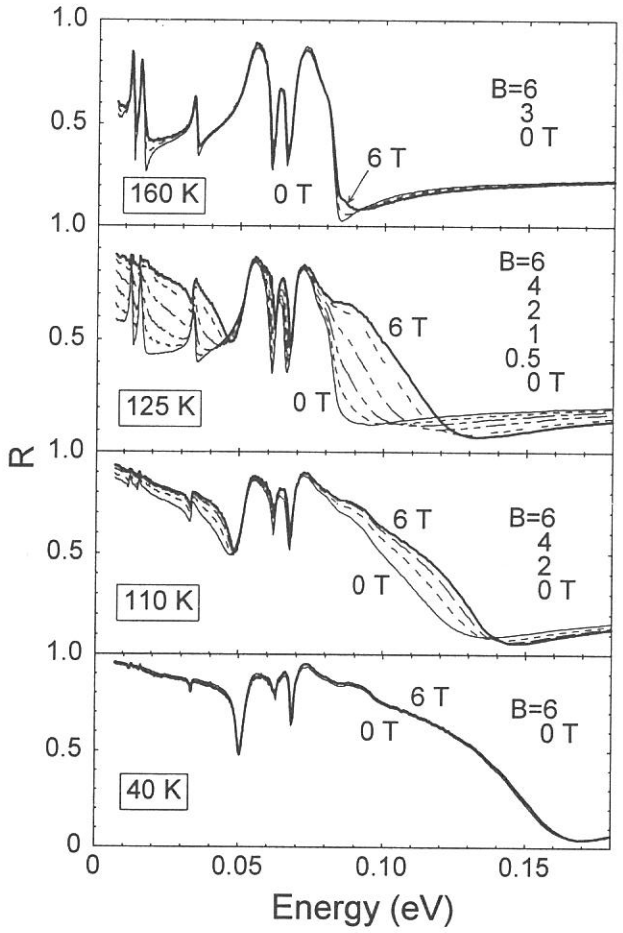

FIG. 1. Reflectivity (R) spectra of $Tl_2Mn_2O_7$ at temperatures 160, 125, 110, and 40 K in various magnetic fields (B).

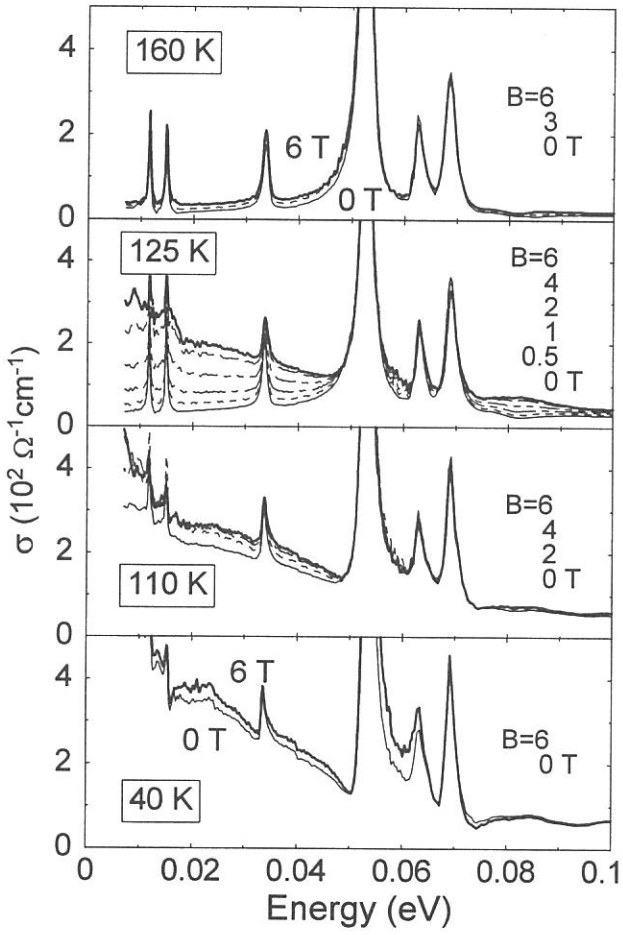

FIG.2 : Optical conductivity (σ) spectra of $Tl_2Mn_2O_7$ at temperatures 160, 125, 110, and 40 K in various magnetic fields (B).

(BL7B)

Responsivity spectra of GaN based UV detectors in VUV region

Atsushi Motogaito[1], Motoo Yamaguchi[1], Kazumasa Hiramatsu[1], Masahiro Kotoh[2], Youichiro Ohuchi[2], Kazuyuki Tadatomo[2], Yutaka Hamamura[3] and Kazutoshi Fukui[4]

[1]*Deptartment of Electrical and Electronic Engineering, Mie University, 1515 Kamihama, Tsu, Mie, 514-8507*

[2]*Photonic Research Laboratory, Mitsubishi Cable Industries, Ltd., 4-3 Ikejiri, Itami, Hyogo, 664-0027*

[3]*Sagamihara Plant, Nikon Co., Ltd., 1-10-1 Asamizodai, Sagamihara, Kanagawa, 228-0828*

[4]*Department of Vacuum UV Photoscience, Institute for Molecular Science, Myodaiji, Okazaki, Aichi, 444-8585*

The group III-nitride semiconductors are promising materials for applications in opt-electronic devices such as laser diodes and field-effect transistors. Ultraviolet (UV) detectors are one of the most attractive devices in the group III-nitride semiconductors. Now, for the measurement UV light, photodetector components with Si such as photodiodes are mainly used. However, light sensitivity often deteriorates due to radiation damage in the VUV region. Several groups have reported on GaN or AlGaN based UV detectors.

Synchrotron radiation (SR) is a powerful light source of X-ray region. However, SR is also the useful light source of V,UV – infrared (IR) region because of its wide wavelength continuity. It gives us the chances not only to investigate the electronic and optical structures, for example in ref.1) and 2), but also to characterize the responsivity spectra of UV detectors in wide wavelength region.

In this report, we describe the responsivity spectra of Schottky type UV detectors between VUV and visible (VIS) light region (λ=41-563 nm, $h\nu$=2-30 eV).

The UV detectors used in this study adopt the Schottky contacts with mesa structures. They consists of a 3 μm thick n-GaN layer (n=2×10^{18} cm^{-3}) and a 2.5 μm thick i-GaN layer (n=1.0×10^{16} cm^{-3}) on (0001) sapphire substrate. These layers are grown by metalorganic vapor phase epitaxy (MOVPE). The Au/Ni Schottky contact with mesa structure composed of 2-μm-electrode regions and 2-μm-window regions by liftoff process is deposited on i-GaN. The diameter of detectors is 6.5 mm.

The responsivity of UV detectors is estimated by measuring photo current illuminating SR at the beam line BL7B of the UVSOR Facility, Institute for Molecular Science. The BL7B is equipped with a 3m normal-incidence monochromator. The details of BL7B are already reported [3, 4]. UV detectors are illuminated with the monochromatic light, which is between $h\nu$=2.2 eV (λ=564 nm) and $h\nu$=30 eV (λ=41 nm). The measurements of photo current are performed at room temperature in the vacuum chamber under the vacuum of 10^{-9} Torr. The photo current is measured as reverse current of Schottky diode with zero bias or applying reverse bias during the illumination of SR. Responsivity of UV detectors is calculated by dividing the photo current by the photon energy.

The responsivity spectra of detectors on photon energy are measured. Figure 1 shows the responsivity spectra at zero bias. No responsivity at the energy lower than 3.4 eV (the absorption edge of GaN)

can be seen clearly. This means these detectors are available for UV or VUV region without filters, which cut off visible light. The ratio of responsivity between UV and VIS region is about 2×10^3. The characteristics of responsivity spectra are considered as follows. In the case of $h\nu$<8.0 eV, there are no photoemission current of Au and GaN so detectors can be used without photoemission. The maximum responsivity of this detector is 0.01 at $h\nu$=4.6 eV (λ=270 nm). In the case of $h\nu$>8.0 eV, photoemission currents of Au and GaN are not negligible now. Especially, $h\nu$>9.5 eV, the photoemission current of GaN, which flows in the reverse direction of photo current, is dominated so the sign of responsivity of detectors is negative. Thus, these detectors can be used between 3.4 eV (360 nm) and 8.0 eV (155 nm). There are no reports on the responsivity spectra in vacuum ultraviolet (VUV) region (λ<200 nm). Therefore this result shows that these Schottky type detectors with mesa structures are effective to detect VUV light (155<λ<200 nm).

1) O. Ambacher et al.: MRS Intern. J. Nitride Semicond. Res. 2 (1997) Article 22.

2) K. Fukui et al.: Jpn. J. Appl. Phys. **38** (1999) Suppl.38-1, 538.

3) K. Fukui, H. Nakagawa, I. Shimoyama, K. Nakagawa, H. Okamura, T. Nanba, M. Hasumoto and T. Kinoshita: J. Synchrotron Rad. **5** (1998) 836.

4) K. Fukui, H. Miura, H. Nakagawa, I. Shimoyama, K. Nakagawa, H. Okamura, T. Nanba, M. Hasumoto and T. Kinoshitato: Nucl. Instrum. & Methods in Phys. Res. A. (to be published).

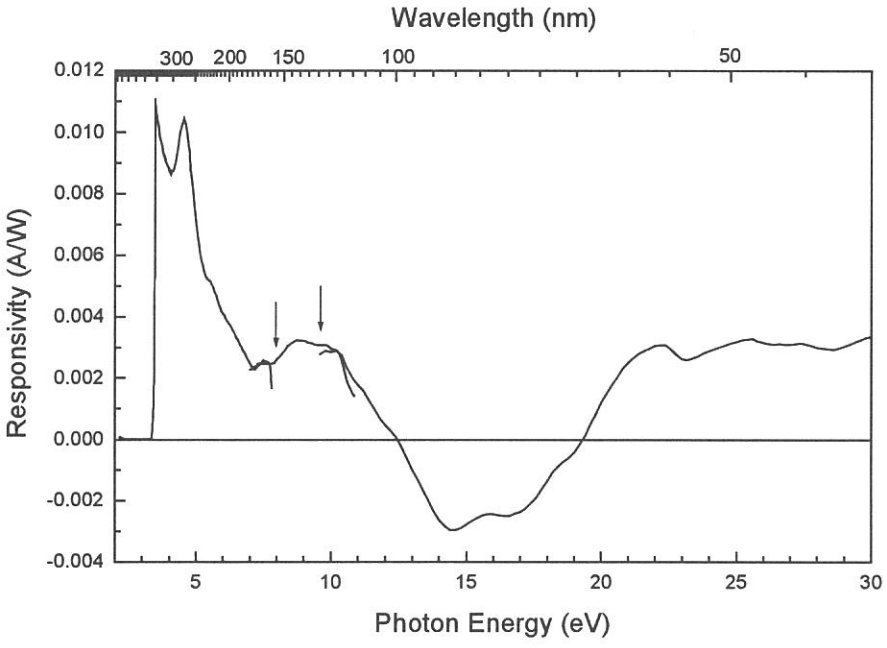

Fig.1. The responsivity spectra of GaN based Shottky type UV detector.

BL-7B

Vacuum Ultraviolet Absorption Spectra of Amino Acids (2): Tryptophan and Methionine

Kazumichi Nakagawa[A)] [1], Hiroyuki Arii[A)], *Yoko Kodama[B)], and **Masahito Tanaka[C)]

[A)]Faculty of Human Development, Kobe University, Tsurukabuto, Nada-Ku, Kobe 657-8501.
[B)]Graduate School of Cultural Studies and Human Sciences, Rokkodai, Nada-Ku, Kobe 657-8501.
[C)]Graduate school of Science and Technology, Tsurukabuto, Nada-Ku, Kobe 657-8501.

Although amino acids are known to be important building block of the life body, little is known about absorption spectra [2], because the main part of oscillator strength of these molecules is in the region of vacuum ultraviolet.

We measured absorption spectra of thin films of tryptophan (Trp) and methionine (Met) evaporated on collodion films. Thickness of amino acid films was estimated to be about 40 nm by a calibration with HPLC technique. Measurement was performed at the BL-7B in the wavelength region from 40 to 350 nm. In order to minimize the error in measurement of very weak transmitted light around 70 nm, we used an electron multiplier as a detector for 40 – 130 nm. Extremely low pressure of amino acid films allowed us measurement in vacuum at room temperature.

Obtained result was shown in Fig. 1.

The 220 nm peak of Trp was analyzed on the basis of peak position of the similar peaks of benzene (185 nm) and that of phenylalanine (198 nm) [2]. On the basis of this comparison, we tentatively concluded that the 220 nm peak of Trp was originated from the benzene ring part of Trp. The 280 nm peak of Trp was analyzed in comparison with absorption spectra of glycine, alanine and aspartic acid [2, 3]. This comparison showed that the 280 nm peak was found only for the case of Trp, which implies that the 280 nm peak was due to the pentagon part of Trp.

In order to confirm these assignments, we made a molecular orbital calculation using the WinMOPAC software. A tentative result showed that a transition due to benzene ring was found around 220 nm and that a transition due to the pentagon part was found around 280 nm. Other results of calculation were in a good harmony with the experimental results. Detailed analysis is being done.

References

[1] E-mail address is nakagawa@kobe-u.ac.jp .
[2] K. Nakagawa et al., in "The role of Radiation in the Origin and Evolution of Life", ed. By M. Akaboshi et al., Kyoto University Press, 2000, Kyoto, Japan, pp. 353-362.
[3] T. Inakagi, Biopolymers 12(1973)1353-1362.

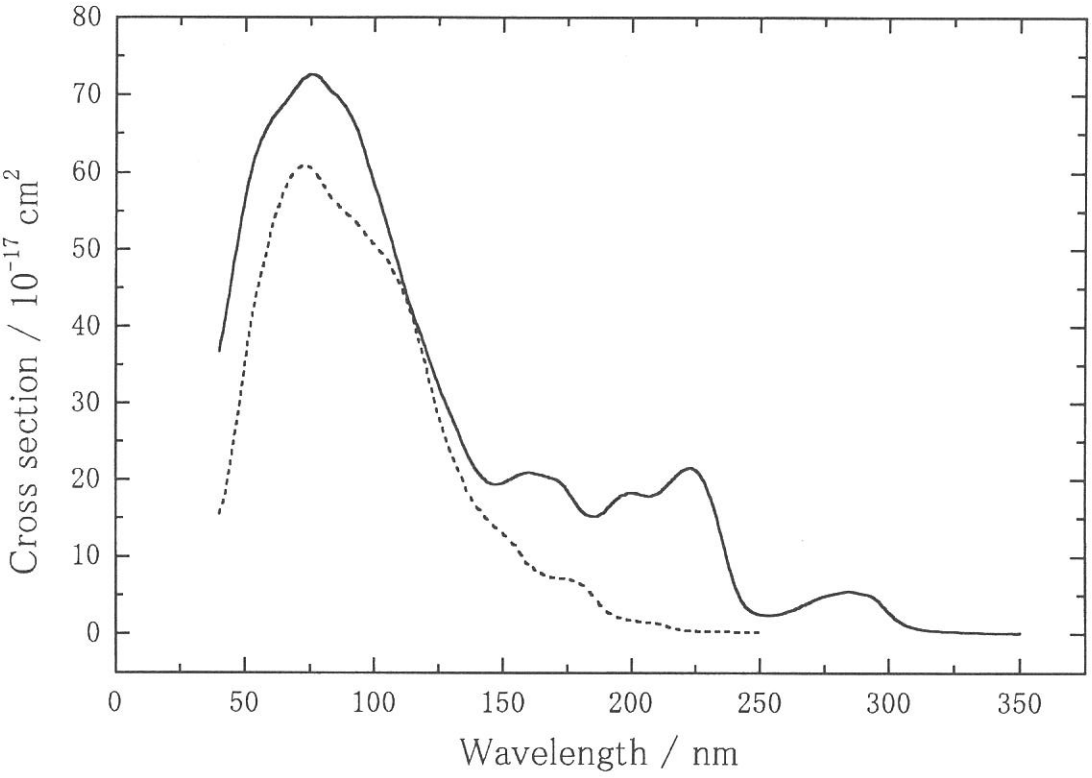

Fig.1. Absorption spectra of L-tryptophan (solid line) and L-methionine (dotted line).

(BL7B)

Luminescence and Reflectance Spectra of $CdBr_2$ Crystal

Kazutoshi FUKUI, Takayoshi Kihara[1], Hideyuki Nakagawa[1]

Institute for Molecular Science, Okazaki 444-8585, Japan

Fax +81-564-54-7079, fukui@fuee.fukui-u.ac.jp

[1] *Faculty of Engineering, Fukui University, Fukui 910-8507, Japan*

The cadmium bromide crystal ($CdBr_2$), which has indirect band gap, is an ionic layer compound. The crystal structure of $CdBr_2$ belongs to the rhombohedral $CdCl_2$ structure [1]. An Cd ion sheet is sandwiched by two I ion sheets and this basic layer stacks with each other. The crystal *c*-axis is perpendicular to these ion sheets. The bonding nature between Cd and Br ions is mainly ionic. However, that between adjacent Br ion sheets is of the Van der Waals force. In this report, we represent the visible – ultraviolet emission spectra, which are excited by the photon energy from near band edge to 30 eV, and their excitation spectra.

The experiments were carried out at BL7B. A single UV optical fiber cable, which was dedicated for ultra high vacuum (UHV) and had 0.6 mm core diameter, were used for detecting VIS and UV luminescence in the UHV chamber. VIS and UV luminescence lights were introduced to the VIS-UV monochromator with CCD array detector via both a UHV fiber optic feedthrough and a 5 m single optical fiber (0.6 mm core diameter). The $CdBr_2$ samples are single crystals, which are grown from the melt by the Stockbarger technique. The starting powder is commercially available $CdBr_2$ powder of 99.99% purity. The purification is carried out by the normal freezing method. The samples were cleaved just before the installation in the vacuum chamber. The incident light is parallel to the *c*-axis. The measurements were carried out in the range of 10^{-9} – 10^{-10} Torr from 15K to

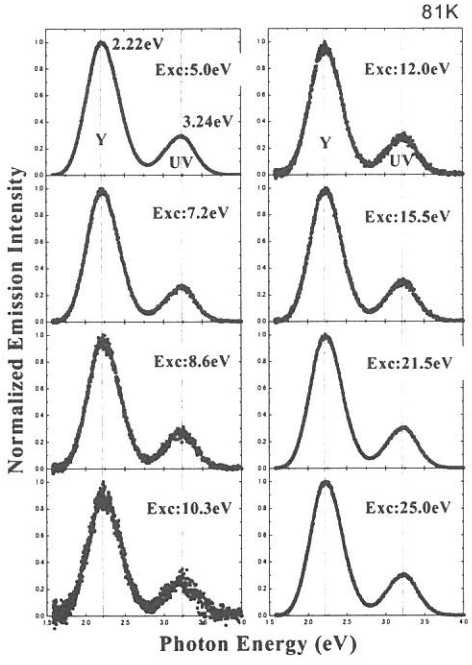

Fig.1 Emission spectra of CdBr2 at 81 K. The excitation energies are from 5.5.0 eV to 25.0 eV.

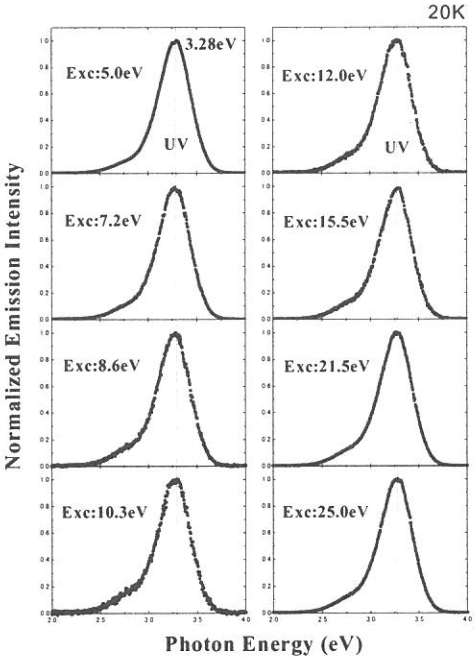

Fig.2 Emission spectra of CdBr2 at 20 K. The excitation energies are from 5.5.0 eV to 25.0 eV.

300 K.

Figure 1 shows the emission spectra at 81K. There are two emission bands. One is UV emission band at about 3.24 eV, the other Y emission band at around 2.22 eV. As shown in Fig. 2, the UV-emission becomes dominant emission band with decreasing temperature. These results are agreement with the previous precise work, which is carried out with D_2 lamp as the excitation light source [1]. The spectral distribution does not depend on the excitation energy from 5.0 to 25.0 eV. It means that the luminescence decay process does not change even though Cd 4*d* (and Br 4*s*) outermost inner core electrons are excited. It also suggests that the spectral distribution of the excitation spectra of both UV and Y emission bands are similar with each other.

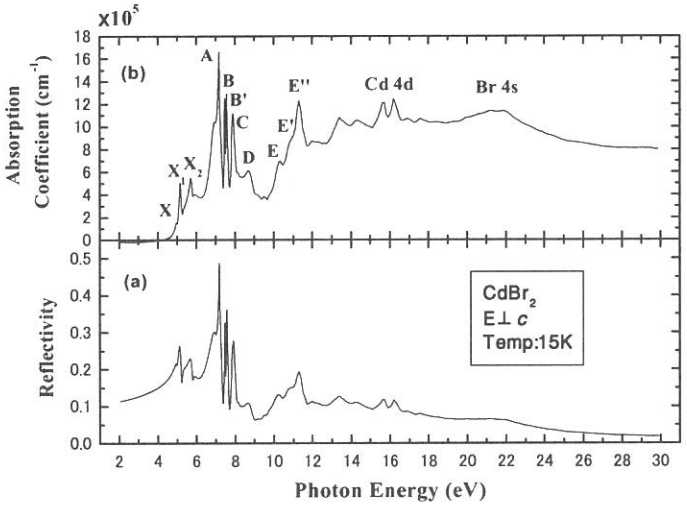

Fig.3 Reflectance spectrum of $CdBr_2$ at 20 K (a) and absorption spectrum (b) derived from (a) through the Kramers-Kronig analysis.

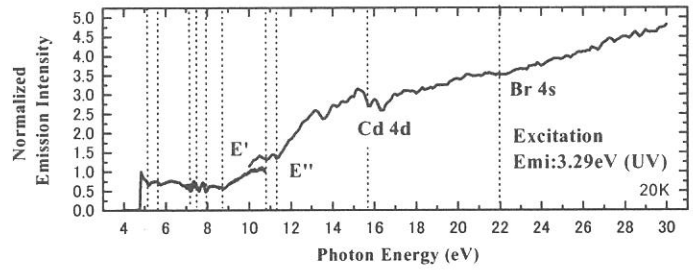

Fig.4 Excitation spectrum of the UV emission band of $CdBr_2$ at 20 K.

The reflectance spectrum at 20 K is shown in Fig. 3(a). Figure 3(b) shows the absorption spectrum derived from Fig. 3(a) through the Kramers-Kronig analysis. These results are agreement with the previous work [2]. The excitation spectrum of UV emission band at 20 K is shown in Fig. 4. The vertical lines indicate the location of the absorption peaks as shown in Fig. 3(b). The emission intensity is increasing with increasing photon energy. The UV emission starts at about 4.8 eV and the upsweep at around 11 eV is due to the transition to the upper conduction band. The dips correspond to the absorption peaks may due to the existence of the surface dead layer or of the other non-radiative decay channel such as photoelectron emission.

References

[1] H. Nakagawa and M. Kitaura, SPIE **2362** (1994) 295.

[2] M. Fujita, H. Nakagawa, H. Matsumoto, T. Miyanaga, M. Watanabe, K. Fukui, E. Ishiguro, Y. Fujii and Y. Sakisaka, J. Phys. Soc. Jpn. **59** (1990) 338.

(BL8B1)

Soft X-ray Excited Visible – Ultraviolet Emission Spectra of AlGaN Crystal

Kazutoshi FUKUI, Hideki HIRAYAMA [1], Satoru TANAKA[2] and Yoshinobu AOYAGI [1]

Institute for Molecular Science, Okazaki 444-8585, Japan

Fax +81-564-54-7079, fukui@fuee.fukui-u.ac.jp

[1] *Institute of Physical and Chemical Research (RIKEN), Wako 351-0198, Japan*

[2] *Research Institute for Electronic Science, Hokkaido University, Sapporo 060-0812, Japan*

The soft X-ray excited Visible (VIS) – Ultraviolet (UV) emission spectra (SXEVUES) of AlGaN have been measured. The emission spectra, which are excited by the band-to-band transition energy region, give us the information of luminescence decay process. SXEVUES gives us not only the excitation energy dependence but also the ion-site dependence of the luminescence decay process. Furthermore, both intensity and time correlation among the SXEVUES, the soft X-ray emission spectra (SXEA), and the photoelectron yield spectra will be interesting for the decay studies of the high photon energy excitation. In this report, we represent the first tentative results of SXEVUES of the wurtzite $Al_{1-x}Ga_xN$ (x= 0.14) and their temperature dependence.

The experiments were carried out at BL8B1. A single UV optical fiber cable, which was dedicated for ultra high vacuum (UHV) and had 0.6 mm core diameter, were used for detecting VIS and UV luminescence in the UHV chamber. VIS and UV luminescence lights were introduced to the VIS-UV monochromator with CCD array detector via both a UHV fiber optic feedthrough and a 5 m single optical fiber (0.6 mm core diameter). Thin film was made by the MOCVD method at RIKEN on SiC substrate. Sample was cleaned with organic solvents just before the installation in the vacuum chamber. No specific surface cleaning of the samples was performed in the vacuum chamber. The SXEVUES measurements were carried out in the range of 10^{-8} Torr from 25K to 200 K.

Figure 1 shows the VIS – UV region emission spectra of $Al_{0.14}Ga_{0.86}N$ thin film from 25K to 201K. The excitation energy is about 330 eV. The spectral distribution does not depend on the excitation energy around the nitrogen K edge (330 – 440 eV). There are at least three emission bands : first one around 3.75 eV (UV), second one around 2.3 eV (Y) and last one around 1.9 eV. According to the similarity of the first two bands in the emission spectrum to those of GaN [1], the first band consists of the exciton peaks, and the band at about 2.3 eV may be associated with deep levels. The deep levels arise due to the cation or nitrogen defects. Figure 2 shows the VIS – UV region emission spectra of SiC substrate from 25K to 208K. In case of SiC substrate, there are at least two emission bands. The first band is located at about 2.6 eV and the other is at about 1.9 eV. The 2.6 eV band on SiC substrate cannot be seen in Fig. 1, so that 3.75 eV and 2.3 eV bands in Fig. 1 are the original emission bands of $Al_{0.14}Ga_{0.86}N$ material. However, the similarity of the 1.9 eV band between Fig. 1 and 2 may suggest that both SiC and $Al_{0.14}Ga_{0.86}N$ surfaces are contaminated by the same material. It may be due to the high vacuum pressure and the surface sensitive character of the SXEVUES.

As shown in Fig. 1, the intensities of the UV and Y bands show the different temperature dependence behavior. The intensity of UV band decreases with increasing temperature even at 25K. However, Y band keeps

its intensity up to 53 K. It means that two bands have different potential barriers in the decay process. Further measurements and the combination with the near band-edge emission measurements will be held.

References

[1] S.C. Jain, M. Willander, R. Van Overstraeten, J. Appl. Phys. **87** (2000) 965.

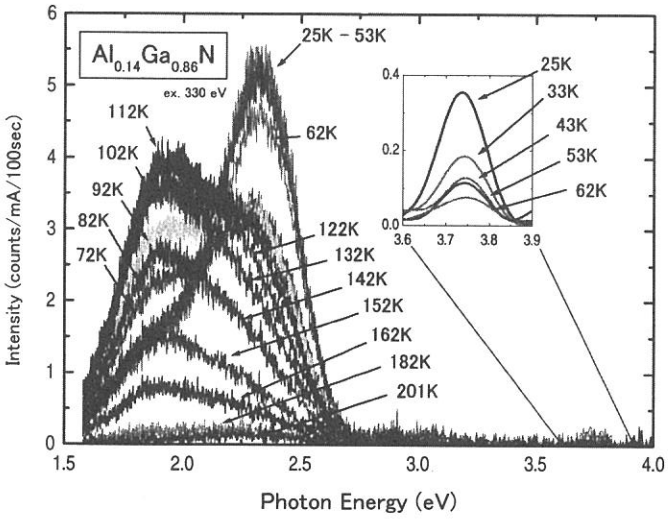

Fig.1 Emission spectra of $Al_{0.14}Ga_{0.86}N$ at various temperature. The excitation energy is 330 eV.

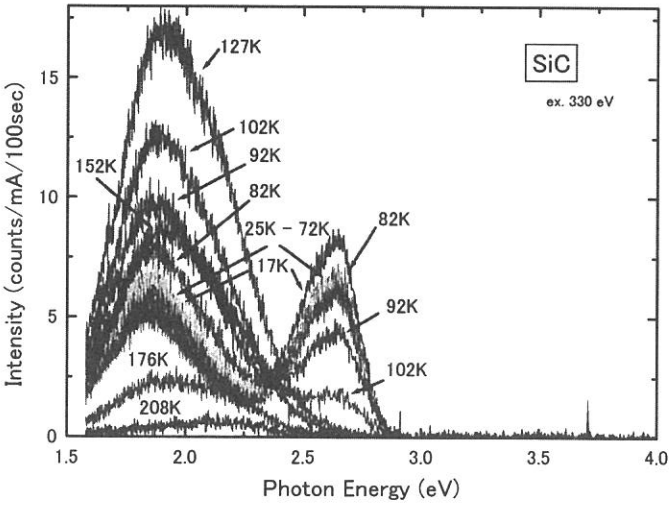

Fig.2 Emission spectra of SiC substrate at various temperature. The excitation energy is 330 eV.

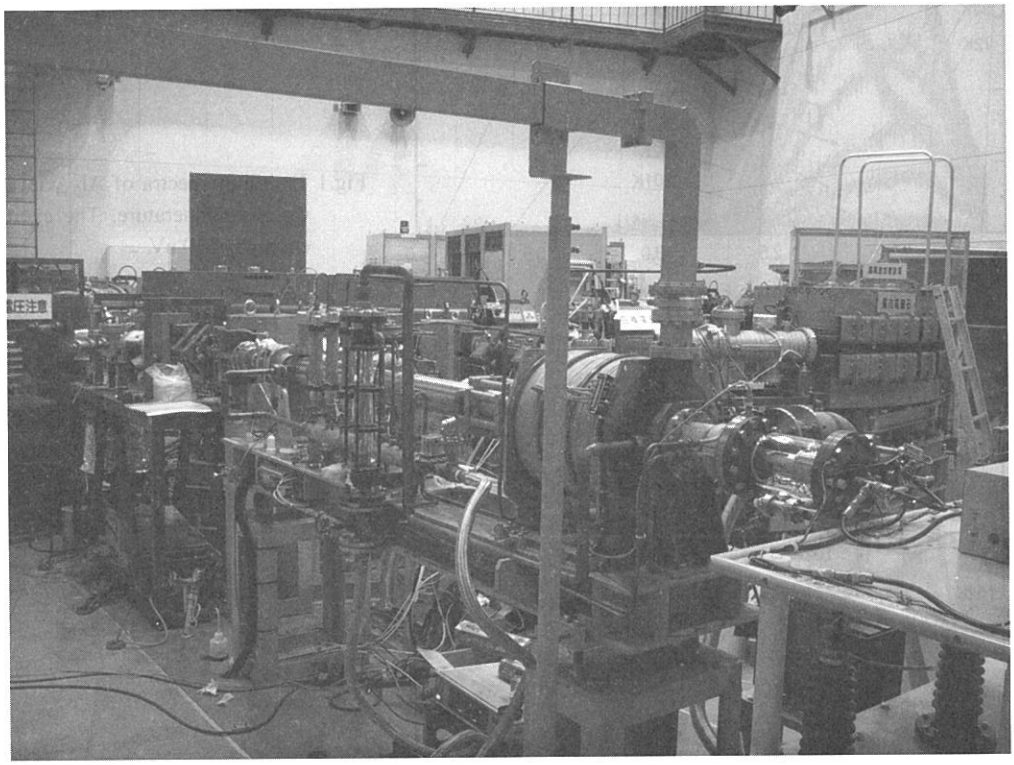

UVSOR

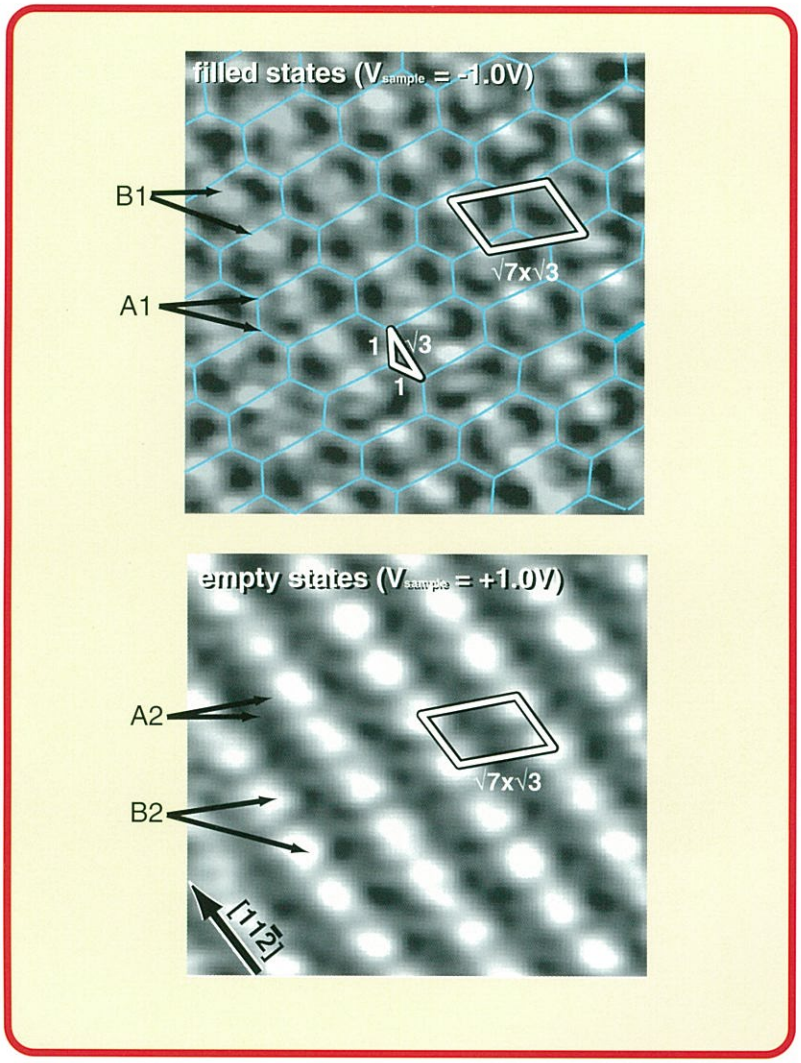

Solid State Spectroscopy II

(XAFS, PES)

BL1A, 5A, 5B, 6A2, 7A, 8B1, 8B2

(BL7A)

Oxidation State of Nickel Ion in Li_xNiO_2 from L-edge Spectroscopy

Takeshi YAO, Naoshi OZAWA, Hiroshi SAWADA and Yoshiharu UCHIMOTO

Department of Fundamental Energy Science
Graduate School of Energy Science
Kyoto University
Yoshida, Sakyo-ku, KYOTO 606-8501 Japan

Secondary lithium batteries using intercalation compounds as the cathode active material have been studied intensively. Among many intercalation compounds, $LiNiO_2$ with layer rock salt structure is one of the most promising cathode material used in lithium ion batteries. It is important to study valency change during charge and discharge process in order to understand their electrochemical properties. In this study, oxidation states of nickel ion in Li_xNiO_2 were determined by using a measurement of Ni L_{23}-edge X-ray absorption near edge structure.

A mixture of Li(OH) and $Ni(OH)_2$ in a mole ratio of 1:1 was heat-treated and $LiNiO_2$ was obtained. The crystal structure of the product was determined by XRD using MoKα radiation to confirm the formation of well characterized $LiNiO_2$. By electrochemical extraction of lithium ion, samples having various x values in Li_xNiO_2 were obtained.

Figure 1 shows the Ni L-edge X-ray absorption spectrum of Li_xNiO_2. The spectra were all attributed to the bivalent nickel ion in high spin state[1]. The change in the shapes of spectra was not so remarkable, it is considered that the valence state of the nickel ion was not changed with the change of the amount of lithium ion. In figure 2, the area ratio of the two sub-peaks in L3-edge (A and B in figure 1) is shown. It is shown that the ratio:B/A increase with the decrease of x, and this indicates that the nickel ion was oxidized with the extraction of lithium ion. It can be concluded that the valence state of the nickel ion was basically unchanged and was bivalent, but slightly oxidized with the extraction of lithium ion.

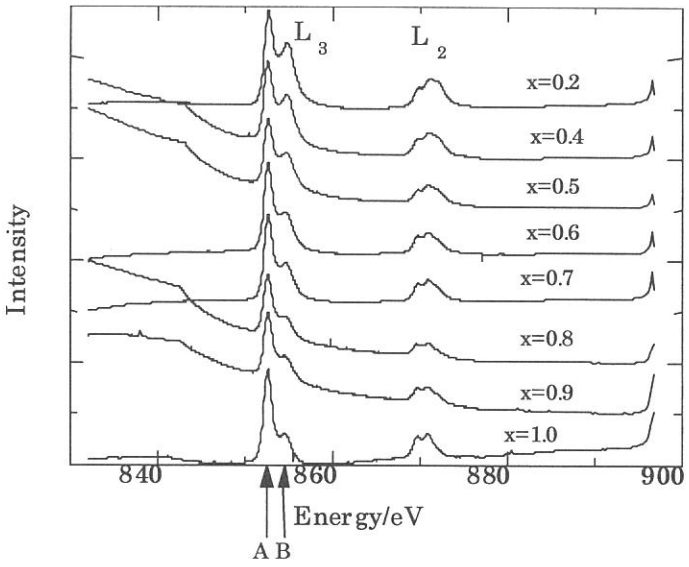

Figure 1 Ni L-edge XANES of Li_xNiO_2

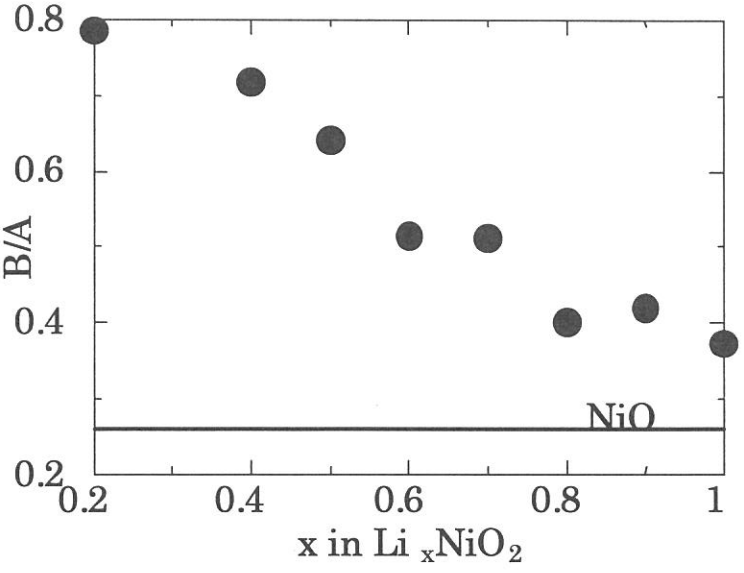

Figure 2 The area ratio of the two sub-peaks in L_3-edge (A and B in figure 1)

Reference
[1] L. A. Montoro, M. Abbate, J.M. Rosolen, J. Electrochem. Soc., **147**, 1651-1657 (2000)

(BL1A)

Ni 2p Photoabsorption and Resonant Photoelectron Spectroscopy of High-spin Ni complex, Ni(*N*,*N*'-dimethylethylenediamine)$_2$Cl$_2$

Hiroshi Oji, Yasutaka Takata, Takaki Hatsui, and Nobuhiro Kosugi

Institute for Molecular Science, Myodaiji, Okazaki 444-8585, JAPAN

In the previous study, we found that the planar Ni complexes with a $3d^8$ low-spin ground state show characteristic resonant behavior in the Ni 3p and 3s resonant photoelectron spectra, which is different from the resonant behaviors of Ni metal and Ni oxide.[1] The kinetic energy of Ni 3p satellite peaks decrease as the photon energy increases, indicating the one electron, or excitonic, feature of the excited states in these systems. In the present study, we measured soft X-ray Ni 2p absorption and resonant Ni 3s and 3p photoelectron spectra of a $3d^8$ high-spin Ni complex, Ni(*N*,*N*'-dimethylethylenediamine)$_2$Cl$_2$ (Ni(DED)$_2$Cl$_2$) to clarify the effect of the spin state on the core-excited states of the system.

For the measurement, the powder of Ni(DED)$_2$Cl$_2$ was compressed into the disk-form, which was fixed to the sample folder by conductive adhesion tape. Measurements of X-ray absorption and photoelectron spectra were performed at BL1A soft X-ray beamline of the UVSOR facility, equipped with the double crystal monochromator. A pair of beryl ($10\bar{1}0$) crystal was used for the monochromator crystal, where the bandpass of monochromatized light was 0.6 eV around the Ni 2p edge. The X-ray absorption spectra (XAS) were measured by the total electron yield mode. A SCIENTA SES-200 hemispherical electron energy analyzer was used for the measurement of photoelectron spectra. The energy resolution of the analyzer was ~0.4 eV and the total energy resolution for the measurements of the photoelectron spectra was ~0.7 eV. The photoelectron spectra of the Cl 2p region were measured to calibrate the electron energy and intensity of the spectra.

The Ni 2p X-ray absorption spectra of Ni(DED)$_2$Cl$_2$ is shown in Fig. 1. At the photon energy labeled as 0-8 in Fig. 1, the off- and on-resonant Ni 3p, 3s photoelectron spectra were measured, as shown in Fig.2. The normal Auger spectra measured at the photon energy of 899.8 eV and 1347.6 eV are also indicated in the upper part of the Fig. 2. Ni 3p and 3s primary ion states labeled with asterisk (*) are not enhanced through the resonant excitation. On the other hand, satellite peaks in the Ni 3p and 3s region (a-g) are enhanced through the resonant excitation. The trend of kinetic energy shift for these satellite peaks are similar to that of primary ion states, indicating their constant binding energy feature. To examine the trend of kinetic energy shift in detail, we have plotted the kinetic energy for the primary ion states and satellite peaks as a function of the photon energy in Fig. 3. This shows nearly linear relationship between the kinetic energy of these satellite peaks and the photon energy with the slope ($\Delta KE/\Delta h\nu$) of +1. This dependence of satellite bands on the photon energy is different from that of the low-spin complexes where the slope becomes negative (e.g. $\Delta KE/\Delta h\nu = -0.55\pm0.05$ for $K_2[Ni(CN)_4]$[1]), but is similar to that of NiO where the electron correlation and multiplet interaction are important. This indicates that the excited states in this high-spin Ni complex cannot be described by the one-electron picture. A series of our studies on the Ni complexes with various electronic states reveals that the resonant behavior of photoelectron spectra reflects the electron configuration of core-excited metal atom which depends on the chemical bonding

state between the metal and the ligand molecules.

Reference

1) Y. Takata, T. Hatsui, and N. Kosugi, *J. Electron Spectrosc. Relat. Phenom.* **88**, 235 (1998).

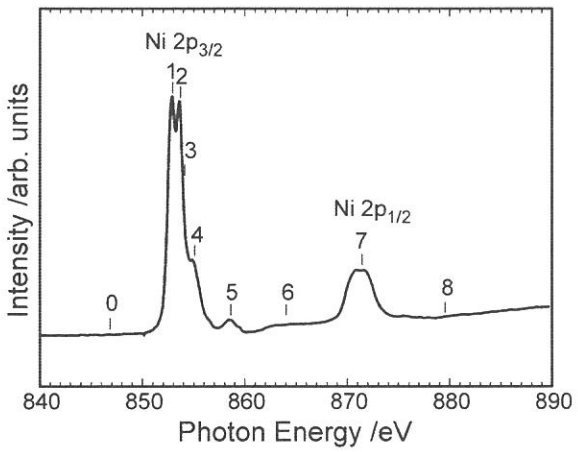

Fig. 1. Photoabsorption spectra at the Ni $2p_{3/2}$ and $2p_{1/2}$ edges for $Ni(DED)_2Cl_2$.

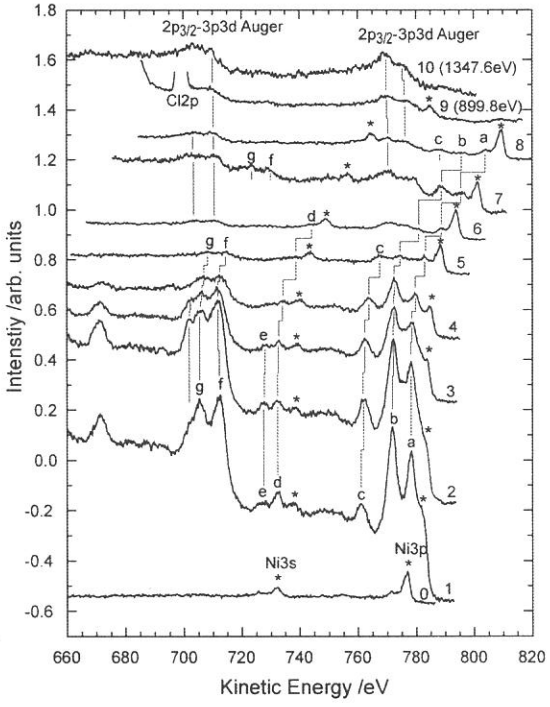

Fig. 2. Off- and on-resonant photoelectron spectra in the Ni 3p and 3s regions at the Ni $2p_{3/2}$ and $2p_{1/2}$ edges for $Ni(DED)_2Cl_2$.

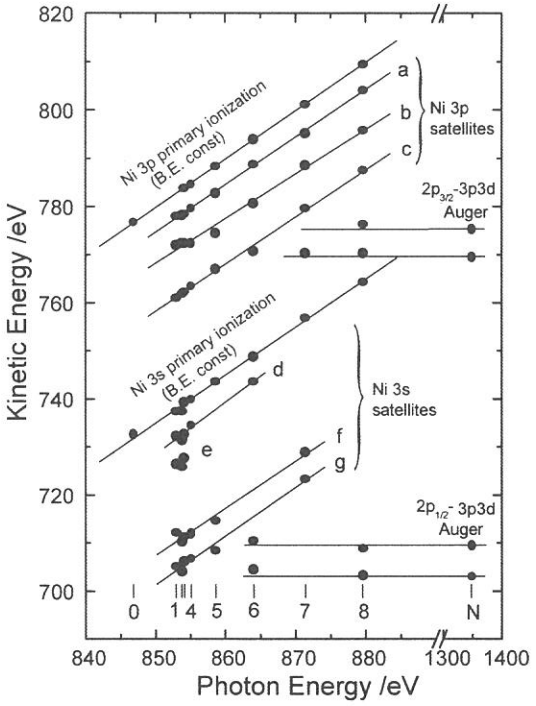

Fig. 3. Photon energy dependence of the kinetic energy for Ni 3p, 3s primary and satellite photoelectron peaks.

(BL5A)

Sn4*d* and Pb5*d* Core-level Photoelectron Spectra of Si(111) $\sqrt{7}\times\sqrt{3}$-(Pb, Sn) Surface

Kazuo SODA, Junji YUHARA, Takashi TAKADA, Osamu YOSHIMOTO, Masahiko KATO, Shinya YAGI, Kenji MORITA and *Masao KAMADA

Graduate School of Engineering, Nagoya University, Furo-cho, Chikusa-ku, Nagoya 464-8603

**UVSOR, Institute for Molecular Science, Myodaiji, Okazaki 444-8585*

Binary adsorbate system on a surface has a possibility of showing new atomic arrangement and properties such as thermal stability, electronic transport, film growth, preferential segregation and so on, which are different from those of single adsorbate system [1]. Recently we have found, by using combined techniques of scanning tunneling microscopy (STM), low energy electron diffraction (LEED), and Rutherford backscattering spectroscopy (RBS), that the coadsorption of Pb and Sn on the Si(111) surface forms a $\sqrt{7}\times\sqrt{3}$ superstructure at coverages of 0.4 ML Pb and 0.4 ML Sn and that Pb atoms on this surface become more stable against heating than those on single adsorbate system [2,3]. Here, 1 ML is defined as 7.8×10^{14} atoms/cm^2. As shown in Fig.1, the STM images of the surface consist of two kinds of bright spots: (A) those aligned zigzag on the T_1 site and (B) those on the T_1 and H_3 sites along the [112] direction. In this study, we have measured the Pb 5*d* and Sn 4*d* photoelectron spectra of the Si(111) $\sqrt{7}\times\sqrt{3}$-(Pb, Sn) surface in order to clarify their bonding properties and the atomic arrangement of the surface.

The Si(111) $\sqrt{7}\times\sqrt{3}$-(Pb, Sn) surface was prepared on a substrate of an n-type Si(111) wafer of 5 Ωcm in a size of $5\times20\times0.5$ mm^3 by annealing at 570 K after depositing about 1 ML Pb onto the Si(111) $\sqrt{3}\times\sqrt{3}$+faint $2\sqrt{3}\times2\sqrt{3}$-Sn surface with the Sn coverage of 0.4 ML, which was made by deposition of 1 ML Sn onto the clean Si(111) 7×7 surface and subsequent annealing at 970 K. Photoelectron measurement was performed at room temperature with the excitation photons of 52 eV and a hemi-spherical analyzer of the angle acceptance of $\pm1^\circ$ at the 45° emission angle. The origin of the binding energy was determined from the Fermi edge of a Ta plate which holds the Si wafer. Total energy resolution was also estimated to be about 0.1 eV from the Ta Fermi edge.

Typical spectra of the Pb 5*d* and Sn 4*d* levels of the Si(111) $\sqrt{7}\times\sqrt{3}$-(Pb, Sn) surface are shown in Figs. 2 and 3 in comparison with those for the single

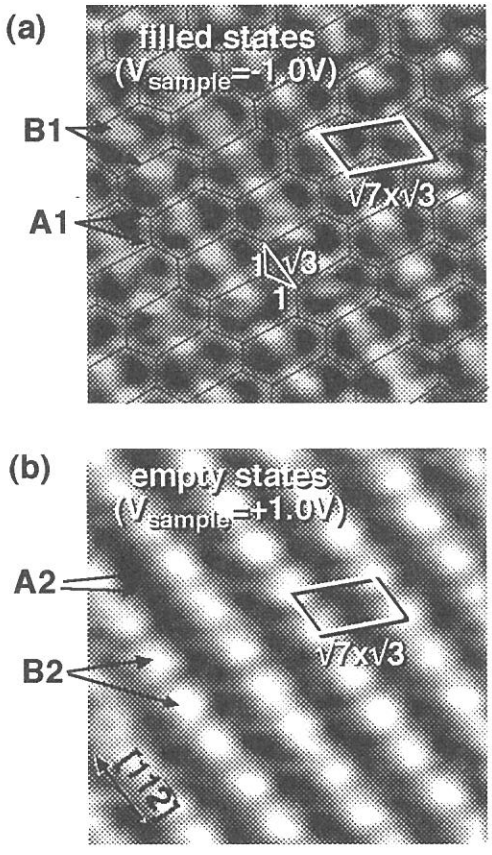

Fig.1 Images of filled states (a) and empty states (b) for the Si(111) $\sqrt{7}\times\sqrt{3}$-(Pb, Sn) surface.

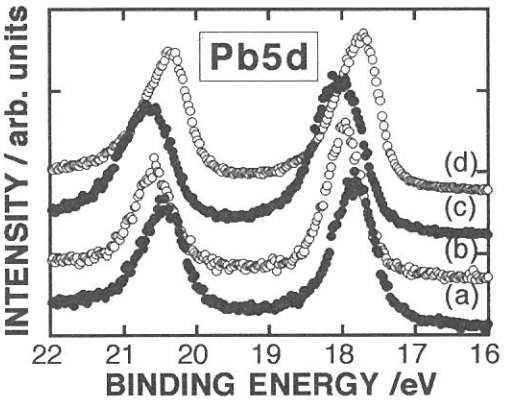

Fig.2 Pb 5*d* photoelectron spectra of Si(111) $\sqrt{7}\times\sqrt{3}$-(Pb, Sn) surface (a), Si(111) $\sqrt{3}\times\sqrt{3}$-Pb surface with 1/6 ML Pb coverage (b), Si(111) $\sqrt{3}\times\sqrt{3}$-Pb surface with 1/3 ML Pb coverage (c), and Si(111) 1×1-Pb surface with 1 ML Pb coverage (d). Intensities of the spectra are normalized at the peaks of the j=5/2 lines.

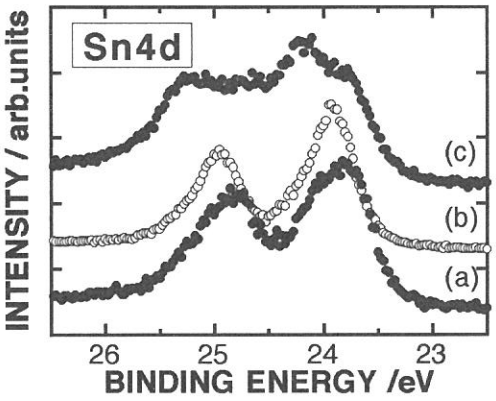

Fig.3 Sn 4*d* photoelectron spectra of Si(111) $\sqrt{7}\times\sqrt{3}$-(Pb, Sn) surface (a), Si(111) $2\sqrt{3}\times2\sqrt{3}$-Sn surface with 1 ML Sn coverage (b), and Si(111) $\sqrt{3}\times\sqrt{3}$-Sn surface with 1/3 ML Sn coverage (c). Intensities of the spectra are normalized at these maxima.

adsorbate system with various coverages of Pb and Sn, respectively. The Pb 5*d* spectrum for the Si(111) $\sqrt{7}\times\sqrt{3}$-(Pb, Sn) surface shows tailing towards the high binding energy side, compared with that for the Si(111) $\sqrt{3}\times\sqrt{3}$-Pb surface with 1/6 ML Pb coverage, where Pb and Si adatoms in T_4 sites form a semiconducting surface [4]. The observed tailing is attributed to metallic nature of the surface, although it is not so extended as the Si(111) 1×1-Pb surface, where about 1 ML Pb is considered to form a metallic layer [5,6]. On the other hand, the Sn 4*d* spectrum exhibits two major components for the Si(111) $\sqrt{3}\times\sqrt{3}$-Sn surface, as reported so far [7,8], and single component for a bulklike α-Sn structure on the Si(111) $2\sqrt{3}\times2\sqrt{3}$-Sn surface [9]. For the Si(111) $\sqrt{7}\times\sqrt{3}$-(Pb, Sn) surface, the Sn 4*d* spectrum also shows shoulder structures at the high binding energy side of the main peaks. This definitely indicates at least two different Sn-Si bonds or inequivalent Sn adsorbing sites on the Si(111) $\sqrt{7}\times\sqrt{3}$-(Pb, Sn) surface. Thus, we ascribe the bright spots at the T_1 site (A) and those at the T_1 and H_3 sites (B) in the STM images to Pb and Sn adatoms, respectively. The present results lend support to a proposed model for the atomic arrangement of the Si(111) $\sqrt{7}\times\sqrt{3}$-(Pb, Sn) surface [3].

References

[1] J. Yuhara, R. Ishigami, K. Morita, Surf. Sci. **326** (1995) 133.

[2] D. Nakamura, J. Yuhara, K. Morita, Appl. Surf. Sci. **130/132** (1998) 72.

[3] J. Yuhara, D. Nakamura, K. Soda, K. Morita, Surf. Sci., *in press*.

[4] C.J. Karlsson, E. Landmark, Y.-C. Chao, and R.I.G. Uhrberg, Phys. Rev. **B**45 (1992) 6321.

[5] J.A. Carlisle, T. Miller, and T.-C. Chiang, Phys. Rev. **B**45 (1992) 3400.

[6] X. Tong, K. Horikoshi, and S. Hasegawa, Phys. Rev. B**60** (1999) 5653.

[7] M. Göthelid, M. Björkqvist, T.M. Grehk, G. Le Lay, and U.O. Karlsson, Phys. Rev. **B**52 (1995) R14352.

[8] R.I.G. Uhrberg, H.M. Zhang, T. Balasubramanian, S.T. Jemander, N. Lin, and G.V. Hansson, Phys. Rev. **B**45 (2000) 8082.

[9] A.H. Levermann, P.B. Howes, K.A. Edwards, H.T. Anyele, C.C. Matthai, J.E. Macdonald, R. Feidenhans'l, L. Lottermoser, L. Seehofer, G. Falkenberg, and R.L. Johnson, Appl. Surf. Sci. **104/105** (1996) 124.

BL5A: Cesiumoxide-GaAs Interface and layer thickness in NEA surface formation

Sam D. Moré [1], Senku Tanaka [2], Shin-ichiro Tanaka [1*], Tomohiro Nishitani [3], Tsutomu Nakanishi [3] and Masao Kamada [1, 2]

[1] *UVSOR Facility, Institute for Molecular Science, Okazaki 444-8585, Japan*
[2] *Department of Structural Molecular Science, The Graduate University for Advanced Studies, Okazaki 444-8585, Japan*
[3] *Department of Physics, Nagoya University, Nagoya 464-8602, Japan*

Negative electron affinity (NEA) surfaces have found applications as efficient photocathodes and the NEA surface of GaAs(100) and its superlattice is known to be a useful emitter of spin-polarized electrons with a high degree of polarization and efficiency. This can be achieved by the 'jo-jo'-technique, where Cs deposition and subsequent oxidation are repeated several times. The details of NEA surface formation, however, are not fully understood: previous reports [2-4] differ considerably both in describing the method of production as well as the underlying chemical and physical mechanism.

Fig. 1 shows the electron yield as a function of sample treatment. Curve (a) shows Cs deposition only. Curve (b) shows the so called Nagoya treatment; Cs is dosed until the electron yield decreases again, the yield raises under O expose. Curve (c) depicts the classical jo-jo treatment; the GaAs surface is alternately exposed to Cs and O, O lowers the electron yield, while Cs increases it. Curve (d) shows a mixed type of activation where during the initial Cs deposition small amounts of O have been added. This treatment involves larger Cs and O amounts. It is characteristic for saturation regimes of both O and Cs, resulting in the generation of overlayers with a larger thickness.

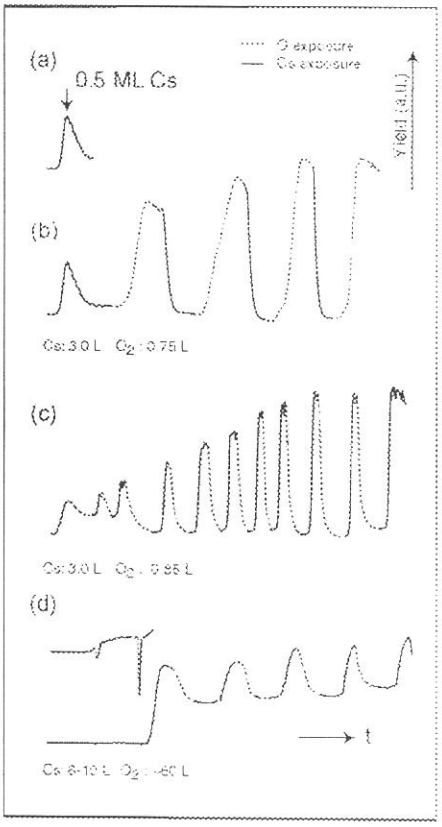

FIGURE 1. Electron yield as a function of sample treatment for different activation processes on GaAs(100): (a) Cs-only activation, (b) so-called Nagoya treatment, (c) classical jo-jo treatment, and (d) a mixed type of activation.

Fig. 2 shows the Ga-3d and As-3d photoemission spectra after the activation. All activations can achieve a high electron yield. The stability of the yield is however different with Phase III activations being frequently less stable than Phase I and Phase II activations. The As-3d peak for Phase I is broadened towards higher kinetic energy, indicating donation of electrons by reaction with Cs. In Phase II the As-3d peak has split into a larger main peak and a smaller peak at 53-54 eV (47-46 eV binding energy), which marks the As=O double bond formation. The broadening to the higher kinetic

energy side is less pronounced. This indicates that Phase II has a larger interface oxidation at the As than Phase I.

Phase III finally shows a strong interface oxidation. The direct Cs-interaction with the substrate seems to be negligible. The Ga and As core-level peaks for Phase III are much broader than the peaks of the previous phases. Also the halfwidth of the Cs-peak is about 25% broader. This indicates that the Cs in this phase consists of more different ionization stages than the one of Phase I. The chemical composition of the thicker overlayer is far more complex and heterogeneous than for the Phases I and II. The lower stability in terms of electron yield for the Phase III surface could be due to an ongoing chemical reaction inside such an overlayer.

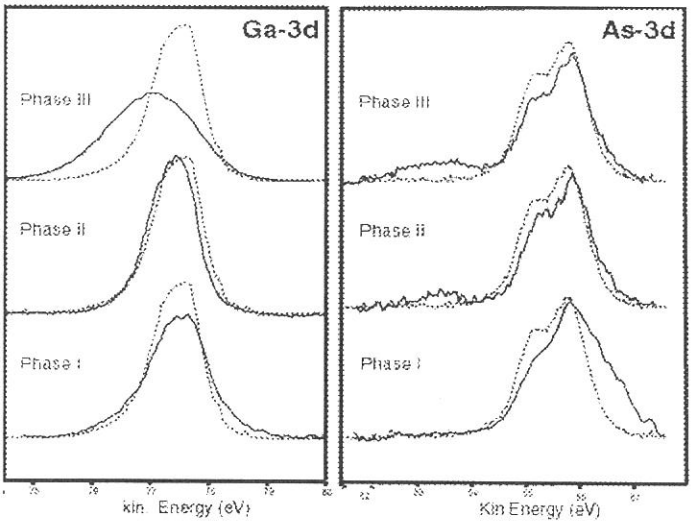

	bandbending	core level shift correction
clean surface	0.85 +/- 0.05 eV	0.00 eV
Phase I	0.35-0.5 eV	0.00 eV
Phase II	0.25 +/- 0.1 eV	0.30 eV
Phase III	0.30 +/- 0.1 eV	0.65 eV

FIGURE 2 Ga-3d and As-3d core-levels representative for different activation processes. Peak positions are corrected for bandbending. The dotted line shows the clean surface. Phase I corresponds to the activation (b), Phase II to the activation (c) and Phase III to the activation (d).

The Table below Fig. 2 gives the bandbending values obtained from the surface photovoltage experiment, which the photoemission data have been corrected for. A stronger oxidation of As is correlated with a decrease in bandbending in our experiment, which is in alignment with previous results from literature [2,3]. The Table shows a decrease in bandbending from Phase I to Phase III. None of the surfaces investigated in our study has shown therefore any increase in bandbending. This contrasts the dipole model as originally proposed [2].

Summarizing, three different NEA activation processes on GaAs(100) have been characterized using high resolution photoemission spectroscopy. Analyzing the influence of the cesiation and oxidation on the bandbending and monitoring the electron yield from bulk GaAs(100), we have been able to distinguish three different phases of activation, which depend on the total thickness of the overlayer, the Cs:O ratio and the resulting chemical interaction with the substrate.

References

1. C.Y. Su, W.E. Spiecer and I. Lindau, *J. Appl. Phys.* **54** (1983) 1413.
2. A. Alperovich, A.G. Paulish, A.S. Terekov, *Surf. Sci.* **331-333** (1995) 1250-1255.
3. M. Besancon, R. Landers and J. Juille, *J. Vac. Sci. Techn.* **A5** (1987) 2025.
4. N. Takahashi, S. Tanaka, M. Ichikawa, Y. Cai and M. Kamada, *J. Phys. Soc. Japan* **66** (1997) 2798.

(BL 5A)

Surface photo-voltage effects on GaAs-GaAsP superlattices studied with combination of SR and laser

Senku Tanaka,[1] Sam D. Moré,[2] Kazutoshi Takahashi,[2] Tomohiro Nishitani,[3] Tsutomu Nakanishi [3] and Masao Kamada [1, 2]

[1] *Department of Structural Molecular Science, The Graduate University for Advanced Studies, Okazaki 444-8585*

[2] *UVSOR Facility, Institute for Molecular Science, Okazaki 444-8585*

[3] *Department of Physics, Nagoya University, Nagoya 464-8602*

Electronic non-equilibrium in the surface layers of photo-excited semiconductors has been attracting much interest from the basic scientific point of view and also from the field of practical applications of photo devices. Many works have been carried out by means of electrical methods using various types of contacting electrodes, but few works have so far been reported on transient non-equilibrium in the interface between semiconductor surfaces and the vacuum. GaAs is one of the most useful semiconducting materials. Especially the negative-electron affinity (NEA) surface of a *p*-type GaAs (100) can provide spin-polarized electrons when it is excited with circularly polarized light. The NEA surface is produced by the so-called yo-yo technique, where cesium and oxygen are deposited repeatedly on clean *p*-GaAs (100) surfaces. It has been pointed out that the electron density saturates when semiconductor photo-cathodes are excited with intense pulsed lasers. Gometz *et al.*[1] have proposed that the surface photo-voltage (SPV) effect plays an important role to cause the saturation and that a metallic overlayer may be useful to prevent the effect from interfering in future high-energy experiments. The use of superlattice photo-cathode as a polarized electron source has been suggested by Togawa *et al.*,[2] since the transport of photo-carriers is expected to be well suppressed in the superlattice system. The SPV effect of superlattice system is therefore of both technical and theoretical interest.

In the present work, the SPV effect on GaAs-GaAsP superlattices has been investigated by using core-level photoelectron spectroscopy with the combination of SR and laser. The schematic energy diagram is shown in Fig. 1. This kind of photoelectron spectroscopy can provide information on the electronic structures in a wide energy range for photo-excited semiconductor surfaces. The core-level photoelectron spectroscopy is more surface-sensitive in comparison with others using

laser and a Kelvin method, since the escape depth of electrons has a minimum around 30-100 eV in kinetic energy. The energy shift of the core-level photoelectron spectra can give us the reliable SPV values as shown in Fig. 1.

The Ga-3*d* photoelectron spectra showed transient energy shifts due to the SPV effect at low temperatures, but not at room temperature. The amount of the SPV effect was about 50 meV, which is very much smaller than that of clean GaAs (100) surfaces. The present result is in good agreement with the proposal by Togawa et al., but the existence of the small amounts of SPV effects even at low temperatures indicates that another mechanism is required in order to suppress the SPV effect completely at any temperature.

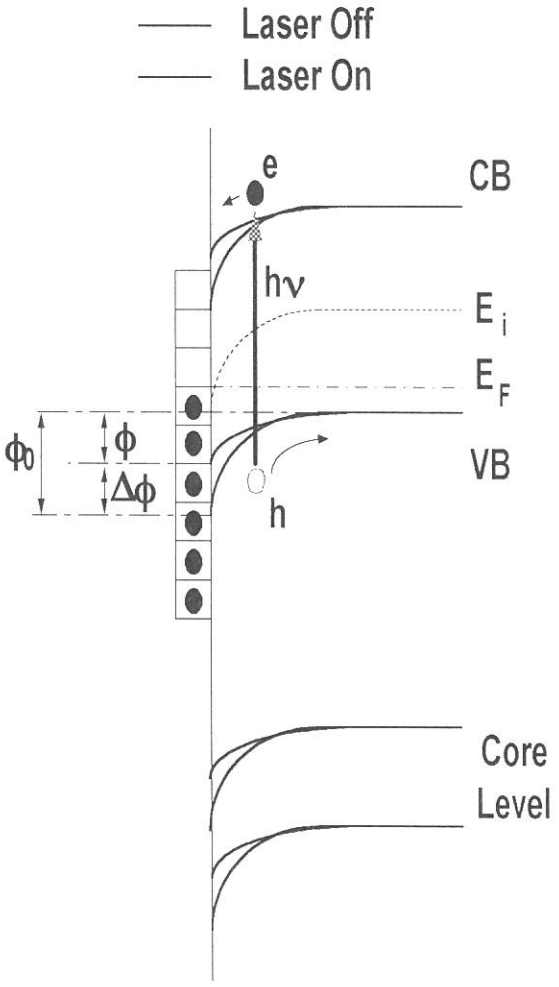

Fig. 1. Schematic diagram of SPV effect

The NEA surface of the superlattice was also prepared by a so-called yo-yo technique. The SPV effects were observed on these NEA surfaces of GaAs (100) and GaAs-GaAsP superlattice, but the amounts of the SPV effect on NEA surface of the superlattice was so small (about 10 meV) in comparison with that of the GaAs.

In conclusion, The SPV effect has been investigated on GaAs-GaAsP superlattices using core-level photoelectron spectroscopy with combination of SR and laser. It was observed that the SPV effects are so small on the clean and NEA surfaces of the superlattice, in comparison with those of bulk GaAs.

References

1) A. Herrera-Gomez, G. Vergara, and W. E. Spicer, J. Appl. Phys. 79, 7318 (1996).

2) K. Togawa, T. Nakanishi, T. Baba, F. Furuta, H. Horinaka, T. Ida, Y. Kurihara, H. Matsumoto, T. Matsuyama, M. Mizuta, S. Okumi, T. Omori, C. Suzuki, Y. Takeuchi, K. Wada, K. Wada, and M. Yoshioka, Nucl. Instrm. Methods A 414, 431 (1998).

(BL 5A)

Time-dependence of the surface photovoltage effect on GaAs (100) studied with combination of SR and laser: Microsecond time-response

Senku Tanaka[A], Kazutoshi Takahashi[B], Sam D Moré[B], and Masao Kamada[A, B]

[A] *The Graduate University for Advanced Studies, Myodaiji, Okazaki, 444-8585*
[B] *UVSOR Facility, Institute for Molecular Science, Myodaiji, Okazaki, 444-8585*

Electronic non-equilibrium in the surface layers of photo-excited semiconductors has been attracting much interest from the basic scientific point of view and also from the field of practical applications of photo devices. Many works have been carried out by means of electrical methods using various types of contacting electrodes, but few works have so far been reported on transient non-equilibrium in the interface between semiconductor surfaces and the vacuum. Photoelectron spectroscopy is one of the most powerful tools to investigate surface electronic properties because of the very short escape depth of photoelectrons. Recently, we have studied photo-induced change in GaAs (100) surface using core-level photoelectron spectroscopy with synchrotron radiation and laser [1], since photoelectron spectroscopy is one of the most powerful tools to investigate surface electronic properties because of the very short escape depth of photoelectrons. It has been observed that the laser-induced core-level shift is caused by the surface photovoltage (SPV) effect. And it has been also found that there are at least two components in the recover process of the SPV. In this report, we present the time response of the SPV effect on GaAs (100).

Experiments have been conducted at BL5A, UVSOR facility. We used the laser (COHERENT Mira 900-F (90 MHz, 800 nm) & RegA (10 KHz, 800 nm)) as the excited light source to cause the SPV effect in the nano-second and micro-second time-domains, respectively. The laser light was transported to the view-port of the measurement chamber using an optical fiber and focused on the sample surface. The OMICRON electron-energy analyzer (EA-125HR) was used to observe the photoelectron spectra. The single signal from the analyzer was used for time-dependent measurements although the analyzer has five channel detectors. Photoelectron signals from the electron analyzer were changed to LED signals in the pre-amplifier circuit in order to decrease the electric noises. Photoelectron signals were transferred to the gate circuit, which was controlled as well as the mechanical shutter. The photoelectron signal was used as a start signal for a time-to amplitude converter (TAC). Laser pulse was monitored by a PIN photodiode, and was used as a stop signal. A couple of TACs has been used, corresponding to the signals with and without laser excitation. By using this system, it is possible to observe the time dependence of photoelectron signals at a fixed kinetic energy. In the present study, it has been observed that the SPV effect caused by the laser excitation decays in the microsecond range as discussed below.

Figure 1 (a) shows Ga-3d core-level photoelectron spectra of GaAs (100). Solid and dotted lines represent Ga-3d spectra with and without laser irradiation, respectively. It is clearly observed that the Ga-3d core-level shifts to the higher kinetic-energy side under irradiation of the laser. This shift originates from the SPV effect caused by the laser-excited photocarriers. Figure 1 (b) represents the time response of the photoelectron intensity at 77.9 eV and 78.8 eV, respectively. It should be noted that there are at least two components in the response curve of the photoelectron intensity; one is the fast component time constant of about 1μs and another has a larger constant of about 13μs. They are attributed to the surface and bulk origin, respectively, since the fast component was not observed on the negative-electron affinity surfaces.

In summary, we have investigated the time-dependence of the SPV effect on GaAs (100) in microsecond region. It has been observed that there are at least two components in the recover process of the SPV effect in microsecond region.

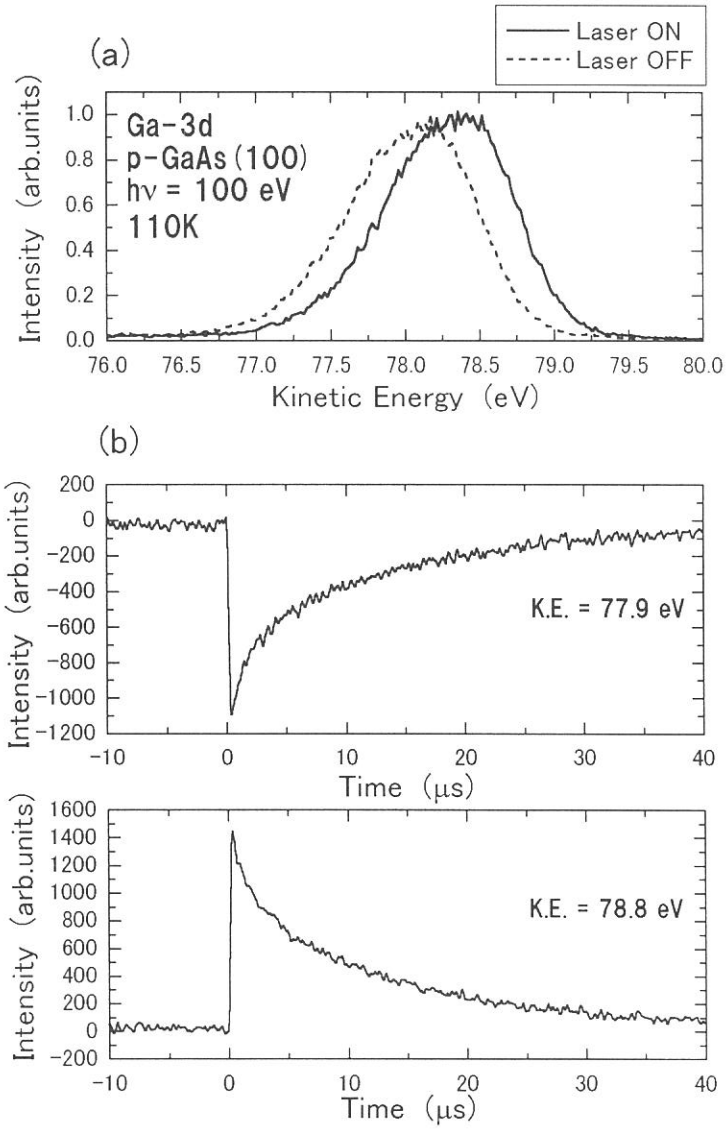

Figure 1. (a) Ga-3d photoelectron spectra of GaAs (100). Solid and dotted lines represent Ga-3d spectra with and without laser excitation, respectively. (b) Temporal profiles of the photoelectron intensity at 77.9 eV and 78.8 eV, respectively.

References

[1] M. Kamada et al., *Surf. Sci.*, **454-456** (2000) 525.

(BL-5B&6A2)

Photoemission Study on the Surface Photovoltage For Si(111) Surface Induced by Laser Light Irradiation

Yuichi Haruyama[A], Taichi Okuda[B], Ayumi Harasawa[B], Toyohiko Kinoshita[B], Shin-ichiro Tanaka[C], Hideo Makino[D], Katsuo Wada[D], Kazutoshi Fukui[E], Masao Kamada[E] and Shinji Matsui[A]

[A]*LASTI, Himeji Institute of Technology, 3-1-2 Kouto, Kamigori, Ako 678-1205, Japan*
[B]*Synchrotron Radiation Laboratory, Institute for Solid State Physics, University of Tokyo, Kashiwa 277-8581, Japan*
[C]*Faculty of Science, Nagoya University, Furo-cho, Chikusa-ku, Nagoya 464-8602, Japan*
[D]*Silicon Technology LTD, 897-20 Kyowa, Mochizuki, Kitasaku-gun, Nagano 384-2204, Japan*
[E]*Institute for Molecular Science, Okazaki 444-8585, Japan*

Recently, the research on the surface photovoltage (SPV) has been performed at super-ACO in France using the FEL light [1]. In the study, it was observed that the band bending is decreased when the synchronized FEL light and SR are irradiated for Si(111) 2x1 and GaAs-Ag surface. At UVSOR, SPV for GaAs surface was also observed using synchronized laser light and SR [2]. In addition, we observed SPV for Si(111) surface using CW laser light irradiation [3]. In these cases, SPV is induced to decrease the band bending between semiconductiong surface and bulk. The mechanism of SPV is explained by a model that the carrier induced by laser light irradiation transfers to the surface. However, it is not clear whether SPV is associated with the surface state. Moreover, it is not clear whether the same senario is applied in the case of the metallic surface or in the case of the semiconducting surface. In order to investigate the relationship between SPV and the surface state, between SPV and the carrier concentration, we have performed the combined study of the photoemission and laser light irradiation.

The experimental setup including the optical alignment was described by Ref. 3 in detail. Photoemission experiments were carried out by using a conventional UHV system (FISONS, ESCALAB-220i-XL) at a base pressure of 2×10^{-8} Pa [4]. Total instrumental energy resolution at room temperature was 0.3~0.5 eV full width at half maximum, depending on the photon energy ($h\nu$) in the energy range of 50~130 eV. Photoemission experiments were also performed with higher energy resolution of ~0.1 eV at PF. The clean surface was obtained by annealing the sample at ~1200°C using the laser light irradiation ($h\nu$ = 1.165 eV) and checked by x-ray photoemission spectroscopy and LEED. The temperature of the sample was measured with an optical pyrometer.

Figure 1(a) and (b) show the Si 2*p* core-level photoemission spectra (closed dots) for n- (P-dope, 9-14Ω) and p-type (B-dope, 10-20 Ω) Si (111) surface at 90K, respectively. Under the laser light irradiation, the photoemission spectra (open dots) for the n-type (p-type) Si(111) surface shift to higher (lower) binding energy side. The shift direction for the n- and p-type Si(111) surface was opposite. It is considered that the observed rigid shift is caused by SPV induced by the laser light irradiation.

Figure 2 shows the impurity (carrier) concentration dependence of SPV obtained by the photoemission spectra. With increasing the impurity concentration, SPV is increased (decreased) for n-type (p-type) Si(111) surface. The shift is associated with the band bending because the band bending is increased with the impurity concentration. However, for the higher doping concentration, the shift was not observed in our measurements.

Figure 3 shows the valence band photoemission spectrum for $\sqrt{3}x\sqrt{3}$ Si (111)-Bi surface (n-type, P-dope 9-14 Ω) at room temperature. For the $\sqrt{3}x\sqrt{3}$ Si (111)-Bi surface, it is known that the surface state near the Fermi level disappears and the band gap is open. Under the laser light irradiation, the photoemission spectrum for the $\sqrt{3}x\sqrt{3}$ Si (111)-Bi surface shifts to higher binding energy side by ~0.2 eV. The shift is identical to that for the clean 7x7 Si(111) surface. This means that SPV is not associated with the surface state in this system.

References

[1] M. Marusi, L. Nahon, D. Garzella, T. Hara, R. Bakker, M. Billardon, A. Delboulbe, G. Indlekofer, and A. Taleb-Ibrahimi, Appl. Phys. Lett. **70** (1997) 895.

[2] M. Kamada, S. Asaka, T. Tsujibayashi, O. Arimoto, M. Watanabe, S. Nakanishi, H. Itho, S. Hirose, and M. Itho, J. Jpn. Soc. for Synchrotron Radiation Research **12** (1999) 48.

[3] Y. Haruyama , T. Kinoshita, S. Tanaka, H. Makino, and S. Matsui, UVSOR Activity Report 1999, p.128.

[4] T. Kinoshita, K. G. Nath, Y. Haruyama, M. Watanabe, S. Yagi, S. Kimura, and A. Fanelsa, J. Electron Spectrosc. Relat. Phenom. **92**(1998)165.

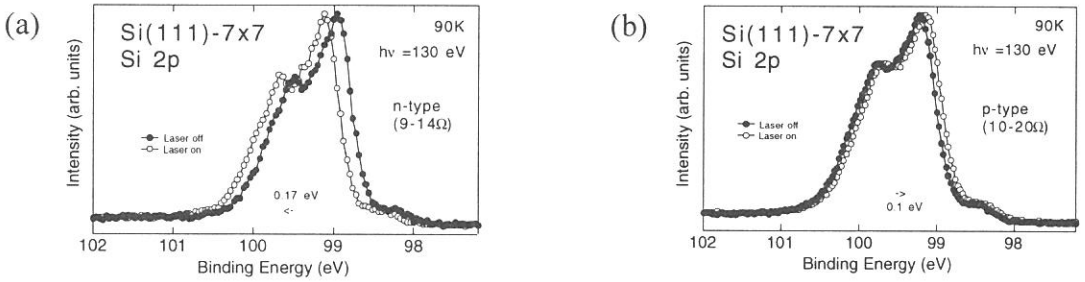

Fig. 1 Si 2*p* core-level photoemission spectrum (a) for the n- and (b) p-type Si(111) surface with laser light irradiation (open dots) and without laser light irradiation (closed dots).

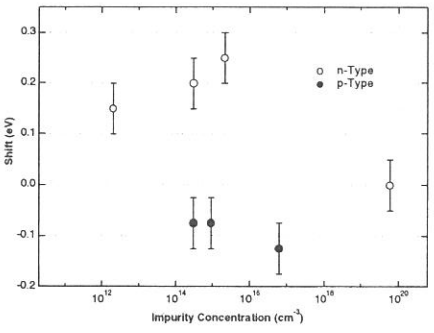

Fig. 2 Impurity concentration dependence of SPV for n- (open dots) and p-type (closed dots) Si (111) surfaces.

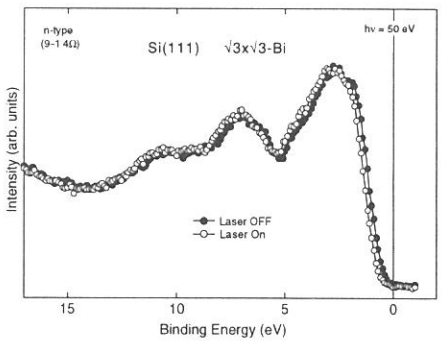

Fig. 3 Valence band photoemission spectrum for Si(111) $\sqrt{3}x\sqrt{3}$-Bi surface with laser light irradiation (open dots) and without laser light irradiation (closed dots).

(BL6A2)

Photoelectron spectroscopic study on photo-induced phase transition in a spin crossover complex $Fe(2\text{-pic})_3)Cl_2EtOH$

Masao Kamada, Yoichiro Doi, [A] Kazutoshi Fukui, [B] Yuichi Haruyama, [C] Takeshi Tayagaki, [E] Naoki Yonemura, [E] and Kouichiro Tanaka [E]

UVSOR Facility, Institute for Molecular Science, Okazaki 444-8585
[A] *College of Engineering, Fukui University, Fukui 910-8507*
[B] *VUV-PhotoScience, Institute for Molecular Science, Okazaki 444-8585*
[C] *LASTI, Himeji University, Hyogo 678-1201*
[E] *Faculty of Science, Kyoto University, Kyoto606-8502*

In recent years, photon-induced phenomena attract much interest. For examples, photon excitation changes the crystal structures, magnetic and optical properties, and so on. These new phenomena are called as photo-induced phase transitions, which are expected to produce new properties of condensed matters.

In order to investigate the photo-induced phase transitions, optical spectroscopic techniques such as optical absorption and reflection have been mostly used, since these techniques can monitor the phenomena in a fast time domain and are easily obtained. However, these techniques have some limitation. For examples, only narrow energy range in the valence electrons can be observed by the optical spectra. The purpose of the present study is to investigate the photo-induced effects on electronic states in wide energy range using photoelectron spectroscopy. We have been developing new techniques based on the combination of synchrotron radiation and laser in recent years. We have applied this technique to the present purpose.

Experiments have been carried out at beam lines BL5B and BL6A2, where a plane-grating monochromator provides photons in a wide energy range from UV to EUV. A VG-microESCA system consisting of XPS and UPS components was used to obtain the photoelectron spectra. A single crystal of $[Fe(2\text{-pic})_3]\ Cl_2EtOH$ was grown at Kyoto university and was filed in a preparation chamber. The sample was attached on the holder of a flow-type He cryostat and was cooled down to about 40 K. The cw Ar^+ laser light was introduced in an analyzing chamber. The sample changed its color from yellow to red and from red to yellow by cooling and photo-excitation, respectively.

Figure 1 shows UPS spectra of valence states of $Fe(2\text{-pic})_3]\ Cl_2EtOH$. The spectra observed at room temperature did not show any change by laser excitation, but it should be noted that the valence states drastically changed by cooling the

sample from RT to 40K and also by the laser-excitation at 40K.

It has been believed from the optical spectroscopic studies that $Fe(2\text{-pic})_3]Cl_2EtOH$ shows high-spin and low-spin states in Fe ions at RT and low temperatures, respectively, and that the low-spin state (low-temperature phase) is changed by photo-excitation to the high-spin state (high-temperature phase). However, the present experimental results indicate that the photo-induced phase transition of $Fe(2\text{-pic})_3]Cl_2EtOH$ is not the same as the high-spin state, where the Fe-3d state may play an important role to trigger the photo-induced phase transition.

Fig. 1. Photoelectron spectra of $Fe(2\text{-pic})_3]Cl_2EtOH$ at RT and 40 K with and witout laser excitation.

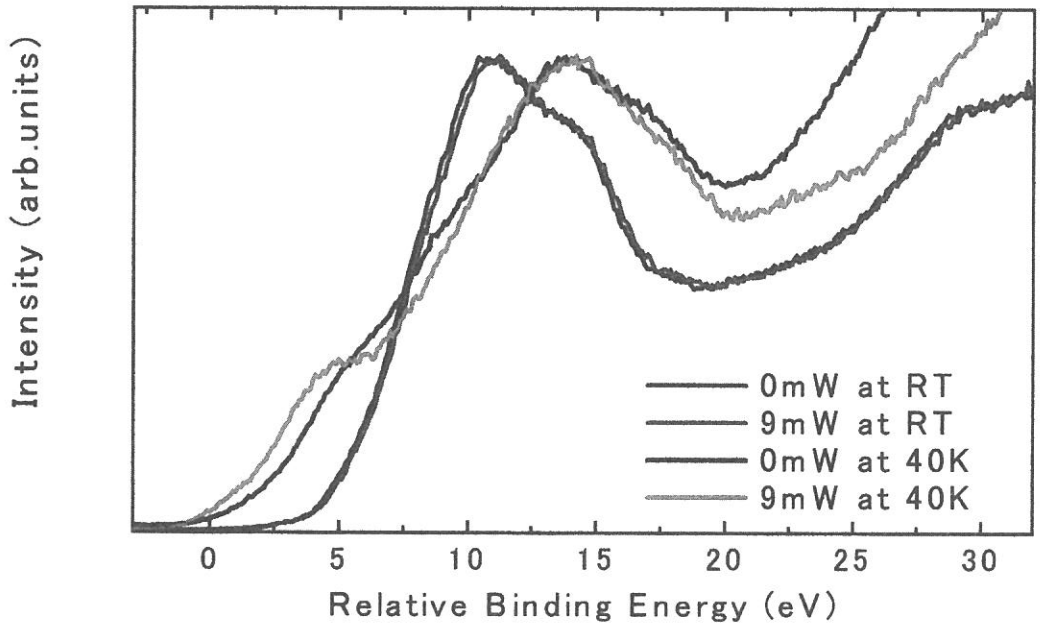

at RT at 40 K with laser at 40 K

(BL6A2)

Comparison of Auger-Free Luminescence and Valence-Band Photoemission in CsCl, CsBr and BaF_2

M. ITOH, M. KAMADA[1] and K. SAWADA

Faculty of Engineering, Shinshu University, Nagano 380-8553

[1] *UVSOR Facility, Institute for Molecular Science, Okazaki 444-8585*

Auger-free luminescence (AFL) has attracted a lot of particular interest in both fundamental and applied research ever since it was discovered in 1983. In the present work, we have studied the line shape of AFL in CsCl, CsBr and BaF_2 in comparison to the data of ultraviolet photoelectron spectroscopy (UPS) of the valence band. The lattice relaxation effect on AFL will be discussed in brief.

A thin film sample was fabricated *in-situ* by evaporation on a gold substrate in a preparation chamber, and was then transferred into an analyzing chamber. The starting materials were crystal ingots obtained from the Horiba Company. Thickness of the specimens was maintained at about 100 Å. Measurements of the luminescence and photoemission spectra were both carried out for the same samples in an identical analyzing chamber to eliminate any uncertainty due to sample preparation. The base pressure in the analyzing chamber was better than 2×10^{-8} Pa during the measurements.

The UPS spectra were measured at 295 K by using an angle-resolved hemispherical analyzer under the multi-bunch operation of SR, with a resolution of 0.21–0.23 eV. On the other hand, the AFL spectra were measured at 295 and 90 K by using a time-resolved detection technique under the single-bunch operation of SR, with a resolution of 0.15–0.20 eV. The obtained luminescence spectra were corrected for the spectral response of the detection system, and were given in arbitrary units of photon numbers per unit energy.

Figure 1 shows UPS spectrum of CsCl excited with 24.7-eV photons. A low-energy band at 7.0 eV is apparently due to the j = 3/2 component of the spin-orbit-split Cs^+ 5*p* levels. A single band at 12.7 eV is referred to the valence band associated with the Cl^- 3*p* states. One may see a weak tail-like structure on the high-kinetic-energy side of the valence band. This signal arises from the gold substrate, indicating that our evaporated film is thin enough to neglect the charging effects. For a direct comparison to the AFL spectrum, the valence-band UPS spectrum has to be replotted relative to the maximum of the Cs^+ 5*p* core band. After the Cs^+ 5*p* band was deconvoluted with a Gaussian instrumental resolution profile, the edge energy was determined as a characteristic energy at which the photoemission intensity decreases to the 1/10 value of the peak intensity. The maximum energy was thus obtained to be 7.86 ± 0.10 eV in Fig. 1.

The AFL spectrum of CsCl measured at 295 K under the excitation with 25.0-eV photons is presented by solid curve in Fig. 2. The result is essentially the same as that of bulk CsCl [1]. The valence-band UPS spectrum replotted relative to the maximum of the core band is also shown by open circles in Fig. 2, where the background structure due to gold substrate has been subtracted from the spectrum. Both curves are normalized to unity at their maxima.

The valence-band UPS spectra of CsBr and BaF_2, replotted relative to the maximum of the core band, are shown by open circles in Figs. 3 and 4, respectively. The AFL of CsBr was stimulated at 295 K with

use of the zero-order SR transmitted through an aluminum filter (transmits radiation between about 16 and 70 eV), while the 90-K AFL spectrum was excited with monochromatized SR at 25.0 eV. These results are depicted by deep and light solid curves in Fig. 3. The solid curve in Fig. 4 shows AFL spectrum of BaF_2 stimulated with 25.0-eV photons at 295 K. The high-energy spectrum above 6.5 eV was reproduced from the data obtained in Ref. [2].

The present results of Figs. 2 - 4 have some common features, which are summarized as follows: (1) The main band of AFL is situated at the bottom of the valence band. (2) The low-energy tail of AFL exists outside of the valence band. (3) The total width of AFL is somewhat narrower than that of the valence band. These facts are explained on the basis of the lattice relaxation model. According to this model, when a hole is generated in the core band, it quickly relaxes into a self-trapped state and deforms the lattice configuration in its immediate vicinity. Because of the Franck-Condon principle, such a deformation is kept well during the radiative transition, leading to the above-mentioned facts (1), (2) and (3).

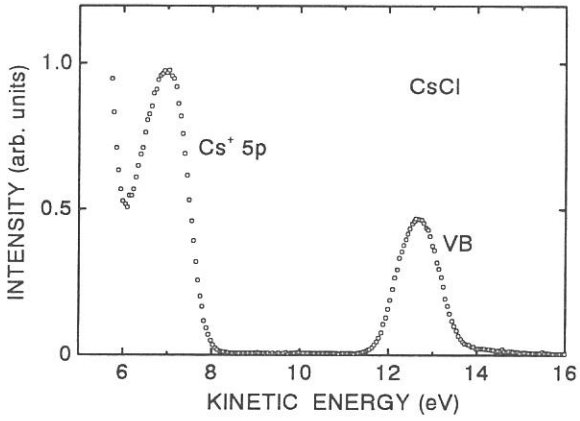

Fig. 1. UPS spectrum of CsCl excited with 24.7-eV photons.

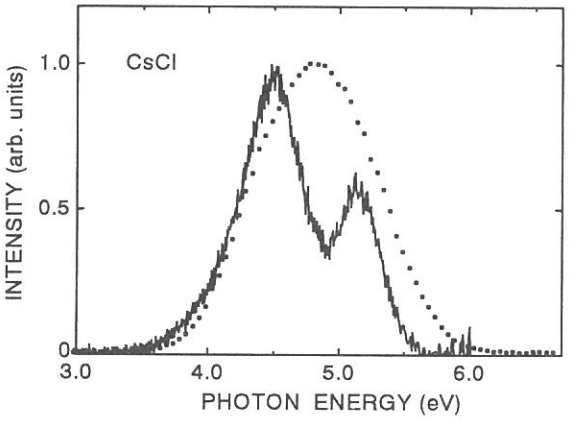

Fig. 2. Comparison of AFL (solid curve) and valence-band UPS (open circles) spectra of CsCl.

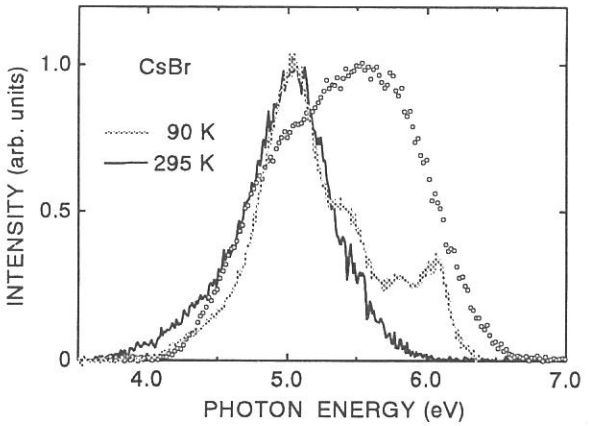

Fig. 3. Comparison of AFL (solid curves) and valence-band UPS (open circles) spectra of CsBr.

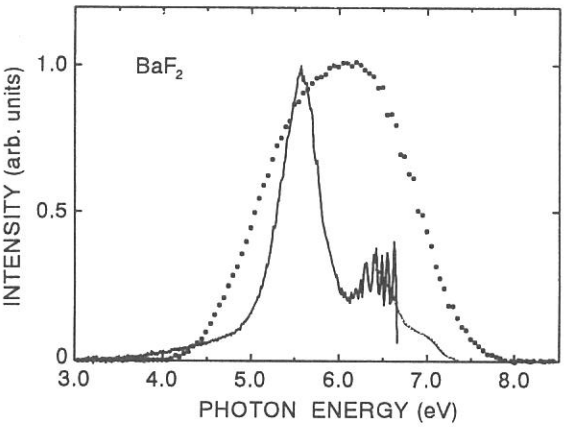

Fig. 4. Comparison of AFL (solid curve) and valence-band UPS (open circles) spectra of BaF_2.

[1] M. Itoh, M. Kamada and N. Ohno : J. Phys. Soc. Jpn. **66** (1997) 2502.

[2] J. L. Jansons, V. J. Krumins, Z. A. Rachko and J. A. Valbis : Phys. Status Solidi B **144** (1987) 835.

(BL7A)

XANES analysis of Cu-MgO/TiO_2 bactericidal material

Tomomi Kosaka, Ayano Yamada, Atsuyuki Miyaji, Mayumi Shiraishi, Sadao Hasegawa

Department of Chemistry, Tokyo Gakugei University, Koganei, Tokyo, 184-8501

TiO_2 was well known for its photocatalytic function such as NOx reduction[1], self-cleaning[2], super-hydrophilic[3]...etc. However, the effects were specifically weakened without UV radiation. Therefore, the noble metal loaded TiO_2 was utilized for keeping its activity even if in the dark place.

Recently, food poisoning was occurred by the water contamination with *O-157 Esherichia coli*, *Staphylococus aureus* and so on. Then, much attention was given to the bactericidal ceramics and the technology of water purification using the materials. It was known that MgO, one of basic catalyst, had the bactericidal function when it involved in the polluted water at higher concentration. However, the mechanism of bactericidal effects was not so clear.

In this report, we prepared MgO/TiO_2 and Cu-MgO/TiO_2 catalysis, investigated that crystal structure and chemical condition of the sample surface from the results of Mg K-edge XAFS analysis.

MgO/TiO_2 and Cu-MgO/TiO_2 catalysis were prepared by the impregnation method and the concentration of MgO was 25wt% in the both samples. They were calcined at 873, 1073, 1273K for 3h in air.

Mg K-edge XAFS measurement was carried out on the BL-7A at UVSOR, Institute for Molecular Science, Okazaki, Japan. The storage ring was operating at electron energy of 750MeV. The spectra were recorded in a total electron yield mode under high vacuum ($<3x10^{-7}$) at room temperature. Data were collected using $KTiPO_4$ [KTP] (011) double crystal monochromator. The samples were put on the first Cu-Be dynode of the electron multiplier using adhesive carbon tape.

Fig.1 were shown Mg K-edge XANES spectra of MgO/TiO_2 samples calcined at various temperatures. Fig.2 were also shown Mg K-edge XANES spectra of some reference samples. The spectra of MgO/TiO_2 calcined over 873K were corresponding to that of $MgTiO_3$. It was indicated that solid phase reaction was occurred between MgO and TiO_2 over 873K. Mg K-edge XANES spectra of Cu-MgO/TiO_2 samples were also shown in Fig.3. In the case of Cu-MgO/TiO_2 samples, the spectra were varied with the calcinations temperature. The spectra at 873K and 1073K were resembled to that of MgO, oxygen atoms in this sample hexagonally surrounded Mg atoms. On the other hand, the change of Mg environmental structure was occurred at 1273K, the resulting coordination number of Mg atoms was 12 (perovskite structure) on the surface. However, the difference of the surface structure due to Cu atom addition was not clarified in this analysis.

The bactericidal effects to *Esherichia coli (IFO 3972)* of these samples were investigated in progress. However, the Mg addition was certainly enhanced the bactericidal function of TiO_2.

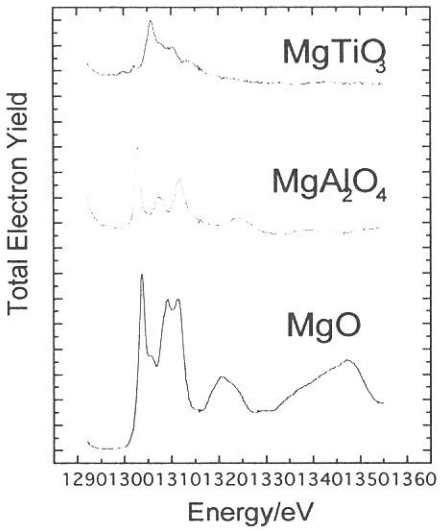

Fig.1 Mg K-edge XANES spectra of Reference samples

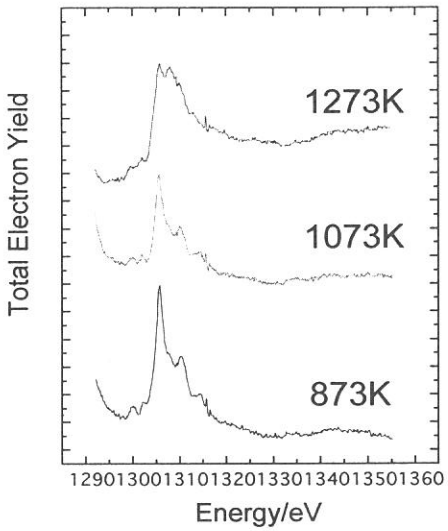

Fig.2 Mg K-edge XANES spectra of 25wt% MgO/Ti_2O

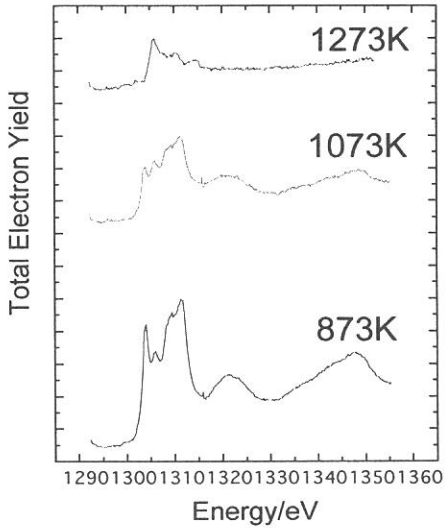

Fig.3 Mg K-edge XANES spectra of Cu-MgO/Ti_2O

1) K. Takeuchi, *Kagaku to Kogyo*, **46**(12), 1839(1993).

2) A. Ishizaki, *Hyomen Gijyutu*, **50**(3), 251(1999).

3) R.Wang et al., *Nature*, **338**, 431(1997)

(BL7A)

Mo L_{III}-edge XANES Study of Molybdena on Silica-Alumina in Contact with Propene

Hirofumi Aritani[a]*, Osamu Fukuda[a], Noboru Tanida[a], Tatsuya Yamamoto[a],
Masato Tamai[a], Atsushi Nakahira[a], Atsuyuki Miyaji[b], and Sadao Hasegawa[b]
[a]*Faculty of Engineering and Design, Kyoto Institute of Technology, Sakyo-ku, Kyoto 606-8585*
[b]*Department of Chemistry, Tokyo Gakugei University, Koganei, Tokyo 184-8501*

Supported molybdena are typical catalysts for olefin metathesis. It is accepted widely that reduced Mo ions such as Mo^{4+} and/or Mo^{5+} should exist as catalytically active center for metathesis. Thus, reductive pretreatment (with H_2 or CO) needs generally to reduce Mo^{6+} ions to form reduced ions as catalytically active species. However, we reported recently that molybdena supported on amorphous silica-alumina exhibit high activity for propene metathesis, which is a typical metathesis reaction, even at room temperature without reductive pretreatment.[1] In this study, it is concluded that support effect of silica-alumina strongly relate to not only structural change but also red-ox performance in contact with propene, and molybdena species on silica-alumina can easily be reduced to form reduced ions as metathesis active species in contact with propene. To obtain detailed structural information about the active molybdena species for metathesis, Mo L_{III}-edge XANES was applied to characterize the active molybdena species. The XANES spectrum probes the orbitals of 4*d* character participating in the Mo-O bonds. The white lines of the spectrum are split, corresponding to the ligand field splitting of Mo 4*d* orbitals. Thus the XANES spectrum is very sensitive to reflect the local structure of Mo ions. In this report, MoO_3/SiO_2-Al_2O_3 catalysts before/after propene metathesis were characterized by means of Mo L_{III}-edge XANES, and structural effect with red-ox behavior was studied in contact with propene.

Supported molybdena catalyst samples were prepared by impregnation of each metal oxide support with an aqueous solution of ammonium heptamolybdate (AHM). The oxide supports used were SiO_2 (Aerosil), Al_2O_3 (Nacalai), and amorphous SiO_2-Al_2O_3 containing 28.6 wt% (JRC-SAH-1, denoted as SAH-1) and 13.8 wt% (JRC-SAL-2, denoted as SAL-2) Al_2O_3. The impregnating solution was stilled at room temperature and evaporated at 343 K for 6 hours, and then the paste was dried for overnight and calcined at 773 K for 6 hours. The Mo L-edge XANES spectra were collected on a facility of BL-7A station of soft X-ray beam line at UVSOR, IMS, with 750 MeV of ring energy. Each powdery sample was mounted on a carbon-tape, and then attached on a beryllium-copper dynode in the first-stage of electron multiplier placed into a vacuum chamber. After the chamber had been evacuated (< 3.0•10-7 Torr), the spectrum was recorded in a total electron yield (TEY) mode at room temperature, using the Ge(111) double-crystal monochromator (2*d* = 0.6532 nm). The photon energy was calibrated by using Mo metal sample at Mo L_{III}-edge (2520 eV).

The Mo L_{III}-edge XANES spectra of supported molybdena samples and reference compounds are shown in Fig. 2 and 3. The detailed interpretation of the spectra was described elsewhere.[2] For MoO_3/SiO_2 and MoO_3/Al_2O_3 samples (Fig. 2), tetrahedral Mo-O_4 species are dominant at low MoO_3 contents (2.5 wt% in MoO_3/SiO_2 and 2.5 - 7.5 wt% in MoO_3/Al_2O_3). With an increase in MoO_3 content, polyanion-like Mo-O_6 octahedra coexist with tetrahedra. For 15.0 wt% MoO_3/SiO_2, the octahedral species exist mainly. These results support the conclusion reported previously by several workers.[3] On the other hand, the XANES spectra of MoO_3/SAH-1 before/after the reaction are shown in Fig. 3. Before the reaction, these spectra indicate that tetrahedral and octahedral species coexist in the whole molybdena contents, and tetrahedral molybdena species exist even at the higher MoO_3 contents. Thus it is suggested that SAH-1 support brings about the formation of disordered molybdena species with tetrahedral local structure. In many cases such as MoO_3/SiO_2, highly dispersed molybdena species on the support consist of tetrahedral Mo-O_4 species. However, the results of UV-Vis spectroscopy showed that the

molybdena on SAH-1 do not consist of highly dispersed tetrahedra but contain polyanion-like species mainly. In fact, it is hardly accepted in 15.0 wt% MoO_3/SAH-1 that highly dispersed tetrahedra are dominant. It may suggest that unique molybdena species are stabilized on SAH-1, and poorly crystallized polymolybdate species with tetrahedra exist mainly. Formation of bulk MoO_3 phase and/or large polyanion clusters proceeds hardly on SiO_2-Al_2O_3 because of peculiar support-interaction.[4] After the reaction at 473 K, molybdena species in 2.5 wt% MoO_3/SAH-1 shows a little change. For 7.5 - 15.0 wt% MoO_3/SAH-1, structural change of tetrahedral species is scarcely brought about by the reaction. In these samples, the white line of higher energy becomes lower by the reaction at 473 K, indicating the decrease of tetrahedra. The XANES of 7.5 wt% MoO_3/SAH-1 shows the most definite change. For this sample, the white line at higher energy side shows less intense with an increase in reaction temperature. Thus it is concluded that tetrahedral species decreases in contact with propene, and reduced Mo ions are formed at the same time. In many molybdena systems reported by many workers, octahedral species can be reduced easier than tetrahedral one.[5] In addition, isolated Mo^{6+}-O_4 tetrahedral species can hardly be reduced thermally. [6] However, tetrahedral molybdenum species on SAH-1 tend to decrease in contact with propene. Thus it can be proposed that tetrahedral species formed on SAH-1 should not isolated ones. In addition, the difference of XANES edge energy is less seen between before and after contact with propene. From the result of ESR, reduction of Mo^{6+} ions proceeds by propene contact. If Mo^{5+} exists mainly after the reaction, the edge energy should be shifted to lower energy. From these results, it is concluded that unique polymolybdate species on SAH-1 are easily reduced in contact with propene, but reduced ions are formed partly and Mo^{6+} ions are still dominant. At the same time, tetrahedral species are consumed during the reaction.

In this study, it is concluded that MoO_3/SAH-1, as a noted metathesis catalyst, consists of poorly-ordered polymolybdate species before the reaction. After contact with propene even at room temperature (293 K), Mo ions are partly reduced to form metathesis active species when tetrahedral species decrease. This red-ox behavior should be brought about by the support effect of SAH-1. It is suggested that the metathesis active sites are not highly dispersed Mo ions in reduced state but exist in poorly crystallized polymolybdena species with reduced ions partly.

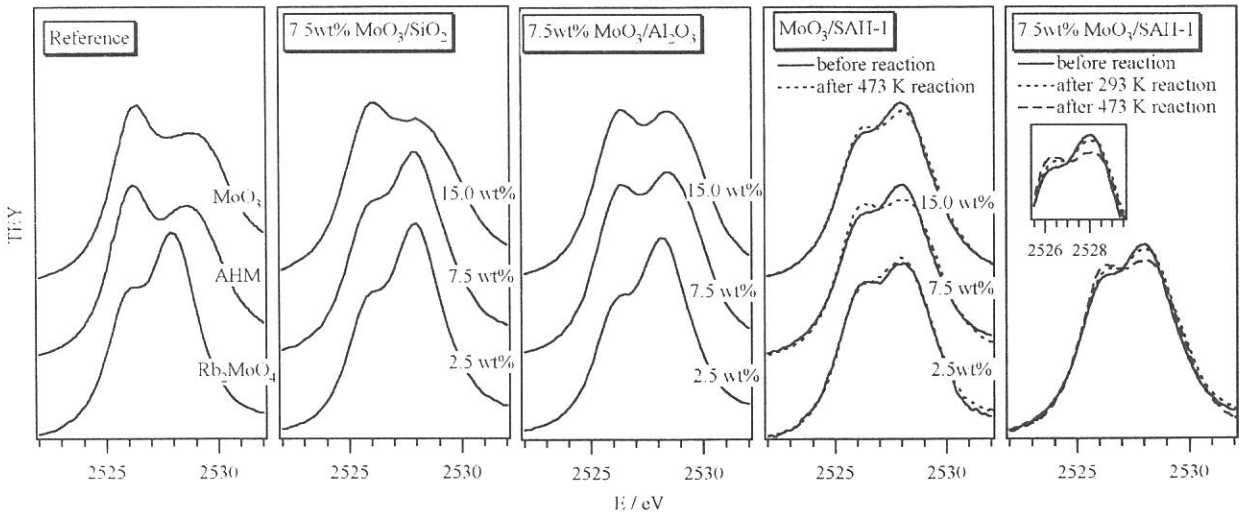

Fig. 1 Mo L_{III}-edge XANES spectra of supported molybdena samples and reference Mo compounds.

[1] H. Aritani, O. Fukuda, T. Yamamoto, T. Tanaka and S. Imamura, Chem. Lett., (2000) 66. [2] H. Aritani, T. Tanaka, T. Funabiki, S. Yoshida, K. Eda, N. Sotani, M. Kudo and S. Hasegawa, J. Phys. Chem., 100 (1996) 19495. [3] H. Shimada, N. Matsubayashi, T. Sato, Y. Yoshimura, A. Nishiyama, N. Kosugi and H. Kuroda, J. Catal., (1992) 746.; H. Prialiaud, Proc. 3rd Int. Conf. Chemistry and Uses of Molybdenum, eds. P. C. H. Mitchell and A. Seamans (Climax Molybdenum Co., Ann Arbor, Michigan, 1976), pp. 195. [4] S. Rajagopal, J. A. Marzari and R. Miranda, J. Catal., 151 (1995) 1995.; S. Rajagopal, H. J. Marini, J. A. Marzari and R. Miranda, J. Catal., 147 (1994) 417. [5] F. E. Massoth, Adv. Catal., (1978) 265.; A. Ueno, Y. Kotera, S. Okuda and C. O. Bennett, Proc. 4th Int. Conf. Chemistry and Uses of Molybdenum, eds. P. C. H. Mitchell and A. Seamans (Climax Molybdenum Co., London, 1982), pp. 250. [6] C. Louis and M. Che, J. Phys. Chem., 91 (1987) 2875.; B. N. Shelimov, I. V. Elev and V. B. Kazansky, J. Catal., 98 (1986) 70.

(BL7A)

Mg-K edge absorption study of MgO-ZnO solid solutions

Teruyasu MIZOGUCHI,[A] Kazuyoshi TATSUMI,[A] Masanobu NAKANO,[A]
Fumiyasu OBA,[A] Masato YOSHIYA,[A] Hirohiko ADACHI,[A] Isao TANAKA,[B]
Tomoko YOSHIDA[C], Hisao YOSHIDA,[D]
Shang-Di MO[E] and Wai-Yim CHING[E]

[A] *Department of Materials Science and Engineering, Kyoto University, Sakyo, Kyoto 606-8501 Japan*
[B] *Department of Energy Science and Technology, Kyoto University, Sakyo, Kyoto 606-8501 Japan*
[C] *Center for Integrated Research in Science and Eng., Nagoya University, Nagoya, 464-8603, Japan*
[D] *Department of Applied Chemistry, Nagoya University, Nagoya, 464-8603, Japan*
[E] *Department of Physics, University of Missouri-Kansas City, Kansas City, Missouri 64110-2499, USA*

Solid solutions of ceramic materials are widely used in modern technology. However, their atomic/electronic structures have not been clarified in most of the cases. X-ray absorption is a versatile tool having potential to elucidate the local atomic/electronic structures of selected atoms. However, it has not been widely applied in ceramic science. One of the greatest reasons is due to the lack of good theoretical tools to interpret experimental spectra. Experimental spectra have thus far been compared with some spectra from reference materials. Information obtained by such a "finger-printing" method is naturally very limited. We have to make a combined effort between experimental XANES and theoretical analysis of the spectra.

High purity MgO powder (2000A, Ube Materials Industries, Japan) and ZnO powder (Seido Chemical Corp., Japan) were used as starting materials. Two powders were mixed by magnetic-starrier for 3h in ethanol. Sintering was done in air at 1623K for 3h for undoped ZnO, and 1933K for 3h for the doped/undoped MgO. The Zn-doped MgO shows only a single crystalline phase of a rock-salt structure by a standard powder x-ray diffraction method. The XAFS were obtained at BL-7A of UVSOR/IMS. Mg-K edge spectra were collected in a total electron yield mode at room temperature using a beryl two-crystal monochrometer. Samples were put on the first photocathode of electron multiplier using adhesive carbon tape.

Figure 1 shows Mg-K edge XANES from four samples with different ZnO concentrations. The series of the spectra shows a continuous change. Relative intensity of the first peak decreases with the increase in Zn-concentration. At the same time, the peak located at around 1310 eV show notable shift toward low energy with rising the Zn-concentration. In the companion paper in this issue, we reported the Zn-$L_{2,3}$ edge XANES from the solid solutions. They are clearly different from the Zn-$L_{2,3}$ edge XANES of wurzite ZnO having 4-fold coordinated Zn. The results confirmed the presence of 6-fold coordinated Zn in the solid solutions. The Mg-K edge XANES should therefore be interpreted by taking the fact into account. Figure 2 shows theoretical XANES by a first principles supercell calculation using the OLCAO (orthogonalized linear combination of atomic orbitals) method. As can be found, the theoretical spectrum can reproduce the experimental XANES quantitatively when a sufficiently large super-cell is used to take into account core-hole effects correctly. Details of the computational procedure can be found elsewhere

[1]. When theory has sufficient predictive power as in the present study, the combined work with good experimental tools should really be useful for elucidating the local atomic/electronic structures of solute atoms. Near edge structures of the core-loss spectra of the electron energy loss spectroscopy (ELNES) is another important tool to provide similar information to XANES. Since ELNES can be measured using a modern transmission electron microscope, it is sometimes more easy to measure than the XANES. In the case of Mg-K edge study, however, the energy resolution as well as the S/N ratio is far better in the XANES as can be seen in Fig. 2.

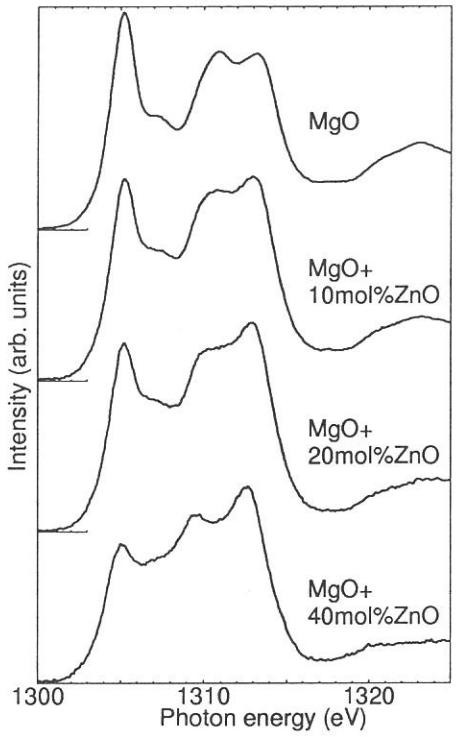

Fig.1 Experimental Mg-K edge XANES from pure MgO and MgO-ZnO solid solutions.

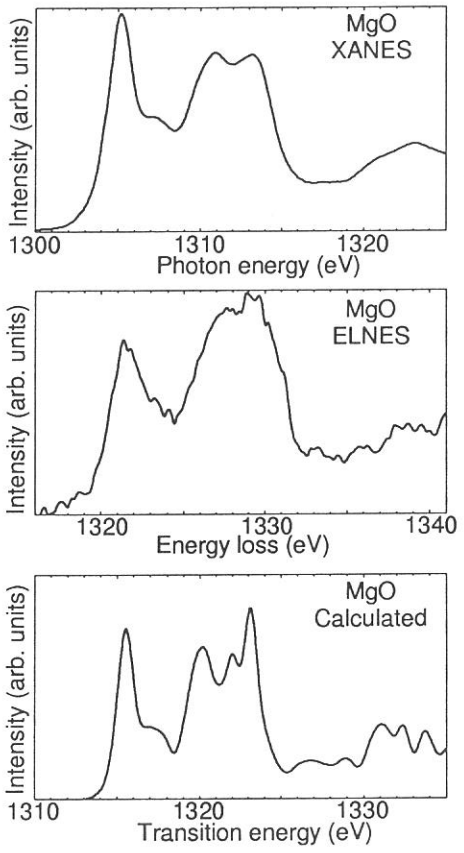

Fig.2 Experimental Mg-K edge XANES and ELNES from pure MgO. Theoretical XANES by the OLCAO calculation using 128 atoms-supercell is shown for comparison.

Acknowledgements This work was supported by Grant-in-Aid for Scientific Research on Priority Areas (No. 751) from Ministry of Education Science, Sports and Culture of Japan .

REFERENCES

[1] Shang-Di Mo, W. Y. Ching, Phys. Rev. B **62** (2000) 7901.

(BL7A)

Zn-$L_{2,3}$ edge absorption study on six-fold coordinated Zn in MgO

Isao TANAKA,[A] Teruyasu MIZOGUCHI,[B] Kazuyoshi TATSUMI,[B] Masanobu NAKANO,[B]
Fumiyasu OBA,[B] Masato YOSHIYA,[B] Hirohiko ADACHI,[B]
Tomoko YOSHIDA[C], Hisao YOSHIDA,[D]

[A] *Department of Energy Science and Technology, Kyoto University, Sakyo, Kyoto 606-8501 Japan*
[B] *Department of Materials Science and Engineering, Kyoto University, Sakyo, Kyoto 606-8501 Japan*
[C] *Center for Integrated Research in Science and Eng., Nagoya University, Nagoya, 464-8603, Japan*
[D] *Department of Applied Chemistry, Nagoya University, Nagoya, 464-8603, Japan*

Small amount of dopants often changes properties of ceramic materials dramatically. However, their atomic/electronic roles have not been clarified in most of the cases. The lack of such information often limits further development of ceramic materials. In the present study, we investigate local structures around Zn^{2+} solute in MgO, which can be a good model system to demonstrate the usefulness of the x-ray absorption method to study the local structures of impurities in ceramic materials.

MgO possesses a simple rock-salt structure. The lattice relaxation associated with the substitution is expected to be simple. Solubility limit of Zn^{2+} in MgO was reported to be 38.7mol% at 1873K [1]. Zn^{2+} is therefore expected to occupy the six-fold coordination site in MgO. Very recent XAFS data confirmed the six-fold coordination [2]. Zn^{2+} in wurzite-ZnO (w-ZnO) or related oxides usually exhibits 4-fold coordination except for the case of high-pressure ZnO having a rock-salt structure (c-ZnO) [3]. We compare Zn-$L_{2,3}$ edge ELNES from w-ZnO and Zn^{2+} doped MgO to see the difference in spectral features between the 4-fold and 6-fold coordinated Zn atoms. Special interests are placed on the analogy to the difference between the Si-$L_{2,3}$ edge ELNES from 4-fold and 6-fold coordinated Si, i.e., α-quartz and stishovite.

In a companion paper, we report Mg-K absorption study of the MgO-ZnO solid solutions. Experimental procedure has been described there. The XAFS were obtained at BL-7A of UVSOR/IMS. Zn-$L_{2,3}$ edge spectra were collected in a total electron yield mode at room temperature using a beryl two-crystal monochrometer.

Figure 1 (left) companion paper included in this issue experimental Zn-$L_{2,3}$ edge XANES from w-ZnO and 10mol%ZnO-doped MgO. The w-ZnO shows four major peaks, while Zn^{2+} in MgO displays only three in the energy range shown in the figure. The major difference can be simply ascribed to the difference in the coordination numbers, i.e., four in w-ZnO and six in Zn-doped MgO.

Si^{4+} in SiO_2 exhibits 4-fold coordination in α-quartz and 6-fold coordination in stishovite. Their Si-$L_{2,3}$ edge XANES have been reported by some groups [4, 5, 6], which agree well with each other. Figure 1 (right) shows the results by Li et al [4]. The 4-fold coordinated Si basically exhibit four sets of peaks in the energy region, whereas the 6-fold coordinated Si shows three-sets. Although the $L_{2,3}$ edge spectra from Zn and Si do not resemble each other at first sight, the origin of the sets is identical: It is derived from the point symmetry within the first coordination unit. Figure 2 schematically shows how the peaks are made out of the molecular orbitals of the primitive units. For simplicity, $(ZnO_4)^{6-}$ and $(ZnO_6)^{10-}$ are taken to be in

tetrahedral (T_d) and octahedral (O_h) symmetries.

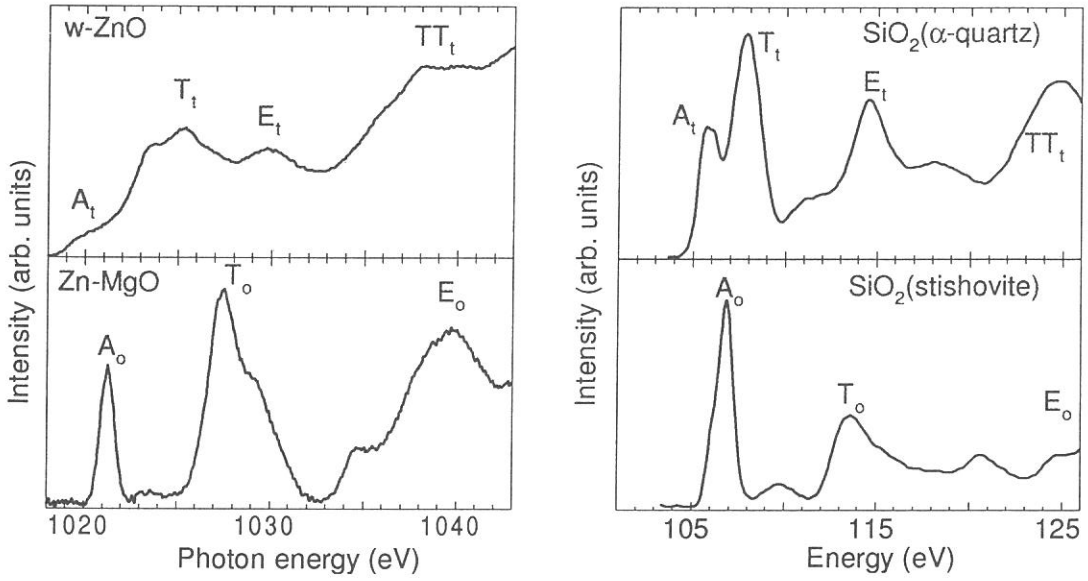

Fig.1 (Left) Experimental Zn-$L_{2,3}$ edge XANES from w-ZnO and 10mol% ZnO doped MgO obtained in the present study. (Right) Experimental Si-$L_{2,3}$ edge XANES for α-quartz and stishovite-type SiO_2 as reproduced from Ref. 4.

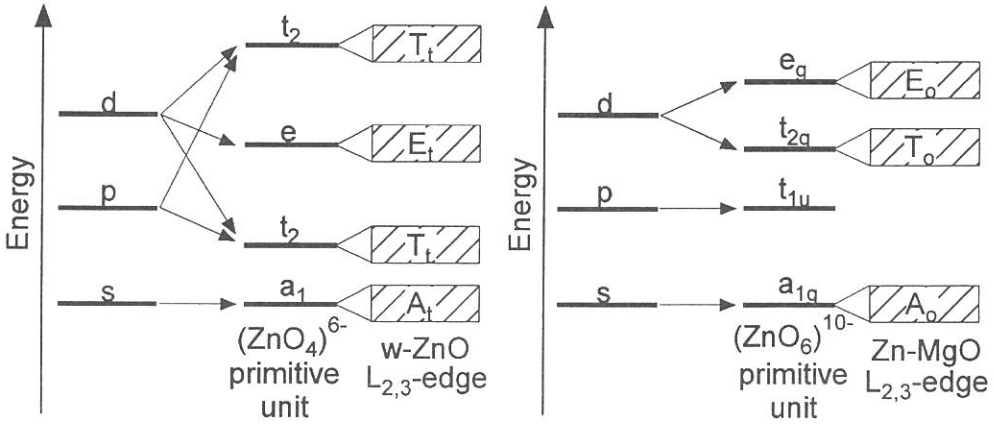

Fig.2 Mechanism of the formation of spectral features of the Zn-$L_{2,3}$ edge XANES from the molecular orbitals of the corresponding primitive units.

Acknowledgements This work was supported by Grant-in-Aid for Scientific Research on Priority Areas (No. 751) from Ministry of Education Science, Sports and Culture of Japan .

REFERENCES

[1] E. R. Segnit, S. E. Hlland, J. Am. Ceram. Soc., **8** (1965) 409.
[2] T. I. Nedoseikina, A. T. Shuvaev, V. G. Vlasenko, J. Phys.: Condens. Matter **12** (2000) 2877.
[3] C. H. Bates, W. B. White, R. Roy, Science **137** (1962) 993.
[4] D. Li, G. M. Bancroft, M. Kasrai, M. E. Fleet, X. H. Feng, K. H. Tan, B. X. Yang, Solid State Commun. **87** (1993) 613.
[5] T. Sharp, Z. Wu, F. Seifert, B. Poe, M. Doerr, E. Paris, Phys. Chem. Minerals **23** (1996) 17.
[6] D. J. Wallis, Ph. D. Thesis, University of Cambridge, 1994.

(BL-7A)

Al *K*-XANES spectra of AlN/Fe multilayered thin films

Masao Takahashi, Akira Asano, Yoshiko Kasama and Hikaru Kobayashi

ISIR, Osaka University, 8-1 Mihogaoka, Ibaraki, Osaka 567-0047

Introduction

Several species are known in the Fe-N system, i.e., α''-$Fe_{16}N_2$, γ'-Fe_4N, ε-$Fe_{2\text{-}3}N$, ζ-Fe_2N and γ'' and γ'''-FeN_y. Among them, iron nitrides with the low nitrogen content have become of an intensive interest after it has been reported that α''-$Fe_{16}N_2$ takes saturation magnetization larger than that of α-Fe.[1] By a reactive sputtering deposition, on the other hand, two iron nitrides, γ'' and γ'''-FeN_y which have not been reported on the equilibrium phase diagram have been prepared and γ'''-FeN_y with Rock salt-like crystal structure takes iron having larger magnetic momentum than α-Fe.[2] Iron nitrides, having both high hardness and corrosion resistance in addition to their magnetic property, therefore, have attracted much attention for one of promising magnetic materials. However, such iron nitrides with fascinating magnetic property are almost thermally unstable. A formation of composites or layered films with non-magnetic and thermally stable material has recently been investigated for an application of such nitrides to a practical magnetic material. It has been reported for multilayered Fe/AlN films that the value of the saturation magnetization of iron could be controlled by regulating thickness of each layer.[3] Fe *K*-XANES spectral feature of these multilayered films was getting different with increasing number of layers in the film, ie., with an increment of the number of the interface, suggesting that the nitridation of iron has occurred at the interface between AlN and Fe films. Al *K*-XAFS spectra for such multilayered Fe/AlN films and AlN film deposited on Fe thick film could elucidate the coordination state of Al near the interface. In the present study, Al *K*-XANES spectra for those films have been compared with that of AlN film.

Experimental

Films were prepared using two target-type rf-sputter deposition apparatus(JEH-430RS, JEOL). Al and Fe metal targets were used for deposition of AlN and Fe, respectively. AlN film was deposited under nitrogen atmosphere, while argon gas was used for formation of Fe film. A silica grass slide was used as a substrate. A base pressure of the deposition chamber was below 1×10^{-4} Pa and the deposition chamber was evacuated down to the base pressure before the deposition of each layer. The sputter gas pressure was kept at 1 Pa and the rf power of 30 or 100 W was applied. Film thickness was controlled by the deposition duration and total film thickness of the multilayered film was 1 μm. $[AlN/Fe]_n$ denotes a multilayered film having n layer(s) of both AlN and Fe. Films were preserved in *n*-hexane.

Al *K*-XANES spectra were measured at BL-7A. YB_{66} was used for the monochromator crystal. Graphite powders were very thinly spread on top of the surface of sample film. The sample film was stuck on the inner surface of first dinode of the electron multipler with a conductive adhesive tape. The total electron yield method was used for the measurement. Gold mesh transmitting 80% of photons was used for the monitor of I_0 current.

Results and Discussion

Al *K*-EXAFS spectra measurements have been executed at BL-7A but unfortunately spectra with good S/N ratio have not been obtained due to the insufficient photn flux, because the wiggler had not been working well.

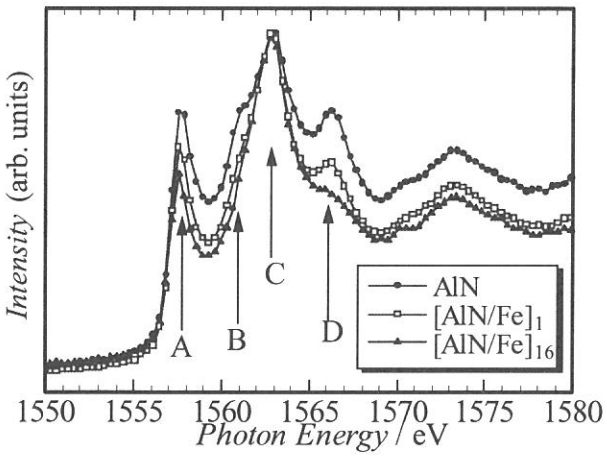

Fig. 1. Al K-XANES spectra for the AlN film and multilayered films, $[Al/FeN]_n$. Full circles, open squares and solid triangles show AlN, $[Al/FeN]_n$ with n = 1 and 16, respectively.

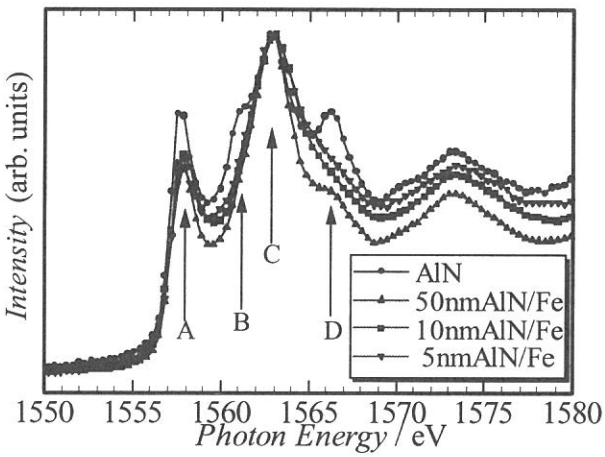

Fig. 2. Al K-XANES spectra for AlN and AlN/Fe films. Circles, triangles, squares and lozenges denote the AlN film and AlN/Fe films with AlN thickness of 50, 10 and 5 nm, respectively.

Instead, Al *K*-XANES spectra have been measured. Though the electronic structure is obtainable from the XANES, the EXAFS, which prolongs more than 1500 eV above the absorption edge, is valuable for the local structure determination. Therefore, the beam line where one can measure the EXFAS with good S/N ratio is required.

Al *K*-XANES spectra for $[AlN/Fe]_n$ multilayered films and AlN/Fe films are shown in Figs. 1 and 2, respectively. There are four peaks, A - D, between photon energy of 1555 and 1570 eV. All spectra in Figs. 1 and 2 are normalized as the peak C of all spectra coincides each other. The intensity of peaks A, B and D apparently decreases with an increase of number of layers, n in $[AlN/Fe]_n$, (Fig. 1) and with a decrease of the film thickness (Fig. 2). The increase in n means the increase of the interface between AlN and Fe layers and the decrease of thickness of AlN layer. The spectrum is measured as the convolution of signals from both the bulk and the interface. The thinner the AlN layer is , the more the spectrum includes information around the interface. Therefore, the change in the spectral shape appears to indicate that the electronic structure of Al at the AlN/Fe interface differs from that of the bulk AlN.

It may be considered from the present change in the spectral shape that a certain kind of thin film effect causes such spectrum change, that is, the electronic structure of AlN itself alters as thickness of the AlN layer decreases. The XPS depth-profile measurements have been showed the possibility of the elimination of nitrogen atoms from AlN at the AlN/Fe interface. Moreover, both the Fe *K*-XANES study and the magnetic property of multilayered $[AlN/Fe]_n$ films point out the posibility of existence of iron nitride, FeN_y. These evidences have supported the existence of the different species from AlN in the vicinity of the interface. Theoretical considerations on the Al *K*-XANES spectra are required to deduce the coordination structure around Al atoms and are presently progressed.

References

1) T.K.Kim and M.Takahashi, *Appl. Phys. Lett.*, **20** (1972) 492.

2) M.Takahashi, H.Fujii, H.Nakagawa, S.Nasu and F.Kanamaru, *Proc. 6th Int Conf. Ferrites*, **1992**, 508.

3) S.Kikkawa, M.Fujiki, M.Takahashi and F.Kanamaru, *Ceramic Microstruct.: Control at the Atomic Level*, ed. by A.P.Tomsia and A.Glaeser, Plenum Press, N.Y., 1998, pp. 605.

(BL7A)

The measurement of soft X-ray excited optical luminescence of a silica glass

Tomoko Yoshida[1], Tetsuo Tanabe[1] and Tatsuya Ii[2]

[1]*Center for Integrated Research in Science and Engineering, Nagoya University, Nagoya 464-8603, Japan*

[2]*Department of Nuclear Engineering, Graduate School of Engineering, Nagoya University, Nagoya 464-8603, Japan*

Introduction

The radiation effects on silica glasses are one of the main concerns for their application as optical windows, insulators and optical fibers under the severe environments such as fusion and fission reactors.[1] Recently, we have made in-situ luminescence measurements of silica glasses induced by in-reactor irradiation, and the in-reactor luminescence was found to be a powerful technique to observe dynamic effects on the electrical property of a silica.[2] However, the detailed effects are still unknown, mainly because many kinds of radiations over the range from γ-ray to optical lights generate and interact each other with a silica in the reactor, which sometimes confused our understanding of dynamic radiation effects. In the present study, to take notice of the effects of soft X-ray, we tried to measure the luminescence from silica glasses under the irradiation of soft X-ray near Si K-edge.

Experimental

The samples used in this work were fused silica glass (T-2030) and synthesized silica glass (T-4040) of 13 mm diameter and 2 mm thickness produced by Toshiba Ceramics, Japan, with different OH content. Nominal impurity levels in these samples are listed in Table 1. The measurement of luminescence of the silica glass induced by soft X-ray irradiation (1.8-1.9 keV) were carried out on the beam line 7A at UVSOR, Insitute for Molecular Science with a stored current of 100-200 mA. The luminescence was focused by a lens in the UVH chamber to the monochromator (CP-200, SEIKO EG&G) and detected by a multi-channel analyser (OMA III, SEIKO EG&G). The photon detecting efficiency especially above 4 eV was reduced.

Results and Discussion

Fig. 1 shows the photoluminescence spectra of a fused silica glass (T-2030) obtained under excitation at various energy (5.1-7.7 eV). These spectra were recorded at BL1B at UVSOR. Two prominent PL bands at 3.1 eV and 4.2 eV were observed. Thomon *et al.*[3] reported the existence of two B_2 bands excited at 5.1 eV, and it is commonly accepted that the PL emission bands at 2.7 eV and 4.4 eV are attributed to the $B_{2\alpha}$ while the $B_{2\beta}$ center generates the 3.1 eV and 4.2 eV PL bands. Therefore, the PL bands for the low-OH fused silica glass (T-2030) are very likely originate from a fair amount of intrinsic oxygen deficiencies assigned as B2β exist in this silica glass.

On the other hand, we succeeded luminescence measurement of the same silica glass under the irradiation of soft X-ray near Si K-edge (ca. 1.83 keV) as shown in Fig. 2, although the energy resolution of this spectrum was very low at the present stage. One can see the similar emission band around at 3.2 eV, therefore, it is very likely that this luminescence mainly originates from

Table 1

Nominal impurity levels in silica glasses (in ppm)

Sample	Al	Fe	Na	K	Cu	B	OH
Fused silica (T-2030)	8	0.8	1	1	0.02	0.3	1
Synthesized silica (T-4040)	0.1	0.05	0.05	0.05	<0.01	<0.01	800

the oxygen deficiencies in the silica glass due to an electron excitation during soft X-ray irradiation. We tried to measure the luminescence of a synthesized silica glass (T-4040) which has few intrinsic defects, and confirmed that no prominent emission band was observed.

In our next study, it will be an important subject to investigate the change in the intensity of the luminescence with the soft X-ray energy as well as its irradiation time.

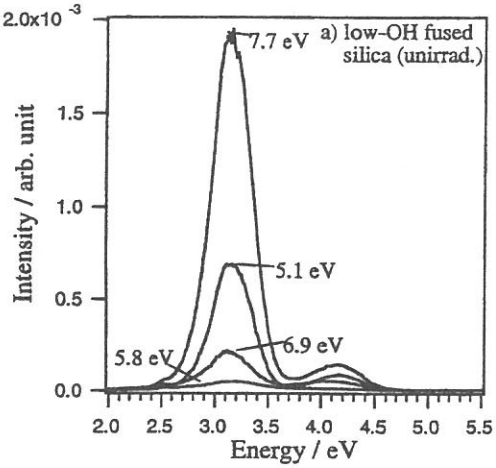

Fig. 1 The photoluminescence emission spectra excited at various energies in a low-OH fused silica glass (T-2030).

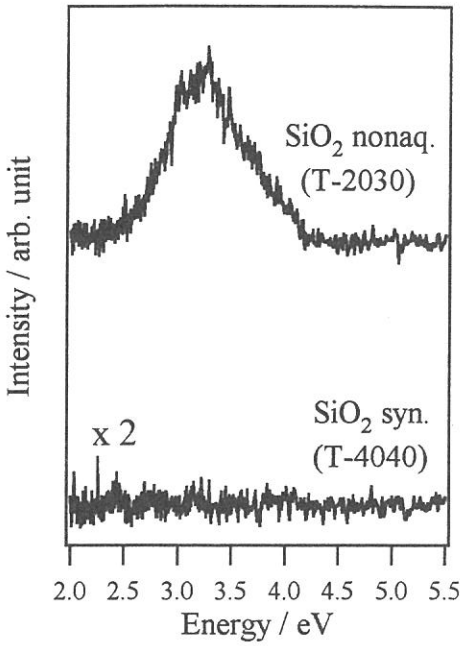

Fig. 2 X-ray excited optical luminescence spectra of silica glasses.

Acknowledgments

The authors are grateful to Prof. Eiji Sigemasa, Prof. Masao Kamata and Mr. Eiken Nakamura of UVSOR for their great help and cooperation in the luminescence measurements.

References

[1] F. W. Clinard Jr., L. W. Hobbs, in : Physics of Radiation Effects in Crystal, Elsevier, Amsterdam, 1986, p. 442.

[2] M. Fujiwara, T. Tanabe, H. Miyamaru and M. Miyazaki, Nucl. Inst. And Meth. B 116 (1996) 536.

[3] R. Tohmon, H. Mizuna, Y. Ohki, K. Sasagane, K. Nagasawa, and Y. Hama, Phys. Rev. B 44 (1989) 1337.

(BL7A)

Improvement electrochemical properties of surface treated natural graphite by aluminum and its mechanisms from Al K-edge XANES

Sung-Soo Kim, Yoshihiro Kadoma, Hiromasa Ikuta, Yoshiharu Uchimoto, and Masataka Wakihara
Department of Applied Chemistry, Graduate School of Science and Engineering, Tokyo Institute of Technology
Ookayama, Meguro, Tokyo 152-8552, Japan.

The rechargeable lithium ion batteries, using a carbon material as anode and transition metal oxide such as $LiCoO_2$, $LiMn_2O_4$ or $LiNiO_2$ as cathode, have been developed. During the past years, there have been a lot of research works to improve of the battery performance carried out on various kinds of carbonaceous material ranges from graphite to disordered carbon by control of various properties such as structure, surface modification[1-3]. Among the several types of carbonaceous materials, natural or synthetic graphitic carbons are commonly found in most commercial products in the market today due to their merits such as flat and low working voltage with respect to lithium metal, relatively high coulombic efficiency, etc. Specifically, natural graphite can be thought as potential materials for anode in lithium ion battery in terms of cost[4]. However, it has been difficult to control the key parameters of natural graphite that affect their characteristics for use as anode because carbon materials have large variations in their electrical properties. Especially, surface properties of natural graphite frequently affect the electrochemical performances such as reversible specific capacity, cycle life, rate capability. Therefore it has been desired to improve by control surface properties of natural graphite. In this work, we investigated the influence of surface and/or structure modification of natural graphite by introducing aluminum compound for electrochemical performances of anode in lithium ion battery. The local structure of amorphous-like alumina on surface of natural graphite was investigated by Al K-edge XANES.

The Aluminum-treated samples were prepared by aluminum tri-etoxide($Al(OC_2H_5)_3$, Soekawa Chemicals) treatment on NG2(Kansai chemicals). The NG2 graphite was soaked in ethanol solution containing 10wt% aluminum tri-etoxide, followed by ultrasonic treatment for 3 hours, filtration and drying above 200°C for 1 day to remove residual of ethanol. The electrochemical measurement was carried out with the use of CR2032 coin-type cell. The working electrodes were prepared by doctor-blade technique on copper foil, spreading paste consisted of 10wt% polyvinylidenefluoride(PVdF) as binder, 10wt% acethylene black as conductive agent, 80wt% treated or pristine NG2 graphite and appropriate amount of 1-methyl-2-pyrrolidinone(NMP) as solvent. After drying of NMP solvent, the electrode was cut into disk(the weight of all sample was controlled around 4mg). Lithium metal was used as counter electrode. The electrolyte used was 1M $LiClO_4$ dissolved in ethylene carbonate(EC)/diethylene carbonate(DEC)(volume ratio 1:1). The cell assembly was operated in a glove box filled with argon gas. The specific capacity was measured by galvanostatically with current density 350mA/g in the ranges between 0 and 2.5V. Al K-edge XAS were measured on BL7A at UVSOR with a ring energy of 750MeV and a stored current of 70-220mA in a mode of total electron yields. The KTP double crystal monochromator was used. The monochromator scanning angle step width was 0.003°, which corresponds to *ca.* 0.1eV at 1560eV.

FT-IR spectra of untreated and Al-treated NG2 samples which were dried at various tempera-

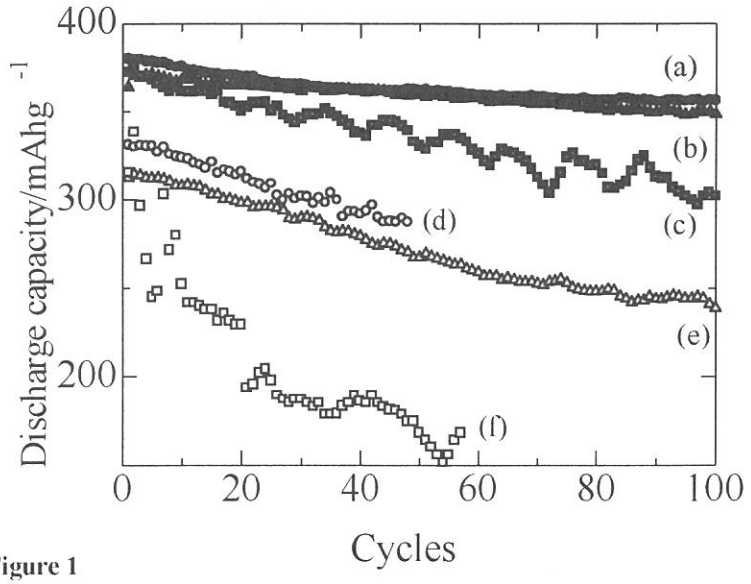

Figure 1
Cycle performances with C-rate of pristine and Al-treated sample. The circle, triangle and rectangular plot respresent 0.2C, 0.5C and 1.0C-rate, respectively. The simple plot and boldic one shows untreated and treated samples, respectively. : (a)treated 0.2C, (b)treated 0.5C, (c)treated1.0C, (d)untreated 0.2C, (e)untreated 0.5C and (f)untreated 1.0C.

ture together with aluminum tri-etoxide ethanol solution. In Spectra of $Al(OC_2H_5)_3$ ethanol solution and Al-treated at 120°C. the band around 1100 cm^{-1} can be attributed to the C-O stretching vibration of ethoxy groups was observed. On the other hand. the band disappeared in dried sample at 200°C and untreated graphite. This result indicates that residual of ethoxy groups at 120°C and the complete removal of ethoxy groups and ethanol solvent takes place above 200°C.

X-ray measurements of untreated and Al-treated NG2 indicated almost consistency in their XRD patterns with no changes in d(002) values. Eventually. we couldn't detect the remarkable influence of small amounts of Al on surface by XRD. which is measurement of total bulk structure. There was noticeable change between untreated and treated graphite in Raman spectroscopy. which reveals mainly the surface structure to the extent of several tens of nanometer. It is well known that graphite shows an intense band at 1580cm^{-1} indicates an E_{2g} vibration mode in the graphite region of carbon(G-band) and relatively weak one at 1360cm^{-1} is an A_{1g} mode arising from the disordering in carbon(D-band) which is Raman inactive for perfect graphite crystals. We could observe the frequency shift and intensified G-band with Al-treatment which is similar phenomena due to the formation of dilute stage1 in initial lithium intercalation. whereas no remarkable changes in D-band. Accordingly the relative intensity $R(I_D/I_G)$. which indicates the ratio of graphite edge plane to the graphite plane. decreased with Al-treatment of surface. The small peak around 1560cm^{-1} due to the oxygen and 1290cm^{-1} in untreated sample is disappeared in Al-treated graphite. Though we could not observe bulk structure change in XRD measurement. the results of Raman spectroscopy is enough to suggest that the Al-treatment causes remarkable modification on graphite surface.

In Fig. 1. the cycle life performance of untreated and Al-treated graphite electrode was represented. The Al-treated graphite shows clearly improved cycle performance compared to untreated one. The periodic fluctuation of capacity in 1C rate (350mA/g) samples can be ascribed to the temperature variation of the testing atmosphere.

To investigate the structure of alumina on the surface of graphite. we measured the Al-K edge XANES. Since accurate structure of alumina are not known except θ -Al_2O_3. the structural analysis of amorphous-like alumina is not so simple. Recently. Al-K-edge XANES measurement combining quantitative analysis was proposed to estimate the local structure of alumina[5]. Only AlO_4 tetrahedra in mordenite was observed. whereas θ - Al_2O_3 has equally distributed between tetrahedral and octahedral coordinations of Al-atoms. It is known that the XANES spectra of AlO_4 tetrahedra and AlO_6 octahedra were clearly identified. A white line 1566eV is characteristics of AlO_4 compound and the peaks at 1568eV and 1572eV can be assigned to AlO_6 octahedral compound. In Fig.3, normalized XANES spectra with calcination temperature of Al-treated graphite samples were shown. We can observe a peak at 1565eV due to AlO_4 and two peaks at 1567eV and 1570eV due to AlO6 and the difference of peak position of AlO_4 and AlO_6 was about 2eV. In addition, the relative intensity of AlO_4 and AlO_6 was varied by calcination temperature. In the range of this study up to the 500°C of calcination temperature. the portion of AlO_4 increased. according to previous report[5], this alumina phase can be thought as boehmite+ γ type alumina. Comparing with the results of rate capability improvement of Al-treated samples (Fig.2). we can assume tetrahedral coordination of Al is more favorable in surface of graphite.

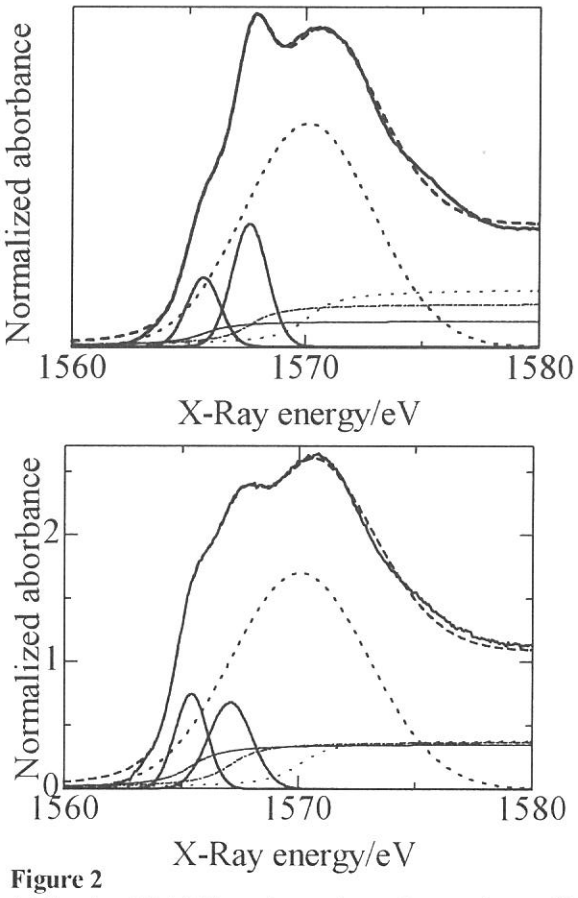

Figure 2
Al K-edge XANES on the surface of natural graphite and its simulated spectrum which composed of three sets of Gaussian and arctangent function. Each samples were calcined at (a) 300°C. and (b) 500°C.

Refedences

[1] E. Peled. G. Menachem. D. Bar-Tow. A. Melman. *J. Electrochem. Soc.*, **143**. L4 (1996).

[2] T. Nakajima. M. Koh. R.N. Singh. M. Shimada. *Electrochim. Acta*. **44**. 2879 (1999).

[3] K.Sumiya. J.Suzuki. R.Takasu. K.Sekine. T.Takamura. *J.Electroanal.Chem.*,**462**. 150 (1999).

[4] K. Fukuta. K. Kikuya. K. Isono. M. Yoshio. *J. Power Sources*, **69**. 165 (1997).

[5] K.Shimizu. Y.Kato. T.Yoshida. H.Yoshida. A.Satsuma and T.Hattori. *Chem. Commun.*,**1999**. 1681 (1999).

(BL7A)

Rb-L Absorption Spectra and Excitation Spectra of Photoluminescence of RbBr

Masahiro MORI, Takashi IKEDA, Takaaki AWATA‡ and Tokuo MATSUKAWA‡

School of Informatics and Sciences, Nagoya University, Nagoya 464-8601
‡ *Naruto University of Education, Naruto, Tokushima 772-8502*

(5: Solid- & liquid-phase spectroscopy 2; soft x-ray, absorption, photo-luminescence)

Soft x-ray excitation spectra of photoluminescence were measured in Rb- and Br-L region as well as the absorption spectra of RbBr. Both the photon energies of Rb- and Br-L edge exist near 1800eV, where only few spectroscopic studies are reported. One of the reasons is that a proper monochromator crystal has been poor, being able to utilized in the soft x-ray region. At the BL7A beam line, stable spectroscopic works have become recently possible by the use of KTP crystal in the photon energy region. The beam line is composed with a double crystal monochromator. We have already performed Br-L absorption measurements on some kinds of alkali bromides.

The purpose is to observe soft x-ray absorption spectra of both Rb- and Br-L edges on RbBr and discuss the excitation spectra of the visible (or/and ultraviolet) light obtained simultaneously. The samples – RbBr thin powder samples – were prepared with the vacuum evaporation on the polyester 2μm thin film and transferred to the sample preparation chamber for each measurement on every sample with different thickness. All measurements were carried out at room temperature. The absorption spectra were obtained by the total photoelectron yield. The excitation spectra were obtained simultaneously with recording the intensity of the visible (ultraviolet) light from the sample. A photo-multiplier tube for the photoluminescence was installed at 45 degrees to incident light direction through a quartz focusing lens of 20mm diameter at 200mm from the sample position. The absorption spectra were obtained by the total photoelectron yield. An electron-multiplier with a Be-Cu anode was set behind the sample film.

Figures 1 and 2 show comparisons of the absorption and the excitation spectrum of RbBr with two kinds of thickness; s. A is 45nm in thickness and s. B is 199nm in thickness. The absorption spectra have a series of fine structures at the edge commonly. Both absorption intensity distribution spectra are the similar with each other, and these have two absorption components which the one on the lower energy results from Rb-L_2 absorption edge and the other on the higher is originated from Rb-L_3 absorption. The Rb-L spectra show no overlap structures because of the large separation of around 50eV between L_2 and L_3 levels. The excitation spectra appear to follow the features of the absorption spectra except the absolute

val"e of the absorption edge depth. In the higher energy region luminescence yields show some structures which corresponds absorption structures as peaks to dips. Thus the excitation spectrum of RbBr shows inverted profiles of the absorption spectrum. It is a well known phenomenon in the ease the luminescence excitation spectra excited with x-ray. Emura *et al.* discussed that the excitation spectra change the profiles among the effective thickness of samples according to a phenomenological model. Their results show that the excitation spectra change their spectral features as the effective thickness change and finally reach the inverted profiles of absorption spectra.

Fig.1

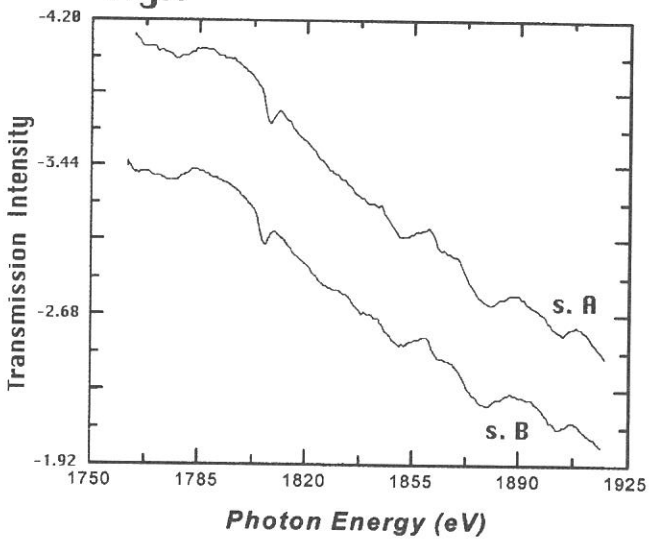

Figure 3 shows the excitation spectrum of RbBr single crystal whose thickness is sufficient about 1mm(1×10^6nm). It shows that the luminescence intensity away from the Rb-L edge increases as a linear function for thickness for the most part. But it near edge is nearly saturated beyond the certain thickness, as the difference value between the edge intensity and off-edge on the sample A is nearly same as that on the sample B. In other words, the excitation spectrum of RbBr changes the feature depending on the thickness. On the other hand, the excitation spectrum of the other alkali bromides increases as a linear function for thickness even in the absorption edge region. This is a strange behavior and becomes a new question for us. Some further studies are needed for this luminescence problem.

Fig.2

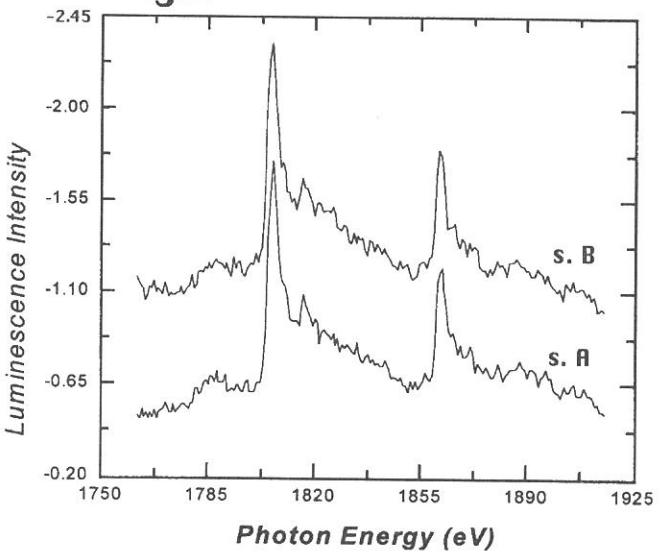

Fig.3

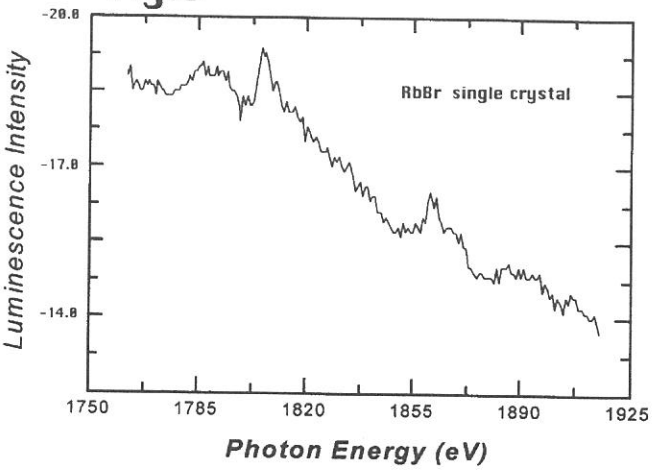

(BL7A)

Thickness Effects of Photoluminescence from Sodium Bromide Film Excited with Soft X-Rays in Na-K Edge Energy

Masahiro MORI, Takashi IKEDA, Takaaki AWATA[‡] and Tokuo MATSUKAWA[‡]

School of Informatics and Sciences, Nagoya University, Nagoya 464-8601
[‡] *Naruto University of Education, Naruto, Tokushima 772-8502*

(5: Solid- & liquid-phase spectroscopy 2; soft x-ray, absorption, photo-luminescence)

We have measured sample thickness dependence of photoluminescence excitation spectra from vacuum evaporated NaBr film excited near the photon energy region of Na-K absorption edge. Na-K spectra have become possible to measure by the use of a beryl crystal as a practical monochromator crystal at BL7A beam line, UVSOR. We have obtained Na-K absorption spectra of sodium halides by the transmission methods and photoluminescence yield spectra from thin samples excited in the energy region. In the case of fine powder samples, the excitation spectra show inverted profiles of absorption spectra in the case of NaBr fine powder sample, whereas other alkali bromides show same profile as the absorption spectra. It has been considered that it might depend on the absorption intensity, that is, the effective sample thickness. The purpose is to observe the relation between sample thickness and excitation spectrum. The excitation spectra were measured on NaBr thin films prepared by vacuum evaporation with different thickness. Although their results do not always show an existence of inverted feature, the intensity of excitation spectra are found to show characteristic variation with sample thickness.

Experiments were performed at the BL7A with a beryl monochromator crystal near the photon energy region of Na-K absorption edge. Several modifications were applied for the beam line. A sample preparation chamber was attached to the sample chamber to evaporate samples in a separated place. Samples were prepared with vacuum evaporation on to a polyester 2μm thin film and transferred to the experimental chamber for each measurements on every sample with different thickness. All measurements were carried out at room temperature. Evaporations were repeated over the one same sample film after a measurement. The thickness of the evaporated sample film was monitored by a quartz thickness monitor and was given by the frequency shift.

A photo-multiplier tube was installed at 45 degrees to incident light direction through a quartz focusing lens of 20mm diameter at 200mm from the sample position. The absorption spectra were obtained by the total photoelectron yield. An electron-multiplier with a Be-Cu anode was set behind the sample film, and absorption spectra were simultaneously obtained by a transmission method getting along with the excitation spectra.

Figure 1 shows the excitation spectrum on sodium bromide excited with a soft x-ray near Na-K edge energy. Spectral features are all common among the samples with the different thickness and with the absorption spectrum except the intensity distribution. As the thickness are small, it is apparent that the photoluminescence intensity increases rapidly.

Figure 2 shows a change of luminescence intensity measured at the energy below the absorption edge, the first, second, third absorption peak and forth peak, which are shown by arrow A, B, C, D and E in Fig. 1, respectively.

Fig.1

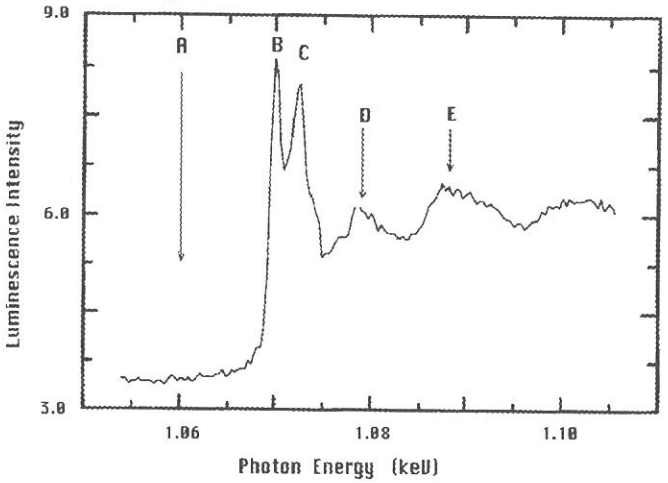

Intensity of the photoluminescence from the thin film, excited with a soft x-ray, is nearly zero independent from sample thickness for very thin thickness, and increases as a linear function for thick. It seems that quantum efficiency curves of A, B, C, D and E are same with each other except their intensity nomalization. It is strange. Because the luminescence intensity depends on the whole amount of creation of inner core holes, and the amount may depends on dose of absorbed x-ray, thus it should be considered to be proportional to the thickness of the sample. The intensity of the light may be unchanged since alkali halides are transparent in visible and UV region, thus no self absorption effects are considered. We have obtained quantum efficiency spectra, ratio spectra of the luminescence and the dose spectra. The dose spectra are given by $(I_0 - I)$ spectra, where I_0 is incident x-ray spectra and I is transmitted x-ray spectra. It shows that all quantum efficiency of A, B, C, D and E are not only linearly changes against the sample thickness as the samples are thin, but also they appear to converge to zero at thickness of about 25nm commonly among A, B, C, D and E. If it is true, it suggests that there is a threshold in the sample thickness to excite the photoluminescence by x-ray.

Fig.2

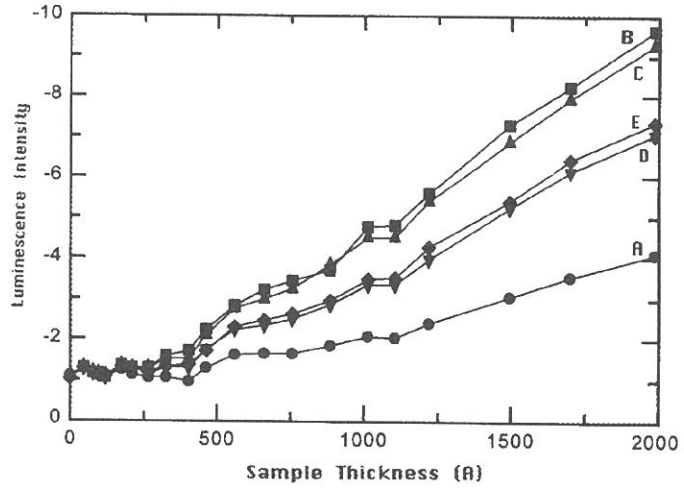

(BL7A)

An electronic static study on the analysis of Al *K* X-ray Absorption Near Edge Structure for Aluminum complexes

K. Shirozu, S. Matsuo, T. Kurisaki, T. Yokoyama, H. Wakita

Department of Chemistry, Faculty of Science, Fukuoka University, Nanakuma, Jonan-ku, Fukuoka 814-0180, Japan

Department of Chemistry, Faculty of Science, Kyushu University, Hakozaki, Higashi-ku, fukuoka 812-8581, Japan

【Introduction】

The characterization of aluminum is one of the most important study in the field of ceramics and glasses. The NMR spectroscopy is a powerful method for studying Al^{3+} complexes in the solution and solid states. In addition to ^{1}H- and ^{13}C- NMR spectra, ^{27}Al- NMR spectra can be obtained in relatively straightforward manner. The chemical shift of NMR spectra is caused by shielding of the magnetic field by electron around nuclear; i.e. the chemical shift depends on the electron density around nuclear.

In this study, the Al *K* XANES spectra of several aluminum complexes, which have different coordinated atoms each other, were measured and discussed the electronic structures. Moreover, electron density of aluminum compounds is analyzed by using a DV-Xα MO calculation, and discussed the correlation between chemical shift of NMR and the result of XANES spectra.

【Experiment and calculation】

The samples of this study are Al(EDTA), Al(lactate) and Al(pentanedionate). Al(EDTA) contains six coordinate Al3+ ions, each of which is bonded to two N atoms and four O atoms. Al(lactate) and Al(pentanedionate) have sixfold coordination, by six O atoms. The Al *K* XANES spectra were collected on the BL7A at the UVSOR of the Institute for Molecular Science in Japan using two KTP(001) monochromator crystals. The storage ring was operating at the electron energy of 750 MeV. All of XANES spectra were detected by a total electron yield method. Based on crystal structures of Na[Ga(EDTA)], [Al(Lactate)] and [Al(Pentanedionate)], the model structures of Na[Al(EDTA)] [Al(Lactate)] and [Al(Pentanedionate)] were constructed for the DV-Xα MO calculation, respectively.

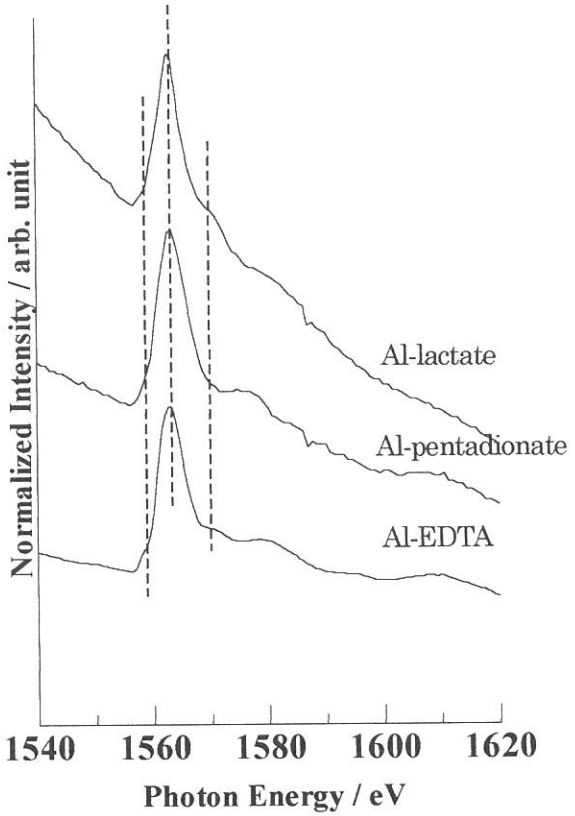

Fig.1 The Al K XANES spectra of aluminum complexes

【Results and discussion】

The Al *K* XANES spectra of these compounds are shown in Fig. 1. For Al *K* XANES spectra, the first peak of *K*-edge shifts higher energy with increasing the coordination numbers of aluminum ions. The absorption edges of three compounds are located on the same energy level. Thus their compounds have the same coordination number. Furthermore, the shapes of XANES spectra are similar to each other, so it can be presumed that there compounds have similar surroundings of aluminum ions. From the result of NMR spectra, the chemical shift of compounds is increasing as follows; Al(lactate) < Al(pentanedionate) < Al(EDTA). Therefore, Al(EDTA) has the poorest electron density of aluminum. We have analyzed the Al *K* XANES spectra of these compounds by a DV-Xα MO calculation. The electron density which was obtained by the DV-Xα MO calculation is increasing in order; Al(lactate) > Al(pentanedionate) > Al(EDTA). So the correlation between the chemical shift and electron density which obtained from XANES spectra analysis is observed in only these three compounds. Further measurement and theoretical study are required.

(BL7A)

A structural study on analysis of Al *K* X-ray Absorption Near Edge Structure for Aluminum complexes with carboxylamine

K. Shirozu, S. Matsuo, T. Kurisaki, T. Yokoyama, H. Wakita

Department of Chemistry, Faculty of Science, Fukuoka University, Nanakuma, Jonan-ku, Fukuoka 814-0180, Japan
Department of Chemistry, Faculty of Science, Kyushu University, Hakozaki, Higashi-ku, fukuoka 812-8581, Japan

【Introduction】

Fulvic acid is a major organic compound in soil solution, and the interaction between this acid and aluminumgives some influence to the behavior of aluminum. Therefore, it is important to understand the behavior of aluminum with this acid on the environmental sciences. Thus for understanding the binding properties of aluminum ion to fulvic acid, it is also important to investigate the interaction between aluminum ion and some model compounds of fulvic acid including carboxyl and amino groups in aqueous solution. We choose EDTA and CyDTA as the model compounds. But the structure of aluminum complexes with these model compounds was not clear yet. As the first step to understand the interaction between aluminum ion and model compounds in aqueous solution, we analyzed the Al *K* XANES spectra of two aluminum complexes using DV-Xα MO calculation, and discussed electronic and steric structure of those complexes in solid state.

【Experiment and calculation】

The Al *K* XANES spectra were collected on the BL7A at the UVSOR of the Institute for Molecular Science in Japan using two KTP(001) monochromator crystals. The storage ring was operating at the electron energy of 750 MeV. All of XANES spectra were detected by a total electron yield method. Based on crystal structures of Na[Ga(EDTA)] and K[Al(CyDTA)], the model structures of Na[Al(EDTA)] and K[Al(CyDTA)] for the DV-Xα MO calculation were constructed, respectively (Fig.1 and 2).

【Result and discussion】

The Al *K* XANES spectra of these compounds are shown in Fig. 3 and 4, and are represented by solid line. The absorption edges of two compounds are located on the same energy level. Furthermore, the shapes of XANES spectra are similar to each other, so it can be presumed that two compounds have the same surroundings of aluminum ions. The DV-Xα calculation was performed for two compounds. The obtained results were shown in Fig. 1 and 2, where straight lines are the probability of electron transition, broken lines are the calculated XANES spectra which were obtained by the probability of electron transition. For the two compounds, calculated XANES spectra reproduce experimental XANES spectra well. From this result, model structures for DV-Xα calculation were thought to be valid. Furthermore from the result of DV-Xα calculation, it is clear that

electron density of aluminum of Al(CyDTA) is more dense than that of Al(EDTA). Bond length of Al-O in Al(CyDTA) is shorter than that in Al(EDTA). This difference of bond length occurs by the difference of flexibility, which is caused by the difference between cyclohexane and ethylene in CyDTA and EDTA, respectively. Shorter the bond length, larger the relative electron density. Thus by not only the coordinated atom but also the degree of flexibility of the ligand, the electronic state of aluminum is influenced

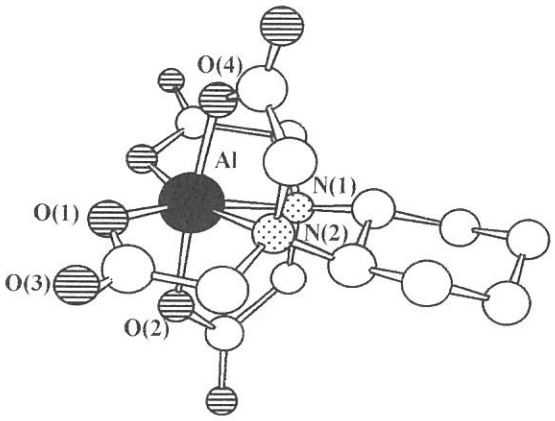

Fig. 1 The model structure of [Al(CyDTA)] for DV-Xα calculation.

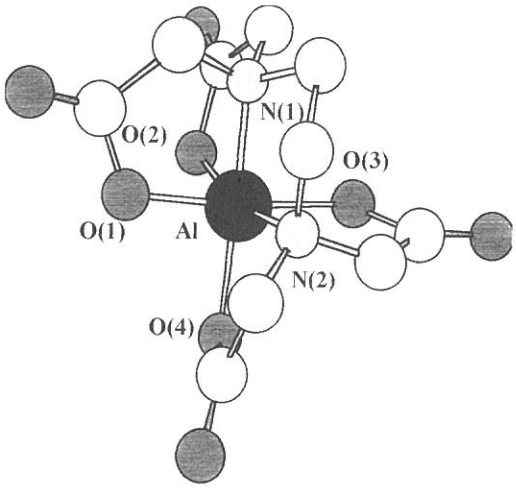

Fig. 2 The model structure of [Al(EDTA)] for DV-Xα calculation.

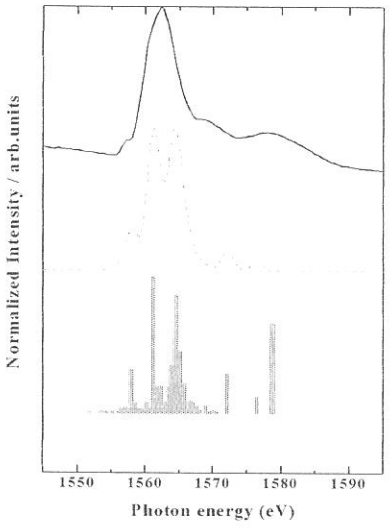

Fig. 3 Experimental and calculated Al *K* XANES spectra of [Al(CyDTA)]

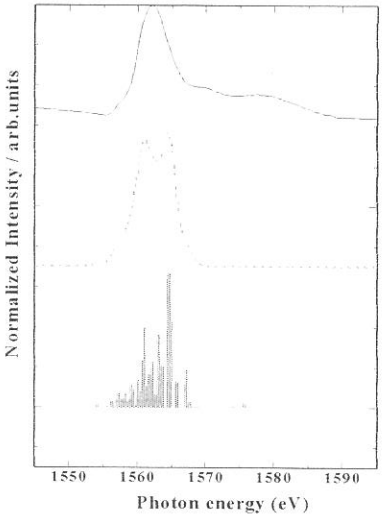

Fig. 4 Experimental and calculated Al *K* XANES spectra of [Al(EDTA)]

(BL8B1)

Changes in Electronic Structure by Li Ion Deintercalation in $LiCoO_2$ From Cobalt *L*-edge and Oxygen *K*-edge XANES

Yoshiharu Uchimoto
Department of Applied Chemistry, Graduate School of Science and Engineering, Tokyo Institute of Technology
Ookayama, Meguro, Tokyo 152-8552, Japan.

Lithium cobalt oxide, $LiCoO_2$, is used as the cathode active material in commercially available 4V-type lithium secondary because of its high theoretical energy density and good cycle performance. In the lithium secondary batteries, which are called 'rocking-chair' batteries, graphite is used as the negative electrode. During the charge and discharge process, lithium ions are transferred from one electrode to the other electrode through an intercalation and/or de-intercalation process. It is important to clarify the change of electronic structure during the charge and discharge process in order to understand the electrochemical properties. Recently first principle molecular orbital calculation studies of the electronic structure of the $Li_{1-x}CoO_2$ have been reported (1, 2). These calculation results indicate that the lithium ion deintercalation increases the covalent interaction between cobalt and oxygen and that the oxidation associated with the deintercalation mainly takes place on oxygen. However experimental information about the electronic structure change during the lithium ion deintercalation is insufficient. To our knowledge, the detailed electronic structure change during electrochemically intercalation and/or de-intercalation process has not yet been reported.

In this study, a measurement of cobalt L_{23}-edge and oxygen K-edge XANES was used to determine the electronic structure changes of $LiCoO_2$ during the electrochemical lithium ion deintercalation.

$LiCoO_2$ powder was prepared by conventional solid state reaction starting with lithium hydroxide (Wako Chemical Co. Inc., 99.9%) and cobalt hydroxide (Wako Chemical Co. Inc., 99.9%). A mixture of Li(OH) and $Co(OH)_2$ in a mole ratio of 1:1 was heated at 700℃ for 13 h in air atmosphere. The crystal structure of the product was determined by XRD using Mo-Ka radiation. $Li_{1-x}CoO_2$ oxides were prepared by electrochemical lithium de-intercalation. A mixture of 82.5 wt% $LiCoO_2$, 15 wt% acetylene black, and 2.5 wt% polytetrafluoropropylene binder was used as working electrode. Lithium metal was used as counter and reference electrode. The electrolyte was 1*M* lithium perchlorate in propylene carbonate solution.

Co L_{23}-edge XANES and oxygen *K*-edge XANES were measured on BL-8B1 beam line at UVSOR (Okazaki, Japan) with ring energy of 750 MeV in a mode of total electron yield at room temperature, respectively.

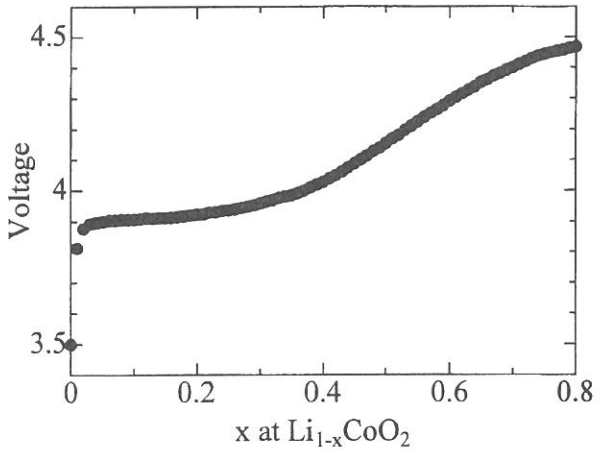

Figure 1
Electrode potential change of the $Li_{1-x}CoO_2$ electrode during the charge process.

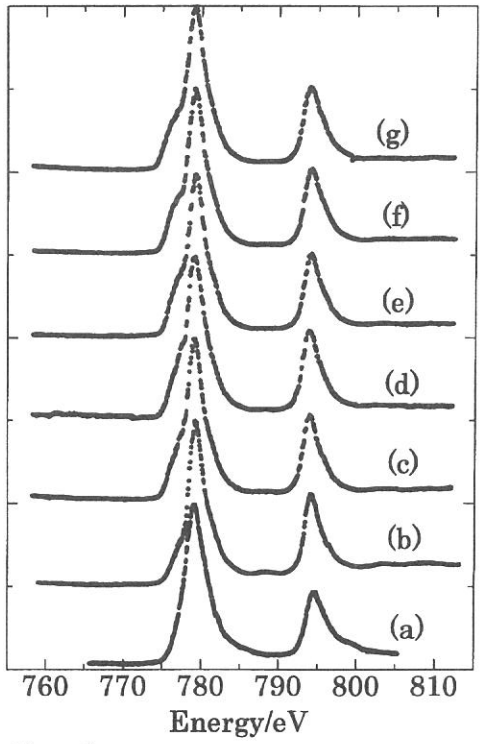

Figure 2
Co 2p absorption spectra of $LaCoO_3$ (a) and $Li_{1-x}CoO_2$ (b-g).
(b) 1.0, (c) 0.8, (d) 0.6, (e) 05, (f) 0.4, (g) 0.2

The XRD pattern of $LiCoO_2$ was indexed to a rhombohedral lattice and is in good agreement of that of $LiCoO_2$ (*R3m*). Figure 1 shows the electrode potential change during the electrochemical extraction of lithium from $LiCoO_2$ in the region from x = 0 to x = 0.8 of $Li_{1-x}CoO_2$. The electrode potential change is in good agreement with the open circuit voltage curve of $Li_{1-x}CoO_2$ reported by Mizushima et.al. (3).

Figure 2 shows the Co *L*-edge XANES of $Li_{1-x}CoO_2$ at various x values together with that of $LaCoO_3$ as model compounds of Co^{3+} oxidation state. The Co *L*-edge XANES shows two strong absorption features due to the spin-orbit splitting of the Co 2p core hole (Abbate *et al.*, 1993). The absorption about 779 eV is $2p_{3/2}$ (L_3) edge and that about 794 eV is $2p_{1/2}$ (L_2) edge. The Co *L*-edge XANES of $LiCoO_2$ is in good agreement that reported by Montoro et.al (4). The shape of the Co *L*-edge XANES of $LiCoO_2$ and $LaCoO_3$ close similarity of low-spin Co^{3+} (4). The Co *L*-edge spectra of $Li_{1-x}CoO_2$ (x=0.2, 0.4, 0.5, 0.6, 0.8, 1.0) do not exhibit chemical shift and the changes of the shape are small. The result that the XANES did not show any chemical shift indicates the Co ion in the $Li_{1-x}CoO_2$ is still trivalent Co^{3+} cations even at low x value of 0.2.

Figure 3 shows the oxygen K-edge XANES of $Li_{1-x}CoO_2$ at various x values. A peak at about 528-530 eV is attributed to transration to the unoccupied band derived from the mixing of the Co 3d states with oxygen 2p states. The broad structure about 535-550 eV is attributed to band of Co 4s and/or 4p character. The peak is broad, so that the peak is difficult to divide two characters. Figure 4 shows a magnified part of Figure 3 between 525 and 535 eV. The peak at about 527 eV increases with decreasing lithium content. This result shows that oxidation also takes place on oxygen 2p orbital and the ground state of $Li_{1-x}CoO_2$ is $Co^{3+}\underline{L}$, where $\underline{L}$ represents a ligand hole state. This phenomenon indicates that the oxidation by anode reaction of lithium deintercalation mainly takes place by using oxygen 2p orbital but Co 3d orbital. This is in good agreement with the result of First-Principles calculation for $Li_{1-x}CoO_2$ oxides (2).

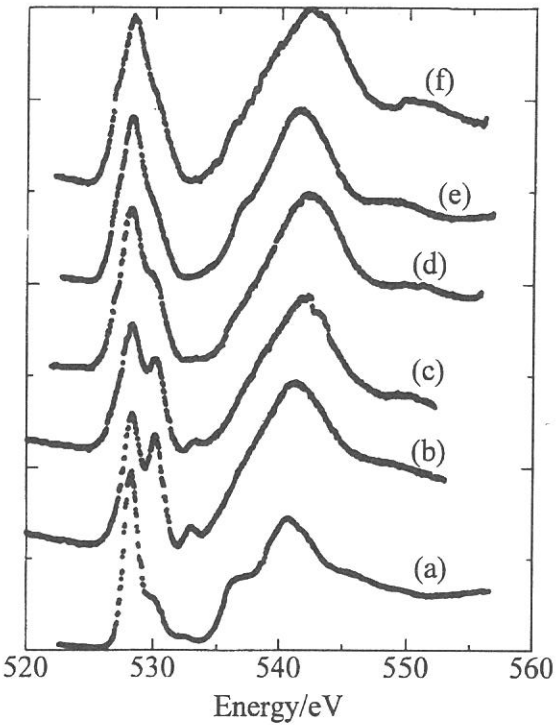

Figure 3
O 1s absorption spectra of $Li_{1-x}CoO_2$.
(a)1.0, (b) 0.8, (c) 0.6, (d) 05, (e) 0.4, (f) 0.2

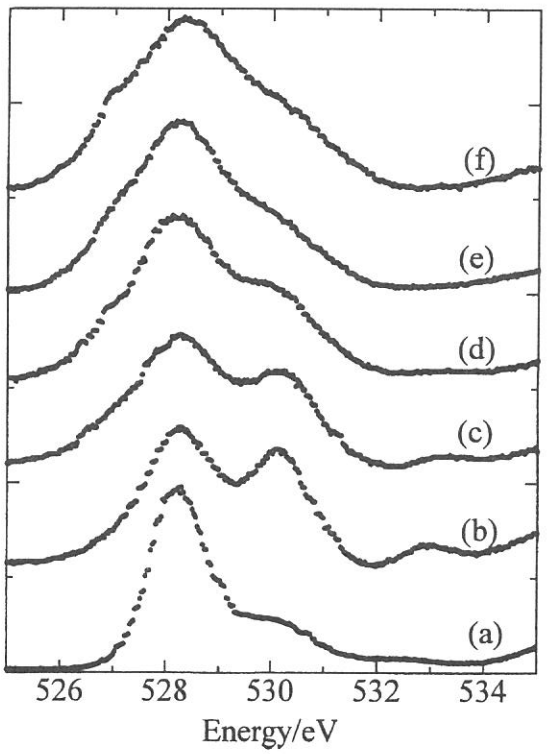

Figure 4
O 1s absorption spectra of $Li_{1-x}CoO_2$ between 525 and 535eV.
(a)1.0, (b) 0.8, (c) 0.6, (d) 05, (e) 0.4, (f) 0.2

References

1) Aydiol, M.K., Kohan, A.F., Cedar, G., Cho, K., & Joannopoulos, J., (1997). *Phys. Review B,* **56**, 1354-1365.

2) Koyama, Y., Tanaka, I., Kim, Y.S., Nishitani, S.R., & Adachi, H., (1999). *Jpn. J. Appl. Pys.*, **38**, 4804-4808.

3) Mizushima,K., Jones, P.C., Wiseman, P.J., & Goodenough, J.B., (1980). *Mater. Res. Bull.*, **15**, 783-789.

4) Montoro, L.A., Abbate, M., Almeida, E.C., & Rosolen, J.M., (1999) *Chem. Phys. Lett.*, **309**, 14-17.

(BL8B2)

Electronic structure and molecular orientation at the surface of poly(9-vinylcarbazole) thin film studied by angle-resolved ultraviolet photoelectron spectroscopy

K.K.Okudaira, Y.Azuma, S.Hasegawa[A], K.Seki[B], and N.Ueno[C]

Graduate School of Science and Technology, Chiba University, Chiba 263-8522
[A]Institute for Molecular Science. Okazaki, 444-8585
[B]Faculty of Science, Nagoya University, Nagoya 464-8602
[C]Department of Materials technology, Faculty of Engineering, Chiba University, Chiba 263-8522

Thin films of pendant group polymers are widely used in practical applications due to molecular stability and facility of preparation. Since the properties of organic devices consisting of the films depend strongly on the molecular orientation at the film surfaces, determination of the surface molecular orientation such as tilt angle distribution of pendant group is very important for understanding the device properties.

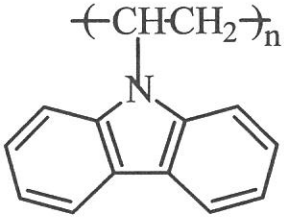

Figure 1 Molecular structure of poly(9-vinylcarbazole)

Angle-resolved ultraviolet photoelectron spectroscopy (ARUPS) using synchrotron radiation offers information on the geometrical structure of thin films as well as on their electronic structures. From the comparison between ARUPS and near-edge X-ray absorption fine structure (NEXAFS) of poly(2-vinylnaphthalene) (PvNp) thin film, we showed that the tilt angle distribution of the pendant groups of PvNp is well described by the three-dimensional isotropic random orientation. [1]

In the report, we investigated the orientation of pendant groups at the surface of poly(9-vinylcarbazole) (PvCz) [see Fig. 1] thin film using ARUPS and NEXAFS spectroscopy. The pendant carbazole group of PvCz has a large π electron system as PvNp. However, it has a larger heterocyclic ring in comparison with the pendant naphthalene group of PvNp. The surface pendant-group orientation of PvCz film is thus expected to be different from that of PvNp.

ARUPS measurements were carried out at the beamline BL8B2 of the UVSOR at the Institute for Molecular Science. ARUPS spectra were measured at hν=40eV and at normal incidence (incidence angle of photon α=0°). Thin films of PvCz were prepared by spincasting on Au-evaporated Si(100) wafers from toluene solutions of 0.3wt/vol%. The film thickness prepared in this way is about 100Å.

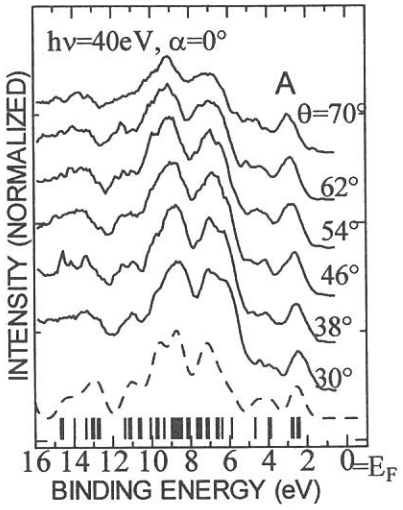

Figure 2 ARUPS of PvCz thin films spincasted from 0.3 wt/vol% toluene solution at hν=40eV and α=0° as a function of take-off angle (θ). The vertical bars show the molecular orbital energies calculated by *ab initio* MO calculation (STO-6G). The density of states (DOS) is represented by (– – – – –) (see text). The calculated binding energy scale was contracted by 1.35 and shifted to fit with the experimental results.

Figure 2 shows the ARUPS spectra of the PvCz thin film as a function of the take-off angle (θ). The intensity of top band A shows slight θ dependence. The calculated density-of-states (DOS) using molecular orbital (MO) calculation (STO-6G) is also shown in Fig.2. The MO calculation was performed for a model compound [CH_3-CH($NC_{12}H_8$)-CH_3] of the polymer unit, and the DOS was obtained by a Gaussian broadening (FWHM = 0.8 eV) of the MO levels. The agreement between the observed spectra and the DOS indicates that the electronic structure of PvCz is well simulated by that of

the model compound. The band A in the spectra originates from two top π states at the pendant carbazole and hereafter we focus on the θ dependence of the intensity of the band A to determine the orientation of the pendant carbazole groups at the surface.

In order to obtain the molecular orientation of the pendant carbazole, we made the analyses of the θ dependence in the single-scattering approximation combined with molecular orbital (SS/MO) approximation.[2] The calculations were performed for the model compound. The phase shift and radial matrix element were calculated for all subshells of the atoms constituting the molecules using the Muffin-tin potential,[3] and the potential between the Muffin-tin spheres was assumed to be zero. In the present calculation we used the phenomenological electron mean-free path of 8 Å to calculate the damping factor.[4] We further assumed an azimuthal disorder for the rotational orientation of the pendant carbazole groups with respect to the surface normal. For the calculation of photoelectron intensity, we introduced an inclination angle (β) of the molecular plane of pendant carbazole groups with respect to the film surface.

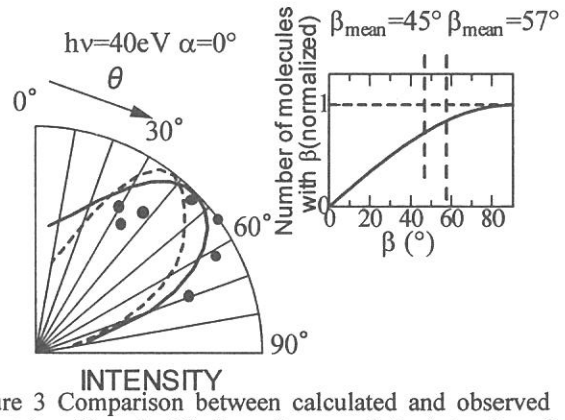

Figure 3 Comparison between calculated and observed (●) take-off angle (θ) dependences of the intensity of the band A. All calculations were carried out by the SS/MO approximation. The calculated result for 3-dimensional isotropic orientation (model 1) shown in the inset is represented by (———). The calculated result for an orientation where an orientation where the tilt angel β varies between 0° and 90° with the uniform distribution (model 2) is represented by (– – – – –). For each model, the β dependence of the number of molecules is shown in the inset.

In Fig. 3, the observed θ dependence of the intensity of the band A is compared with calculated results for two orientation models, namely (1); three-dimensional isotropic random orientation model which has a mean β value (β_{mean}) of 57°, and (2) an orientation model where the tilt angel β varies between 0° and 90° with the uniform distribution; thus β_{mean} = 45°. The calculated θ pattern for the model 1 is in better agreement with observed one than that for the model 2. It should be noted, however, that the observed θ dependence peaks clearly at larger θ than the calculated one for the model 1. It indicates that at the surface of PvCz film there are more pendant groups with large tilt angles than the orientation model 1. This different pendant-group orientation between PvCz and PvNp film can be ascribed to the difference in the size and chemical structure of pendant groups.

The β value of 60° determined by the NEAXFS study (not shown) is slightly larger than β_{mean} of 57° for the model 1. This result is consistent with that obtained from the ARUPS analyses. The present results indicate that the surface electronic states of PvCz may be rather dominated by σ(C-H) states at the pendant carbazole group than π states.

REFERENCES

[1]E.Morikawa, V.Saile, K. K. Okudaira, Y.Azuma, K.Meguro, Y.Harada, K.Seki, S.Hasegawa, and N.Ueno, J. Chem. Phys. **112** 10476(2000)

[2]N.Ueno, A.Kitamura, K.K.Okudaira, T.Miyamae, S.Hasegawa, H.Ishii, H.Inokuchi, T.Fujikawa, T.Miyazaki, and K.Seki, J.Chem.Phys., **107** 2079(1997).

[3]D.Dill and J.L.Dehmer, J.Chem.Phys., **61** 692 (1974).

[4]K. K. Okudaira, E. Morikawa, D.A.Hite, S. Hasegawa, H. Ishii, M. Imamura, H. Shimada, Y. Azuma, K. Meguro, Y. Harada, V. Saile, K. Seki, and N. Ueno, J.Electron Spectrosc.Relat.Phenom. 101-103, **389**(1999).

(BL8B1)

Changes in Electronic Structure by Li Ion Deintercalation in $LiNiO_2$ from Nickel *L*-edge and O *K*-edge XANES

Yoshiharu Uchimoto
Department of Applied Chemistry, Graduate School of Science and Engineering, Tokyo Institute of Technology
Ookayama, Meguro, Tokyo 152-8552, Japan.

$LiNiO_2$ oxide with a layered α-$NaFeO_2$ structure is one of the most promising cathode materials used in 4V-type lithium ion batteries because its low cost and high theoretical energy density. It is important to clarify the change of electronic structure during charge and discharge process in order to understand the electrochemical properties. Recently, first-principle molecular orbital calculations of the electronic structure of the $Li_{1-x}NiO_2$ have indicated that lithium ion deintercalation increases the covalent interaction between Ni and oxygen, and that the oxidation associated with the deintercalation mainly takes place on oxygen. [1-2] However, experimental studies of the electronic structure change during the lithium ion deintercalation are insufficient.In this study, Ni L_{23}-edge and O *K*-edge X-ray Absorption Near Edge Structure (XANES) was determined the electronic structure of $LiNiO_2$ during lithium ion deintercalation.

$LiNiO_2$ powder was prepared by conventional solid state reaction starting with lithium hydroxide (Wako Chemical Co. Inc., 99.9%) and nickel hydroxide (Wako Chemical Co. Inc., 99.9%). A mixture of Li(OH) and $Ni(OH)_2$ in a mole ratio of 1:1 was heated at 770°C for 30 h in an oxygen atmosphere. The crystal structure of the product was determined by XRD using Mo-K radiation. Li_xNiO_2 was prepared by electrochemical lithium deintercalation. A mixture of 82.5 wt% $LiNiO_2$, 15 wt% acetylene black, and 2.5 wt% polytetrafluoropropylene binder was used as working electrode. The electrolyte was a 1*M* $LiClO_4$ in PC solution. Ni L_{23}-edge XANES spectra were measured on the BL-7A beam line and O *K*-edge XANES were measured on the BL-8B1 beam line at UVSOR (Okazaki, Japan) with a ring energy of 750 MeV in a mode of total electron yield at room temperature.

The XRD pattern for $LiNiO_2$ was indexed in a rhombohedral *R3m* space group. The first-cycle discharge capacity is 140 mAh g^{-1}. Fig. 1 shows the Ni *L*-edge XANES of Li_xNiO_2 for various x values. The Ni *L*-edge XANES shows two strong absorption features of the spin-orbit splitting of the Ni 2p core hole. [3] The absorption near 852-856 eV is the $2p_{3/2}$ (*L3*) edge and that near 868-872 eV is the $2p_{1/2}$ (*L2*) edge. The XANES for $LiNiO_2$ is similar to that for NiO, which shows the Ni ions in $LiNiO_2$ to be Ni^{2+} ions in a high-spin state. [4] The spectra for Li_xNiO_2 (x=0.2, 0.4, 0.5, 0.6, 0.7, 0.8, 0.9, 1.0) do not exhibit chemical shift and the change in shape are small, indicating the Ni ion in the Li_xNiO_2 is still Ni^{2+} even at as low an x value as 0.2.

Fig. 2 shows the O *K*-edge XANES for Li_xNiO_2 for various x values. The peak at about 532 eV (●) is attributed to oxygen in the substrate. A peak at about 533 eV is attributed to the band derived from the mixing of the Ni 3d states with O 2p states. The broad structure near 535-550 eV is attributed to a Ni band with 4sp character. The peak at near 528 eV increased with decreasing lithium content. This result shows that oxidation influences the oxygen 2p orbital and the ground state of Li_xNiO_2 ($x<1.0$) is $Ni^{2+}\underline{L}$, where $\underline{L}$ represents a ligand hole state. [4] This indicates that the lithium deintercalation reaction does not involve Ni but oxygen.

REFERENCES

1) M.K. Aydinol, A.F. Kohan and G. Cedar, *J. Power Sources*, **68**, 664(1997).
2) Y. Koyama, Y.S. Kim, I. Tanaka and H. Adachi, *Jpn. J. Appl. Pys.*, **38**, 2024 (1999).
3) J. van Elp, B.G. Searle, G.A. Sawatzky and M. Sacchi, *Solid State Communication*, **80**, 67 (1991).
4) P. Kuiper, G. Kruizinga, J. Ghijsen, G.A. Sawatzky and H. Verweij, *Phys. Rev. Lett.*, **62**, 221 (1989).

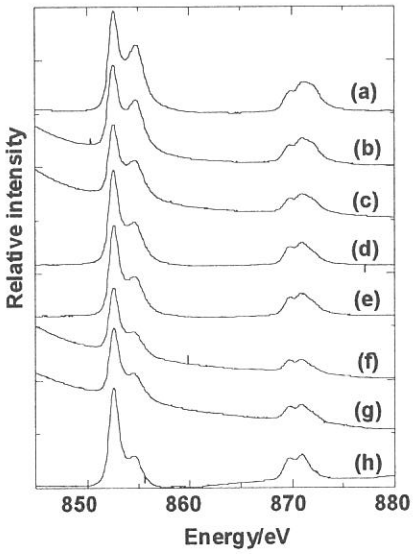

Fig. 1 Ni 2p absorption spectra for Li_xNiO_2:
(a) 0.2, (b) 0.4, (c) 0.5, (d) 0.6, (e) 0.7, (f) 0.8, (g) 0.9, (h) 1.0

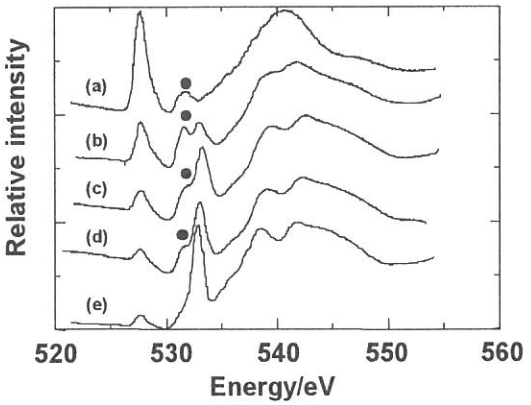

Fig. 2 O 1s absorption spectra for Li_xNiO_2:
(a) 0.2, (b) 0.5, (c) 0.6, (d) 0.8, (e) 1.0

UVSOR

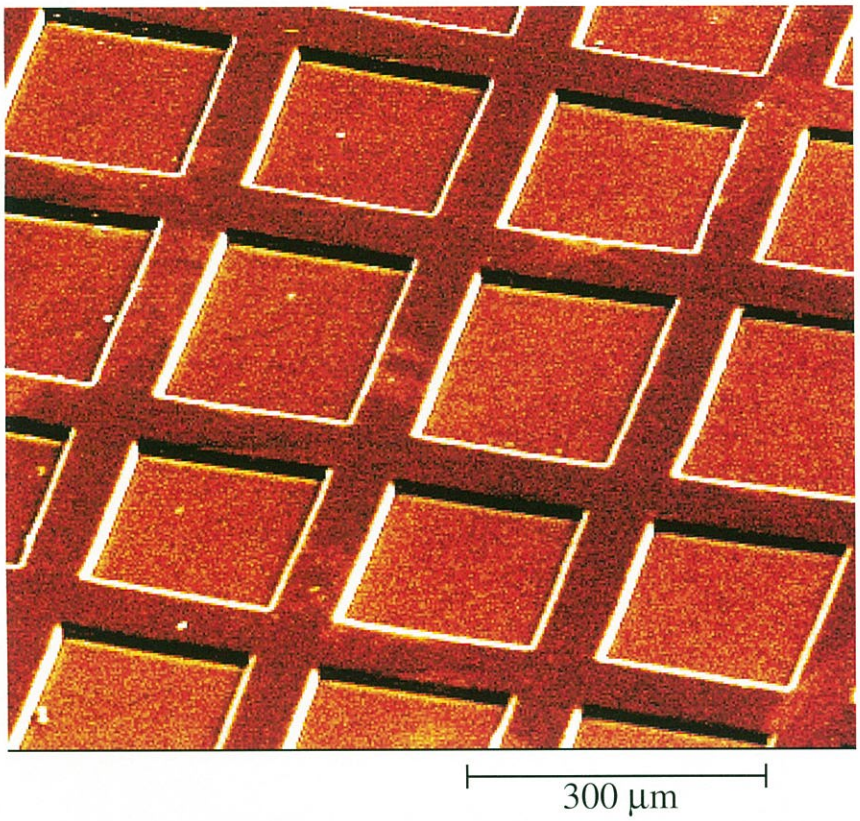

Surface and Photochemistry

BL2B1, 3A1, 4A1, 4A2, 5B, 6B, 8A

BL4A-2

Ideal H-terminated Si(100) Surface Formation By Dry Process And Its Reactive Properties

Zhihong Wang[1], Hideyuki Noda [1], Youichi Nonogaki[2] and Tsuneo Urisu [2]
([1]The Graduate University for Advanced Studies, [2]Institute for Molecular Science)

The preparation of ideal Si(100) surfaces which are free of contamination and defects is important in both the fields of semiconductor device fabrication technology and surface science. The wet treatment using HF solution can only provides ideal H-terminated Si(111) surfaces, but it results in rough Si(100) surfaces. Concerning H-terminated Si(100) surfaces, we have found that they are very stable under synchrotron irradiation. However, the chemical stability against contamination is not well known. In this work, an ideal H-terminated Si(100) surface prepared in ultrahigh vacuum by the dry process is monitored with BML-IRRAS to investigate the chemical stability of the surface. Figure 1 shows the dependence of the coupled Si-H symmetric stretching peak integrated absorbance (IA) and its peak position on the adsorption temperatures. Figure 2 shows the adsorption temperature dependence of the peaks width. If we assume that the coverage θ of the Si-H at the stationary state is given by $\theta = \Gamma/(k+\Gamma)$, (k and Γ are the desorption and the adsorption rate, respectively). The coverage θ of Si-H is calculated by fitting the equation to the observed IA and using the reported activation energy 2.82eV for k as show in Fig. 1. From these data, it is concluded that the ideal H-terminated surface is given at the temperature range T$\approx$400 ~ 440 °C (θ >0.99). The chemical stability of this surface for the H_2O and D_2O exposures is going to be investigated.

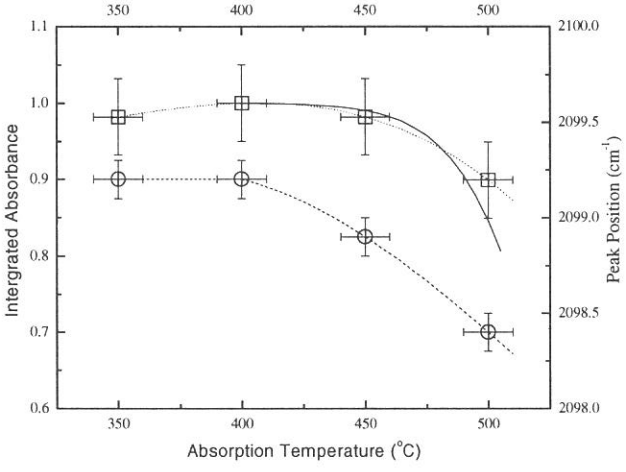

Fig.1 Dependence of IA(□) and the peak position(○) of the Si-H symmetric stretching peak on the hydrogen atom adsorption. ------: smoothly fitted line, —— : calculated coverage of Si-H. IA is normalized to 1 at the maximum.

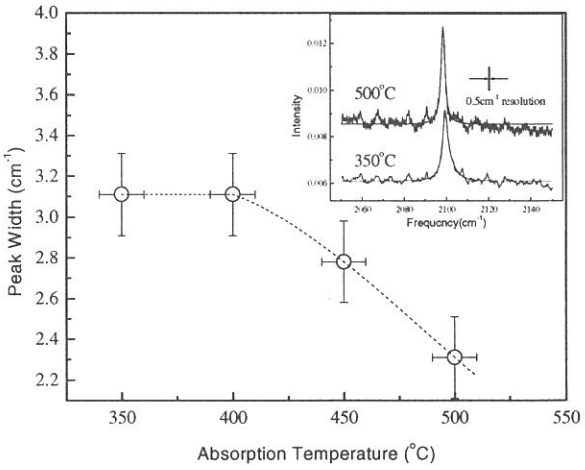

Fig. 2 Dependence of the peak width of the Si-H symmetric stretching peak on the hydrogen atom adsorption temperature.
Inserted figure is the observed IR spectra.

(BL2B1)

Layer-Resolved Auger Spectra of $CF_3CD(OH)CH_3$ on a Si(100) Surface

Shin-ichi NAGAOKA, Arinobu NAKAMURA,[A] Kazuhiko MASE[B] and Shin-ichiro TANAKA[C]

Institute for Molecular Science, Okazaki 444-8585

[A]Department of Chemistry, Faculty of Science, Ehime University, Matsuyama 790-8577

[B]Photon Factory, Institute of Materials Structure Science, High Energy Accelerator Research Organization, 1-1 Oho, Tsukuba 305-0801

[C]Department of Physics, Graduate School of Science, Nagoya University, Chikusa-ku, Nagoya 464-8602

The study of adsorbate properties and behaviors on substrates has attracted considerable attention. Chiang et al. previously reported the observation of layer-resolved shifts of photoemission spectra from physisorbed rare-gas multilayers [1]. The shifts were explained in terms of difference in final-state hole-screening energy. We previously studied the photoelectron spectra (PES) of $CF_3CD(OH)CH_3$ (TFIP-d_1) on Si(100) and found that similar shifts can be revealed in the binding energies of the C:1s core-level, the O:1s core-level and the valence level [2]. In the present study, we have studied the Auger spectra of TFIP-d_1 on Si(100) and found that similar shifts are also evident in the Auger spectra.

TFIP-d_1 was prepared with the reaction of CF_3COCH_3 and $LiAlD_4$. The amount-regions of gas exposure corresponding to the monolayer coverage and the multiplayer coverage were determined by observing the development of the ion intensity as a function of the amount of gas exposure; the plot of the ion intensity versus the amount of gas exposure was discontinuous between the two regions. The experiments were performed using a double-pass cylindrical-mirror electron-energy analyzer (ULVAC-PHI) and a home-built time-of-flight ion-detection assembly coupled to a grasshopper monochromator (Mark XV) installed on the BL2B1 beamline [3].

Figures 1a-3a show the C, O and F:KVV normal Auger spectra (NAES) of TFIP-d_1 monolayer and multiplayer on a Si(100) surface. Figures 1b-3b show the C, O and F:KVVσ^* resonant Auger spectra (RAES) . The peaks in the spectrum of the multilayer are shifted to lower kinetic energies from those of the monolayer. The absolute values of the shift are summarized in Table 1. As in the case of rare-gas [1], the shift in NAES is three times as large as that in the corresponding PES, and thus can be explained in terms of difference in final-state hole-screening energy.

Table 1 Spectral shift in eV between monolayer and multiplayer

	PES	NAES	RAES
C:1s	0.5	1.5	0.7
O:1s	0.5	1.5	0.7
F:1s	<0.3	0.6	0.4

Further investigations on the site-specific fragmentation in TFIP-d_1 [4,5] are in progress.

[1] T.-C. Chiang, G. Kaindl and T. Mandel, Phys. Rev. B **33**, 695 (1986).

[2] S. Nagaoka, A. Nakamura, K. Mase and S. Tanaka, UVSOR Activity Report, **27**, 120 (1999).

[3] S. Tanaka, N. Takahashi, K.-P. Lee and M. Kamada, J. Electron Spectrosc. Relat. Phenom. **80**, 205 (1996).

[4] A. Nakamura, S. Nagaoka, K. Mase, S. Tanaka and T. Urisu, UVSOR Activity Report, **26**, 100 (1998).

[5] K. Mase, S. Tanaka, S. Nagaoka and T. Urisu, Surf. Sci. **451**, 143 (2000).

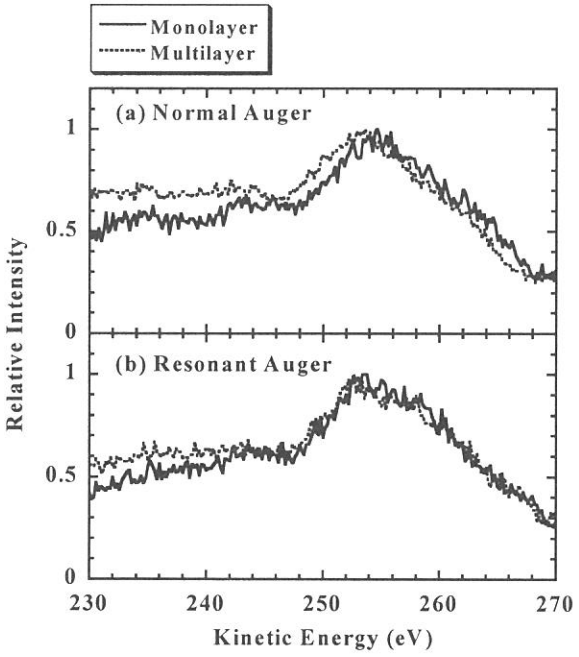

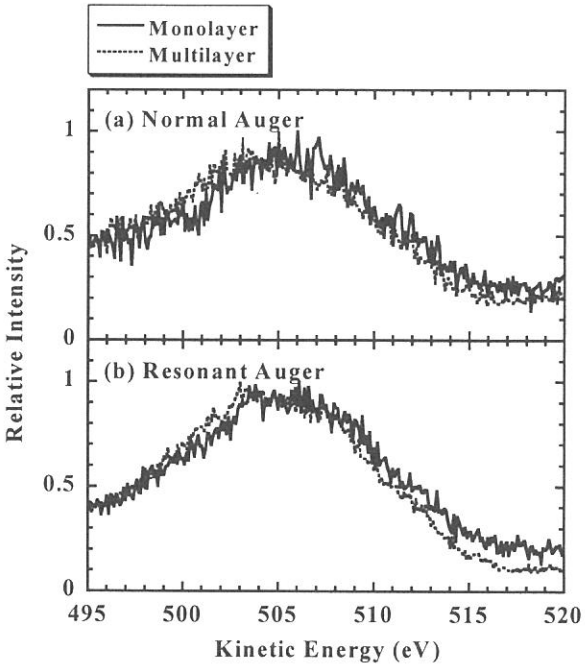

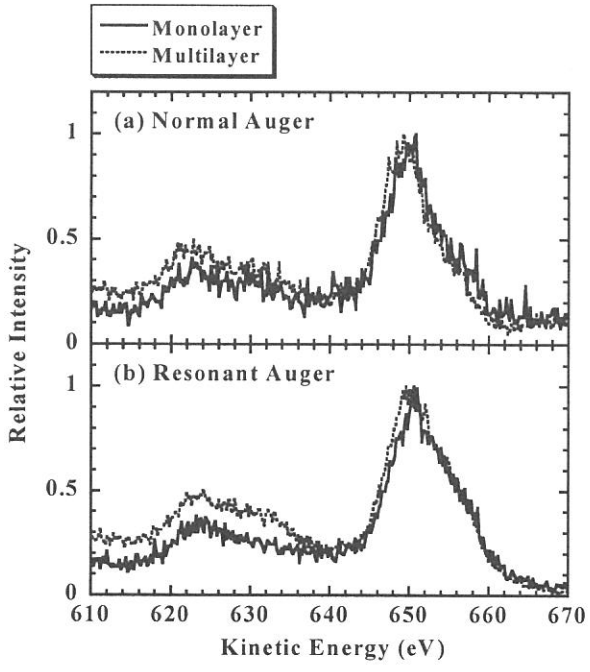

Figure 1 (upper left-hand side). C:1s Auger spectrum of TFIP-d_1 on a Si(100) surface. (a) KVV NAES. (b) KVVσ* RAES.

Figure 2 (upper right-hand side). O:1s Auger spectrum of TFIP-d_1 on a Si(100) surface. (a) KVV NAES. (b) KVVσ* RAES.

Figure 3 (bottom). F:1s Auger spectrum of TFIP-d_1 on a Si(100) surface. (a) KVV NAES. (b) KVVσ* RAES.

(BL2B1)

Site-Specific Fragmentation Following C:1s Core-Level Photoionization of $CF_3CD(OH)CH_3$ on a Si(100) Surface

Shin-ichi NAGAOKA, Arinobu NAKAMURA,[A] Shin-ichiro TANAKA[B] and Kazuhiko MASE[C]

Institute for Molecular Science, Okazaki 444-8585

[A]Department of Chemistry, Faculty of Science, Ehime University, Matsuyama 790-8577

[B]Department of Physics, Graduate School of Science, Nagoya University, Chikusa-ku, Nagoya 464-8602

[C]Photon Factory, Institute of Materials Structure Science, High Energy Accelerator Research Organization, 1-1 Oho, Tsukuba 305-0801

Synchrotron radiation has provided a powerful means to obtain information about core-level excitations, and the dynamic processes following the core-level excitations in molecules have long been a subject of interest. In contrast to valence electrons that are often delocalized over the entire molecule, the core electrons are localized near the atom of origin. Although core electrons do not participate in the chemical bonding, the energy of an atomic core-level in the molecule depends on the chemical environment around the atom. A shift in the energy levels of core electrons that is due to a specific chemical environment is called a chemical shift.

Monochromatized synchrotron radiation can excite core electrons of an atom in a specific chemical environment selectively, discriminating the core electrons from those of like atoms having different chemical environments. This site-specific excitation often results in site-specific fragmentation, which is of importance in understanding localization phenomena in chemical reactions and which is potentially useful for synthesizing materials through selective bond breaking. Synchrotron radiation can indeed play the part of an optical knife for molecules. When bond dissociation around an atomic site is required in the synthesis, one can use the optical knife that has the photon energy corresponding to the specific excitation of that site.

To elucidate the site-specific fragmentation, we have studied the spectroscopy and dynamics following core-level photoionization of various molecules condensed on surfaces [1-4]. In the present work, we have used the energy-selected-photoelectron photoion coincidence (ESPEPICO) method to study the site-specific fragmentation following C:1s photoionization of $CF_3CD(OH)CH_3$ (TFIP-d_1) on a Si(100) surface. Since the chemical environments of a C atom bonded to three F atoms (C[F]), of C bonded to three H atoms (C[H]) and of C bonded to an OH group (C[O]) are different from one another, TFIP shows occurrence of different chemical shifts [4]. Thus it seems likely that TFIP-d_1 will show site-specific fragmentation.

Figures 1a, b and c respectively show the ESPEPICO spectra obtained with emissions of the C[O]:1s, C[H]:1s and C[F]:1s electrons of TFIP-d_1 monolayer adsorbed on a Si(100) surface. Figures 2a-c show the corresponding spectra of TFIP-d_1 monolayer adsorbed on Si(100) and

annealed at room temperature. Figures 3a-c show the corresponding spectra of TFIP-d_1 multilayer condensed on Si(100). H^+ ion is predominantly desorbed coincidentally with the C[H]:1s and C[O]:1s electrons in Figures 2a and b. In contrast, F^+ ion is predominantly desorbed coincidentally with the C[F]:1s electron. Such site-specific fragmentation is not clearly revealed in Figures 1 and 3. Further investigations are clearly needed on the reason for this difference.

[1] S. Nagaoka, K. Mase, M. Nagasono, S. Tanaka, T. Urisu and J. Ohshita, J. Chem. Phys. **107**, 10751 (1997).

[2] S. Nagaoka, K. Mase and I. Koyano, Trends Chem. Phys. **6**, 1 (1997).

[3] S. Nagaoka, K. Mase, M. Nagasono, S. Tanaka, T. Urisu, J. Ohshita and U. Nagashima, Chem. Phys. **249**, 15 (1999).

[4] K. Mase, S. Tanaka, S. Nagaoka and T. Urisu, Surf. Sci. **451**, 143 (2000).

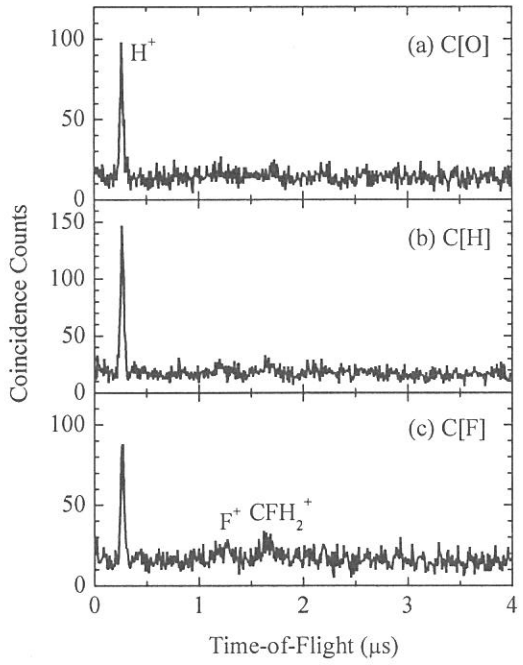

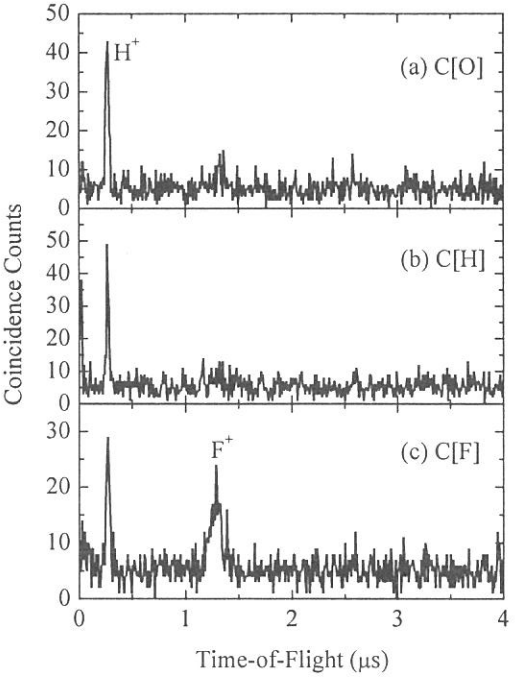

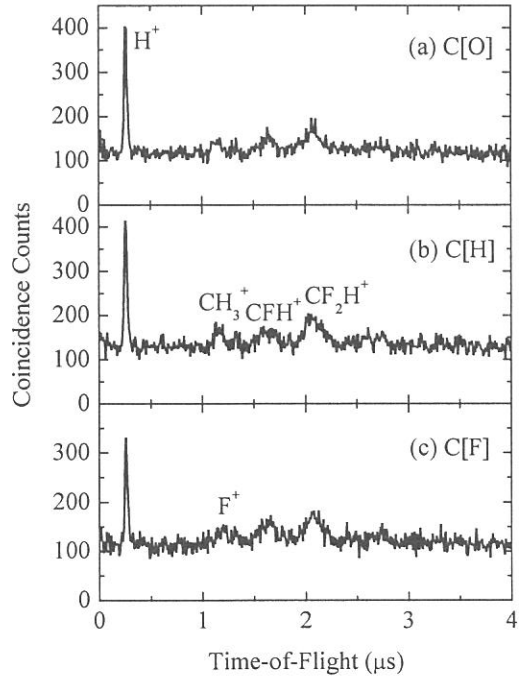

Figure 1 (left-hand side). ESPEPICO spectra of TFIP-d_1 monolayer adsorbed on a Si(100) surface. The spectra were taken at a photon energy of 398.1 eV and the data collection time was 4500 s.

Figure 2 (right-hand side). ESPEPICO spectra of TFIP-d_1 monolayer adsorbed and annealed on a Si(100) surface at room temperature. 4200 s.

Figure 3 (bottom). ESPEPICO spectra of TFIP-d_1 multilayer condensed on a Si(100) surface. 3900 s.

(2B1)

Observation of the surface states on the TiO_2(110) surface by using the photo-stimulated ion desorption.

S. Tanaka[1], S. Nagaoka[2] and K. Mase[3]

[1]Department of Physics, Graduate School of Science, Nagoya University, Furo-cho, Chikusa, Nagoya 464-8602, Japan

[2]Institute for Molecular Science, Myodaiji, Okazaki 444-8585, Japan

[3]Institute for Material Structure Science, Tsukuba 305-0801, Japan

Introduction A number of investigations have been carried out on the surface of the TiO_2, and a rutile (110) surface has been particularly studied by many authors. However, many things still remain unknown. For instance, intrinsic surface states of the rutile (110) surface have not yet experimentally observed although some theoretical calculations have predicted that they would have different binding energies. In this report, we measure the photo-stimulated desorption in order to observe the NEXAFS (Near edge X-ray absorption fine structure) of the rutile (110) surface, and detected the surface (unoccupied) states.

Experiments All experiments have been carried out at the BL2B1 of the UVSOR, IMS. Soft-X ray of photon energies near the Ti-$L_{2,3}$ and O-K thresholds were monochromized by a grasshopper monochromator, and injected to the rutile (110) surface. Ejected ions and electrons as functions of photon energies were detected by a home-made EICO (Electron-Ion Coincidence) apparatus which equipped with a CMA (Cylindrical Mirror Analyzer) for electrons and a TOF tube for ions. Coincidence measurements with electrons and ions were separately carried out in order to determine ion species. The rutile (110) surface was cleaned by Ar^+ sputtering and heating followed by annealing in oxygen (10^{-6} Torr). It was a nearly perfect surface, in which a number of oxygen vacancies was small as observed with the photoelectron spectroscopy.

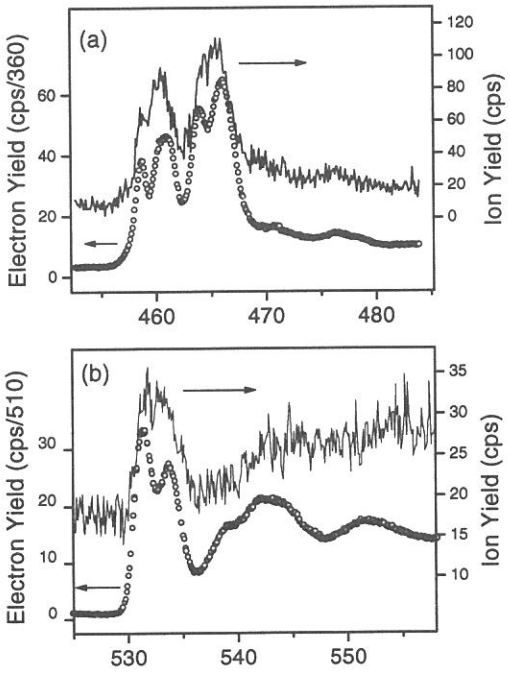

Figure 1

Results and Discussion Figure 1 shows electron (open circles) and ion (solid lines) yields near (a):Ti-$L_{2,3}$ and (b):O-Kedges. The electron yield predominantly represents the bulk absorption, and ion yield the surface absorption. In these spectra, desorbed ions were mostly O^+ according to the coincidence measurements. Here, we focus on near edge structures, because it is expected that they show electronic structures (density of states) of the unoccupied states. In figure 2, curves (a) and (b) show the ion yields and (c) and (d) show the electron yields, where the x axis represents the relative energies referred to the threshold at Ti-L_3 (a and c) and O-K (b and d) edges, which approximately indicates the binding energy of the unoccupied states from the Fermi level. Because the core electron is strongly localized, the absorption curve is expected to indicate the partial density of states at the atoms involving the core electron to participate the transition. Thus, the spectra at the O-K edges approximately show the O-2p contribution to the unoccupied levels, and those at the Ti-L_3 edges show the Ti-3d contribution. The density of states observed in fig. 2 for Ti-3d and O-2p are rather similar to each other both in electron (bulk sensitive) and ion (surface sensitive) yields. It indicates that the hybridization between the Ti-3d and O-2p is strong in the unoccupied states of the rutile, and rules out a simple picture that the rutile is an ionic crystal where O-2p is fully occupied and Ti-3d is fully empty. Ti-3d splits into t_{2g} and e_g levels due to the crystal field made by surrounding oxygen ions. It is interesting to point out that the e_{2g} energies observed in the ion yields is shifted by about 1 eV compared to the electron yield while the t_{2g} levels do not show such differences. It is known that the energy of e_g is more sensitive to the symmetry of the crystal field than that of the t_{2g}. Thus, it is reasonable to conclude the 1 eV shift is a bulk-to-surface shift in the binding energies of the e_g level at the rutile surface. This shift is consistent with the experimental work. This is the first observation of the intrinsic surface states on the rutile(110) surface to our knowledge.

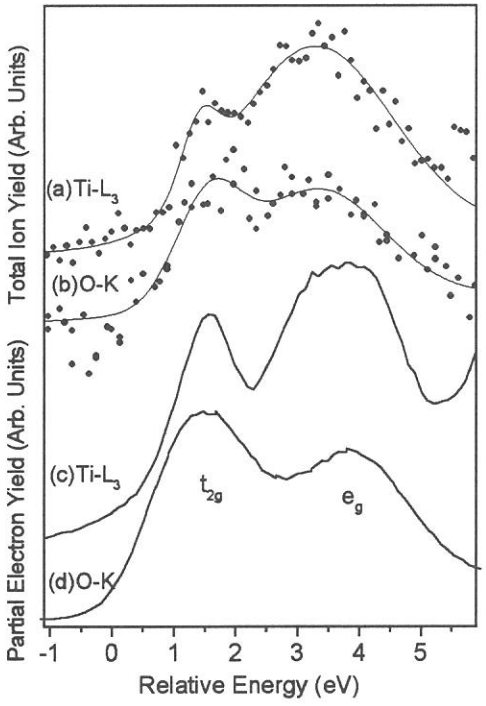

Figure 2

(2B1)

Ion Desorption from $H_2O/ZnO(10\bar{1}0)$ and $H_2O/TiO_2(110)$ surfaces induced by the core-level excitation

S. Tanaka[1], S. Nagaoka[2] and K. Mase[3]

[1]Department of Physics, Graduate School of Science, Nagoya University, Furo-cho, Chikusa, Nagoya 464-8602, Japan

[2]Institute for Molecular Science, Myodaiji, Okazaki 444-8585, Japan

[3]Institute for Material Structure Science, Tsukuba 305-0801, Japan

Ion desorption from solid surfaces is one of the most fundamental processes in the photochemical reaction. In this report, a comparison in the hydrogen ion desorption from water-chemisorbed ZnO and TiO_2 surfaces will be presented, and a mechanisms of them will be discussed.

A nominal electronic configuration of ZnO is $(Zn3d)^{10}(O2p)^6$, and that of TiO_2 is $(Ti3d)^0(O2p)^6$. However, in both metal oxides, the hybridization among electrons in metal and oxygen atoms is considerably large. It is generally accepted that water dissociates on $ZnO(10\bar{1}0)$ and $TiO_2(110)$ surfaces and the OH species is bonded to the metal (Zn and Ti) atoms mainly at the oxygen vacant site according to previous studies.

We made photoelectron-photoion coincidence measurements on both surfaces. The experiments have been carried out at BL2B1 of UVSOR. The samples were cleaned by Ar^+ sputtering and annealing in UHV and oxygen ($1x10^{-6}$ Torr). Samples were heated to high temperature (about >900K) in UHV at the final stage of the cleaning to produce oxygen vacancies at the surfaces, then exposed to H_2O gas at room temperature.

Figure 1 shows a photoelectron and photoelectron-photoion coincidence spectra for the water-chemisorbed $ZnO(10\bar{1}0)$ surface. The left-hand side shows a photoelectron spectrum and the right-hand side shows TOF spectra of ions to be triggered by the detection of photoelectrons whose kinetic energies are indicated by bars in the left-hand side. The photon energy used was 680 eV. Peaks observed in the photoelectron spectrum are ascribed to the oxygen

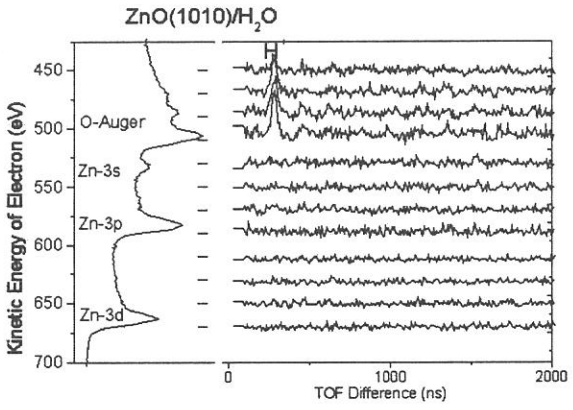

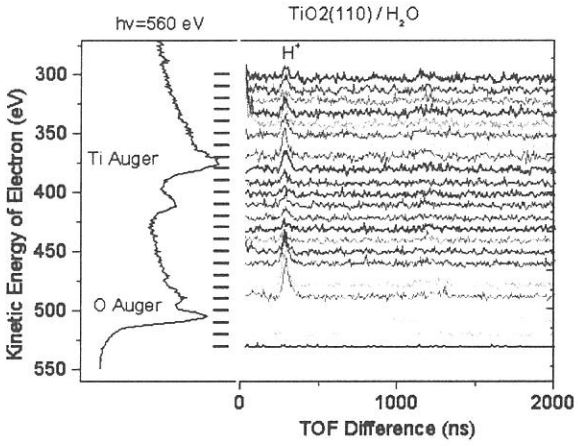

KVV Auger electron emission and the core-level photoelectron emission from Zn as shown in the figure. In the coincidence spectra, the desorption of H^+ is observed at the oxygen Auger electron emission, and no coincidence was observed with the electron emission from Zn. This indicates that the excitation and decay within the oxygen atom leads to the H^+ desorption from the OH species. Meanwhile, the excitation and decay at Zn, which is not bonded to H, dose not yield any ion desorption. A results for the water-chemisorbed TiO_2(110) is drastically different from ZnO(1010). The H^+ desorption coincides not only with the electron emission from O, but also with that from Ti as shown in figure 2. Thus, in the case of the TiO_2, the excitation and decay at Ti, which is not directly bonded to H, can yield the H^+ desorption.

In the classical Knotek Feiblman model for TiO_2, the ion desorption is induced by holes at O2p created by the inter-atomic Auger decay of the Ti3p hole (which can be produced by the Auger decay of any Ti core levels deeper than Ti3p), because there are no higher levels than Ti3p except O2p. However, it seems to be difficult to explain the results shown above with that scenario, because 1) the valence band of TiO_2 is strongly hybridized, and the decay of the Ti core levels without any inter-atomic Auger process is possible and 2) Zn3d level is the highest level at Zn which is below the O2p level, so, similar mechanism might be expected in ZnO as well as TiO_2. Thus, it is necessary to find another mechanism. It is reasonable to assume that the mechanism of the ion desorption induced by the Ti-core level excitation should be related to a presence of the empty Ti3d level in TiO_2, because this is the most significant difference between TiO_2 and ZnO. We propose a model in which the charge transfer from O2p to Ti3d through the hybridization induced by the Ti3p core hole potential (similar to the Kotani-Toyozawa model in the photoelectron spectroscopy) is responsible for the charge transfer from O to Ti and also for the ion desorption. This model is consistent with the experimental result shown above because the process is inhibited in ZnO because Zn3d is not empty.

(BL2B1)

Adsorption, Desorption And Dissociation of Nitrous Oxide over Palladium (110) at Low Temperatures

H. Horino,[a] S. Wako,[a] T. Matsushima,[b] S. Nagaoka,[c] E. Nakamura,[c] S. Tanaka[d] and M. Kamada[c]

[a] *Graduate School of Environmental Earth Science, Hokkaido University, Sapporo 060-0810, Japan*
[b] *Catalysis Research Center, Hokkaido University, Sapporo 060-0811, Japan*
[c] *Institute for Molecular Science, Myodaiji Okazaki 444-8585, Japan*
[d] *Department of Physics, Nagoya University, Senju, Nagoya 464-0814, Japan*

Catalytic N_2O decomposition on metal surfaces has attracted much attention because N_2O is harmful, yielding a remarkable greenhouse effect, and is also a by-product in catalytic NO decomposition. In the latter, this species was recently identified as the intermediate emitting N_2 on Pd(110)[1]. N_2O decomposition depends strongly on the kind of metals and also their surface structures. Desorption of N_2O(a) is completed without dissociation at 90-120 K on Pt(111), Ir(111), Ni(111) and Ag(111). On the other hand, N_2O(a) dissociates at around 100 K on Ru(001) and W(110). This abstract delivers the first report of NEXAFS data of N_2O on Pd(110), showing a molecular adsorption state, and also of decomposition on this surface at low temperatures, showing four N_2 desorption peaks with different angular distributions.

Experimental

[Near-edge X-ray absorption fine-structure] The angle of X-ray incidence (χ) with respect to the surface normal was varied by rotating a Pd(110) crystal such that the electric vector of the X-ray, $\boldsymbol{E}$, was oriented in a plane parallel to or perpendicular to the [1$\bar{1}$0] direction. The crystal was kept below 70 K during the NEXAFS measurements. The NEXAFS spectra were recorded by an Auger electron yield mode with the kinetic energy of the nitrogen KLL Auger electrons at 382 eV [2].

[Angle-resolved thermal desorption] A UHV system with three chambers was used. The reaction chamber was equipped with LEED-AES, an Ar+ gun, and a mass spectrometer for angle-integrated (AI) analysis [3]. The collimator had a slit on each end and the analyzer had another mass spectrometer for angle-resolved (AR) measurements. The crystal was set on the top of a rotatable manipulator to change the desorption angle (θ ;polar angle). This angle was scanned in a plane along the [001] direction because N_2 desorption was concentrated in this plane. The surface after flashing to 1100 K was exposed to $^{15}N_2O$ through a gas doser when the surface temperature (T_S) was below 95 K. Hereafter, isotope ^{15}N is designated as N.

Results and Discussion

[NEXAFS] On a clean surface, no signal peaks were found in raw NEXAFS spectra in the photon energy range from 395 eV to 430 eV. On the other hand, two resonance states were clearly seen in NEXAFS spectra at 403.2±0.5 and 406.7±0.5 eV when the surface was exposed N_2O at 70 K (Fig. 1). The former was assigned to the transition from the 1S state of the terminal nitrogen atom to 3 π *, and the latter due to the excitation of a 1S electron of the center nitrogen to 3 π *. This energy difference of 3.3 eV agrees well with the results on Ni(111) and confirms the molecular form of N_2O.

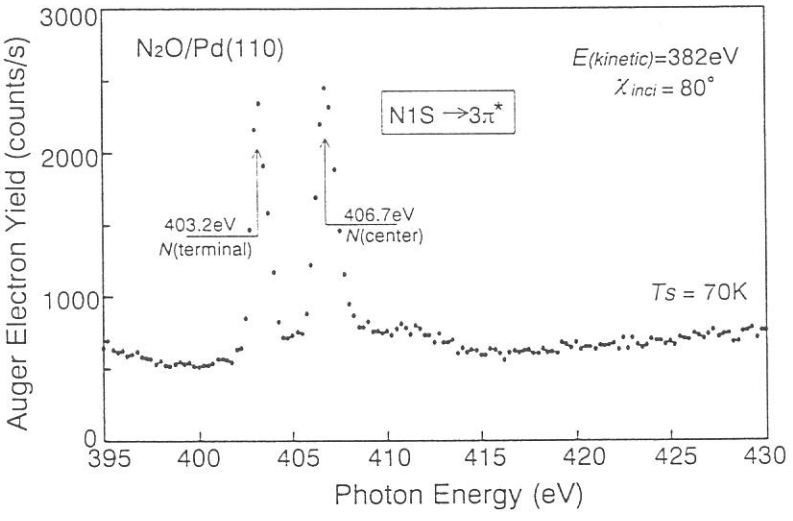

Fig. 1 NEXAFS spectra of N_2O ad-molecules at an incidence angle (χ) of 80 °
The electric vector $\boldsymbol{E}$ was in a plane along the [001] direction.

[AR-TDS] N_2O(a) is mostly decomposed during heating procedures, emitting N_2 (g) and leaving O(a). N_2 showed four desorption peaks, β_1-N_2 at 140-160 K, β_2-N_2 at 132-138 K, β_3-N_2 at 123-127 K and β_4-N_2 at 105-111 K (Fig. 2a)[4]. The first was found at high N_2O exposures and the last at very low exposures. Both β_1-N_2 and β_3-N_2 revealed sharp and inclined emission collimated at θ =43° off the surface normal in the (001) plane, β_4-N_2 sharply collimated around θ =55° , and β_2-N_2 showed a cosine form below half saturation. The total amount of emitted N_2 showed a good linearity with increasing N_2O exposure and a passing at the origin of the exposure curve, indicating that N_2O including the product of N_2 is trapped on the surface at 95 K. No removal of product N_2 was noticed during exposure at 95 K.

The AR signal of N_2 showed different peak shapes as shown in Fig. 2b. The β_4-N_2 peak became clear at Θ_{N2O}=0.03 and around θ =50 ° , where Θ_{N2O} is the relative coverage of N_2O normalized to the desorption maximum of N_2 and N_2O. It is maximized at around θ = +55 ° and -55 ° in the (001) plane, as approximated by $\cos^{40}(\theta +55) + \cos^{40}(\theta -55)$. At this coverage, the β_3-N_2 was not significant. The β_2-N_2 peak in AI form was higher than the others, however, its intensity in AR form was lower than the others. The value at θ = 90 ° remained about 60 % of that at θ = 0 ° . This remaining signal is due to N_2 molecules that did not pass through the slits directly from the surface, but were first desorbed into the reaction chamber and penetrated from there into the analyzer. This extraneous signal was subtracted from the observed AR signal at θ <90° when the signal was plotted against θ . The resultant β_2-N_2 showed a simple cosine distribution.

At high Θ_{N2O} values, β_3-N_2 was enhanced especially around θ =43 ° , whereas β_4-N_2 was relatively suppressed and β_2-N_2 increased. β_3-N_2 sharply peaked at around θ = +43 ° and -43 ° in the [001] plane, as represented by $\cos^{51}(\theta +43) + \cos^{51}(\theta - 43)$ (Fig. 2c). β_1-N_2 was sensitive to θ at around θ =43 ° . It showed a sharp collimation at around ±43° off the surface normal direction. On the other hand, β_2-N_2 became sensitive to θ at around ±43 ° at high exposures. This is probably due to the contribution from enhanced β_1-N_2 and β_3-N_2.

[Inclined desorption] Prior to decomposition, N_2O(a) must lie on the surface because oxygen is released on it. A simple dissociation of inclined N_2O bonding to metal through the O-end may emit N_2 into an inclined way, although such configuration has not been confirmed by vibrational spectroscopy. In N_2O dissociation, a surface parallel momentum can be transferred to nascent N_2 from the other product oxygen atom immediately after N_2O dissociation, because a high energy (about 2 eV) is released in the subsequent formation of O-metal bond.

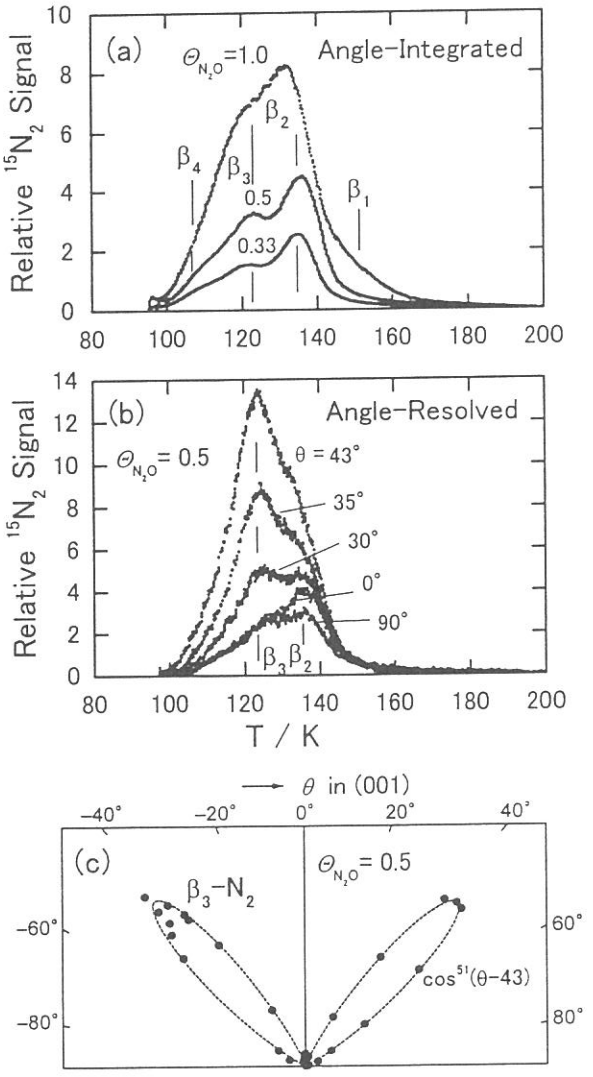

Fig. 2 TDS spectra of N_2 from N_2O-covered Pd(110) in (a) angle-integrated and (b) angle-resolved forms at different θ values in the (001) plane. The heating rate was 0.4 K/s. (c) Angular distribution of desorbing β_3-N_2 in the (001) plane at Θ_{N2O} = 0.5.

Reference

1. I. Kobal, K. Kimura, Y. Ohno, H. Horino,I. Rzeznicka, T. Matsushima, Stud. Surf. Sci. and Catal. 130 (2000) 1337-1342.
2. S. Wako, M. Sano, Y. Ohno, T. Matsushima, S. Tanaka, M. Kamada, Surf. Sci. 461 (2000) L537-542.
3. I. Rzeznicka, Y. Ohno, H. Horino, I. Kobal, K. Kimura, T. Matsushima, Hetero. Catal. Proc. 9th Intern. Symp. Eds. L. Petrov, Ch. Bonev, G. Kadinov, (2000) page 97-102.
4. H. Horino, S. Liu, M. Sano, S. Wako, Y. Ohno, A. Hiratsuka, T. Matsushima, Topics in Catal. in press (2001) .

(BL3A-1)

Investigation of Photo-dissociation Process of Organo-metallic Compounds : TEOS($Si(OC_2H_5)_4$) and TEOG($Ge(OC_2H_5)_4$)

Yasuhiro Kawasaki, Hideaki Yanagida, Kou Kurosawa, Eiken Nakamura and Masao Kamada

Department of Electrical and Electronic Engineering, Miyazaki University
Institute for Molecular Science, Okazaki, 444-8585

SiO_2 and GeO_2 thin films have been prepared by photo-chemical vapor deposition (Photo-CVD) at room temperature from organo-metallic compounds: $Si(OC_2H_5)_4$ and $Ge(OC_2H_5)_4$, The photo-dissociation processes have not been clear yet. In this work, we have identified species dissociated from $Si(OC_2H_5)_4$ and $Ge(OC_2H_5)_4$ molecules by vacuum ultraviolet radiation and discussed about the photo-dissociation processes. The chemical structures are illustrated in Fig.1

TEOS and TEOG were supplied at 3.0×10^{-7} Torr and 7.0×10^{-6} Torr into a stainless steel pipe, respectively. The 10.7 eV photon beam was introduced into the pipe, which was provided by adjusting the undulator gap to be 35mm. The average photon density was 8.0×10^{13}photon/cm^2/100mA/sec.

The mass spectra taken from TEOS and TEOG before-radiation and during-radiation are shown Figs.3(a) and (b) and Fig.4(a) and (b), respectively. Our main aim of this study is to identify the final products associated with Si and Ge photo-dissociated from these molecules, so that we focus on the spectra at 28 (Si), 44 (SiO), 60 (SiO2), and 76 (SiO4) for TEOS, and 72(Ge), 88(GeO), 104 (GeO2), 120 (GeO3), and 136 (GeO4) for TEOG. By comparing the spectra from TEOS and TEOG, we can conclude that SiO and Ge are the main final products. In case of TEOS, a small amount of Si are produced. Taking into

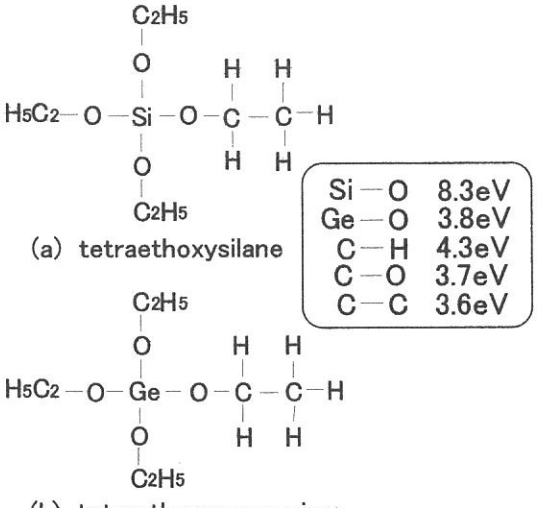

Fig.1 Chemical structure
(a) TEOS (b) TEOG

account of a fact that the bonding energies of Si-O and Ge-O are 8.3 eV and 6.9 eV, respectively, the difference induces the different final products.

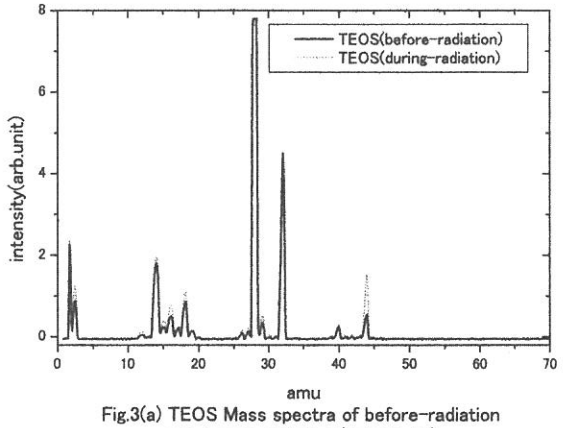

Fig.3(a) TEOS Mass spectra of before-radiation and during-radiation (m/e=1-70)

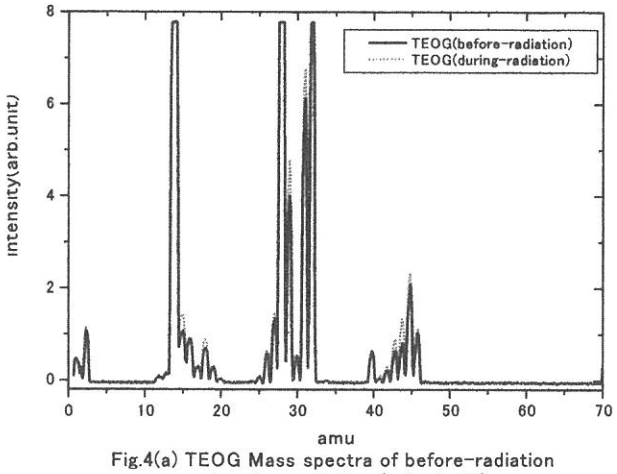

Fig.4(a) TEOG Mass spectra of before-radiation and during-radiation (m/e=1-70)

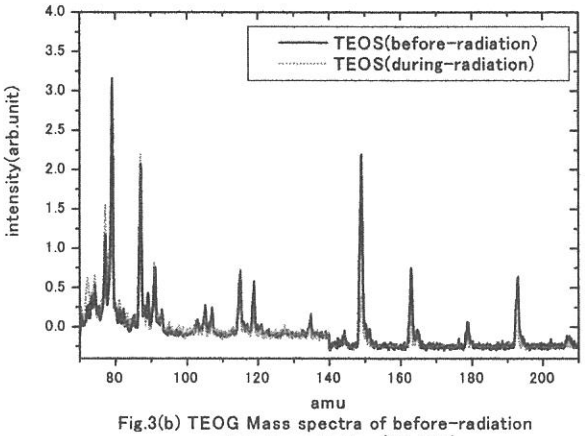

Fig.3(b) TEOG Mass spectra of before-radiation and during-radiation (70-210)

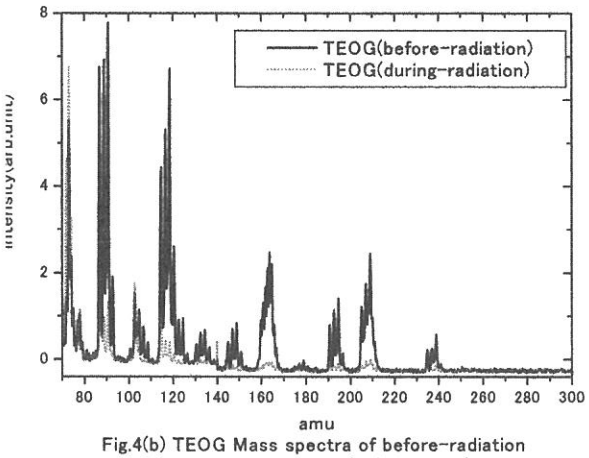

Fig.4(b) TEOG Mass spectra of before-radiation and during-radiation (m/e=70-300)

(BL4A)

Assignments of bending and stretching vibrational spectra and mechanisms of thermal decomposition of SiH_2 on Si(100) surfaces

Hideyuki Noda[a], Tsuneo Urisu[b]

[a]*The Graduate University for Advanced Studies, Myodaiji, Okazaki, 444-8585*
[b]*Institute for Molecular Science, Myodaiji, Okazaki, 444-8585*

Infrared (IR) absorption spectroscopy has contributed to identification of the chemical species on the hydrogen-adsorbed Si surface (H/Si) and elucidation of their structures. Despite extensive IR studies of H/Si systems, however, many fundamental problems in the assignment of vibrational modes and thermal reaction mechanisms remain unsettled. Even in the stretching vibrational region, reported assignments are still inconsistent. Most previous IR studies of H/Si surfaces have used the technique of attenuated total reflection (ATR), which can only provide spectra above about 1400 cm^{-1} because of Si lattice absorption. Buried metal layer-infrared reflection absorption spectroscopy (BML-IRRAS) has an advantage in that it supplies spectra with high sensitivity and high resolution (0.5-2 cm^{-1}) for the SiH_n bending and wagging vibrations, which appear in the so-called fingerprint region, <1000 cm^{-1} as well as the SiH_n stretching vibration. In this work, we have assignned the SiH_2 modes in the stretching and bending regions consistently by analyzing the temperature dependence of this spectrum and discussed mechanisms of the thermal decomposition of SiH_2 species.

Figure 1 shows typical BML-IRRAS spectra obtained after 500 L hydrogen exposure at different temperatures. The RHEED patterns were 1x1 for the sample exposed at 300 K and 3x1 for that exposed at 400 K. The spectra shown in Figs. 1(a) and (b) consist of the stretching and bending modes near 2100 and 900 cm^{-1}, respectively. The peak-resolved spectra for these vibrations, calculated assuming that the shape of each peak is Lorentzian, are also shown in Fig. 1. The stretching part is resolved to at least four clear peaks at 2082, 2100, 2107, and 2138 cm^{-1}. Assignments of the 2100 cm^{-1} peak are made with reference to these works to the symmetric stretching mode of coupled monohydride (M_{ss}), the broad peaks at 2138 and 2130 cm^{-1} to the SiH_3 stretching modes (T_s) and the 860 cm^{-1} peak to the SiH_3 symmetric deformation (T_{sd}) mode. The assignments of the 860 and 2138 cm^{-1} peaks to the SiH_3 species are also supported by their clear intensity decrease by the change from 1x1 to 3x1.

As for the dihydride species, in previous reports, the weak peak at 2091 cm^{-1} was assigned to the SiH_2 symmetric stretching (D_{ss}), the 2114 cm^{-1} peak to the D_{ss} and the 2108 cm^{-1} peak for the HF-treated Si(100) surfaces to the D_{ss} of SiH_2 perpendicular to the Si(100) plane.

Of particular interest is the doublet peak in the bending vibration region that splits into two distinct peaks at 902 and 913 cm^{-1}. The IR absorption spectra of hydrogenated

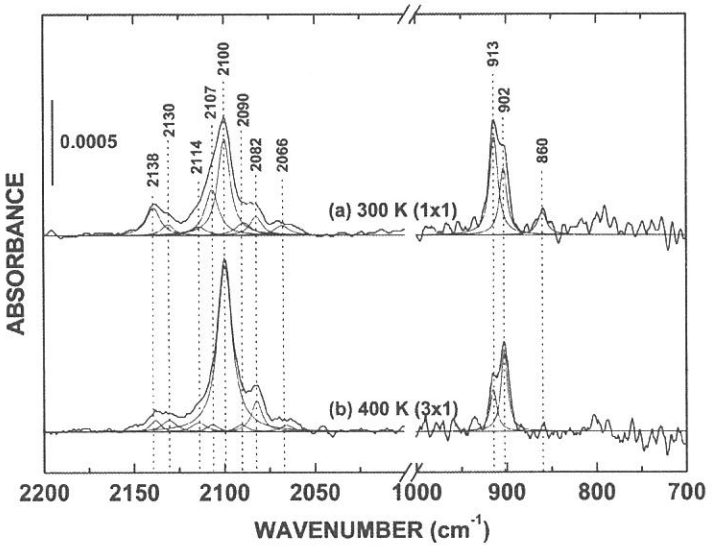

Fig. 1. p-Polarized BML-IRRAS spectra associated with H/Si(100) surfaces with (a) 1x1 (b) 3x1. Narrow lines show peak-resolved spectra calculated assuming that the the shape of each peak is Lorentzian.

porous silicon and the Si_2H_6 gas suggest that this doublet peak is a result of the SiH_2 bend scissors mode (D_{sci}) overlapping the degenerate deformation mode of SiH_3 (T_{dd}). McGonigal et al. assigned the small peak at 930 cm^{-1} to the T_{dd} and the strong peak at 860 cm^{-1} to the T_{sd} in their BML-IRRAS study of H on the polycrystalline Si surface. Since IR data with Si_2H_6 adsorbed porous Si and ab initio calculations imply that T_{dd} is much weaker (1/3 to 1/5) than that of the T_{sd} observed at 860 cm^{-1}, the SiH_3 bending mode, T_{dd}, should be weaker than the observable level in the present case. Moreover, the 907 cm^{-1} peak observed in a recent high-resolution (13 cm^{-1}) EELS study of H/Si(100) surfaces was assigned to the D_{sci} of the terrace dihydride and the small peak at 933 cm^{-1} to the T_{dd}. Therefore, we conclude that the 902 and 913 cm^{-1} peaks observed in the present work should both be assigned to D_{sci}. Furthermore, given the structures of 3x1 and 1x1 surfaces, we believe that there is adjacent dihydride (*AD*: H-Si-H H-Si-H), in addition to isolated dihydride (*ID*: H-Si-Si-H H-Si-H H-Si-Si-H), on the 1x1 surface that includes many phase boundaries of the 3x1 structures. It is also known that the vibrational frequencies of adsorbates on a solid surface are easily influenced by the neighboring species. In the IR absorption spectra of a-Si:H, the observed D_{sci} of the polysilane-like chain segment $(SiH_2)_n$ is about 10 cm^{-1} higher than that of the normal SiH_2. We therefore assign the 902 cm^{-1} peak in Fig. 1 to the bend scissors mode of *ID* (ID_{sci}), and that the 913 cm^{-1} peak to the same mode of *AD* (AD_{sci}). These assignments are also supported by that the 913 cm^{-1} peak is weaker for the 3x1 structure (Fig. 1(b)) than that for the 1x1 structure (Fig. 1(a)).

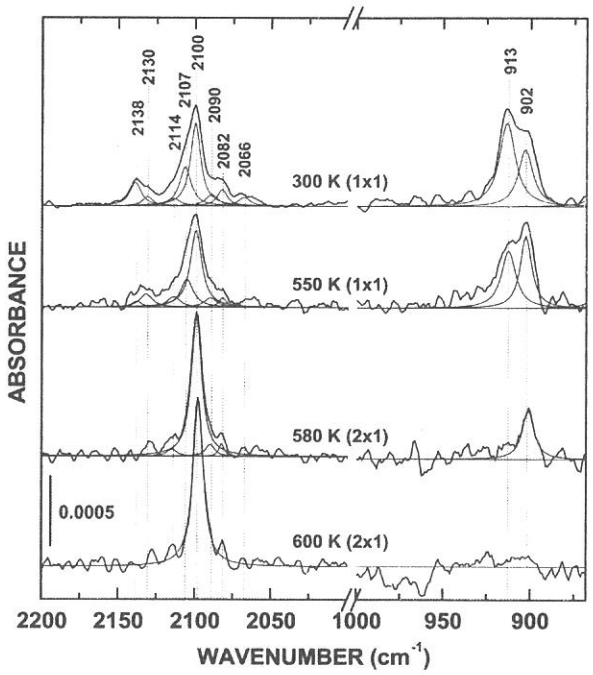

Fig. 2. BML-IRRAS spectra obtained at various annealing temperatures. Narrow lines show peak-resolved spectra calculated assuming that the the shape of each peak is Lorentzian.

To confirm the assignments of the SiH_2 species, we investigated the dependence of this peak intensity for the 1x1 surface on the annealing temperature (Fig. 2). The IA of the 2100 cm^{-1} peak starts to increase at about 500 K and that of the 913 cm^{-1} peak starts to decrease at nearly the same temperature. As shown in Fig. 2, the temperature dependence of the 913 cm^{-1} peak almost coincides with that of the 2107 cm^{-1} peak. We therefore assign the 2107 cm^{-1} peak to the symmetric stretching mode of *AD* (AD_{ss}). It is difficult to account for the temperature dependence of the two peaks at 2090 and 2114 cm^{-1} in detail from the data shown in Fig. 2, but both peaks are found in the spectra of samples annealed up to 550 or 580 K, in contrast to those of samples annealed at higher temperatures. Both peaks are therefore assigned to the vibrational modes of the dihydride species. Furthermore, because the temperature dependence of the 2090 cm^{-1} peak shown in Fig. 2 is similar to that of the 902 cm^{-1} peak, we assign the former peak to the symmetric stretching mode of *ID* (ID_{ss}), as reported by Chabal et al. On the other hand, Dumas et al. assigned the 2114 cm^{-1} peak observed in their IR study of the HF-treated Si(100) surface to the asymmetric stretching of the tilted dihydride ("horizontal" dihydride on the (111) facets) on an atomically rough H-terminated Si(100) surface; we therefore assign the small peak at 2114 cm^{-1} to the SiH_2 asymmetric stretching mode (D_{as}) on defect sites.

From the annealing temperature dependence shown in Fig. 2, we conclude that *AD* is slightly less stable than *ID* and that both *AD* and *ID* produce coupled monohydride by thermal decomposition. *AD* can easily generate coupled monohydride by thermal decomposition via second-order kinetics, the thermal reaction of *ID* may generate coupled monohydride by the decomposition reaction accompanied by the rearrangement of hydrogen.

(BL4A)

Initial Stage of Hydrogen Etching of Si Surfaces Investigated by Infrared Reflection Absorption Spectroscopy

Hideyuki Noda[a], Tsuneo Urisu[b]

[a]*The Graduate University for Advanced Studies, Myodaiji, Okazaki, 444-8585*
[b]*Institute for Molecular Science, Myodaiji, Okazaki, 444-8585*

Hydrogen-adsorbed Si (H/Si) surfaces have attracted considerable interest in the fields of semiconductor technologies, because H plays important roles in the passivation effect and in several chemical-vapor-deposition reactions on the Si surface. Recently, some studies by temperature-programmed-desorption (TPD) and scanning tunneling microscopy (STM) have also shown the evidence of etching reactions involving by H atoms adsorbed on Si surfaces. This indicates that H atoms break Si back bonds and remove the Si atom from the surface. Clarifying the H-etching process will be significant in future nanoprocesses including atom-level control. In this work, we have investigated the initial stage of etching reaction of Si(100) and Si(111) surfaces induced by H-exposure using buried metal layer-infrared reflection absorption spectroscopy (BML-IRRAS).

Figure 1 shows IRRAS spectra of H/Si(100) surface formed at room temperature (RT) as a function of H-exposure. The three peaks at 902, 913 and 860 cm^{-1} in the bending part have been assigned to the isolated SiH_2 scissors (ID_{sci}), adjacent SiH_2 scissors (AD_{sci}) and SiH_3 symmetric deformation (T_{sd}) modes, respectively. The detection of the T_{sd} peak indicates that the initial stage of H-etching (breaking of the Si-Si back bonds) is occuring and that trihydride is forming. The H-exposure dependence of the integrated absorbance of these bending vibrations, calculated assuming the shape of Lorenzian, are plotted in Fig. 2. As shown in Figs. 1 and 2, the ID_{sci} peak appears and saturates at relatively low H-exposures (50 L). On the other hand, the AD_{sci} peak becomes clear at around 100 L and tends to saturate at 200-500 L. We can see that the T_{sd} appears and begins to increase gradually at the same time when the AD_{sci} almost saturates above 200 L. This means that the adjacent SiH_2 structure is a precusor to the SiH_3 formation.

Figure 3 shows a series of IRRAS spectra of H/Si(111) surface obtained by H-exposures at RT. At low exposures (~10 L), adatom monohydride (M'_s), observed at 2074 cm^{-1} is mainly formed on the surface. With increasing exposures (~30 L), the intensity of the M'_s peak decreases and the 905 cm^{-1} peak (D_{sci}) appears. This means that one back bond of Si adatom is broken, and that the adatom dihydride forms. As the exposure increases above 70 L, the 860 cm^{-1} peak (T_{sd}), which indicates the formation of adatom trihydride, increase gradually and saturates at 500 L. The formation of adatom higher hidrides by breaking of the adatom back bonds enlarges the H-terminated 1x1 area. Therefore, the 2080 cm^{-1} peak (M_s) increases remarkably as the exposure increases from 500 to 2000 L. Figure 4 shows IRRAS spectra of H/Si(111) surface obtained at RT by much higher

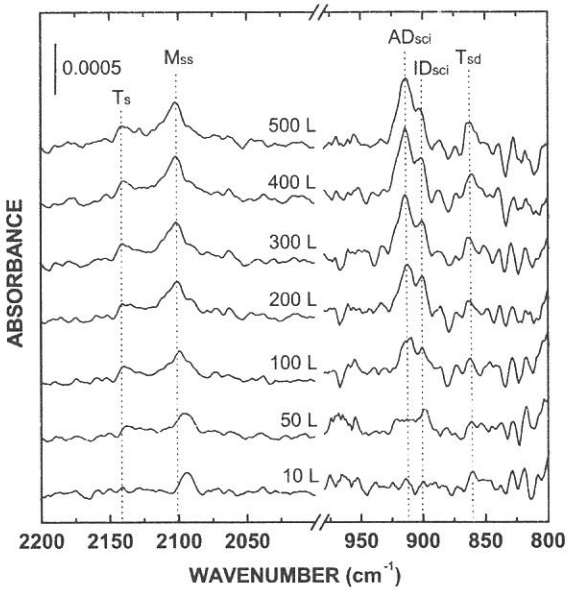

Fig. 1. BML-IRRAS spectra of p-polarization for H/Si(100) formed by H-exposure at RT.

H-exposure of 5000, 10000 and 50000 L. The most important result is that the SiH_3 symmetric deformation vibration peak (T_{dd}: 940 cm^{-1}) is observed at above 10000 L. Appearance of the T_{dd} peak means that the initial stage of etching of the 1x1 rest-atom layer occurs and the tilted trihydrides are formed. As for the adatom trihydride of which the symmetry axis is perpendicular to the surface, p-polarized IR beam excite the T_{sd} mode but not the T_{dd} mode. On the other hand, as for the trihydride formed by the etching of the 1x1 terrace having tilted symmetry axis against the (111) direction, both peaks of T_{dd} and T_{sd} are observable. The etching of the 1x1 terrace is also supported by the distinct decrease and broadening of the M_s peak indicating the increase of the surface roughness.

Initial stage of etching reactions on Si(100) and Si(111) surfaces, induced by H-exposure at RT, has been investigated by BML-IRRAS. The SiH_2 scissors and SiH_3 deformation modes have been observed as clear indicators at the initial stage of etching reactions. On the Si(100) surface, the etching reaction started in the relatively low exposure region of ≥300 L. We found that the adjacent dihydride is a precursor structure of breaking the Si back bonds. On the Si(111) surface, adatom's back bonds were easily broken at a low H-exposure of 30-500 L. Adding to this dominant reaction, the etching of rest-atom layer was observed at higher H-exposures than 10000 L.

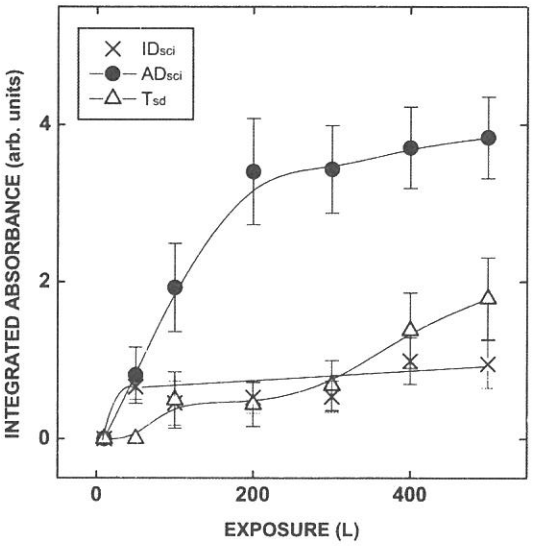

Fig. 2. Dependence on H-exposure of the integrated absorbances for the ID_{sci}, AD_{sci} and T_{sd} peaks in the Fig. 1 spectra.

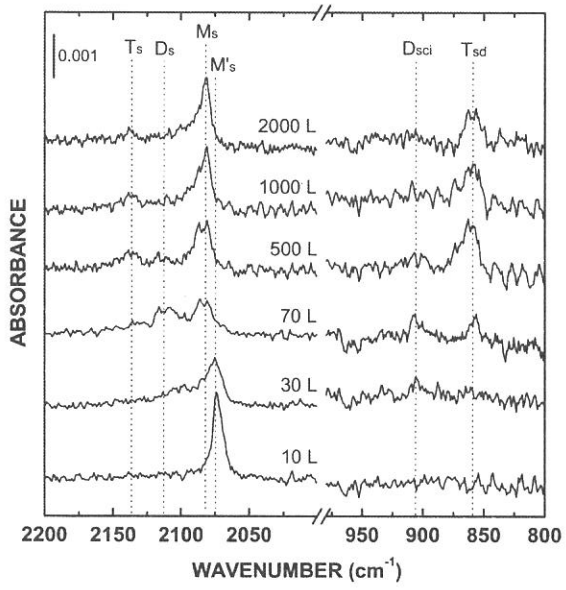

Fig. 3. BML-IRRAS spectra of p-polarization for H/Si(111) formed by H-exposure at RT.

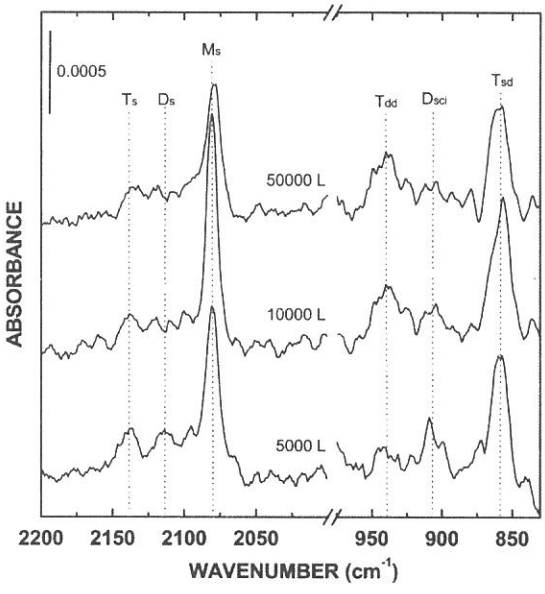

Fig. 4. BML-IRRAS spectra of p-polarization for H/Si(111) formed by high H-exposure of 5000, 10000 and 50000 L.

(BL-4A1)

X-ray lithography of PMMA sheets using white beam of the beam line BL4A1

Harutaka Mekaru[a], Yuichi Utsumi[a], Tadashi Hattori[a], and Tsuneo Urisu[b]

[a]Laboratory of Advanced Science and Technology for Industry, Himeji Institute of Technology, koto, kamigorii, Ako, 678-1205
[b]Institute for Molecular Science, Myodaiji, Okazaki, 444-8585

LIGA process, that utilizes a useful industrial application of SR, is one of the promising technologies for fabrication of extremely tall three-dimensional microstructures with a large aspect ratio. This process was invented at the Institut Fur Mikrostrukturtechnik (IMT) of the Karlstuhe Nuclear Center (KfK) in 1980 [1]. Microstructures with height of over a few hundreds μm have been widely applied to various fields such as micro-mechanics, micro-optics, sensor and actuator technologies, and chemical, medical and biological engineering.

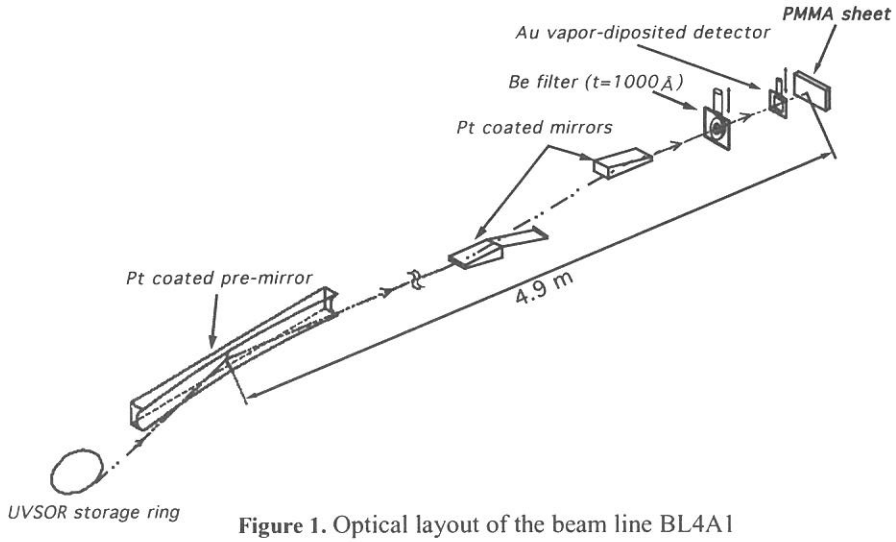

Figure 1. Optical layout of the beam line BL4A1

An X-ray deep lithography of the LIGA process needs the photon energies of 2 keV to 6 keV. The depth to which X-rays penetrate a resist depends on the resist's absorption coefficient for X-rays. The vacuum ultraviolet (VUV) photons contained in the SR can excite almost all electronic states, including core electrons. However, the penetration depth for PMMA in the photon energy range of the VUV has never been examined. This report is intended as an investigation of the X-ray lithography in the photon energy range less than 2 keV.

Figure 1 shows optical layout of a beam line BL4A1 in the UVSOR. The multilayered-mirror (MLM) monochromator beam line had been constructed specially for SR stimulated process. When the MLM is not used, the SR beam is reflected by a pair of Pt coated plane mirrors with grazing incident angles of 2 degrees in the white beam chamber

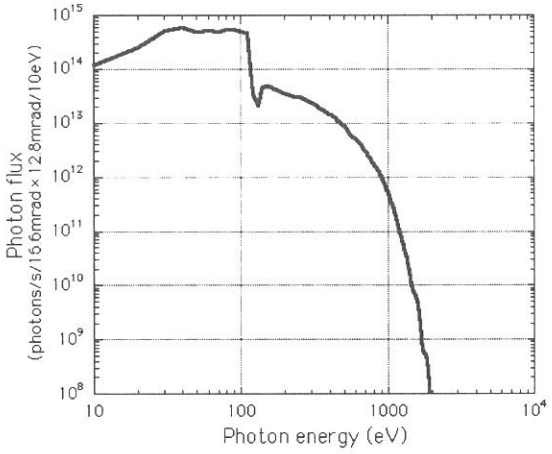

Figure 2. Calculated spectra of the photon flux of white beam in the beam lines BL4A1 of the UVSOR.

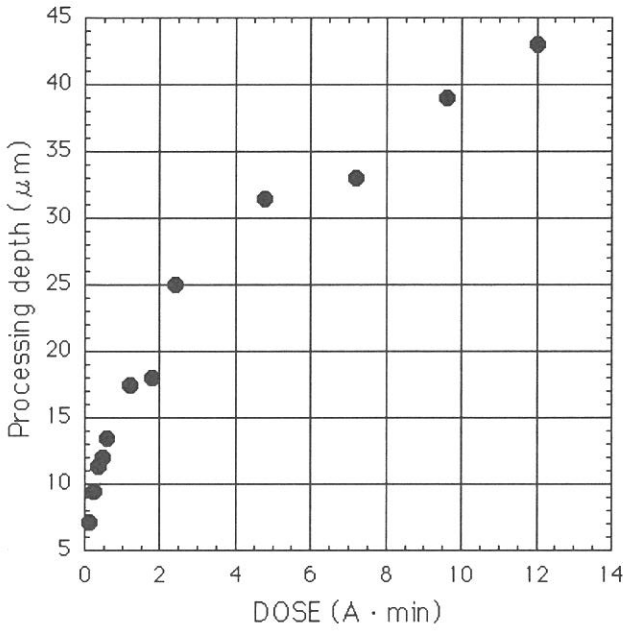

Figure 3. The dose dependence of PMMA sheet processing depth using the beam line BL4A1 of the UVSOR.

to keep the output beam at the same height as that of the output beam from the MLM monochromator. A Be filter is set to cut off low-energy photons, and an Au vapor-deposited detector is set to measure photo-current.[2], [3]

Figure 2 shows calculated the photon flux of the output beam at a point downstream of the exposure stage as a function of photon energy taking into consideration the acceptance angles and reflectivity of the pre-mirror, the reflectivity of two Pt-coted mirrors, and the transmission of the Be filter. The transmission (84%) of the mesh holding the thin Be film was also considered in addition to the transmission of the 0.1-μm-thick Be filter. The values of the optical constants used in the calculation were cited from reference 4.

As a fundamental data to estimate the required X-ray dose energy to process the required depth, the dependencies of processing depth and irradiated X-ray energy without any X-ray mask are measured. The processing depths after SR exposure and development were estimated maximum depths measured by the surface profiler (Dektak^3 ST). As shown in Fig. 3, processing depth increased linearly at low doses, while at high exposure doses it showed to gradually becoming saturation. The etching rate is estimated lower than that of the hard X-ray lithography in the photon energy range more than 1 keV. Furthermore, at the exposure doses more than 1.8 A• min, PMMA sheets become degenerating by thermal.

Finally, a patterning of the PMMA sheet was demonstrated by using the output beam with an Au wire mesh. The output beam irradiated on a 0.5 mm-thick PMMA sheet with an Au wire mesh at an exposure dose of 3.6 A• min. The diameter of the Au wire is 70 μm. Figure 4 shows the SEM image of PMMA microstructures. The patterning of the PMMA sheet was successfully demonstrated by using the output beam of the beam line BL4A1.

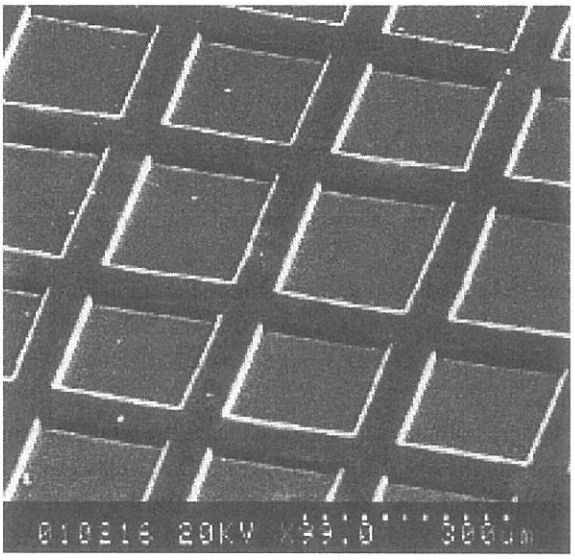

Figure 4. SEM image of PMMA microstructures.

REFRENCES

[1] E. W. Becker, *et. al.*, *Microelectron. Eng.*, **4**, pp.35-42 (1986).
[2] H. Mekaru, *et. al.*, *UVSOR Activity Report*, 38 (1999).
[3] H. Mekaru, *et. al.*, *Rev. Sci. Instrum.*, **70**, 2601-2605 (1999).
[4] B. L. Henke, E. M. Gullikson, and J. C. Davis, Atomic Data and Nuclear Data Tables, **54**, 216 (1993).

(BL5B)

Measurements of Total Photo-Desorption Yields from Solid Krypton by Exciton Creation

Takashi Adachi, Satoshi Ishii, Takato Hirayama, Ichiro Arakawa and Makoto Sakurai*

Department of Physics, Gakushuin University , Mejiro, Toshima, Tokyo 171-8588.

**Department of Physics, Kobe University, Rokkodai-cho, Nada-ku, Kobe 657-8501.*

1. Introduction

Desorption induced by electronic transitions (DIET) of various kinds of particles from rare gas solids has been extensively studied in these 10 years [1]. Investigation of the desorption characteristics such as desorption yields, kinetic energies and angular distributions, will reveal the dynamics of the electronic excitations and the relaxations.

We reported the absolute photo-desorption yields from the surface of solid neon [2] and argon [3, 4] at excitonic excitation energy and revealed the main desorption channel by the quantitative analysis. For a thick neon film, the desorption yield was 1-2 atoms/photon by bulk exciton excitation and 2-10 atoms/photon by bulk ionization. These values were quantitatively explained by the internal sputtering mechanism. In the case of argon, the absolute photo-desorption yield was 0.05-0.1 atoms/photon by bulk exciton excitation. The results agreed with the calculated value using the classical molecular dynamics by Cui et al [5]. The dissociation of excimer in the bulk was found to play an important role in the desorption mechanism of argon.

Here, we present the preliminary results of the total photo-desorption yields from the surface of solid krypton. The "total" means that we detected all the krypton particles desorbed, i.e., atoms and clusters in ground, electronically excited, and ionized states. In this report, we show only the relative desorption yields because the absolute number of incident photon have not been measured in the wavelength range of the exciton creation energy for solid krypton (100-130 nm).

2. Experiments

The experimental procedure and set-up have been described in detail elsewhere [2] and are briefly summarized here. Experiments have been carried out at the beam line BL5B in UVSOR of the Institute for Molecular Science, Okazaki. A liquid helium cryostat was installed in an ultrahigh-vacuum chamber with a base pressure of 5×10^{-9} Pa. Krypton gas was introduced into the main vacuum chamber and was condensed on the surface of a platinum substrate attached to the liquid helium cryostat. The temperature of the sample was 6 K or lower. The thickness of a krypton film was calculated from the exposure on the assumption that the condensation coefficient of the krypton on the sample surface was unity. The film thickness was between 10 and 2400 atomic layers.

Desorption rate was calculated from the total pumping speed for krypton and the rise of the krypton partial pressure in the vacuum chamber during the irradiation of the sample. The pumping speed for krypton of a turbo molecular pump and the cold surface of the cryostat was 0.068 ± 0.01 m^3/s in total. The partial pressure of krypton was measured by a quadrupole mass spectrometer which was calibrated with an ionization gauge at each run of the experiment.

3. Results

Figure 1 shows the wavelength dependence of the total desorption yields for solid krypton. In case the film thickness is 10 atomic layers, a peak is observed at 125 nm which corresponds to the excitation energy of the first order surface exciton (S1(3/2)). For the film of 2400 atomic layers in thickness, additional peaks appear at the wavelengths corresponding to the first order bulk (B1, 122 nm (3/2), 114 nm (1/2)) excitons. The small shoulders at 110, 116 and 112 nm in the spectrum for 2400 atomic layers film are due to the creation of the second order bulk (B2(3/2)), the first order surface (S1(1/2)) and the second order surface (S2(3/2)) excitons, respectively. The background signal is mainly due to the ionization by the second order light from the monochromater.

The thickness dependencies of the desorption yields at each exciton excitation energy are shown in figure 2. The desorption yield at the surface exciton creation energy should have no thickness dependence because the "thickness of the surface" is constant for any thickness of the film, which was indeed the case for neon [2] and argon [3,4]. However, in figure 2, the desorption yield at the first order surface exciton (3/2) excitation energy gradually decreases with the increase of the thickness of krypton film. This decrease can be the contribution of the residual gas adsorption on the sample surface. To make a thick krypton film, the substrate was exposed to gaseous krypton with rather high pressure (~ 1 x 10^{-4} Pa) for more than 10 minutes. After the exposure, we had to wait for about 1 hour or more in order to get a low pressure (< 2 x 10^{-8} Pa), which was essential for a good signal to background ratio in the present experiments. The sample surface can be partly covered with the residual gas (H_2, H_2O, CO, etc.) during this period, which resulted in the decrease of the desorption yield. This very slow pressure decrease was not observed in the measurements for neon and argon, which is explained by the difference of their vapor pressure at the temperature of the cryostat which has a temperature distribution from 4.2 K to the room temperature.

The desorption yields at the bulk exciton creation energies increase with the thickness of krypton film and saturated at about 200 atomic layers. The saturated value for B1 (3/2) and B1 (1/2) is roughly estimated at 0.01~0.1 krypton/photon. The measurements of the absolute intensity of the incident light at the wavelengths of the exciton creation for krypton (100-130 nm) will be done in the next machine time, which will give the absolute desorption yield. This will make it possible to discuss the desorption mechanism quantitatively.

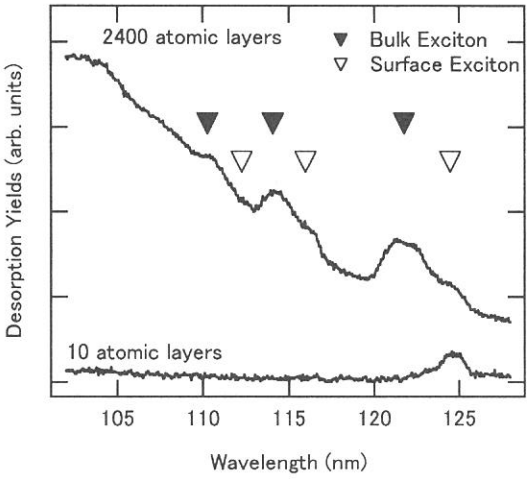

Fig.1 Wavelength dependence of total desorption yields of argon for thin (10 layers) and thick (2400 layers) films.

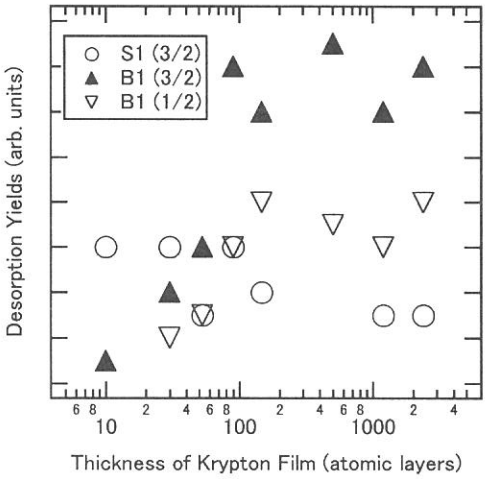

Fig.2 Thickness dependence of desorption yields at the bulk and surface exciton creation energies.

[1] for recent review, see I. Arakawa, Molec. Crystal Liq. Crystal, **314**, 47 (1998), M. Runne and G. Zimmerer, Nucl. Instrum. Meth. Phys. Res. B **101**, 156 (1995).

[2] I. Arakawa, T. Adachi, T. Hirayama and M. Sakurai, Surf. Sci. **451**, 136 (2000).

[3] T. Adachi, T. Hirayama, I. Arakawa and M. Sakurai, UVSOR Activity Report 1999, UVSOR-27, (2000) 178.

[4] T. Adachi, T. Hirayama, I. Arakawa and M. Sakurai, in preparation.

[5] S. Cui, R. E. Johnson, and P. Cummings, Surf. Sci. **207**, 186 (1988).

(BL-6B)

In-situ observation of synchrotron-radiation-stimulated process of surface reaction

Takafumi Tanaka[1,2], Hideaki Yanagida[1,2], Kou Kurosawa[1], Yoichi Nonogaki[1], and Tsuneo Urisu[1]

[1]Institute for Molecular Science, Okazaki, 444-8585 Japan

[2]Department of Electrical and Electronic Engineering, Miyazaki University, Miyazaki, 889-2192 Japan

Nano structures must open new windows not only for surface physics and chemistry but also for electronic and photonic devices. Synchrotron-radiation-stimulated surface chemical reactions have been a most promising way to fabricate nano structures, because they offer a process with the advantage of high-site selectivity by core electron excitation and also free-of damage with atomic scale. However, the detailed reactions have not been elucidated yet.

We have set and operated ultra-high vacuum scanning tunneling microscope (UHV-STM) and low energy electron diffraction (LEED) for atomic-resolution characterization of surfaces in the new beam line BL-6B. Figure 1 shows the outline of the beam line and observation system. The observation chamber is evacuated down to 1×10^{-10} Torr with turbo molecular, ion sputter, Ti-sublimation and NEG pumps. We have observed HOPG(0001) and Si(111) surfaces. We can obtain a clean surface of HOPG easily, but a clean surface of Si can not appear without sample heating, because the surface is covered with native oxide and carbonized layers. We have prepared the sample with wet chemical treatment called Shiraki method. By heating the sample to remove the layers, the clean surface is obtained. Figures 2 and 3 show the STM images of HOPG and Si surfaces. HOPG has been observed under such conditions that are scan width $1.5\times1.5nm^2$, scan speed 202nm/s,tunnel current 0.89nA, and bias voltage 0.089V. The conditions of Si are scan width $100\times100nm^2$, scan speed 3280nm/s, tunnel current 0.1nA, and bias voltage 2.0V. In the

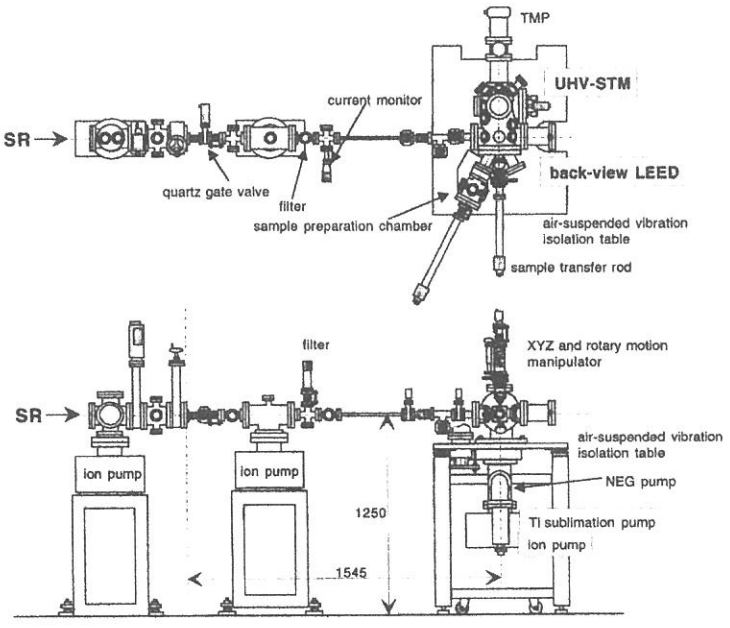

Figure 1. Schematic drawing of the BL-6B beam line and observation system.

figures, white appearing areas part correspond to the upper parts and black appearing ones are to the lower parts. In the case of the HOPG images, the atomic distances are found to agree with the theoretical values. In the case of Si images, steps with monoatomic height are shown in Figure 3. The LEED pattern inserted in the figure indicates that the Si(111) surface has a 7×7 reconstruction structure. At the present stage, the atomic images of Si(111) have not been obtained with STM yet. There is a problem in the system that the vacuum is not enough to keep Si (111) surfaces clean for a long time. Evacuating the preparation and observation chambers down to the order of 10^{-11} Torr and further optimize the observation conditions, we could observe the atomic images in the storage ring room on UVSOR.

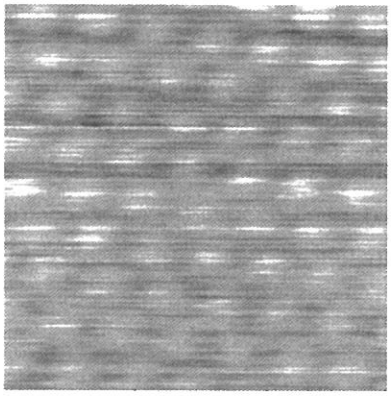

Figure 2. STM image of HOPG

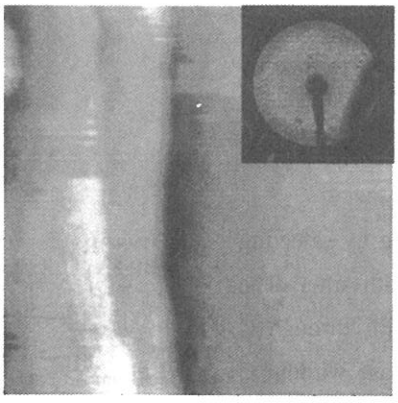

Figure 3. STM image of Si(111). The second insert of the LEED pattern.

(BL8A)

Investigation of Fragment from Polytetrafluoroethylene by Synchrotron Radiation Ablation

Hisao Nagai, Masaru Hori and Toshio Goto,
*Koji Katou and *Mineo Hiramatsu

Department of Quantum Engineering, Nagoya University,
Chikusa-ku, Nagoya, 464-8603
**Department of Electrical and Electronic Engineering, Meijo University,*
Tempaku-ku, Nagoya, 468-8502

INTRODUCTION

Fluorocarbon polymer has excellent properties such as chemical stability, potential biocompatibility and nonwetting property, and so on. Previously, we demonstrated the anisotropic micromachining and film formation of Teflon (fluorocarbon polymer) using synchrotron radiation (SR) ablation process [1,2]. Moreover, in order to clarify the mechanism of SR ablation, we have performed polytetrafluoroethylene (PTFE) micromachining by selecting the photon energy of SR beam with filter. From these results, we clarified that photon energies absorbed by carbon (C) and fluorine (F) atoms contribute to the ablation of PTFE. In this report, we have investigated the variation of fragments generated by PTFE ablation by quadraple mass spectroscopy (QMS).

EXPERIMENT

The experiments were carried out at beam line BL-8A of UVSOR. Figure 1 shows a schematic diagram apparatus used in this study. The PTFE target was set perpendicularly to the SR beam in the reaction chamber (base pressure of 10^{-4} Pa). A Nickel (Ni) mesh (square pattern of 77 μm) was used as the contact mask. The SR beam irradiated the samples through the Ni contact mask in vacuum at a room temperature. This experimental apparatus was equipped with QMS. In order to selecting the photon energy of SR beam, carbon (C) filter and C&MgFx filter was used. The thickness of C and C&MgFx filter were 100 nm, 200 nm, respectively. These filter were formed by electron beam evaporation.

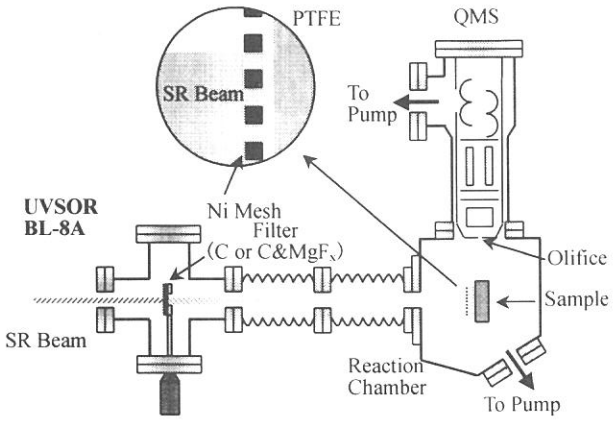

Fig. 1. Schematic diagram apparatus used in this study.

RESULTS AND DISCUSSION

We have performed PTFE etching by selecting the photon energy of SR beam with filter. The total photon flux irradiated on PTFE through C filter was the same as that in the case without C filter. As a result, the ablation rate with C filter was smaller than that of without C filter.

Figures 2 (a)-(b) show the QMS spectra of the fragments from PTFE target. Figure 2(a) shows

the QMS spectrum of CF fragment obtained from the target irradiated with white SR beam. Figure 2(b) shows the fragments after the SR beam passed through the C filter. These intensities were normalized to the maximum signal intensity (CF_3:Mass Number 69) and intensities of mass numbers above 70 was multiplied by 10 times. A big difference was not observed in the distribution of these spectra. Therefore, PTFE ablation with and without C filter would be identical in the ablation mechanism.

As shown Figs. 2 (a) and (b), the 69 fragment compared with the 31 fragment (CF) was dominated. T. Katoh *et al* reported that the domination at 69 indicated the main gaseous products by SR ablation should be the saturated fluorocarbon (CF_3-C_nF_{2n}-CF_3), while the domination at 31 indicated the main products are the monomers [3,4]. Thus, the domination at 31 would contribute to thermal decomposition of PTFE and domination at 69 would contribute to the saturated fluorocarbon generated by photochemical decomposition of PTFE irradiated SR beam. In this study, it is considered dominately reaction of SR ablation is photochemical decomposition.

SUMMARY

We have performed PTFE micromachining by selecting the photon energy of SR beam with filter and investigated the variation of fragments generated by PTFE ablation by QMS.

The dominate reaction of PTFE ablation by SR would be photochemical decomposition. The PTFE ablation with and without C filter would be identical in the ablation mechanism.

REFERENCES

[1] M. Inayoshi, M. Ito, M. Hori, T. Goto, M. Hiramatsu, and A. Hiraya, Jpn. J. Appl. Phys., **34**, L1675 (1995).

[2] M. Inayoshi, M. Ito, M. Hori, T. Goto, and M. Hiramatsu, J. Vac. Sci. Technol., **B 17**, 949 (1999).

[3] T. Katoh and Y. Zhang, Appl. Phys. Lett., **68**, 865 (1996)

[4] T. Katoh, Journal of Japan Society for Precision Engineering, **64**, 1008 (1998)

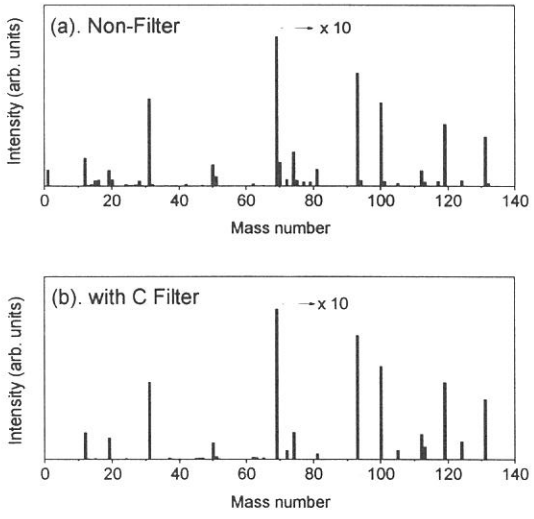

Fig. 2. QMS spectra of the fragments obtained from PTFE.
(a) fragment irradiated with white SR beam.
(b) passing SR beam through the C filter.

(BL8A)

Photoluminescence of ZnTe homoepitaxial films deposited by synchrotron-radiation-excited growth

Mitsuhiro Nishio, Kazuki Hayashida, Hiroki Harada, Toru Tanaka, Chiharu Ohata, Masahiko Tsujita, Yoshiaki Mitsuishi, Qixin Guo and Hiroshi Ogawa

Department of Electrical and Electronic Engineering, Saga University, Saga 840-8502, Japan

Synchrotron-radiation (SR) excited growth is promising as a new non-thermal technique, since virtually any reactants can be decomposed effectively at room temperature by using a high photon flux density in the vacuum ultraviolet region. Several attempts have so far been carried out using SR light to perform the deposition of semiconductors at low temperatures. In order to improve the film quality, it is important to investigate the photoluminescence (PL) spectrum of the film deposited by SR-excited growth. However, such investigations do not exist except for our previous papers, which described luminescence of ZnTe films grown using hydrogen carrier gas. In this study, we deal with PL properties of ZnTe films deposited by SR-excited growth technique using nitrogen carrier gas

The growth experiments were carried out using the SR beam line, BL8A. The beam line supplies only white light. Diethylzinc (DEZn) and diethyltelluride (DETe) were used as source materials. These source materials were independently fed into the chamber together with nitrogen carrier gas by means of mass flow controller and variable leak valve. The deposition of ZnTe was carried out at very low pressure of $10^{-5}\sim10^{-4}$ Torr in the growth chamber. In order to clarify the effect of nitrogen carrier gas upon PL spectrum of the deposited film, the growth experiments have been carried out under almost the same growth conditions as the previous ones using hydrogen carrier gas.

We have found that there is no remarkable difference in the growth rate of the deposited film between hydrogen and nitrogen carrier gases. Thus, hydrogen seems not to play an important role in the growth reaction due to a use of the low pressure. However, we have discovered that PL spectrum of ZnTe film is significantly different from that in the case of hydrogen carrier gas. Figure 1(a) shows the PL spectra of ZnTe films for various source transport rates. In order to clarify the influence of carrier gas upon PL spectrum, the results in the case of hydrogen carrier gas are also shown in fig.1 (b). Here, we select samples corresponding to a Zn rich, nearly stoichiometric and Te rich conditions based on the growth rate behavior. It should be noticeable that in the PL spectrum of the film grown under a Zn rich condition, no deep level emissions can be detected whereas the PL spectrum of the film grown using hydrogen carrier gas exhibits strong deep level emissions with two broad bands centered at around 2.1 eV and 1.85 eV. The deep level emissions may be due to the generation of defects such as vacancy-impurity complex in the film. The deep-level luminescence obtained here can be found in the experimental results by Tews et al., who have attempted laser-induced diffusion in ZnTe with Cl.

As pointed out previously, in the case of hydrogen carrier gas, a Zn rich condition may facilitate Cl inclusion into a Te lattice site. Actually, a decrease of DEZn transports rate seems to bring about significant reduction of deep level bands. In the case of nitrogen carrier gas, a sharply excitonic emission (I_a) at 2.375 eV is detected prominently in the spectrum. This peak is attributed to shallow acceptors. Thus, a use of nitrogen carrier gas may be effective for suppression of deep level emission. It is well known that nitrogen is substituted on the Te lattice site and acts as a shallow acceptor. It is possible that nitrogen is included in the film and so participates shallow acceptors related to I_a peak. SR-excited growth may be effective for a use of thermally stable nitrogen as dopant, as shown in the growth of silicon nitride using nitrogen source. Similar feature can be found in the spectrum of the film grown under nearly stoichiometric condition. The appearance of strong I_a line may be due to a decrease in the numbers of deep-level centers such as Te vacancy complex accompanied by inclusion of nitrogen. On the other hand, the PL spectrum of the film grown under a Te rich condition exhibits new deep-level emission band in addition to I_a peak, as supported by the fact that the PL spectrum in the case of hydrogen carrier gas shows only donor-acceptor pair bands together with I_a line. Thus, a use of nitrogen carrier gas under a Te rich condition may bring about an increase in the numbers of deep-level centers such as Zn vacancy complex, different from the case of hydrogen carrier gas. Finally, we emphasize that near band gap luminescence can be observed even in the films grown at room temperature under Zn rich condition together with nearly stochiometric one by using nitrogen carrier gas.

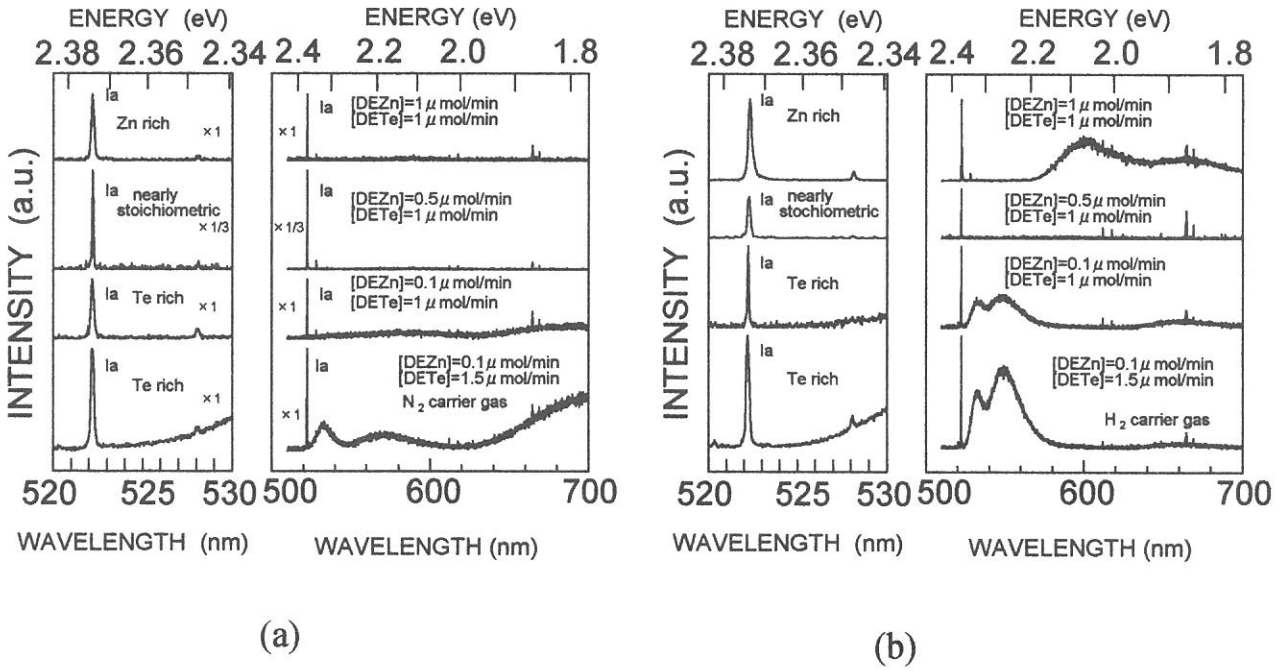

Fig. 1 PL spectra of ZnTe films for various source transport rates when substrate temperature was kept at 27℃. Fig. (a) corresponds to the case of nitrogen carrier gas, while fig. (b) the case of hydrogen carrier gas.

(BL8A)

Characterization of Polytetrafluoroethylene Thin Films Deposited by Synchrotron Radiation

M.Uchida, M.Ishizaka, H.Okada, A.Wakahara and A.Yoshida

Department of Electrical and Electronic Engineering, Toyohashi University of Technology, Tempaku, Toyohashi 441-8580

The polytetrafluoroethylene (PTFE) has been widely used in many application fields for a long time because of its unique properties such as chemical stability, thermal durability, hydrophobicity and low surface friction. Furthermore, electrical property of PTFE as the insulator is feasible for large-scale integrated circuits (LSIs) due to its low dielectric constant of ε_s=2.1 which value is smaller than that of SiO_2(ε_s=3.9). However, formation technique of the thin PTFE film having microscale pattern is not established yet. Recently, irradiation of the vacuum ultraviolet light from the SR beam is found to be useful for the micro processing of these materials in the small scale with very high rate even at room temperature.

In this report, we have investigated the deposition of PTFE by SR beam. Investigation was also made on the selective area etching of the PTFE with SR beam.

The experimental setup is shown in Fig.1. In the PTFE deposition experiment, PTFE target was put in the reaction chamber. A Si(100) substrate was placed in the position which countered with the target. The distance between target and the substrate is 3 cm. Before the deposition, the reaction chamber was evacuated below 1×10^{-6} Torr. With this setup, we investigated characteristics of the deposited films that were deposited with various beam current, target and substrate temperatures. Selective area etching of the deposited PTFE thin film was carried out by shadowing method. Here, we used the Ni mesh mask with the hole of $7.5\times7.5\ \mu$m and was closely placed on the PTFE thin film surface.

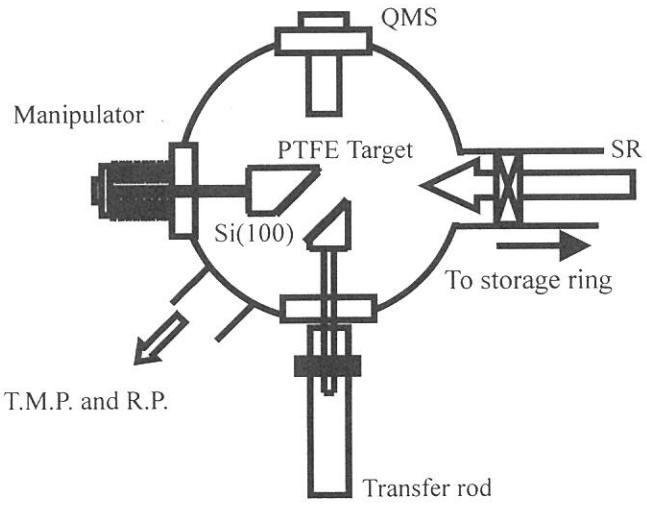

Fig.1 Experimental setup for deposition.

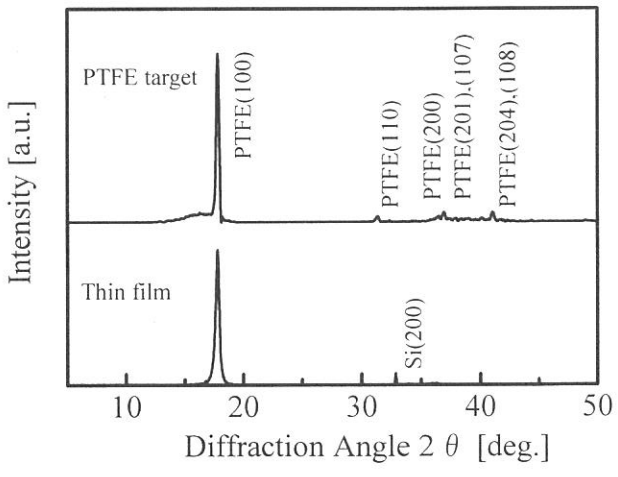

Fig.2 XRD spectra of PTFE target and PTFE thin film.

After the SR beam irradiation, we obtained PTFE deposition on Si substrate. Fig.2 shows XRD spectra of PTFE target and PTFE thin film deposited by SR beam. Both the PTFE target and the deposited thin film showed distinct peak at around 18° which was assigned to the peak from crystal portion of the PTFE. However, peak at 16° in the spectrum of the PTFE target was vanished in that of the deposited film. According to the previous report, sub-peak at around 16° indicates existence of the amorphous portion in the PTFE. Thus, better crystallinity of the PTFE thin film deposited by SR beam was demonstrated.

The surface morphology of the deposited PTFE thin film was characterized by atomic force microscope (AFM). AFM images of PTFE thin films deposited with beam current of 150 mA and 220 mA are shown in Figs.3(a) and 3(b), respectively, in range of 10 × 10 μm. In the case of the beam current of 150 mA shown in Fig.3(a), cracks are observed on the whole PTFE film surface. Depth of this cracks is in the range of 10 to 20 nm. On the other hand, as shown in Fig.3(b), such a crack is not observed on the PTFE film surface deposited with the beam current of 220 mA. These results indicate that smooth surface can be deposited with relatively large beam current. However, mechanism of the crack is not cleared yet. Further investigation is needed here.

Figure 4 shows a scanning electron microscope (SEM) image of selective area etched PTFE films by mesh shadowing method. Mesh patterned PTFE having sharp edge was obtained. Thus, selective area etching with SR beam exposure was succeeded.

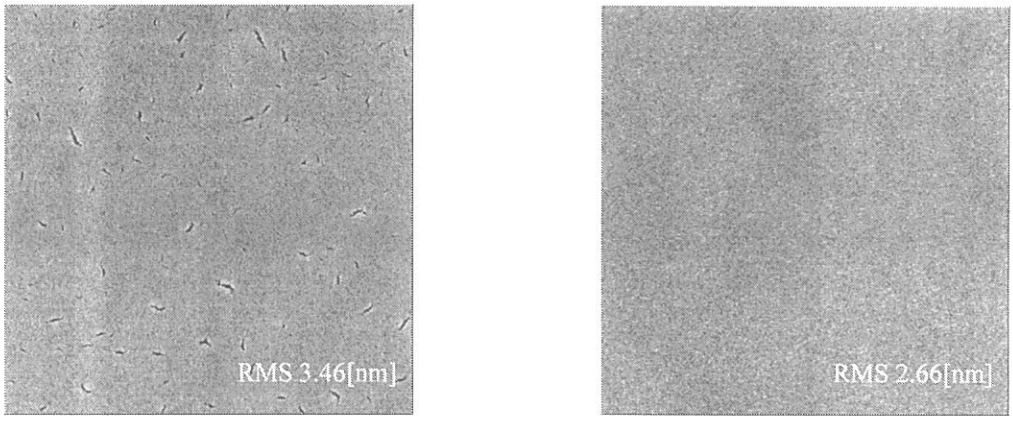

(a) Beam current 150[mA]　　(b)Beam current 220[mA]

Fig.3 AFM images of PTFE thin film(10×10 μm).
(RMS was calculated in the portion without a crack.)

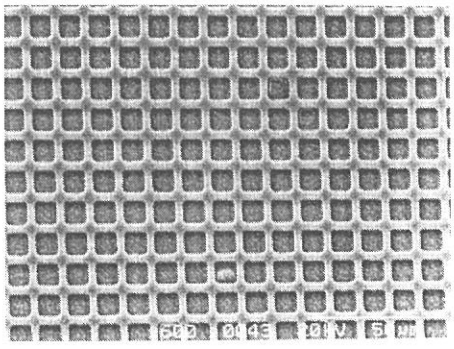

50 μm

Fig.4 SEM image of selectively etched of PTFE thin film

List of Publications

LIST OF PUBLICATIONS (2000)

I. Arakawa, T. Adachi, T. Hirayama and M. Sakurai
Absolute Measurement of Total Photo Desorption Yield of Soled Neon in Vacuum Ultraviolet Range
Surf. Sci. **451,** 136 (2000).

I. Arakawa
Exciton Induced Desorption at the Surface of Rare Gas Solids
Mol. Cryst. Liq. Cryst. **314,** 47 (1998).

H. Aritani, H. Yamada, T. Nishio, T. Shiono, S. Imamura, M. Kudo, S. Hasegawa, T. Tanaka and S. Yoshida
Characterization of Li-Doped MgO Catalysts for Oxidative Coupling of Methane by Means of Mg K-edge XANES
J. Phys. Chem. B **104**, 10133 (2000).

Y. Azuma, T. Hasebe, T. Miyamae, K. K. Okudaira, Y. Harada, K. Seki, E. Morikawa, V. Saile and N. Ueno
Angle-resolved UV Photoelectron Spectra (UPS) of Thin Films of Perylene-3,4,9,10-Tetracarboxylic Dianhydride on MoS_2
J. Synchrotron Rad. **5**, 1044 (1998).

Y. Azuma, S. Akatsuka, K. K. Okudaira, Y. Harada and N. Ueno
Angle-resolved Ultraviolet Photoelectron Spectroscopy of In-[Perylene-3,4,9,10-Tetracarboxylic Dianhydride] System
J. Appl. Phys. **87**, 76 (2000).

A. Ejiri and K. Arakaki
Vacuum UV Photoelectric Yield and Photoluminescence in CsCl and CsBr
Solid State Commun. **110**, 575 (1999).

M. Fujita, M. Itoh, Y. Bokumoto, H. Nakagawa, D. L. Alov and M. Kitaura
Optical Spectra and Electronic Structures of Lead Halides
Phys. Rev. B **61**, 15731 (2000).

Y. Gao, H. Mekaru, T. Miyamae and T. Urisu
Scanning Tunneling Microscopy Study of Surface Morphology of Si(111) after Synchrotron Radiation Stimulated Desorption of SiO_2
J. Vac. Sci. Technol. A **18**, 1153 (2000).

Y. Gao, H. Mekaru, T. Miyamae and T. Urisu
Scanning Tunneling Microscopy Study of Si(111) Surface Morphology after Removal of SiO_2 by Synchrotron Radiation Illumination
Appl. Phys. Lett. **76**, 1392 (2000).

K. Hamaguchi, S. Machida, K. Mukai, Y. Yamashita and J. Yoshinobu
Adsorption State of 1,4-cyclohexadiene on Si (100)(2×1)
Phys. Rev. B **62**, 7576 (2000).

Y. Haruyama, T. Kinoshita, K. Takimiya, T. Otsubo, C. Nakano and K. Yakushi
Electronic Structures of Organic Salts DMTSA-BF_4 Using Photoelectron Spectromicroscopy
J. Electron Spectrosc. Relat. Phenom. **114-116**, 1013 (2001).

A. Hayama, T. Kuninobu, T. Hirayama and I. Arakawa
Desorption of Metastable Particles Induced by Electronic Excitation at the Surface of Rare-gas Solid with Physisorbed Hydrogen
J. Vac. Sci. Technol. A **16**, 979 (1998).

M. Hayashi, M. Nakayama, T. Nanba, T. Matsumoto, J. Tang and S. Nagata
Optical Response of $CuIr_2X_4$ (X=S,Se) due to Metal-insulator Transition
Physica B **281&282**, 631 (2000).

Y. Homma, P. Finnie, T. Ogino, H. Noda and T. Urisu
Aligned Island Formation Using Step-band Networks on Si(111)
J. Appl. Phys. **86**, 3083 (1999).

M. Hosaka, S. Koda, J. Yamazaki and H. Hama
Temporal Stability of the UVSOR-FEL Micropulse
Nucl. Instrum. Meth. A **445**, 208 (2000).

T. Ibuki, K. Okada, K. Saito and T. Gejo
Molecular Size Effect on the Site-specific Fragmentation of N and O K Shell Excited CH_3OCOCN and CH_3OCOCH_2CN Molecules
J. Electron Spectrosc. Relat. Phenom. **107**, 39 (2000).

T. Ibuki, K. Okada, T. Gejo and K. Saito
Angle-resolved Photofragmentation of the N K-shell Excited CF_3CN Molecule
Chem. Phys. Lett. **328**, 147 (2000).

M. Itoh, D. L. Alov and M. Fujita
Exciton Luminescence of Scheelite- and Raspite-structured $PbWO_4$ Crystals
J. Lumin. **87-89**, 1243 (2000).

M. Itoh and M. Fujita
Optical Properties of Scheelite and Raspite PbWO4 Crystals
Phys. Rev. B **62**, 12825 (2000).

M. Kamada, J. Murakami, S. Tanaka, S. D. More, M. Itoh and Y. Fujii
Photo-induced Change of the Semiconductor-vacuum Interface of p-GaAs(100) Studied by Photoelectron Spectroscopy
Surf. Sci. **454-456**, 525 (2000).

M. Kamada, J. Murakami and N. Ohno
Excitation Spectra of a Long-persistent Phosphor $SrAl_2O_4$:Eu, Dy in Vacuum Ultraviolet Region
J. Lumin. **87-89**, 1042 (2000).

K. Kanda, M. Kono, T. Nagata, A. Hiraya, K. Tabayashi and K. Shobakake
Photodissociation Spectroscopy of ClCN in the Vacuum Ultraviolet Region
Chem. Phys. **255**, 369 (2000).

S. Kimura, H. Kitazawa, G. Kida and T. Suzuki
Electronic Structure in the Magnetically Ordered States of CeSb studied by Infrared Magneto-Optical Spectroscopy
J. Phys. Soc. Jpn. **69**, 647 (2000).

S. Kimura, F. Arai and M. Ikezawa
Optical Study on Electronic Structure of Rare-Earth Sesquioxides
J. Phys. Soc. Jpn. **69**, 3451 (2000).

S. Kimura, H. Kitazawa, G. Kido and T. Suzuki
Optical and Magneto-optical Studies on Magnetic-phase Transition of CeSb and CeBi
Physica B **281&282**, 449 (2000).

M. Kitaura, A. Ohnishi
Thermal Stability of Trapped Holes in $PbCl_2$ Crystals
J. Phys. Sco. Jpn. **69**, 2360 (2000).

Y. Kobayashi, K. Sumitomo, K. Shiraishi, T. Urisu and T. Ogino
Control of Surface Composition on Ge/Si(001) by Atomic Hydrogen Irradiation
Surf. Sci. **436**, 9 (1999).

K. Mase, S. Tanaka, S. Nagaoka and T. Urisu
Ion Desorption Induced by Core-Electron Transitions Studied with Electron-Ion Coincidence Spectroscopy
Surf. Sci. **451**, 143 (2000).

T. Masuoka
Anisotropic Angular Distribution of Ionic Fragments in the Dissociation of CO_2^{2+}
J. Electron Spectrosc. Relat. Phenom. **101-103**, 53 (1999).

T. Masuoka and A. Kobayashi
Dissociative Photoionization of CF_4 from 23 to 120 eV
J. Chem. Phys. **113**, 1559 (2000).

T. Masuoka and A. Kobayashi
Angular Distribution of Ionic Fragments in the Dissociation of SO_2^{2+}
J. Chem. Phys. **113**, 6634 (2000).

K. Mitsuke, H. Hattori and Y. Hikosaka
Superexcitation and Subsequent Decay of Triatomic Molecules Studied by Two-dimensional Photoelectron Spectroscopy
J. Electron Spectrosc. Relat. Phenom. **112**, 137 (2000).

K. Mitsuke
SR-Pump and Laser-Probe Experiments for the Photofragmentation Dynamics of Atoms and Molecules
The Physics of Electronic and Atomic Collisions, 172 (2000).

K. Mitsuke, Y. Hikosaka and K. Iwasaki
Laser Photoionization of Polarized Ar Atoms Produced by Excitation with Synchrotron Radiation
J. Phys. B: At. Mol. Opt. Phys. **33**, 391 (2000).

K. Mitsuke and H. Nakamura
Photo-Dynamics and Reaction Dynamics of Molecules
Comments on Modern Physics **2**, D75 (2000).

S. More, S. Tanaka, S. Tanaka, Y. Fujii and M. Kamada
Coadsorption of Cs and O on GaAs: Formation of Negative Electron Affinity Surfaces at Different Temperatures
Surf. Sci. **454-456**, 161 (2000).

E. Morikawa, V. Saile, K. K. Okudaira, Y. Azuma, K. Meguro, Y. Harada, K. Seki, S. Hasegawa and N. Ueno
Pendant Group orientation of Poly (2-vinylnaphthalene) Thin Film Surface Studied by Near-edge X-ray Absorption Fine Structure Spectroscopy (NEXAFS) and Angle-resolved Ultraviolet Photoelectron Spectroscopy (ARUPS)
J. Chem. Phys. **112**, 10476 (2000).

S. Nagaoka, S. Tanaka and K. Mase
Site-Specific Fragmentation Following C:1s Core-Level Photoionization of 111-Trifluorethane Condensed on a Au Surface and of a 222-Trifluoroethanol Monolayer Chemisorbed on a Si(100) Surface
J. Phys. Chem. B **105**, 1554 (2001).

M. Niibe, T. Watanabe, H. Nii, T. Tanaka and H. Kinoshita
Contrast Measurement of Reflection Masks Fabricated from Cr and Ta Absorbers for Extreme Ultraviolet Lithography
Jpn. J. Appl. Phys. **30**, 6815 (2000).

H. Niikura, M. Mizutani and K. Mitsuke
Rotational State Distribution of N_2^+ produced from N_2 or N_2O Observed by a Laser-Synchrotron Radiation Combination Technique
Chem. Phys. Lett. **317**, 45 (2000).

M. Nishio, K. Hayashida, H. Harada, Y. Mitsuishi, Q. Guo and H. Ogawa
Recent Studies on ZnTe Homoepitaxial Films Deposited by Synchrotron-radiation-excited Growth
Proc. SPIE. **4086**, 158 (2000).

M. Nishio, Q. Guo and H. Ogawa
Low Temperature Epitaxial Growth of II-VI Compound Semiconductors Using Synchrotron Radiation as a Light Source
Crystal Growth Research **5**, 1 (1999).

H. Noda and T. Urisu
Assignments of Bending and Stretching Vibrational Spectra and Mechanisms of Thermal Decomposition of SiH_2 on Si(100) Surfaces
Chem. Phys. Lett. **326**, 163 (2000).

H. Noda, T. Urisu, Y. Kobayashi and T. Ogino
Initial Stage of Hydrogen Etching of Si Surfaces Investigated by Infrared Reflection Absorption Spectroscopy
Jpn. J. Appl. Phys. **39**, 6985 (2000).

T. Noma, K. S. Seol, M. Fujimaki, H. Kato, T. Watanabe and Y. Ohki
Photoluminescence Analysis of Plasma-deposited Oxygen-rich Silicon Oxynitride Films
Jpn. J. Appl. Phys. **39**, 6587 (2000).

Y. Nonogaki, H. Hatate, R. Oga, S. Yamamoto, Y. Fujiwara, Y. Takeda, H. Noda and T. Urisu
SR-stimulated Etching and OMVPE Growth for Semiconductor Nanostructure Fabrication
Mat. Sci. Eng. B **74**, 7 (2000).

Y. Ohki, T. Toyoda Y. Hama, W. Wei and F. Massines
Photoluminescence in Polypropylene Induced by Ultraviolet Laser Irradiation
Proceedings of The 6th International Conference on Properties and Applications of Dielectric Materials **1**, 439 (2000).

H. Okamura, J. Kawahara, T. Nanba, S. Kimura, K. Soda, U. Mizutani, Y. Nishino, M. Kato, I. Shimoyama, H. Miura, K. Fukui, K. Nakagawa, H. Nakagawa and T. Kinoshita
Pseudogap Formation in the Intermetallic Compounds $(Fe_{1-x}V_x)_3Al$
Phys. Rev. Lett. **84**, 3674 (2000).

N. Ohno, Y. Yamasaki, H. Yoshida and M. Fujita
Optical Spectra of Orthorhombic $SnBr_2$ *Crystals*
Phys. Status Solidi B **223**, 723 (2001).

K. K. Okudaira, S. Hasegawa, H. Ishii, K. Seki, Y. Harada and N. Ueno
Structure of Copper-and H_2*-phthalocyanine Thin Films on* MoS_2 *Studied by Angle-resolved Ultraviolet Photoelectron Spectroscopy and Low Energy Electron Diffraction*
J. Appl. Phys. **85**, 6453 (1999).

K. K. Okudaira, E. Morikawa, D. A. Hite, S. Hasegawa, H. Ishii, M. Imamura, H. Shimada, Y. Azuma, K. Meguro, Y. Harada, V. Saile, K. Seki and N. Ueno
Surface Molecular Orientation of Poly(2-vinylnaphalene) Thin Films: ARUPS and NEXAFS Studies
J. Electron Spectrosc. Relat. Phenom. **101-103**, 389 (1999).

K. Ozawa, T. Noda, T. Nakane, M. Yamazaki, K. Edamoto, S. Tanaka and S. Otani
Potassium Adsorption on the Polar ZrC(111) Surface: Photoemission Spectroscopy Study
Surf. Sci. **446**, 229 (2000).

K. Ozawa, T. Yoshii, T. Noda, K. Edamoto, S. Tanaka and S. Otani
Cs Adsorption on ZrC(111): Photoemission Spectroscopy Study
Jpn. J. Appl. Phys. **39**, 4325 (2000).

K. S. Seol, T. Watanabe, M. Fujimaki, H. Kato, Y. Ohki and M. Takiyama
Time-resolved Photoluminescence Study of Hydrogenated Amorphous Silicon Nitride
Phys. Rev. B **62**, 1532 (2000).

K. Shimizu, H. Maeshima, H. Yoshida, A. Satsuma, and T. Hattori
Crystal Field Effect on the Chemical Shift in Cu L-III XANES Spectra of Copper(II) Compounds
Chem. Lett. (2000) 210.

K. Shimizu, H. Maeshima, H. Yoshida, A. Satsuma and T. Hattori
Spectroscopic Characterization of Cu-Al_2O_3 Catalyst for Selective Catalytic Reduction of NO with Propene
Phys. Chem. Chem. Phys. **2**, 2435 (2000).

S. Tanaka, K. Mase, M. Nagasono, S. Nagaoka and M. Kamada
Electron-ion Coincidence Study for the TiO_2(110) Surface
Surf. Sci. **451**, 182 (2000).

S. Tanaka, K. Mase, M. Nagasono, S. Nagaoka, M. Kamada, E. Ikenaga, T. Sekitani and K. Tanaka
Electron-Ion Coincidence Spectroscopy as a New Tool for Surface Analysis -An Application to the Ice Surface
Jpn. J. Appl. Phys. **39**, 4489 (2000).

T. Tsujibayashi, M. Watanabe, O. Arimoto, M. Itoh, S. Nakanishi, H. Itoh, S. Asaka, and M. Kamada
Two-photon Excitation Spectra of Exciton Luminescence in CaF_2 Obtained by Using Synchrotron Radiation and Laser
J. Lumin. **87-89**, 254 (2000).

Y. Uchimoto and T. Yao
Electronic Structure in $LiMn_2O_4$ Based Spinel Oxides from Transition Metal L-edge and O K-edge XANES
Abstract of 10th International Meeting on Lithium Batteries, 242 (2000).

S. Wako, M. Sano, Y. Ohno, T. Matsushima, S. Tanaka and M. Kamada
Orientation of Oxygen Ad-molecules on Stepped Platinum (112)
Surf. Sci. **461**, L537 (2000).

K. Yamaguchi, K. Ebitani, T. Yoshida, H. Yoshida and K. Kaneda
Mg-Al Mixed Oxides as Highly Active Acid-Base Catalysts for Cycloaddition of Carbon Dioxide to Epoxides
J. Am. Chem. Soc. **121**, 4526 (1999).

Y. Yamashita, K. Hamaguchi, S. Machida, K. Mukai, J. Yoshinobu, S. Tanaka and M. Kamada
Adsorbed States of Cyclopentene, Cyclohexene and 1,4-cyclohexadiene on Si(100)(2×1): Towards the Fabrication of Novel Organic Films/Si Hybrid Structures
Appl. Surf. Sci. **169-170**, 172 (2001).

T. Yoshida, H. Yoshida, T. Hara, M. Sakai, A. Omori and T. Tanabe
XAFS Study on D^+ Irradiated Si Surface
J. Synchrotron Rad. **6**, 734 (1999).

T. Yoshida, T. Tanabe, H. Yoshida, Y. Yazawa, T. Hara, M. Sakai, H. Yamamoto and Y. Baba
XANES and XPS analyses of Silicon Irradiated by Deuterium Ions
Jpn. J. Appl. Phys. **38**, 305 (1999).

T. Yoshida, T. Tanabe, T. Ii, T. Hara, M. Sakai and Y. Inaki
In-Reactor Luminescence from Silica Glasses
Nucl. Instrum. Meth. B **166-167**, 476 (2000).

T. Yoshida, H. Yoshida, T. Hara, T. Ii, T. Okada, T Tanabe
XAFS Study on Silica Glasses Irradiated in a Nuclear Reactor
Nucl. Instrum. Meth. B **166-167**, 48 (2000).

T. Kinoshita and Y. Haruyama
Photoelectron Spectromicroscopy
J. Jpn. Soc. Synchro. Rad. Res. **13**, 10 (2000).

(Japanese)
H. Aritani, H. Yamada, T. Nishio, S. Imamura, S. Hasegawa, T. Tanaka, T. Funabiki and S. Yoshida
Distribution of Defect Species in Li-doped MgO and Catalytic Activity of the Species for Methane Oxidation
Shokubai **41**, 429 (1999).

R. Kano, K. Kumagai, S. Tsuneta, H. Hara, K. Shinoda, T. Sakao, S. Nagata and K. Kabayashi
Evaluation and Selection of Back-Illuminated CCDs for solar-B X-Ray Telescope
Report of the National Astronomical Observatory of Japan **5**, 19 (2000).

S. Kimura
Utilization of Circularly Polarized Synchrotron Radiation in Infrared Region -Infrared Magnetic Circular Dichroism-
J. Jpn. Soc. Synchro. Rad. Res. **13**, 62 (2000).

K. Mase
Study of Ion Desorption Induced by Core-Electron Transitions -Auger-Final-State-Selected Study Using Auger Electron Photoion Coincidence Spectroscopy –
Chemistry and Chemical Industry **53**, 111 (2000).

K. Nakagawa
Study of Origin of Life using Synchrotron Radiation
J. Jpn. Soc. Synchro. Rad. Res. **13**, 57 (2000).

Y. Uchimoto
(TIC, Kyoto, 2000)

Workshops

UVSOR Workshop VII

Current Status and Applications of Insertion Devices in VUV·SX Region

27 and 28 November, 2000

27 Nov. (Mon) 13:00 – 18:00
Insertion Devices

13:00 - 13:15 Introduction — N. Kosugi (IMS)

13:15 - 13:35 Fundamentals of insertion devices(1)
-- Principles of undulators and properties of undulator radiation
K. Tsuchiya (KEK-PF)

13:35 - 13:55 Fundamentals of insertion devices (2)
-- Modern techniques for undulators — R. Tanaka (SPring-8)

13:55 - 14:15 Fundamentals of insertion devices (3)
-- Novel ideas on undulators — T. Hara (SPring-8)

14:15 - 14:30 Fundamentals of insertion devices (4)
-- Effects of undulators on electron beams — M. Katoh (IMS)

14:30 - 15:00 Present status of VUV-SX undulators at KEK-PF
K. Tsuchiya (KEK-PF)

15:00 - 15:30 Present status of VUV-SX undulators at SPring-8
R. Tanaka(SPring-8)

15:30 - 16:30 coffee break

16:00 - 16:15 Status of insertion devices and free electron laser in UVSOR
M. Hosaka (IMS)

16:15 - 16:30 Status of HiSOR undulators — K. Goto (HiSOR, Hiroshima Univ.)

16:30 - 16:45 An overview of the insertion devices development at NewSUBARU — S. Hashimoto (LASTI, Himeji Inst. of Tech.)

16:45 - 17:00 Present status of the insertion devices and free electron lasers at ETL — N. Sei (ETL)

17:00 - 17:15 An upgrade plan for UVSOR — M. Katoh (IMS)

17:15 - 17:30 Improvement of the straight sections at the PF ring — Y. Kobayashi (KEK-PF)

17:30 - 17:45 Insertion devices for the VSX light source — N. Nakamura (ISSP, Univ. of Tokyo)

17:45 - 18:00 Insertion devices at Tohoku university Synchrotron Radiation Facility (TSRF) — S. Sato (Tohoku Univ.)

28 Nov. (Tue) 9:00 – 12:20
Present Status of Undulator Beamlines and Their Applications

9:00 - 9:30 Gas phase experiments using a figure-8 undulator at SPring-8 — H. Yosida (Hiroshima Univ.)

9:30 - 10:00 Performance of a soft x-ray helical undulator beamline BL25SU at SPring-8 — Y. Saitoh (SPring-8/JAERI)

10:00 - 10:30 Insertion device beamlines at Photon Factory — T. Koide (KEK-PF)

10:30 - 10:50 coffee break

10:50 - 11:20 Performance of insertion device beamline of ISSP and experience in monochromator calibration — M. Fujisawa (ISSP, Univ. of Tokyo)

11:20 - 11:40 Commissioning and present status of undulator beamlines at HiSOR — K. Shimada (HiSOR, Hiroshima Univ.)

11:40 - 12:00 Characteristics of insertion device beamlines of UVSOR and their evaluation — M. Kamada (IMS)

12:00 - 12:20 Techniques for mirror cooling and beam monitoring — M. Hasumoto (IMS)

28 Nov. (Tue) 13:30 – 17:10
Experiments using Undulator Beamlines and Future Projects

13:30 - 14:00 Scientific targets of SX long undulator at SPring-8
T. Miyahara (Tokyo Metropolitan Univ.)

14:00 - 14:30 An aim of 11m undulator in NewSUBARU
M. Niibe (LASTI, Himeji Inst. of Tech.)

14:30 - 15:00 Study projects of 27m long undulator at the VSX light source
T. Kinoshita (ISSP, Univ. of Tokyo)

15:00 - 15:30 coffee break

15:30 - 15:50 Laser induced fluorescence spectroscopy of fragments produced by VUV photoexcitation of gaseous molecules
K. Mitsuke (IMS)

15:50 - 16:10 Undulator is a dream light source for the research of SR stimulated processes T. Urisu (IMS)

16:10 - 16:30 Research on binary metal adsorbates system on the Si(111) surface by use of insertion device beamline
K. Soda (Nagoya Univ.)

16:30 - 16:50 Light amplification within a nanometer-sized layer under undulator radiation M. Itoh (Shinshu Univ.)

16:50 - 17:10 Present status of soft X-ray photochemistry beamline BL27SU
H. Ohashi (JASRI)

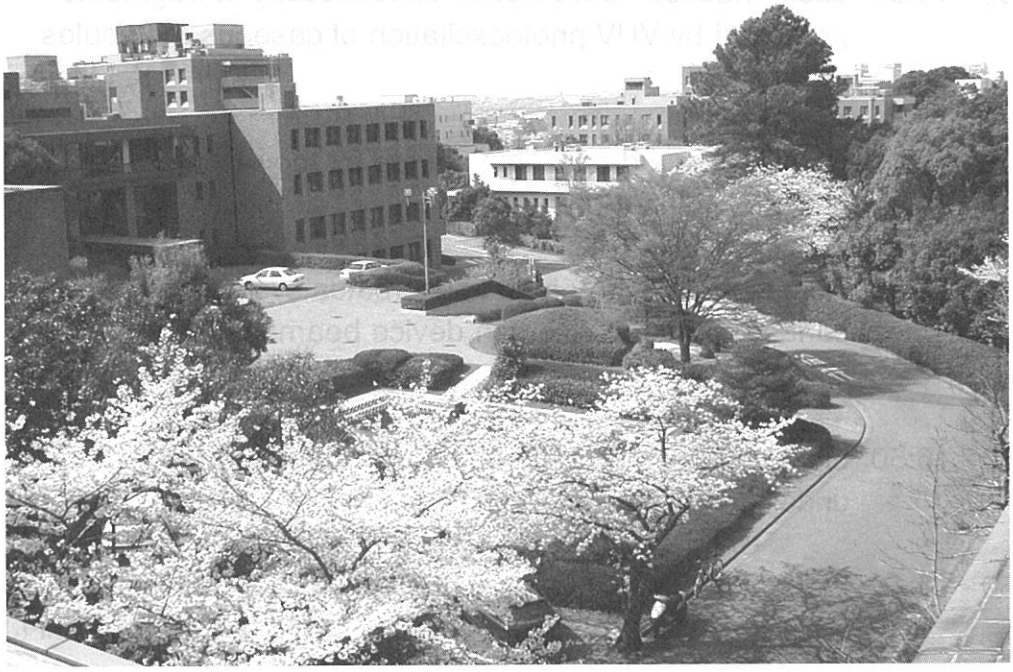

Appendix

ORGANIZATION

Director

Nobuhiro Kosugi	Professor	kosugi@ims.ac.jp

Accelerator Division

Masahiro Katoh	Associate Professor	mkatoh@ims.ac.jp
Masahito Hosaka	Research Associate	hosaka@ims.ac.jp
Shigeru Kouda	Research Associate	kouda@ims.ac.jp
Toshio Kinoshita	Unit Chief Engineer	kinoshita@ims.ac.jp
Jun-ichiro Yamazaki	Unit Chief Engineer	yamazaki @ ims.ac jp
Kenji Hayashi	Engineer	h-kenji@ims.ac.jp

Beamline Division

Masao Kamada	Associate Professor	kamada@ims.ac.jp
Eiji Shigemasa	Associate Professor	sigemasa@ims.ac.jp
Tatsuo Gejo	Research Associate	gejo@ims.ac.jp
Kazutoshi Takahashi	Research Associate	ktakahashi@ims.ac.jp
Osamu Matsudo	Section Chief Engineer	mastudo@ims.ac.jp
Masami Hasumoto	Unit Chief Engineer	hasumoto@ims.ac.jp
Eiken Nakamura	Engineer	eiken@ims.ac.jp
Tadanori Kondo	Engineer	kondo@ims.ac.jp
Suekichi Matsuo	Supporting Engineer	mastuo@ims.ac.jp
Bunichi Kamimoto	Supporting Engineer	kamimoto@ims.ac.jp

Guest Scientist

Shin-ichi Kimura	Associate Professor	skimura@kobe-u.ac.jp
Sam Dylan Moré	JSPS Research Fellow	more@ims.ac.jp (-Oct. 2000)
Junpei Azuma	JSPS Research Fellow	azuma@ims.ac.jp (Apr. 2001-)

Secretary

Hisayo Hagiwara		hagiwara@ims.ac.jp
Naoko Onitake		onitake@ims.ac.jp

Graduate Student

Senku Tanaka		senku@ims.ac.jp

STEERING COMMITTEE

(April 2000 - March 2001)

Nobuhiro Kosugi	UVSOR IMS	Chairperson
Masao Kamada	UVSOR IMS	
Masahiro Katoh	UVSOR IMS	
Eiji Shigemasa	UVSOR IMS	
Shin-ichi Kimura	UVSOR IMS	
Tatsuhisa Katoh	IMS	
Tatsuya Tsukuda	IMS	
Hayao Kobayashi	IMS	
Tsuneo Urisu	IMS	
Toyohiko Kinoshita	Univ. of Tokyo	
Akira Yagishita	KEK	
Nobuo Ueno	Chiba Univ.	
Yasuo Udagawa	Tohoku Univ.	
Keiichiro Nasu	KEK	
Takao Nanba	Kobe Univ.	
Ken-ichiro Tanaka	Hiroshima Univ.	

JOINT STUDIES

(Financial Year 2000)

Cooperative Research Projects	: 27
Use-of-UVSOR Projects	: 160
Workshop	: 1
Machine Time for Users	: 37 weeks

UVSOR staffs

Location

Ultraviolet Synchrotron Orbital Radiation (UVSOR) is located at Okazaki. Okazaki (population 320,000) is 260 km southwest of Tokyo, and can be reached within 3 hours from Tokyo via the Tokaido Shinkansen and the Meitetsu line.

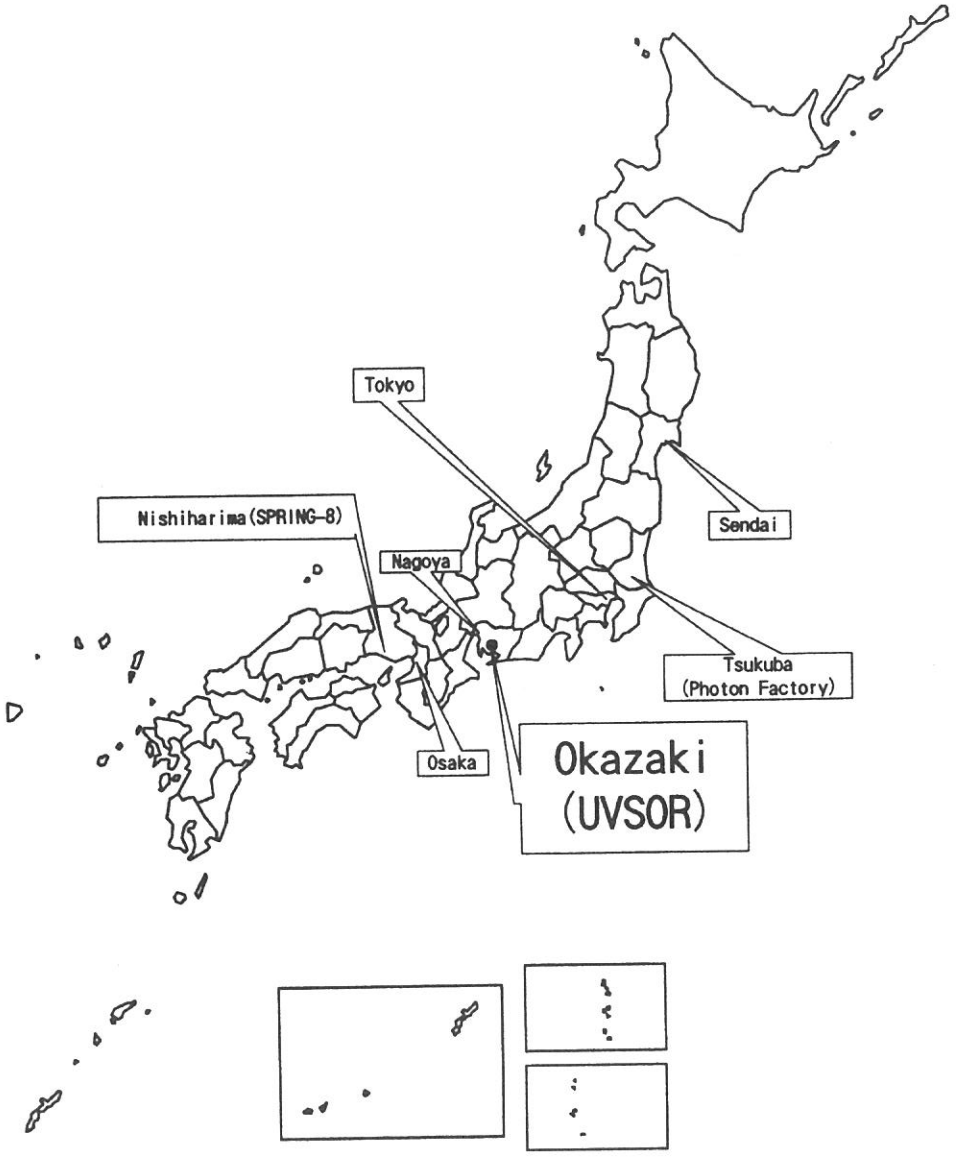

Address

UVSOR Facility
Institute for Molecular Science
Myodaiji, Okazaki 444-8585, JAPAN

PHONE : +81-564-55-7402 (Secretary)
+81-564-52-6101
FAX : +81-564-54-7079
Telex : 4537475 KOKKEN J (IMS)
Homepage : http://www.uvsor.ims.ac.jp/